Department of Geological Sciences
University of Cape Town

LANDSCAPE EVOLUTION AND EQUILIBRIUM IN SOUTHERN AFRICA:

INSIGHTS FROM COSMOGENIC NOBLE GASES IN KAROO DOLERITES AND GEOSPATIAL ANALYSES

BY

JOHN E. DECKER
B.SC., B.SC.(HONS), M.SC.

THESIS SUBMITTED IN AUGUST 2010 IN FULFILLMENT OF THE REQUIREMENTS FOR THE DEGREE OF DOCTOR OF PHILOSOPHY IN GEOLOGY

Supervisors:

Prof. Maarten J. de Wit
Africa Earth Observatory Network (AEON) and
Department of Geological Sciences, University of Cape Town

Dr Samuel Niedermann
Deutsches GeoForschungsZentrum, Potsdam

Nothing can last, I do believe, for long
In the same image. The ages of the world
From Golden passed to Iron. How many times
The fortunes of a place have been reversed!
I've seen myself how solid stable ground
Became the open sea; I've seen the ocean
Turn to dry land; and sea shells often lie
Far from the shore; and on a mountain top
Is found a rusty anchor centuries old.
A plain is made a valley by the force
Of falling waters; floods have washed away
Mountains to make a plain; a marsh dries out
In parching dunes; a thirsty wilderness
Lies flooded and becomes a swampy fen.

- Ovid (43 B.C. - 17 A.D.)
The Doctrines of Pythagorus
Book XV, Metamorphoses

Translated by A.D. Melville (1986),
Oxford University Press, 486 p.

DECLARATION

I declare that this thesis is my own work, and has not been submitted for examination previously. All external contributions are duly cited, referenced and acknowledged.

Signed:

J.E. Decker

August 2010

ABSTRACT

Southern Africa's landscape is characterised by a high plateau (elevation > 1,000 m) bound by escarpments and extensional continental margins, and the region has been influential in the development of geomorphological theory. However, the evolution of this landscape in response to tectonic and climatic forcing remains poorly understood, and is investigated here though an analysis of the topography and surface exposure history of early Jurassic (~183 Ma) Karoo dolerites.

Quantitative GIS-based analyses indicate that Karoo dolerite elevation and relief is generally higher than that of neighbouring lithologies, but depends upon intrusion geometry and neighbouring rock type. At a small catchment scale (~100-2,400 km^2), mean relief values for various lithologies are shown to be independent of each other, although general differences in local elevation and relief of different lithologies are observed, suggesting equilibrium between lithology and form.

Abundances of cosmogenic noble gas nuclides (^{3}He, ^{21}Ne and ^{38}Ar) in pyroxenes are used here to constrain surface exposure histories for 22 Karoo dolerite surface samples from southern Africa's southern escarpment, central plateau and eastern regions. Minimum exposure ages range from ~20 ka to ~500-700 ka and corresponding maximum erosion rates range from ~0.6 m/Myr to ~20 m/Myr, with most values < ~4 m/Myr. This data indicates a decline in denudation rates over time, as recent surface process rates are too low to account for the form of topographic features. Low maximum erosion rates are interpreted as weathering rates, but do not correlate with lithological and present-day climatic variables. However, dolerite weathering rates are similar to theoretical basalt weathering fluxes modelled as a function of present-day temperature and run-off. Regional discrepancies between measured and model values may be interpreted as an indication of a variable late Quaternary palaeoclimate. Dolerite weathering rates are similar to stratigraphically determined Holocene denudation rates, suggesting that denudation has been weathering-limited over this time period. Finally, if Karoo dolerite maximum erosion rates are interpreted as soil production rates, it is estimated that modern rates of soil erosion in southern Africa are up to two orders of magnitude higher than rates of soil production, implying that modern land-use practices are unsustainable.

ACKNOWLEDGEMENTS

I should like to express my sincere gratitude to my supervisors, Prof. Maarten de Wit (University of Cape Town) and Dr Samuel Niedermann (Deutsches GeoForschungsZentrum), for all the guidance and support received from them for the duration of this research. Prof. de Wit's demand for excellence and enthusiasm for frontier science has been a source of inspiration and encouragement for most of my geological career. Together with Prof. Brian Horsfield (GFZ), Prof. de Wit is also thanked for establishing the highly successful German-South African bilateral research initiative *Inkaba yeAfrika*, within which this research was framed and funded, and without which it would surely never have taken place. Dr Niedermann kindly hosted me for a year at the GFZ noble gas laboratory. He is thanked in particular for his patient instruction, formidable expertise and meticulous analytical support, and for always being only an email away for even the slightest technical query.

Prof. Judith Masters (University of Fort Hare) is thanked for securing initial funding for this thesis, for teaching me much about Madagascar and lemurs, and for inadvertently guiding me towards sampling sites. Dr Fenton "Woody" Cotterill (UCT) is thanked for field assistance, and for posing for scale in sometimes inclement weather conditions. Numerous landowners are thanked for access to their properties during fieldwork. The UCT Department of Geological Sciences provided me with access to their cutting and crushing laboratory, and Mr Ernest Stout is thanked for instruction in the use thereof. The Department is also thanked for the production of thin sections (Mr David Wilson), and access to photomicrography and XRD facilities (Prof. David Reid and Ms Ronel August, respectively). Numerous colleagues at UCT are thanked for their advice, including Mr Eugene Grosch (petrography and mineral chemistry), and Dr Frank Eckardt, Mr Christian Mielke and Mr Tyrel Flügel (GIS). Mr Mielke also kindly permitted use of his digitised erosion surface map, and Mr Flügel is thanked for access to his unpublished GPS readings and for proof-reading. Dr Luc Chevallier (Council for Geoscience) is thanked for generously donating digitised 1:250,000 scale geological maps, and Prof. Stephanie de Villiers (UFH) is thanked for discussion on the use of river chemistry to determine weathering rates.

I should like to thank Prof. Jörg Erzinger (Inorganic and Isotope Geochemistry Head) for his help and hospitality during my research visit to the GFZ. Numerous

colleagues at the GFZ are thanked for their assistance. I am particularly grateful to Mr Enzio Schnabel for his friendly guidance and assistance in the noble gas laboratory. Dr Cassandra Fenton and Dr Nicole Stroncik are thanked for advice on cosmogenic nuclides, noble gases and sample preparation. Dr Johannes Glodny and Ms Juliane Herwig are also thanked for sample preparation advice, and for permission to use the mineral separation laboratory. Dr Robert Trumbell is thanked for access to his petrography laboratory. I am grateful to Ms Sabine Tonn for conducting ICP-AES analyses on my behalf, and to Mr Rudolf Naumann for XRD analyses. Additional rock crushing was performed by members of the GFZ technical staff. Dr Jacek Stankiewicz and Mrs Samantha Stankiewicz are thanked for the initial accommodation, advice and athletic training regime which they offered in Berlin. The Potsdam Internationales Begegnungszentrum der Wissenschaften and Ms Carolin Switala are thanked for accommodation. Fellow researchers in residence, in particular Drs Lachlan and Rachel Campbell, are thanked for their friendliness and for putting up with the bagpipes.

I offer my thanks to the many colleagues whose discussions I have benefited from at conferences and workshops, and at UCT and GFZ. I am also very grateful for all the support and encouragement that I have received from my family and friends over the years. Thanks are especially due to my wife Catherine for doing everything she could to assist me in my work, from proof-reading to following me to Germany. The Petroleum Agency of South Africa is thanked for granting me time to complete this work during its final stages. Funding for this project from the Deutsches GeoForschungsZentrum and the National Research Foundation is gratefully acknowledged.

TABLE OF CONTENTS

LIST OF FIGURES

Chapter 1

Figure 1.5: Timeline of significant events in the geological history of southern Africa; based on Tankard *et al.* (1982), Johnson *et al.* (2006) and de Wit, M.J. (2007) and references therein, with use of the geochronological divisions of Gradstein *et al.* (2004). Vertical axis is not to scale. The amalgamation and breakup of Gondwana represents the most recent phase of sediment accumulation and subsequent denudation in the long tectonic history of the region.

Figure 1.6: Chronostratigraphic map of southern Africa, modified from the 1:5,000,000 International Metallogenic Map of Africa (Veselinovic-Williams and Frost-Killian, 2002), with Jurassic Karoo dolerites modified from the 1:1,000,000 Metallogenic Map of South Africa, Lesotho and Swaziland (Vorster, 2001).

Figure 1.7: Lithological map of southern Africa, compiled from the same sources as in **Figure 1.6**.

Figure 1.8: Schematic map of southern Africa's tectonic basement, modified from de Wit, M.J. (2007). The Archean Azanian Craton domain (> 2.5 Ga) in the central-eastern region is bound by Palaeo- and Mesoproterozoic mobile belts (2.5-1.0 Ga) and Neoproterozoic (1.0-0.5 Ga) suture zones. Black lines are political boundaries.

Chapter 2

Figure 2.1: The topography of Africa and the bathymetry of the surrounding oceans relative to sea level, rendered from the 2 arc-minute (≤ 3.7 km) resolution ETOPO2 digital elevation dataset (U.S. Department of Commerce, National Oceanic and Atmospheric Administration, National Geophysical Data Center, 2001). Note the high elevation of the southern African region.

Figure 2.2: The topography of Africa south of 20ºS. Elevation given here and elsewhere is from a processed version the SRTM 3 arc-second (~90 m) resolution digital elevation model dataset (Jarvis *et al*., 2006) unless otherwise stated. The locations of key topographic features in the region are indicated.

Figure 2.3: The drainage of southern Africa. Drainage shown here and elsewhere is compiled from the AEON digital database and from data downloaded from the S.A. Department of Water Affairs and Forestry: www.dwaf.gov.za. Rivers (both perennial and non-perennial) with Strahler stream orders ≥ 3 are shown.

Figure 2.4: Frequency distribution for integer elevation values in the SRTM digital elevation model in **Figure 2.2**. Elevation displays a bimodal distribution, with the dominant mode of elevation at approximately 1000 m, representing southern Africa's interior plateau. Significant single value spikes represent waterbodies.

Figure 2.5: The elevation of southern Africa and the distribution of Karoo dolerite outcrop in southern Africa. The southern limit of Karoo dolerite outcrop coincides with much of the southern escarpment, although these features diverge as the Karoo dolerite limit is followed towards the southeast coast, resulting in semi-parallel "true" (drainage divide defined) and "false" (dolerite outcrop controlled) escarpments (see also **Figure 2.6**).

Figure 2.6: Top: The "false escarpment" (green line), defined approximately by the southern limit of Karoo dolerite outcrop (pale pink), south of the "true escarpment" (orange line), defined by the drainage divide between interior and coastal drainage. The "false escarpment" also forms the drainage divide between coastward flowing tributaries of the Sundays and Great Fish rivers, and the northward-flowing tributaries of the Great Fish and Kei rivers. Below: Schematic illustration of a possible model for development of drainage, where an initial escarpment (1) migrates inland (2), following headward erosion or drainage capture by coastal rivers, and finally resulting in the present configuration (top). Thus the "false escarpment" might represent the former divide between coastal and inland drainage.

Figure 2.7: Probable drainage capture of the plateau's Slang River (presumably a former tributary of the interior Vaal/Orange river) across the escarpment by a tributary of the coastward-draining Tugela River. The extent of Karoo dolerite outcrop is also shown.

Figure 2.8: Examples of discordant coastal drainage across the Lebombo (Pongola and Mbuluzi rivers, above) and Cape Fold Belt mountain ranges of the Swartberg, Rooiberg and Langeberg (Gourits River, below).

Figure 2.9: Block diagrams illustrating the development of (a) superimposed drainage and (b) antecedent drainage, modified from Plummer and McGeary (1996).

Figure 2.10: Sketch of factors that may influence the evolution of an escarpment and extensional continental margin, from Summerfield (1991): U_T = thermally-driven uplift; U_I = isostatic uplift associated with denudational unloading, S_T = thermally driven subsidence, S_I = isostatic subsidence associated with sediment loading, E = erosion through escarpment retreat. An extensional continental margin might therefore experience some rotation (r) due to the combination of U_I and S_I. S.l. denotes sea level.

Figure 2.11: Diagrammatic representation of diachronous age relations for L.C. King's cyclic pediplanation surfaces, after Summerfield (1991). A cyclic surface's initial age represents the age of base level fall, following which scarp retreat inland occurs (e.g. surface A). As a result, the initial ages for the surfaces above increase with elevation, i.e. D > C > B > A. The local age for a surface is the age of the surface where an overlying sedimentary deposit gives a minimum age constraint (e.g. for surfaces A and C), and is younger that the initial age of the surface. Eventual complete removal of a surface (D) through the growth of a younger surface represents the older surface's terminal age.

Figure 2.12: King's (1967) diagrammatic profile of world cyclic denudational landscapes, based on a global correlation of landscapes with that of southern Africa.

Figure 2.13: Partridge and Maud's (1987) erosion surfaces for South Africa, Lesotho and Swaziland (map based on GIS data digitised from the original by C. Mielke). The location of van Niekerk *et al.*'s (1999) $^{40}Ar/^{39}Ar$ cryptomelane age for a duricrust correlated with the Post-African I erosion surface is also shown.

Figure 2.14: Sketch demonstrating the Gipfelflur hypothesis of accordant summits, from Sparks (1960) based on Baulig (1952). Here uniform summit heights are a result of uniform slopes (due to constant mass shear strength in a lithologically homogeneous area) and uniform stream spacing, as is common, for example, in areas of trellis drainage in the Drakensberg Escarpment or in the Cape Fold Belt (Stankiewicz, 2004). In this case, the accordance of summit heights may not be used to infer the existence of a dissected erosion surface.

Figure 2.15: Moore's (1999) hypothetical axes of epeirogenic flexure, revised from those proposed by du Toit (1933).

Figure 2.16: Long-term denudation rate estimates for southern Africa based on thermochronology and other geological indicators, as listed in **Table 2.1**. Horizontal lines between points each indicate the time period over which the denudation rate was averaged. Values are calculated medians where a range of values was indicated in the literature. For Brown, R.W. *et al*.'s (2002) estimate for 130-0 Ma, Kounov *et al*.'s (2009) estimate for the interior plateau, and Flowers and Schoene's (in press) estimate for 60-0 Ma, values given are maximum estimates. Error bars are not shown for the sake of clarity.

Figure 2.17: Approximate locations of long-term denudation rate estimates from the literature (**Table 2.1**) for the Cretaceous, late Jurassic and early Tertiary (above) and for the Cenozoic and late Cretaceous (below). Note the general decrease in denudation rates over time across the southern African region.

Figure 2.18: Approximate locations of previous cosmogenic nuclide studies in southern Africa (Fleming *et al*., 1999; Cockburn *et al*., 1999, 2000; Bierman and Caffee, 2001; Van der Wateren and Dunai, 2001; Kounov *et al*., 2007; Codilean *et al*., 2008).

Figure 2.19: Contrasting (strike-averaged) topographic profiles for the development of escarpments through plateau degradation (above; where an initial inland drainage divide exists) and escarpment retreat (below; where the escarpment coincides with a

drainage divide), as predicted by the modeling of van der Beek *et al*. (2002). Red arrows each signify the relative extent of drainage divide migration for each case.

Chapter 3

Figure 3.1: Karoo-aged basins of south-central Gondwana (orange), relative to the tectonic plate configuration at ~250 Ma, including the position of the Main Karoo Basin of southern Africa (black square, **Figure 3.2**). Image modified from Reeves and de Wit (unpublished data).

Figure 3.2: Geological map of the Main Karoo Basin and surrounding Karoo-aged sedimentary sub-basins and volcanic outliers in South Africa, Lesotho and Swaziland, modified from Vorster (2001).

Figure 3.3: *Top:* Dolerite ring outcrops and interpreted cross-section along line A-B after Walker and Poldevaart (1949), who inferred that the rings represent the surface expression of an undulating dolerite sheet. *Bottom:* Alternative interpretation of the three-dimensional geometry of dolerite rings, after Chevallier and Woodford (1999). Here, sills at different elevations are connected by an inclined dolerite sheet or ring dyke.

Figure 3.4: *Main image:* The distribution of dolerite dykes in the Main Karoo Basin, after Chevallier and Woodford (1999). *Left inset (a)* and *right inset (b):* Structural and geodynamic interpretations, respectively, of Chevallier and Woodford (1999), who inferred a failed transform rift with an east-west right-lateral shear sense and a triple junction off the east coast at the time of dolerite dyke emplacement, resulting in the intrusion of north-northwest trending dolerite dykes.

Figure 3.5: Map of N-values (solid lines) in southern Africa, after Weinert (1965). The N-value is a climatic measure of the relative dominance of physical over chemical weathering in dolerites, where $N < 5$ signifies the dominance of chemical weathering, and $N > 5$ signifies the dominance of physical weathering. Thus for weathered doleritic material, the $N = 5$ contour coincides with the boundary (dashed

line) between western areas of sound engineering performance (Atterberg liquid limit < 10; Atterberg plasticity index < 30), and eastern areas of less sound performance.

Figure 3.6: The locations of the three digitised 1:250,000 geological map sheets used in these analyses: *3222 Beaufort West*, *3024 Colesberg* and *2730 Vryheid*, relative to the distribution of Karoo dolerites in southern Africa.

Figure 3.7: Geology modified from the *3222 Beaufort West* map sheet (Marsh, 1979). Labelled river catchments after Schulze (2007) are also shown.

Figure 3.8*:* Elevation (Z, colour scale) and relief (R, greyscale) for the same area as in **Figure 3.7**, derived from the SRTM DEM (Jarvis *et al*., 2006). The location of the town Beaufort West and the boundaries of river catchments are also shown.

Figure 3.9: Composite map of geology, relief and river catchments for the map sheet *3222 Beaufort West* (Marsh, 1979).

Figure 3.10: Comparison of Z_{mean} values for the Abrahamskraal Fm. (top), Teekloof Fm. (middle) and Cenozoic alluvium (bottom), with those of Karoo dolerite in the map sheet *3222 Beaufort West* (**Figures 3.7**, **3.8** and **3.9**). Note the higher average elevation of Karoo dolerites in comparison with the other geological units for almost all catchments.

Figure 3.11: Comparisons between catchment-specific Z_{mean} values for the Abrahamskraal Fm., Teekloof Fm. and Cenozoic alluvium in the map sheet *3222 Beaufort West* (**Figures 3.7**, **3.8** and **3.9**). The mean elevations of the Teekloof Fm. are generally higher than for the Abrahamskraal Fm. and Cenozoic alluvium, with the Abrahamskraal Fm. and Cenozoic alluvium both occurring at similarly low elevations.

Figure 3.12: Comparisons of catchment-specific R_{mean} values for the Abrahamskraal Fm. (top), Teekloof Fm. (middle) and Cenozoic alluvium (bottom), with those of Karoo dolerite in the map sheet *3222 Beaufort West* (**Figures 3.7**, **3.8** and **3.9**). Note

the generally higher relief of Karoo dolerite, and the poor statistical correlation between corresponding R_{mean} values.

Figure 3.13: Comparisons of R_{mean} values for the Abrahamskraal Fm., Teekloof Fm. and Cenozoic alluvium in the map sheet *3222 Beaufort West* (**Figures 3.7**, **3.8** and **3.9**). The R_{mean} values for the Teekloof Fm. are generally higher than for the Abrahamskraal Fm., which in turn generally displays higher R_{mean} values than the Cenozoic alluvium.

Figure 3.14: Geology modified from the *3024 Colesberg* map sheet (Le Roux, 1998). River catchments after Schulze (2007) are also shown.

Figure 3.15: Composite map of elevation (Z, colour scale) and relief (R, greyscale) for the same area as in **Figure 3.14** (derived from the SRTM DEM; Jarvis *et al*., 2006). The faint diagonal lines visible in the northeast (low relief) sector of the map represent artefacts in the SRTM DEM. The locations of Vanderkloof Dam and Gariep Dam along the northwest-flowing Orange River, and the town of Colesberg, are also shown.

Figure 3.16: Composite map of geology, relief and river catchments for the map sheet *3024 Colesberg* (Le Roux, 1998).

Figure 3.17: Comparisons of Karoo dolerite Z_{mean} values for the Tierberg Fm. (top left), Balfour Fm. (top right), Katberg Fm. (bottom left) and Quaternary alluvium (bottom right) in **Figure 3.14** (*3024 Colesberg*; Le Roux, 1998). Karoo dolerites generally display higher Z_{mean} values than the Tierberg Fm., Balfour Fm., and Quaternary alluvium, and correlate significantly with Z_{mean} values for the Katberg Fm. and Quaternary alluvium.

Figure 3.18: Comparisons of Z_{mean} values for non-dolerite units in **Figure 3.14**. In none of the catchments on the map *3024 Colesberg* were outcrops of both the Tierberg and Katberg Formations present.

Figure 3.19: Comparisons of R_{mean} values for the Tierberg, Balfour and Katberg Formations and Quaternary alluvium with R_{mean} values of Karoo dolerite for the catchments in **Figure 3.14**.

Figure 3.20: Comparisons of R_{mean} values for non-dolerite units in **Figure 3.14**. R_{mean} values for the Tierberg and Balfour Formations are comparable, with R_{mean} values for the Katberg Fm. generally higher and R_{mean} values for the Quaternary alluvium generally lower. No significant correlations between R_{mean} values occur.

Figure 3.21: Geology modified from the *2730 Vryheid* map sheet (Wolmarans, 1988). River catchment outlines after Schulze (2007) are also shown. For the purpose of clarity, catchment name labels are shown separately in **Figure 3.22**.

Figure 3.22: Labelled river catchments after Schulze (2007) for the *2730 Vryheid* mapsheet (**Figure 3.21**). In addition, the relief of the area is shown (see also **Figure 3.23**).

Figure 3.23: Composite map of elevation (Z, colour scale) and relief (R, grey scale) for the same area as **Figure 3.21**, derived from the SRTM DEM (Jarvis *et al*., 2006). Catchment outlines and the locations of the incised Pongola River valley and the town of Vryheid are also shown.

Figure 3.24: Composite map of geology, relief and catchments for the *2730 Vryheid* map area in **Figure 3.21**.

Figure 3.25: Comparison of Z_{mean} values of Karoo dolerite with those of other lithologies in the map *2730 Vryheid* (**Figure 3.21**).

Figure 3.26: Comparison of Z_{mean} values for non-dolerite lithologies in the map *2730 Vryheid* (**Figure 3.21**).

Figure 3.27: Comparison of R_{mean} values of Karoo dolerite with those of other lithologies in the map *2730 Vryheid* (**Figure 3.21**).

Figure 3.28: Comparison of R_{mean} values for non-dolerite lithologies in the map *2730 Vryheid* (**Figure 3.21**).

Figure 3.29: Comparison of R_{mean} and Z_{mean} values for Karoo dolerite for the three geological map sheets analysed in this study (top). The generalised topographic fields pertaining to Karoo dolerites each map area are delineated in the miniature reproduction (below). Note that no positive correlation exists between Z_{mean} and R_{mean} in any of the maps.

Chapter 4

Figure 4.1: Neon three-isotope diagram showing mixing trends between atmospheric Ne ($^{21}Ne/^{20}Ne$ = 0.002959 and $^{22}Ne/^{20}Ne$ = 0.1020; Eberhardt *et al*., 1965) and various other Ne components. A mixture of only atmospheric Ne and cosmogenic Ne must plot on the "spallation line" (shown here for quartz). The vertical and horizontal dotted lines represent mixing with nucleogenic ^{22}Ne and ^{21}Ne respectively (here produced, for example, through the interaction of ^{19}Fe and ^{18}O nuclei with α-particles emitted by the radioactive decay of neighbouring U and Th nuclei). Contributions of both nucleogenic ^{22}Ne and ^{21}Ne may thus result in a Ne measurement plotting on the spallation line even though a significant nucleogenic component may be present.

Figure 4.2: Flow chart illustrating the data evaluation procedure for standard, blank and sample measurements.

Chapter 5

Figure 5.1: The topography of southern Africa according to the SRTM digital elevation model (Jarvis *et al*., 2006), the extent of Karoo dolerite outcrop in South Africa, Lesotho and Swaziland (AEON database) and the locations of sites sampled for cosmogenic nuclide analysis. Sites are shown in more detail in maps A to E in **Figures 5.2**, **5.3** and **5.4**

Figure 5.2: Locations of sample sites in box A of **Figure 5.1** relative to relief-shaded elevation (top), and the erosion surfaces of Partridge and Maud (1987) as digitized

from the authors' 1:2,500,000 scale map by C. Mielke (bottom). The drainage divide of the northward-draining Orange River basin according to Schulze (2007) is also shown.

Figure 5.3 Locations of sample sites in boxes B, C and D of **Figure 5.1** and in **Figure 5.2** relative to relief-shaded elevation**.** Geographical features mentioned in the text are also shown for reference. The course and tributaries of the Orange River (Strahler stream order ≥ 2; data from the Department of Water Affairs and Forestry: www.dwaf.gov.za) are shown in D.

Figure 5.4: Locations of sample sites in area E of **Figure 5.1** relative to relief-shaded elevation. The courses of the Pongola and Mkuze rivers (Strahler stream order ≥ 2) are also given. The approximate extent of Partridge and Maud's (1987) "African Surface (dissected)", according to their 1:2,500,000 erosion surface map, is shown with cross-hatching. These authors classified the remaining area of this figure as a part of "other dissected areas".

Figure 5.5: Locations of sample sites, dolerite outcrop, and median January rainfall (austral summer; previous page, top), median July rainfall (austral winter; previous page, bottom), and mean annual precipitation (above) according to Schulze (2007). Rainfall and precipitation data is interpolated from stations with ≥ 15 years of daily records (Schultz, 2007).

Figure 5.6: Locations of sample sites, dolerite outcrop, mean January temperature (austral summer; previous page, top), mean July temperature (austral winter; previous page, bottom) and mean annual temperature (above) according to Schulze (2007). Data is interpolated from stations with daily records ranging from 3 to >75 years (Schultz, 2007).

Figure 5.7: Locations of sample sites, dolerite outcrop and Weinert's (1965) dolerite weathering index, $N = 12(E_{Jan}/P)$, where E_{Jan} is potential evaporation in January and P is mean annual precipitation. N is calculated from the E_{Jan} and P values of Schulze (2007).

Figure 5.8: Top: BW3 sample site (arrow) on scarp face of dolerite sill, viewed from Molteno Pass, looking east. Bottom: Close-up view of sample BW3, viewed towards the south. Sample is being held back in place after removal from the exfoliating dolerite face.

Figure 5.9: Sample DV5 from the low relief region, *Die Vlakte*, south of the escarpment zone between Beaufort West and Graaff Reinet.

Figure 5.10: Sample DV6, viewed to the north, with the escarpment zone on the horizon. A thin, white calcrete coating on the dolerite is observable in the right foreground.

Figure 5.11: Sample DV9 viewed towards the south. The dolerite sill from which the sample is collected forms a slight local topographic high on the low relief plain. The mountains of the Cape Fold Belt are faintly visible on the horizon.

Figure 5.12: Samples GR1 (top) viewed towards the east and GR2 (bottom) viewed towards the south from a dolerite ridge north of Graaff-Reinet.

Figure 5.13: Sample site GR3 from a dolerite sill north of Graaf-Reinet, viewed towards the north.

Figure 5.14: Sample site GR5 from a dolerite outcrop at the top of Lootsberg Pass.

Figure 5.15: Sample site CB1 from an inclined exfoliating scarp face south of Colesburg.

Figure 5.16: Sample sites GD1 (arrow 1), GD2 and GD3 (arrow 2,3), from a dolerite sill forming the resistant caprock to a flat-topped hill, or *koppie*, overlooking Gariep Dam on the Orange River. Photograph viewed towards the south.

Figure 5.17: Samples GD1 (arrow 1, above) and GD2 (arrow 2, below, with Gariep Dam in the background), both viewed towards the south.

Figure 5.18: Sample GD3 (arrow 3) viewed to the west, a few metres adjacent to sample GD2, with the Orange River in the background.

Figure 5.19: Sample OR3 from the top corestone of a dolerite inselberg or tor between Colesberg and Vanderkloof Dam. Photograph viewed to the east.

Figure 5.20: Sample OR1 from an inclined dolerite hillslope near Vanderkloof Dam on the Orange River. Photograph viewed to the west.

Figure 5.21: Sample OR2 from the summit of a *koppie* overlooking the Orange River near Vanderkloof Dam. Photograph viewed to the west, with a bridge crossing the Orange River in the background.

Figure 5.22: Stone quarry from the side of the koppie from which OR2 is sampled, displaying unweathered dolerite corestones within a weathered saprolite. The upper rock face (background) displays orthogonal joints within the dolerite. In the foreground, subsurface weathering along the joints of the dolerite has resulted in the development of fresh corestones surrounded by saprolite.

Figure 5.23: Sample IT6 from a dolerite sill (top, viewed to the southwest), overlooking the incised meanders of the Pongola River (bottom, viewed to the northwest).

Figure 5.24: Sample IT5 from a dolerite sill at the base of the Karoo sedimentary sequence, viewed to the west. Valley of a Pongola River tributary in the background.

Figure 5.25: Sample IT1, viewed towards the northwest.

Figure 5.26: Sample IT3, from an exposed dolerite pavement littered with dolerite boulders.

Figure 5.27: Samples IT8 (arrow 1) and IT9 (arrow 2) from an exfoliating dolerite pavement, viewed towards the southwest (top) and the north (below).

Figure 5.28: Sample IT10 viewed towards the south.

Figure 5.29: Photomicrographs of sample GR5 in plane-polarised light (PPL, top) and cross-polarized light (XPL, bottom), displaying an ophitic texture with euhedral laths of plagioclase enclosed by a clinopyroxene phenocryst.

Figure 5.30: Sample IT8 (PPL top; XPL bottom), a plagioclase cumulate with intercumulate pyroxene. Note the extensive alteration of plagioclase feldspar to white mica ("sericitisation").

Figure 5.31: Sample OR2 (PPL top; XPL bottom), showing alteration of olivine to green "bowlingite" pseudomorphs. Besides pyroxene and plagioclase, biotite and chlorite are also present.

Figure 5.32: Sample BW3 (PPL top; XPL bottom), showing primary mineral phases cross-cut by a vein infilled with white mica, biotite and chlorite, and alteration of neighbouring pyroxene to a brown fibrous amphibole.

Figure 5.33: Sample DV9 (PPL top; XPL bottom) showing alteration of pyroxene to amphibole, and alteration of plagioclase to white mica. The white mica, in turn, displays extensive alteration to clay minerals.

Figure 5.34: Comparative net cosmogenic production rates for ^{3}He and ^{21}Ne (normalized to sea level and at high latitude with no topographic shielding) for all pyroxene mineral separates. These are calculated from pyroxene mineral chemistry according to the elemental production rates of Masarik and Reedy (1996), Kober *et al*. (2005) and Fenton *et al*. (2009), and displayed as P1, P2 and P3, respectively.

Chapter 6

Figure 6.1: Neon three-isotope diagram of analyses of sample BW3 at 600 ºC, 900 ºC and 1750 ºC. Schäfer *et al.*'s (1999) pyroxene spallation line ($y = (1.069 \pm 0.035)x + 0.099$) and the composition of air ($^{21}Ne/^{20}Ne = 0.002959$) are also shown here and in subsequent Ne three-isotope diagrams.

Figure 6.24: ^{3}He vs. ^{21}Ne minimum exposure ages according to the nuclide production rate of Fenton *et al.* (2009) and the scaling factors of Lal (1991), top, and Dunai (2000a), bottom.

Figure 6.25: Top: ^{3}He vs. ^{21}Ne maximum erosion rates according to the nuclide production rate of Fenton *et al.* (2009) and the scaling factor of Lal (1991). Bottom: Detail of maximum erosion rates of 0-5 m/Myr.

Figure 6.26: Top: ^{3}He vs. ^{21}Ne maximum erosion rates according to the nuclide production rate of Fenton *et al.* (2009) and the scaling factor of Dunai (2000a). Bottom: Detail of maximum erosion rates of 0-5 m/Myr.

Figure 6.27: Comparison of the difference between ^{21}Ne and ^{3}He minimum exposure ages (according to Lal (1991) scaling) and ^{4}He abundances. A negative regression line where $R^2 = 0.32$ indicates that no positive correlation exists. Therefore, if higher ^{21}Ne T estimates are a result of a significant nucleogenic ^{21}Ne component, the ^{4}He abundance cannot be used as a proxy for the nucleogenic ^{21}Ne contribution.

Figure 6.28: ^{38}Ar/^{36}Ar analyses presented in **Table 6.5**. Although the majority of analyses plot within error of the composition of air (^{38}Ar/^{36}Ar = 0.1880; Nier, 1950), 10 of the analyses at 1750 ºC display significantly higher ^{38}Ar/^{36}Ar values, which may be attributed to a cosmogenic Ar component.

Figure 6.29: Comparison of $^{38}Ar_c$ concentrations normalized to Ca with ^{3}He (top) and with ^{21}Ne normalized to Mg (bottom). Lines defining the relations determined by Niedermann *et al.* (2007) are also shown.

Figure 6.30: ^{38}Ar minimum exposure ages compared with the corresponding estimates from cosmogenic ^{3}He (top; Lal (1991) scaling) and ^{21}Ne (bottom; Dunai (2000a) scaling).

Figure 6.31: ^{38}Ar maximum erosion rates compared with the corresponding estimates from cosmogenic ^{3}He (top; Dunai (2000a) scaling) and ^{21}Ne (bottom; Lal (1991)

scaling). The three samples with the highest ^{38}Ar ε values (CB1, GR2 and IT9) are not shown for the sake of clarity.

Figure 6.32: Comparison of ^{38}Ar minimum exposure ages with ^{3}He (Dunai (2000a) scaling; top) and ^{21}Ne estimates (Lal (1991) scaling; bottom) for nine samples where the ^{38}Ar T estimates do not plot within error of zero (sample OR3 excluded).

Figure 6.33: Total $^{36}Ar/^{132}Xe$ vs. $^{84}Kr/^{132}Xe$ ratios for samples in this study.

Figure 6.34: $^{36}Ar/^{132}Xe$ vs. $^{84}Kr/^{132}Xe$ ratios for crushing and total heating analyses in this study, compared with results from Hawaiian basalts (Valbracht *et al*., 1996) and the composition of air.

Chapter 7

Figure 7.1: Schematic illustration of chemical weathering and granular disintegration. For a rock surface (1), one or more chemical mineral phases (e.g. mineral phase 1) may experience chemical alteration, followed by removal of the weathering products in solid state or in solution. This results in lowering of the surface (2), following which the remaining rock (e.g. mineral phases 2 and 3) may also experience chemical alteration on exposure, and/or be removed through gravity, water or wind action.

Figure 7.2: Schematic illustration of rock exfoliation, here resulting from pressure release, modified from Plummer and McGeary (1996). In this instance, a granitic dome experiences exhumation and unloading, due to surface denudation caused by regional uplift. This pressure release results in the formation of surface parallel joints, causing the detachment of rock sheets parallel to the surface (exfoliation). Tension release joints may also result from thermal expansion due to insolation or fire, incipient chemical weathering, or frost wedging.

Figure 7.3: Schematic illustration of (a) rock falls and (b) rock slides, modified from Clowes and Comfort (1987). Rock falls occur at steep rock surfaces and generate scree slopes or debris cones below them, whereas rock slides occur along inclined

planes of weakness, and result in less disruption of the mobile mass (Clowes and Comfort, 1987).

Figure 7.4: Schematic illustration of landscape denudation through initial chemical weathering followed by physical erosion, modified from Sawyer (1970). In Stage I, the rate of bedrock weathering along fractures exceeds the rate of erosion of the weathered material, leading to Stage II, where a regolith is formed and a subsurface weathering front (B-B') has developed beneath the ground surface (A-A'). Should the rate of physical erosion of the regolith then exceed the rate of chemical weathering of the bedrock, the weathering front is then exposed at the surface (Stage III).

Figure 7.5: The positions of samples BW3, DV5, DV6 and DV9, relative to SRTM elevation and relief (Jarvis *et al*., 2006). The position of the topographic profile intersecting these sample sites along line A-B-C (**Figure 7.6**) is also shown.

Figure 7.6: Topographic profile A-B-C from northwest to southeast (**Figure 7.5**), showing ^{3}He minimum exposure ages (T, above) and maximum erosion rates (ε, below) according to Fenton *et al*.'s (2009) production rates and Dunai's (2000a) scaling factors. The model scarp retreat rate, E, determined from the minimum exposure age of sample BW3, is also shown (above).

Figure 7.7: The positions of samples GR1, GR2, GR3, GR5 and CB1 relative to SRTM elevation and relief (Jarvis *et al*., 2006). The position of the topographic profile intersecting these sample sites along line D-E-F-G (**Figure 7.8**) is also shown.

Figure 7.8: Topographic profile D-E-F-G from south to north (**Figure 7.7**), showing ^{3}He minimum exposure ages (T, above) and maximum erosion rates (ε, below) according to Fenton *et al*.'s (2009) production rates and Dunai's (2000a) scaling factors. The model scarp retreat rate, E, determined from the minimum exposure age of sample CB1, is also shown (above).

Figure 7.9: Schematic illustration of the slope from which CB1 is sampled. The model scarp retreat rate perpendicular to the scarp, E (determined from the minimum exposure age T, and an assumed rock fall thickness of 1.15 m, equivalent to 3

effective attenuation lengths here), may be resolved into horizontal and vertical components. For E = 44-76 m/Myr and an inclined surface of dip angle 44º, the erosion rate in the horizontal direction is 31-53 m/Myr, and the vertical downwearing rate is 32-55 m/Myr.

Figure 7.10: The positions of samples GD1, GD2 and GD3 relative to SRTM elevation and relief (Jarvis *et al*., 2006). The position of the topographic profile intersecting these sample sites along line H-I (**Figure 7.11**) is also shown.

Figure 7.11: Topographic profile H-I from southwest to northeast (**Figure 7.10**), showing ^{3}He minimum exposure ages (T, above) and maximum erosion rates (ε, below) according to Fenton *et al*.'s (2009) production rates and Dunai's (2000a) scaling factors. The model scarp retreat rate, E, determined from the minimum exposure age of sample GD1, is also shown (above).

Figure 7.12: The location of samples OR1 and OR2 relative to the 1:50,000 topographic map *2924DC Havengabrug* (Chief Director of Surveys and Mapping, 1988a). The location of topographic profile J-K-L (**Figure 7.l3**) is also shown.

Figure 7.13: Topographic profile J-K-L from west to east (**Figure 7.12**), showing ^{3}He minimum exposure ages (T, above) and maximum erosion rates (ε, below) according to Fenton *et al*.'s (2009) production rates and Dunai's (2000a) scaling factors. Elevation is derived from the SRTM DEM (Jarvis *et al*., 2006).

Figure 7.14: The location of sample OR3 relative to the 1:50,000 topographic map *3024BA Petrusville* (Chief Director of Surveys and Mapping, 1988b). The location of topographic profile M-N (**Figure 7.15**) is also shown.

Figure 7.15: Topographic profile M-N from south to north (**Figure 7.14**), showing the ^{3}He minimum exposure age (T, above) and maximum erosion rate (ε, below) according to Fenton *et al*.'s (2009) production rates and Dunai's (2000a) scaling factors. Elevation is derived from the SRTM DEM (Jarvis *et al*., 2006).

Figure 7.16: The positions of samples IT1, IT3, IT5, IT6, IT8, IT9 and IT10 relative to SRTM elevation and relief (Jarvis *et al*., 2006). The position of the topographic profile intersecting these sample sites along line O-P-Q-R-S-T-U-V (**Figure 7.17**) is also shown.

Figure 7.17: Previous page: Schematic geological cross-section along topographic profile O-P-Q-R-S-T-U-V (**Figure 7.16**). This page: Topographic profile O-P-Q-R-S-T-U-V showing ^{3}He minimum exposure ages (T, above) maximum erosion rates (ε, below) according to Fenton *et al*.'s (2009) production rates and Dunai's (2000a) scaling factors. The model scarp retreat rate, E, determined from the minimum exposure age of sample IT6, is also shown (above).

Figure 7.18: ^{3}He minimum exposure ages and maximum erosion rates, based on Dunai's (2000a) scaling factors and Fenton *et al*.'s (2009) cosmogenic nuclide production rates, for vertical and inclined surfaces (red diamonds, $\alpha = 90^{o} - 30^{o}$) and horizontal surfaces (blue diamonds, $\alpha = 12^{o} - 0^{o}$).

Figure 7.19: Maximum erosion rates and median pyroxene grain sizes of 19 samples where $\varepsilon < 4$ m/Myr. No statistical correlation exists between these variables, and samples that exhibit cumulate and ophitic textures, respectively, display similar ranges of ε values.

Figure 7.20: Maximum erosion rates and slope angles for 19 dolerite surfaces where $\varepsilon < 4$ m/Myr, displaying no statistical correlation.

Figure 7.21: Maximum erosion rates and mean annual temperatures (Schulze, 2007) for 19 dolerite surfaces where $\varepsilon < 4$ m/Myr, displaying no statistical correlation.

Figure 7.22: Maximum erosion rates and mean annual precipitation (Schulze, 2007) for 19 dolerite surfaces where $\varepsilon < 4$ m/Myr, displaying no statistical correlation.

Figure 7.23: Maximum erosion rates and N values (Weinert, 1965, with data from Schulze, 2007) for 19 dolerite surfaces where $\varepsilon < 4$ m/Myr, displaying no statistical

correlation. A negative correlation would be expected if ε values and N values both depended upon the absolute chemical weathering rate.

Figure 7.24: Maximum erosion rates and model basaltic weathering fluxes in the same units (calculated according to Dessert *et al*., 2003) for catchments corresponding to the 19 samples where ε < 4 m/Myr. No statistical correlation exists ($R^2 = 0.42$ for the best fit linear regression line, where y = -0.627x + 2.65, not shown for clarity). Model basaltic weathering fluxes yield a range of values < 3 m/Myr, similar to the range of values for maximum erosion rates. However, the model weathering fluxes are generally lower than maximum erosion rates in the more arid western (southern escarpment and central plateau) region, and generally higher than maximum erosion rates in the more humid eastern (Pongola) region.

Figure 7.25: Antarctic atmospheric temperature relative to the present (dark blue line), according to deuterium and oxygen isotope proxies in the Vostok ice core (Petit *et al*., 1999; data from Petit *et al*., 2001). Individual Vostok core sample points are omitted for clarity. The characteristic erosion timescales (T_ε) of the 19 samples where the maximum erosion rate is < 4 m/Myr are superimposed on the background of the graph (blue bars), and ranked from longest (bottom) to shortest (top), with analytical error bars omitted for clarity. This illustrates that the maximum erosion rates for all these samples are integrated over time periods that experienced dramatic shifts in global climate.

Figure 7.26: Comparison between ^{3}He maximum erosion rates for Karoo dolerites, according to Dunai (2000a) scaling and Fenton *et al*.'s (2009) production rates, and literature estimates of modern rates of soil erosion in the vicinity of sample sites, according to Rooseboom (1978), Le Roux (1990), Schulze (2007) and Compton *et al*. (2010). Note that if Karoo dolerite maximum erosion rates are assumed to represent soil production rates, soil erosion rates are higher than long-term production rates at any site by a factor of between ~2 and ~280.

LIST OF TABLES

Chapter 2

Chapter 3

Table 3.4: R_{mean} values for geological units in **Figure 3.21** for a total of 73 catchments in the area (labelled in **Figure 3.22**). Areas of whole quaternary catchments (including portions beyond the map margins, according to Schulze, 2007) are also shown.

Table 3.5: Percentages of catchments in the three geological maps where Z_{mean} and R_{mean} values for Karoo dolerites are less than those for Karoo sedimentary units and Cenozoic/Quaternary alluvial deposits. The number of catchments involved in each comparison is also given.

Chapter 4

Table 4.1: Values for coefficients a_0, a_1, a_2 and a_3 as a function of geomagnetic latitude (λ_m) for the calculation of atmospheric nuclear disintegration rate $N(\lambda_m)$ according to Lal (1991) (equation 4.4), with h in km, based on the data of Lal and Peters (1967).

Table 4.2: Values for coefficients in equations 4.6 and 4.7 for the calculation of $N_{1030}(I)$ and $\Lambda(I)$ (Dunai, 2000a).

Table 4.3: Literature estimates of the terrestrial cosmogenic production rates of the noble gas nuclides ^{3}He, ^{21}Ne and ^{38}Ar at sea level and at high latitudes (>60°), in atoms per gram of element per year.

Table 4.4: Maximum and minimum blank values estimated for ^{4}He, ^{20}Ne, ^{40}Ar, ^{84}Kr and ^{132}Xe in cm^3 STP for the evaluation of sample analyses.

Chapter 5

Table 5.1: Geographic locations and elevations of sample sites, as well as cosmogenic nuclide production rate scaling factors and shielding factors.

Table 5.2: Mean annual precipitation, mean annual temperature and Weinert's (1965) N values, as well as river catchments and theoretical erosion surfaces (Partridge and Maud, 1987), corresponding to Karoo dolerite sample sites.

Table 5.3: Petrographic summary of the samples analysed for cosmogenic noble gases, with estimated mineral concentration given as percentages. Abbreviations are as follows: psdm = pseudomorph, a = accessory, op = ophitic pyroxene, pc = plagioclase cumulate. Modal percentages are estimated from thin section. Accessory phases are defined as those that consititute less than 10 % of the rock volume.

Table 5.4: Results of ICP-AES analyses (above) and calculated major element compositions (below) for pyroxene separates.

Table 5.5: Cosmogenic ^{3}He and ^{21}Ne production rates for pyroxene separates calculated according to Masarik and Reedy (1996), Kober *et al*. (2005) and Fenton *et al.* (2009), abbreviated as P1, P2 and P3, respectively. All production rates are in atoms per gram at sea level and high latitude (> 60º). Ratios and averages are also given for the purpose of comparison.

Chapter 6

Table 6.1: Results of all ^{4}He, ^{20}Ne, ^{3}He/^{4}He, ^{22}Ne/^{20}Ne and ^{21}Ne/^{20}Ne measurements after sample heating or crushing. Totals from heating measurements are also given for each sample.

Table 6.2: ^{3}He and ^{21}Ne excesses calculated for all samples in 10^{6} atoms per gram of pyroxene.

Table 6.3: ^{3}He and ^{21}Ne minimum exposure ages, according to the production rates calculated from Fenton *et al*. (2009). Results are reported according to the scaling factors of both Lal (1991) and Dunai (2000a).

Table 6.4: ^{3}He and ^{21}Ne maximum erosion rates, according to the production rates calculated from Fenton *et al*. (2009). Results are reported according to the scaling factors of both Lal (1991) and Dunai (2000a).

Table 6.5: Results of all ^{40}Ar, ^{40}Ar/^{36}Ar and ^{38}Ar/^{36}Ar measurements after heating or crushing. Calculated ^{36}Ar abundances and totals from heating measurements are also given.

Table 6.6: Estimates for the ^{38}Ar excess above air, $^{38}Ar_{ex}$, the ^{38}Ar/^{36}Ar neutron spallation production ratio, $(38/36)_{sp}$, the ^{36}Ar produced from thermal and epithermal neutron capture of ^{35}Cl and subsequent decay of ^{36}Cl, 36_{Cl}, and the Ca-normalised cosmogenic ^{38}Ar concentration, $^{38}Ar_{c}$, for each sample.

Table 6.7: ^{38}Ar minimum exposure ages (T) and maximum erosion rates (ε) according to both Lal's (1991) and Dunai's (2000a) scaling factors.

Table 6.8: Results of all ^{84}Kr and ^{132}Xe analyses. The ^{84}Kr/^{132}Xe ratios and the total ^{36}Ar/^{132}Xe ratios are also shown.

Chapter 7

Table 7.1: Effective neutron spallation attenuation lengths (perpendicular to the sample surface) for non-horizontal surfaces (i.e. where surface dip, $\alpha > 0^{o}$). Also shown are depths in cm equivalent to 1, 2, 3 and 4 effective attenuation lengths, where the cosmogenic nuclide production ratio is 37 %, 15 %, 5.0 % and 1.8 % of that at surface (based on a dolerite density of 3.0 g/cm^{3}).

Table 7.2: ^{3}He minimum exposure ages and maximum erosion rates for Karoo dolerite surfaces analysed in this study, based on Fenton *et al.*'s (2009) production rates and Dunai's (2000a) scaling factors. The dip angle from the azimuth for each surface is also shown.

Table 7.3: Mean annual temperature, mean annual runoff and the modeled basaltic weathering flux, as calculated in equation 3.6, according to Dessert *et al*. (2003), for

catchments where dolerite samples were collected for cosmogenic nuclide analysis. Catchment names and runoff values are from Schulze (2007), and catchment mean annual temperatures are calculated from Schulze (2007) by averaging mean annual temperature pixel values in each catchment area.

Table 7.4: Literature estimates of modern soil erosion rates for areas that encompass Karoo dolerite sample sites. Rooseboom (1978) provides only maximum values.

CHAPTER 1: INTRODUCTION AND FRAMEWORK

1.1 Introduction

This chapter begins with a brief history of the development of geomorphological theory. The aims of the thesis are then addressed from this perspective. The scope of the thesis is discussed and the outline of following chapters is presented. Finally, a brief account of southern Africa's geology is provided.

1.2 Theoretical framework

W.M. Davis (**Figure 1.1**) defined the theoretical basis of geomorphology by stating that all landscapes are a function of three variables: structure (i.e. underlying geology, including lithology and structural geology), process and time (Davis, 1899). Although recognising the importance of all these three variables, Davis' primary interest lay in the evolution of landscapes over time, leading to the development of his geographical cycle (Davis, 1899; Hart, 1986; **Figure 1.2**). This was defined for an originally horizontal surface that experiences rapid uplift followed by fluvial incision and downwearing in a humid environment (although later modified to account for other environmental conditions), eventually resulting in the development of an "old" landscape of low relief, worn near to base level - a peneplain (Davis, 1899, 1905).

Thus Davis (1899) championed a time-dependent, evolutionary approach to landscape analysis, with form and structure playing apparently subsidiary roles, although landscape age was only defined according to the relative terms of youth, maturity and old age. According to Higgins (1975), Davis' theory of landscape evolution was probably greatly influenced by Darwin's (1859) theory of biotic evolution, an idea much in vogue at the time. Davis' approach may be contrasted with that of his contemporary, G.K. Gilbert (**Figure 1.1**), who had a background in physics and embraced thermodynamic concepts in his study of landforms (Thorn, 1988). Gilbert (1877) proposed that a dynamic equilibrium was established when more resistant rocks developed steeper slopes, so that "where the ratio of erosive action as dependent on declivities [i.e. slopes] becomes equal to the ratio of resistances as dependent on rock character, there is equality of action." (Gilbert, 1877; p. 116; **Figure 1.3**). Gilbert (1877) thus incorporated the concept of negative feedback or self-regulation into landform development, with slope reciprocally determined by erodibility.

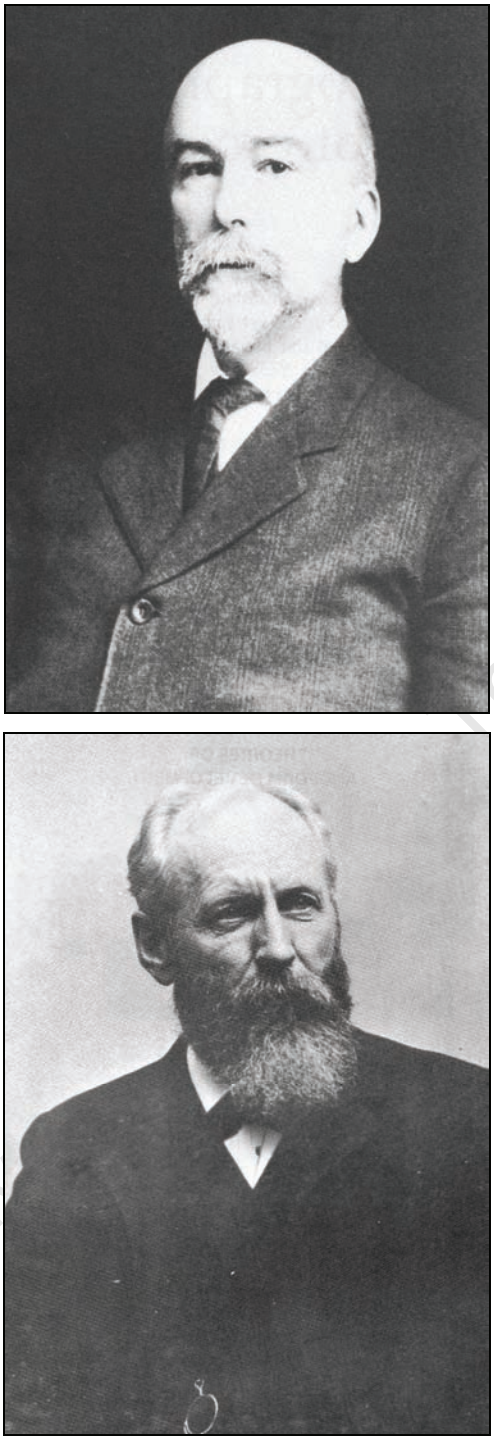

Figure 1.1: W.M. Davis (above) and G.K. Gilbert (below), pioneers of geomorphology who focused on evolutionary and equilibrium concepts, respectively, in the study of landscapes. Photographs are from Hart (1986) and Melhorn and Flemal (1980), respectively.

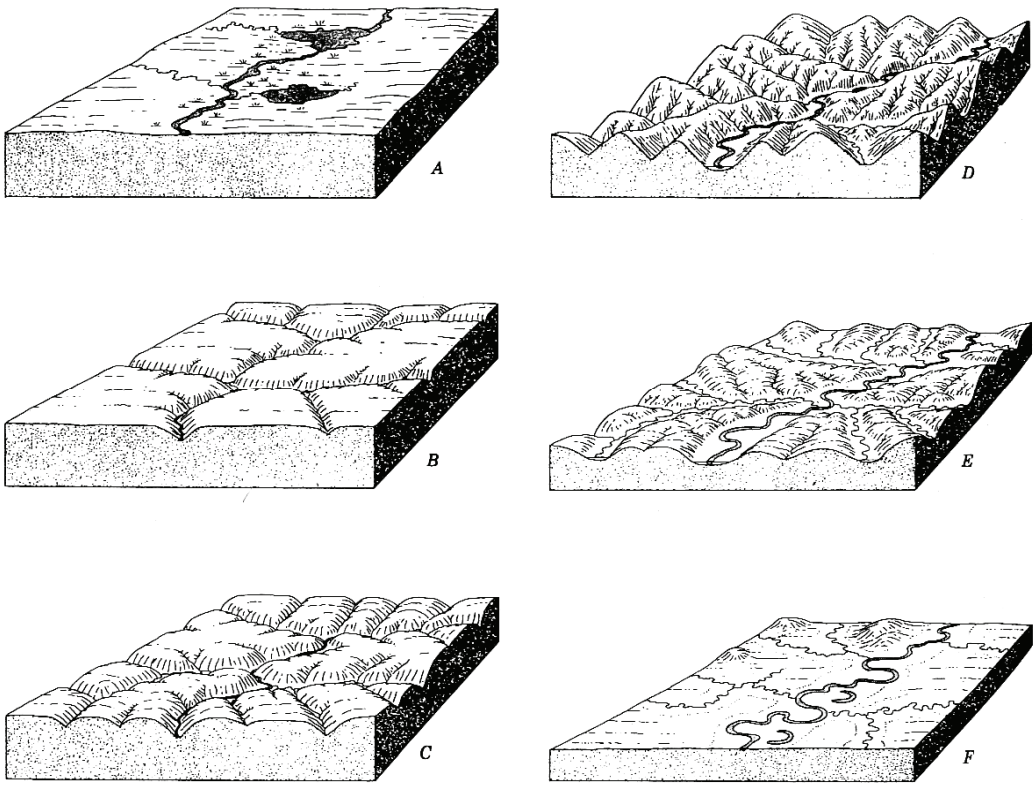

Figure 1.2: Davis' geographical cycle of landform evolution in a humid climate, modified from Summerfield (1991) and references therein. A surface of low relief (A) experiences uplift, initiating a "youthful" stage characterized by fluvial incision (B) followed by the grading of rivers and lateral erosion (C). A "mature" stage is reached where the flat uplands have been removed and relief is at a maximum (D). Lowering of interfluves then exceeds the lowering of channels, leading to a decline in relief and the development of floodplains and meandering channels (E). By the time "old age" is reached (F), local relief has been significantly reduced and floodplains are extensive, and the surface, a peneplain, resembles the initial condition in (A).

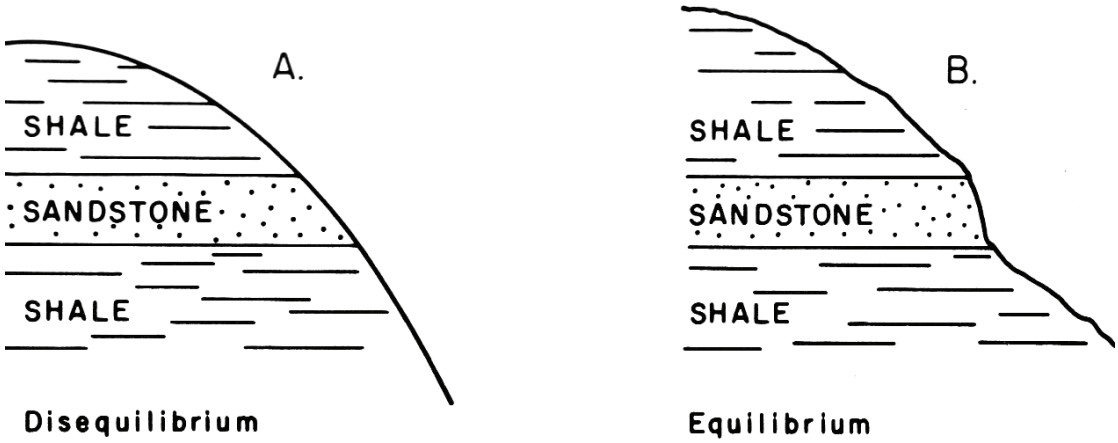

Figure 1.3: Schematic representation of Gilbert's (1877) argument for the development of an equilibrium hillslope profile, after Bull (1975). Hillslope A is in a state of disequilibrium because differences in the erodibility of two rock types (sandstone and shale) have not been compensated for by changes in slope steepness. Greater erosion of less resistant (shale) units leads to hillslope B, which is in equilibrium if the differing slopes for the different rock units balance their differences in erodibility. This slope then experiences an equality of action, i.e., a uniform rate of erosion, across the slope.

Comparison of Gilbert's (1877) theory of landscape equilibrium with Davis' (1899) theory of landscape evolution raises an apparent paradox, suggesting that landscapes both retain an equilibrium form and undergo progressive change through time (Summerfield, 1991). However, despite the way in which the term is often used in the literature (e.g. Hack, 1960), a state of equilibrium may not necessarily imply a steady state but rather a trending mean, and thus the relative usefulness of equilibrium and evolutionary concepts may well depend on the temporal and spatial scales of landscape investigation (Thorn, 1988; Summerfield, 1991; Thorn and Welford, 1994). Therefore, while Davis saw temporal variation as signal and spatial variation as noise, Gilbert may be interpreted to advocate the reverse approach, with spatial variability being primarily a result of the adjustment between structure and process (Thorn, 1988). Disagreement over the relative importance of spatial versus temporal approaches to landscape analysis has long since contributed to the somewhat arbitrary and subjective debate over whether geomorphology should be considered more properly a field of geography or geology, or an independent discipline in its own right (Sparks, 1960; Twidale, 1996).

Davis' theoretical approach to geomorphology initially overshadowed that of Gilbert's, and it became the dominant mode of analysis in the early 20th Century. According to Higgins (1975) this was perhaps due, in part, to the aesthetic appeal of its treatment of time as cyclic, an idea reminiscent of Hutton (1788). However, some early criticisms were presented. A notable early critic was W. Penck, whose work was published in German after his early death in 1923 (Penck, 1924), but unfortunately frequently misunderstood in the anglophone world (e.g. Davis, 1932) and only translated accurately into English many years later (Penck, 1953). Penck (1953) stressed the importance of backwearing over downwearing in landscapes, and attempted to relate landscape morphology to crustal movements. Although he rejected Wegener's (1920) theory of continental drift, he saw slope development as being self-regulatory and dependent on the rate of crustal uplift, an alternative to Davis' (1899) initial assumption of rapid uplift initiating landscape evolution (Penck, 1953).

Penck's (1924) emphasis on the importance of backwearing provided the stimulus for one of Davis' most vocal later critics, L.C. King, who proclaimed that the peneplain should be redefined as an imaginary landform (King, 1953; Thorn, 1988). Unlike

Penck (1953), King (1951; 1967) embraced a cyclic (ironically, essentially Davisian) methodology in his analysis of landscapes, but proposed the theory of pediplanation as an alternative to peneplanation (**Figure 1.4**). Pediplains, defined as plains formed through the parallel recession of scarps and the coalescence of sub-scarp low angle pediments, proved to be particularly useful to King (1951; 1967) as a way of explaining the persistence of relief (and particularly escarpments) in the presumably "old" landscape of southern Africa. He also proposed that an erosion cycle was initiated by isostatic uplift following a threshold amount of denudation (King, 1955), thus incorporating a periodic self-regulatory mechanism into his scheme of landscape evolution.

However, by the mid-20th Century the focus of geomorphological research had shifted towards process-orientated studies, and scepticism over the existence of discrete erosion surfaces had grown (Thorn, 1988). In contrast, Gilbert's (1877) use of a dynamic-equilibrium principle was revisited by Hack (1960; 1975), who proposed that although the inheritance of form is always possible, where a dynamic equilibrium exists between uplift and rock resistance on the one hand, and erosion and relief on the other, variation in the morphology of landscapes could be related to spatial variables such as lithology, i.e. landscapes may be investigated in non-historical terms.

The effects of spatially variable climatic conditions on process have also been emphasised, for example by Büdel's (1963; 1969) climatic approach to geomorphology, although due to changes in climatic conditions over time, this approach acknowledges an historical aspect to landscapes too. In fact, the possible effect of more than one climatic condition on the form of a landscape has lead to some landscapes being described as being of a palimpsest nature (Twidale, 1973). Besides temporal variations in process, the effect of structure on a landscape may also vary over time, resulting in, for instance, superimposed drainage patterns, or the development of terraces upstream of resistant outcrops that are later removed by erosion.

The historical approach of landscape analysis, although revisited on occasion in the southern hemisphere (e.g. Partridge and Maud, 1987), was largely neglected by

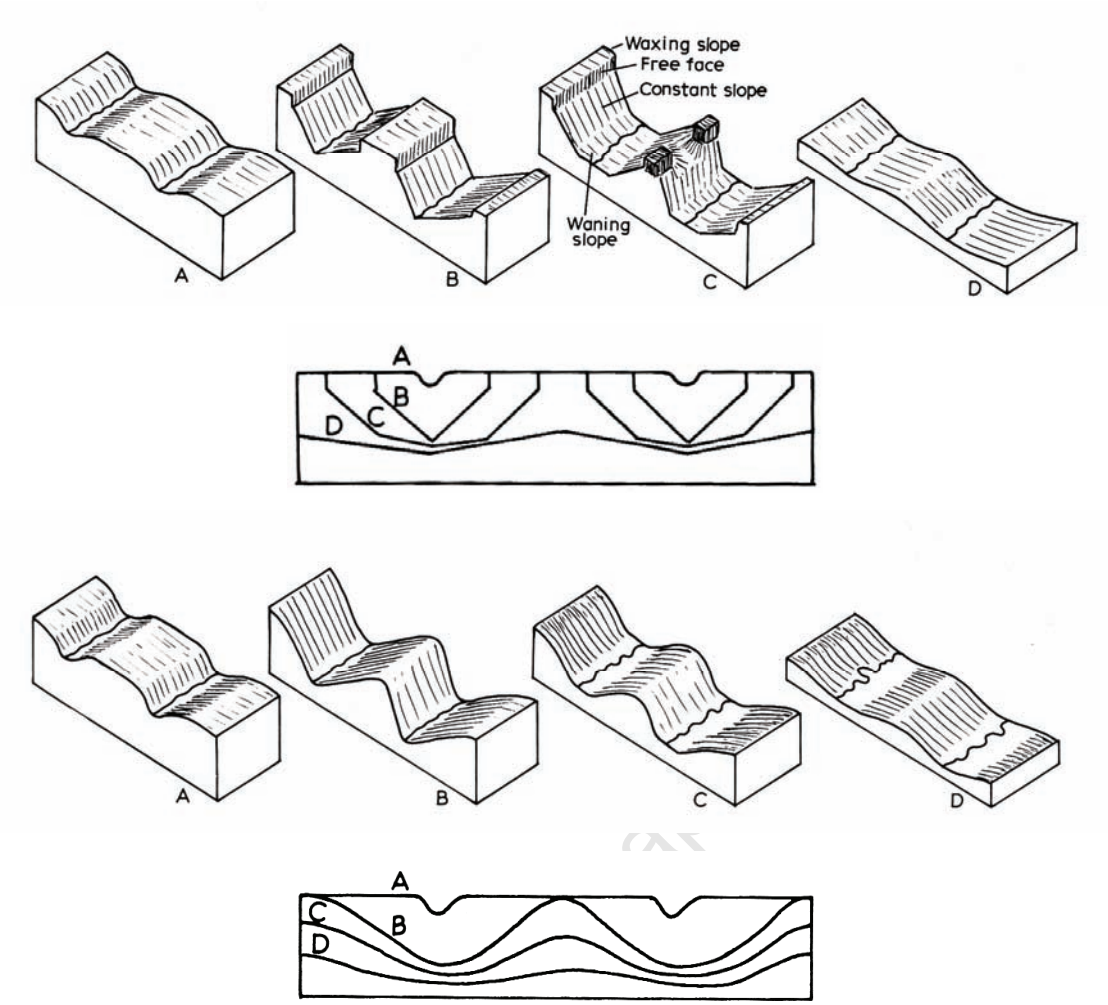

Figure 1.4: Block diagrams and cross-sections representing models for the progressive evolution of landscapes over time (stages A to D), modified from Sawyer (1970) and references therein. King's cycle of pediplanation (above), showing parallel slope recession, is contrasted with Davis' cycle of peneplanation (below), showing slope decline.

geomorphologists for much of the late 20th Century, leading to an emphasis on more readily observable phenomena, i.e. process geomorphology (Summerfield, 2005a). However, during the last two decades, advances in geochronological techniques, particularly fission track thermochronology and cosmogenic nuclide analysis, have revived interest in testing models of denudation chronology (e.g. Fleming *et al*., 1999; Tinker *et al.*, 2008a). Additional stimuli have been provided by the recent availability of high resolution digital elevation data and the greater computing power now available for numerical models that can simulate landscape evolution (Summerfield, 2005b).

In recent times, geomorphology has also been increasingly viewed within an earth systems science context (Murray *et al*., 2009), most notably as the dynamic interface between processes in the solid earth and its fluid envelope. Weathering and erosion play a central role in this regard, and whilst the potential role of silicate weathering in modulating global climate through the capture of atmospheric carbon has long been recognised (Ebelmen, 1845; Urey, 1952; Walker *et al*., 1981), the relative importance of climate and tectonics in controlling long-term silicate weathering rates remains a complex subject of vigorous debate (Raymo and Ruddiman, 1992; Molnar, 2003). For instance, low denudation rates along southern Africa's western coastal margin (the Namib desert) might be due to both a hyper-arid climate and tectonic stability, with aridity being a result of oceanic circulation, and so ultimately a function of tectonic plate configuration (Van der Wateren and Dunai, 2001).

1.3 Aims

The general aim of this thesis is to contribute towards the understanding of landscape development in southern Africa, a region already noted for being important in the development of geomorphological theory (e.g. King, 1951). In the context of the theoretical approaches to geomorphology outlined above, the central conceptual question to be investigated in this study may be phrased as follows:

- To what degree may southern Africa's landscape be described as a function of spatial variation in structure and process, and to what extent does it reflect a history of responses to tectonic events and climatic changes?

Whether or not an equilibrium or evolutionary account of southern Africa's topography is more appropriate is likely to depend on the scale of analysis, as the relaxation time of a landscape (the period required to adjust to change in a system) depends on both the scale and connectivity of the landscape under consideration and the rates of relevant processes (Summerfield, 1991). Here the use of cosmogenic nuclides has the potential to provide a unique perspective. This technique allows for constraints to be placed on the rates of weathering and erosion on time periods of 10^3-10^6 yr, intermediate between shorter periods addressed by process geomorphology and longer periods addressed by denudation thermochronology studies.

In this thesis, an attempt is made to address the following questions with reference to the landscape of southern Africa:

- How did key regional topographic features develop?
- Do cyclic landsurfaces exist (or, is their existence falsifiable)?
- To what degree is topography structurally (lithologically) controlled?
- What are the current rates of weathering and erosion of landforms?
- How and why have erosion rates changed over time?
- Do weathering rates depend on climatic conditions?

At this point, some clarification on the definition of the terms *weathering*, *erosion* and *denudation* is necessary, particularly as these terms have been used ambiguously in the literature. This study follows Sparks (1960) in using the following definitions:

- *Weathering:* Chemical or physical alteration of rock at the surface or subsurface.
- *Erosion:* Removal of rock mass from the surface, whether through physical (mechanical) processes or chemical processes such as dissolution.
- *Denudation:* Synonymous with erosion as defined above.

Although erosion is often defined as the removal of rock through mechanical processes only, and denudation is defined as the combined loss of mass resulting from (physical) erosion and chemical dissolution which accompanies weathering (e.g. von Blanckenburg, 2005), the cosmogenic nuclide literature often refers to denudation rates as erosion rates, and so the definitions above are adopted to avoid confusion. It

should also be noted that for many surfaces, mechanical erosion and chemical weathering may operate in tandem.

1.4 Scope

More specifically, this thesis constitutes an investigation of the geomorphology of Karoo dolerites in southern Africa, a common lithology found across the region. The reasons for this approach are threefold:

- Karoo dolerites are topographically significant. They are commonly assumed to be highly resistant to erosion (e.g. King, 1951), and they define a number of ubiquitous landscape features, including *koppies* (inselbergs) and escarpments.
- Karoo dolerites bear pyroxene minerals which quantitatively retain cosmogenic noble gas nuclides, notably ^{3}He, ^{21}Ne and ^{38}Ar. Noble gas mass spectrometry allows for the abundances of these cosmogenic nuclides to be determined, allowing for quantitative constraints to be placed on the rates of dolerite weathering and erosion.
- Karoo dolerites are found across the southern African region, enabling the spatial comparison of weathering and erosion rates and topography for a relatively uniform lithology across a large, climatically variable region.

In 1899, W.M. Davis wrote:

"Evidently a longer period is required for the complete denudation of a resistant than for that of a weak mass, but no measure in terms of years or centuries can now be given to the period needed for the effective wearing down of highlands to featureless lowlands" (Davis, 1899; in Johnson, 1909, p. 251).

Fortunately, this situation no longer applies. Cosmogenic nuclide analysis allows for the determination of rock denudation rates, although, as will be seen in later chapters, the extrapolation of this data to long timescales (>10^6 yr) remains interpretative.

Emphasis will also be given to the role of Karoo dolerites in determining spatial variability in the southern African landscape, and a quantitative assessment of the elevation and relief of Karoo dolerites in comparison with neighbouring lithologies will be presented. The possibility of spatial variation in Karoo dolerite weathering and

erosion rates will also be investigated, particularly with reference to possible controls on weathering rates for basaltic rocks, which may be important for regulation of the long term carbon cycle.

1.5 Outline

The remainder of this chapter provides a brief account of southern Africa's geology. In the following Chapter 2, an introduction to southern Africa's regional geomorphology is provided by highlighting significant topographic features and presenting a critical review of the relevant literature. Key studies are summarised from the early work of A.L. du Toit and L.C. King to the present day, where denudation thermochronology and cosmogenic nuclide analysis have allowed for re-evaluations of longstanding theories.

Chapter 3 reviews previous studies relevant to the emplacement, weathering and topography of Karoo dolerites. The topography of Karoo dolerites is then assessed with reference to a high resolution (90 m) digital elevation model, and detailed (1:250,000 scale) digital geological maps of select areas in South Africa. A catchment-scale comparison of the mean elevation and relief of Karoo dolerites and neighbouring lithologies explores the expression of Karoo dolerites in the landscape, and whether this may reflect a state of dynamic equilibrium.

Chapter 4 introduces the theory of cosmogenic noble gas nuclide analysis, and discusses the analytical methods employed in this study. The geomorphological context of the samples analysed is then presented in Chapter 5, together with all data relevant to the interpretation of the cosmogenic nuclide abundances.

Chapter 6 presents and evaluates the results of the noble gas analyses. The abundances of the cosmogenic components of the nuclides ^{3}He, ^{21}Ne and ^{38}Ar are determined, and minimum exposure ages and maximum erosion rates are calculated from this data.

In Chapter 7, the significance of minimum exposure ages and maximum erosion rates is dicussed, with particular reference to the various geomorphological processes that may result in the denudation of Karoo dolerite. Various possible influences on

weathering and erosion rates are then investigated. Following this, comparisons between published cosmogenic nuclide data and long-term denudation rate estimates are presented. Finally, soil erosion rate estimates for the 20th Century are discussed from the perspective of cosmogenic nuclide-based rates of soil production.

Chapter 8 presents a summary of the findings of this study with reference to the aims of the thesis presented in Section 1.3. Recommendations for future research and concluding remarks are then presented.

1.6 Geological framework

The general geology of a region may be relevant to its geomorphology in two primary respects. Firstly, geological units provide the substrate from which the landscape is composed, and secondly, the geological history of a region also provides a chronology in which the development of a landscape may be interpreted. In southern Africa, this distinction is to a large degree time-dependent, with the majority of surface rocks pre-dating the break-up of Gondwana in the Mesozoic, and with the uplift and denudation of most topography probably either coincident with or post-dating this important tectonic event. In addition, lithospheric structure may also be important in determining crustal (and thus landscape) responses to tectonic forcing and denudational unloading.

The geological history of southern Africa is summarised in the timeline in **Figure 1.5**, based on the extensive reviews of Tankard *et al.* (1982) and Johnson *et al.* (2006) from which the following synopsis is derived in part. Chronostratigraphic and lithostratigraphic maps of the region's geology are given in **Figures 1.6** and **1.7** respectively.

Southern Africa boasts a rich geological history dating back approximately 3.6 billion years. The Archean crustal rocks of the "Azanian Craton" (joint Kaapvaal and Zimbabwe Cratons; de Wit, M.J., 2007) form the basement geology across north-eastern South Africa, Lesotho, Swaziland, Zimbabwe and eastern Botswana (**Figure 1.8**). This crust is underlain by thickened and chemically depleted subcontinental lithosphere, estimated to be between 140 km and 400 km thick, and bound in the east and south by Palaeoproterozoic and Mesoproterozoic mobile belts and Neoproterozoic

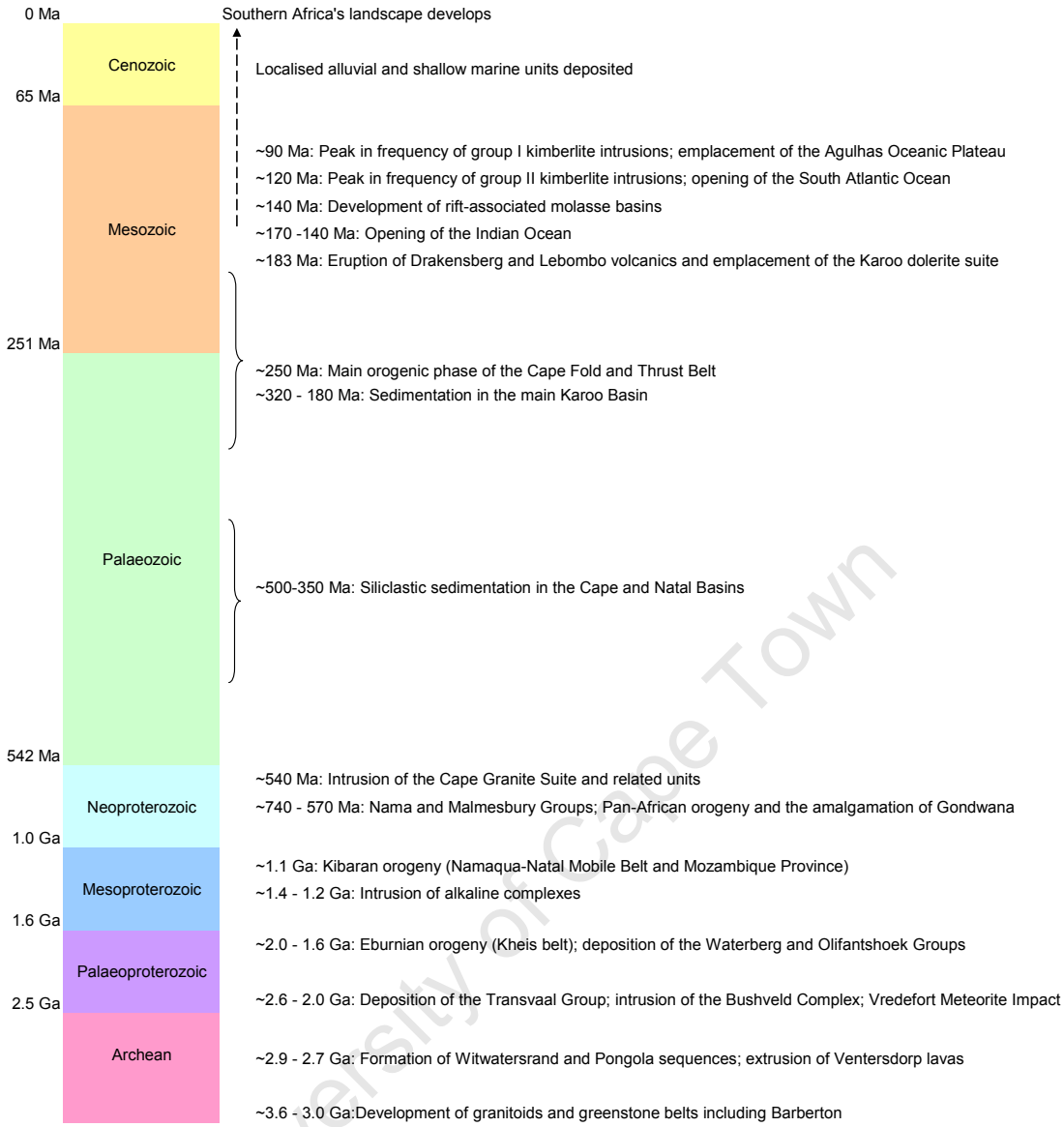

Figure 1.5: Timeline of significant events in the geological history of southern Africa; based on Tankard *et al.* (1982), Johnson *et al.* (2006) and de Wit, M.J. (2007) and references therein, with use of the geochronological divisions of Gradstein *et al.* (2004). Vertical axis is not to scale. The amalgamation and breakup of Gondwana represents the most recent phase of sediment accumulation and subsequent denudation in the long tectonic history of the region.

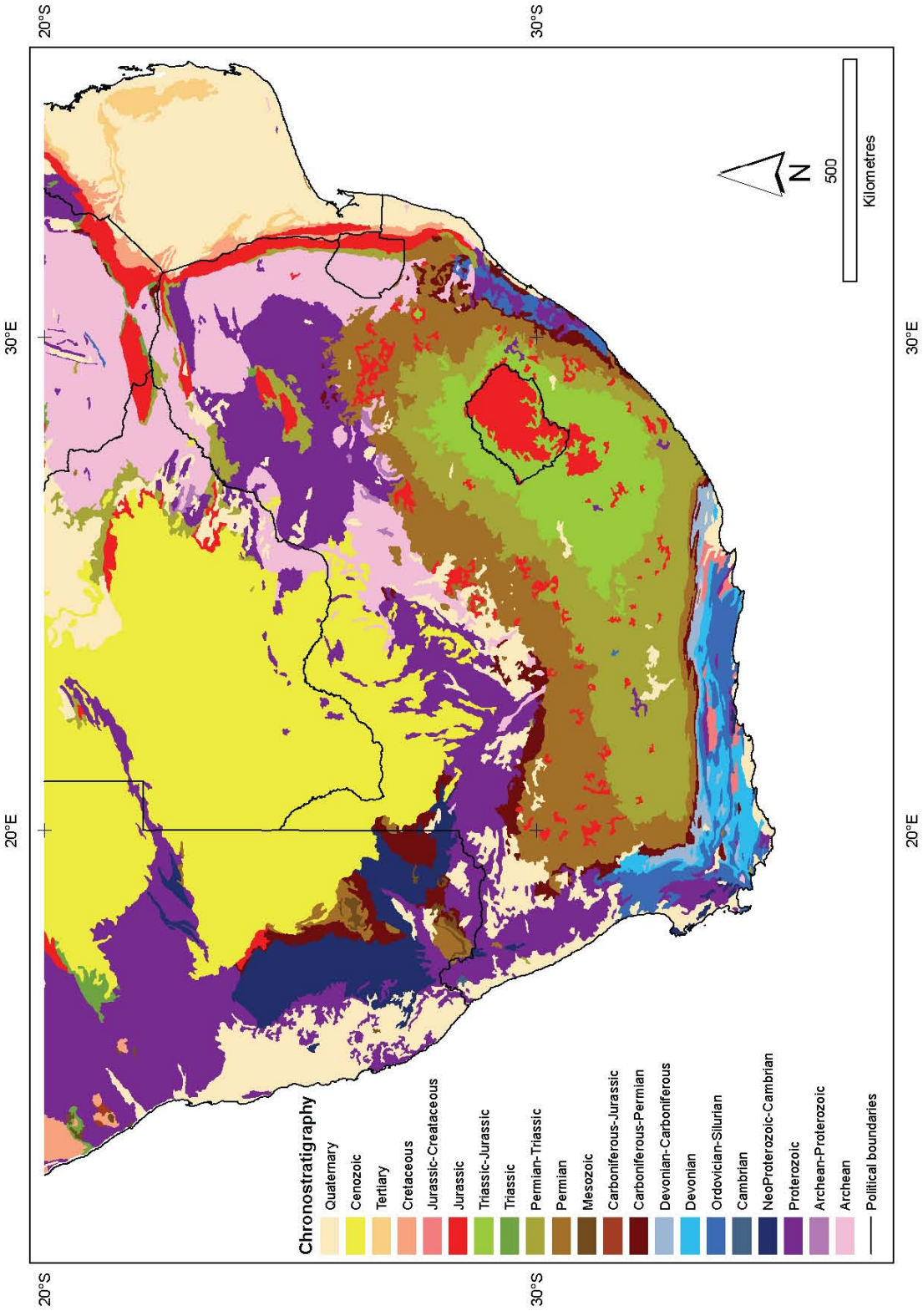

Figure 1.6: Chronostratigraphic map of southern Africa, modified from the 1:5,000,000 International Metallogenic Map of Africa (Veselinovic-Williams and Frost-Killian, 2002), with Jurassic Karoo dolerites modified from the 1:1,000,000 Metallogenic Map of South Africa, Lesotho and Swaziland (Vorster, 2001).

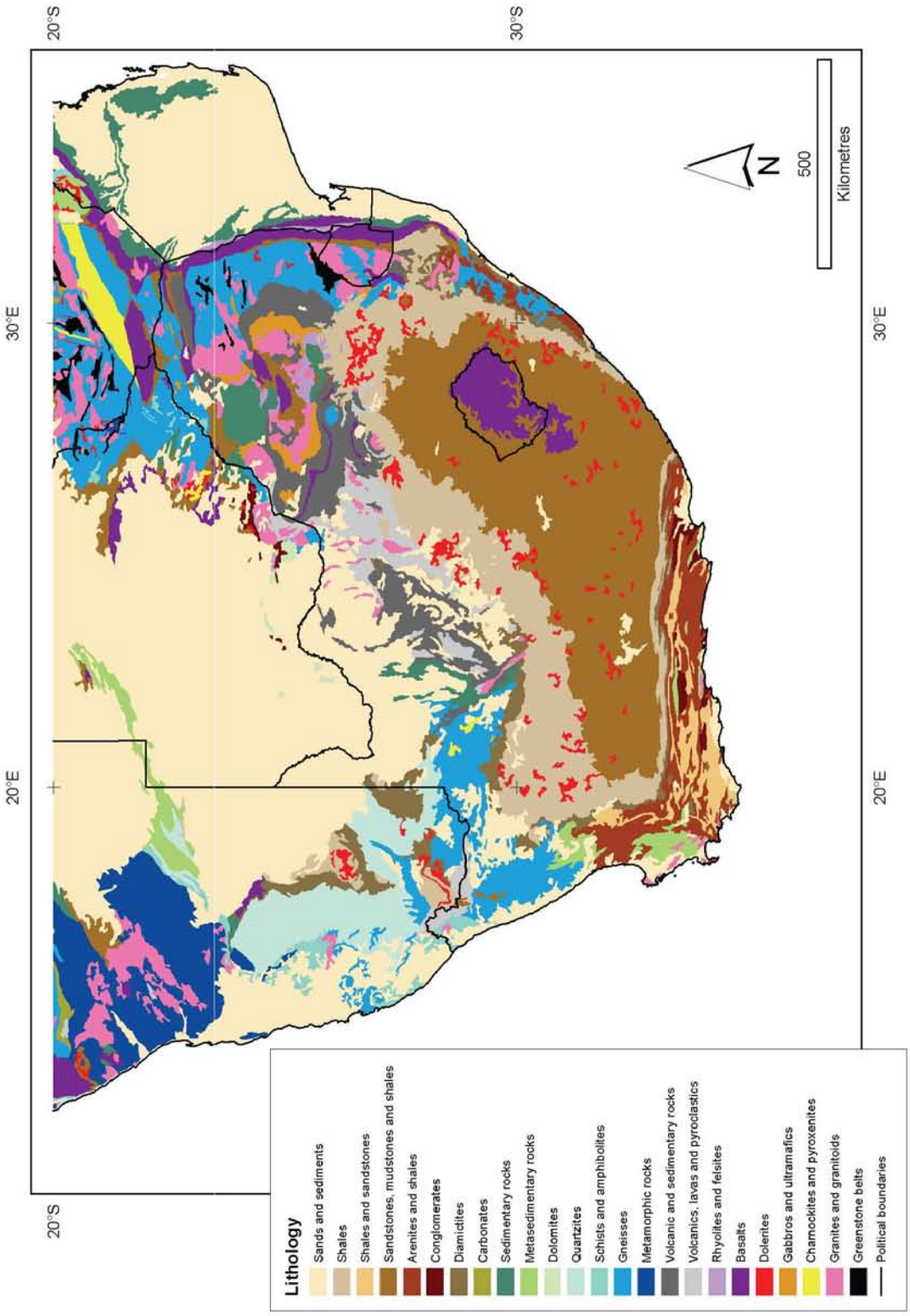

Figure 1.7: Lithological map of southern Africa, compiled from the same sources as in **Figure 1.6**.

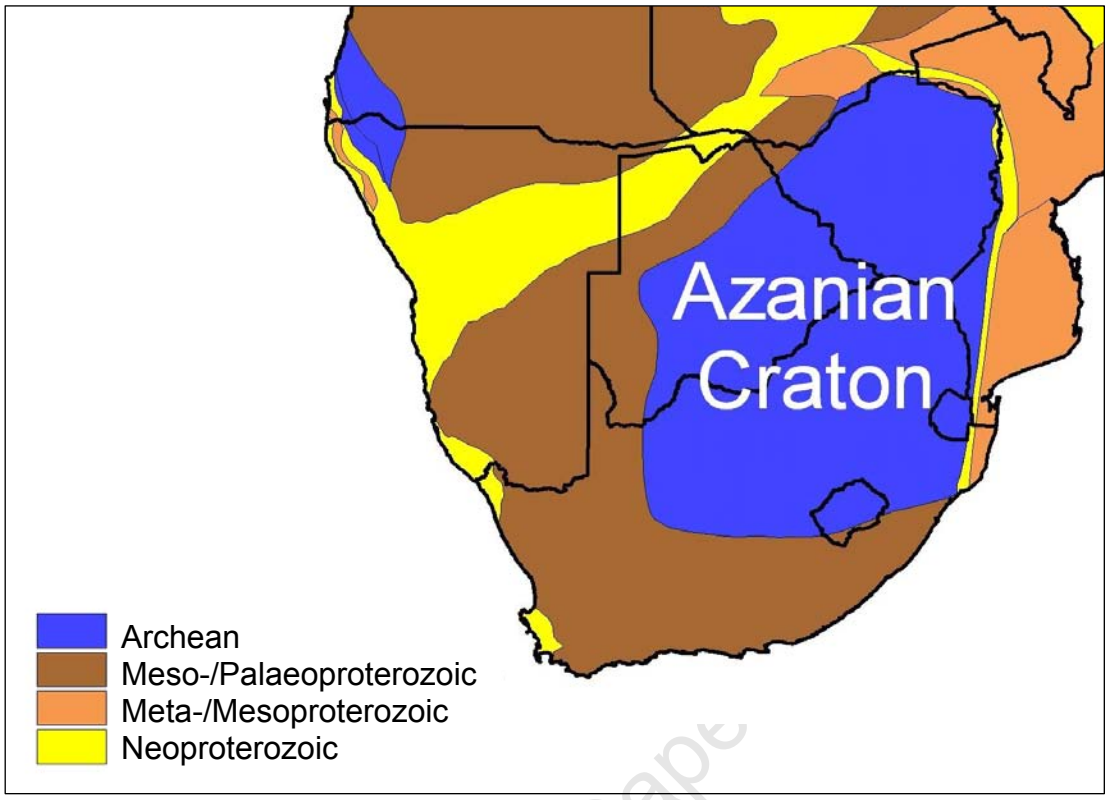

Figure 1.8: Schematic map of southern Africa's tectonic basement, modified from de Wit, M.J. (2007). The Archean Azanian Craton domain (> 2.5 Ga) in the central-eastern region is bound by Palaeo- and Mesoproterozoic mobile belts (2.5-1.0 Ga) and Neoproterozoic (1.0-0.5 Ga) suture zones. Black lines are political boundaries.

suture zones with thinner (< 120 km) lithospheric keels (de Wit, M.J., 2007 and references therein). Neoproterozoic sutures represent the Pan-African orogeny which resulted in the amalgamation of Gondwana and subsequent sedimentation in the supercontinent's interior. The most notable Gondwanan sequences in southern Africa were deposited in the Palaeozoic (Cambrian-Carboniferous) Cape Basin, the siliciclastic sediments of which were deformed during the Cape Orogeny to form the Cape Fold and Thrust Belt in the southern and western regions of South Africa at ~250 Ma, and the Palaeozoic-Mesozoic (Carboniferous-Jurassic) Karoo Basin, the rocks of which now crop out across much of the interior of southern Africa.

Protracted sedimentation in the Karoo Basin from the Carboniferous through to the early Jurassic progressed from glacial deposition to deep marine, shallow marine, alluvial and finally aeolian deposition (Smith *et al*., 1993). However, the magmatism of the Karoo Large Igneous Province at ~183 Ma (Duncan *et al*., 1997) comprising the Drakensberg basalts, Lebombo basalts and rhyolites and Karoo dolerites, signalled the end of sedimentation in the Main Karoo Basin. Later, sediments of the Kalahari Group (possibly Late Cretaceous; Haddon and McCarthy, 2005) began to accumulate over Karoo-aged sediments in the Kalahari Basin to the north of the Main Karoo Basin, although the age, stratigraphy and tectonic setting of this sequence remains poorly understood (B. Linol, personal communication, 2009).

The eruption of the Karoo Large Igneous Province also pre-empted the fragmentation of Gondwana. During the Jurassic, extensional and strike-slip tectonics lead to the development of small syn-rift graben and half-graben basins along southern Africa's south and east coasts (Shone, 2006). The progressive opening of the Indian Ocean at ~170-140 Ma and the opening of the south Atlantic at ~120 Ma (de Wit, M.J., 2007 and references therein), resulted in the establishment of marine sedimentation around southern Africa's margins during the Cretaceous, particularly in the Natal Basin (east coast), Bredasdorp, Pletmos and Algoa Basins (south coast) and Orange Basin (west coast) (Macmillan, 2003; Broad *et al.,* 2006).

The late Jurassic and Cretaceous periods also witnessed an increase in the frequency of kimberlite magmatism, as well as the eruption of the submarine Agulhas Plateau off the southern Africa south coast and the Paraná-Etendeka flood basalts in both

Brazil and Namibia. As will be discussed in the following chapter, it is at this time that thermally-induced uplift of southern Africa might have been initiated (de Wit, M.J., 2007; Tinker *et al*., 2008a), although alternative interpretations suggest that the uplift of the region occurred predominantly during the Tertiary (Burke, 1996). The high topography of southern Africa has probably been generally maintained since then, as Tertiary marine deposits are generally localised and of limited thickness. With the exception of the Kalahari basin, extensive Quaternary marine, alluvial and aeolian cover is limited to the low elevation Mozambique and Namibian coastal plains, with more localised deposition occurring in the interior.

CHAPTER 2: THE GEOMORPHOLOGY OF SOUTHERN AFRICA

2.1 Introduction

The continent of Africa displays an asymmetrical bimodality in topography (**Figure 2.1**). Western and northern Africa is characterised by extensive low-lying plains and isolated mountains, whilst eastern and southern Africa display rugged scarps that surround high plateaux. Whilst eastern Africa's high plateau is associated with Cenozioc volcanism and active rift systems, suggesting impingement of a mantle plume (e.g. Ebinger and Sleep, 1998), major rifting and volcanism in southern Africa dates back to the Mesozoic, and the origin of southern Africa's present-day high topography remains controversial (de Wit, M.J., 2007). This chapter provides an introduction to the regional geomorphology of southern Africa, and reviews the relevant literature on the subject.

2.2 Regional topography and drainage

The topography of southern Africa is illustrated in **Figure 2.2**, and the drainage of the region is shown in **Figure 2.3**. An elevation frequency curve for this region, based on the data in **Figure 2.2**, reflects a major mode of elevation at approximately 1000 m (**Figure 2.4**), reflecting southern Africa's extensive elevated interior plateau.

The plateau is drained principally by the large, westward-draining Orange River basin and is separated from the lower-lying coastal regions by a narrow region of high relief known as the Great Escarpment or, alternatively, as the escarpment zone. The exact position of this important topographic feature can sometimes be ill-defined, and although roughly parallel to the coastline, it is also characterised by a number of coast-facing 'embayments'. Parts of the southern African plateau may be referred to as the Karoo (the semi-arid southwest), the Highveld (the more humid east), and the Kalahari (the arid central region of especially low relief). The most mountainous region in southern Africa is the Drakensberg mountainland or Lesotho Highlands, encompassing the Kingdom of Lesotho and coinciding with the extent of the Drakensberg basalts (~183 Ma; Duncan *et al*., 1997), the eastern-most boundary of which defines the southeast (Drakensberg) escarpment.

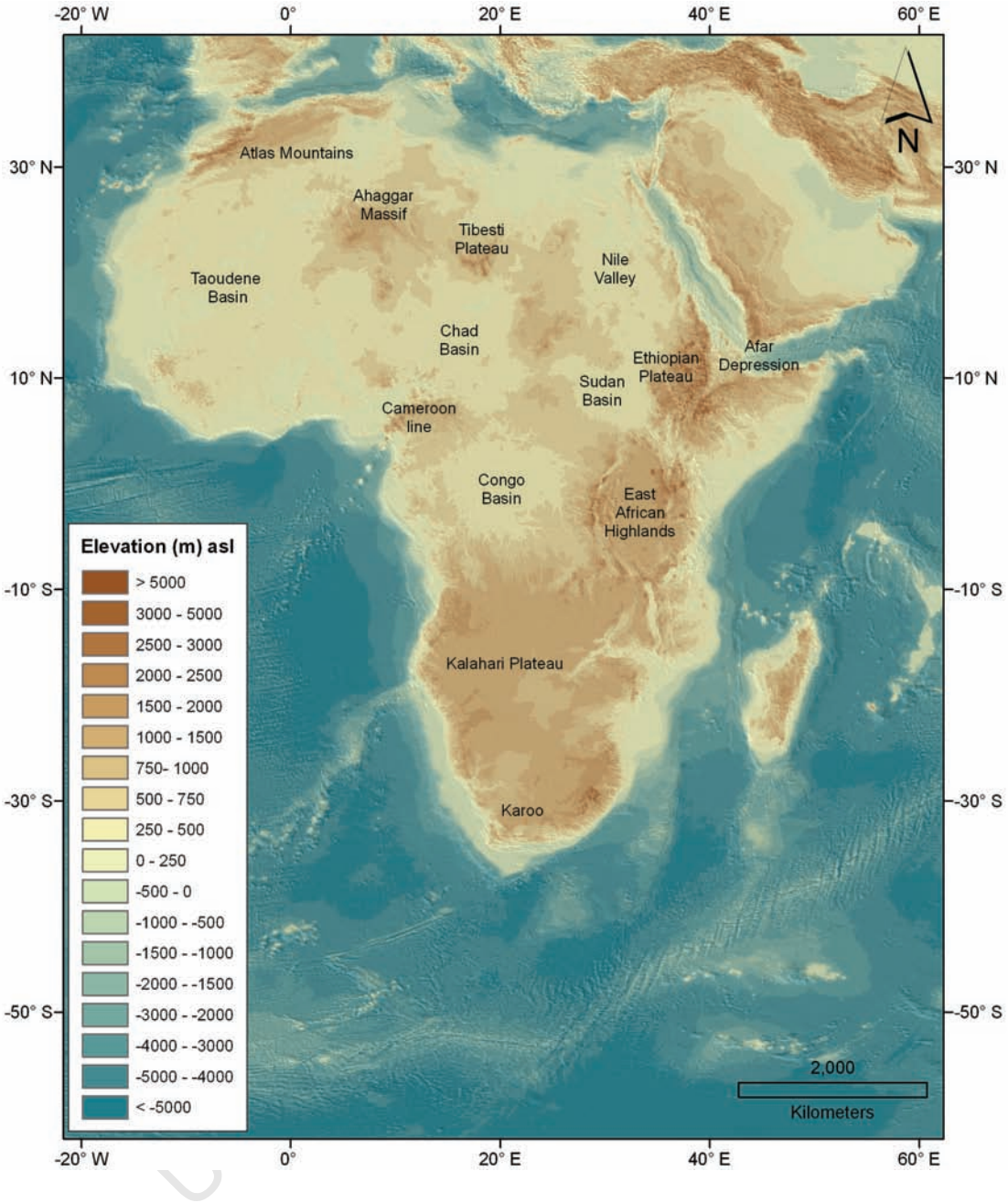

Figure 2.1: The topography of Africa and the bathymetry of the surrounding oceans relative to sea level, rendered from the 2 arc-minute (≤ 3.7 km) resolution ETOPO2 digital elevation dataset (U.S. Department of Commerce, National Oceanic and Atmospheric Administration, National Geophysical Data Center, 2001). Note the high elevation of the southern African region.

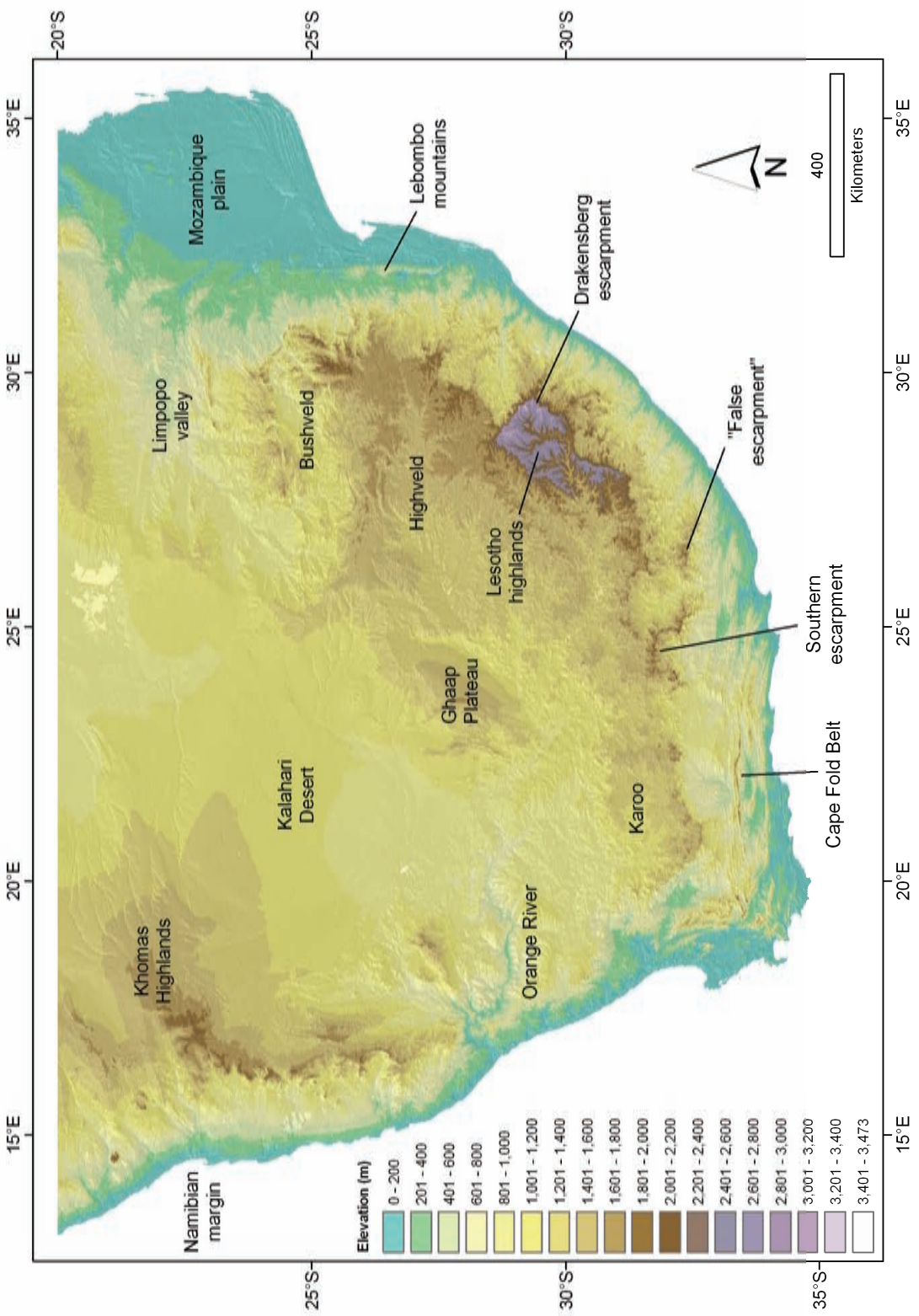

Figure 2.2: The topography of Africa south of 20ºS. Elevation given here and elsewhere is from a processed version the SRTM 3 arc-second (~90 m) resolution digital elevation model dataset (Jarvis *et al*., 2006) unless otherwise stated. The locations of key topographic features in the region are indicated.

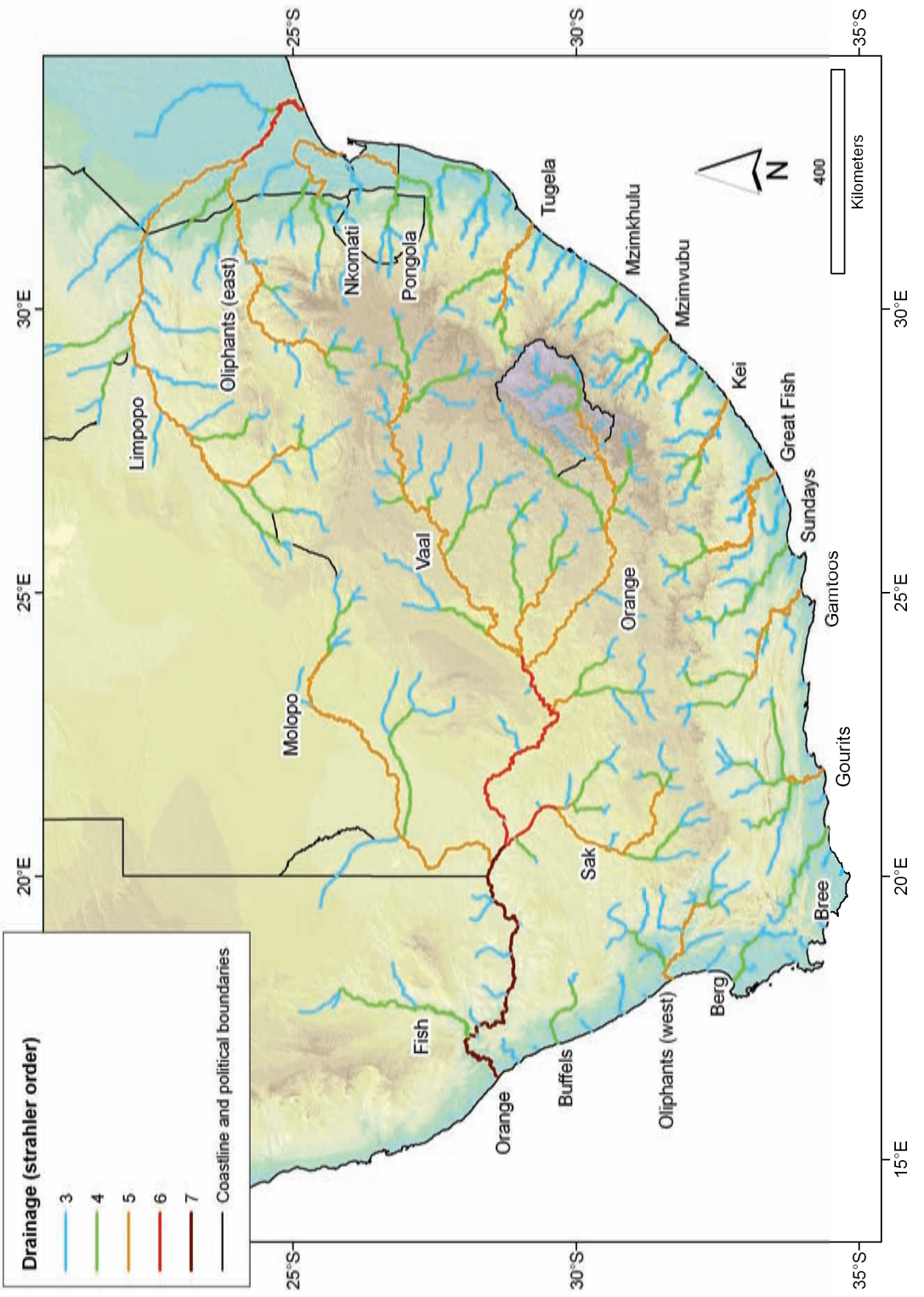

Figure 2.3: The drainage of southern Africa. Drainage shown here and elsewhere is compiled from the AEON digital database and from data downloaded from the S.A. Department of Water Affairs and Forestry: www.dwaf.gov.za. Rivers (both perennial and non-perennial) with Strahler stream orders ≥ 3 are shown.

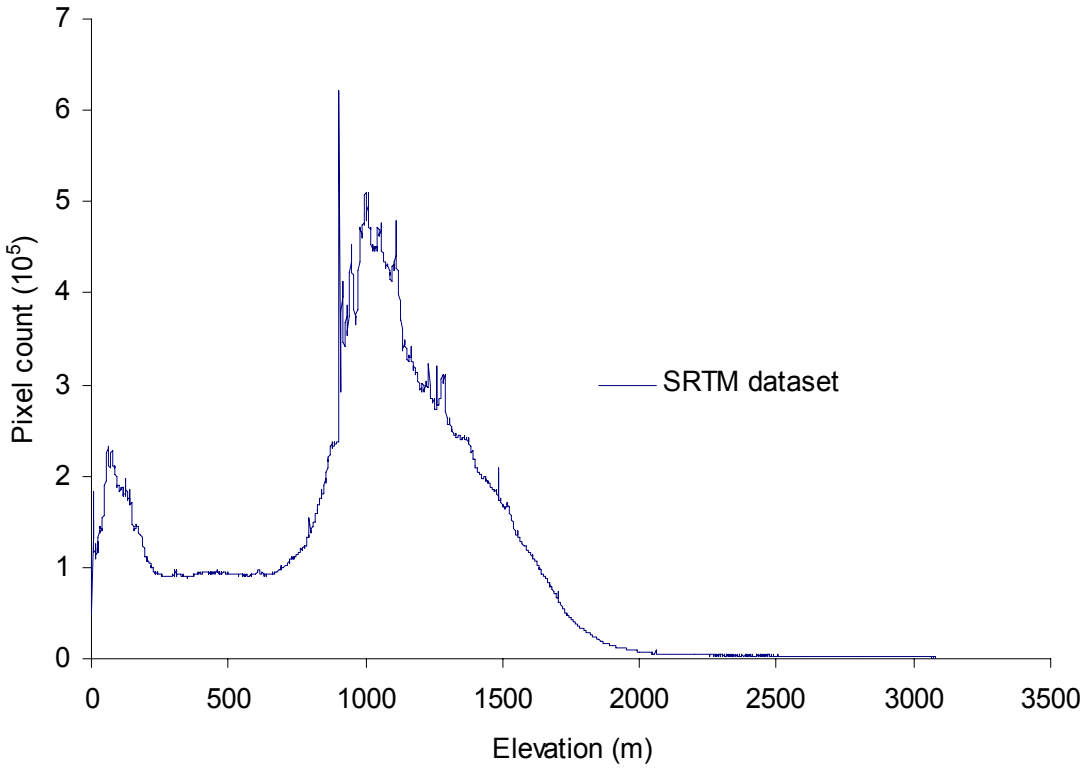

Figure 2.4: Frequency distribution for integer elevation values in the SRTM digital elevation model in **Figure 2.2**. Elevation displays a bimodal distribution, with the dominant mode of elevation at approximately 1000 m, representing southern Africa's interior plateau. Significant single value spikes represent waterbodies.

A visual comparison of topography and the extent of Karoo dolerite outcrop reveals that the southern escarpment is largely coincident with the southerly extent of the Karoo dolerites (**Figure 2.5**). However, in places along the southern escarpment, the position of the Orange River drainage divide – the boundary between coastal and interior drainage – does not always coincide with the zone of highest relief defined by the Karoo dolerites. At the eastern end of the southern escarpment zone, in the region of the Sundays, Great Fish and Kei rivers, a second or "false" escarpment south of the Orange River drainage divide forms where the outcrop of Karoo dolerites extends towards the coastline, whilst the Orange River drainage divide migrates inland (**Figure 2.6**). This "false escarpment" is in fact the drainage divide between southward-flowing tributaries of the Sundays and Great Fish rivers, and the north-flowing tributaries of the Great Fish and Kei rivers, which eventually reverse their courses and flow towards the south coast. The "true" escarpment, on the other hand, is defined by a coastward facing embayment. This configuration of drainage and topography may be interpreted as evidence of one or more of the following scenarios:

- Headward erosion of the escarpment by the Great Fish River;
- Piracy (or capture) of plateau (formerly Orange) drainage by the Great Fish and Kei rivers, meaning that the "false escarpment" defines the former position of the escarpment;
- Superimposition of former drainage on the exhumed pattern of dolerite outcrop, resulting in discordant drainage (see further discussion of discordant drainage below).

A speculative model depicting the possible enlargement of the Great Fish and Kei river catchments over time through headward erosion and river capture is illustrated in **Figure 2.6**. King (1951) regarded the headwaters of the Great Fish as representing plateau drainage, presumably implying that part of the "false escarpment" denoted in **Figure 2.6** is in fact the Great Escarpment (true escarpment), yet he also remarked that the area does not reflect a "simple" river capture (King, 1951; p. 264). A more convincing example of stream piracy is provided by the Slang River, a westward-flowing plateau tributary of the coastward-draining Tugela River that was presumably captured from the Vaal/Orange drainage system (King, 1951; **Figure 2.7**). Stream piracy is obvious here because there is little evidence of post-capture escarpment

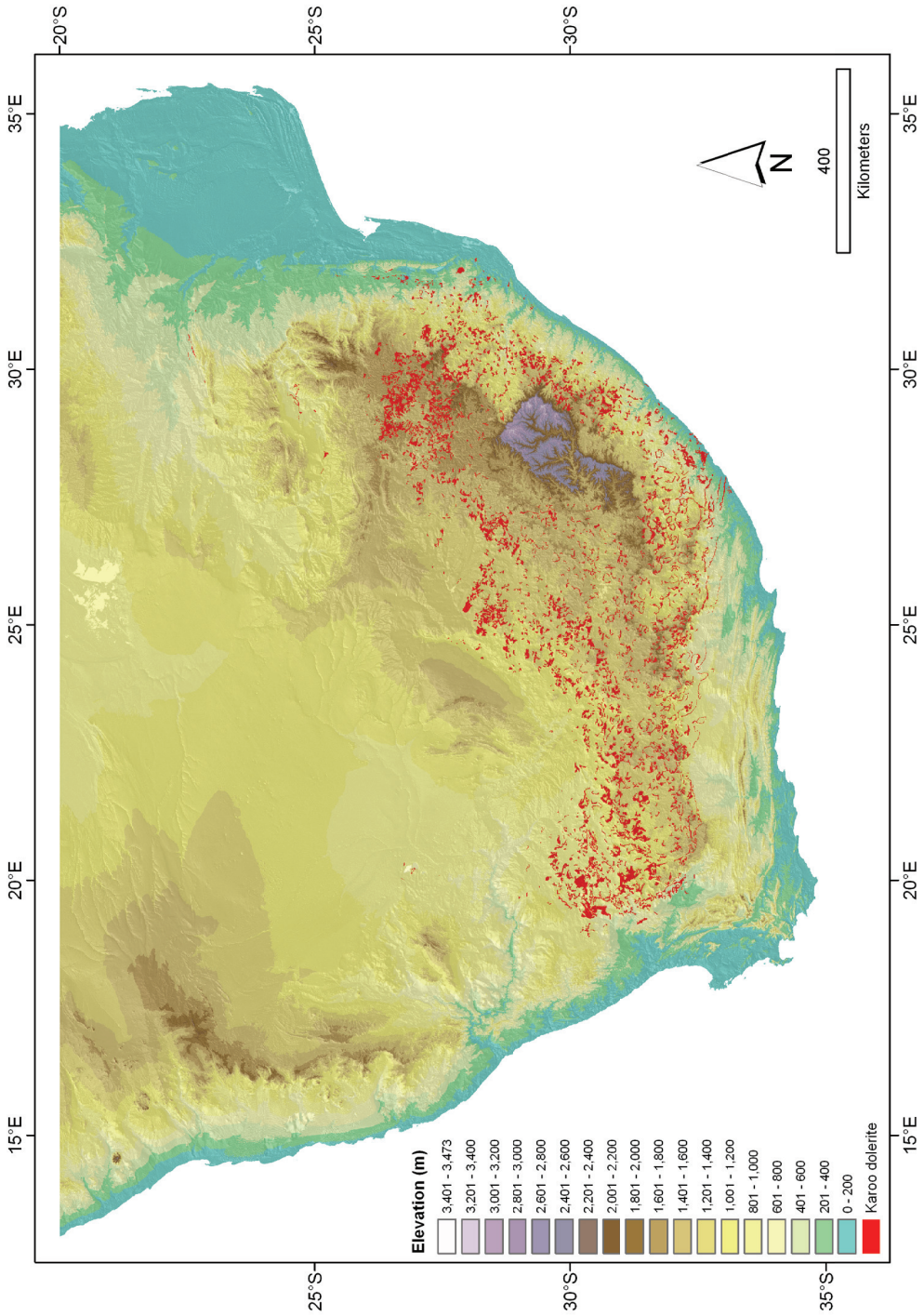

Figure 2.5: The elevation of southern Africa and the distribution of Karoo dolerite outcrop in southern Africa. The southern limit of Karoo dolerite outcrop coincides with much of the southern escarpment, although these features diverge as the Karoo dolerite limit is followed towards the southeast coast, resulting in semi-parallel "true" (drainage divide defined) and "false" (dolerite outcrop controlled) escarpments (see also **Figure 2.6**).

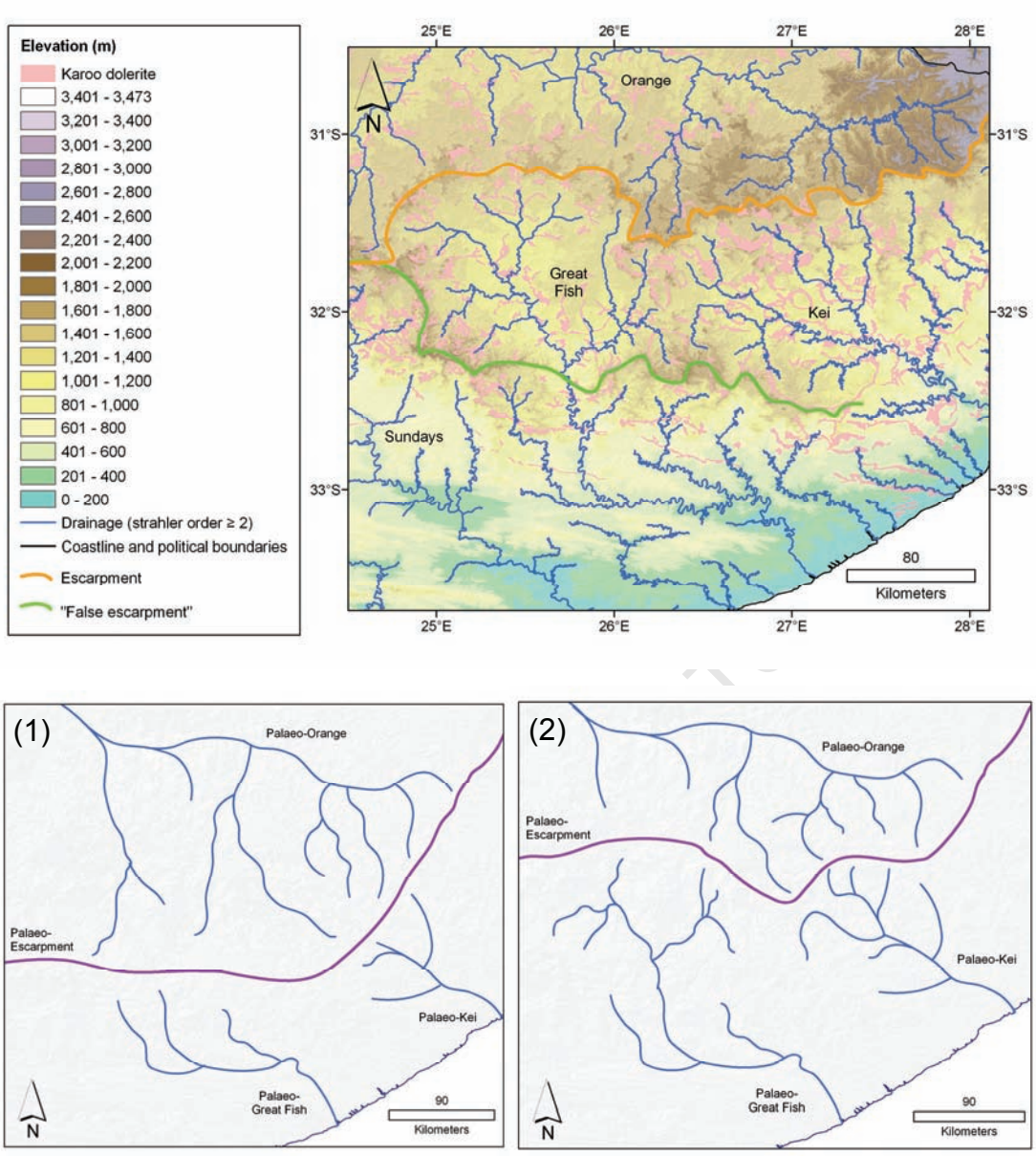

Figure 2.6: Top: The "false escarpment" (green line), defined approximately by the southern limit of Karoo dolerite outcrop (pale pink), south of the "true escarpment" (orange line), defined by the drainage divide between interior and coastal drainage. The "false escarpment" also forms the drainage divide between coastward flowing tributaries of the Sundays and Great Fish rivers, and the northward-flowing tributaries of the Great Fish and Kei rivers. Below: Schematic illustration of a possible model for development of drainage, where an initial escarpment (1) migrates inland (2), following headward erosion or drainage capture by coastal rivers, and finally resulting in the present configuration (top). Thus the "false escarpment" might represent the former divide between coastal and inland drainage.

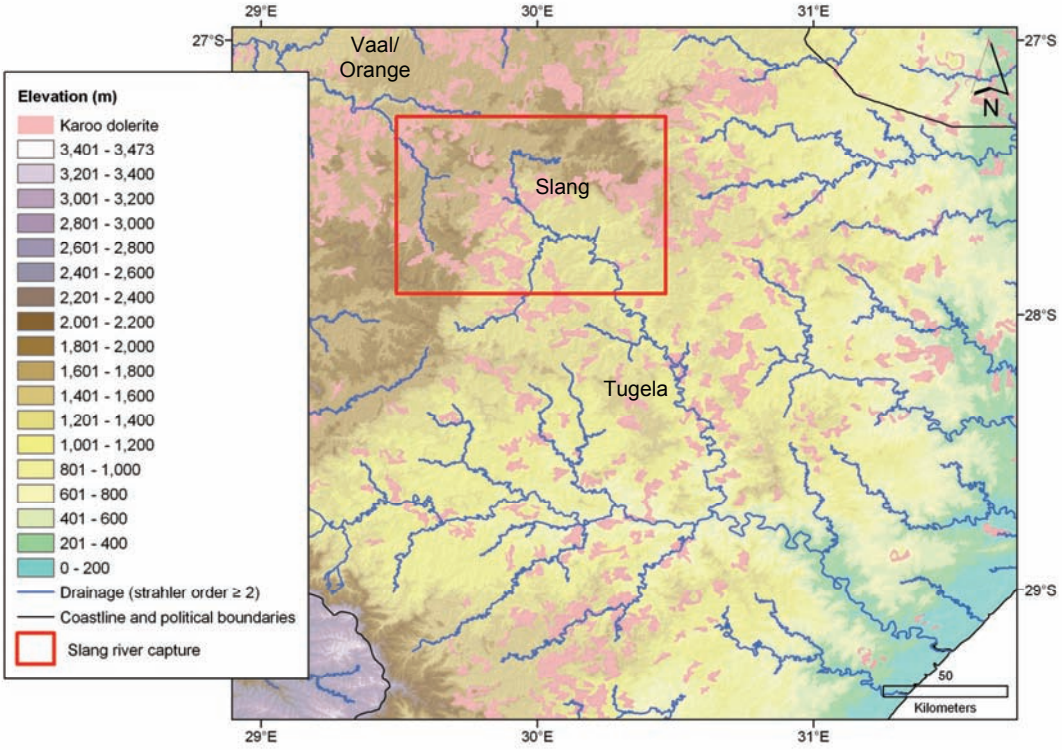

Figure 2.7: Probable drainage capture of the plateau's Slang River (presumably a former tributary of the interior Vaal/Orange river) across the escarpment by a tributary of the coastward-draining Tugela River. The extent of Karoo dolerite outcrop is also shown.

modification, although the strike of the escarpment in this region is distinctly irregular. On a larger scale, the modern outlet of the Orange River basin also has been interpreted to be the result of stream piracy by a coastal river that dissects the escarpment (e.g. de Wit, M.C.J., 1993). However, Partridge and Maud (1987) suggest that dissection of the escarpment by the Limpopo River may instead be due to the river's course predating uplift of the escarpment (i.e. antecedence).

Two significant mountain ranges occur seawards of southern Africa's escarpment:

1) The east-west striking southern limb of the Cape Fold Belt Mountains, defined by the erosionally resistant Palaeozoic quartz arenites of the Cape Supergroup that were folded and thrusted during the Cape Orogeny in the Permo-Triassic (Newton *et al*., 2006); and
2) The north-south striking Lebombo mountains, defined by the rhyolites of the Lebombo Suite of the ~183 Ma (Duncan *et al*., 1997) Karoo Large Igneous Province, erupted along the Lebombo monocline. Whether the Lebombo represents a failed rift pre-empting the onset of true rifting by some 30 Ma, or the true rift margin between Africa and Antarctica, has long remained a subject of debate (e.g. du Toit, 1929; Cox, 1992; Watkeys, 2006; Klausen, 2009).

Interestingly, major rivers that drain the eastern and southern escarpments display discordant drainage patterns where trunk streams cross these linear, coast-parallel mountain ranges, although the positions of tributaries may be structurally controlled and flow along the strike of these ranges (Stankiewicz, 2004; **Figure 2.8**). These trunk streams also display incised meanders, which characterise much of the drainage of southern Africa's eastern and southern coastal zones.

Given the control that underlying geology usually exercises on drainage patterns (e.g. Horton, 1945), drainage that does not reflect the structure of the rocks over which it flows may be termed discordant or transverse drainage, and may result from:

1) Superimposition (or inheritance) of drainage (**Figure 2.9**) from a former plain or from an unconformable cover of rocks which have since been removed through erosion;

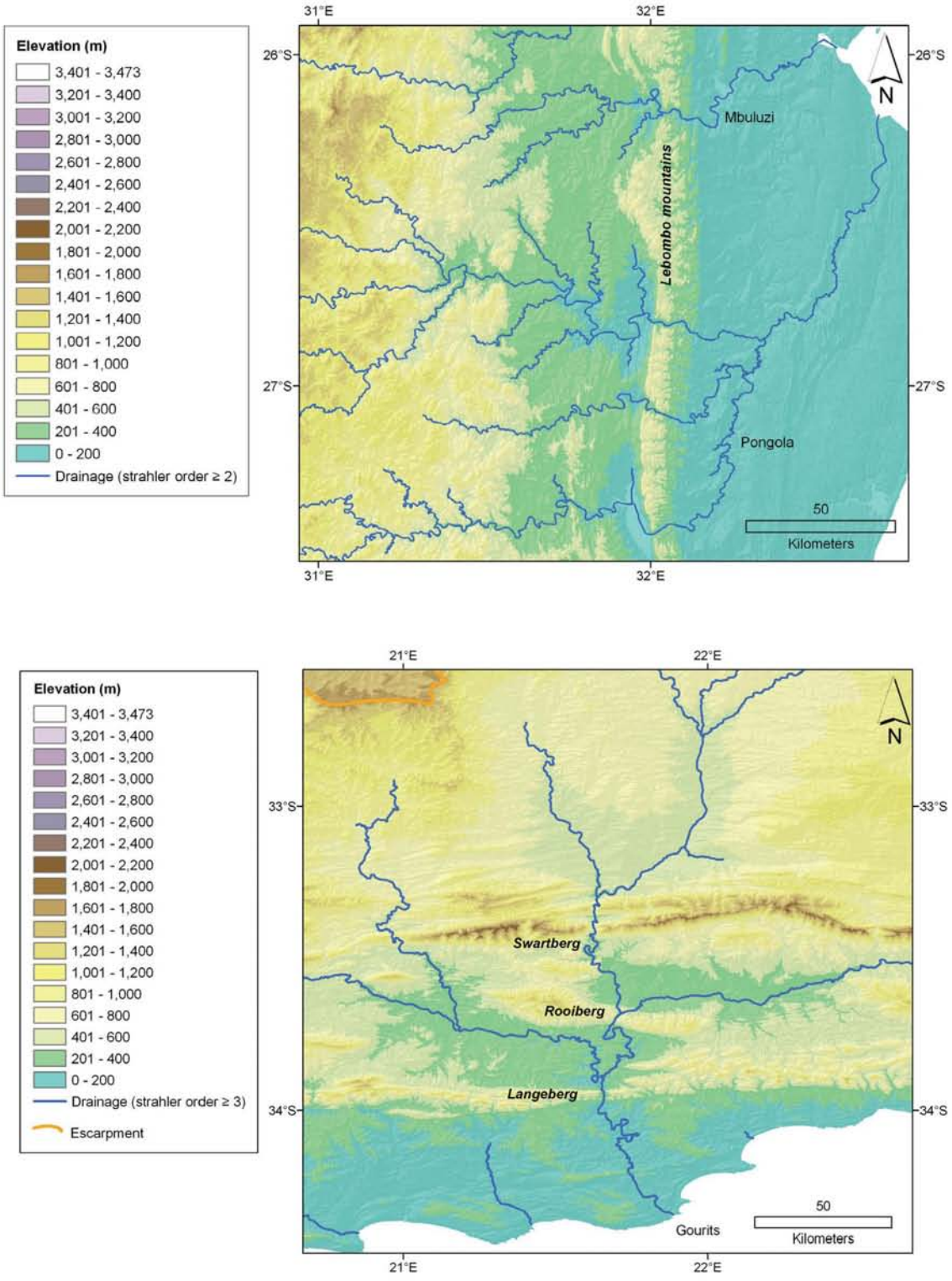

Figure 2.8: Examples of discordant coastal drainage across the Lebombo (Pongola and Mbuluzi rivers, above) and Cape Fold Belt mountain ranges of the Swartberg, Rooiberg and Langeberg (Gourits River, below).

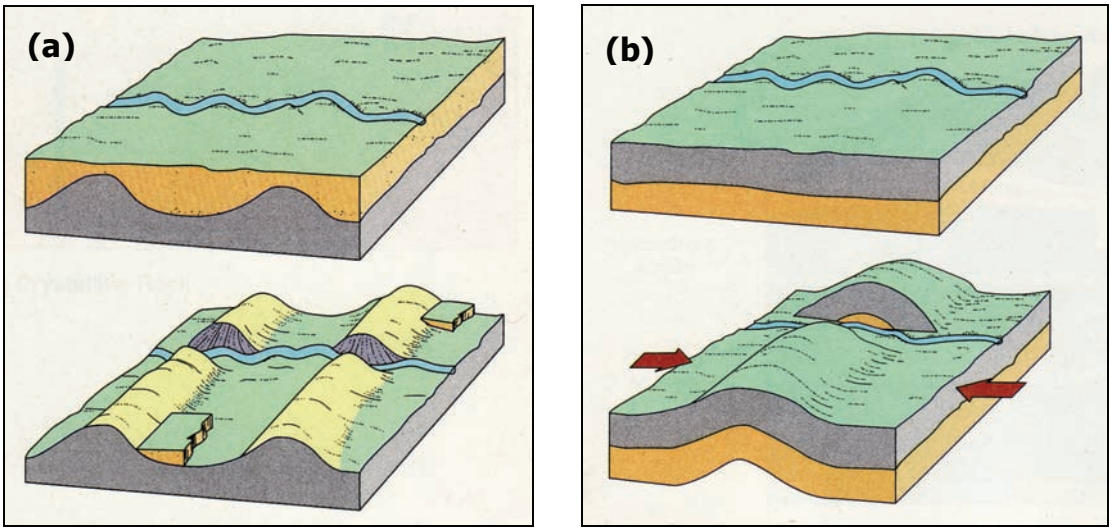

Figure 2.9: Block diagrams illustrating the development of (a) superimposed drainage and (b) antecedent drainage, modified from Plummer and McGeary (1996).

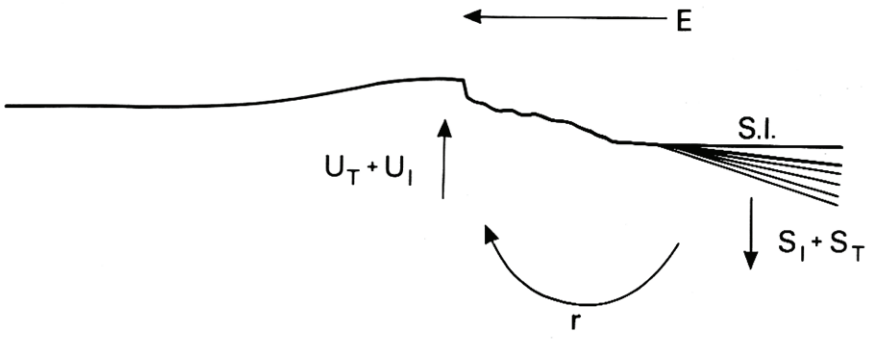

Figure 2.10: Sketch of factors that may influence the evolution of an escarpment and extensional continental margin, from Summerfield (1991): U_T = thermally-driven uplift; U_I = isostatic uplift associated with denudational unloading, S_T = thermally driven subsidence, S_I = isostatic subsidence associated with sediment loading, E = erosion through escarpment retreat. An extensional continental margin might therefore experience some rotation (r) due to the combination of U_I and S_I. S.l. denotes sea level.

2) Antecedence (**Figure 2.9**), where a stream maintains its course despite crustal displacement, such as where a rising fold crosses its path;
3) Overflow, where a ponded lake behind a ridge over-spills at the lowest point, resulting in incision of the ridge; or
4) Piracy by drainage at a lower base level (e.g. Sparks, 1960; Plummer and McGeary, 1996; Douglass and Schmeeckle, 2007).

For the Lebombo and Cape Fold Belt, (1) suggests that simple denudational exhumation of the erosionally resistant rhyolites and quartz arenite lithologies occurred, (2) suggests that flexural or local isostatic uplift occurred along the strike of these ranges and (3) and (4) suggest that incision of meandering courses resulted from the breaching of downstream resistant lithologies. Note that Partridge *et al*. (2010) interpret the discordant drainage across the Lebombo as superimposed drainage, inherited from a formerly continuous ("African") pediplanation surface (see Section 2.4.1). However, these same authors interpret the discordant drainage across the Cape Fold Belt as antecedent drainage dating from even before the onset of the Cape Orogeny in the Permian-Triassic (Partridge *et al*., 2010). Moreover, most coastal drainage, including the discordant drainage across the Cape Fold Belt, flows perpendicularly to the strike of the roughly coast-parallel Great Escarpment. Thus it is the interpretation of the present author that this incised drainage does not pre-date Gondwana rifting and escarpment formation.

In summary, if the above interpretations are accepted, a basic sequence of events may be inferred for the development of southern Africa's topography:

- An initial coast-parallel drainage divide or proto-escarpment developed gradually or rapidly, during or after, Gondwana rifting at ~140-120 Ma;
- Subsequent to the establishment of this coastward-flowing escarpment drainage, discrete or continuous drainage incision occurred as a result of local or regional drop(s) in relative base level, and at least minor modification of the escarpment's position occurred through the capture of interior drainage.

Clearly, drainage patterns may well record the topographic evolution of an area, but an unambiguous interpretation based on a visual appraisal of their form remains

elusive. This generalised account of regional landscape evolution in southern Africa, based on a first-order interpretation of topography and drainage, may be considered as a starting point for investigating the topographic evolution of the region. Most models of landscape evolution in southern Africa are generally consistent with this (admittedly imprecise) sequence of events, but differ from each other significantly concerning the timing, rates and mechanisms of uplift and erosion that are involved (e.g. Partridge and Maud, 1987; van der Beek *et al.*, 2002).

2.3 Geodynamics

2.3.1 Origin of the escarpment

Escarpments are characteristic of extensional continental margins throughout the world (e.g. southern Africa, southeast Australia, western India, eastern Madagascar, the Red Sea), suggesting that these regional topographic features date from the time of extensional tectonics, although escarpments are also notably absent from some other extensional continental margins (e.g. Argentina, South Australia; Gallagher and Brown, R., 1999). For young rifts such as the post-Eocene Gulf of Suez, broadly uplifted rift flanks of over 1000 m in elevation have been interpreted to be a result of small-scale mantle convection induced by large horizontal heat gradients following lithospheric thinning (Steckler, 1985). A "permanent" state of uplift may result from plastic necking (regional isostatic compensation of the thinned lithosphere; Braun and Beaumont, 1989), although the maintenance of this relief in response to denudation would require further isostatic compensation (Gilchrist and Summerfield, 1990).

In contrast, Burke (1996) and Burke and Gunnell (2008) propose that the southern African escarpment is unrelated to continental rifting, but is rather a result of a topographic swell developing at ~30 Ma when Africa apparently came to "rest" with respect to the lithospheric mantle. Whilst this model of mid-Tertiary uplift and denudation is apparently inconsistent with the results of a number of recent denudation thermochronology studies from the region (Sections 2.4.2 and 2.5 below), a number of processes may potentially alter an extensional margin escarpment. These processes include escarpment retreat through erosion, thermally-driven uplift and subsidence, onshore isostatic uplift due to denudational unloading, and offshore isostatic subsidence due to sediment loading (**Figure 2.10**; Summerfield, 1991). A full appraisal of these factors is necessary if it is to be determined whether the

southern African escarpment has been maintained in a statistically-invariant form (i.e. a steady state) since the time of lithospheric extension, whether it has decayed in equilibrium with the processes acting upon it, or whether it records a history of responses to punctuated geodynamic forcing.

2.3.2 Isostasy

The potential role of isostasy in maintaining the topography of southern Africa has long been recognised. For example, du Toit (1933) viewed the anomalously high topography of southern Africa as being "simply and convincingly the results of unloading under erosion, uncomplicated by other disturbing influences" (du Toit, 1933; p. 4). Isostatic responses have also been important to the development of cyclic landsurface models in southern Africa. For instance, King (1951; 1955) proposed that regional isostatic uplift would follow a threshold amount of denudation, and would result in a new cycle of scarp retreat and pediplanation.

However, according to Gilchrist and Summerfield (1991), isostatic responses to lithospheric loading occur effectively continuously with a period of ~10^4-10^5 yr, unlike the typical timescale of ~10^7 yr envisaged by King (1951; 1955). This continuous isostatic response was incorporated into the model of Gilchrist and Summerfield (1990), who proposed that scarp retreat from an initial high relief margin may result in an isostatic upwarp that is eroded due to its high relief. Here the relief is maintained due to isostatic rebound, and so a continuing focus of erosion results in retreat of the scarp (Gilchrist and Summerfield, 1990). Van der Beek *et al*. (2002) note that the only unequivocal evidence of uplift in the region, Late Cretaceous-Eocene marine sediments at elevations of up to 400 m in the onshore Algoa Basin along the southern coast, may be explained as a result of isostatic uplift if eustatic sea level variations are also taken into account.

2.3.3 Tectonics, far-field effects and thermal epeirogeny

Southern Africa is not associated with any convergent tectonic plate boundaries. This eliminates orogeny as a direct contributing factor towards southern Africa's high elevation, and contrasts southern Africa with most other plateau regions on Earth, such as the Tibetan Plateau and the Andean Cordillera, which are associated with orogenic belts. In fact, more than 90 % of the African Plate's tectonic boundary is

extensional, with the exception of a northern convergent plate boundary between Eurasia and Africa (Doucouré and de Wit, M.J., 2003). If horizontal stresses have had any notable effect on the uplift of southern Africa, this is likely to have been principally a result of far-field effects, perhaps where a slowing of plate motion resulting from the collision of Africa and Eurasia may have had an effect on the thermal balance between the African lithosphere and its underlying mantle (e.g. Burke, 1996, de Wit, M.J. 2007). Indeed some post-rifting adjustment of the African crust is necessary if a tight tectonic fit between Africa and South America is to be achieved (de Wit, M.J. *et al*., 2008).

Whether or not thermally-induced epeirogenic uplift in southern Africa is related to horizontal plate motions is uncertain, but a direct role played by mantle dynamics in the uplift of the region seems plausible. Nyblade and Robinson (1994) demonstrated that the anomalous topography of southern and eastern Africa is contiguous with a broad swell in offshore bathymetry. They named this anomalous feature the "African Superswell", and related it to a high in the African-Atlantic geoid, and a low seismic velocity zone - interpreted to signify elevated temperatures or chemical differences - in the asthenospheric mantle (Nyblade and Robinson, 1994).

The period for which this anomalous velocity zone has persisted is unknown, but if this zone does represent a significant thermal anomaly or mantle "superplume", associated buoyancy forces may be invoked. Partridge (1998) used this anomaly to account for a proposed phase of extensive uplift in southern Africa during the Neogene (see Section 2.4.1), and interpreted it to represent the progressive southward migration of the East African Rift into southern Africa. However, more detailed recent studies (Stankiewicz *et al*., 2002; Montelli *et al*., 2006) have indicated that the upper mantle beneath southern Africa is not anomalously warm at present. This suggests that heat transfer is not presently responsible for southern Africa's high elevation; instead, heat may be convecting laterally from the low-mid mantle beneath Southern Africa to the upper mantle beneath East Africa (de Wit, M.J., 2007).

When, then, did southern Africa attain its high elevation? Reconstruction of Cretaceous topography suggests that southern Africa was already anomalously high at this time (Doucouré and de Wit, M.J., 2003). Whilst absolute palaeoelevations of a

continental surface are difficult to determine (England and Molnar, 1990), the denudational history of a region provides a useful starting point for inferring its topographic history. To this end, fission track thermochronology and cosmogenic nuclide studies have been particularly useful in providing quantitative estimates of denudation rates over time.

2.4 Denudation chronology

2.4.1 Cyclic erosion surfaces and relative dating

Early attempts at defining a denudation chronology for southern Africa (e.g. King, 1951) were made through the identification and correlation of erosion surfaces formed during pediplanation cycles. Correlation of these surfaces across the region was performed on the basis of relative elevation, and the assignment of ages was based on inferred correlations between subaerially exposed landsurfaces and basal unconformities beneath dated sediments. Because planar surfaces were interpreted to have developed through progressive backwearing (scarp retreat), the ages of correlated surfaces were presumed to be diachronous, and where surface deposits were present, these deposits indicated a minimum age for the surface at that point (e.g. King, 1951; **Figure 2.11**). The names given to these surfaces referred to their time of *initiation*. For instance, the "African" surface referred to the proposed initiation of an extensive erosion surface post-dating the rifting of Gondwana and the birth of the African continent in the Cretaceous. It may be noted that the rifting of Gondwana occurred over a lengthly period, with the opening of the Indian Ocean at ~170-140 Ma, the opening of the Atlantic Ocean at ~130-120 Ma and the final separation of the Falkland Plateau from Africa along a strike-slip southern margin at ~100-90 Ma (de Wit, M.J., 2007 and references therein).

L.C. King correlated erosion surfaces not only across southern Africa, but across the continent and even globally (King, 1967; **Figure 2.12**), leading to his eventual rejection of the modern plate tectonic synthesis in favour of an expanding earth hypothesis (King, 1983). However, a revision of King's cyclic erosion surface model for southern Africa was presented by Partridge and Maud (1987), who followed King's pediplanation-based approach of correlating erosion surfaces on the basis of relative elevation. This correlation was performed relative to the local elevation of the oldest surface, the "African surface". The "African surface", in turn, was correlated

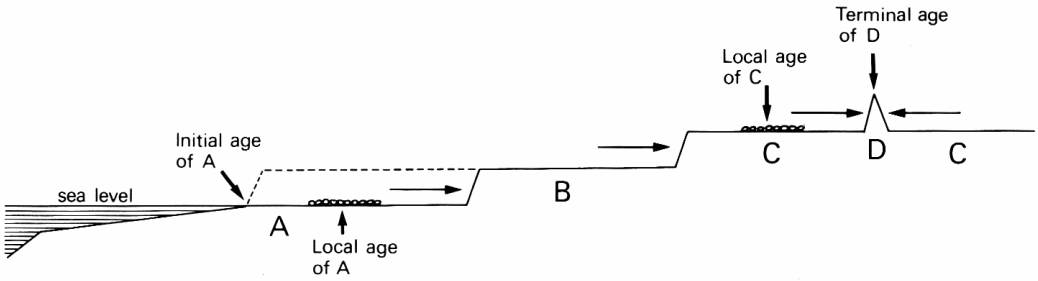

Figure 2.11: Diagrammatic representation of diachronous age relations for L.C. King's cyclic pediplanation surfaces, after Summerfield (1991). A cyclic surface's initial age represents the age of base level fall, following which scarp retreat inland occurs (e.g. surface A). As a result, the initial ages for the surfaces above increase with elevation, i.e. D > C > B > A. The local age for a surface is the age of the surface where an overlying sedimentary deposit gives a minimum age constraint (e.g. for surfaces A and C), and is younger that the initial age of the surface. Eventual complete removal of a surface (D) through the growth of a younger surface represents the older surface's terminal age.

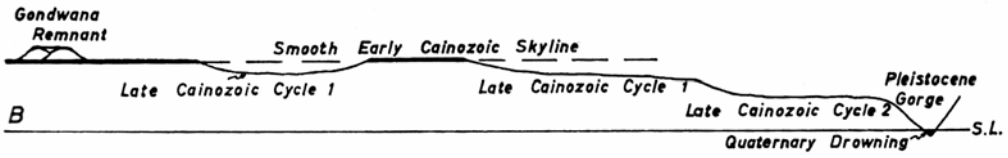

Figure 2.12: King's (1967) diagrammatic profile of world cyclic denudational landscapes, based on a global correlation of landscapes with that of southern Africa.

primarily on the basis of "diagnostic" deep kaolinisation (Partridge and Maud, 1987), as it was presumed that this surface had been deformed after extensive pediplanation had occurred.

Partridge and Maud (1987) recognised three major erosion surfaces formed through scarp retreat: the "African" (Cretaceous and younger), the "Post-African" (early Miocene and younger) and the "Post-African II" (late Pliocene and younger; **Figure 2.13**). These three surfaces were proposed to have been initiated by the rifting of southern Africa during Gondwana break-up, an uplift event of 150-300 m in the early Miocene, and an uplift event of <100-900 m at the end of the Pliocene (Partridge and Maud, 1987, although Cowling *et al*. (2009) place the second uplift event in the late Miocene). The maximum magnitude of these latter uplift events was proposed to have taken place along an axis approximately 75-175 km inland of the southern and eastern coasts, resulting in deformation of earlier surfaces, tilting of the subcontinent down in the west, and incision of drainage in the southern and eastern coastal regions (Partridge and Maud, 1987). Interestingly, an increase in topographic heterogeneity resulting from the proposed uplift event in the early Miocene has been invoked as the driving mechanism behind the exceptional radiation of plant diversity in the Cape Floristic Region that is thought to have occurred at this time (Cowling *et al*., 2009).

The details of erosion surface recognition and correlation in southern Africa, as well as the general validity of the cyclic approach to denudation chronology, have long been debated (e.g. Wellington, 1955; de Swardt and Bennet, 1974; 1976; King, 1976; Summerfield, 1985; Brown, R.W. *et al*., 2000). More recently, Mielke (2009) demonstrated that the cyclic erosion surfaces of Partridge and Maud (1987) in the southern Cape region could not be delineated by using an automated classification of quantitative morphometric parameters derived from remotely-sensed topography. (Note that Partridge *et al*. (2010) reported morphometric parameters for geomorphic 'provinces' in southern Africa, but that these provinces do not correspond with proposed planation surfaces. Instead, Partridge *et al*.'s (2010) provinces were delineated for use in biodiversity conservation studies, and were modified from similar provinces defined by King (1967) on the basis of "expert judgement.")

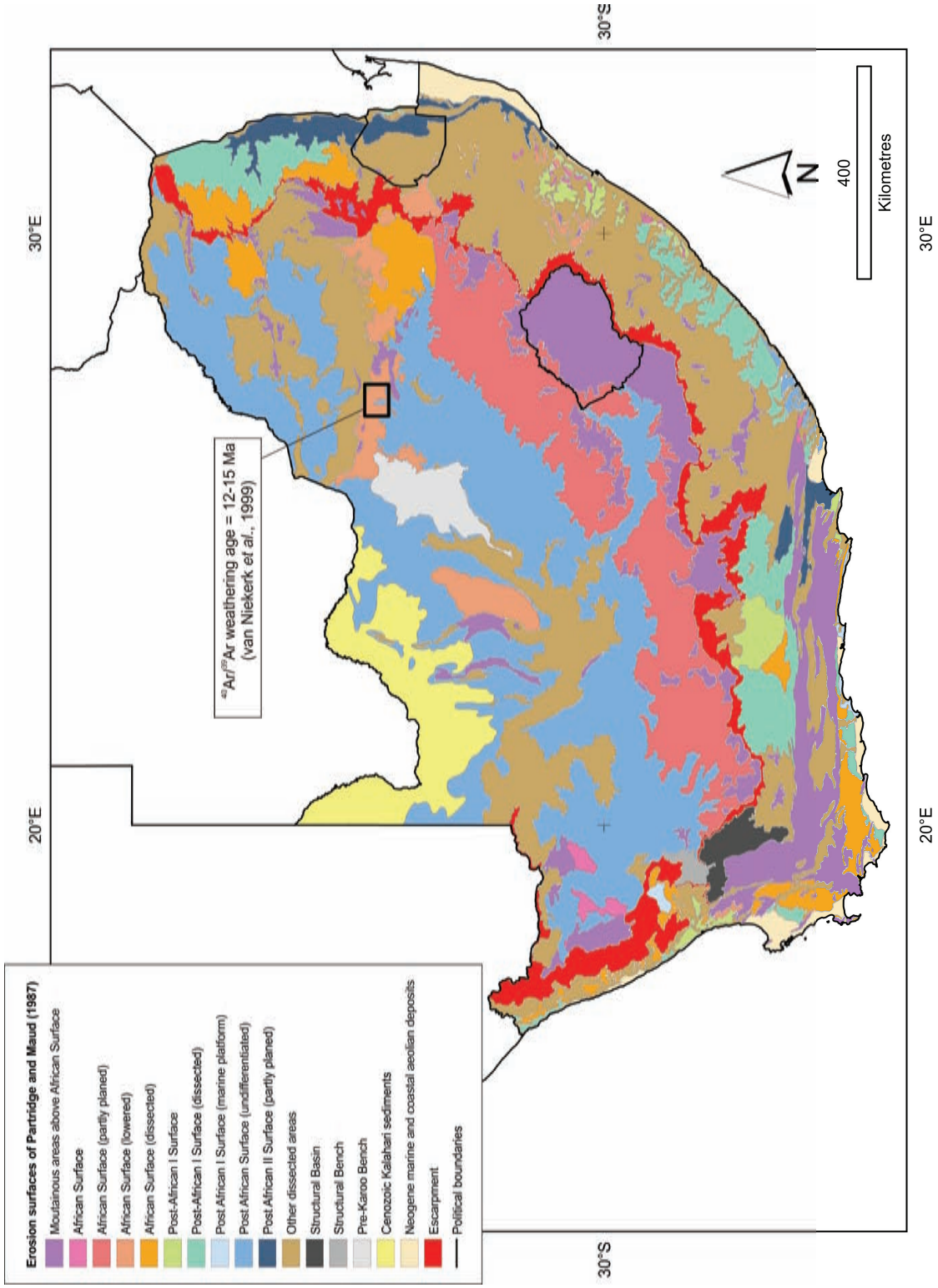

Figure 2.13: Partridge and Maud's (1987) erosion surfaces for South Africa, Lesotho and Swaziland (map based on GIS data digitised from the original by C. Mielke). The location of van Niekerk *et al.*'s (1999) $^{40}Ar/^{39}Ar$ cryptomelane age for a duricrust correlated with the Post-African I erosion surface is also shown.

As mentioned above, Partridge and Maud (1987) noted the potential shortcomings of correlating surfaces on the basis of altitude alone, and preferred the use of weathering profiles as a correlative tool for the "African surface". Indeed, accordant summit heights, sometimes used to infer the existence of a former, dissected plain, may merely reflect the development of uniform slopes in a region of uniformly spaced drainage (the Gipfelflur hypothesis; Sparks, 1960; **Figure 2.14**). Unfortunately, Partridge and Maud's (1987) correlation of the "African surface" on the basis of deep weathering is not necessarily any more robust, because the argument that such weathering is diagnostic of this surface is circular. There seems little reason to presuppose that the development of a deep weathering profile should necessarily relate to a single cycle of planation (e.g. Brown, R.W. *et al*., 2000). On the other hand, van Niekerk *et al*. (1999) determined an $^{40}Ar/^{39}Ar$ age of 12-15 Ma for cryptomelane (K-Mn oxyhydroxide) samples from a pedogenic manganese crust in a saprolite developed below a surface assigned by Partridge and Maud (1987) to the "Post-African I" cycle (**Figure 2.13**). This weathering mineral age is at least consistent with the corresponding erosion surface's proposed Miocene age of initiation, although more work on supergene mineral geochronology is needed from across the region.

As a further criticism, inferring long wavelength deformation of a reconstructed erosion surface presupposes an original horizontality for which no evidence exists, and infers the existence of a flexural axis about which crustal deformation may occur. The existence of flexural axes in southern Africa is debatable, although they have long been invoked, for example, to explain the position of drainage divides (du Toit, 1933; Pretorius, 1973; Partridge and Maud, 1987; Moore, 1999; **Figure 2.15**). In a recent study, de Wit, M.C.J. *et al*. (2009) reported that Cretaceous palaeo-current directions for alluvial gravels on the Ghaap Plateau (north central South Africa, **Figure 2.2**) were towards the northwest, and consistent with the flow directions of modern drainage. This new sedimentological data is contrary to the southeastwards palaeoflow direction proposed by Partridge (1998), and negates the need to infer axial uplift in this region in order to generate drainage reversal, as proposed, for example, by Moore (1999). Another possible point of contention is the proposed origin of the east-to-west asymmetry in the elevation of southern Africa's plateau, which might not be a result of westward-tilting, as proposed by Partridge and Maud (1987). Instead,

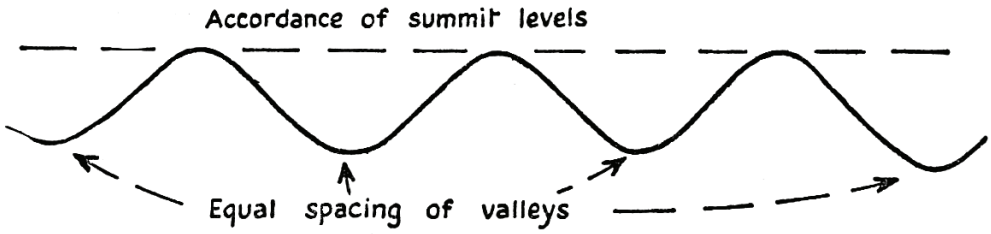

Figure 2.14: Sketch demonstrating the Gipfelflur hypothesis of accordant summits, from Sparks (1960) based on Baulig (1952). Here uniform summit heights are a result of uniform slopes (due to constant mass shear strength in a lithologically homogeneous area) and uniform stream spacing, as is common, for example, in areas of trellis drainage in the Drakensberg Escarpment or in the Cape Fold Belt (Stankiewicz, 2004). In this case, the accordance of summit heights may not be used to infer the existence of a dissected erosion surface.

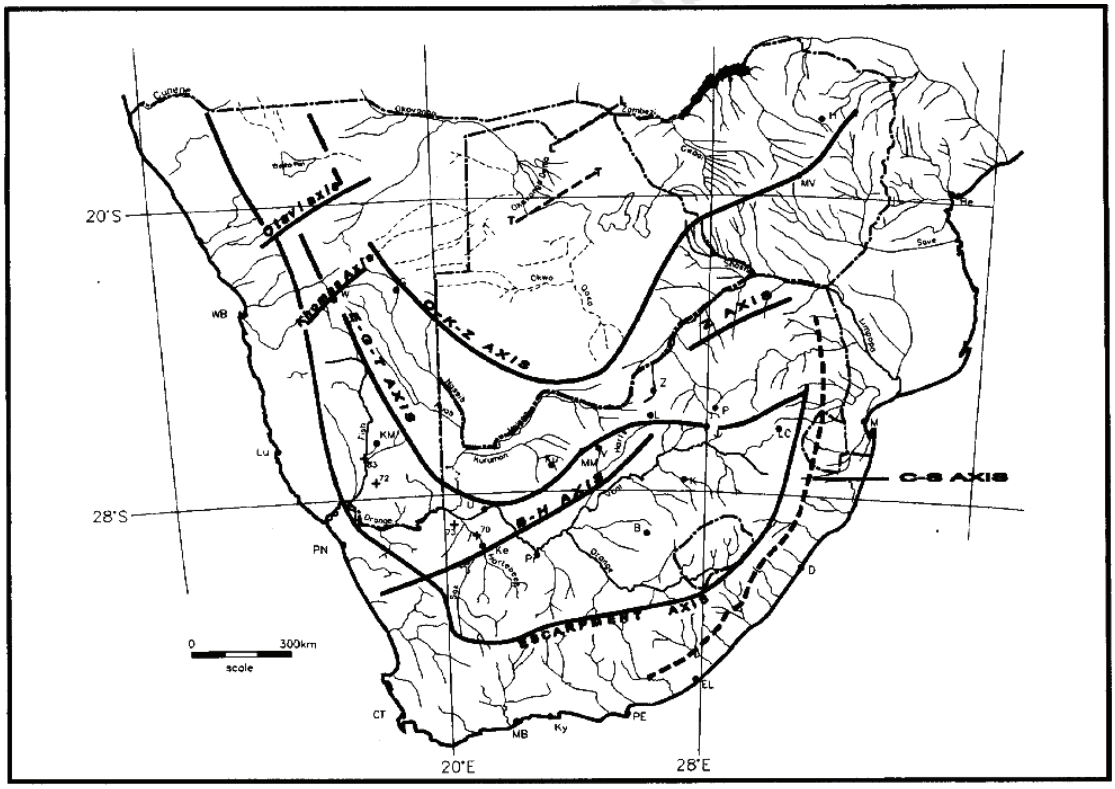

Figure 2.15: Moore's (1999) hypothetical axes of epeirogenic flexure, revised from those proposed by du Toit (1933).

this may simply reflect the development of a concave-upward long-profile for the westward-draining Orange River basin since the birth of southern Africa (> 100 Ma).

Relating planar surfaces at various elevations to palaeo-sea level is also problematic. It ignores, for example, the possibility that surface erosion down to local, structurally-controlled base levels may be more dominant. Römer (2010) demonstrated that, for southern Zimbabwe, multivariate statistic analysis of morphometric parameters indicates a strong association between lithology and terrain types. Also, numerical modelling suggests that lithological controls are likely to exert a long-term impediment to the continuous transmission of base level change through a landscape, meaning that the vertical separation of surfaces cannot be used to infer episodic tectonic displacements (Römer, 2010). Furthermore, some planation surfaces may in fact be older, exhumed surfaces, i.e. unconformities exposed at the surface due to the erosion of overlying rocks. For instance, de Wit, M.J. (2007) noted that an Archean erosion surface that cuts across granite-greenstone basement rocks crops out in a number of places across the Azanian Craton, due to stripping of the overlying marine carbonates and quartzites at the base of the ~2.6-2.0 Ga Transvaal Supergroup.

Finally, cosmogenic nuclide studies generally confound the assignment of absolute ages to landsurfaces, as even very stable landforms appear to be eroding, albeit slowly, over time (e.g. Bierman and Caffee, 2002). In fact, only in exceptional environments, such as the Dry Valleys area of Antarctica (Summerfield *et al*., 1999), the Atacama Desert of Chile (Dunai *et al.*, 2005) and possibly the Namib Desert (Van der Wateren and Dunai, 2001; see section 2.4.3 below) does the concept of an age for a landscape appear to be potentially appropriate. More typically, a landform's age may refer to the time of its initial development, and due to subsequent erosion, its residual appearance may merely mimic its original form (e.g. Watchman and Twidale, 2002). This implies that the question of a landscape's age is essentially semantic, and that the landscape ages proposed by cyclic erosion models might not be falsifiable.

2.4.2 Long-term denudation rates from fission track and (U-Th)/He thermochronology

Fortunately, more precise long-term temporal constraints on denudation may be determined from thermochronology. Following the early work of Haack (1983), a number of fission track thermochronology studies have been conducted in southern

Africa over the past two decades (Brown, R.W. *et al*., 1990; 1994; 2002; Gallagher and Brown, R., 1999; Raab *et al*., 2002; Tinker *et al*., 2008a; 2008b; Kounov *et al*., 2008; 2009). Because of the annealing of fission tracks (damage features resulting from the spontaneous fission of ^{238}U) with increasing temperatures, the analysis of fission tracks yields detailed information on the thermal histories of rocks at temperatures of below ~350 ºC for zircon and below ~120 ºC for apatite, a temperature range characteristic of the upper 4-5 km of the continental crust (Gallagher *et al*., 1998; Gallagher and Brown, R., 1999). By assuming a palaeogeothermal gradient, preferably determined from a deep borehole, this cooling history may be used to reveal an exhumation history for rocks sampled from the present-day landsurface or from boreholes. A summary of long term (>10^6 yr) denudation rate estimates for southern Africa based on apatite fission track data and other geological indicators is given in **Table 2.1** and shown graphically in **Figures 2.16** and **2.17**.

Reviews of fission track studies from southern Africa's western margin by Gallagher and Brown, R. (1999) and Brown R.W. *et al.* (2000) showed that almost all apatite fission track data from surfaces in this region yielded Cretaceous cooling ages, ranging from 166 ± 6 Ma to 70 ± 5 Ma, and that ages predating rifting at ~134 Ma only occur within inland elevated regions lying over 1000 m in elevation, although some younger ages (~70 Ma) occur up to 600 km inland. Apatite fission track data also indicates that cooling to near-surface temperatures generally occurred in two phases:

1) in the early Cretaceous (~140-120 Ma) and
2) in the mid-Cretaceous (~100-80 Ma), although in northern Namibia this later phase of cooling occurred in the late Cretaceous to earliest Tertiary (~80-60 Ma), possibly associated with a tectonic reactivation of pre-existing crustal structures (Brown, R.W. *et al*., 2000, and references therein; Raab *et al*., 2002).

Modelling of fission track data by Cockburn *et al*. (2000) suggests that denudation rates along the western margin have decreased from ~40 m/Myr (~130-36 Ma) to ~5 m/Myr (~36-0 Ma).

Method	Source	Area	Approximate time interval (Ma)	Average denudation rate (m/Myr)
Kimberlite facies analysis	Partridge and Maud (1987) and references therein	Letseng, Drakensberg mountainland	87 - 0	3.4
	Hanson *et al*. (2009)	Kimberley region, central plateau	120 - 85	15
			85 - 0	10
Offshore stratigraphy	Rust and Summerfield (1990)	Atlantic (western) margin	152 - 113	41 - 82
			37 - 0	7 - 9
Apatite fission track thermochronology	Gallagher and Brown, R. (1999)	Atlantic (western) margin	140 - 0	7 - 36
	Cockburn *et al*. (2000)	Atlantic (western) margin	130 - 36	40
			36 - 0	5
	Brown, R.W. *et al*. (2002)	Coastward of Drakensberg (southeast) escarpment	130 - 0	≥ 35
			91 - 69	95 ± 43
		Inland of Drakensberg (southeast) escarpment	78 - 0	15 - 28
			78 - 64	82 ± 43
	Tinker *et al*. (2008a)	Coastward of southern escarpment	100 - 80	125 -175
			80 - 0	10 - 15
	Kounov *et al*. (2009)	Atlantic (western) margin of South Africa: coastal plain	115 - 90	60 - 108
		Atlantic (western) margin of South Africa: Interior plateau	115 - 90	<40
Apatite (U-Th)/He thermochronology	Flowers and Schoene (in press)	Eastern escarpment transect from South Africa to Swaziland	65 - 0	11-14

Table 2.1: Summary of long-term (> 10^6 yr) denudation rates for the southern African region reported in the literature. Denudation rates referenced from Partridge and Maud (1987) and references therein, Kounov *et al*. (2009) and Flowers and Schoene (in press) are rates that have been calculated from the estimated thicknesses of denudation over discrete periods given in these sources.

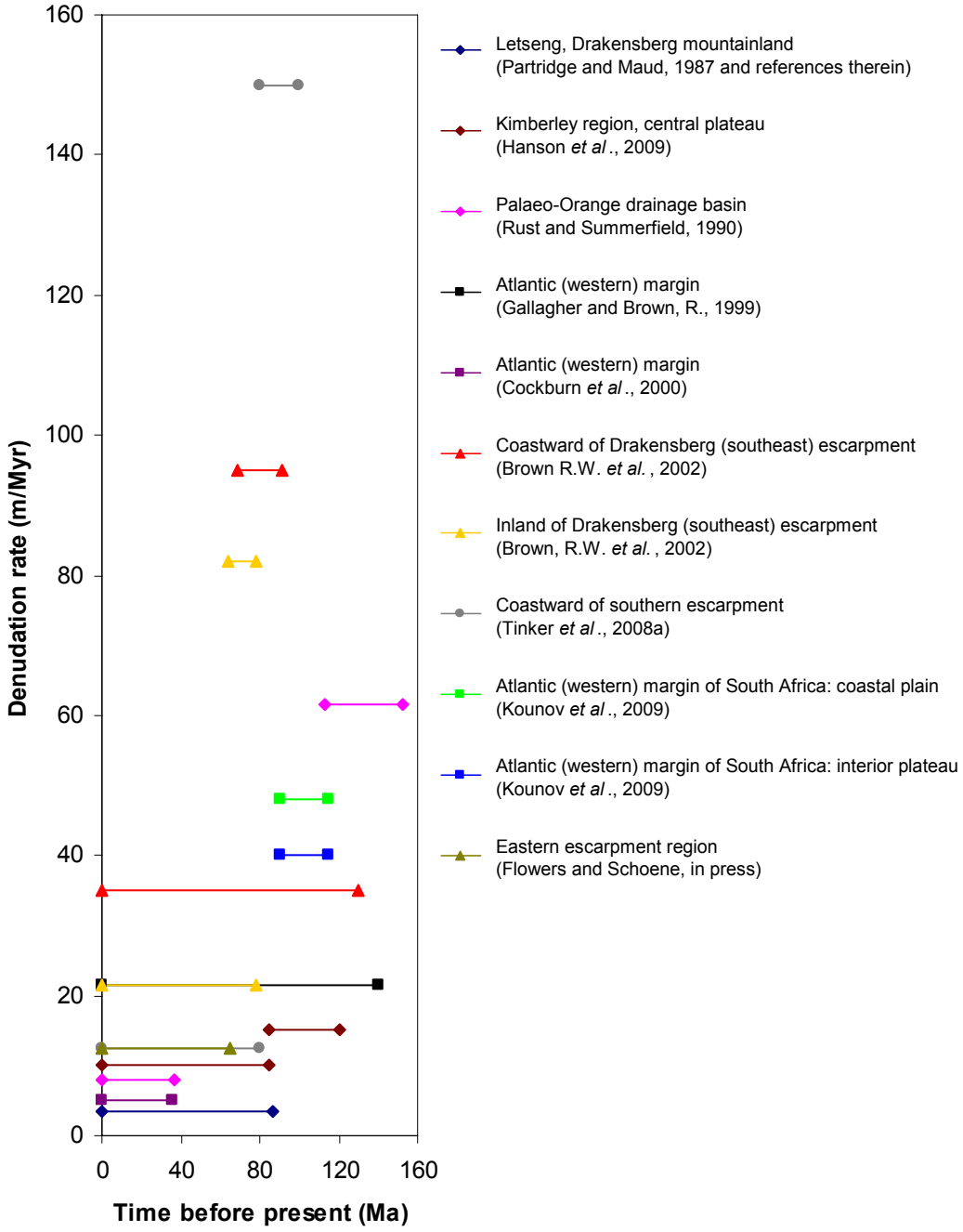

Figure 2.16: Long-term denudation rate estimates for southern Africa based on thermochronology and other geological indicators, as listed in **Table 2.1**. Horizontal lines between points each indicate the time period over which the denudation rate was averaged. Values are calculated medians where a range of values was indicated in the literature. For Brown, R.W. *et al.*'s (2002) estimate for 130-0 Ma, Kounov *et al.*'s (2009) estimate for the interior plateau, and Flowers and Schoene's (in press) estimate for 60-0 Ma, values given are maximum estimates. Error bars are not shown for the sake of clarity.

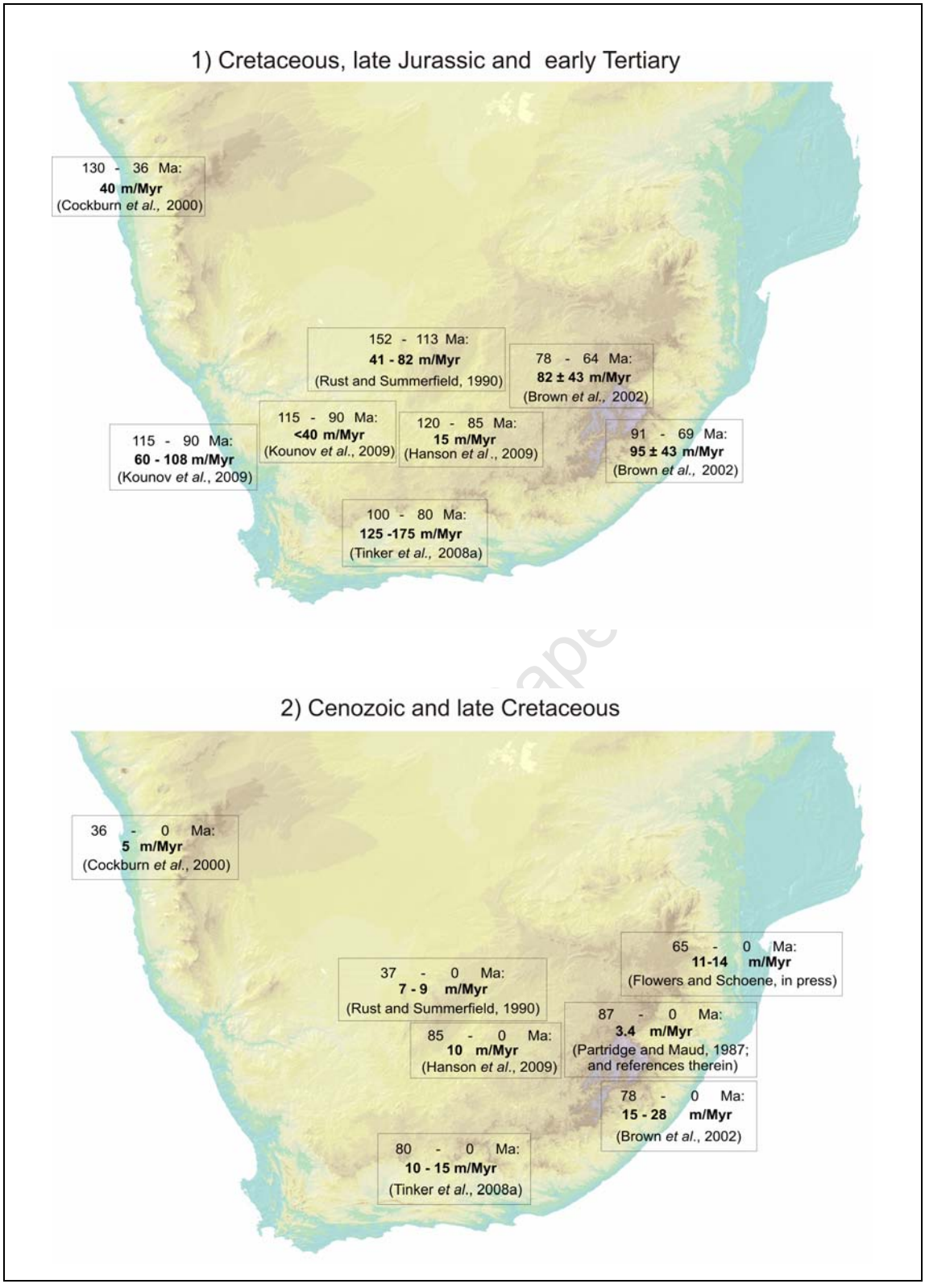

Figure 2.17: Approximate locations of long-term denudation rate estimates from the literature (**Table 2.1**) for the Cretaceous, late Jurassic and early Tertiary (above) and for the Cenozoic and late Cretaceous (below). Note the general decrease in denudation rates over time across the southern African region.

More recently, Kounov *et al.* (2009) reported apatite fission track data from two traverses perpendicular to South Africa's west coast across the escarpment zone, and reported fission track ages for surface samples ranging from 180 to 86 Ma. Modelling of these results indicates two distinct cooling events, separated by a period of quiescence:

1) Between 160 and 138 Ma only in rocks from the Karoo basin above the escarpment, possibly due to post-Karoo magmatism thermal relaxation, and
2) Accelerated cooling between 115 and 90 Ma, consistent with a proposed pulse of tectonically induced denudation of up to 2.5 km of rock from the coastal zone and less than 1 km of rock from the elevated continental interior (Kounov *et al*., 2009).

For southern Africa's southeast (Drakensberg) margin, apatite fission track data for a ~500 km long transect perpendicular to the coastline was presented by Brown, R.W. *et al*. (2002), who combined outcrop and borehole sample data to demonstrate that at least 4.5 km of rock has been denuded from the coastal zone since ~130 Ma. Notably, an apatite fission track profile from a borehole approximately 30 km east (seaward) of the Drakensberg escarpment (SW1/67) reveals a phase of accelerated denudation of 2.1 ± 0.9 km at a mean rate of 95 ± 43 m/Myr from approximately 91 Ma to 69 Ma (Brown, R.W. *et al*., 2002). Inland of the escarpment, another borehole (LA 1/86) shows that 1.7 ± 0.5 km of denudation has occurred since ~78 Ma, with a period of accelerated denudation (82 ± 43 m/Myr) between 78 Ma and 64 Ma (Brown, R.W. *et al*., 2002).

A similar pattern emerges from southern Africa's southern margin, where Tinker *et al*. (2008a) conducted an apatite fission track study perpendicular to southern Africa's southern margin, across the Cape Fold Belt to the southern escarpment, also using surface and borehole samples. Tinker *et al*.'s (2008a) modelled results indicate that 2.5-3.5 km of denudation occurred seawards of the escarpment in the mid-late Cretaceous (100-80 Ma) at a rate of 125-175 m/Myr, and that less than 1 km of regional denudation occurred since the late Cretaceous, at a rate of 10-15 m/Myr (80-0 Ma), although these authors conceded that minor episodes of uplift and river incision might have occurred throughout the Cenozoic.

Most recently, long-term denudation rates from a transect across southern Africa's eastern escarpment from South Africa to Swaziland were determined by Flowers and Schoene (in press) with the use of apatite (U-Th)/He thermochronology. Flowers and Schoene (in press) reported apatite (U-Th)/He ages from both above and below the eastern escarpment that were only Cretaceous in age. There was no correlation observed between cooling ages and sample elevations, and their modeled results indicated that the region experienced relatively rapid cooling between 130 and 100 Ma (Flowers and Schoene, in press). Given that this constrains Cenozoic denudation to ≤ 0.7-0.9 km due to (U-Th)/He thermochronology being sensitive to temperatures as low as 30 ºC (Flowers and Schoene, in press) and given that the current relief of the eastern escarpment is ~1.5 km, Flowers and Schoene (in press) concluded that ≥ 0.6 km of relief (i.e. a palaeo-escarpment close to the current escarpment position) must have existed by the end of the Cretaceous.

In summary then, the emerging picture from apatite fission track and (U-Th)/He thermochronology in southern Africa suggests that a major regional episode of denudation occurred in the mid- to late Cretaceous with significantly lower denudation rates for the Cenozoic (**Figures 2.16** and **2.17**). Earlier periods of cooling during the Jurassic and early Cretaceous may have been due to thermal relaxation following Karoo magmatism or enhanced denudation associated with the onset of rifting. However, besides determining regional denudation rates, fission track thermochronology may also be used for more detailed studies of topographic evolution, due to the dependence of subsurface isotherms on topography. Kounov *et al.* (2008) reported that fission track data from the Krom River valley (western South African margin) is consistent with a high relief precursor to the current river valley already being in existence between ~120 and ~100 Ma. This supports previous models (for instance, on sedimentological grounds by de Wit, M.C.J., 1993) that this river valley was the original coastal exit of southern Africa's interior (palaeo-Orange) drainage, before drainage capture by the more northerly Orange river.

2.4.3 Other geological indicators

In addition to fission track data, an independent account of southern Africa's long-term denudational history may be provided by the region's offshore stratigraphic record, which is well-known from seismic reflection data and petroleum exploration

wells (e.g. Brown, L.F., *et al*., 1995; Macmillan, 2003). Phases of onshore denudation should correspond with phases of offshore sedimentation if sediment transport from land to sea is efficient, and if offshore sediments are not significantly redistributed by marine currents.

With reference to their account of landscape evolution in southern Africa, Partridge and Maud (1987) noted a general lack of evidence for enhanced Tertiary denudation episodes in the offshore sedimentary record. However, they explained this mismatch with their model of landscape evolution as a result of sediment redistribution off the continental shelf. Partridge and Maud (1987) also noted that peaks in offshore sedimentation occurred shortly after rifting in the early Cretaceous (Valanginian-Barremian; 131-115 Ma) and in the late Cretaceous (Coniacian-Santonian; 86-78 Ma), and that these periods are bracketed by a significant Turonian unconformity coincident with widespread kimberlite intrusions at ~90 Ma (Dingle *et al*., 1983; Partridge and Maud, 1987 and references therein). As a result, Partridge and Maud (1987) admitted that associated tectonic disturbances may have occurred onshore at these times, meaning that the "African cycle" could therefore be polycyclic. Similarly, Rust and Summerfield (1990) analysed the stratigraphic record off southern Africa's west coast, and proposed that the denudation rate for the palaeo-Orange catchment had decreased from approximately 82-41 m/Myr in the early Cretaceous (~152 - 113 Ma), to 9-7 m/Myr in the late Tertiary (~37 - 0 Ma) (**Table 2.1**; **Figures 2.16** and **2.17**).

For the Algoa Basin (south coast), Tinker *et al.* (2008b) compared the denudation record for the southern margin proposed by Tinker *et al*. (2008a) with the offshore sedimentary record, and found that peaks in sediment accumulation in the early Cretaceous (~130-120 Ma) and mid-late Cretaceous (~93-67 Ma) coincided with peaks in denudation inferred from apatite fission track analysis, although the absolute volumes of offshore sediment accumulation did not match the calculated volumes of eroded material.

Other independent estimates for long-term denudation rates in southern Africa have been based on the analysis of kimberlite pipes of a known eruption age, as an estimation of the depth of denuded material is made possible by the depth dependence

of kimberlite facies. Partridge and Maud (1987) referenced the study of Hawthorne (1975), who inferred the erosion of some 300 m of Drakensberg basalt at Letseng in Lesotho since the emplacement of kimberlite pipes at ~87 Ma (Davis, 1977). As Partridge and Maud (1987) pointed out, this may be taken as evidence that the intact preservation of a Jurassic or "Gondwana" erosion surface in the region (King, 1951) is untenable. Furthermore this yields an average denudation rate of ~3.4 m/Myr for Drakensberg basalts here since ~87 Ma (**Table 2.1**; **Figures 2.16** and **2.17**). In a recent study based on the analysis of kimberlites and their country rock xenoliths, Hanson *et al*. (2009) inferred denudation rates of ~15 m/Myr from ~120 Ma to ~85 Ma (during which predominantly Drakensberg basalts were removed in this region) and ~10 m/Ma from ~85 Ma to the present (during which Karoo sediments were eroded). Hanson *et al*. (2009) also infer an eastward migration of the western limit of the erosional remnant of Drakensberg basalts during the Cretaceous, based on the spatial distribution of Drakensberg basalt xenoliths in older (Group II, ~120 Ma) versus younger (Group I, ~85 Ma) kimberlites. Hanson *et al.* (2009) thus propose a model of internal escarpment retreat at a rate of ~2 km/Myr.

2.4.4 Cosmogenic nuclide studies

Long-term estimates of denudation rates may be augmented with cosmogenic nuclide-based studies, which yield quantitative denudation rate estimates on a finer temporal and spatial scale than available from apatite fission track and (U-Th)/He thermochronology. A number of cosmogenic nuclide studies have been conducted in southern Africa over the past decade, the results of which are summarised in **Table 2.2**, with the approximate locations given in **Figure 2.18**.

In the only published cosmogenic nuclide study from the southeastern part of southern Africa to date, Fleming *et al*. (1999) conducted a study of cosmogenic ^{36}Cl abundances in bulk basalt samples from the Drakensberg (southeast coast) escarpment. Vertical denudation (downwearing) rates at the escarpment summit were reported to range between 1.4 m/Myr and 10 m/Myr (average 6 m/Myr), with ridge top denudation seaward of the escarpment being higher, at ~27 m/Myr. Scarp face retreat (horizontal backwearing) was determined in two samples 175 km apart, and found to be at least 49 m/Myr and 63 m/Myr respectively (assuming uniform, steady-state erosion), and at most 83 m/Myr and 95 m/Myr respectively (assuming erosion

Study	Nuclides	Material analysed	Region	Lithology	Landform	Location	Denudation rate (m/Myr)
Fleming *et al*. (1999)	^{36}Cl	Basalt	Drakensberg (southest) escarpment	Basalt	Face		49 - 83; 63 - 95
					Ridge summit	Seaward of escarpment	26.9 ± 1.7
					Escarpment summit		10.0 ± 0.5 - 1.4 ± 0.1; mean = 6 (n = 3)
Cockburn *et al*. (1999; 2000)	^{10}Be, ^{26}Al	Quartz	Central Namibian (western) margin	Biotite-granite	Coastal inselbergs (bornhardts)		5.1 ± 1.1 (n = 6)
				Granite-gneiss	Escarpment faces and ridges		10 (n = 10)
				Quartzite	Escarpment summit (Gamsberg)		0.4 ± 0.1 (n = 4)
Bierman and Caffee (2001)	^{10}Be, ^{26}Al	Quartz	Central Namibian (western) margin	Granite, granite gneiss, quartzite, pegmatite	Outcrops, including inselbergs	Inland of escarpment	3.2 ± 1.5 (n = 9)
						Seaward of escarpment	3.6 ± 1.9 (n = 38)
				Sediment	Small streams	Escarpment	16
						Highlands	5
						Coastal plain	8
					Large rivers		6.4 ± 2.9 (3 - 9; n = 4)
Van der Wateren and Dunai (2001)	^{21}Ne	Quartz	Central Namibian (western) margin	Quartz (veins in granitic and metamorphic rocks)	Pediments and terraces		0.11 ± 0.01 - 1.04 ± 0.07
				Quartz (amalgamated pebble samples)	Kuiseb river (incision rate)		40 - 160
Kounov *et al*. (2007)	^{3}He, ^{21}Ne	Quartz	Southwestern Karoo	Quartzite	Plateau surfaces		1.5 - 3 (n = 3)
		Pyroxene	Southwestern Karoo	Dolerite			1.0 - 2.1 (n = 7)
Codilean *et al*. (2008)	^{10}Be		Central Namibian (western) margin	Sediment	Gaub River subcatchments		7.97 ± 0.49 - 14.12 ± 0.88
Dirks *et al*. (2010)	^{10}Be	Quartz		Quartz (veins in chert breccia)	Plateau surface		3.6 ± 1.1 (n = 4)
					Grootvleispruit River (incision rate)		53 ± 9

Table 2.2: Denudation rates for southern Africa, based on cosmogenic nuclide studies. With the exception of Fleming *et al*.'s (1999) escarpment retreat rates and Van der Wateren and Dunai's (2001) and Dirks *et al*.'s (2010) fluvial incision rates, based on the extrapolation of minimum exposure ages, denudation rates here are all maximum denudation rates (assuming a constant rate of denudation and an infinite period of exposure).

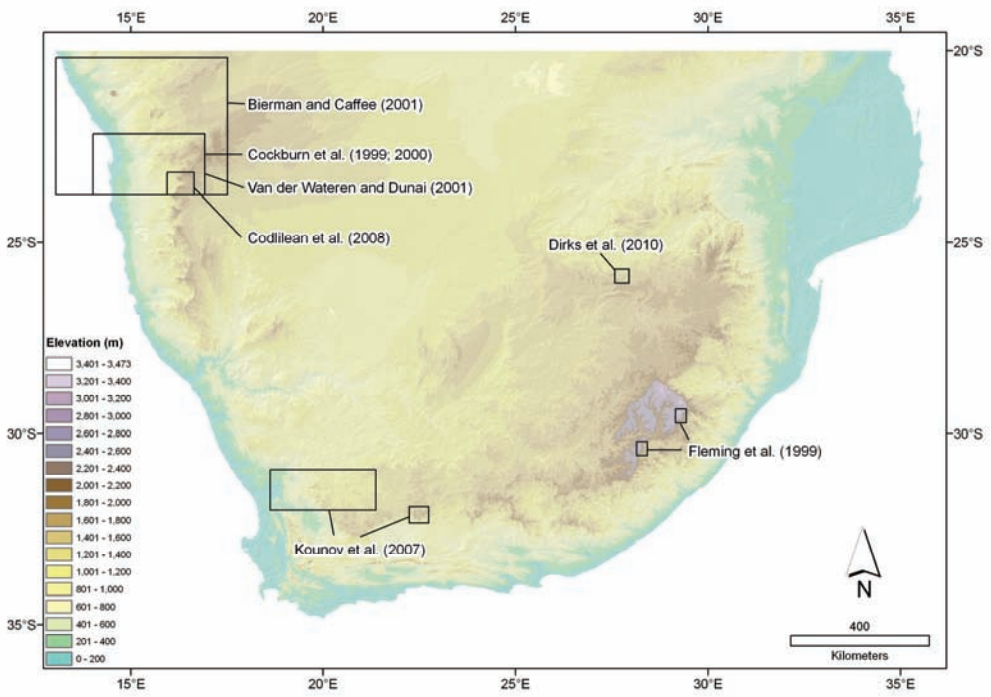

Figure 2.18: Approximate locations of previous cosmogenic nuclide studies in southern Africa (Fleming *et al*., 1999; Cockburn *et al*., 1999, 2000; Bierman and Caffee, 2001; Van der Wateren and Dunai, 2001; Kounov *et al*., 2007; Codilean *et al*., 2008).

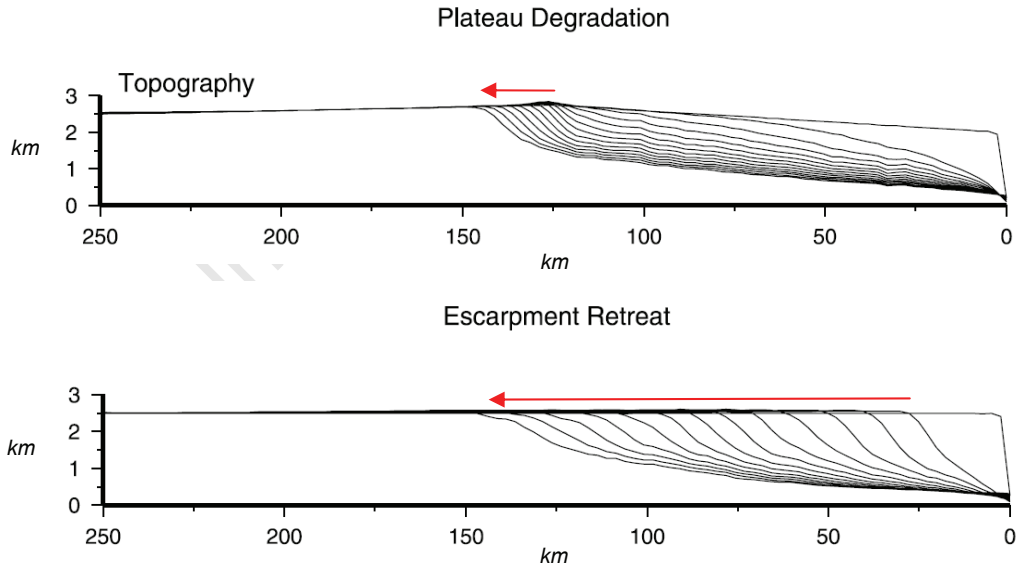

Figure 2.19: Contrasting (strike-averaged) topographic profiles for the development of escarpments through plateau degradation (above; where an initial inland drainage divide exists) and escarpment retreat (below; where the escarpment coincides with a drainage divide), as predicted by the modeling of van der Beek *et al*. (2002). Red arrows each signify the relative extent of drainage divide migration for each case.

through regular rockfalls equal to the attenuation length for ^{36}Cl, i.e. ~0.5 m). These rates confirm Partridge and Maud's (1987) inference of the non-existence of a preserved Gondwanan (Jurassic) erosion surface at the summit of the escarpment (contrary to King, 1951), and are compatible with the post-Cretaceous long term denudation rates that may be inferred from kimberlite facies analysis in Lesotho (~3.4 m/Myr since ~87 Ma; Partridge and Maud, 1987 and references therein). Furthermore, Fleming *et al.*'s (1999) maximum model values for the rate of scarp retreat are still an order of magnitude too low, when extrapolated, to permit for a constant rate of escarpment recession from the coastline since Gondwana break-up (cf. King, 1951).

Other cosmogenic nuclide studies in southern Africa have generally focused on the western coastal and escarpment regions. Using ^{10}Be and ^{26}Al in quartz, Cockburn *et al*. (1999; 2000) reported a mean rate of escarpment retreat of 10 m/Myr from granitic free face and ridges (n = 10), a mean denudation rate of 0.4 ± 0.1 m/Myr (n = 4) for the quartzite summit of Gamsberg mountain on the escarpment, and a mean denudation rate of 5.1 ± 1.1 m/Myr for the summits of granitic bornhardts (domed inselbergs) on the coastal plain (Namib desert) seaward of the Namibian escarpment. Although low, these denudation rates for inselbergs in the Namib are higher than denudation rates given for some other granitic inselbergs, such as in the Eyre Peninsula, central-south Australia (Bierman and Turner, 1995; 0.7 ± 0.1 m/Myr, n = 6). Cockburn *et al*. (1999) attributed this to the effect of enhanced salt weathering in Namibia's coastal environment.

The low rate of present denudation along the Namibian margin (particularly when compared to Cretaceous denudation rates determined from fission track thermochronology, **Table 2.1**), has been confirmed by subsequent studies (Bierman and Caffee, 2001; Van der Wateren and Dunai, 2001; Codilean *et al*., 2008). Also using ^{10}Be and ^{26}Al in quartz, Bierman and Caffee (2001) determined denudation rates for outcrops (predominantly inselbergs) both inland and seaward of the escarpment, yielding indistinguishable average rates of 3.2 ± 1.5 m/Myr (n = 9) and 3.6 ± 1.9 m/Myr (n = 38) respectively. These denudation rates were observed to be independent of the quartz-bearing lithology sampled (granite, granite-gneiss, quartzite, pegmatite) and insensitive to trends in local rainfall, elevation or distance from the escarpment. Bierman and Caffee (2001) remarked that the independence of

the weathering rates from rainfall may indeed result from the salt weathering of inselbergs in the more arid Namib coastal zone, as suggested by Cockburn *et al*. (1999), and from the rapid drainage of water from bare rock outcrops. The authors noted that the paired ^{26}Al and ^{10}Be data for bedrock surfaces is consistent with simple exposure histories (continuous surface exposure or steady erosion). In contrast, ^{10}Be and ^{26}Al activities reported for quartz pavement clasts yielded long and sometimes complex exposure histories, with minimum total exposure histories as long as 2.7 Myr, consistent with the interpretation that these clasts are recycled from older Miocene gravels (Bierman and Caffee, 2001 and references therein).

Bierman and Caffee (2001) also presented denudation rates calculated from the analysis of quartz from sediment samples. Four large rivers yielded denudation rates that ranged from 3 to 9 m/Myr (Bierman and Caffee, 2001), and three smaller catchments yielded variable denudation rates, with the highest denudation rate being from a small catchment with schistose bedrock within the escarpment zone (16 m/Myr), and with lower denudation rates for small catchments in the highlands (5 m/Myr) and for the coastal plain (8 m/Myr). As argued by Bierman and Caffee (2001), even if the higher denudation rate for the catchment in the escarpment zone is characteristic of the entire escarpment, and not a result of the more friable bedrock lithology in that catchment, the rate of escarpment retreat would be nearly two orders of magnitude lower than required for parallel retreat of the escarpment from the coastline to have occurred since continental breakup. Again, these findings are inconsistent with King's (1951) pediplanation model. Due to the lower denudation rates for bedrock samples than for stream sediments, Bierman and Caffee (2001) suggested that inselbergs may grow from the surrounding landscape with time, until being consumed by erosion from their margins. In summary, these workers suggest that the Namibian landscape is approaching a geomorphic steady state under present conditions, where the overall form of the landscape has changed little, if at all, over the time periods addressed by their data (Bierman and Caffee, 2001).

Through the analysis of cosmogenic ^{21}Ne in quartz, Van der Wateren and Dunai (2001) also studied the development of the central Namibian margin. Whilst also advocating low Neogene denudation rates for the region, their results offered a slightly different interpretation. Van der Wateren and Dunai (2001) reported

denudation rates for *in situ* quartz veins cropping out on pediment surfaces and on river cut surfaces of granitic and metamorphic rocks. They also determined an incision rate for the escarpment-draining Kuiseb River, based on the exposure ages of amalgamated quartz pebble samples on river terraces and shielded samples. Van der Wateren and Dunai's (2001) minimum exposure ages for their quartz veins ranged from 0.57 ± 0.04 Ma to 5.18 ± 0.18 Ma (n = 4), and corresponding to maximum denudation rates of between 1.04 ± 0.07 m/Myr and 0.11 ± 0.01 m/Myr. Van der Wateren and Dunai (2001) proposed that such rates are more representative of the central Namibian margin than the inselberg-based value of 5.1 ± 1.1 m/Ma proposed by Cockburn *et al*. (2000). They also suggested that the latter value may be due to an accelerated denudation rate for these inselbergs, or because these inselbergs may have been excavated from a regolith during the Pleistocene following regional fluvial rejuvenation. Indeed, based on the average exposure ages of amalgamated surface pebble and shielded terraces of the Kuiseb River, Van der Wateren and Dunai (2001) proposed that incision of the river was initiated after 2.81 ± 0.11 Ma, slowing or stopping to create terraces at 1.28 Ma and 0.47 Ma. This implies a river incision rate of 40-160 m/Myr during the Pliocene and Pleistocene (Van der Wateren and Dunai, 2001). The authors also correlated these terraces with others according to the results of a heavy mineral-based sediment provenance study. They then suggested that drainage incision at this time was regional in extent, and probably a result of increasingly wet conditions upstream in response to Plio-Pleistocene global cooling (Van der Wateren and Dunai, 2001).

These authors thus chose to reject the model of Plio-Pleistocene tectonic uplift proposed by Partridge and Maud (1987), as they stated that they found no evidence for deformation of the pre-incision surface (Van der Wateren and Dunai, 2001). In summary, Van der Wateren and Dunai (2001) favoured a model of an extremely stable central Namibian margin with very low denudation rates, interrupted by pulses of rapid denudation due to climate-driven river incision. It may be noted, however, that structural evidence for onshore and offshore neotectonic activity along the southwestern African margin since at least the Pleistocene has been proposed by other workers (Viola *et al*., 2005; Andreoli *et al*., 2009).

Incidentally, it might be alleged that the extremely old exposure ages and consistently lower erosion rates reported by Van der Wateren and Dunai (2001) relative to the ^{10}Be and ^{26}Al erosion rates reported by Cockburn *et al.* (1999, 2000) and Bierman and Caffee (2001) may be due to a possible overestimation of the cosmogenic ^{21}Ne abundances in their quartz samples. The potential to overestimate the cosmogenic ^{21}Ne abundance in a sample is a common problem for cosmogenic ^{21}Ne studies, and stems from the difficulty in determining the abundance of crustal ^{21}Ne (nucleogenic ^{21}Ne trapped in fluids from crustal rocks; see Section 4.8 for a discussion). Van der Wateren and Dunai (2001) argued that their Ne isotope measurements from all but one of their heating extractions are at least consistent with negligible nucleogenic ^{21}Ne being present in their samples, and that this is supported by low radiogenic (crustal) ^{4}He concentrations. Unfortunately, this is not necessarily evidence of the absence of significant nucleogenic ^{21}Ne (Niedermann *et al*., 1993; see also Section 6.3 for a discussion of nucleogenic ^{21}Ne in pyroxene samples from this study). Elevated ^{21}Ne/^{20}Ne ratios relative to ^{22}Ne/^{20}Ne ratios at higher temperature extractions, as reported by these authors for some of their samples, might also be interpreted as evidence of a significant crustal component. On the other hand, Van der Wateren and Dunai (2001) sampled different landscape elements than Cockburn *et al.* (1999, 2000) and Bierman and Caffee (2001), and their data, particularly the relative ages of their terraces, does display internal consistency.

In a further study from this region, Codilean *et al*. (2008) studied the Gaub River (a tributary of the Kuiseb), and presented four new cosmogenic ^{10}Be measurements for sediment samples from subcatchments (yielding denudation rates of 7.97 ± 0.49 m/Myr - 14.12 ± 0.88 m/Myr). According to these authors, this new data, together with results from Cockburn *et al*. (2000) and Bierman and Caffee (2001), suggests that spatially variable erosion rates in this area are linearly related to mean subcatchment slope angle, as determined from a 30 m resolution digital elevation model (Codilean *et al*., 2008). This slope dependence for erosion rates would imply that the Gaub catchment is *not* in a topographic steady state (Codilean *et al*., 2008). This interpretation apparently contradicts the conclusions of Bierman and Caffee (2001) and Van der Wateren and Dunai (2001). However, a "steady state" is a somewhat relative term, and its applicability depends upon the timescale of interest (Section 1.2). Codilean *et al*. (2008) also reported that by assuming this linear relation

between mean slope and erosion rate, the spatial variation in erosion rates for the Gaub catchment is reflected in the frequency distribution of cosmogenic ^{21}Ne in quartz pebbles leaving the catchment.

In the only study yet reported from the southwestern margin (Karoo plateau region) of South Africa, Kounov *et al.* (2007) reported ^{3}He and ^{21}Ne denudation rates for dolerite outcrops on the interior plateau above the western and southern escarpments (n = 7), and ^{21}Ne denudation rates for Ordovician-Silurian quartzite (or quartz arenite; Thamm and Johnson, 2006; **Figures 1.6** and **1.7**) samples of the Cape Supergroup from a flat erosional surface just above the edge of the western escarpment (n = 3). Samples were all from horizontal or sub-horizontal surfaces (inclination ≤ 7º) with the exception of an inclined (30º) quartzite surface. Kounov *et al*.'s (2007) cosmogenic ^{3}He and ^{21}Ne abundances were corrected for non-air and non-cosmogenic components revealed by crushing experiments, and they reported model exposure ages and maximum erosion rates relative to a number of possible scaling factors and nuclide production rate estimates (see discussion in Sections 4.2 and 4.7). Nevertheless, their results revealed consistently low although slightly different denudation rate for quartzites (1.0 – 2.1 m/Myr) and dolerites (1.5 – 3 m/Myr), and Kounov *et al*. (2007) thus suggested that their data pointed to a lithological control on denudation rates. They also mentioned other possible determining factors, including climate, with lower dolerite denudation rates observed for samples from the drier, western escarpment region, and local topography, where the accumulation of water on flat surfaces may serve to enhance the rate of bedrock weathering (Kounov *et al*., 2007).

Most recently, Dirks *et al*. (2010) reported cosmogenic ^{10}Be data from the Malapa caves region on the central eastern plateau, in order to assess the development of the caves from which new hominin fossils (*Australopithecus sediba*; Berger *et al*., 2010) have been described. Dirks *et al*. (2010) report a mean maximum erosion rate of 3.6 ± 1.1 m/Myr for quartz vein samples in chert breccia (n = 4) on the plateau. They also report three ^{10}Be model exposure ages of 41.4 ± 1.1 ka, 50.5 ± 1.7 ka and 115.2 ± 3.2 ka for a resistant chert breccia layer near the course of the Grootvleispruit River (Limpopo tributary), and propose that these ages may be interpreted as evidence of progressive local river incision at a rate of 53 ± 9 m/Myr, due to stripping of an

erodable overlying shale layer over this period (Dirks *et al*., 2010 and online supplementary data).

In summary, cosmogenic nuclide studies have been broadly in agreement with each other regarding the low denudation rates prevailing in the region during at least the last few hundred thousand years (**Table 2.2**). However, alternative interpretations of the data and competing hypotheses regarding the origin of certain landforms have emerged (e.g. the development of Namib inselbergs; Cockburn *et al*., 2000; Van der Wateren and Dunai, 2001). Moreover, somewhat different ideas have been proposed regarding the stability of the southern African landscape, with accounts of near steady state (Bierman and Caffee, 2001); extreme steady state punctuated by rapid change (Van der Wateren and Dunai, 2001) and non-steady state (Codilean *et al*., 2008) being invoked by studies sampling different landscape elements within the same area. Local river incision during the Pleistocene has also been inferred in places (Van der Wateren and Dunai, 2001; Dirks *et al*., 2010). Hypotheses emphasising the relative roles of slope (Codilean *et al*., 2008), lithology and climate (Kounov *et al*., 2007) have been proposed, and are in need of testing. These developments affirm the potential of cosmogenic nuclide studies to continue to yield new insights into the development of the southern African landscape.

2.5 Synthesis

The quantitative denudation studies discussed above, primarily based on fission track thermochronology and cosmogenic nuclides, have yielded a consensus that denudation rates along southern Africa's margins were highest during the Cretaceous and experienced a decrease during the Tertiary. Denudation rates were also low during the Quaternary, and lower than for certain intervals of the Cretaceous by as much as two orders of magnitude (e.g. Kounov *et al*., 2007 versus Tinker *et al*., 2008a). In a general sense, this is consistent with the long held notion that widespread erosion of southern Africa's landscape occurred during the Cretaceous (e.g. Partridge and Maud's (1987) "African" cycle). Yet, one of the emerging patterns from fission track data is that no younging trend exists for the cooling ages of surface samples from the coastline towards the escarpment (Brown, R.W. *et al*., 2002; Tinker *et al*., 2008a), as would be expected if the escarpment had progressively retreated from the coast. Coupled with other criticisms of cyclic models highlighted in Section 2.4.1, this

observation has lead these authors to reject earlier, simple pediplanation-based models such as those proposed by King (1951; 1967) and Partridge and Maud (1987).

The lack of any evidence for significant mid-Cenozoic cooling from these fission track studies has also lead to a rejection of Burke's (1996) model of regional uplift and denudation at ~30 Ma. Partridge *et al*. (2006) and Burke and Gunnell (2008) have in turn criticised the robustness and resolution of fission track thermochronology as a method for distinguishing between competing hypotheses regarding the timing of major uplift and escarpment formation in southern Africa. Burke and Gunnell (2008) point out that apatite fission track annealing ages from surface samples do not necessarily reflect the period of major uplift. However, the sum of the evidence remains compelling, particularly when newer denudation thermochronology studies based on apatite fission track data from deep borehole cores (Tinker *et al*., 2008a) and apatite (U-Th)/He thermochronology data (Flowers and Schoene, in press) are also considered. Furthermore, cosmogenic nuclide data from studies within the escarpment zone (Fleming *et al*., 1999; Bierman and Caffee, 2001; Van der Wateren and Dunai, 2001; Codilean *et al*., 2008) infer currents rates of backwearing that are one or even two orders of magnitude too low to account for the development of the escarpment through a constant rate of escarpment retreat from the coastline.

Moore and Blenkinsop (2006), favouring Partridge and Maud's (1987) scarp retreat model, argued that the rapid denudation event recorded seaward of the Drakensberg escarpment by Brown, R.W. *et al*. (2002) in the late Cretaceous reflects the passage of the escarpment after rifting, and that scarp retreat has slowed considerably since then, due to lithological variability and climate change. Yet this interpretation ignores the emerging evidence from across southern Africa for a peak in denudation rates during the Cretaceous (Dingle *et al*., 1983; Partridge and Maud, 1987; Brown, R.W. *et al*., 1990; Rust and Summerfield, 1990; Brown, L.F. *et al*., 1995; Tinker *et al*., 2008a,b). De Wit, M.J. (2007) notes that this peak in denudation is synchronous with a peak in the frequency of group I kimberlite intrusions and the magmatism of the submarine eruption of the Agulhas oceanic plateau, and suggests that mantle induced uplift may have triggered this regional denudational event. However, conclusively relating proposed regional denudational events to specific landforms remains an unfinished task.

Numerical modeling studies have proposed that the pre-existing drainage along an extensional margin exerts a first-order control on post-breakup escarpment development (Kooi and Beaumont, 1994; Van der Beek *et al*., 2002). According to these models, for significant escarpment retreat to occur, the escarpment should coincide with a drainage divide, whereas if a pre-existing drainage divide exists inland of the escarpment, rapid seaward incision of the plateau (plateau degradation) occurs, and an escarpment forms close to the position of the initial drainage divide. The evolution of topographic profiles corresponding to these two models is given in **Figure 2.19**, with the degree and direction of drainage divide migration for each case shown by arrows.

The model of plateau degradation is favoured by van der Beek *et al.* (2002), as its predictions are consistent with observations from fission track and cosmogenic nuclide data (Brown, R.W. *et al*., 2002; Fleming *et al*., 1999). Van der Beek *et al*. (2002) attribute the pre-existence of a drainage divide to possible thickness variations in the pile of Drakenberg basalt. However, for this model to be applicable for the whole of southern Africa's margin, a pre-existing topographic high must presumably have existed parallel to, but inland from, the entire rift margin. For the interior of southern Africa's plateau, Hanson *et al.* (2009) present evidence from kimberlites for the progressive eastward removal of overlying basalt as evidence of internal scarp retreat above the Great Escarpment (Section 2.4.3). This scenario is also consistent with the provenance of certain Cretaceous gravel deposits on the plateau (de Wit, M.C.J., 2009). However, these observations would also be compatible with a model of interior plateau degradation controlled by an eastern drainage divide.

In keeping with developments over the past two decades, it seems likely that the revision and refinement of models for the development of southern Africa's topography will continue. Nevertheless, it is imperative that the relative merits of new numerical models for landscape evolution continue to be assessed in the light of quantitative constraints on how the rates of denudation across southern Africa have changed through time, as may be established through fission track thermochronology and cosmogenic nuclide studies. Results from future studies using other modern geochronological techniques such as laterite geochronology (e.g. van Niekerk *et al*., 1999; see review by Vasconcelos, 1999) and (U/Th)-He denudation

thermochronology (e.g. Flowers and Schoene, in press) are also likely to be useful in this regard.

CHAPTER 3: EMPLACEMENT, WEATHERING AND TOPOGRAPHY OF KAROO DOLERITES

3.1 Introduction

In order to appreciate the geomorphological significance of cosmogenic nuclide-based constraints on Karoo dolerite surface exposure histories, an understanding of the geometry, weathering and topography of these intrusions is required. This chapter begins by reviewing previous relevant research on these subjects. The topography of the Karoo dolerites is then examined further with the use of a GIS (Geographic Information System).

3.2 Distribution, geometry and emplacement of Karoo dolerites

The erosional remnants of the Karoo Large Igneous Province (LIP) in southern Africa are characterised by a large proportion of intrusive rocks - the Karoo dolerite suite - and a smaller proportion of extrusive lithologies, comprising the Drakensberg and Lebombo Group basalts and rhyolites. Intrusions of the Karoo dolerite suite occur throughout the horizontal and sub-horizontal siliciclastic sediments of the Carboniferous-Jurassic Karoo Supergroup, both in the Main Karoo Basin of South Africa, and in adjacent Karoo sub-basins within the region (Walker and Poldevaart, 1949; Duncan and Marsh, 2006; **Figures 3.1** and **3.2**). Associated basic intrusions are found in Karoo-aged sediments in Africa as far away as Malawi, as well as on other Gondwanan remnants (e.g. in Brazil, Antarctica and Tasmania; du Toit, 1954; Jokat *et al*., 2003).

3.2.1. Age of the Karoo dolerites

Duncan *et al*. (1997) reported ^{40}Ar-^{39}Ar ages for feldspar separates and whole rocks from the Karoo LIP in South Africa, Namibia and Antarctica that ranged from ~184 Ma to ~179 Ma, with a clustering of ages at 183 ± 1 Ma, suggesting plume-related magmatism of short duration. More recent augmentation of this dataset for southern Africa, particularly from Karoo LIP rocks in Botswana and in the more easterly Lebombo and Mwenzi regions (adjacent to the South Africa-Mozambique and Zimbabwe-Mozambique borders) by Jourdan *et al*. (2005, 2007), has indicated that Karoo LIP magmatism in the region was more protracted than Duncan *et al*. (1997) supposed, and was active over ~10 Myr from ~184 Ma to ~178 Ma.

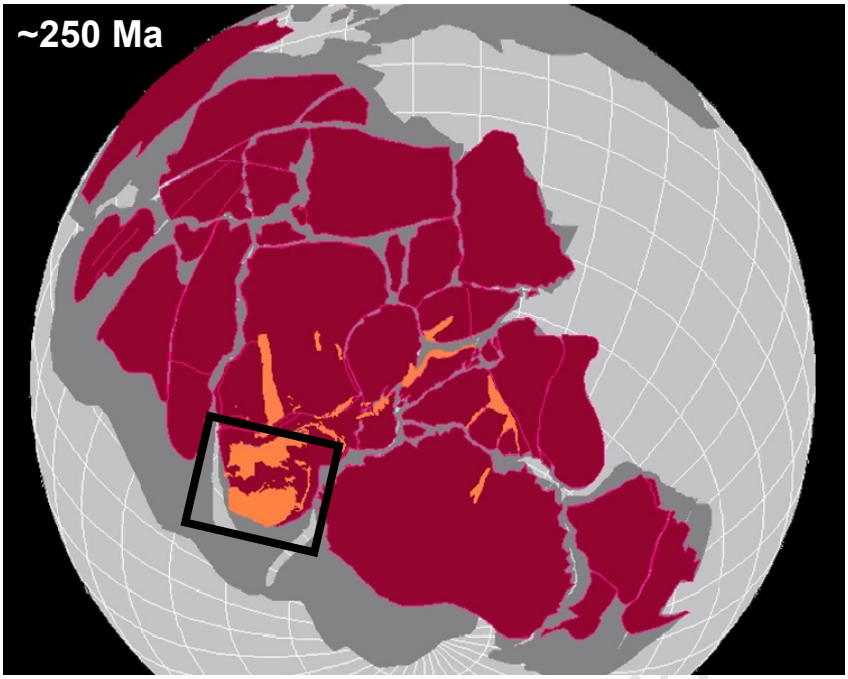

Figure 3.1: Karoo-aged basins of south-central Gondwana (orange), relative to the tectonic plate configuration at ~250 Ma, including the position of the Main Karoo Basin of southern Africa (black square, **Figure 3.2**). Image modified from Reeves and de Wit (unpublished data).

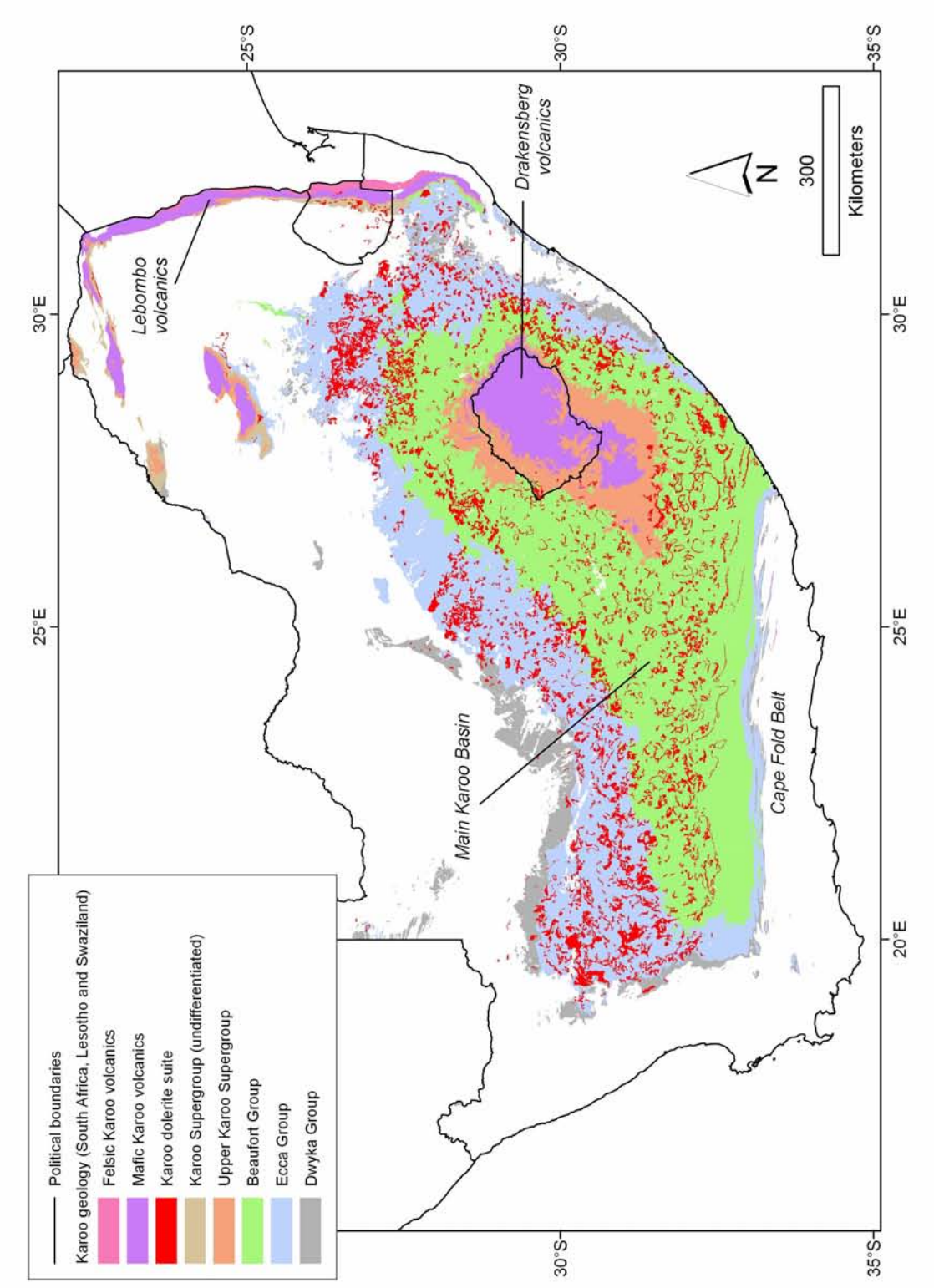

Figure 3.2: Geological map of the Main Karoo Basin and surrounding Karoo-aged sedimentary sub-basins and volcanic outliers in South Africa, Lesotho and Swaziland, modified from Vorster (2001).

However, Karoo dolerites of the Main Karoo Basin were apparently generally intruded during the early stages of Karoo LIP magmatism. Jourdan *et al*. (2008) reported ^{40}Ar-^{39}Ar ages for Karoo dolerites that generally lay between 181 Ma and 184 Ma, suggesting that major Karoo dolerite intrusion occurred over this ~3 Ma period. U-Pb zircon/baddeleyite ages of 183.7 ± 0.6 Ma and 182.5 ± 0.4 Ma (2σ uncertainty) have also been reported for Karoo dolerites in the Main Karoo Basin by Encarnacion *et al.* (1996) and Svensen *et al*. (2007), respectively. Given these considerations, an approximate emplacement age of ~183 Ma, as reported previously by Duncan *et al*. (1997), is assumed for Karoo dolerites for the purposes of this study.

3.2.2 Geometry of Karoo dolerite intrusions

The geometry of Karoo dolerite intrusions is apparently highly variable, and dolerite bodies have been described as horizontal sills, inclined sheets, vertical dykes, plugs, pipes, rings, laccoliths and pods (du Toit, 1920, 1954; Walker and Poldevaart, 1949 and references therein; Chevallier and Woodford, 1999). Sill thicknesses vary from less than a meter to more than 300 m. Dolerite dykes are generally thinner (2-9 m) but may be regionally continuous for more than 60 km, and pods are often 300-600 m thick (Walker and Poldevaart, 1949; du Toit, 1954).

Chevallier and Woodford (1999) noted that many Karoo dolerite intrusive bodies display a complex interconnectivity, and that a single dyke may act as a feeder for two different sills, or an individual sill may be fed by dykes of various orientations. Model geometries for dolerite rings include:

- Undulating dolerite sheets that may form basins and domes that intersect the surface as rings (Walker and Poldevaart, 1949 after Rogers and Schwarz, 1902 and du Toit, 1905; **Figure 3.3**);
- Horizontal sills connected by inclined sheets (du Toit, 1920);
- Laccoliths connected to a central intrusion; and
- Sills at varying elevations connected by ring dykes (Chevallier and Woodford, 1999 and references therein; **Figure 3.3**).

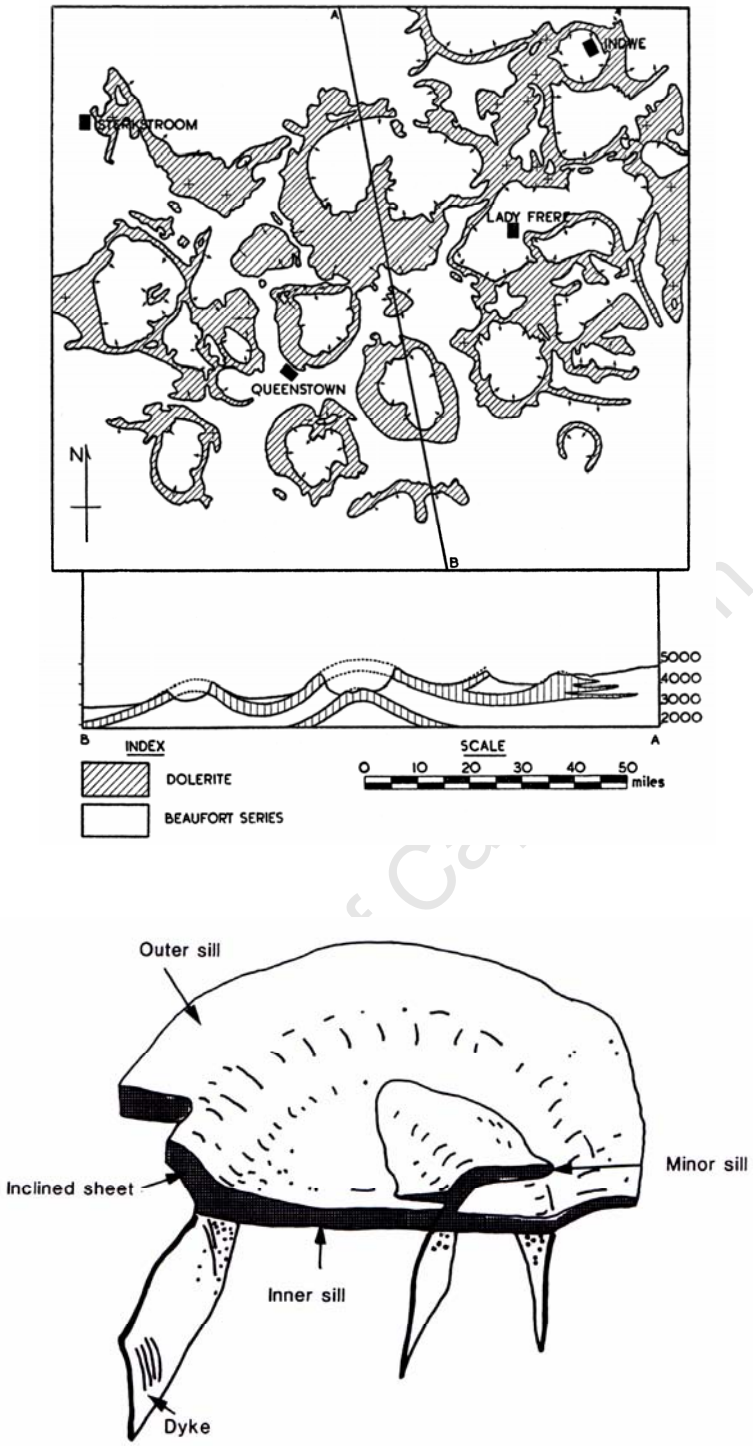

Figure 3.3: *Top:* Dolerite ring outcrops and interpreted cross-section along line A-B after Walker and Poldevaart (1949), who inferred that the rings represent the surface expression of an undulating dolerite sheet. *Bottom:* Alternative interpretation of the three-dimensional geometry of dolerite rings, after Chevallier and Woodford (1999). Here, sills at different elevations are connected by an inclined dolerite sheet or ring dyke.

3.2.3 Distribution of Karoo dolerites

In southern Africa, pre-Karoo Supergroup outcrops are rarely penetrated by the Karoo dolerite suite, and then only by minor intrusions that are usually dykes (du Toit, 1920). Karoo dolerite is also largely absent from outcrops and borehole cores in the Main Karoo Basin's southern and southwestern margins that were deformed by the Cape Fold Belt (e.g. Walker and Poldevaart, 1949; du Toit, 1954; Tinker *et al*., 2008a). However, Karoo dolerite sheets have been observed to be abundant within the alluvial mudstones and sandstones of the lower Beaufort Group, but relatively scarce within the glacial diamictites of the Dwyka Group (Walker and Poldevaart, 1949). Du Toit (1920) noted that preferential intrusion of Karoo dolerites occurs at the contact between the Dwyka and Ecca Groups, at the contact between the Whitehill and Prince Albert Formations (black shale units within the Ecca Group), and at the Ecca-Beaufort Group contact.

According to Woodford and Chevallier (2002) and van Zijl (2006), Karoo dolerite intrusions in the Main Karoo Basin may be grouped into three generalised vertical zones. These are:

1) A lower zone at the base of the Karoo Supergroup, where horizontal sills intrude into well-laminated shales of the lower Ecca Group;
2) A middle zone, extending from the upper Ecca Group through the overlying Beaufort Group and into the upper Karoo Supergroup, consisting of a dense network of basin-shaped intrusions amongst interbedded sandstones, mudstones and shales; and
3) An upper zone at the top of the Karoo sedimentary pile, characterised by steeply dipping dolerite sheets and dykes.

Spatially, large intrusive dolerite suites may be typically expressed in radiating dyke swarms (e.g. the Central Atlantic Magmatic Province), but no such radiating style of intrusion has been found within the Karoo dolerite suite (Chevallier and Woodford, 1999). Chevallier and Woodford (1999) recognised that Karoo dolerite dykes are aligned principally along east-west and north-northeast trends (**Figure 3.4**), and they interpreted this as an indication of pre-rifting shear stresses at the time of dolerite emplacement. Multiple phases of dolerite magma injection have also been demonstrated by intrusive contacts (du Toit, 1954), although debate remains over the

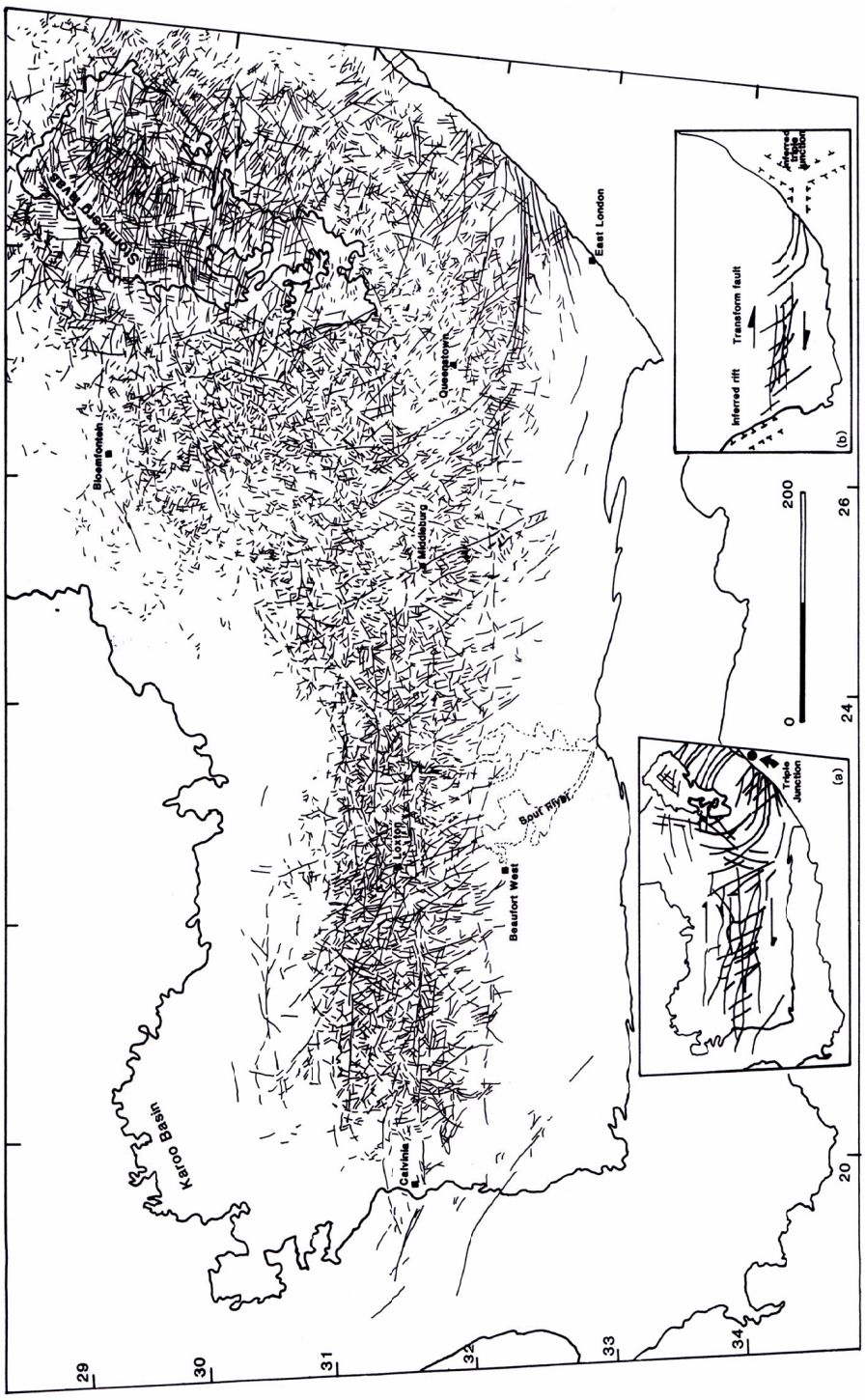

Figure 3.4: *Main image:* The distribution of dolerite dykes in the Main Karoo Basin, after Chevallier and Woodford (1999). *Left inset (a)* and *right inset (b):* Structural and geodynamic interpretations, respectively, of Chevallier and Woodford (1999), who inferred a failed transform rift with an east-west right-lateral shear sense and a triple junction off the east coast at the time of dolerite dyke emplacement, resulting in the intrusion of north-northwest trending dolerite dykes.

possible mechanisms of Karoo dolerite emplacement (e.g. Chevallier and Woodford, 1999 and references therein; van Zijl, 2006).

3.2.4 Effects of Karoo dolerite emplacement

Hydrothermal vent complexes and breccia pipes have been identified within the Karoo Basin, and have been related to the intrusion of Karoo dolerites (Jamtveit *et al*., 2004; Svensen *et al*., 2007). Although previously identified as volcanic diatremes or a result of phreatomagmatic activity, hydrothermal vents within the upper Karoo Supergroup might rather have been generated shortly after dolerite sill intrusion, possibly through the explosive release of fluids near the upper sill surface (Jamtveit *et al*., 2004 and references therein). Breccia pipes associated with the black shales of the Prince Albert and Whitehill Formations in the Ecca Group are similar sub-vertical cylindrical structures that Svensen *et al*. (2007) interpreted as having erupted through gas pressure build-up during contact metamorphism.

Apparent synchroneity between the intrusion and eruption of the Karoo Large Igneous Province and a mass extinction event in the early Jurassic at the Pliensbachian-Toarcian boundary (183.0 ± 1.5 Ma; Gradstein *et al*., 2004), has caused some workers to invoke a causal relationship between these events, where volcanic degassing may have resulted in global warming, a significant sea level rise and widespread oceanic anoxia (Pálfy and Smith, 2000). Jourdan *et al*. (2005), however, maintained that the Early Jurassic extinction event was a relatively minor, second-order biotic crisis, and that Karoo magmatism occurred over a relatively protracted period of time across the entire southern African region (see Section 3.2.1). Yet Svensen *et al*. (2007) argued that intrusion of Karoo dolerites into the Main Karoo Basin may have occurred in a relatively short period of time during the initial stages of Karoo LIP magmatism, and that the contact metamorphism of organic shales may have resulted in the explosive release of up to 27 400 Gt of CO_2 into the atmosphere from thousands of breccia pipes, triggering global warming, ocean anoxia and the extinction of marine species. These authors also noted that the zircon date of 182.5 ± 0.4 Ma for a dolerite sill related to a number of these breccia pipes supports a causal link with the Pliensbachian-Toarcian biotic crisis (Svensen *et al*., 2007). The possibility of a causal link was acknowledged by Jourdan *et al*. (2008), who noted that either pipe eruption may have coincided with sill emplacement over a ~3 ± 1 Myr period, or pipes may

have erupted over a much shorter period of time after the build up of gas pressure in the Karoo Basin.

3.3 The weathering of Karoo dolerites

3.3.1 Basaltic rocks and climate

Whilst the emplacement of Karoo dolerites (and the eruption of associated lavas) may have resulted in the release of significant amounts of CO_2 into the atmosphere, the weathering of Karoo dolerites and lavas may have resulted in the capture of large amounts of carbon from the atmosphere. This is because dolerite is composed principally of feldspar and pyroxene minerals, and the weathering of calcium and magnesium silicates results in the long-term removal of CO_2 from the atmosphere (Berner, 1991). For instance, the hydrolysis of calcium-rich plagioclase feldspar (anorthite) leads to the formation of kaolinite:

$$CaAl_2Si_2O_8 + 2CO_2 + 3H_2O \rightarrow Al_2Si_2O_5(OH)_4 + Ca^{2+} + 2HCO_3^- \quad (3.1)$$

and the subsequent precipitation of carbonate in the oceans:

$$Ca^{2+} + 2HCO_3^- \rightarrow CaCO_3 + CO_2 + H_2O \quad (3.2)$$

which results in the net burial of one mole of CO_2 for every mole of plagioclase weathered (e.g. Gislason *et al*., 2009). The net transfer of carbon between Ca and Mg silicates and the ocean-atmosphere may thus be generalized according to the following two equations:

$$CO_2 + CaSiO_3 \leftrightarrow CaCO_3 + SiO_2 \quad (3.3)$$

$$CO_2 + MgSiO_3 \leftrightarrow MgCO_3 + SiO_2 \quad (3.4)$$

where the forward reactions occur during rock weathering, resulting in carbonate precipitation and burial, and the reverse reactions occur during metamorphism and magmatism, with the thermal breakdown of carbonate minerals and the resulting liberation of CO_2 back to the ocean and atmosphere (e.g. Urey, 1952; Berner, 1991).

For the Deccan Trap flood basalts, modelling by Dessert *et al.* (2001) suggests that the combined effect of their eruption at the end-Cretaceous (~65 Ma, e.g. Courtillot *et al*., 1986) and their subsequent weathering has lead to a net decline in atmospheric

CO_2. For the Karoo Large Igneous Province, de Wit, M.J. (2007) estimated that in the mid-Cretaceous, some 6×10^6 km^3 of Drakensberg basalt may have been denuded within 10 million years, and that the weathering of these basalts may have resulted in the capture of 1.5×10^{18} mol of atmospheric CO_2 – more than double the highest estimates for Cretaceous CO_2 levels. Furthermore, de Wit, M.J. (2007) suggested that the capture of atmospheric carbon may have triggered the onset of global cooling at the end of the Turonian (~89 Ma).

Thus silicate weathering may be an effective means of temperature regulation at the Earth's surface (Walker *et al.*, 1981; but an idea first proposed by Ebelmen, 1845, according to Berner, 1998 and Dupré *et al*., 2003). Conversely, as is implied by the literal meaning of the term *weathering*, the chemical weathering of rocks may depend on climatic variables, principally moisture and temperature (e.g. Ollier, 1984). White and Blum (1995), based on their analysis of solute fluxes from watersheds, considered that weathering rates of granitoid rocks vary linearly with precipitation and non-linearly with temperature. An empirical characterisation of this latter non-linearity is provided by the classical Arrhenius equation:

$$k = Ae^{-E_a / RT} \tag{3.5}$$

where k, the rate constant of a reaction, depends on the activation energy, E_a, temperature, T, and the gas constant, R, and where A is a pre-exponential factor (e.g. White and Blum, 1995). Similarly, Dessert *et al*. (2003) argued that run-off and temperature are also the main parameters that control the chemical weathering of basaltic rocks. They proposed that the weathering flux for a catchment may be predicted as a function of local climate, according to the relation:

$$f_w = R_f \times 18.41e^{0.0553T} \tag{3.6}$$

where f_w is the weathering flux in $kg/km^2/yr$, R_f is the catchment mean annual run-off in mm, and T is the mean annual temperature in °C (Dessert *et al*., 2003).

The case for the dependence of basaltic rock weathering rates on climate has been further strengthened, for example, by Gislason *et al*. (2009), who studied a 44-year record of chemical and mechanical weathering fluxes from 8 nearly pristine Icelandic

river catchments. These workers reported significant linear positive correlations between mean annual temperature and both mechanical and chemical weathering fluxes in all catchments, as well as significant correlations between mean annual precipitation and runoff on the one hand, and mechanical and chemical weathering on the other, in 3 of the least glaciated catchments (Gislason *et al*., 2009).

3.3.2 Non-climatic effects on weathering rates

Tectonics may also be crucial in controlling the rate of rock weathering and the resultant long-term capture of atmospheric CO_2. Tectonically active regions such as Himalaya orogen are characterized by high rates of physical erosion that facilitate the exposure of fresh mineral surfaces to chemical weathering (e.g. Raymo *et al*., 1988). As a result, the dependence of chemical weathering on climate may only be significant in high relief (weathering limited) environments where soils are rapidly eroded (Dupré *et al*., 2003). By contrast, lowland tropical environments (e.g. the Congo and Amazon basins) have low chemical weathering rates despite apparently optimal climatic conditions, due to thick soil or regolith protecting the bedrock from chemical weathering (Gaillardet *et al*., 1999; Oliva *et al*., 2003). However, for very high erosion rates (e.g. 2000 - 5000 m/Myr in the high Himalayas; Burbank *et al*., 2003), the low residence time of minerals allows them to be transported virtually unaltered from a catchment, although the subsequent weathering of these minerals in floodplains may be considerable (Gabet and Mudd, 2009).

Vascular plants may also have a significant effect on the rate of rock weathering (Oliva *et al*., 1999); including the weathering of basaltic rocks (Cochran and Berner, 1996). Organic acids, including humic acids, may affect mineral dissolution rates directly through at least three mechanisms, namely by:

1) Affecting the dissolution rate far from equilibrium, through decreasing pH or forming complexes with cations at the mineral surface;
2) Affecting the saturation state of the solution with respect to the mineral; and
3) Affecting the speciation of ions such as Al^{3+} that also affect the mineral dissolution rate (Drever and Stillings, 1997).

Organic acids may also indirectly influence silicate mineral dissolution rates through the dissolution of secondary iron and aluminium hydroxide phases, which in turn increases permeability and accelerates transport (Drever and Stillings, 1997). In

addition, plant roots make fresh mineral surfaces available to chemical weathering by mechanically disintegrating bedrock, although they also bind fine particles and aid the accumulation of soil (e.g. Drever and Stillings, 1997).

3.3.3 Karoo dolerite weathering studies

The possible effect of climate on the weathering of Karoo dolerite was examined in detail by Weinert (1961, 1965). Due to the widespread use of weathered Karoo dolerite and crushed fresh Karoo dolerite as a road-building material in South Africa at the time, Weinert (1961) conducted a range of standard engineering tests on weathered Karoo dolerite material throughout the region, including the determination of Atterberg liquid limits and Atterberg plasticity indices. Atterberg plastic and liquid limits express the weight of contained water as a percentage of the weight of dry soil at the stages where the material exhibits, when stressed, a transition from elastic to plastic behaviour, or plastic to liquid behaviour, respectively, and the Atterberg plasticity index is defined as the liquid limit minus the plastic limit (e.g. Summerfield, 1991). Thus a higher Atterberg liquid limit is indicative of a greater swelling capacity and unsound engineering performance, e.g. due to the presence of smectite clays, and a higher plasticity index indicates a greater moisture range over which a soil may exhibit plastic behaviour (Summerfield, 1991). Weinert (1961) reported that doleritic material displayed sound engineering performance (Atterberg liquid limit < 10 % and Atterberg plasticity index < 30 %) in the western parts of South Africa (west of ~27 ºE) but performed more poorly further east (Weinert, 1961). Furthermore, Weinert (1961) proposed that in these eastern regions, Karoo dolerites typically displayed well developed soil profiles, and were especially prone to "decomposition" (chemical weathering) and the generation of soils, whilst western dolerites typically displayed "disintegration" (physical weathering), and the generation of a dolerite gravel with only partial chemical alteration (Weinert, 1961). This predominance of physical weathering in western regions and chemical weathering in eastern regions was attributed by Weinert (1961) to the significant increase in rainfall from west to east in the interior, summer rainfall region of southern Africa. Weinert (1961) proposed that the 500 mm isohyet (rainfall contour) for mean annual rainfall marked the approximate boundary between chemical versus physical weathering dominated regions (Weinert, 1961).

In addition to annual precipitation, Weinert (1965) found that the engineering performance of dolerite material also coincided with the contours for two other climatic factors, namely potential evaporation and total precipitation in the warmest month (January for South Africa). Weinert (1965) thus combined these climatic factors as a ratio, R:

$$R = \frac{E_J}{P_J} \tag{3.7}$$

where E_J is January potential evaporation, P_J is January precipitation, and where lower values for R favour chemical weathering over physical weathering. The apparent importance of the balance between E_J and P_J emphasizes the importance of summer precipitation in chemical weathering, and it seems reasonable that warmer water should weather rocks more effectively (e.g. equation 3.5). On the other hand, because evaporation is higher during the warm summer months than during the cooler winter months, the amount of time during which water may weather a rock may be less for summer precipitation events than for events occurring in winter (Weinert, 1965). In order to take this seasonal effect into account, Weinert (1965) expressed rainfall seasonality as the ratio D:

$$D = \frac{12 \times P_J}{P_a} \tag{3.8}$$

where P_J is again January precipitation and P_a is annual precipitation (Weinert, 1965). Where $D > 1$, summer rainfall is indicated, where $D < 1$, winter rainfall is indicated, and where $D \approx 1$, rainfall is distributed fairly evenly throughout the year (Weinert, 1965). Multiplication of R by D yields Weinert's (1965) N-value, where:

$$N = 12\frac{E_J}{P_a} \tag{3.9}$$

Weinert (1965) proposed that the N-value thus constitutes a numerical expression of the balance of those climatic factors that are important for Karoo dolerite weathering, and that the contour N = 5 represents the boundary between regions where chemical weathering predominates ($N < 5$) and where physical weathering predominates ($N > 5$; **Figure 3.5**). However, Weinert (1965) also acknowledged that the validity of N-

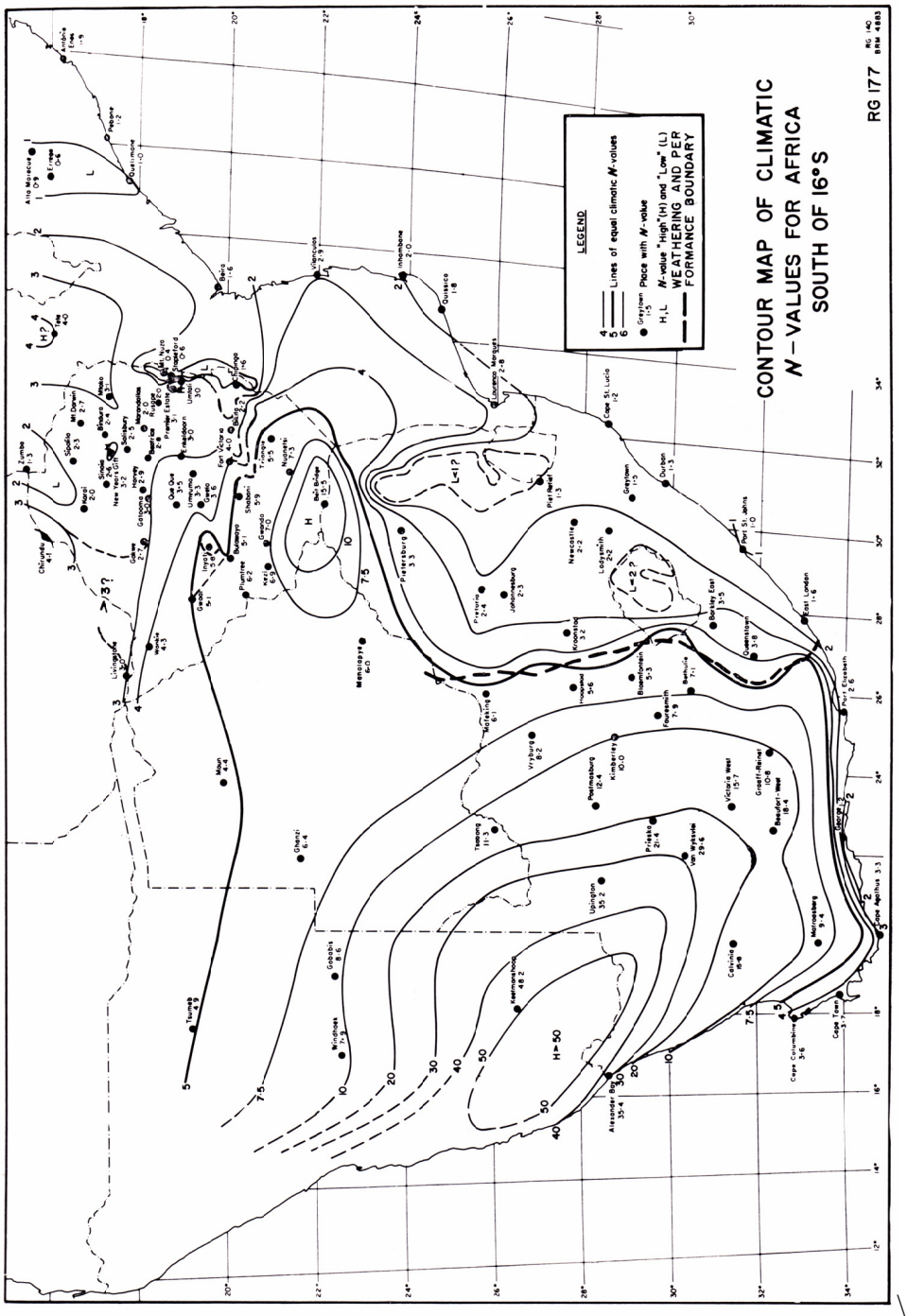

Figure 3.5: Map of N-values (solid lines) in southern Africa, after Weinert (1965). The N-value is a climatic measure of the relative dominance of physical over chemical weathering in dolerites, where N < 5 signifies the dominance of chemical weathering, and N > 5 signifies the dominance of physical weathering. Thus for weathered doleritic material, the N = 5 contour coincides with the boundary (dashed line) between western areas of sound engineering performance (Atterberg liquid limit < 10; Atterberg plasticity index < 30), and eastern areas of less sound performance.

values is apparently restricted to areas with similar climates to southern Africa (warm semi-arid or warm with seasonal rainfall). In cooler climates such as in northern Europe, Weinert (1965) found that physical weathering was more predominant than expected from N-values, and in tropical regions, a double rainy season and fairly uniform temperatures throughout the year made the determination of N-values problematic (Weinert, 1965).

Weinert (1965) also admitted that the products of weathering that remain in the contemporary southern Africa landscape may have been produced at some time in the geological past, under different climatic conditions. Indeed, various authors have identified, for example, products of Pleistocene glacial and periglacial mechanical weathering within the contemporary southern African landscape, particularly in the Lesotho highlands and Cape Fold Belt mountains, although such interpretations are frequently contentious (Boelhouwers and Meiklejohn, 2002, and references therein). Marker (1986) proposed a periglacial origin for scree slopes below dolerite scarps in the eastern Cape, but this was disputed by Sumner and de Villiers (2002) who found no evidence for such an interpretation, but noted that the region was previously subjected to a phase of enhanced mechanical weathering and block production.

Variables other than climate may also be important for determining the nature and intensity of Karoo dolerite weathering. Beater (1947) was of the opinion that the deep chemical weathering of Karoo dolerite observed in coastal KwaZulu-Natal (southeast South Africa) was determined more by local groundwater conditions than by climate. Walker and Poldevaart (1949) proposed that greater weathering of dolerite occurred on poorly drained, flat surfaces, and emphasised the role of grain size and mineralogy in determining the relative extent of chemical weathering, stating that fine-grained ophitic dolerites are less subject to chemical weathering than coarser-grained varieties (Walker and Poldevaart, 1949). These authors also proposed that dolerites that had experienced hydrothermal alteration were more subject to surface weathering (Walker and Poldevaart, 1949). Indeed, according to Bell and Jermy (2000; and references therein), unweathered Karoo dolerite material may experience rapid disintegration to gravel- or sand-sized particles when placed on stockpiles after quarrying - a phenomenon attributed to the hydration of secondary hydrothermal mineral phases such as montmorillonite and chlorite.

Recently, Røyne *et al*. (2008) emphasized the coupling of chemical and physical processes in the weathering of dolerite. Based on observations from a field site with an annual rainfall of 600-800 mm, they presented a reaction-induced hierarchical fracturing model for Karoo dolerites. In this model, chemical weathering initiates volumetric expansion, which not only causes spheroidal weathering, but results in successive generations of fracturing and subsequent weathering, causing the dolerite to weather at an accelerating rate (Røyne *et al*., 2008).

3.4 Karoo dolerite topography

As mentioned in Section 2.2, much of the southern Great Escarpment coincides with the southern limit of Karoo dolerite outcrop, and as discussed in Section 3.2, dolerites may form prominent topographic rings, although the three-dimensional geometry of these intrusions remains a subject of debate. Indeed, the general positive relief exhibited by Karoo dolerites has frequently been remarked upon in the literature. For instance, Hatch and Corstorphine (1905) observed that the Karoo dolerites form prominent surface features, but proposed that dolerites were less conspicuous in northern and eastern outcrop regions (former Orange Free State and southern Transvaal) than in western and southern outcrop regions (former Cape Colony), due to more argillaceous country (host) rocks in the Cape being more easily weathered.

Walker and Poldevaart (1949) stated that even in humid eastern regions, the Karoo dolerites form "bold" (i.e. high relief) escarpments (p. 595). They observed that dolerite sills formed the caprocks for abundant table mountains (mesas) and narrower *koppies* (buttes or inselbergs), or formed boulder-strewn plateaux, but mentioned that dolerite dykes were generally inconspicuous in the landscape (Walker and Poldevaart, 1949). Other workers such as King (1951) and du Toit (1954) made similar observations to Walker and Poldevaart (1949), with du Toit (1954) also commenting that dolerite outcrops produced chains of hills that rise above the flatter ground built of Karoo sedimentary rocks. King (1951) remarked that in the Lesotho region, dolerite dykes formed positive features in shales but negative features in the massive aeolian sandstones of the Clarens Formation. Furthermore King (1951) noted that inclined dolerite sheets may give rise to "pseudo-*cuestas*" (a *cuesta* is a ridge with a gentle slope on one side and a steep scarp on the other, formed by tilted sedimentary rocks, e.g. Cruden, 2003). King (1951) also observed that the Howick Falls, a 200 ft

(~60 m) waterfall on the Umgeni River in Natal (southeast southern Africa), is formed entirely by a dolerite sill.

The significance of Karoo dolerites to stream development has been emphasised more recently by a model of drainage evolution proposed by Tooth *et al*. (2002; 2004). These authors showed that resistant dolerite sills in three tributaries of the Vaal river catchment form local erosion base levels, and are associated with steeper stream gradients and straighter river courses. In contrast, low-gradient, meandering streams and wetlands were reported to develop upstream of the dolerites in laterally eroding valleys of sedimentary country rocks, until breaching of the dolerite and subsequent river incision apparently causes floodplain abandonment (Tooth *et al*., 2002, 2004). In this model, the denudation of dolerites is thus the rate-determining step in the overall lowering of the landscape.

Although widespread in the literature, arguments that dolerites are topographically significant are generally based on qualitative field observations, and perhaps subject to individual bias. Here, a quantitative geospatial assessment of Karoo dolerite topography is presented, based on the analysis of a high resolution digital elevation model (DEM) and a geological database within a geographic information system (GIS). This analysis includes an attempt to test Hatch and Corstorphine's (1905) claim that the relief of Karoo dolerites is variable and dependent on country rock lithology, as well as Walker and Poldevaart's (1949) claim that dolerite relief is relatively invariable and not dependent on local climate. If the relative degree of dolerite chemical weathering varies across the region as a function of climate, as proposed by Weinert (1961, 1965), Walker and Poldevaart's (1949) claim is perhaps surprising.

3.5 Geospatial analysis of Karoo dolerite topography

A GIS is a problem-solving platform that allows for the querying of digital geospatial data with a degree of sophistication not possible with hard-copy maps. The aims of this analysis are:

1) To compare the topography of areas of Karoo dolerite outcrop with the topography of neighbouring rocks; and
2) To examine how variable the topographic expression of Karoo dolerite across southern Africa is, and what the cause of any variation might be.

All analyses here are conducted with the use of ArcGIS 9.3 software.

3.5.1 Topography

The topography of an area may be described according to a number of topographic (or morphometric) parameters that are calculated from a DEM (i.e. from spatial elevation data in raster format). In this study, the following two parameters are determined:

1) Average elevation, Z_{mean}, which is the mean value for elevation Z in a defined area.
2) Average relief, R_{mean}, which is the mean value for R in a defined area, where R is the local relief, defined as:

$$R = (Z_{max} - Z_{min})_r \tag{3.10}$$

where Z_{max} and Z_{min} are the maximum and minimum elevation values, respectively, within a defined neighbourhood r of a given pixel (e.g. Formento-Trigilio and Pazzaglia, 1998). In this study, a 1 pixel neighbourhood is used. Local relief is therefore an indication of the local change in elevation, and is thus a proxy for slope that is dependent upon the spatial resolution of the DEM. Relief was chosen as a parameter of interest instead of slope angle *per se*, because numerical errors have been shown to arise when slope angles are calculated in ArcGIS 9 (Mielke, 2009).

The DEM (digital elevation model) used in this study is based on the SRTM (Shuttle Radar Topography Mission) 3 arc-second (~90 m) resolution dataset, acquired onboard the Space Shuttle Endeavour in February 2000 (Rabus *et al*., 2003). A processed version (also known as Version 3) released by Jarvis *et al*. (2006) was downloaded from the site http://srtm.csi.cgiar.org. This processed version is a result of:

- Substantial editing by the National Geospatial Intelligence Agency to define waterbodies and coastlines, and remove single pixel errors - “spikes” and “wells” (http://www2.jpl.nasa.gov/srtm); and
- Data void filling through interpolation techniques and the use of auxillary DEMs by the Consortium for Spatial Information (CSI), an initiative within

the Consultative Group for International Agriculture Research (CGIAR; Jarvis *et al*., 2006).

SRTM data for Africa south of 20 ºS was downloaded in 5 º × 5 º tiles in ASCII format, converted to ESRI grid files and mosaicked. Pixels with values below 0 were then identified within the dataset along coastlines and the mouths of rivers, and were judged as processing artefacts and normalised to a value of 0. The resulting DEM, projected on a geographical coordinate (latitude/longitude) grid and with elevation in meters above sea level (WGS1984 coordinate system; EGM96 geoid) is displayed in the previous chapter (**Figure 2.2)**.

The vertical accuracy of SRTM data globally is stated to be better than 16 m at the 90 % confidence limit (Jarvis *et al*., 2004). Rodriguez *et al.* (2006) estimated that for SRTM data covering Africa, 90 % error limits in absolute geolocation were 11.9 m, and 90 % error limits in absolute vertical height were 5.6 m. In southern Africa (Botswana and Zambia), ground-truthing using precision GPS measurements (n = 32) by T. Flügel (unpublished data, 2009) show that, except in highly forested and/or topographically complex areas, absolute accuracy of SRTM elevation relative to orthometric height (height relative to the geoid) is ± 8 m at the 95 % confidence limit. Much of this error is systematic, with a strong linear relation between SRTM elevation and orthometric height, such that normalization of SRTM elevation data according to this relation yields an accuracy of ± 4 m at the 95 % confidence limit (T. Flügel; unpublished data, 2009). However, it must also be borne in mind that the SRTM DEM simply reflects the elevation of the earth's surface as determined by radar, although not necessarily the ground surface, and includes the height of man-made structures and dense vegetation (e.g. Nelson *et al*., 2009). Nevertheless, given the generally low height of vegetation (typically bushes and grasses) and the low population densities in the generally rural areas examined in this study, vegetation and man-made structures are unlikely to have a significant effect on the calculation of the parameters defined above.

3.5.2. Geology

Digital geological data used for this analysis was modified from unpublished data obtained from the Council for Geoscience, South Africa. This data had been digitised

by the Council for Geoscience from three published 1:250,000 scale geological maps, *3222 Beaufort West* (Marsh, 1979), *3024 Colesberg* (Le Roux, 1998) and *2730 Vryheid* (Wolmarans, 1988). Printed copies of these maps were also used in this study for data verification and the augmentation of attribute tables. These three particular maps were chosen because they correspond to widely spaced regions from which dolerite samples were collected for cosmogenic nuclide analysis. The positions of these map sheets relative to the Karoo dolerite distribution in southern Africa are shown in **Figure 3.6**.

These maps represent the highest resolution source of geological data available for this study. Given the discontinuous nature of Karoo dolerite outcrops, the spatial resolution of these maps is likely to be a limiting factor in the accuracy of the results presented here. A visual comparison of the geological data and the SRTM data suggests a slight spatial displacement, in places, of the geological data used, typically by a few pixels of the DEM, which is likely a result of errors arising during map projection or digitization. However, recalculation of Z_{mean} and R_{mean} values after manually shifting the locations of polygons demonstrates that the effects of this offset in the determination of these catchment-averaged topographic parameters such as R_{mean} and Z_{mean} is likely to be insignificant (i.e. no more than a few meters). Furthermore, to correct the geological data on the basis of a non-correlation with topography assumes a direct dependence of geology on topography - the very subject of inquiry here.

3.5.3 Catchments

In order to compare the R_{mean} and Z_{mean} values of dolerites with those of other rocks, it was judged necessary to define meaningful spatial units for which Z_{mean} and R_{mean} values could be calculated. Instead of defining arbitrary areas according to geographical coordinates, small river catchments were chosen as the units of comparison. Catchments represent the natural spatial units within which fluvial erosion occurs, and thus allow for the comparison of elevation and relief relative to a common local erosional base level. The "quaternary river catchments" defined by the Department of Water Affairs, South Africa, and sourced from Schulze (2007), are the units for which lithology-specific topographic parameters were calculated. These catchments are fourth-order catchments defined within a system of linked, cascading

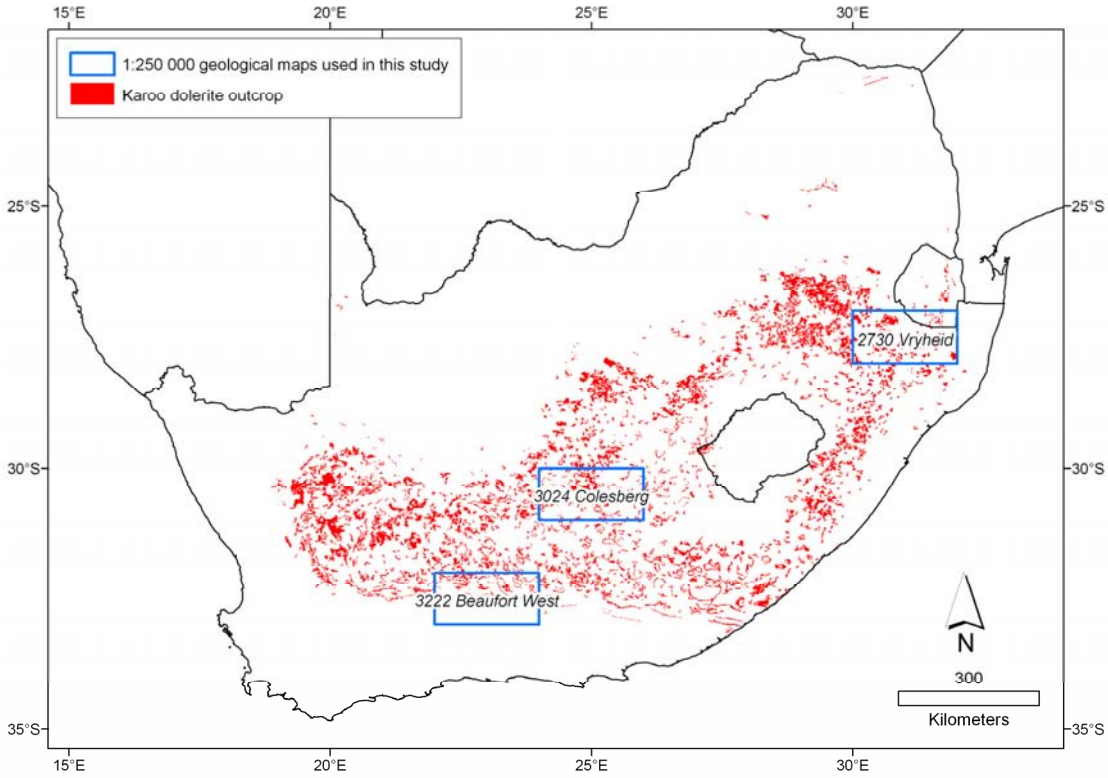

Figure 3.6: The locations of the three digitised 1:250,000 geological map sheets used in these analyses: *3222 Beaufort West*, *3024 Colesberg* and *2730 Vryheid*, relative to the distribution of Karoo dolerites in southern Africa.

catchments used in hydrological modelling and national water management studies, and their alphanumeric names, as given by Schulze (2007), are used herein. Lithology-specific topographic parameters were thus calculated for those catchments or parts of catchments that overlapped with the areas covered by the geological data.

3.5.4 Comparison of topography and geology

The Council for Geoscience's 1:250,000 geological maps for South Africa were mapped by different authors at different times, and so mapped units do not continue seamlessely across map boundaries. Furthermore, the stratigraphic nomenclature used in these maps is not consistent, partially due to lateral facies changes in regionally extensive sedimentary units such as the Beaufort Group (Rubidge *et al*., 1995). Thus it was decided to conduct three separate analyses for the three separate map sheets. The results of these analyses are presented below.

3222 Beaufort West

The digitised and modified map of *3222 Beaufort West* (Marsh, 1979) and associated catchments (Schulze, 2007) is shown in **Figure 3.7**. The SRTM elevation and relief of this area is shown in **Figure 3.8**, and a composite map of geology, catchments and relief is provided in **Figure 3.9**. The structurally-deformed Dwyka Group and Ecca Group (Ripon, Fort Brown and Waterford formations) crop out along the southeastern border of the map, but no Karoo dolerite occurs in the same catchments as these units. The three main geological units that do crop out in the same catchments as Karoo dolerite are:

1. The Abrahamskraal Formation of the Adelaide Subgroup, Beaufort Group, described within the database as mudstone (generally greenish-grey) and subordinate sandstone;
2. The Teekloof Formation, also of the Adelaide Subgroup, Beaufort Group, described as mudstone (brownish-red and greenish-grey) and subordinate siltstone and sandstone; and
3. Cenozoic alluvium, an amalgamation of units described in the database as Cenozoic alluvial slope deposits, Quaternary alluvium and scree, and Quaternary waterbodies.

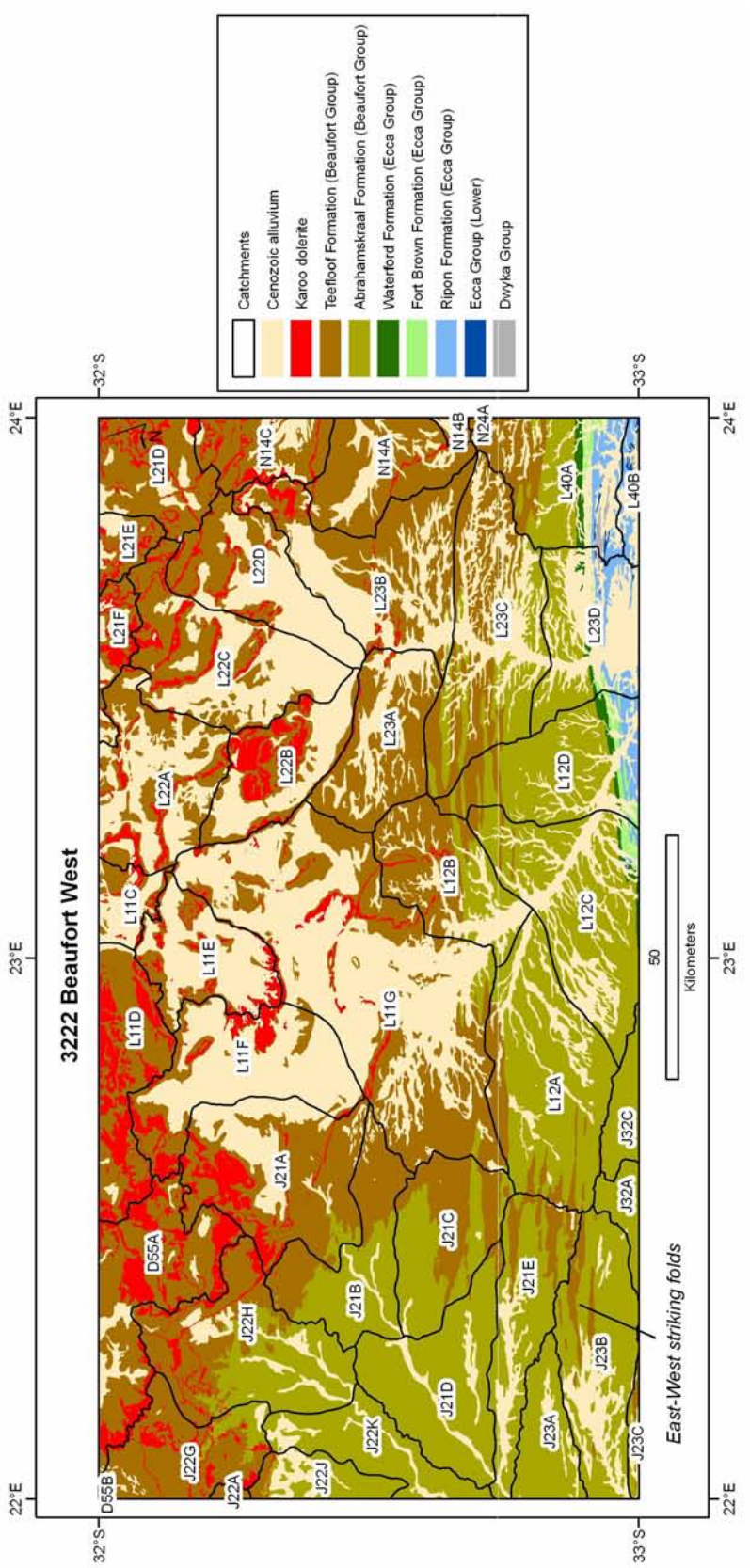

Figure 3.7: Geology modified from the *3222 Beaufort West* map sheet (Marsh, 1979). Labelled river catchments after Schulze (2007) are also shown.

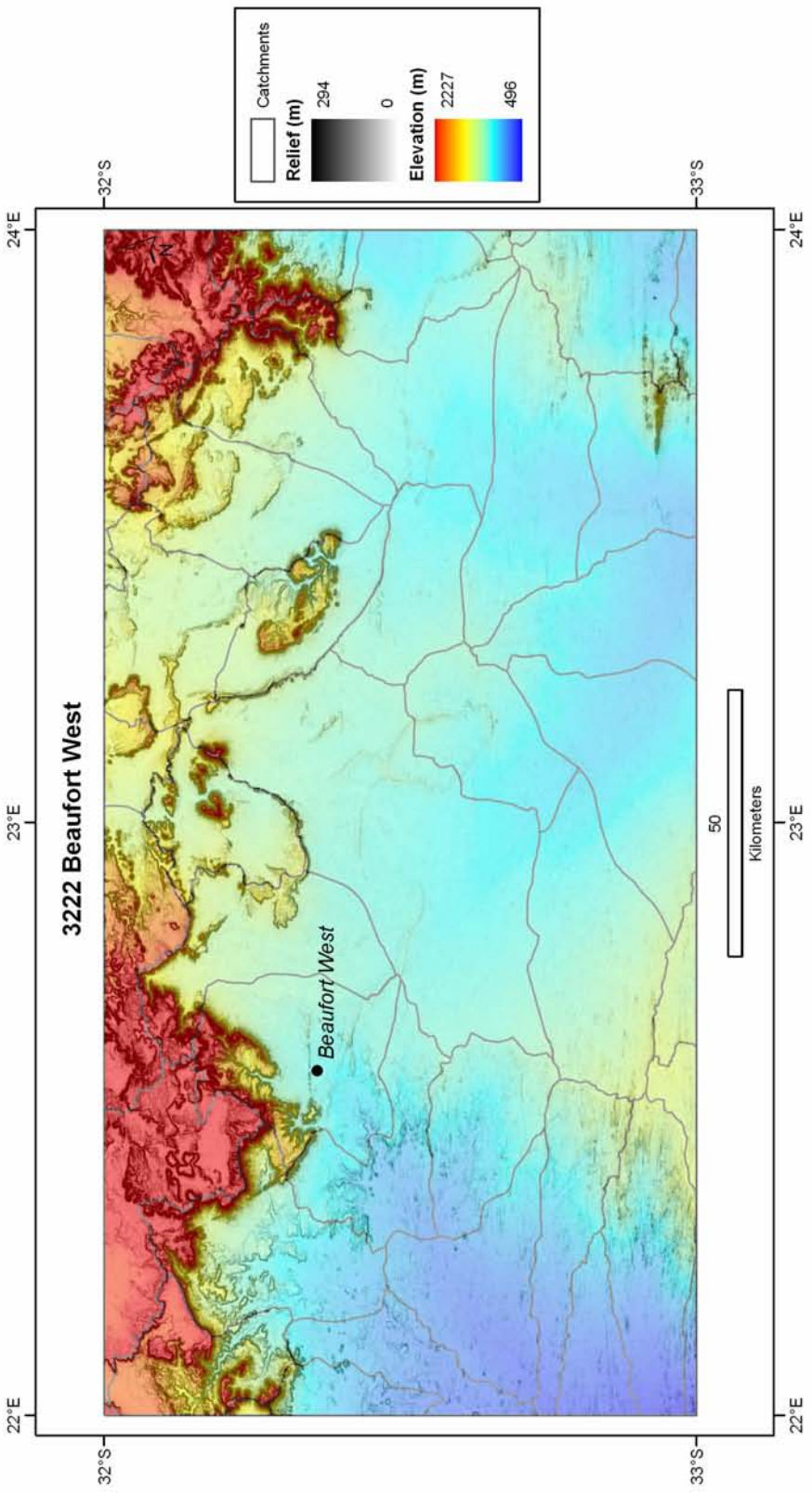

Figure 3.8: Elevation (Z, colour scale) and relief (R, greyscale) for the same area as in **Figure 3.7**, derived from the SRTM DEM (Jarvis *et al*., 2006). The location of the town Beaufort West and the boundaries of river catchments are also shown.

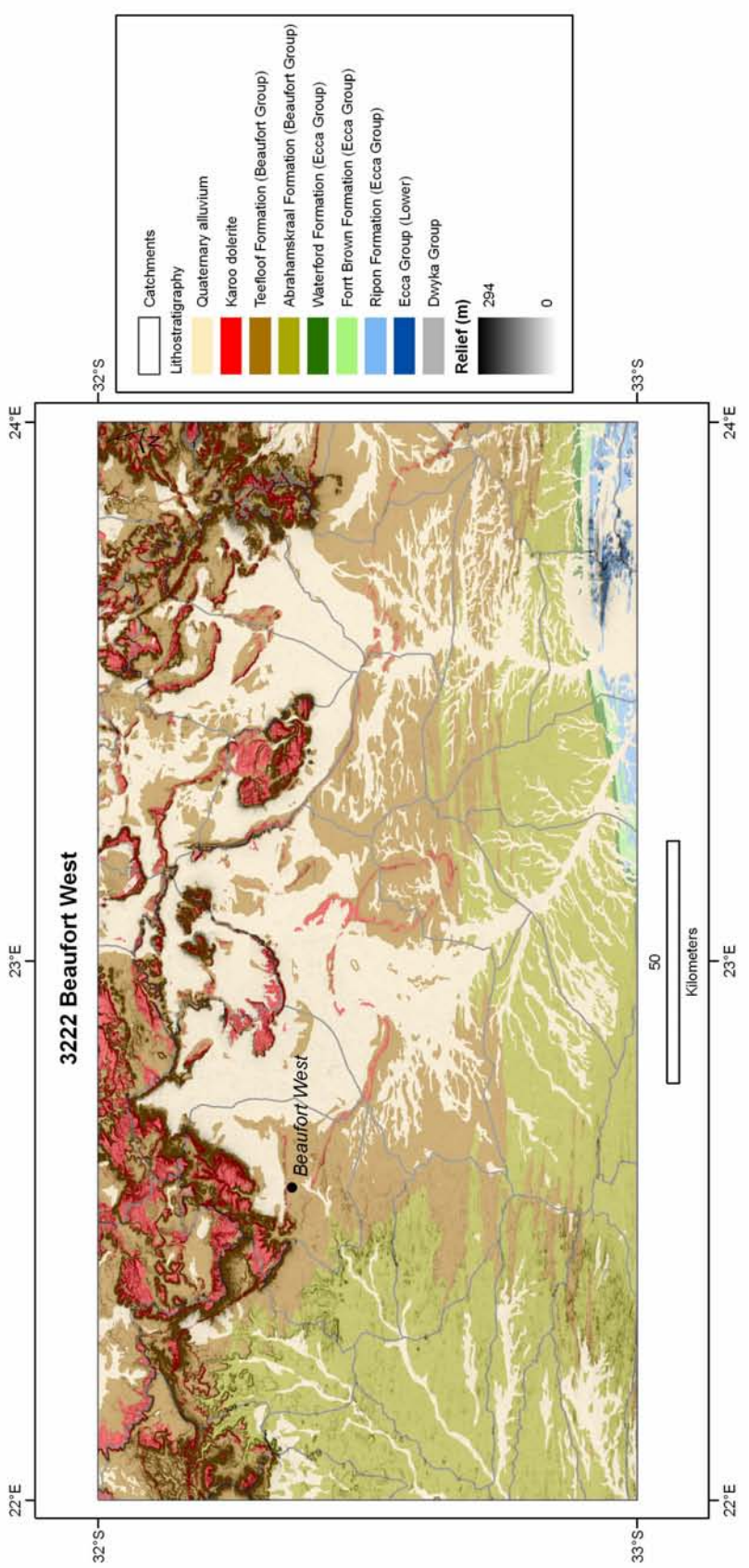

Figure 3.9: Composite map of geology, relief and river catchments for the map sheet *3222 Beaufort West* (Marsh, 1979).

Z_{mean} and R_{mean} values calculated for each of these units, and for Karoo dolerite, are given in **Table 3.1**, for a total of 43 catchments.

Z_{mean} values are compared in **Figures 3.10** and **3.11**. **Figure 3.10** shows that Z_{mean} for Karoo dolerite is in all cases higher than for the other geological units in the same catchments (sometimes by more than 500 m), with the exception of 1 catchment out of 28 (*L11E;* central northern region in **Figure 3.7**), which yields a slightly higher mean elevation for the Teekloof Fm. (by 4 m). **Figure 3.11** demonstrates that for nearly all catchments, the mean elevation of the Teekloof Fm. is in turn higher than the mean elevation of the Abrahamskraal Fm. and the Cenozoic alluvium. An exception is catchment *N24A* (eastern border of the area, **Figure 3.7**), where only a marginal proportion of the catchment area is present in the map area. Mean elevation values for the Abrahamskraal Fm. and for the Cenozoic alluvium are comparatively low, with only 11 out of 23 catchments having higher Z_{mean} values for the Abrahamskraal Fm. Some covariance of Z_{mean} values occurs for most pairs of geological units ($R^2 > 0.5$), due to the dependence of both variables on the general catchment elevation. However, no correlation exists between the Z_{mean} values of the Abrahamskraal Fm. and those of the Karoo dolerite or the Teekloof Fm. ($R^2 = 0.02$ and 0.22, respectively), and the mean elevation of the Abrahamskraal Fm. is consistently low. The most significant correlations occur between the Z_{mean} values of the Teekloof Fm. and Z_{mean} values of Karoo dolerite and Cenozoic alluvium ($R^2 = 0.76$ and $R^2 = 0.83$, respectively).

R_{mean} values are compared in **Figures 3.12** and **3.13**. Unlike mean elevation values, mean relief values do not co-vary significantly. Karoo dolerite displays higher R_{mean} values than the Abrahamskraal Fm. or the Cenozoic alluvium in all catchments where they both crop out, and higher R_{mean} values than the Teekloof Fm. in 22 out of 28 catchments (**Figure 3.12**). In the 6 catchments where the mean relief of the Teekloof Fm. is greater than or equal to that of the Karoo dolerite (*D55B, J22K, L11E, L11F, L21F* and *L22B*), dolerite outcrops are either very limited (e.g. catchment *J22K*, western margin of the area) or form extensive, sub-horizontal sills (e.g. catchment *L22B*, central eastern region). A comparison of the R_{mean} values for the Teekloof and Abrahamskraal Formations shows that the Teekloof exhibits greater average relief in 17 of 22 catchments (**Figure 3.13**). The Teekloof and Abrahamskraal Formations

Catchment	Area (km^2)	Abrahamskraal Fm.		Teekloof Fm.		Karoo dolerite		Cenozoic alluvium	
		Z_{mean} (m)	R_{mean} (m)	Z_{mean} (m)	R_{mean} (m)	Z_{mean} (m)	R_{mean} (m)	Z_{mean} (m)	R_{mean} (m)
D55A	1873			1579	16	1666	23	1494	5
D55B	1261			1421	18	1460	10		
J21A	855	787	10	984	19	1284	45	915	6
J21B	531	755	10	853	8	1175	81	758	5
J21C	526	791	7	849	6			739	4
J21D	650	679	6	848	6			654	5
J21E	505	801	8	938	9			711	5
J22A	437			1229	43	1534	71		
J22G	567	901	19	1280	28	1361	41	1164	4
J22H	808	815	9	1172	34	1403	51	887	8
J22J	378	727	9	1080	45	1109	80	784	6
J22K	479	691	7	986	73	1098	54	718	6
J23A	763	643	6					641	5
J23B	783	834	11	895	13			676	6
J23C	515	651	11	735	15			622	9
J32A	708	1046	5	1085	13			1035	4
J32C	225	1011	6	1070	13				
L11C	568			1140	18	1181	23	1073	7
L11D	1287			1350	24	1453	27	1247	6
L11E	456			1129	40	1126	35	1006	9
L11F	745			1249	37	1358	34	953	6
L11G	2025	835	4	884	5	953	18	878	4
L12A	906	913	4	917	4			866	4
L12B	519	818	4	868	4	878	9	821	4
L12C	1068	828	4	841	4			813	4
L12D	870	788	4	855	5			745	3
L21D	865			1545	30	1728	42	1430	18
L21E	712			1469	28	1484	36	1275	10
L21F	576			1273	28	1340	28	1140	12
L22A	1073			1047	10	1137	30	1026	5
L22B	475			1019	31	1086	28	935	7
L22C	760			1139	19	1237	34	947	5
L22D	530			1195	32	1250	50	960	6
L23A	516	822	4	866	4	873	8	846	3
L23B	818	804	3	917	10	1338	46	886	7
L23C	891	813	4	851	4			818	3
L23D	665	790	3					801	6
L40A	361	832	5	903	8			814	6
L40B	378							779	6
N14A	505			865	7	1018	41	840	4
N14B	389			915	8	932	17	888	4
N14C	655			1174	39	1454	68	1041	29
N24A	666			914	6	989	38	926	4
Average	724	807	7	1058	19	1247	38	914	6

Table 3.1: Z_{mean} and R_{mean} values for the Abrahamskraal Formation, Teekloof Formation, Karoo dolerite and Cenozoic alluvium per catchment in **Figure 3.7**. Areas of whole quaternary catchments (including portions beyond the map margins, according to Schulze, 2007) are also shown.

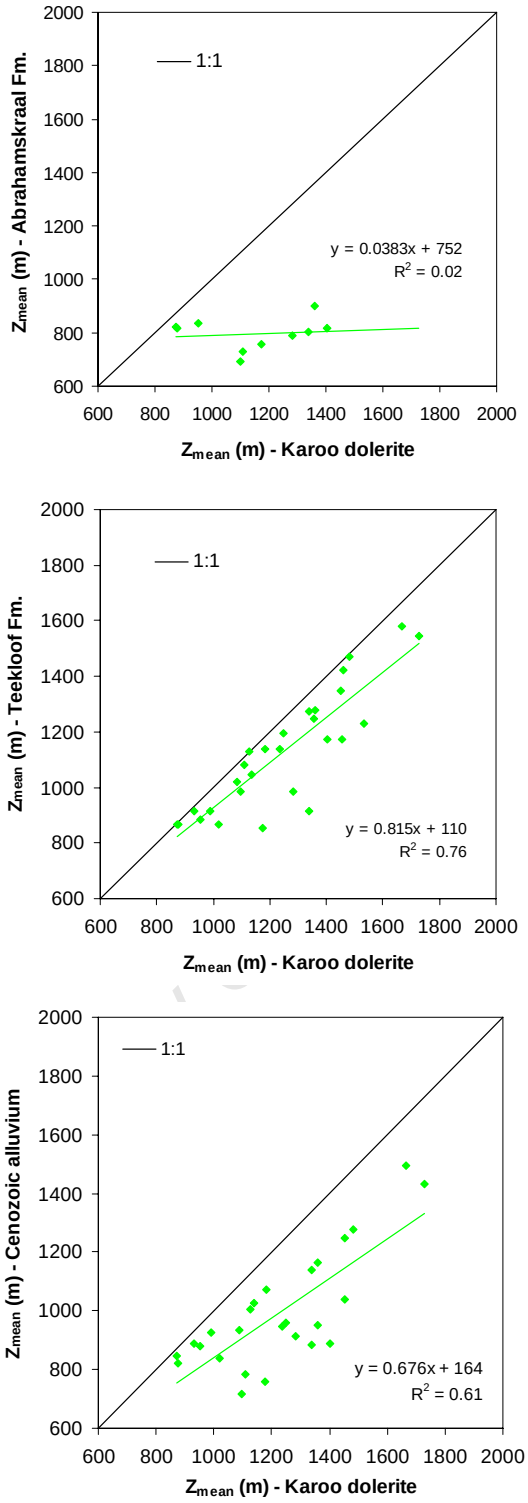

Figure 3.10: Comparison of Z_{mean} values for the Abrahamskraal Fm. (top), Teekloof Fm. (middle) and Cenozoic alluvium (bottom), with those of Karoo dolerite in the map sheet *3222 Beaufort West* (**Figures 3.7**, **3.8** and **3.9**). Note the higher average elevation of Karoo dolerites in comparison with the other geological units for almost all catchments.

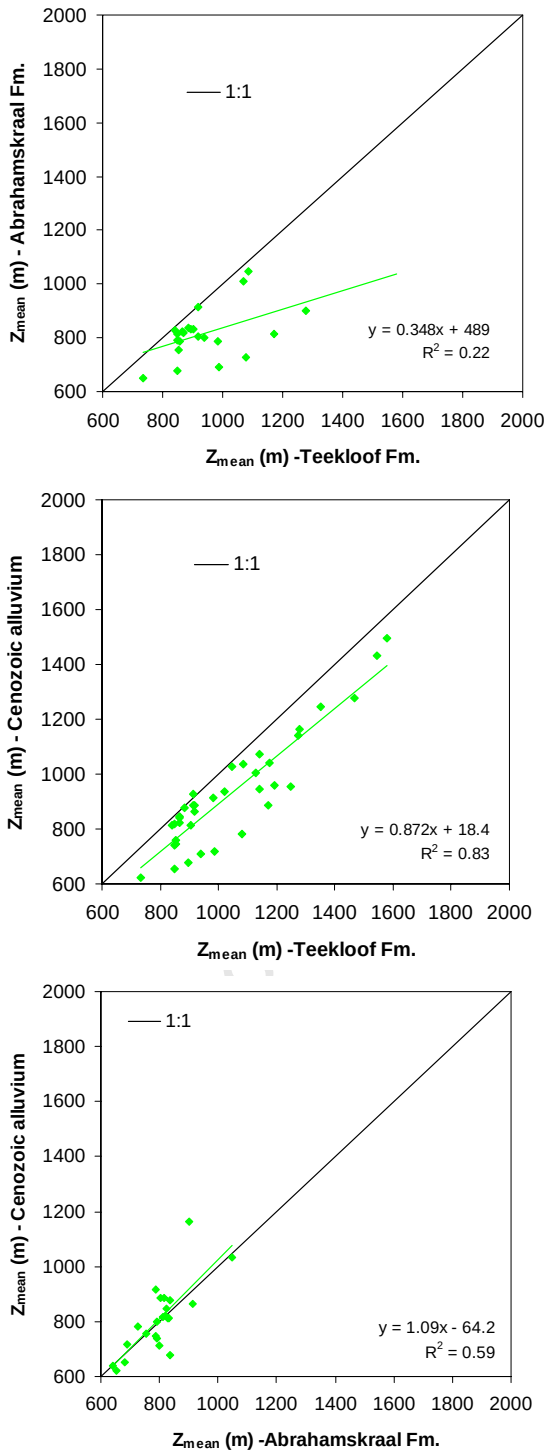

Figure 3.11: Comparisons between catchment-specific Z_{mean} values for the Abrahamskraal Fm., Teekloof Fm. and Cenozoic alluvium in the map sheet *3222 Beaufort West* (**Figures 3.7**, **3.8** and **3.9**). The mean elevations of the Teekloof Fm. are generally higher than for the Abrahamskraal Fm. and Cenozoic alluvium, with the Abrahamskraal Fm. and Cenozoic alluvium both occurring at similarly low elevations.

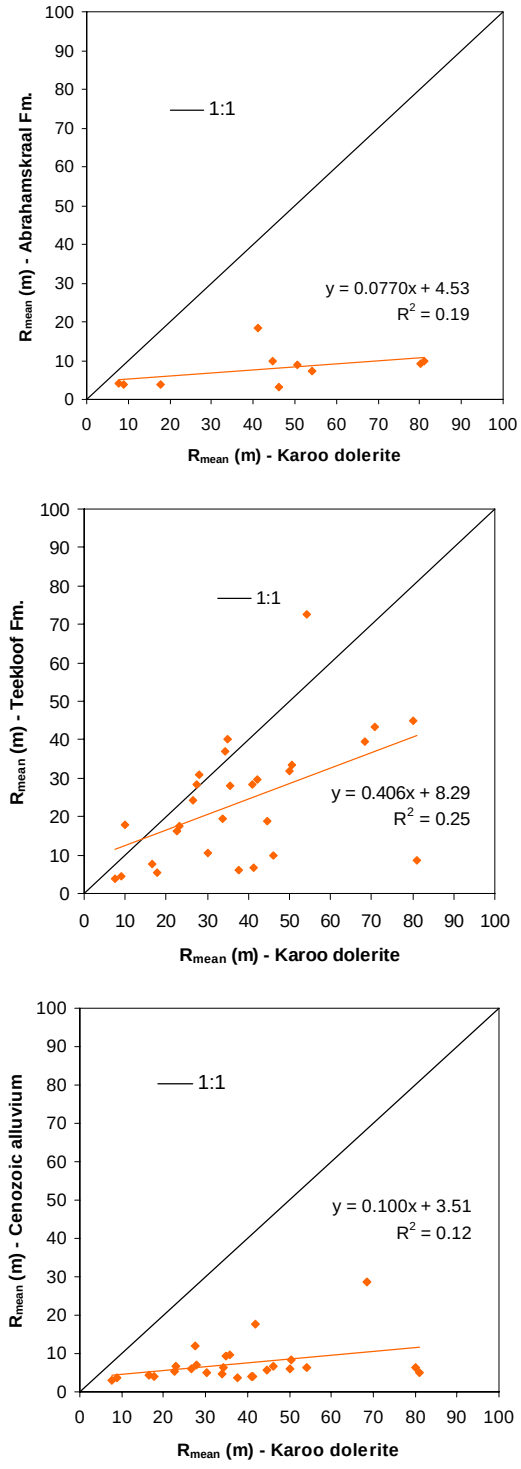

Figure 3.12: Comparisons of catchment-specific R_{mean} values for the Abrahamskraal Fm. (top), Teekloof Fm. (middle) and Cenozoic alluvium (bottom), with those of Karoo dolerite in the map sheet *3222 Beaufort West* (**Figures 3.7**, **3.8** and **3.9**). Note the generally higher relief of Karoo dolerite, and the poor statistical correlation between corresponding R_{mean} values.

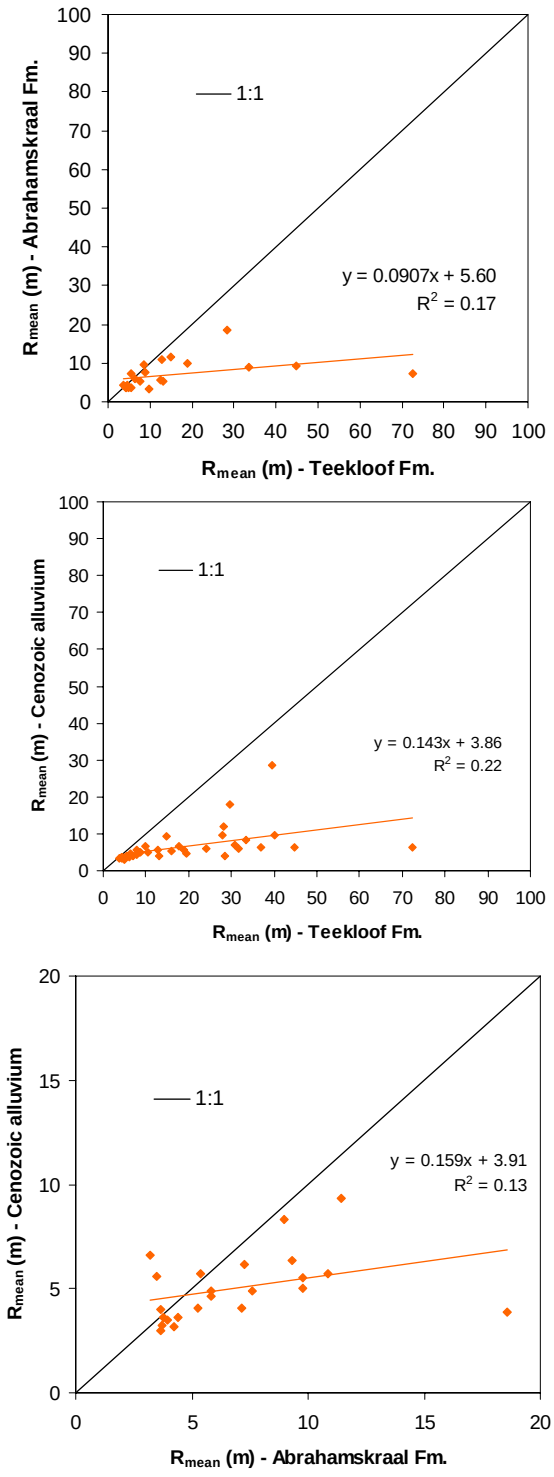

Figure 3.13: Comparisons of R_{mean} values for the Abrahamskraal Fm., Teekloof Fm. and Cenozoic alluvium in the map sheet *3222 Beaufort West* (**Figures 3.7**, **3.8** and **3.9**). The R_{mean} values for the Teekloof Fm. are generally higher than for the Abrahamskraal Fm., which in turn generally displays higher R_{mean} values than the Cenozoic alluvium.

have equivalent R_{mean} values in 5 catchments (*L12A, L12B, L12C, L23A* and *L23C,* central southern and southeastern regions), with higher R_{mean} values for the Abrahamskraal in 2 catchments (*J21B* and *J21C,* central western region). In all cases where the Teekloof Fm. does not exhibit a greater R_{mean} than the Abrahamskraal Fm., Karoo dolerite outcrops are either absent or of limited areal extent. The Teekloof Fm. exhibits higher average relief than the Cenozoic alluvium in 34 of 37 catchments, with equivalent R_{mean} values in the remaining 3 catchments (*L12A, L12B* and *L12C* in the southern central region). R_{mean} values are higher for the Abrahamskraal Fm. than for the Cenozoic alluvium in 15 out of 23 catchments, with 4 catchments (*L11G, L12A, L12B, L12C)* showing equivalent average relief of 4 m for both units, and 3 catchments (*L23B, L23D* and *L40A*) showing higher average relief for Cenozoic alluvium.

In summary, a comparison of the mean elevation and mean relief of 4 different geological units in a total of 43 catchments demonstrates that Karoo dolerites do indeed dominate the topography of the *3222 Beaufort West* map region. Karoo dolerites generally exhibit higher average elevation and relief than other lithologies, although in some catchments, when present as extensive sub-horizontal sills, dolerites may exhibit lower average relief yet high local elevation. Furthermore, the Teekloof Formation of the Beaufort Group (the country rock into which most dolerites are intruded) displays higher R_{mean} values in catchments where a significant amount of dolerite is also present.

The generally higher elevation of the Teekloof Fm. relative to the Abrahamskraal Fm. may be explained in areas of sub-horizontal bedding as simply due to their relative stratigraphic positions. However, even in southern catchment areas where units are folded along the east-west striking northern edge of the Cape Fold Belt, the Teekloof Fm. generally occupies higher ground. This is suggestive of a local contrast in lithology. Indeed, according to the South African Committee for Stratigraphy (1980), the Abrahamskraal-Teekloof Formation contact may be drawn at the base of the Poortjie Member, which is defined as a series of arenaceous zones in the lower part of the Teekloof Fm. The Teekloof Fm. often exhibits greater relief than the Abrahamskraal Fm., although this is not always the case, particularly in the low relief southern region of the *3222 Beaufort West* map area where no Karoo dolerite crops

out. Unsurprisingly, Cenozoic alluvium generally exhibits the lowest R_{mean} and Z_{mean} values in most catchments, although the relief of the alluvium is comparable with that of the two Beaufort Group units in the low relief southern region. Finally, the general lack of correlation between R_{mean} values for all pairs of geological units ($R^2 \leq 0.25$) indicates that the average relief of a given geological unit in a catchment is not influenced significantly by the overall relief of the catchment.

3024 Colesberg

The digitised and modified map of *3024 Colesberg* (Le Roux, 1998) and associated river catchments of Schulze (2007) is shown in **Figure 3.14**. The SRTM elevation and relief of the area is shown in **Figure 3.15**, and a composite map of geology, catchments and relief is provided in **Figure 3.16**. The geology of the area may be divided into five principal units in the following stratigraphic order:

1. The Tierberg Formation of the Ecca Group, described in the database as grey shales with interbedded siltstones in the upper part;
2. The Balfour Formation of the Adelaide Subgroup, Beaufort Group, described as comprising greenish- to bluish-grey and greyish-red mudstones with subordinate sandstones;
3. The Katberg Formation of the Tarkastad Subgroup, Beaufort Group, described in the database as sandstone (pebbly in places) and mudrock (but predominantly arenaceous, according to the South African Committee for Stratigrapy, 1980);
4. The Karoo dolerite suite; and
5. Quaternary alluvium, incorporating alluvium and calcrete of Quaternary age, as well as present-day waterbodies.

According to vertebrate biostratigraphy, the Permian-Triassic boundary lies within the uppermost member of the Balfour Formation, below the Katberg Formation (Rubidge *et al*., 1995).

The map *3024 Colesberg* covers a smaller range of surface elevation (1112 - 1779 m) and relief (≤ 213 m) than the map *3222 Beaufort West* (elevation = 496 - 2227 m; relief ≤ 294 m), as it covers the central southern African plateau, rather than the southern escarpment. Karoo dolerite outcrop occurs in every catchment covered by the *3024 Colesberg* map, and the most continuous dolerite outcrops generally occur as

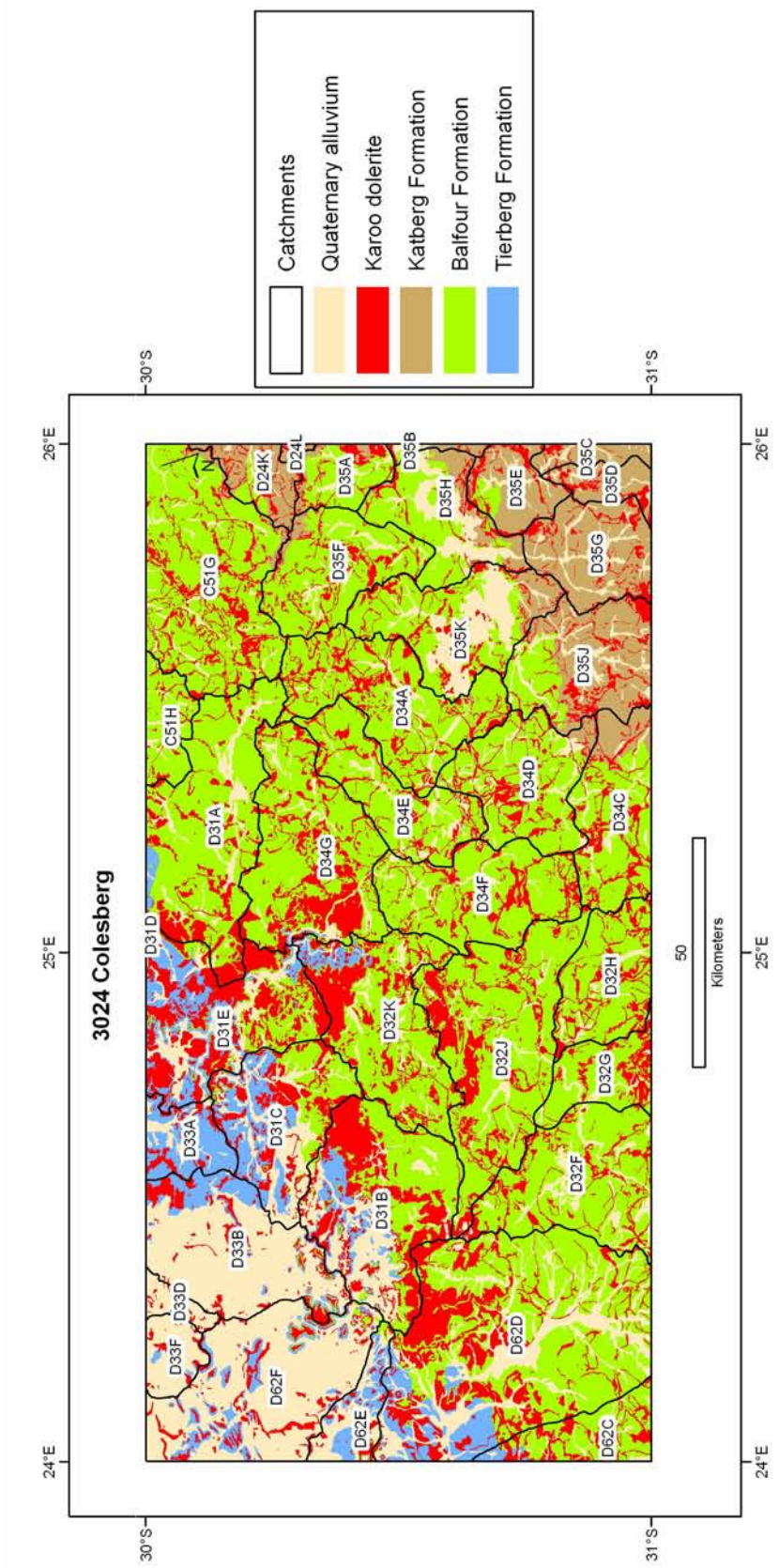

Figure 3.14: Geology modified from the *3024 Colesberg* map sheet (Le Roux, 1998). River catchments after Schulze (2007) are also shown.

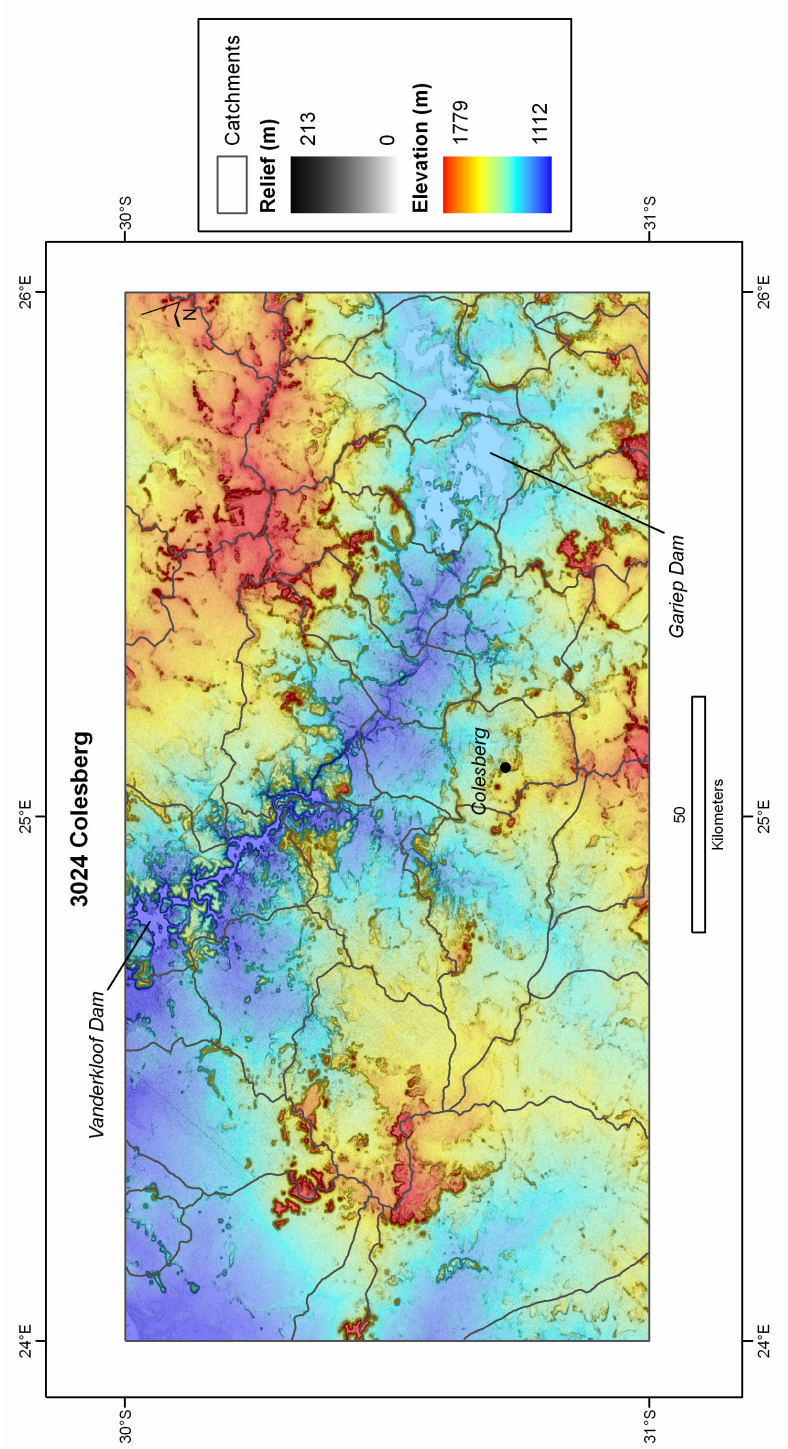

Figure 3.15: Composite map of elevation (Z, colour scale) and relief (R, greyscale) for the same area as in **Figure 3.14** (derived from the SRTM DEM; Jarvis *et al.*, 2006). The faint diagonal lines visible in the northeast (low relief) sector of the map represent artefacts in the SRTM DEM. The locations of Vanderkloof Dam and Gariep Dam along the northwest-flowing Orange River, and the town of Colesberg, are also shown.

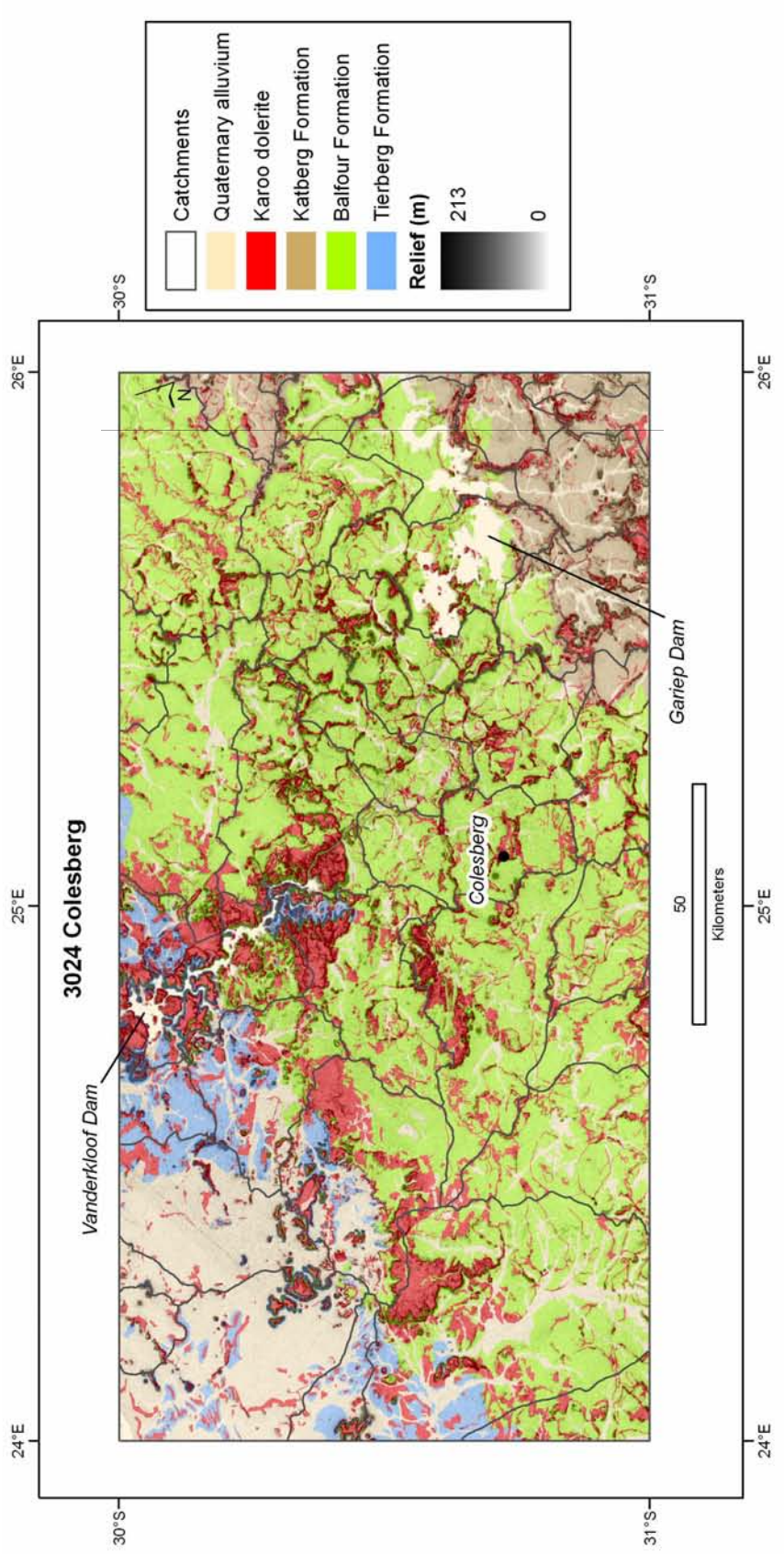

Figure 3.16: Composite map of geology, relief and river catchments for the map sheet *3024 Colesberg* (Le Roux, 1998).

extensive sills intruded close to the Tierberg-Balfour Formation boundary (i.e. close to the Ecca-Beaufort Group contact, as noted by du Toit, 1920, Section 3.2.3). Z_{mean} and R_{mean} values for geological units in a total of 38 catchments are given in **Table 3.2**.

Z_{mean} values of Karoo dolerites are compared with those of other lithologies in **Figure 3.17**. Despite the relatively uniform topography of this region in comparison with the *3222 Beaufort West* map area, Karoo dolerites still generally display higher Z_{mean} values than the Tierberg Formation, Balfour Formation and Quaternary alluvium in the corresponding catchments. In the 2 out of 14 catchments where the Tierberg Fm. displays a higher Z_{mean} value than Karoo dolerite (*D31A*, north-central margin, and *D33D*, north-western margin), Tierberg Fm. outcrop is relatively limited. However, in 6 out of 32 catchments, the Balfour Fm. displays a higher Z_{mean} value than Karoo dolerite (*D31A, D31C, D33A, D33B, D62E* and *D62F*). As illustrated in **Figures 3.14, 3.15** and **3.16**, dolerite rings may form high elevation drainage divides, whilst extensive dolerite sills may occupy broad lower regions (catchment valley floors). Interestingly, there appears to be little systematic difference between the Z_{mean} values of the sandstone-dominated Katberg Formation and those of Karoo dolerite (**Figure 3.17**). The degree to which Z_{mean} values for Karoo dolerites correlate with Z_{mean} values of other units is variable, and ranges from a poor correlation with the Balfour Fm (R^2 = 0.16) to a good correlation with Quaternary alluvium (R^2 = 0.78). The good correlation with Quaternary alluvium is probably due to the fact that Quaternary surficial deposits and waterbodies are likely to accumulate in the lowest parts of any catchment, and thus be most dependent upon the overall catchment elevation.

The Z_{mean} values of the non-dolerite units are compared in **Figure 3.18.** In all relevant catchments, the Katberg Fm. exhibits a higher mean elevation than the Balfour Fm., which in turn exhibits a higher mean elevation than the Tierberg Fm. It is likely that this is predominantly due to the relative stratigraphic positions of these sub-horizontal units. The Tierberg Fm. and Quaternary alluvium occupy similarly low elevations. The degree of correlation between Z_{mean} values for different non-dolerite lithologies within catchments varies from poor (Tierberg Fm. vs. Balfour Fm.; R^2 = 0.18) to strong (Balfour Fm. vs. Katberg Fm.; R^2 = 0.80).

Catchment	Area (km^2)	Tierberg Fm.		Balfour Fm.		Katberg Fm.		Karoo dolerite		Quaternary alluvium	
		Z_{mean} (m)	R_{mean} (m)	Z_{mean} (m)	R_{mean} (m)	Z_{mean} (m)	R_{mean} (m)	Z_{mean} (m)	R_{mean} (m)	Z_{mean} (m)	R_{mean} (m)
C51G	1836			1486	7	1563	11	1515	15	1455	4
C51H	1782			1474	8			1511	21	1450	5
D24K	877			1491	5	1511	7	1531	13	1467	4
D24L	511					1525	16	1535	17		
D31A	1159	1420	6	1448	7			1413	13	1432	5
D31B	995	1369	19	1429	9			1434	13	1405	8
D31C	676	1258	12	1318	14			1298	15	1271	8
D31D	1108			1437	31			1458	16		
D31E	969	1262	32	1281	28			1306	22	1201	12
D32F	1441			1375	5			1398	8	1362	4
D32G	1044			1354	6			1401	12	1341	4
D32H	572			1431	7			1442	11	1399	6
D32J	1113			1363	8			1389	18	1328	6
D32K	824	1241	38	1332	10			1357	20	1272	8
D33A	592	1231	13	1448	54			1259	17	1185	7
D33B	1017	1301	18	1533	51			1355	17	1281	7
D33D	950	1327	66					1250	9	1227	6
D33F	861	1238	15					1262	15	1226	8
D34A	794			1370	14			1427	30	1286	9
D34C	760			1434	8	1455	9	1467	20	1399	5
D34D	599			1332	9	1454	9	1359	23	1336	6
D34E	519			1325	12			1364	26	1253	8
D34F	692			1335	9			1377	18	1256	6
D34G	949	1215	61	1355	14			1379	25	1290	15
D35A	255			1401	8	1474	21	1451	17	1370	4
D35B	260			1274	4	1360	9	1353	19	1269	4
D35C	944					1405	12	1434	20	1355	7
D35D	587					1433	10	1450	19	1394	6
D35E	312			1293	6	1343	9	1377	23	1298	5
D35F	558			1448	7	1563	22	1472	15	1401	4
D35G	552					1381	13	1459	20	1340	5
D35H	499			1297	6	1317	16	1339	20	1262	2
D35J	1002			1325	6	1416	16	1494	24	1347	6
D35K	674			1322	10	1340	11	1355	25	1264	2
D62C	2126	1271	5	1346	7			1350	11	1323	5
D62D	2397	1284	6	1359	7			1388	12	1315	5
D62E	1920	1348	8	1504	40			1413	16	1325	6
D62F	1697	1262	16	1516	45			1306	13	1261	5
Average	958	1288	23	1389	14	1436	13	1398	18	1323	6

Table 3.2: Z_{mean} and R_{mean} values for the Tierberg Formation, Balfour Formation, Katberg Formation, Karoo dolerite and Quaternary alluvium per catchment in **Figure 3.14**. Areas of whole quaternary catchments (including portions beyond the map margins, according to Schulze, 2007) are also shown.

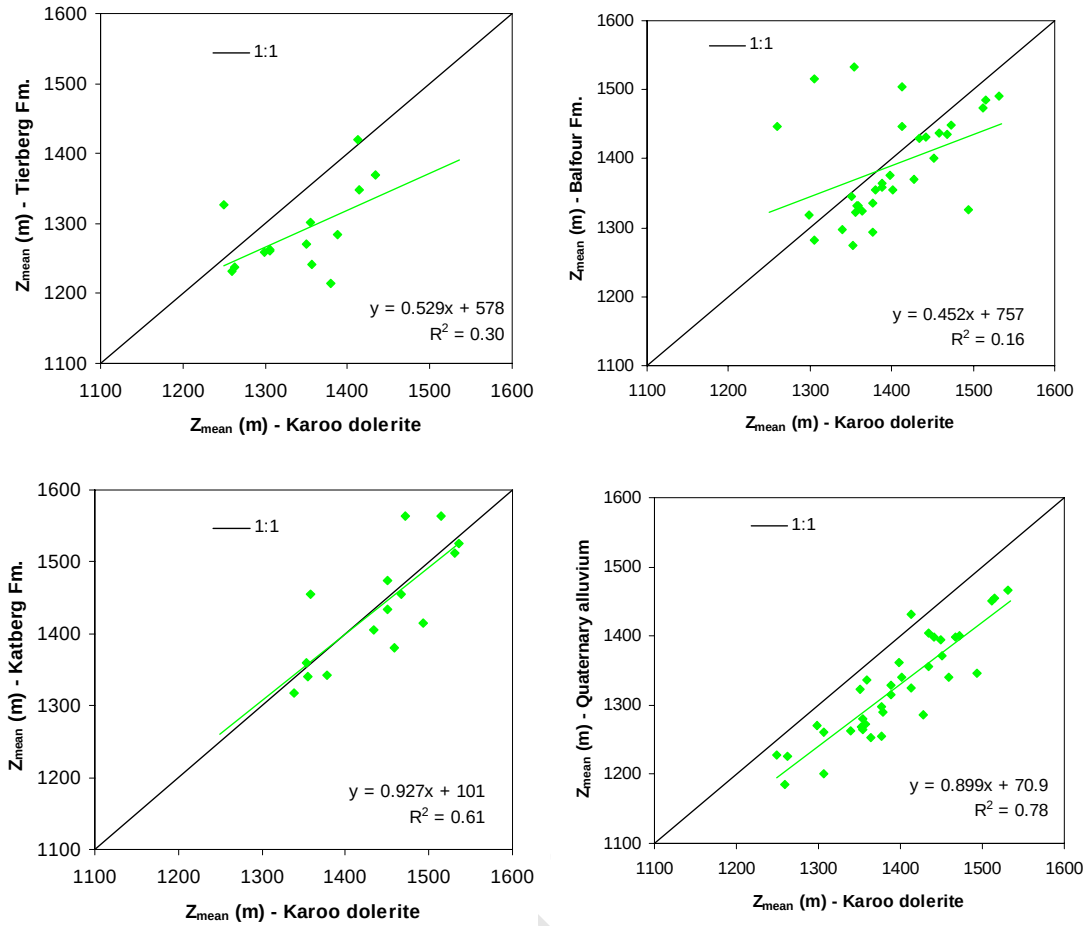

Figure 3.17: Comparisons of Karoo dolerite Z_{mean} values for the Tierberg Fm. (top left), Balfour Fm. (top right), Katberg Fm. (bottom left) and Quaternary alluvium (bottom right) in **Figure 3.14** (*3024 Colesberg*; Le Roux, 1998). Karoo dolerites generally display higher Z_{mean} values than the Tierberg Fm., Balfour Fm., and Quaternary alluvium, and correlate significantly with Z_{mean} values for the Katberg Fm. and Quaternary alluvium.

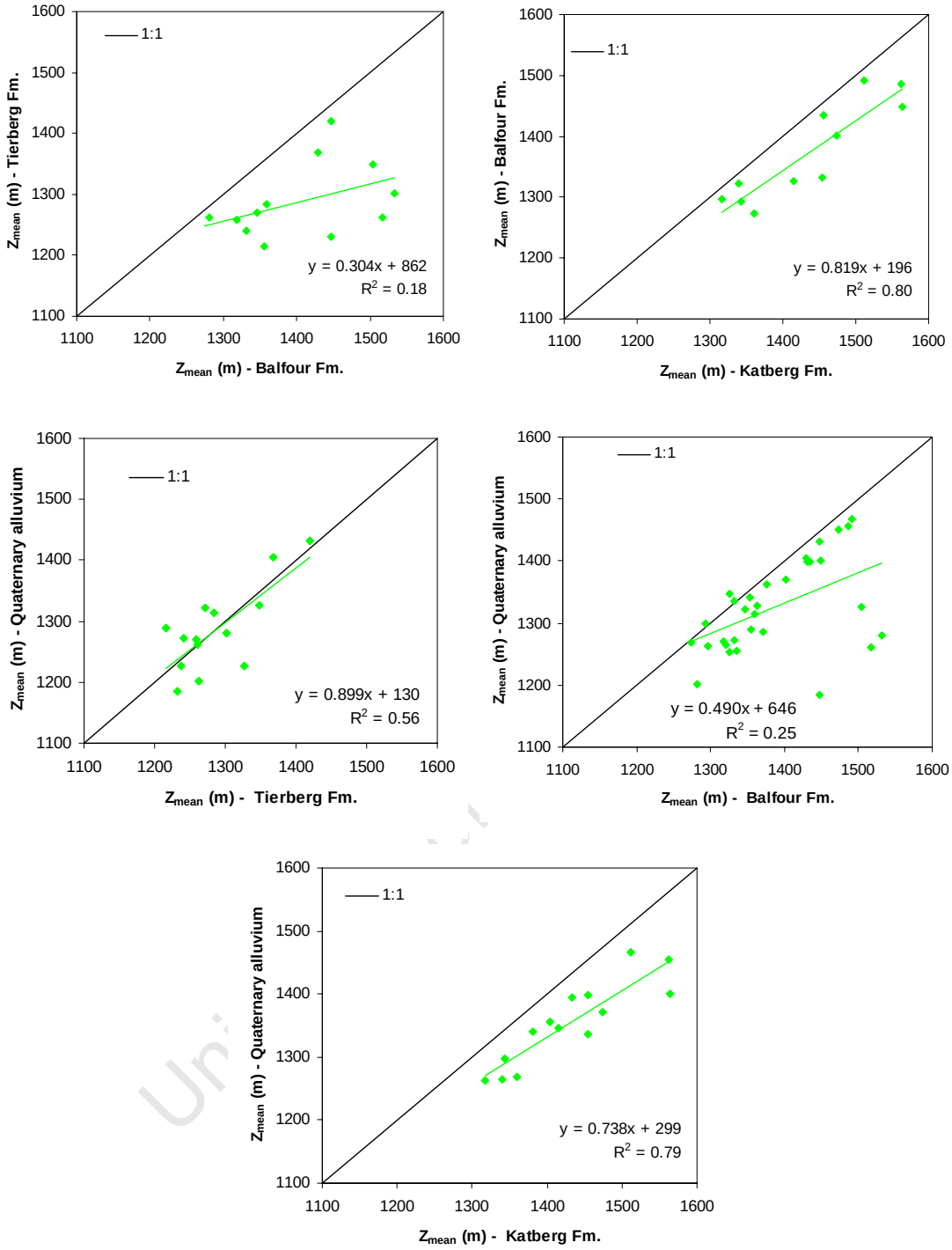

Figure 3.18: Comparisons of Z_{mean} values for non-dolerite units in **Figure 3.14**. In none of the catchments on the map *3024 Colesberg* were outcrops of both the Tierberg and Katberg Formations present.

R_{mean} values for Karoo dolerites are compared with those of other geological units in **Figure 3.19**, and a comparison of R_{mean} values for non-dolerite units is given in **Figure 3.20**. No correlation occurs between R_{mean} values for any pair of lithologies. 13 out of 15 catchments display a greater R_{mean} value for Karoo dolerite than for the Katberg Fm., even though, as noted above, Z_{mean} values for these units are comparable. An examination of **Figures 3.14, 3.15** and **3.16** reveals that in catchments where these two units both crop out (eastern and south-eastern parts of the map), the Katberg Fm. may occupy relatively elevated plateaux, but these may be encircled by high relief dolerite rings. It seems possible that the sandstone country rocks that characterize the Katberg Fm. may have been less easily intruded by the dolerites than the potentially more ductile shales and mudstones of the Tierberg and Balfour Formations, and were thus more conducive to the formation of complex ring structures. In 26 out of 32 catchments, Karoo dolerite has a higher R_{mean} value than the Balfour Fm. In those catchments where R_{mean} values for the Balfour Fm. are higher than for Karoo dolerite (*D31D, D31E, D33A, D33B, D62E* and *D62F*), the Balfour Fm. typically crops out along slopes below lower relief Karoo dolerite sills, i.e. the Karoo dolerite forms resistant caprocks. The same is true for those 7 out of 14 catchments where the Tierberg Fm. displays a higher R_{mean} than Karoo dolerite (*D31B, D31E, D32K, D33B, D33D, D34G* and *D62F*). Interestingly, all R_{mean} values > 30 m occur for either catchment areas of Balfour Fm. or Tierberg Fm. outcrop. No systematic difference occurs between R_{mean} values for the Tierberg and Balfour Formations in catchments where they both crop out, but R_{mean} values for the (sandstone-dominated) Katberg Fm. are generally higher than for the (mudstone-dominated) Balfour Fm. (the Katberg and Tierberg Formations do not crop out together in any of the catchments in the area). All three of the Karoo sedimentary units generally display higher R_{mean} values than Quaternary alluvium.

In summary, the topographic expression of Karoo dolerites across the *3024 Colesberg* map area is strong, although less pronounced than in the *3222 Beaufort West* map area. The average elevation and relief of Karoo dolerites, relative to the Ecca and Beaufort Group units into which they intrude, appears to depend upon:

1) The style of Karoo dolerite intrusion: Catchment areas of extensive sill outcrop may exhibit lower average relief and are sometimes at lower average

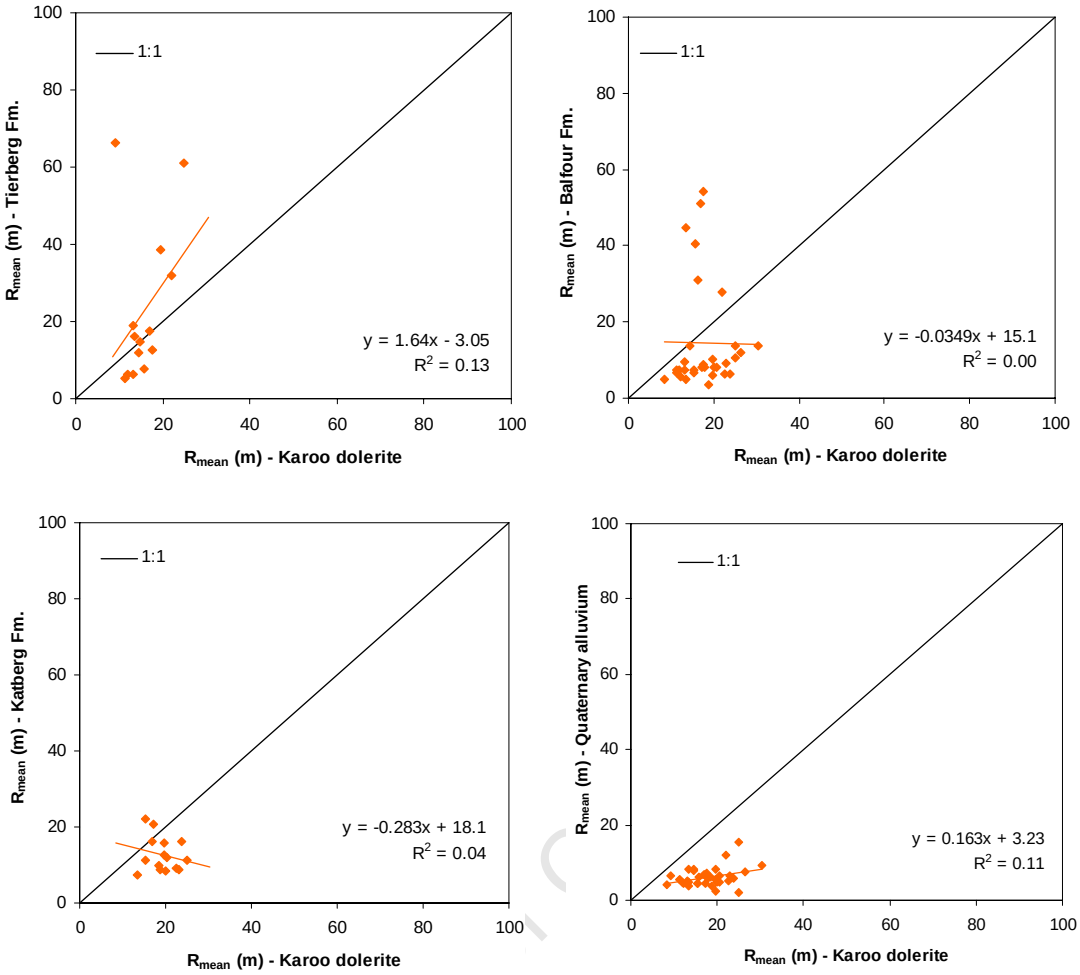

Figure 3.19: Comparisons of R_{mean} values for the Tierberg, Balfour and Katberg Formations and Quaternary alluvium with R_{mean} values of Karoo dolerite for the catchments in **Figure 3.14**.

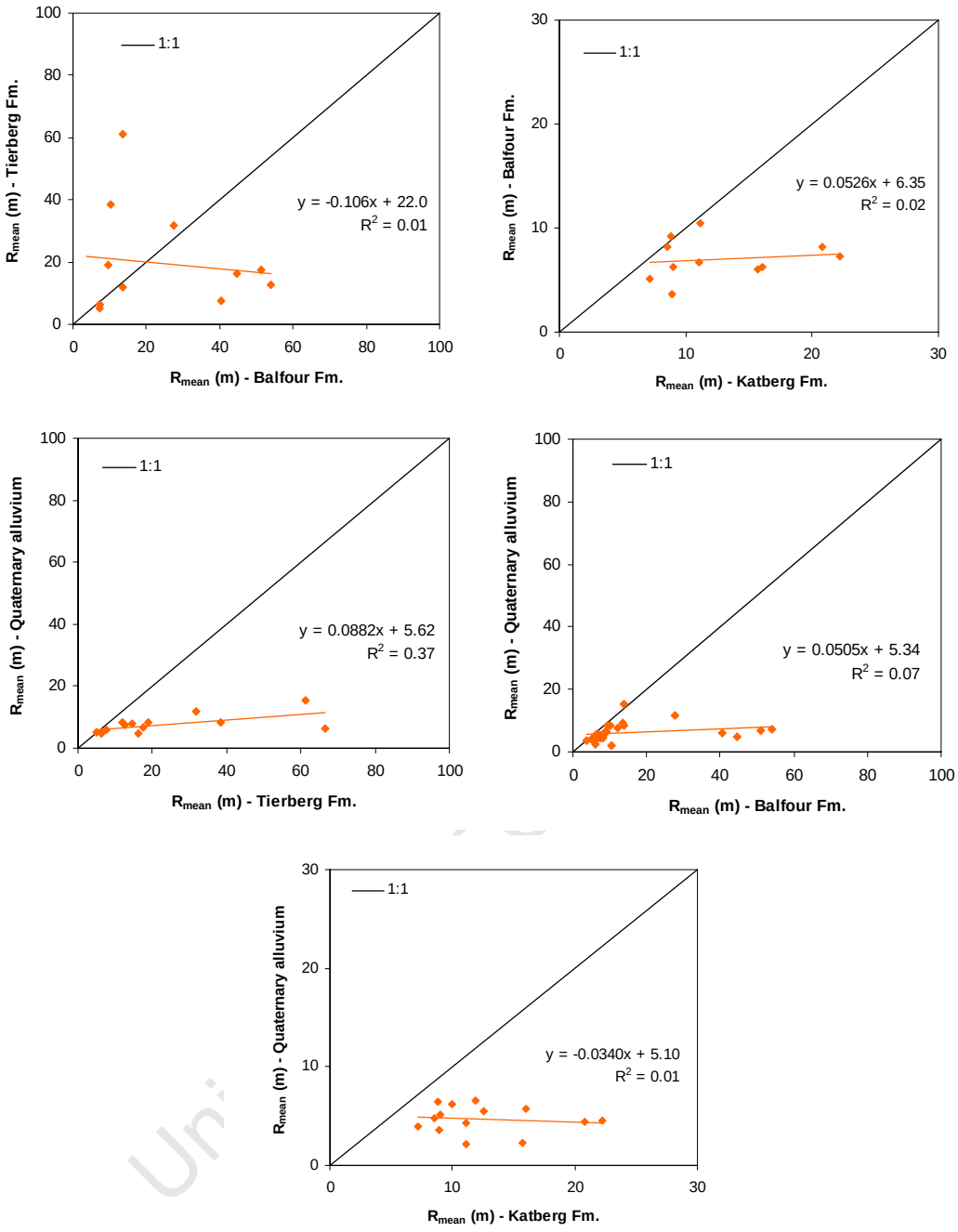

Figure 3.20: Comparisons of R_{mean} values for non-dolerite units in **Figure 3.14**. R_{mean} values for the Tierberg and Balfour Formations are comparable, with R_{mean} values for the Katberg Fm. generally higher and R_{mean} values for the Quaternary alluvium generally lower. No significant correlations between R_{mean} values occur.

elevation, but areas of dolerite ring outcrop form high relief ridges at higher elevations.

2) The erodibility of the country rocks: The predominately argillaceous Tierberg and Balfour Formations may exhibit higher relief than overlying protective dolerite sill caprocks. This suggests that the erosion of these dolerite caprocks may depend upon the erosion of underlying shale from their flanks. In contrast, the more arenaceous Katberg Fm. occurs at similar average elevations to the sinuous Karoo dolerite ring intrusions, yet exhibits generally lower relief than Karoo dolerite in these catchments. This suggests that Karoo dolerites form protective scarps here that help retard the erosion of Katberg Fm. material.

2730 Vryheid

A digitised and modified map of *2730 Vryheid* (Wolmarans, 1988) is given in **Figure 3.21**, with catchments after Schulze (2007) labelled in **Figure 3.22**. The corresponding elevation and relief of the area is given in **Figure 3.23**. A composite map of the geology, relief and catchments of the area is provided in **Figure 3.24**.

The geology of the *2730 Vryheid* map is more complex than the geology of the *3024 Colesburg* and *3222 Beaufort West* maps, and, for the purposes of this study, is simplified into 9 geological units on the basis of stratigraphy and a first-order visual comparison of geology and topography. These units are:

1. Archean granitoids and greenstone belts. This unit comprises the oldest basement rocks in the area, and includes medium- and coarse-grained Archean granites, as well as Archean amphibolites, schists, cherts and iron formations.
2. The Pongola sequence and other pre-Karoo. This unit comprises the Neo-Archean meta-sedimentary Pongola sequence and associated intrusives. As such, this unit includes a diverse array of tectonically deformed lithologies, including quartzite, conglomerate, siltstone, shale, iron formation, phyllite, schist, hornfels, amphibolite, tuff, lava, diabase, gabbro, dunite, diorite and granite.
3. The Dwyka Group, which forms the base of the Karoo Supergroup and consists predominantly of tillite, as well as subordinate shale, dropstone-bearing shale, and sandstone.

4. The Ecca Group, which here consists of the Pietermaritzburg Formation (shale and siltstone), the Vryheid Formation (sandstone, shale and grit with coal and oil-shale bands) and the Volksrust Formation (shale and siltstone), with the Vryheid Formation being the most aerially extensive unit in the region.
5. The Beaufort Group and upper Karoo. In the western outcrop region of the map, this consists of the Normadien Formation (formerly Escourt Formation; Wolmarans, 1988) from the base of the Beaufort Group, and is described by Wolmarans (1988) as comprising sandstone, mudstone and siltstone with thin coal seams. In the eastern part of the map just west of the Lebombo mountains, the Beaufort Group and the upper Karoo is represented by the Emakwenzini Formation (sandstone, siltstone and shale with thin coal seams), the Ntabene Formation (sandstone and subordinate shale), the Nyoka Fomation (shale, siltstone, subordinate maroon mudstone and sandstone) and the Clarens Formation (fine-grained sandstone).
6. The Karoo dolerite suite.
7. The basalts of the Lebombo Suite (extrusive equivalents of the Karoo dolerites), which here comprise the Letaba Formation.
8. The rhyolites of the Lebombo Suite, which here comprise the Jozini Formation.
9. Quaternary alluvium, which here includes the Masotcheni Formation (clay, gravel, laterite, silcrete and soil of Quaternary age), units simply described as Quaternary alluvium, and present-day waterbodies.

Much of the northeastern part of the map *2730 Vryheid* covers the southern Kingdom of Swaziland, from which no geological data is presented in this source (Wolmarans, 1988). However, the region covers a greater range of elevation (115 m - 2276 m) and relief (≤ 327 m) than the *3024 Colesberg* and *3222 Beaufort West* maps, and stretches from the eastern escarpment and plateau in the west to the Lebombo monocline in the east. The incised meanders that typify drainage in this region have been discussed earlier in Section 2.2. The quaternary river catchments of Schulze (2007) are generally smaller in this area than in the areas covered by the the *3024 Colesberg* and *3222 Beaufort West* maps (average area of 420 km^2, versus 958 km^2 and 724 km^2, respectively), and thus topographic parameters for geological units were typically determined for smaller areas also. Z_{mean} values for geological units on the *2730*

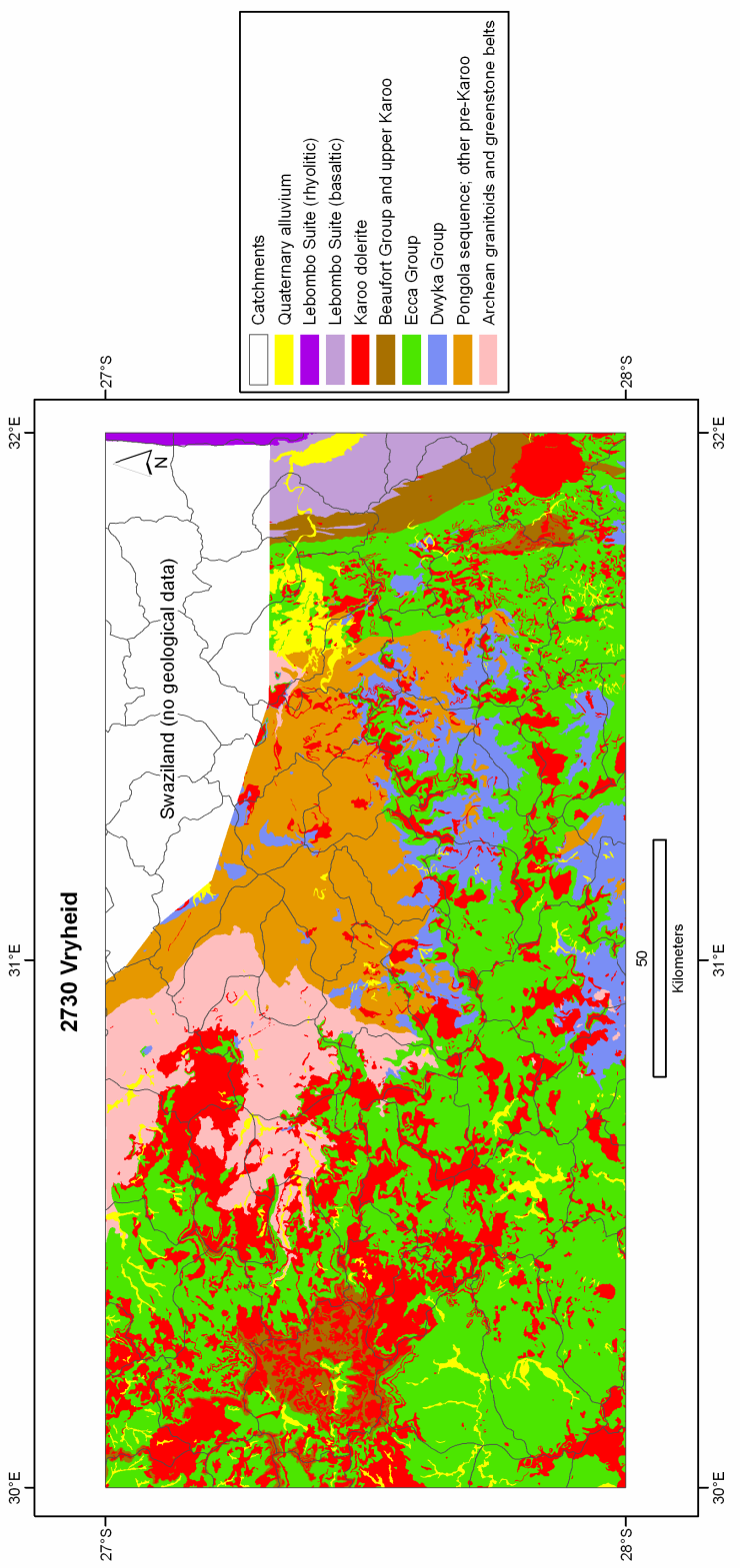

Figure 3.21: Geology modified from the *2730 Vryheid* map sheet (Wolmarans, 1988). River catchment outlines after Schulze (2007) are also shown. For the purpose of clarity, catchment name labels are shown separately in **Figure 3.22**.

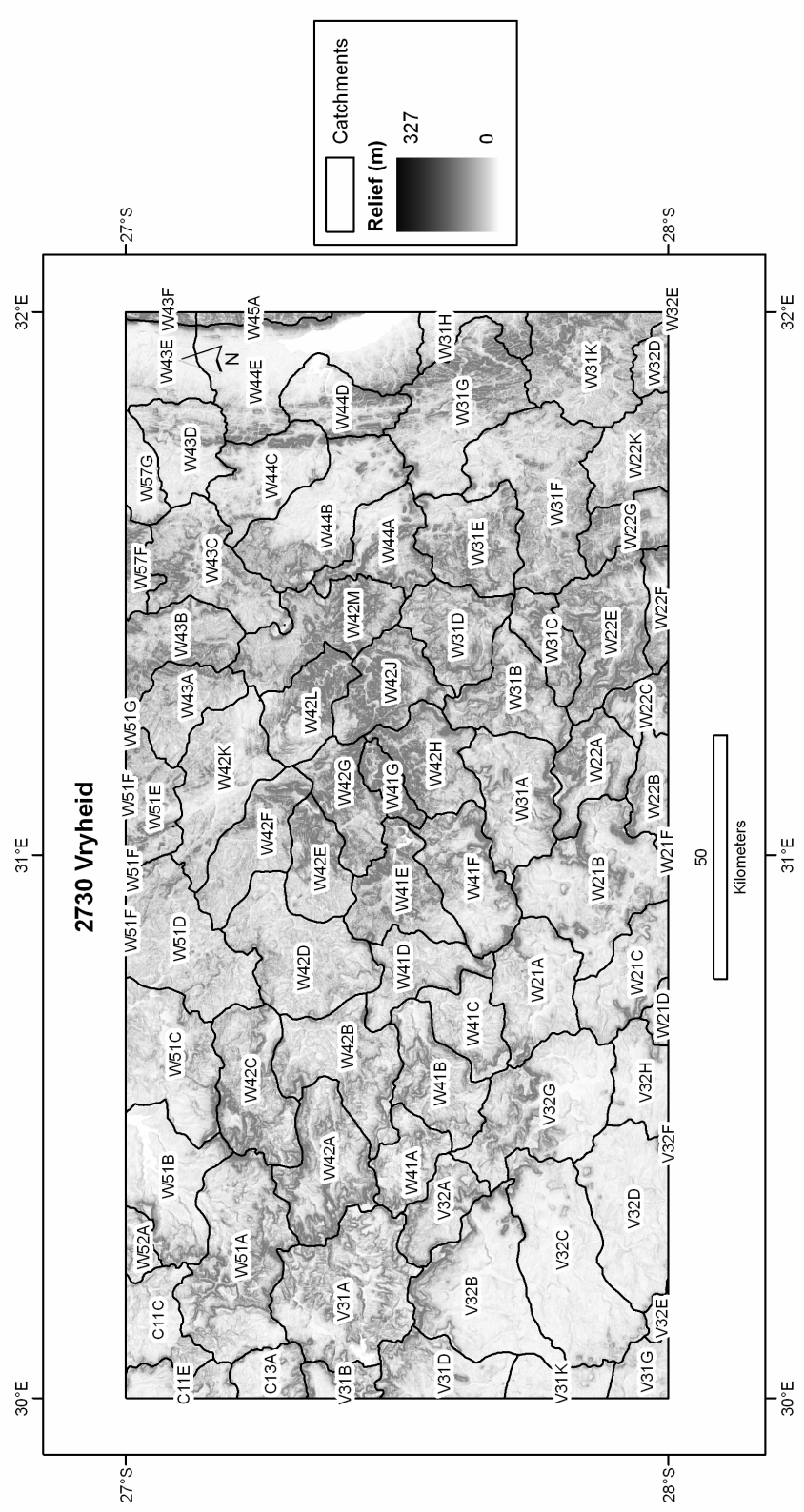

Figure 3.22: Labelled river catchments after Schulze (2007) for the *2730 Vryheid* mapsheet (**Figure 3.21**). In addition, the relief of the area is shown (see also **Figure 3.23**).

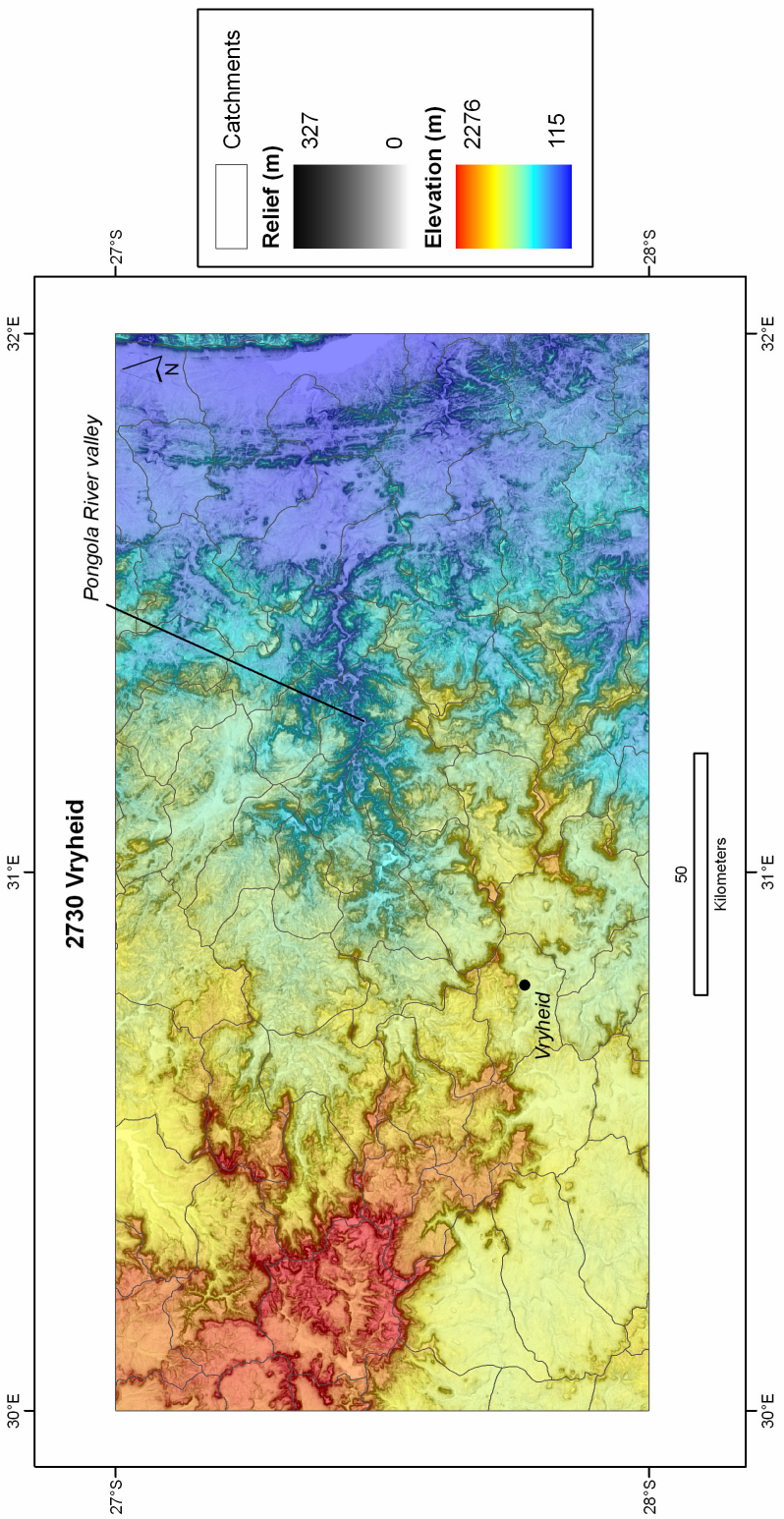

Figure 3.23: Composite map of elevation (Z, colour scale) and relief (R, grey scale) for the same area as **Figure 3.21**, derived from the SRTM DEM (Jarvis *et al*., 2006). Catchment outlines and the locations of the incised Pongola River valley and the town of Vryheid are also shown.

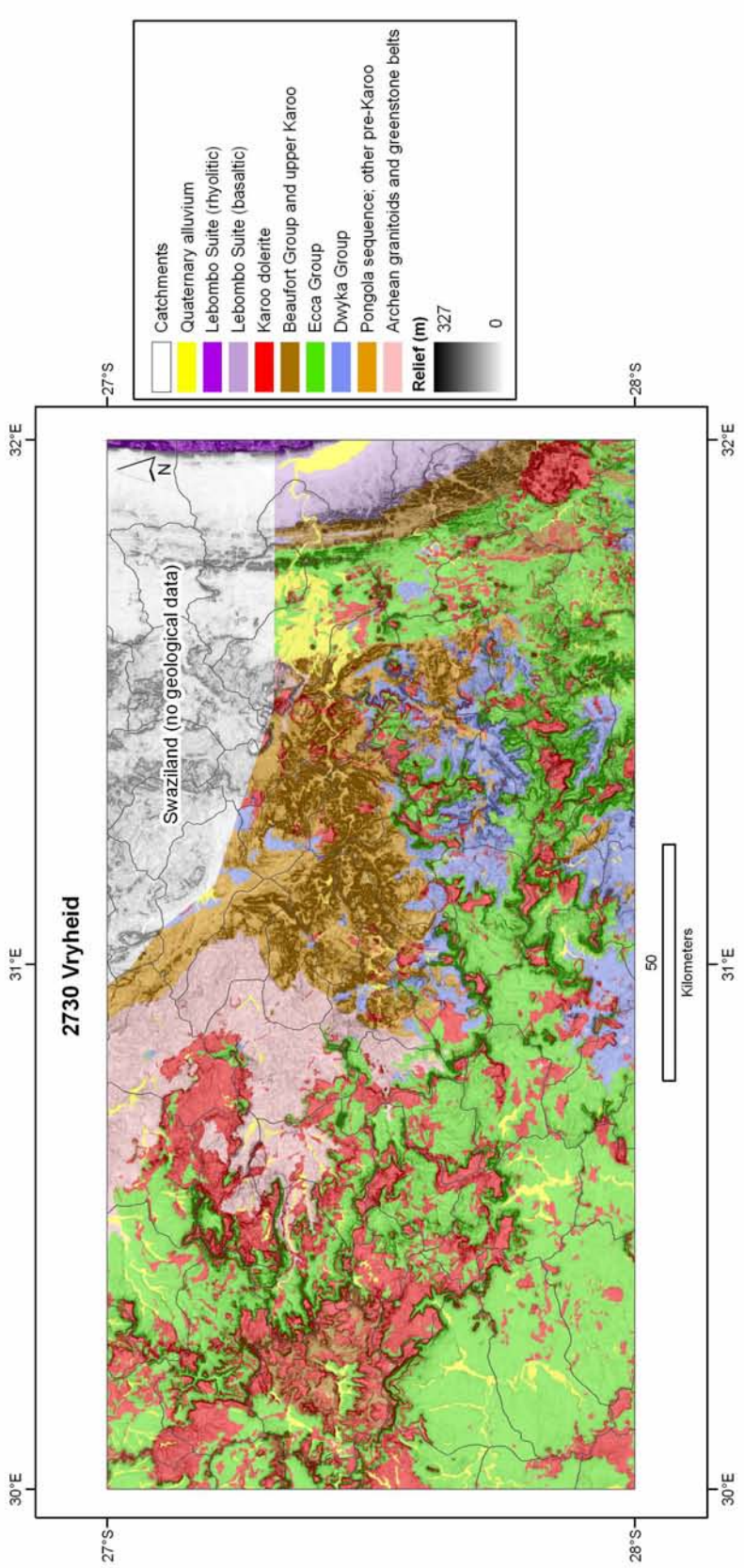

Figure 3.24: Composite map of geology, relief and catchments for the *2730 Vryheid* map area in **Figure 3.21**.

Vryheid map are presented in **Table 3.3**, and corresponding R_{mean} values are presented in **Table 3.4**.

Z_{mean} values for Karoo dolerite are compared with those of other lithologies in **Figure 3.25**. Karoo dolerites yielded higher Z_{mean} values than the Archean granitoids and greenstone belts for 17 out of 22 catchments, higher Z_{mean} values than the Pongola sequence and other pre-Karoo for 24 out of 25 catchments, higher Z_{mean} values than the Dwyka Group for 31 out of 34 catchments, higher Z_{mean} values than the Ecca Group for 52 out of 60 catchments, and higher Z_{mean} values than the Quaternary alluvium for 50 out of 54 catchments. However, in 15 out 23 catchments, Z_{mean} values were greater for the Beaufort Group and upper Karoo than for the Karoo dolerite. These 15 catchments include both low elevation catchments in the east, and high elevation catchments in the west, but include a greater proportion of the western catchments (**Figure 3.25**). Z_{mean} values for the two Lebombo Group units are not compared graphically with Z_{mean} values for Karoo dolerite in **Figure 3.25**. Karoo dolerite does not crop out in the same catchments as Lebombo rhyolite anywhere in the study area. However, Karoo dolerite displays higher Z_{mean} values than the Lebombo basalt in the three catchments in which the two units both crop out.

A comparison of Z_{mean} values for non-Karoo units is shown graphically in **Figure 3.26**. Basement units (Archean granitoids and greenstone belts; Pongola sequence and other pre-Karoo) exhibit Z_{mean} values that are generally similar to those of the overlying Dwyka Fm. However, the Archean granitoids and greenstone belts display higher Z_{mean} values than the Pongola sequence and other pre-Karoo in 9 out of 10 catchments, with the exception being catchment *W42M*, which lies east of the main Archean granitoid body. Whilst this may be expected, due to the Pongola sequence lying eastward of the Archean granitoids (i.e. coastward and thus topographically lower), examination of **Figures 3.23** and **3.24** reveals preferential incision of the Pongola River into the Pongola sequence (see also discussion of R_{mean} values below). Z_{mean} values for the Karoo Basin sedimentary units are generally in stratigraphic order, i.e. Dwyka Group < Ecca Group < Beaufort Group and upper Karoo. However, this trend is most pronounced for higher elevation catchment areas (Z_{mean} > ~750 m). In fact, for the eastern, lower elevation catchments where the Ecca Group and Beaufort and upper Karoo both crop out, the Ecca Group yields higher Z_{mean} values

Catchment	Area (km^2)	Z_{mean} (m)								
		Archean granitoids and Barberton sequence	Pongola sequence and other pre-Karoo	Dwyka Group	Ecca Group	Beaufort Group and upper Karoo	Karoo dolerite	Lebombo Group (basaltic)	Lebombo Group (rhyolitic)	Quaternary alluvium
C11C	453				1712	1796	1764			1697
C11E	1165				1734	1816	1817			1687
C13A	599				1836	1973	1874			1799
V31A	627				1796	1895	1926			1758
V31B	510				1779	1945	1829			1634
V31D	471				1332	1817	1444			1254
V31G	257				1253		1328			1210
V31K	229				1216		1289			1175
V32A	197				1543	1953	1668			1250
V32B	562				1267	1808	1578			1187
V32C	636				1236	1712	1345			1190
V32D	596				1214		1248			1223
V32E	791				1322		1358			
V32F	203				1343		1412			1330
V32G	550				1321		1505			1204
V32H	523				1224		1288			1180
W21A	344	1102			1246		1293			1183
W21B	587	1087		1015	1179		1192			1018
W21C	374	1049		1029	1128		1152			1132
W21D	474				1188		1372			1140
W21F	246			1016	1069		1114			
W22A	242		839	764	1145		1248			908
W22B	336		826	780	1061		1179			646
W22C	188		776	616	927		1011			
W22E	391			462	833		1041			467
W22F	316		365	350	587		802			397
W22G	253				563		741			468
W22K	482			443	597	525	593			606
W31A	374			988	1206		1302			986
W31B	308		752	868	1091		1154			1344
W31C	174		583	734	1001		1160			
W31D	298		639	708	957		975			556
W31E	339		542	649	462		654			
W31F	592		515	607	513	438	517			449
W31G	527		381	335	380	368	392	305		252
W31H	328					472		233		
W31K	869				472	448	418	325		409
W32D	271			433	458	424	492			
W41A	189				1608	1954	1764			1699
W41B	309	1170			1368		1507			
W41C	220	1176			1321		1394			
W41D	241	1076		1107	1227		1264			1134
W41E	307	1028	956	934	1163		1025			801
W41F	347	1125	1003	1011	1204		1103			937
W41G	97		791				993			
W42A	401	1246		1395	1522	1962	1578			1227
W42B	421	1179		1114	1401	1807	1364			1179
W42C	381	1253			1599	1929	1541			1298
W42D	495	1092		1107	1271		1241			1041
W42E	234	1016	960	895			975			1107
W42F	309	1070	949				1246			1057
W42G	251		871	815			917			560
W42H	276		897	974	1082		1211			979
W42J	294		696	880	1126		928			
W42K	421	1190	1006	923			975			902
W42L	254		774	867			818			
W42M	397	580	617	799	866		714			305
W43C	401		719	770	819		893			
W43E	269								521	
W43F	642								479	
W44A	258	534	498	570	492		548			285
W44B	493	493	439	486	336		455			273
W44C	319				266	307	295			207
W44D	240				374	300	455	208		151
W44E	722					594		226	567	140
W45A	1310								615	
W51A	630				1570	1889	1729			1830
W51B	501	1316			1381	1906	1515			1312
W51C	685	1256			1383		1398			1244
W51D	533	1218	1165	1149	1355		1357			1193
W51E	278		1064	1009						
W51F	596	1344	1280							
W52A	292				1548		1723			1515
Average	420	1073	774	817	1125	1335	1173	259	546	1002

Table 3.3: Z_{mean} values for geological units in **Figure 3.21** for a total of 73 catchments in the area (labelled in **Figure 3.22**). Areas of whole quaternary catchments (including portions beyond the map margins, according to Schulze, 2007) are also shown.

Catchment	Area (km^2)	R_{mean} (m)								
		Archean granitoids and Barberton sequence	Pongola sequence and other pre-Karoo	Dwyka Group	Ecca Group	Beaufort Group and upper Karoo	Karoo dolerite	Lebombo Group (basaltic)	Lebombo Group (rhyolitic)	Quaternary alluvium
C11C	453				11	28	17			9
C11E	1165				15	42	22			8
C13A	599				13	47	23			9
V31A	627				17	31	28			6
V31B	510				25	66	30			10
V31D	471				18	62	23			7
V31G	257				10		15			7
V31K	229				7		15			6
V32A	197				33	54	25			11
V32B	562				12	77	38			4
V32C	636				8	95	20			6
V32D	596				8		14			13
V32E	791				12		14			
V32F	203				24		40			19
V32G	550				17		24			4
V32H	523				8		21			3
W21A	344	10			17		22			5
W21B	587	34		15	26		25			11
W21C	374	25		14	17		22			26
W21D	474				18		37			24
W21F	246			11	18		19			
W22A	242		37	22	43		37			16
W22B	336		34	22	35		40			13
W22C	188		39	22	50		34			
W22E	391			26	48		43			22
W22F	316		17	14	39		34			20
W22G	253				38		42			22
W22K	482			31	22	18	30			19
W31A	374			18	29		27			17
W31B	308		30	34	37		39			21
W31C	174		11	36	44		42			
W31D	298		36	31	40		36			14
W31E	339		44	33	23		37			
W31F	592		25	29	24	20	27			18
W31G	527		13	12	24	46	28	34		14
W31H	328					52		18		
W31K	869				27	35	39	23		13
W32D	271			32	26	19	32			
W41A	189				25	47	22			7
W41B	309	6			23		31			
W41C	220	16			16		23			
W41D	241	19		17	26		27			14
W41E	307	28	46	22	33		38			20
W41F	347	10	35	23	44		25			20
W41G	97		65				48			
W42A	401	26		38	40	73	39			10
W42B	421	18		14	30	73	28			9
W42C	381	25			44	82	38			10
W42D	495	17		25	32		25			10
W42E	234	18	50	30			21			18
W42F	309	20	42				23			17
W42G	251		49	27			26			34
W42H	276		48	23	56		42			21
W42J	294		57	28	45		36			
W42K	421	22	21	10			17			5
W42L	254		49	14			33			
W42M	397	34	48	38	36		43			41
W43C	401		57	67	72		25			
W43E	269								88	
W43F	642								65	
W44A	258	47	46	38	28		35			13
W44B	493	44	41	34	20		27			9
W44C	319				30	30	32			9
W44D	240				49	36	69	17		10
W44E	722					72		18	86	0
W45A	1310								44	
W51A	630				25	60	28			10
W51B	501	4			13	117	27			3
W51C	685	15			18		26			8
W51D	533	18	28	16	21		18			11
W51E	278		25	14						
W51F	596	8	15							
W52A	292				27		24			12
Average	420	21	37	25	27	53	30	22	71	13

Table 3.4: R_{mean} values for geological units in **Figure 3.21** for a total of 73 catchments in the area (labelled in **Figure 3.22**). Areas of whole quaternary catchments (including portions beyond the map margins, according to Schulze, 2007) are also shown.

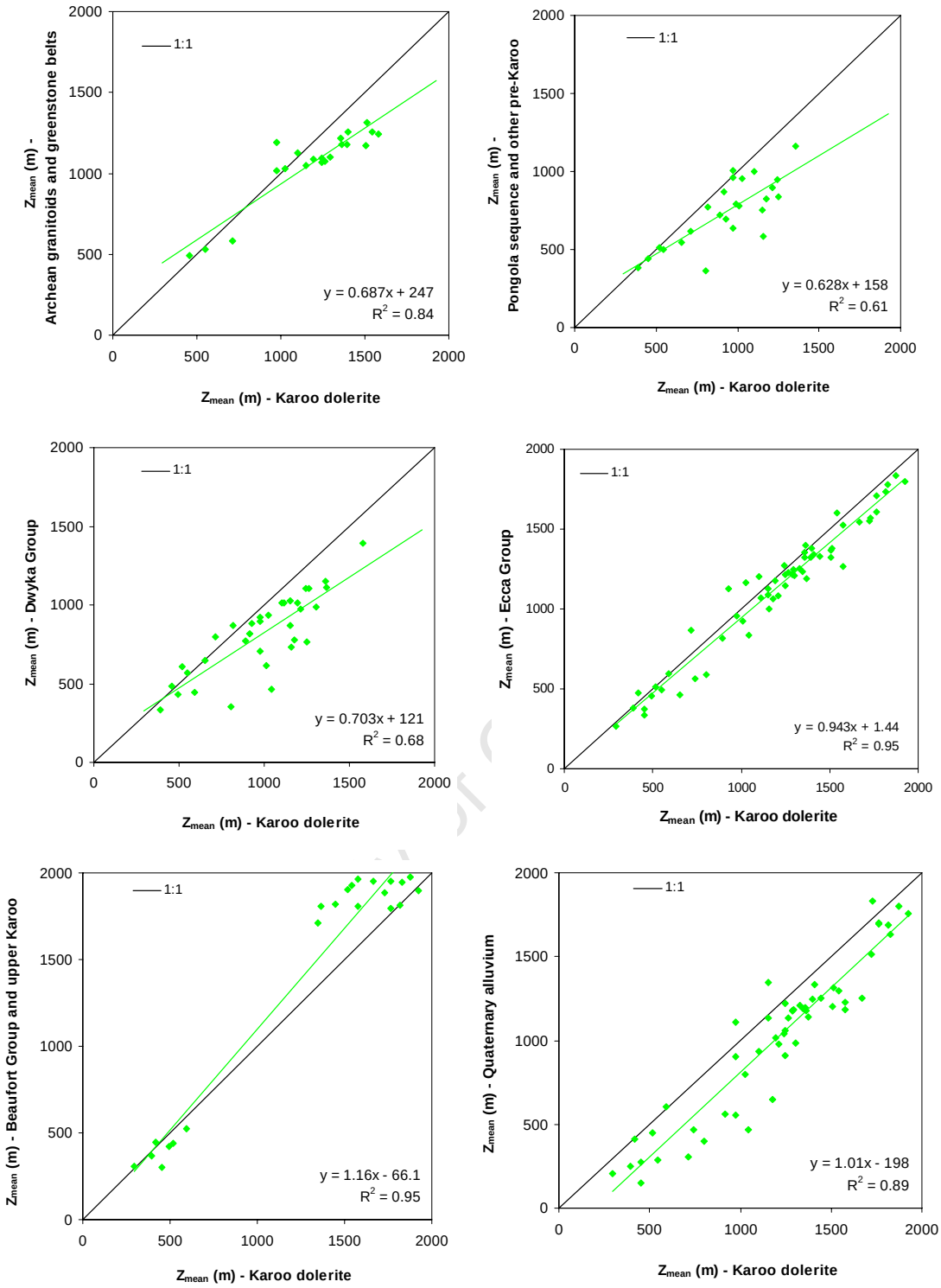

Figure 3.25: Comparison of Z_{mean} values of Karoo dolerite with those of other lithologies in the map *2730 Vryheid* (**Figure 3.21**).

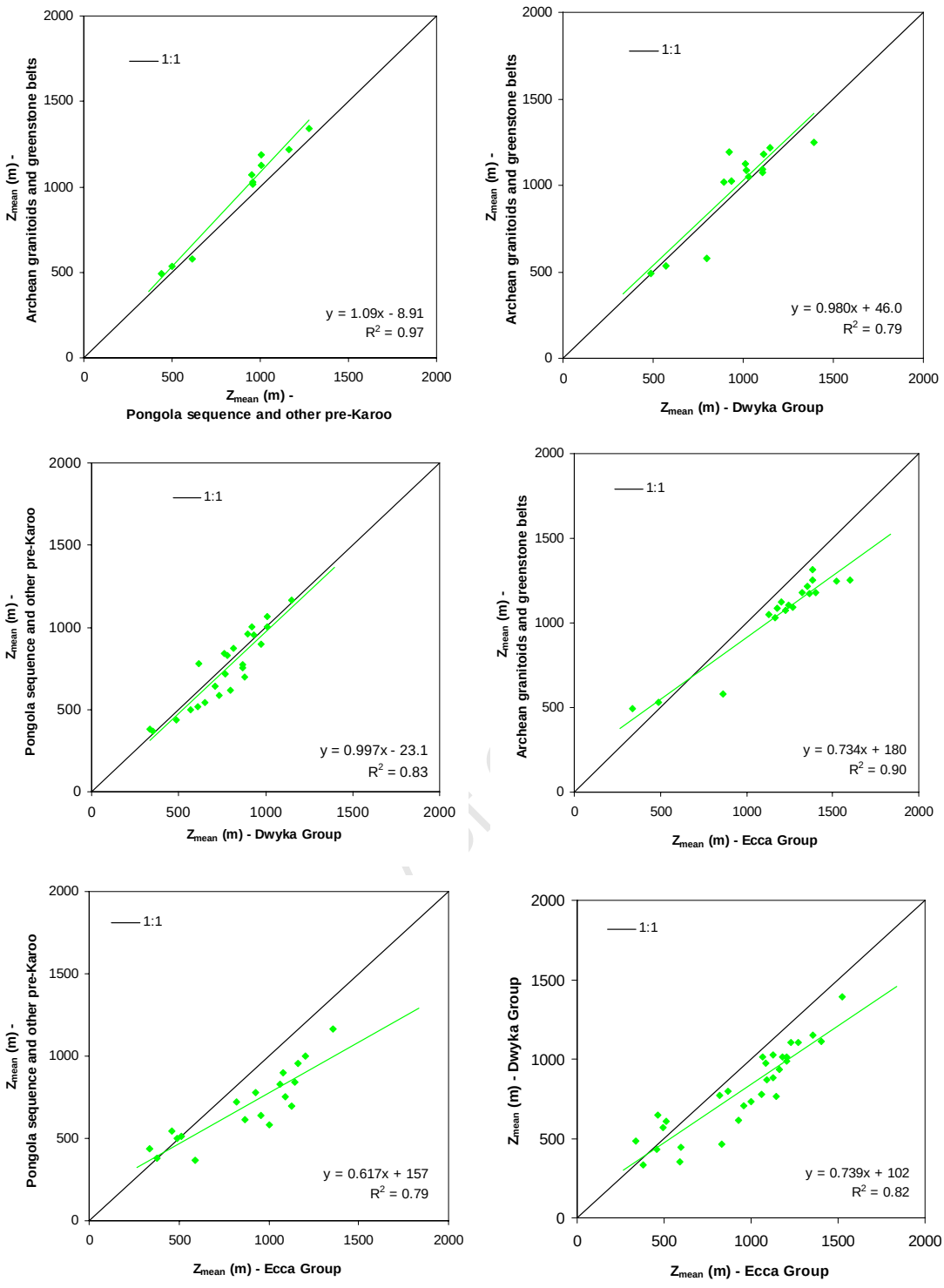

Figure 3.26: *(Continued on following page).*

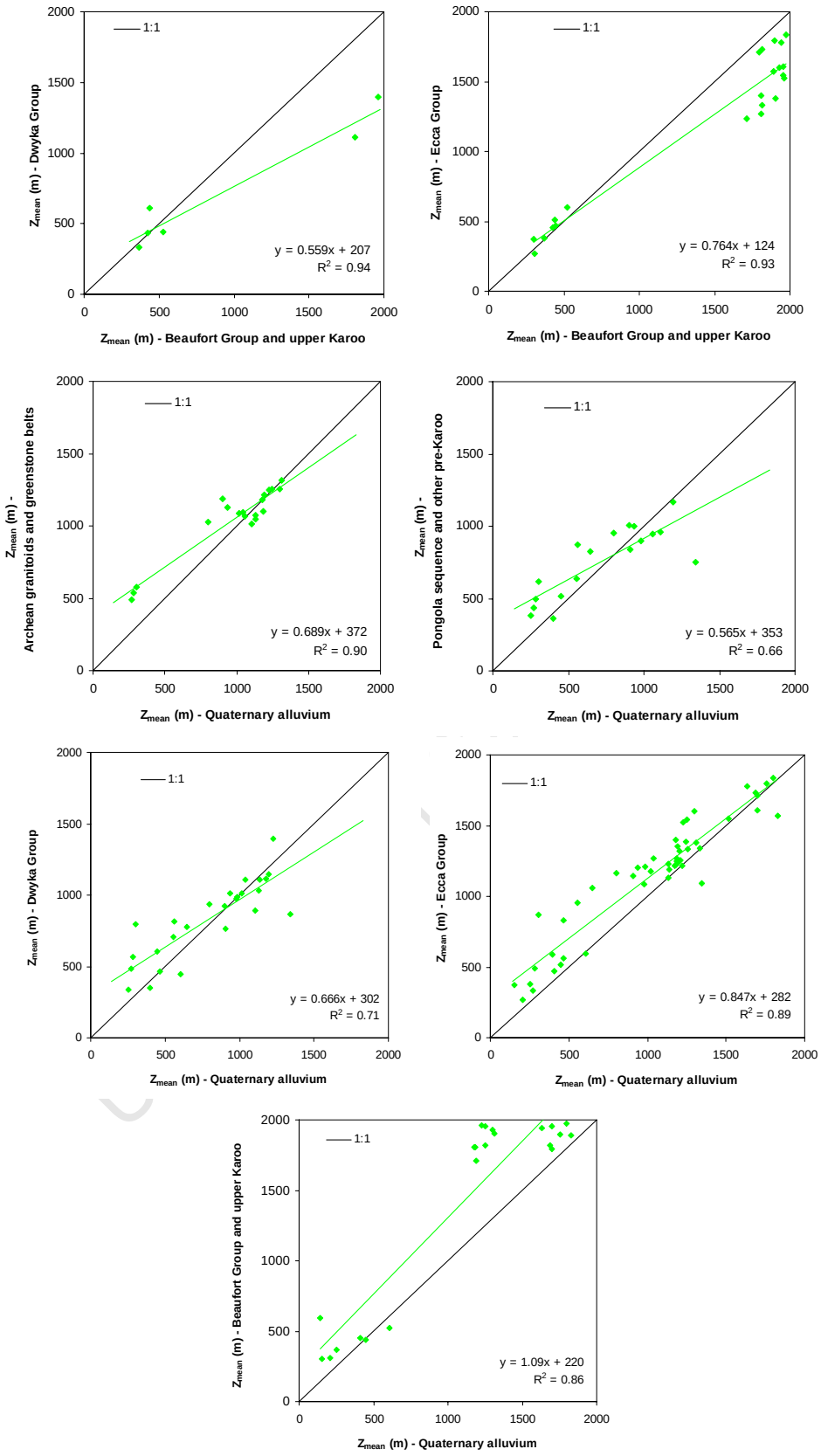

Figure 3.26: *(Continued from previous page).* Comparison of Z_{mean} values for non-dolerite lithologies in the map *2730 Vryheid* (**Figure 3.21**).

for 6 out of 7 catchments. This is probably due to the Beaufort and upper Karoo cropping out further east (i.e. at lower elevations towards the coast) because of a 20º to 30º eastward dip, and thus the role of lithological contrasts in determining the relative elevations of different Karoo sedimentary strata seems relatively weak here. As expected, Z_{mean} values for Quaternary alluvium are generally lower than for other geological units, although this is not always the case, particularly at higher elevations (e.g. where Z_{mean} values for Quaternary alluvium are > 1000 m), where alluvium may have been trapped in the upper parts of a catchment. Catchment *W44E* is the only catchment where the Lebombo rhyolite crops out in the same catchment as other units. Here the Lebombo rhyolite displays a higher Z_{mean} value than the Quaternary alluvium, the Lebombo basalt and the Beaufort Group and upper Karoo. Lebombo basalt, on the other hand, displays lower Z_{mean} values than all other geological units in the 4 catchments in which it crops out, with the exception of Quaternary alluvium in 2 of the 4 catchments in which they both occur. As with the two previous map areas, the Z_{mean} values of all geological units display fair to strong correlations with each other (R^2 = 0.61 to R^2 = 0.95), with Z_{mean} values being controlled primarily by the overall elevation of each catchment in this topographically diverse area.

R_{mean} values for Karoo dolerites are compared graphically with other lithologies in **Figure 3.27**, and R_{mean} values for non-dolerite units are compared with each other in **Figure 3.28**. As with the *3222 Beaufort West* and *3024 Colesburg* maps, R_{mean} values do not co-vary significantly ($R^2 \leq 0.40$ for all pairs of geological units). Karoo dolerites generally show higher R_{mean} values than the Archean granitoids and greenstone belts (15 out of 21 catchments), the Dwyka Group (24 out of 34 catchments), the Ecca Group (40 out of 60 catchments) and the Quaternary alluvium (52 out of 54 catchments). Karoo dolerites display higher R_{mean} values than Lebombo basalts in 2 out of 3 catchments. However, the Pongola sequence and other pre-Karoo displays higher R_{mean} values than the Karoo dolerite in 17 out of 25 catchments, and the Beaufort Group and upper Karoo displays higher R_{mean} values than the Karoo dolerite in 16 out of 22 catchments.

The Pongola sequence and other pre-Karoo displays higher R_{mean} values than the Archean granitoids and greenstone belts in 7 out of 10 catchments, and also higher R_{mean} values than the Dwyka Group in 20 out of 24 catchments. The high relative

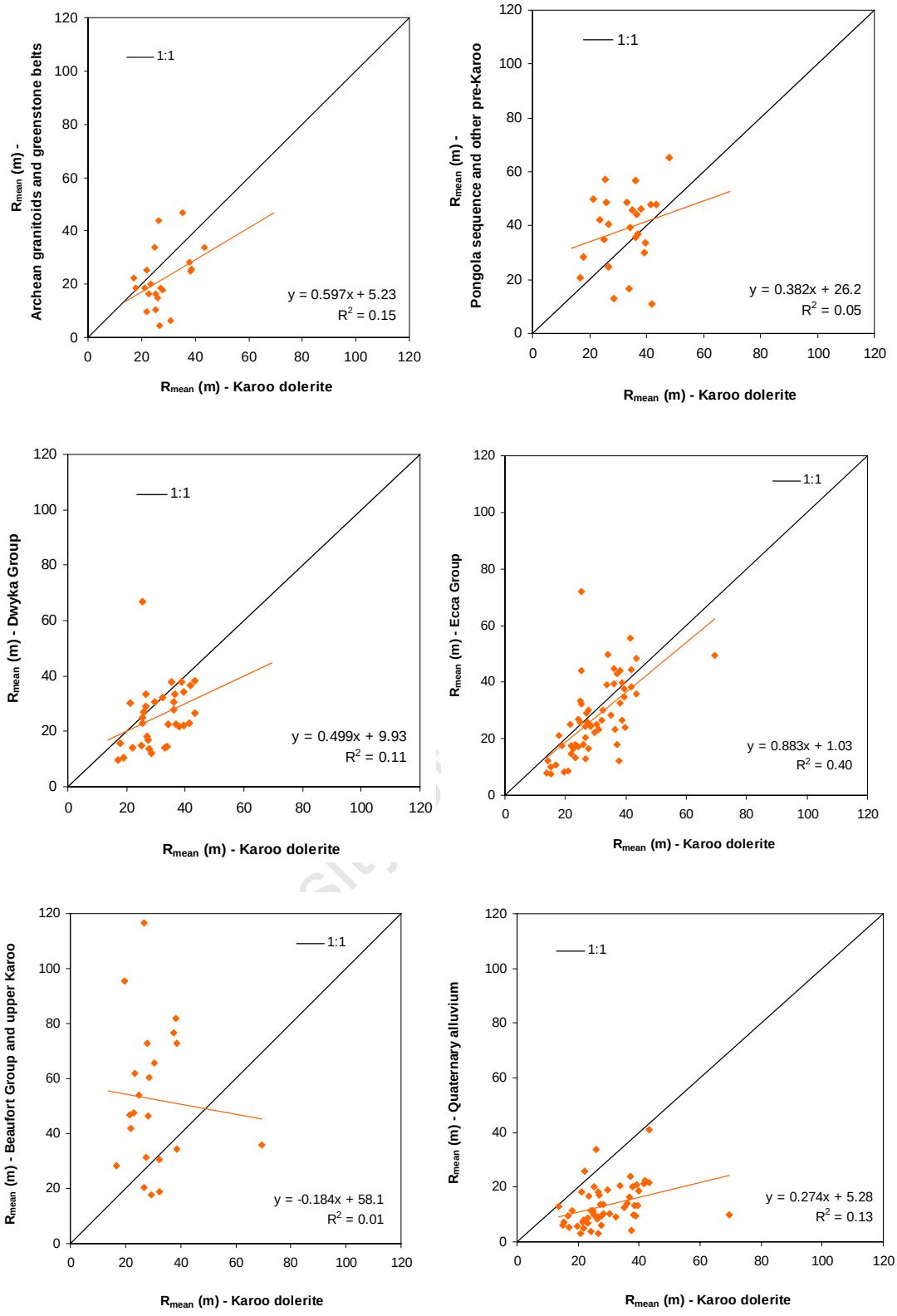

Figure 3.27: Comparison of R_{mean} values of Karoo dolerite with those of other lithologies in the map *2730 Vryheid* (**Figure 3.21**).

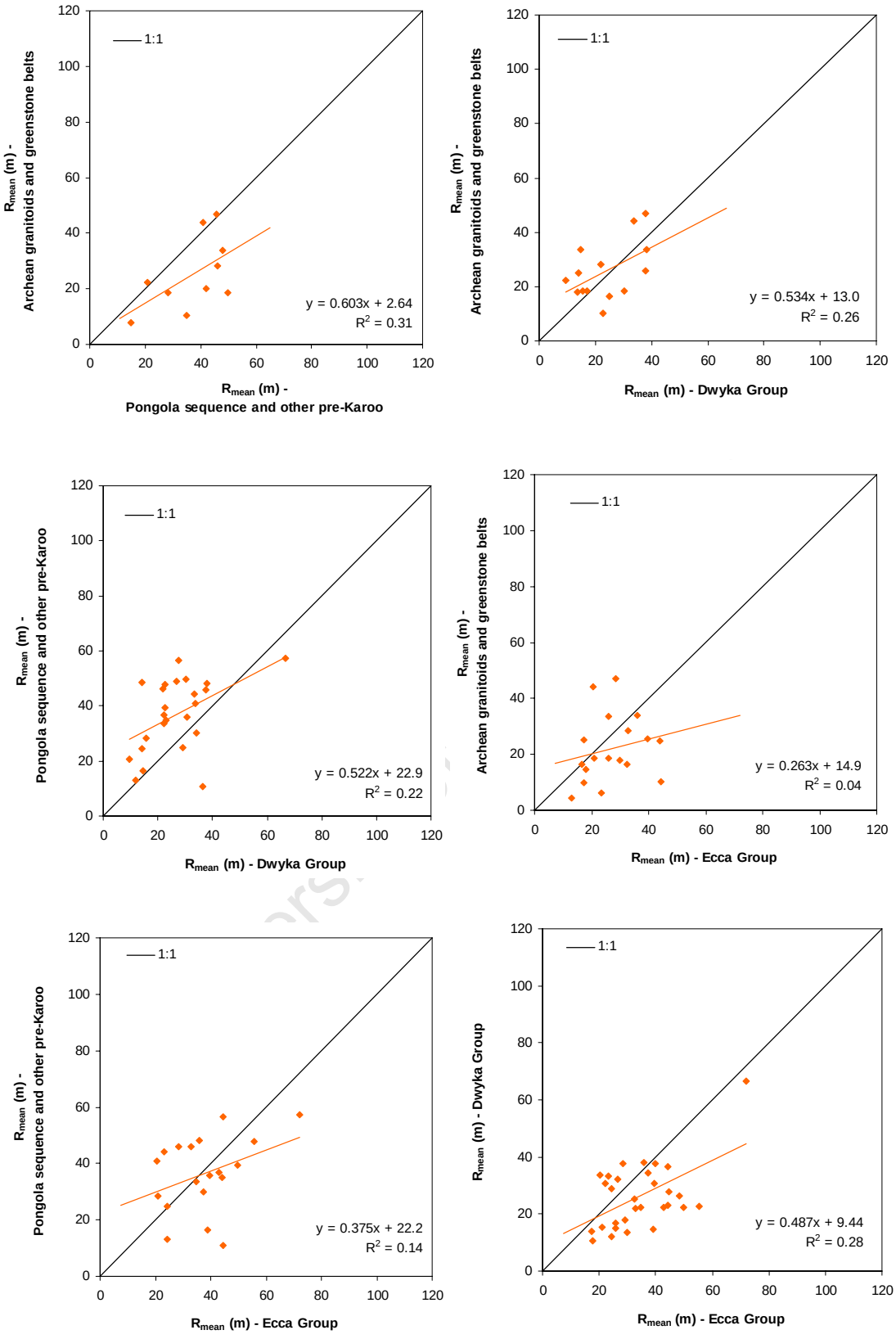

Figure 3.28: *(Continued on following page).*

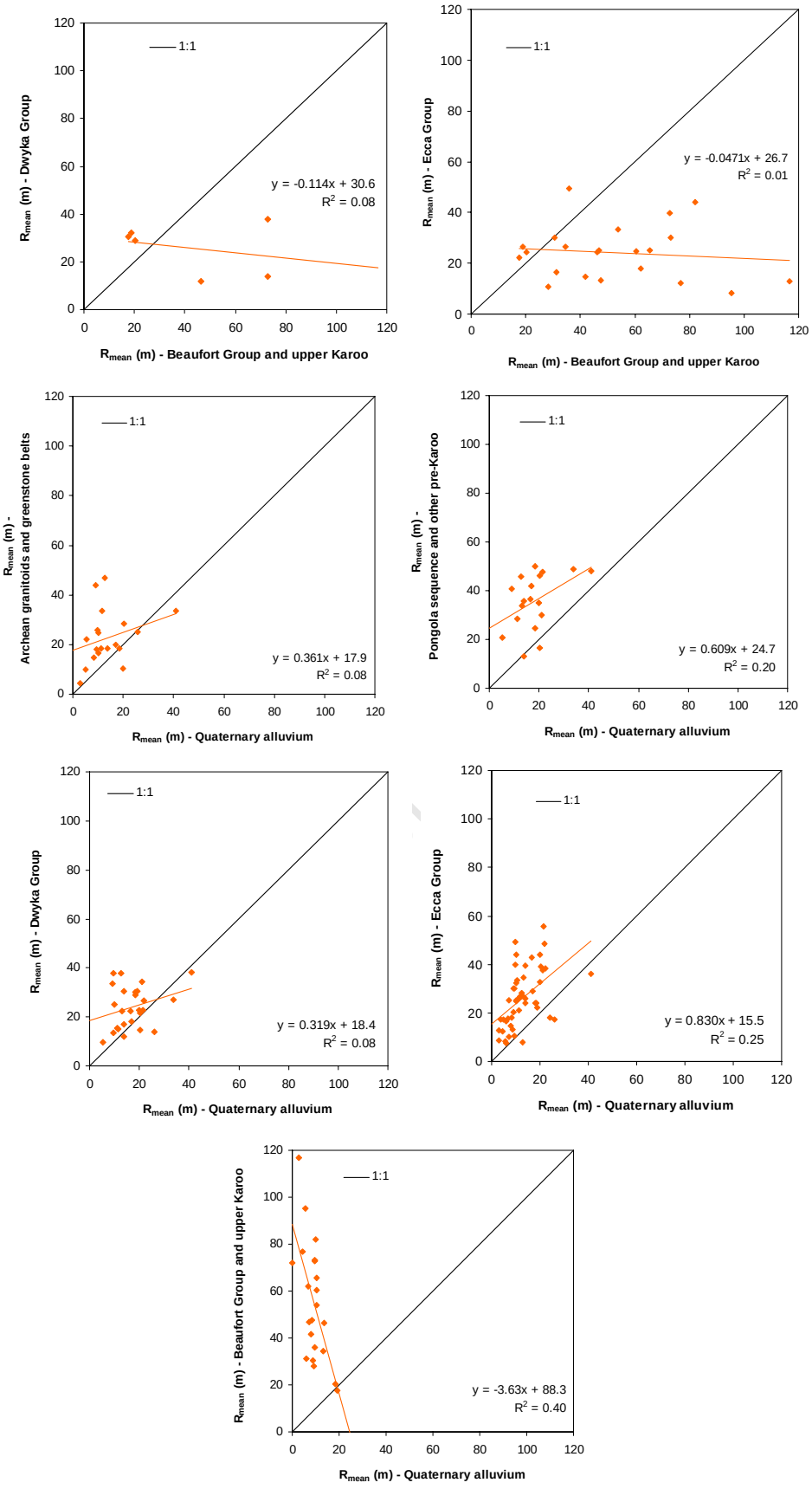

Figure 3.28: *(Continued from previous page).* Comparison of R_{mean} values for non-dolerite lithologies in the map *2730 Vryheid* (**Figure 3.21**).

relief of the Pongola sequence and other pre-Karoo is primarily due to the preferential incision of the Pongola River into the Pongola sequence, as mentioned above. R_{mean} values for the Dwyka Group and the Artchean granitoids and greenstone belts are generally comparable, but with higher R_{mean} values for Archean granitoids in 9 out of 14 catchments.

The Ecca Group displays higher R_{mean} values than the Archean granitoids and greenstone belts in 13 out of 18 catchments, and higher R_{mean} values than the Dwyka Group in 23 out of 30 catchments, although R_{mean} values for the Ecca Group are higher than for the Pongola sequence and other pre-Karoo in only 11 of 19 catchments. The Beaufort Group and upper Karoo display the greatest range of R_{mean} values in the study (18 - 117 m), including the highest R_{mean} values in the area. The Beaufort Group and upper Karoo have greater R_{mean} values than the Dwyka Group in 3 out of 6 catchments (although by as much as 59 m), and greater R_{mean} values than the Ecca Group in 17 out of 22 catchments.

In contrast, Quaternary alluvium generally displays lower R_{mean} values than the Archean granitoids and greenstone belts (15 out of 19 catchments), the Pongola sequence and other pre-Karoo (16 out of 18 catchments), the Dwyka Group (21 out of 26 catchments), the Ecca Group (46 out of 50 catchments) and the Beaufort Group and upper Karoo (21 out of 22 catchments). Quaternary alluvium also displays lower R_{mean} values than the Lebombo Group basalts and/or rhyolites in the 4 catchments in which they both crop out. In 4 out of 5 catchments where Lebombo basalts crop out, the basalts display lower R_{mean} values than all other units, with the exception of Quaternary alluvium. The exceptional catchment, *W31G*, yields an R_{mean} value for Lebombo basalt that is higher than for all other units, with the exception of the Beaufort Group and upper Karoo. The Lebombo rhyolite, which only crops out with other units in catchment *W44E*, displays a higher R_{mean} value than any of the other units in this catchment.

Discussion

The *2730 Vryheid* map differs from the *3222 Beaufort West* and *3024 Colesberg* maps in that, in addition to Karoo sedimentary rocks, Karoo dolerites and alluvium, there are igneous and metamorphic basement rocks, as well as basaltic and rhyolitic

extrusives, that crop out in the area. The Pongola sequence (predominantly low grade metapelites, quartzites and metavolcanics) and the Lebombo rhyolites, both of which are unique to the *2730 Vryheid* map, contribute towards the higher relief of this area.

The relative relief and elevation of Karoo dolerites relative to Karoo and Cenozoic/Quaternary units is summarised in **Table 3.5**. Here, the percentage of catchments in each of the three maps in which Z_{mean} and R_{mean} values are higher for Karoo dolerites than for Karoo sedimentary units or Cenozoic/Quaternary alluvium is given. The number of catchments for which each percentage is calculated is also shown. The only instances where the percentage of catchments with greater Z_{mean} values for Karoo dolerite is < 80 % are when comparisons are made with the (sandstone-dominated) Katberg Formation (67 %, *3024 Colesberg* map) or with the Beaufort Group and upper Karoo in the *2730 Vryheid* map (32 %). Similarly, the only instances where the percentage of catchments with greater R_{mean} values for Karoo dolerite is < 70 % are where the comparison is made with the Tierberg Formation (43 %, *3024 Colesberg* map, where dolerites form extensive low relief sills) or with the Ecca Group (67%) or Beaufort Group and upper Karoo (27%), both in the *2730 Vryheid* map.

The observation that the Beaufort Group and upper Karoo displays greater average elevation and relief than Karoo dolerite in the *2730 Vryheid map* in 68% and 73% of catchments, respectively, is surprising. One possibly important factor to take into account is that Beaufort Group and Upper Karoo units only crop out over a very restricted area in the *2730 Vryheid* map (**Figures 3.21**), particularly when compared to the *3222 Beaufort West* and *3024 Colesberg* maps (**Figures 3.7** and **3.14**), and thus topographic statistics may be less representative here. The number of catchments in which the Beaufort Group and upper Karoo unit crops out in the *2730 Vryheid* map is comparable with the numbers of catchments for which these statistics are determined for the other two maps (**Table 3.5**). However, the average area of the catchments in the *2730 Vryheid* map is 420 km^2 (**Table 3.4**), significantly smaller than the average catchment areas in the *3222 Beaufort West* and *3024 Colesburg* maps (724 km^2 and 958 km^2 respectively; **Tables 3.1** and **3.2**). Also, for the few catchments in the western parts of the *2730 Vryheid* map in which Beaufort Group and upper Karoo do crop out, extensive low relief horizontal dolerite sills are often intruded at the

Map sheet	Geological unit			Catchments (%) where:		Number of catchments
	Group	Subgroup	Formation	Z_{mean} (Karoo dolerite) > Z_{mean} (sedimentary unit)	R_{mean} (Karoo dolerite) > R_{mean} (sedimentary unit)	
3222 Beaufort West	Beaufort	Adelaide	Abrahamskraal	100	100	10
			Teekloof	96	79	28
	Cenozoic alluvium			100	100	26
3024 Colesberg	Ecca		Tierberg	86	43	14
	Beaufort	Adelaide	Balfour	81	81	32
		Tarkastad	Katberg	67	87	15
	Quaternary alluvium			97	100	36
2730 Vryheid	Dwyka			91	74	34
	Ecca			87	67	60
	Beaufort and upper Karoo			32	27	22
	Quaternary alluvium			93	96	54

Table 3.5: Percentages of catchments in the three geological maps where Z_{mean} and R_{mean} values for Karoo dolerites are less than those for Karoo sedimentary units and Cenozoic/Quaternary alluvial deposits. The number of catchments involved in each comparison is also given.

Beaufort-Ecca Group contact. It should also be noted that *V31A*, the catchment in the west of the *2730 Vryheid* west of the map with the most substantial Beaufort Group and upper Karoo outcrop (here the Normandien Formation), displays a lower Z_{mean} value for this unit than for the Karoo dolerite. On the other hand, Karoo dolerites do not form particularly continuous outcrops in many parts of the *2730 Vryheid* map region, especially in comparison with dolerite areas in the *3222 Beaufort West* and *3024 Colesberg* maps.

Another possibility is that Beaufort Group and upper Karoo unit on the *2730 Vryheid* map generally consist of more erosionally resistant lithologies than any of the corresponding Beaufort Group units assessed in the *3222 Beaufort West* and *3024 Colesberg* maps. However, examination of the geological database used and referral to the South Africa Committee for Stratigraphy (1980) provides little evidence to support this hypothesis, as sandy units such as the Clarens and Ntabane (Molteno equivalent) Formations are restricted to the easternmost outcrops adjacent to the Lebombo, and more widespread formations such as the Emakwizini Formation (lower Beaufort Group equivalent) are shale- and mudstone-dominated (South African Committee for Stratigraphy, 1980). It should also be noted that in the majority of relevant catchments in the *3024 Colesberg* map, even the sandstone-dominated Katberg Formation displays lower elevation and relief than Karoo dolerite. The extent to which Beaufort Group units in the *3024 Colesberg* map area have been hardened by contact metamorphism during dolerite intrusion is unknown, but there seems little reason to expect this effect to have been significantly greater here than in the other two map areas examined in this study, where abundant dolerite intrusions occur.

The Z_{mean} and R_{mean} values for Karoo dolerite for the three maps are compared graphically in **Figure 3.29**. *3024 Colesberg* displays the most restricted range of Karoo dolerite Z_{mean} values, 1250 - 1515 m, and also the most restricted range of R_{mean} values, 8 - 30 m, due to its location on southern Africa's central escarpment. *3222 Beaufort West* displays a larger Z_{mean} range of 873 - 1723 m and a substantially larger R_{mean} range of 9 - 81 m, as the Karoo dolerites sharply define the southern escarpment zone in this region. For *2730 Vryheid*, however, Karoo dolerites display a more modest R_{mean} range of 14 - 69 m (or 14 - 48 m for 65 of the 66 catchments with Karoo dolerite), but the greatest range of Z_{mean} values: 295 - 1926 m. Given that, as noted

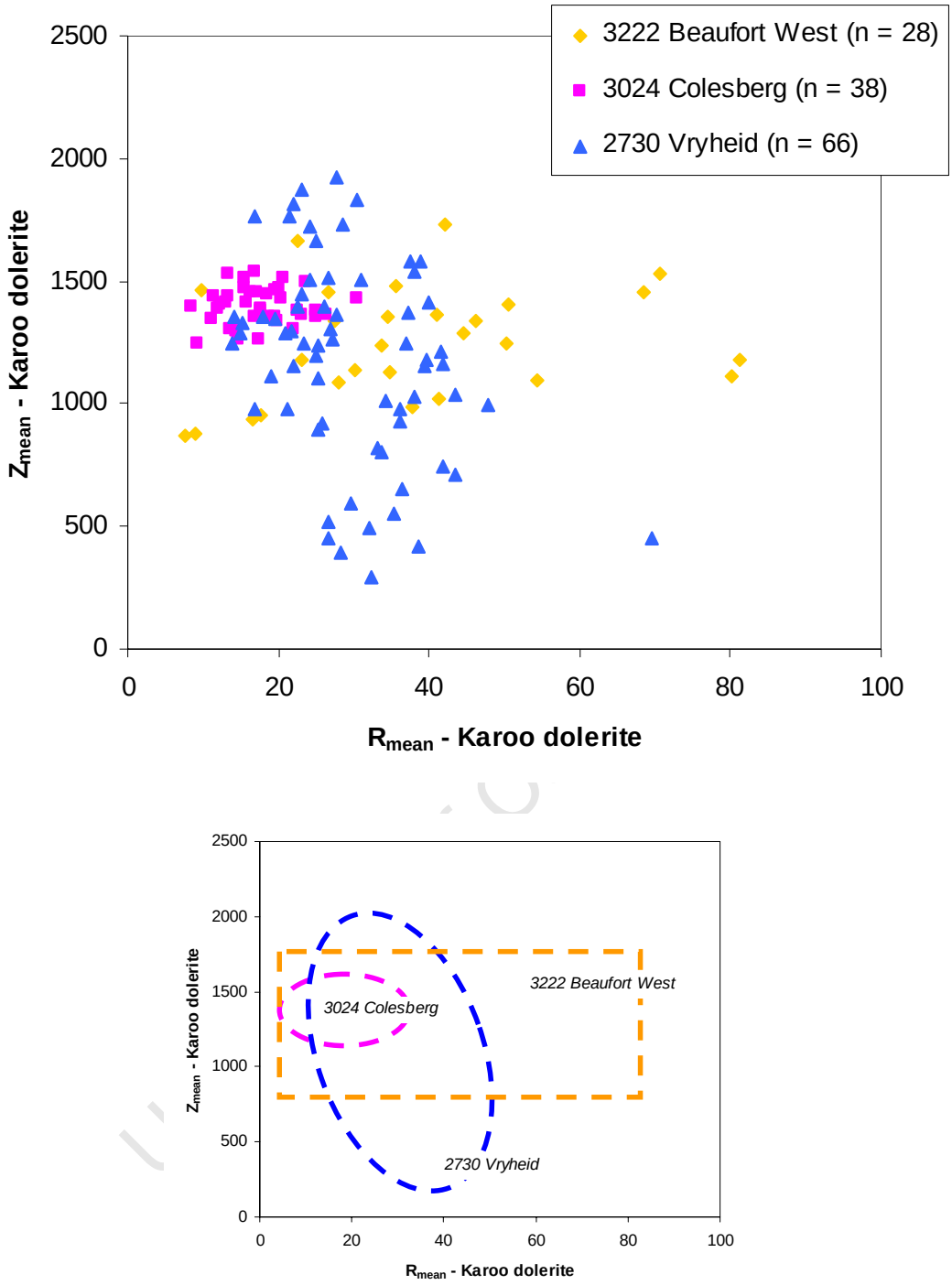

Figure 3.29: Comparison of R_{mean} and Z_{mean} values for Karoo dolerite for the three geological map sheets analysed in this study (top). The generalised topographic fields pertaining to Karoo dolerites each map area are delineated in the miniature reproduction (below). Note that no positive correlation exists between Z_{mean} and R_{mean} in any of the maps.

above, the average size of catchments over which these parameters are calculated is smallest for the *2730 Vryheid* map, the more modest range of R_{mean} values is somewhat surprising. Indeed, the greater general relief of this area (maximum relief = 327 m; **Figure 3.23**) would suggest that Karoo dolerites should also exhibit greater relief, although the greater relief of this area is partly due to the presence of the higher relief Pongola sequence rocks and Lebombo rhyolites that are absent in the two other maps. Yet the two highest R_{mean} values determined for the map area (117 m and 95 m) occur for Beaufort Group and upper Karoo areas of catchments within the eastern escarpment zone. It is worth noting that for none of the three maps does a significant positive correlation between Z_{mean} and R_{mean} values exist, indicating that the average elevation and relief of dolerites in catchments are generally independent of each other on the scale of the analyses. As noted above, the positive linear correlations observed between Z_{mean} values for different lithologies indicates the strong influence of overall catchment elevation in determining this parameter. Thus the non-correlation between Z_{mean} and R_{mean} values for Karoo dolerites indicates the average relief of Karoo dolerite in a catchment does not depend upon its relative elevation in the landscape.

According to Weinert (1965), the *2730 Vryheid* region is characterised by a predominance of chemical weathering over physical weathering for Karoo dolerites and more mature soil profiles, in contrast to the *3222 Beaufort West* and *3024 Colesber*g regions (**Figure 3.5**). If the climate of the *2730 Vryheid* area is such that the chemical weathering rate of Karoo dolerite is enhanced, making dolerite more erodable, this may explain the absence of particularly high relief areas of Karoo dolerite in this humid eastern escarpment region. If this is the case, one might also speculate that the weathering rate of the siliciclastic Karoo country rocks might be less dependent on climatic variation than the weathering rate of the mafic Karoo dolerites, as this would help explain the observation that Karoo dolerite exhibits generally lower Z_{mean} and R_{mean} values than the Beaufort Group and upper Karoo here. However, for this explanation to be plausible, the present-day longitudinal climatic gradient in southern Africa must have persisted for a period long enough to result in significant regional differences in topography.

3.6 Concluding remarks

A comparison of average elevation and average relief for different lithologies in catchments from areas where Karoo dolerites crop out was presented in the previous section. The results of this analysis strongly suggest that lithological contrast ("structure", e.g. Davis, 1899) is the dominant factor that determines topographic variation across the region. Karoo dolerite is clearly one of the most topographically significant lithologies in the Karoo Basin, often exhibiting high local elevation and relief relative to other lithologies, although the topographic prominence of Karoo dolerites clearly depends on country rock lithology, as well as the geometry of the dolerite intrusions. These conclusions, based on a quantitative geospatial analysis, support qualitative field observations made by early workers such as Hatch and Corstorphine (1905), as well as recent models of river catchment development by workers such as Tooth *et al.* (2002; 2004).

The lack of correlation between R_{mean} values for different geological units throughout the region is also interesting. A correlation between the R_{mean} values of different lithologies in the same catchment would be expected if relief was determined by some external factor, such as spatially variable uplift along flexural axes (e.g. Moore, 1999) or the presence of different pediplanation surfaces of variable relief (e.g. Partridge and Maud, 1987). Instead, R_{mean} values are simply indicative of a strong lithological control on topography. This observation is consistent with the hypothesis that southern Africa may exhibit an equilibrium landscape in a topographic steady state, and may, at the scale of these analyses, be described as a function of a time-independent variable, i.e. lithology (Gilbert, 1877; Hack, 1960; Section 1.2). Note, however, that such an interpretation, if based only on topographic data and made without any knowledge of relative denudation rates throughout the landscape, is non-exclusive. Nevertheless, the topography yields no historical information.

The topographic parameters also demonstrate that, somewhat in contrast to the statements of Walker and Poldevaart (1949), the average relief of Karoo dolerites in catchments in the eastern escarpment region is generally lower than in the southern escarpment region (only 1 out of 66 versus 7 out of 28 catchments have Karoo dolerite R_{mean} values $\geq$ 50 m, despite the smaller average catchment size). Also, in the area of the more easterly *2730 Vryheid* map, the mean elevation and relief of Karoo

dolerites in catchments is usually lower than the mean elevation and relief of Beaufort Group country rocks, in contrast with the two map areas (*3222 Beaufort West* and *3024 Colesberg*) from the more arid central-western parts of southern Africa, where Karoo dolerites are generally more topographically prominent. It is possible that these differences are due to regional differences in the geometry of dolerite intrusions and in the sizes and shapes of catchments. However, it remains possible that these regional topographic differences are the expression of regional variation in climate-dependent rates of weathering and erosion, as has been suggested, for instance, to explain latitudinal variations in the topography of the Andes (Strecker *et al*., 2007). Whether denudation rates for Karoo dolerites are indeed higher in this currently wetter, eastern region than in the more arid, western parts of southern Africa will be investigated with the use of cosmogenic nuclide analysis in the following chapters of this thesis.

A final factor that might warrant consideration as an influence on the topography, weathering and erosion of Karoo dolerites in southern Africa is vegetation. Due to greater humidity, the eastern regions of southern Africa boast a greater net primary productivity (natural vegetative yield) than the more arid western regions (Rosenzweig, 1968; Schulze, 2007), and this greater plant biomass might cause an acceleration of dolerite rock weathering through the release of organic acids and the disintegration of rock by plant roots (Section 3.3.2). However, according to Rutherford (1997) different vegetation biomes also occur in the three map regions assessed in this analysis, with the Nama Karoo Biome (grassy, dwarf shrubland) in the two more arid western regions, and with the Grassland Biome (grasses - at higher altitude) as well as the Savannah Biome (grasses with woody plants - at lower altitude) in the more humid *2730 Vryheid* region. One may only speculate, at this point in time, on the possible effects that different plant species may have on dolerite chemical weathering rates, but this may prove to be an interesting area of future research. A greater plant biomass may also result in a longer residence time of weathered dolerite material at the surface, due to more plant roots binding material and retarding soil erosion. Whilst this may retard the actual rate of bedrock weathering, due to soil shielding, the retention of weathered material may result in the eventual development of more chemically weathered soil profiles - a possible alternative explanation that may account for the observations of Weinert (1961, 1965).

CHAPTER 4: THEORY AND METHODS OF TERRESTRIAL COSMOGENIC NOBLE GAS ANALYSIS

4.1 Introduction

Cosmogenic nuclides are produced through the interaction of high-energy cosmic ray particles (primarily from our galaxy) with target nuclei in the earth's atmosphere (Libby, 1946), in meteorites (Paneth *et al*., 1952), and in terrestrial rocks (Davis and Schaeffer, 1955). The interactions between cosmic rays and the earth's atmosphere mean that terrestrial cosmogenic nuclides (TCNs) produced *in situ* at the earth's surface are several orders of magnitude less abundant than in meteorites, and it is only in recent years that technological advances have enabled their routine analysis and application to studies of earth surface processes (Gosse and Phillips, 2001; Niedermann, 2002).

The production of cosmogenic nuclides occurs through a variety of mechanisms, namely spallation, thermal neutron capture, negative muon capture and fast muon induced reactions (e.g. Niedermann, 2002). Although the cosmic ray flux at the top of the atmosphere is dominated by protons (~87 %), spallation reactions within the earth's atmosphere create a cascade of secondary particles, and the cosmic ray flux at the earth's surface is dominated by secondary cosmic ray neutrons (Niedermann, 2002). Spallation, which may be defined as the nuclear reaction of a fast incoming particle with a nucleus in which a few protons and neutrons are sputtered off, leaving behind a lighter nucleus, is the quantitatively dominant mechanism for TCN production in surface rocks (Niedermann, 2002). For the analysis of subsurface rock samples, or for very high erosion rates over long time periods investigated with radionuclides, muogenic TCN production may become important (Niedermann, 2002), but these scenarios are not applicable to this study.

The abundance of TCNs within a given rock is a function of the cosmic ray flux experienced by the rock, as well as the relative abundance of parent (target) nuclei. For geomorphological applications, the TCN concentration in a rock surface is typically used to estimate an age of exposure at the earth's surface, or a surface denudation rate, under the assumption that other determining factors, such as spatial

and temporal variations in cosmic irradiation, and the dependence of production rates on mineral chemistry, are well-constrained (Lal, 1991).

4.2 Latitudinal and altitudinal variations in the cosmic ray flux

Although the cosmic ray flux in space is isotropic, the flux at the earth's surface is latitudinally variable. This is because the geomagnetic field deflects primary (charged) cosmic rays (protons and α-particles), such that only particles with a high "rigidity" (energy to charge ratio) can reach the earth's surface; such particles must exceed a threshold, or cutoff, rigidity, P_c:

$$P_c = \frac{M\mu_0 c}{16\pi R^2}\cos^4 \lambda_m \tag{4.1}$$

where M is the dipole moment of the geomagnetic field (7.9×10^{22} Am^2), μ_0 is the magnetic permeability of free space ($4\pi \times 10^{-7}$ Vs/Am), R is the radius of the earth (6.37×10^6 m), and λ_m is the geomagnetic latitude (Niedermann, 2002). Because the cutoff rigidity at latitudes ≥ 60º is lower than the minimum rigidity of cosmic rays in the solar system, the cosmic ray flux intensity is negligibly affected by the geomagnetic field at such high latitudes (Niedermann, 2002).

The cosmic ray flux on earth also decreases with altitude, due to attenuation as a result of particle interactions in the atmosphere. This may be expressed as:

$$N = N_0 e^{-d/\Lambda} \tag{4.2}$$

where N is the number of particles at the altitude of interest, N_0 is the number of particles at the top of the atmosphere, d is the atmospheric depth in g/cm^2 and Λ is the attenuation length (or mean free path) in g/cm^2 (Niedermann, 2002). The value for Λ varies with latitude, in accordance with the latitudinal variation of P_c.

Because of these effects, TCN production rates vary systematically with both latitude and altitude. As a result, formalised scaling methods have been introduced in order to estimate comparable nuclide production rates at different locations. Because the cosmic ray intensity at a given location is proportional to the nuclear disintegration rate in the atmosphere at that point, Lal (1991) proposes that:

$$P(\lambda_{m,} h) = N(\lambda_m, h) \times P_n / 563.4$$

(4.3)

where $P(\lambda_m,h)$ is the production rate of a nuclide at geomagnetic latitude λ_m and altitude h, $N(\lambda_m,h)$ is the nuclear disintegration rate in the atmosphere at the same location and P_n is the production rate of the nuclide at sea level and high latitudes (≥ 60º). $N(\lambda_m,h)$ is derived from the polynomial:

$$N(\lambda_{m,} h) = a_0 + a_1 h + a_2 h^2 + a_3 h^3$$

(4.4)

where $a_{0,}$ $a_{1,}$ a_2 and a_3 are coefficients that vary according to geomagnetic latitude $\lambda_{m,}$ and are estimated from fitting the observational data of Lal and Peters (1967). These values are given in **Table 4.1**.

The scaling method of Lal (1991) has been criticized by Dunai (2000a) on the basis that although Lal (1991) assumes the geomagnetic field to be a dipole as in equation 4.1, the real geomagnetic field has a significant non-dipole component, of between 10 % and 25 %, that has an effect on the cosmic ray flux (Dunai, 2000a, and references therein). Instead, Dunai (2000a) does not use geomagnetic latitude and altitude to derive his scaling factors, but rather expresses the cosmic ray (neutron) flux as a function of measured geomagnetic field inclination, and atmospheric depth:

$$N(\Delta d, I) = N_{1030}(I) \times e^{\Delta d / \Lambda(I)}$$

(4.5)

where N is the nuclear disintegration rate (i.e. nuclide production rate) at the point of interest, Δd is the difference in atmospheric depth between sea level and the altitude of interest (given as $\Delta d = \Delta p/g$ where Δp is the difference in atmospheric pressure and g is gravitational acceleration, 9.80665 m/s^2), I is the inclination of the geomagnetic field, $N_{1030}(I)$ is the disintegration rate at sea level (1030 g/cm^2 atmospheric depth), and $\Lambda(I)$ is the attenuation path length in g/cm^2. Values for $N_{1030}(I)$ and $\Lambda(I)$ may be calculated from the following two equations:

$$N_{1030}(I) = Y + \frac{A}{\left[1 + e^{-\left(\frac{I-X}{B}\right)}\right]^C}$$

(4.6)

λ_m	a_0 ($g^{-1}yr^{-1}$)	a_1	a_2	a_3
0º	330.7	255.9	98.43	20.50
10º	337.9	252.1	111.0	20.73
20º	382.1	272.1	132.5	24.83
30º	469.3	394.6	97.76	47.20
40º	525.6	505.4	142.0	58.87
50º	571.1	588.1	170.9	76.12
60-90º	563.4	621.8	177.3	78.91

Table 4.1: Values for coefficients a_0, a_1, a_2 and a_3 as a function of geomagnetic latitude (λ_m) for the calculation of atmospheric nuclear disintegration rate $N(\lambda_m)$ according to Lal (1991) (equation 4.4), with h in km, based on the data of Lal and Peters (1967).

Coefficients for $N_{1030}(I)$		Coeffiecients for $\Lambda(I)$	
A	0.4450	a	19.85
B	4.1703	b	-5.430
C	0.3350	c	3.590
X	32.698	x	62.050
Y	0.5555	y	129.55

Table 4.2: Values for coefficients in equations 4.6 and 4.7 for the calculation of $N_{1030}(I)$ and $\Lambda(I)$ (Dunai, 2000a).

$$\Lambda(I) = y + \frac{a}{\left[1 + e^{-\left(\frac{I-x}{b}\right)}\right]^c}$$

(4.7)

where A, B, C, X, Y, a, b, c, x, and y are all coefficients derived by the fitting of observational data (Dunai, 2000a,b). These values are given in **Table 4.2**. The long-term (> 10-20 kyr) averaged value for I may be calculated from the geomagnetic latitude λ_m:

$$\tan I = 2 \tan \lambda_m$$

(4.8)

because the long-term geomagnetic field can be described as a geocentric axial dipole field for periods greater than ~20 kyr (Dunai, 2000a). The average geomagnetic latitude at a site of interest may then also be assumed to be equal to the current geographic latitude, as the earth's magnetic dipole approximates the position of the earth's geographic poles when averaged over millennial timescales (Ohno and Hamano, 1992).

In comparison with Lal (1991), Dunai's (2000a) scaling factors estimate production rates that are up to 18 % lower at sea level and latitudes between 20º and 40º, and more than 30 % higher for high altitudes at higher latitudes (Dunai, 2000a). Whether the scaling factors of Lal (1991) or Dunai (2000a) are more appropriate has been the subject of debate (Desilets *et al*., 2001; Dunai, 2001a; Desilets and Zreda, 2001) and is an issue that is currently unresolved (Kounov *et al*., 2007). Further refinements of these scaling factors have also been published, proposing higher production rates for Antarctica, due to the region's anomalously low air pressure (Stone, 2000) and reassessing the attenuation of spallation reactions with increasing atmospheric depth (Desilets and Zreda, 2003; Desilets *et al*., 2006). Since the methods of Lal (1991) and Stone (2000) on the one hand, and Dunai (2000a), Desilets and Zreda (2003) and Desilets *et al*. (2006) on the other, yield very similar scaling factors in most cases, this study reports exposure ages/erosion rates according to Lal's (1991) and Dunai's (2000a) scaling factors.

4.3 Temporal variations in the cosmic ray flux

The cosmic ray flux at a given point on the earth's surface also varies with time. For instance, galactic cosmic rays that reach the solar system are modulated by solar magnetic fields, and periods of high solar activity correspond with significant decreases in the flux of lower energy cosmic rays at high latitudes (Niedermann, 2002; Lifton, 2005). However, because most solar magnetic field variations occur according to the 11-year solar cycle, and most TCN investigations are concerned with cosmic ray exposures on far longer time spans (> 10^3 yr), this factor may usually be ignored (Gosse and Phillips, 2001; Niedermann, 2002).

More importantly, the dipole and non-dipole components of the earth's geomagnetic field have been variable over time. For periods of < 10-20 kyr, the geomagnetic field cannot be approximated by a dipole, and magnetic field inclination should be estimated from local palaeomagnetic records when scaling TCN production rates (Dunai 2001b; Niedermann, 2002).

The effect of long-term variations in the geomagnetic field intensity (and thus the cutoff rigidity $P_{c,}$ and resulting cosmic ray flux at low latitudes) on TCN production rates is poorly understood and currently debated (Niedermann, 2002). For older exposure ages of up to 50 ka, lack of local palaeomagnetic information may introduce an uncertainty of up to 10-15 % at sea level in some places (Dunai, 2001b), although Masarik *et al*. (2001) suggest more conservative systematic errors, with required corrections of < 12 % for low latitudes and exposure ages of 10-40 ka, and less than a few percent for all latitudes > 35º.

4.4 Surface shielding

The cosmic ray flux experienced by a rock surface can be decreased by surface shielding, and this effect must be modeled accordingly (Dunne *et al*., 1999). For a horizontal surface, the total incident cosmic radiation flux, F, may be given as:

$$F = \int_{\phi=0}^{2\pi} \int_{\theta=0}^{\pi/2} I(\theta,\phi) \cos\theta d\theta d\phi \qquad (4.9)$$

where θ is the inclination angle measured up from the horizontal in radians, ϕ is the azimuthal angle of the incident cosmic rays in radians, and $I(\theta,\phi)$ is the cosmic ray intensity:

$$I(\theta,\phi) = I_0 \sin^m \theta \tag{4.10}$$

for $\theta \geq 0$, where I_0 is the (maximum) cosmic radiation intensity in the vertical direction (Dunne *et al*., 1999). This effect occurs because the atmospheric depth through which cosmic rays must travel is greatest for horizontal ray paths and least for the vertical direction (i.e. zenith), where the flux attains a maximum (e.g. Niedermann, 2002). The commonly estimated value for *m* is 2.3 (Gosse and Phillips, 2001; Niedermann, 2002). Although other values for *m* have been used (Niedermann, 2002, and references therein) such differences have a minor effect (Gosse and Phillips, 2001).

The cosmic ray flux is a maximum for unshielded and horizontal surfaces, as the cosmic ray flux is incident from the entire upper half-space (Niedermann, 2002). Thus, Dunne *et al*. (1999) give this maximum possible flux, $F_{max,}$ as:

$$F_{\max} = \frac{2\pi I_0}{m+1} \tag{4.11}$$

Shielding of the sky by an object thicker than the cosmic ray attenuation length for that material can therefore be determined by placing appropriate limits on the integrals in equation 4.9, or by calculating the missing flux from the shielded region of sky and subtracting it from F_{max} (Dunne *et al*., 1999). This missing flux, δF, may be calculated for a rectangular object as follows:

$$\delta F = \frac{I_0 \Delta\phi}{m+1} \sin^{m+1} \theta_0 \tag{4.12}$$

where the obstruction blocks cosmic rays from the horizontal up to a constant inclination angle θ_0 that extends through an azimuth of $\Delta\phi$ (Dunne *et al*., 1999).

Therefore, the cosmogenic nuclide production rate for a shielded surface may be scaled using the production shielding factor, *S*, which is the ratio of the remaining flux to the maximum flux, and may be calculated as:

$$S = 1 - \frac{1}{2\pi} \sum_{i=1}^{n} \Delta\phi_i \sin^{m+1} \theta_i \tag{4.13}$$

for a set of *n* rectangular obstructions, each with a corresponding θ_i and $\Delta\phi_i$ (Dunne *et al*., 1999).

The shielding effect of a triangular shielding object may be modeled as a rectangular object over the same azimuthal range as the base of the triangular object, by using the following polynomial:

$$\phi_R = 0.62\phi_T - (6.5 \times 10^{-4})\phi_T^2 \tag{4.14}$$

where ϕ_R is the equivalent rectangular inclination angle for the inclination of a triangular object, ϕ_T, both measured here in degrees (Dunne *et al*, 1999).

It should be noted that in addition to changing the surface rate of production, the effective attenuation length of cosmic rays through rock also changes in a complex way with surface shielding, e.g., an obstruction close to the horizon can increase the proportion of cosmic rays close to normal incidence, resulting in a longer effective attenuation length (Dunne *et al*., 1999).

4.5 Self shielding and surface inclination

Due to particle interactions, the cosmic ray flux attenuates in a rock with depth (Lal, 1991):

$$I(d) = I(0)e^{-d/\lambda} \tag{4.15}$$

where I(d) is the flux intensity after traveling a distance d through a rock, I(0) is the unattenuated flux and λ is the attenuation length in a single direction, dependent on particle energy, type and direction.

If a rock surface is inclined, the incident cosmic ray flux will also be reduced from that experienced by a horizontal surface. The extent of shielding varies in a complex way with azimuthal angle (Dunne *et al*., 1999). If a slope has a maximum dip of α where the azimuthal direction ϕ is defined as zero, the dip γ for any azimuthal direction is given by:

$$\tan\gamma = \cos\phi \tan\alpha \tag{4.16}$$

(Dunne *et al*., 1999). Thus for a target located a distance z perpendicularly below the inclined surface, the flux penetration distance d depends on cosmic ray inclination ϕ and slope angle γ in that azimuthal direction, such that:

$$d = \frac{z\cos\gamma}{\cos\alpha\sin(\theta-\gamma)} \tag{4.17}$$

which is valid for $\theta > \gamma$; if $\theta < \gamma$, the incident cosmic ray is being blocked by the surface (Dunne *et al*., 1999).

Thus the total flux intensity F from all directions (θ, ϕ), at a point at perpendicular depth z, on a slope of inclination angle α, is given as:

$$F = \int_{\phi=0}^{2\pi}\int_{\theta=0}^{\pi/2} I(\theta,\phi)e^{-d/\lambda}\cos(\theta)d\theta d\phi \tag{4.18}$$

which may be solved numerically for a given distribution of cosmic rays (Dunne *et al*., 1999).

A decline in the cosmogenic nuclide production rate corresponds to the attenuation of the cosmic ray flux as described in equation (4.15), such that:

$$P(d) = P(0)e^{-\rho d/\Lambda} \tag{4.19}$$

where P(d) and P(0) are the production rates at depth d and at the surface, respectively, ρ is the rock density (g/cm^3) and Λ is the nuclide attenuation length in all directions (decrease in production rate with mass encountered by a factor of 1/e) in g/cm^2 (Niedermann, 2002). A value of 160 g/cm^2 is given by Gosse and Phillips

(2001) as the neutron spallation attenuation length for an unobstructed, horizontal surface.

Therefore, because the cosmogenic nuclide production rate is proportional to the cosmic ray flux, the ratio of the cosmic ray flux F at perpendicular depth z and inclination α (equation 4.18) to the maximum possible flux F_{max} (z = 0; α = 0) also defines a cosmogenic nuclide production rate scaling factor, S:

$$S(z,\alpha) = \frac{F}{F_{\max}} \tag{4.20}$$

(Dunne *et al*., 1999). Substitution with equation 4.18 (which may be solved using the intensity distribution given in equation 4.10, where *m* = 2.3) produces an incomplete gamma function which may be modeled as the following exponential that closely approximates the scaling factor:

$$S(z,\alpha) = (1 - 3.6\times10^{-6}\alpha^{2.64})e^{-\left(\frac{z}{\Lambda}\right)\left(1+\frac{\alpha^2}{5000}\right)} \tag{4.21}$$

where Λ, the nuclide production attenuation length, has been related to λ, the cosmic ray attenuation length, such that λ = 1.3 Λ, and α is in degrees (Dunne *et al*., 1999). This scaling factor thus holds for all cases, including subsurface samples on horizontal surfaces (α = 0°, z > 0) and surface samples on inclined surfaces (α > 0, z = 0). For z = 0 and α = 90° (e.g. a cliff face), S = 0.5 because cosmic rays are blocked from half the upper half-space.

4.6 Erosion rates and exposure ages

Once the production rate of a cosmogenic nuclide is known, and scaled appropriately for the effects of latitude, altitude, shielding and surface inclination, its cosmogenic nuclide abundance may be interpreted in terms of a cosmic ray exposure history.

Both stable (e.g. ^{3}He and ^{21}Ne) and unstable (e.g. ^{10}Be, ^{26}Al and ^{36}Cl) nuclides can be applied to geomorphological studies. Paired analyses of unstable nuclides with differing half-lives (e.g. ^{10}Be with ^{26}Al) allow for the study of complex exposure histories which include episodes of burial (Lal, 1991), but unless used in conjunction with cosmogenic radionuclides, the stable cosmogenic noble gases do not provide

such information. However, cosmogenic noble gases do allow for long exposure periods to be measured accurately, as their abundances do not reach saturation, and they also allow for shorter surface exposures to be studied, due to the high production rate of ^{3}He. Cosmogenic noble gases even allow for the study of palaeo-exposures that have later been covered and shielded from cosmic rays (e.g. Libarkin *et al*., 2002).

Erosion removes irradiated surface rock, such that the TCN production in a surface rock formerly at depth was lower in the past. The shielding depth z(-t) of a rock at time t before present can be expressed as:

$$z(-t) = z_p + \int_{-t}^{0} \varepsilon(t')dt' \tag{4.22}$$

and for a constant erosion rate:

$$z(-t) = z_p + \varepsilon t \tag{4.23}$$

where ε(t) is the erosion rate and z_p is the present shielding depth (Niedermann, 2002). Similarly, if t = 0 is defined as the time of emplacement in the subsurface, and z_0 as the initial shielding depth, then:

$$z(t) = z_0 - \varepsilon t \tag{4.24}$$

Substitution of z(t) for d in equation 4.19 yields:

$$P(z,t) = P(0)e^{-\rho(z_0-\varepsilon t)/\Lambda} \tag{4.25}$$

where P(z,t) is the resulting production rate. The change in the nuclide concentration C over time is determined by P(z,t) and the nuclide decay constant, λ:

$$\frac{dC(z,t)}{dt} = P(0)e^{-\rho(z_0-\varepsilon t)/\Lambda} - \lambda C(z,t) \tag{4.26}$$

and integration of equation 4.26 provides a solution for C:

$$C(z,t) = C(z,0)e^{-\lambda t} + \frac{P_0}{\lambda + \rho\varepsilon/\Lambda} e^{-\rho(z_0-\varepsilon t)/\Lambda}(1 - e^{-(\lambda+\rho\varepsilon/\Lambda)t}) \tag{4.27}$$

(Niedermann, 2002). Assuming that the surface production rate P_0, the decay constant λ, the attenuation length Λ and the rock density ρ are well constrained, equation 4.27 contains two free parameters: t (exposure age) and ε (erosion rate). For geomorphological applications, equation 4.25 can therefore be used to define two limiting cases which interpret a measurement of C, either to calculate an exposure age T, where ε = 0:

$$T = \frac{C(z_0, T)}{P_0 e^{-\rho z_0 / \Lambda}} \tag{4.28}$$

or to calculate a constant erosion rate ε, where t = ∞:

$$\varepsilon = \frac{\Lambda}{\rho}\left(\frac{P_0}{C}\right) \tag{4.29}$$

both of which hold for stable cosmogenic nuclides (λ=0) where the initial concentration $C(z_0,0) = 0$ (Lal, 1991, Niedermann, 2002, Bierman and Caffee, 2002). Equations 4.28 and 4.29 therefore provide the minimum exposure age and maximum erosion rate compatible with the data (Niedermann, 2002). The maximum erosion rate ε is by definition valid for the time taken to erode the thickness of rock equivalent to the cosmogenic nuclide attenuation length Λ.

As mentioned in Section 4.5, a value of 160 g/cm^2 is typically used as the neutron spallation attenuation length for an unobstructed, horizontal surface. However, if this value is used in equation 4.29 to calculate the erosion rate for surface of dip > 0º, only an apparent erosion rate will be determined, which will be greater than the true erosion rate perpendicular to the surface. This is because the effective attenuation length perpendicular to the surface depends on slope angle in a complex manner (Dunne *et al*., 1999), due to the lower energy of cosmic ray neutrons with lower angles of incidence (Section 4.4). According to Hermanns *et al.* (2004), the true erosion rate for an inclined surface ε may be calculated from an apparent erosion rate ε* by using the numerical approximation:

$$\varepsilon = \frac{\varepsilon^*}{\left(1 + \frac{\alpha^2}{5000}\right)} \tag{4.30}$$

where α is the slope angle in degrees.

Finally, it is important to note that, as stated in Section 1.3, the commonly used term for ε, maximum "erosion" rate, as derived above from a cosmogenic nuclide concentration, might be more correctly referred to as a maximum denudation rate, as it reflects the total removal of rock, whether through mechanical or chemical processes (von Blanckenburg, 2005).

4.7 Cosmogenic noble gas production rates

Craig and Poreda (1986) and Marti and Craig (1987) were first to measure the abundance of cosmogenic ^{3}He and ^{21}Ne in pyroxenes, although at that time, the nuclide production rates were only approximately known (Marti and Craig, 1987). Since then, efforts have been made to determine the production rates of ^{3}He and ^{21}Ne experimentally in mafic minerals (e.g. Kurz *et al*., 1990; Cerling, 1990; Poreda and Cerling, 1992; Cerling and Craig, 1994). Young volcanic rocks have been especially useful in this regard, as the absence of erosion can be confirmed by the presence of surface textures, and exposure ages are identical to radiometric eruption ages (Niedermann, 2002).

However, cosmogenic ^{3}He and ^{21}Ne production rates actually depend on target mineral chemistry, as these nuclides are each produced through a range of spallation reactions with different cross-sections (probabilities), and therefore different production rates. The Mg content of pyroxenes is especially important for ^{21}Ne production due to the high cross-section for the ^{24}Mg(n,α)^{21}Ne reaction (e.g. Masarik and Reedy, 1996). Following initial approximations by Lal (1991), Masarik and Reedy (1995) used cross-sections derived from measurements of extra-terrestrial materials to model elemental coefficients for TCN production. Production rate estimates have been proposed for these nuclides by Masarik and Reedy (1996), Schäfer *et al*. (1999) and Masarik (2002), as well as by Kober *et al*. (2005) where the elemental ^{21}Ne production rate is calibrated to the experimentally determined production rate of ^{21}Ne from Si in quartz (Niedermann *et al*., 1994; Niedermann, 2000).

Fenton *et al*. (2009) compared the accuracy of experimentally determined production rates (Poreda and Cerling, 1992; Cerling and Craig, 1994) with elemental model production rates (Masarik, 2002; Kober *et al*, 2005) for cosmogenic ^{3}He and ^{21}Ne in pyroxene and olivine separates from radiometrically-dated lava flows. They found that the radiometrically-calibrated nuclide production rates gave more accurate surface exposure ages, but that these rates should be adjusted to the chemical composition of any given sample in order to obtain the best agreement between ^{3}He and ^{21}Ne ages (Fenton *et al*., 2009). Thus Fenton *et al.* (2009) proposed that a calibrated version of Masarik's (2002) elemental production rates be used, by multiplying all Masarik's (2002) elemental production rates for ^{3}He by a normalization factor of 1.099 and the corresponding ^{21}Ne elemental production rates by a normalization factor of 0.851.

Another cosmogenic noble gas nuclide produced in pyroxene is ^{38}Ar, which is a potential tool for cosmogenic exposure studies using Ca- and K-rich minerals, despite obstacles such as the high atmospheric background of ^{38}Ar, and the production of ^{36}Ar through β^- decay of cosmogenic ^{36}Cl (half-life 3×10^5 yr), produced from ^{35}Cl through thermal and epithermal neutron capture (Renne *et al*., 2001; Niedermann *et al*., 2007).

The suggested elemental production rates for ^{3}He, ^{21}Ne and ^{38}Ar from Lal (1991), Niedermann *et al*., (1994), Masarik and Reedy (1996), Schäfer *et al*. (1999), Niedermann (2000), Masarik (2002), Kober *et al*. (2005), Niedermann *et al*. (2007) and Fenton *et al*. (2009) are given in atoms per gram of element per year in **Table 4.3,** normalised to sea level and high latitudes (> 60º).

4.8 Noble gas components

The noble gas inventory in a rock is always a mixture of a number of components. In addition to a cosmogenic component, these nuclides may also originate from atmospheric, mantle or crustal gases trapped within the crystal lattice or in fluid inclusions, or they may be radiogenic, i.e. formed by the radioactive decay of U, Th, and ^{40}K (Niedermann, 2002). Alternatively, they may be "nucleogenic", i.e. produced by non-cosmic ray induced nuclear reactions, such as $^{18}O(\alpha,n)^{21}Ne$ or $^{24,25}Mg(n,\alpha)^{21,22}Ne$, where the incident alpha-particles are derived from U and Th

Nuclide	Authors	Elemental production rate (atom/g/yr)								
		O	Na	Mg	Al	Si	Ca	Fe	Ti	Ni
^{3}He	Lal (1991)	83		50	47	66		28		
	Masarik and Reedy (1996)	135		116	107	111	61	40		
	Masarik (2002)	128.7		110.8	102	106	57.7	38.5		
	Kober *et al. (*2005)	191		182	160	129		95		91
	Fenton *et al*. (2009)[4]	141.4		121.8	112.1	116.5	63.7	42.3	42.3	
^{21}Ne	Lal (1991)			110	24	18		0.24		
	Niedermann *et al*. (1994)[1]					45				
	Masarik and Reedy (1996)		98	131	65	39	4	0.20		
	Schäfer *et al*. (1999)			196	54	45				
	Niedermann (2000)[2]					40.7 ± 7.9				
	Masarik (2002)		102	175.1	62.4	41.7	1.8	0.187		
	Kober *et al*. (2005)		208	189	60	44	17	1		1
	Fenton *et al*. (2009)[4]		86.8	148.9	52.8	35.7	1.7	0.159	0.159	
^{38}Ar	Lal (1991)						200	1.7		
	Knight *et al.* (2003)[5]						100			
	Niedermann *et al*. (2007)[3]						191± 21 - 254±28			

[1] experimental determination

[2] revised from Niedermann *et al*. (1994)

[3] based on two different "sets" of estimates for ^{3}He and ^{21}Ne production rates; see Niedermann *et al.* (2007) for details

[4] modified from Masarik (2002) using experimentally determined normalization factors

[5] first-order estimate based on neutron activation experiments

Table 4.3: Literature estimates of the terrestrial cosmogenic production rates of the noble gas nuclides ^{3}He, ^{21}Ne and ^{38}Ar at sea level and at high latitudes (>60°), in atoms per gram of element per year.

Temperature		^{4}He		^{20}Ne		^{40}Ar		^{84}Kr		^{132}Xe	
		10^{-8} cm^3 STP	± 2σ	10^{-12} cm^3 STP	± 2σ	10^{-8} cm^3 STP	± 2σ	10^{-12} cm^3 STP	± 2σ	10^{-12} cm^3 STP	± 2σ
crushed	min.	0.00030	0.00020	0.33	0.12	0.0050	0.0050	0.0110	0.0040	0.0070	0.0040
	max.	0.0016	0.0010	0.73	0.20	0.028	0.010	0.035	0.010	0.055	0.020
600 ºC	min.	0.00070	0.00020	0.40	0.10	0.0100	0.0030	0.0150	0.0080	0.0110	0.0030
	max.	0.00080	0.00020	0.50	0.15	0.0200	0.0080	0.025	0.010	0.020	0.010
900 ºC	min.	0.00050	0.00020	1.00	0.30	0.080	0.020	0.120	0.040	0.037	0.010
	max.	0.00080	0.00030	1.90	0.60	0.160	0.050	0.20	0.15	0.100	0.060
1750 ºC	min.	0.0035	0.0015	0.80	0.40	0.050	0.030	0.040	0.020	0.015	0.010
	max.	0.0130	0.0080	2.50	0.90	0.170	0.050	0.220	0.080	0.060	0.020

Table 4.4: Maximum and minimum blank values estimated for ^{4}He, ^{20}Ne, ^{40}Ar, ^{84}Kr and ^{132}Xe in cm^3 STP for the evaluation of sample analyses.

decay and the neutrons from other (α,n) reactions, or from U fission (Niedermann, 2002). Fortunately, pyroxenes are not only characterized by a high He and Ne retentivity, but also have typically low concentrations of U, Th and K (Niedermann, 2002).

If the isotopic ratio of the trapped component is assumed, or determined independently, then the excess (non-trapped component) of a noble gas nuclide may be determined from a measured isotopic ratio and the measured abundance of the reference isotope:

$$^{3}He_{ex} = \left[\left(^{3}He/^{4}He\right)_{m} - (^{3}He/^{4}He)_{tr}\right] \times ^{4}He_{m} \tag{4.31}$$

for ^{3}He, and

$$^{21}Ne_{ex} = \left[\left(^{21}Ne/^{20}Ne\right)_{m} - (^{21}Ne/^{20}Ne)_{tr}\right] \times ^{20}Ne_{m} \tag{4.32}$$

for ^{21}Ne, where ^{4}He and ^{20}Ne are the respective reference isotopes, and the subscripts *ex*, *m* and *tr* denote excess, measured and trapped, assuming that $^{4}He_{ex}$ and $^{20}Ne_{ex}$ can be ignored (Niedermann, 2002). The trapped noble gas component may be determined through crushing *in vacuo* to preferentially release gas in fluid inclusions, or partially separated through stepwise heating, which is useful for Ne, where, for pyroxene, the major fraction of the cosmogenic component is often released at temperatures ≥ 900°C (Niedermann, 2002 and references therein).

For Ne, three-isotope systematics may also be used, because in addition to ^{21}Ne, the isotopes ^{22}Ne and ^{20}Ne are also produced through cosmic-ray neutron spallation, and thus cosmogenic Ne from a given target material has a unique ^{21}Ne/^{22}Ne/^{20}Ne ratio (Niedermann, 2002). Therefore, when the measured ^{21}Ne/^{20}Ne ratio is plotted against the measured ^{22}Ne/^{20}Ne ratio, any mixture in which cosmogenic Ne and atmospheric Ne (^{21}Ne/^{20}Ne = 0.002959; Eberhardt *et al*., 1965) are the only significant components must fall on the "spallation line" - the mixing line between these two components (**Figure 4.1**; Niedermann *et al*., 1993). If measured ratios deviate from the spallation line, the excess Ne cannot be assumed to be purely cosmogenic. Contamination by other components is implied, and can be corrected for, but only if it is known that

there is only one contaminant, e.g. nucleogenic ^{21}Ne (Niedermann, 2002). In the event that the measured Ne does plot on the spallation line, significant contributions from other components might still be present, but occur in such proportions that they remain unresolved (**Figure 4.1**).

The slope of the spallation line depends upon where the cosmogenic component plots on the Ne three isotope diagram, which is a result of the relative cosmogenic production rates of ^{20}Ne, ^{21}Ne and ^{22}Ne for a target mineral. Relative cosmogenic nuclide production rates may be determined through studies of extraterrestrial samples and model calculations. However, the slope of the pyroxene spallation line has been experimentally defined with much more accuracy by Bruno *et al*. (1997) and Schäfer *et al*. (1999) as 1.055 ± 0.017 and 1.069 ± 0.035 respectively, by plotting Ne isotope data for a range of Antarctic samples with long exposure histories. Variations in the chemistry of the pyroxene target have apparently little effect on the slope of the spallation line (S. Niedermann, personal communication, 2008).

For cosmogenic Ar, both ^{38}Ar and the reference isotope ^{36}Ar are produced through neutron spallation, and ^{36}Ar is also produced through ^{36}Cl decay (Niedermann *et al.*, 2007). The cosmogenic ^{38}Ar ($^{38}Ar_c$) component may thus be resolved as:

$$^{38}Ar_c = \frac{(38/36)_{sp}}{(38/36)_{sp} - (38/36)_{air}} \times \{36_{tot}\left[(38/36)_{tot} - (38/36)_{air}\right] + 36_{Cl}(38/36)_{air}\} \quad (4.33)$$

where 38 and 36 denote the respective Ar isotopes, the subscript *tot* denotes total measured, *air* denotes the assumed ratio in air (e.g., $(38/36)_{air}$ = 0.1880 ± 0.0003; Nier, 1950), *sp* denotes the spallation production rate (e.g., $(38/36)_{sp}$ = 1.5 ± 0.2 for Ca measured in lunar material; Hohenberg *et al*., 1978; Niedermann *et al*., 2007) and *Cl* denotes the concentration produced from thermal and epithermal neutron capture of ^{35}Cl and subsequent decay of ^{36}Cl to ^{36}Ar, which is typically less than the analytical uncertainty of total ^{36}Ar for samples with Cl concentrations of <100 ppm (Niedermann *et al*., 2007). It must also be noted that $(38/36)_{sp}$ = 1.5 is only valid where secular equilibrium between production and decay of ^{36}Cl has been attained, i.e. for long exposure ages of ~1 Ma (~3 half lives of ^{36}Cl) or more; for younger exposures $(38/36)_{sp}$ is time dependent (Renne *et al*., 2001; Niedermann *et al*., 2007).

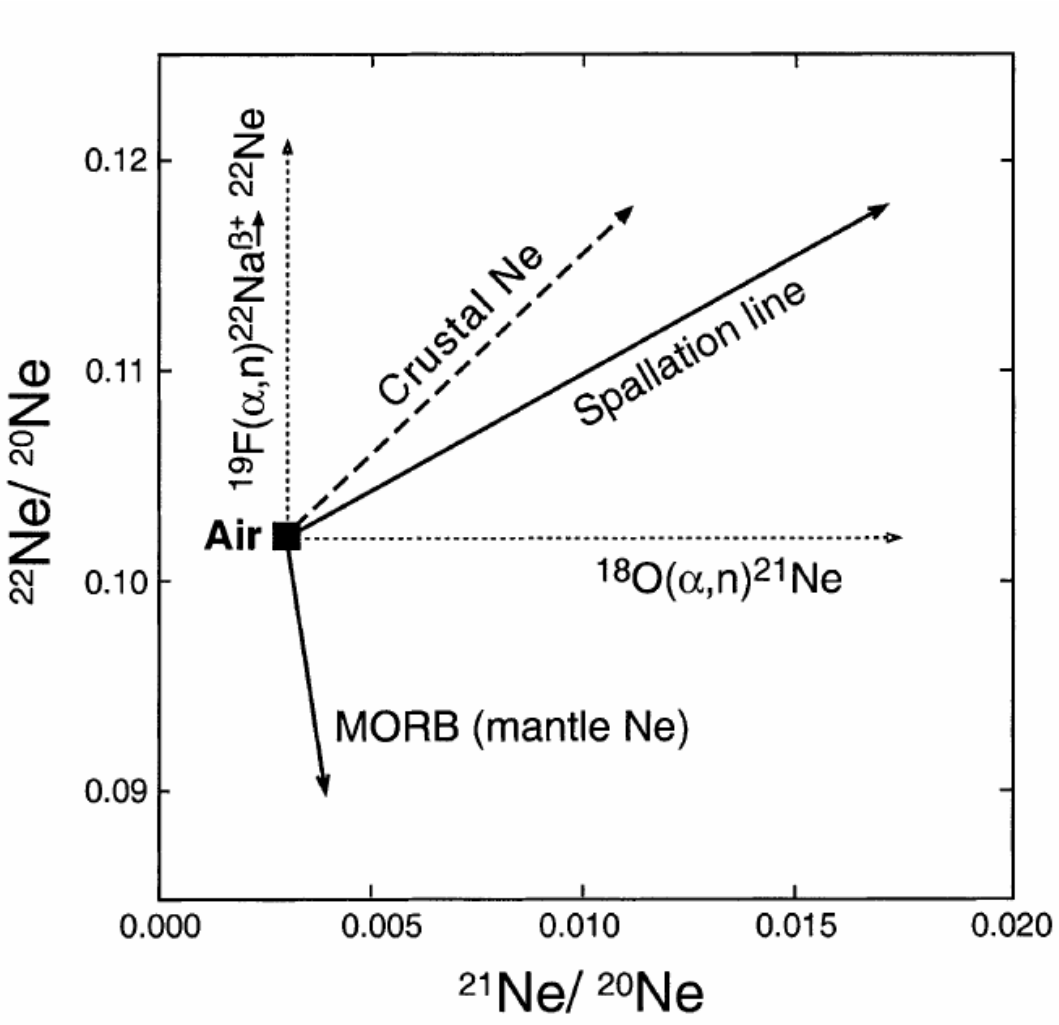

Figure 4.1: Neon three-isotope diagram showing mixing trends between atmospheric Ne (^{21}Ne/^{20}Ne = 0.002959 and ^{22}Ne/^{20}Ne = 0.1020; Eberhardt *et al.*, 1965) and various other Ne components. A mixture of only atmospheric Ne and cosmogenic Ne must plot on the "spallation line" (shown here for quartz). The vertical and horizontal dotted lines represent mixing with nucleogenic ^{22}Ne and ^{21}Ne respectively (here produced, for example, through the interaction of ^{19}Fe and ^{18}O nuclei with α-particles emitted by the radioactive decay of neighbouring U and Th nuclei). Contributions of both nucleogenic ^{22}Ne and ^{21}Ne may thus result in a Ne measurement plotting on the spallation line even though a significant nucleogenic component may be present.

4.9 Sample preparation and analysis

For this study, rock samples were recovered in the field with a hammer and chisel once their geographic location and altitude were recorded with a GPS, and their surface inclination measured with a clinometer. The extent of cosmic ray shielding by obstructions on the horizon was measured with an Abney level and a compass.

For each sample, the top 5 cm of the exposed rock surface was removed with a circular saw for further analysis, and the excess rock used to produce thin sections for petrographic examination. Samples were then crushed with a jaw crusher and sieved, and the 250-600 μm fraction was washed with distilled water in an ultrasonic bath.

Magnetic and density separation techniques were then applied. The general mineral separation procedure was varied slightly for individual samples, depending on individual sample mineral chemistry, texture, and degree of chemical weathering. Magnetic separation was performed with an electromagnetic separator in order to remove a large proportion of the metal oxide and plagioclase feldspar grains; these corresponded to the magnetic fraction for a 0.20 A current and the non-magnetic fraction for 1.0 A current, respectively, for a 20° side tilt. Density separation with diiodomethane (CH_2I_2, ρ = 3.325 g/cm^3) was then used to remove the light fraction from the sample. Slightly diluted diiodomethane was sometimes used to recover a lighter fraction. Further magnetic separation was then usually performed by trial and error in order to concentrate the fresh pyroxenes in the non-magnetic fraction. Currents between 0.30 A and 0.20 A for a 15° side tilt often proved useful in this regard. Etching with concentrated HCl to remove metal oxides, and with HF to remove weathered pyroxene grain surfaces, was also applied.

Approximately 650 mg of pyroxene grains were handpicked from each sample, with a typical grain diameter of 250-300 μm. A split of ~500 mg was used for noble gas mass spectrometry, and ~150 mg was used for major element determination though ICP-AES (inductively-coupled plasma atomic emission spectrometry). Extra sample was sometimes handpicked for XRD (X-ray diffraction) analysis, in order to confirm the success of the mineral separation procedure.

Noble gas analysis was performed at the noble gas laboratory of the Deutsches GeoForschungsZentrum in Potsdam, Germany, using a MM5400 noble gas mass spectrometer, equipped with an ultrahigh vacuum furnace, an ultrahigh vacuum mechanical crusher, a gas preparation line and a cryogenic adsorber.

All samples were analysed through stepwise heating and some samples were also analysed through crushing. For crushing analyses, the sample was loaded into the ultrahigh vacuum crusher and baked at 100 °C for 24 hours. The sample was then crushed between two hard metal jaws in order to release gases trapped between grain boundaries and within fluid inclusions, and the extracted gas was expanded into the gas preparation line. After crushing, the crushed sample material was then recovered and used in subsequent heating analyses.

For all heating analyses (both for pre-crushed and uncrushed samples), each sample was wrapped in aluminium foil, deposited in a sample carousel, placed under vacuum, dropped into a tantalum crucible and heated by a graphite heating jacket. Samples were then heated in two or three temperature steps: 600°C and/or 900°C and 1750°C, and after each temperature step the gas was expanded into the gas preparation line and ultimately into the mass spectrometer for separate analysis.

In the gas preparation line, condensable gases such as H_2O were frozen in a dry-ice cooled trap, and other chemically active gases (e.g. O_2, N_2, CO_2, H_2, hydrocarbons etc.) were absorbed in two titanium sponge and two ZrAl getters, with two additional ZrAl getters in the source and detector parts of the mass spectrometer, in order to maintain a low background of active gases during the measurements.

For each analysis (crushed, 600 ºC, 900 ºC, or 1750 ºC), measurement of noble gas spectra (and other associated spectra for interference corrections) was performed in three separate stages - first for He, then for Ne, and finally for Ar, Kr and Xe together. Sequential release of these gases into the mass spectrometer was achieved with the use of the cryogenic adsorber which could be cooled to 12 K, and then heated in separate steps. Gases were then ionized through electron bombardment with a modified Nier-type ion source, accelerated by a 4.5 kV voltage, focused through a system of electric lenses, and deflected through a 90° magnetic sector field according

to their mass to charge ratio (m/e), for measurement by a Faraday cup or an electron multiplier detector, depending on the ion current strength.

4.10 Data reduction and evaluation

For each noble gas analysis (i.e. He, Ne or Ar-Kr-Xe), noble gas nuclides of interest as well as species necessary for isobaric interference corrections were measured over 11 scans. Isobaric interferences occur between species with the same m/e ratio. $^{12}C^{+++}$ (m/e = 4), $H_2{}^{18}O^+$ and $^{40}Ar^{++}$ (m/e = 20), $^{12}C^{16}O_2{}^{++}$ (m/e=22), $H^{35}Cl$ (m/e = 36), and $H^{37}Cl$ (m/e=38) interfere with the measurements of ^{4}He, ^{20}Ne, ^{22}Ne, ^{36}Ar and ^{38}Ar respectively.

The $^{12}C^{+++}$ contribution to the m/e = 4 peak was determined during blank measurements (typically 1-1.5 × 10^{-6} V) and subtracted from the ^{4}He sample measurements. The contribution of $H_2{}^{18}O^+$ on the ^{20}Ne measurement was small enough to avoid a correction by setting the m/e=20 peak measurement slightly off the peak centre. The peaks of $^{40}Ar^+$ and $^{12}C^{16}O_2{}^+$ were monitored during Ne measurements as proxies for the contributions of $^{40}Ar^{++}$ and $^{12}C^{16}O_2{}^{++}$ to the m/e = 20 and m/e = 22 peaks respectively. However, the $CO_2{}^+/CO_2{}^{++}$ and $^{40}Ar^+/^{40}Ar^{++}$ ratios vary systematically with the mass spectrometer background of $H_2{}^+$, $CH_4{}^+$ and $CO_2{}^+$ (Niedermann *et al*., 1997 and references therein), and so all these species were also monitored so that the ^{20}Ne and ^{22}Ne measurements could be corrected appropriately. For Ar measurements, $^{35}Cl^+$ was similarly measured as a proxy for $H^{35}Cl^+$ and $H^{37}Cl^+$ contributions at m/e = 36 and m/e = 38; the $H^{35}Cl^+/^{35}Cl^+$ and $H^{37}Cl^+/^{35}Cl^+$ ratios do not depend on the background, but remain constant for constant ion source conditions (Niedermann *et al*., 1997).

Some samples yielded a high ^{4}He voltage peak greater than the Faraday cup's upper detection limit of 10 V, presumably due to an accumulation of *in situ*-produced radiogenic ^{4}He. For these samples, measurements had to be made after 2 minutes of pumping the mass spectrometer and subsequently re-expanding the remaining gas from the part of the line next to the mass spectrometer inlet, and an experimentally-determined correction factor was applied in order to estimate the true ^{4}He abundance.

Once interference corrections were made, measurements of nuclide abundances ($^{4}He_{F}$, $^{20}Ne_{m}$, $^{40}Ar_{F}$, $^{84}Kr_{m}$, $^{132}Xe_{m}$) and isotopic ratios ($^{3}He_{m}/^{4}He_{F}$, $^{20}Ne_{m}/^{22}Ne_{m}$, $^{21}Ne_{m}/^{20}Ne_{m}$ or $^{20}Ne_{m}/^{21}Ne_{m}$, $^{36}Ar_{F}/^{40}Ar_{F}$, $^{36}Ar_{m}/^{40}Ar_{F}$, $^{38}Ar_{m}/^{36}Ar_{m}$) from the 11 scans were each reduced to a single value with uncertainty, based on mean, linear or exponential extrapolation to the time of gas admission, as appropriate. The subscripts m and F denote measurements on the electron multiplier and Faraday cup detectors, respectively.

In order to evaluate the sample analyses and determine the true abundances of the reference isotopes and the correct isotope ratios for the samples, standard and blank measurements were also required. The data evaluation procedure is illustrated schematically as a flow chart in **Figure 4.2**. Analyses of a standard gas aliquot were conducted regularly in order to determine (1) the sensitivity of the detectors (ε, relating measured voltage to gas amounts in cm^3 STP) (2) the relative sensitivity of the electron multiplier detector compared to that of the Faraday detector (the multiplier gain) and (3) mass discrimination effects affecting the measured values of isotope ratios. The standard gas analyses measured the Faraday cup and electron multiplier sensitivities for $^{4}He_{F}$, $^{20}Ne_{F}$, $^{40}Ar_{F}$, $^{84}Kr_{m}$, $^{132}Xe_{m}$, the electron muliplier's gain for $^{20}Ne_{m}/^{20}Ne_{F}$ and $^{36}Ar_{m}/^{36}Ar_{F}$, the effect of mass discrimination on $^{20}Ne_{m}/^{22}Ne_{m}$, $^{21}Ne_{m}/^{20}Ne_{m}$, $^{40}Ar_{F}/^{36}Ar_{F}$ and $^{38}Ar_{m}/^{36}Ar_{m}$, and the combined effect of mass discrimination and multiplier gain on $^{3}He_{m}/^{4}He_{F}$ and $^{40}Ar_{F}/^{36}Ar_{m}$.

Blank analyses for $C^{+++}{}_{m}$, $^{4}He_{m}$, $^{20}Ne_{m}$, $^{40}Ar_{F}$, $^{84}Kr_{m}$ and $^{132}Xe_{m}$ were performed in between the sample analyses in order to monitor the background levels of gas within the mass spectrometer. These blank analyses included extraction analyses for empty Al foil wrappers that were step-heated to temperatures of 600 ºC, 900 ºC and 1750 ºC, as the melting of the Al foil at 660 °C generally makes a significant contribution to the background levels of the gases (with the exception of ^{4}He). Blank values were estimated separately for individual analyses as the background varied with time and with the temperature of the analysis. The maximum and minimum blank values that were estimated for ^{4}He, ^{20}Ne, ^{40}Ar, ^{84}Kr and ^{132}Xe for each temperature step are given in **Table 4.4**.

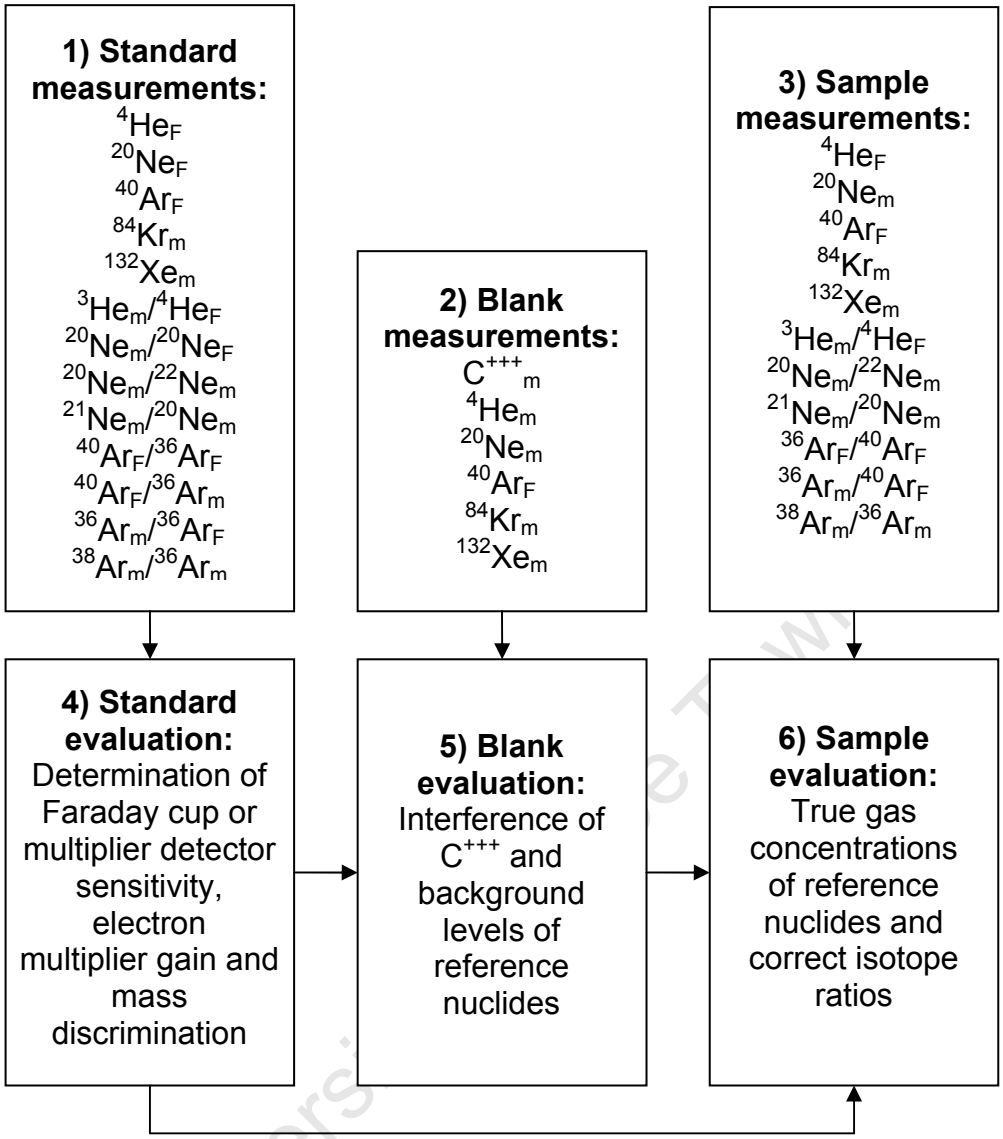

Figure 4.2: Flow chart illustrating the data evaluation procedure for standard, blank and sample measurements.

CHAPTER 5: GEOMORPHOLOGICAL AND CLIMATIC CONTEXT, PETROGRAPHY, MINERALOGY AND COSMOGENIC ^{3}HE AND ^{21}NE PRODUCTION RATES FOR KAROO DOLERITE SAMPLES

5.1 Introduction

This chapter describes the geomorphological and climatic context of the Karoo dolerite samples collected for cosmogenic nuclide analysis. A brief account of each sample's petrography is also presented. Finally, cosmogenic ^{3}He and ^{21}Ne production rates for pyroxene mineral separates are calculated according to pyroxene mineral chemistry and published elemental production rates.

5.2 Sample sites

Previous cosmogenic nuclide studies in southern Africa have concentrated on Namibia's highlands, escarpment and coastal plain (Cockburn *et al*., 1999; 2000; Bierman and Caffee, 2001; van der Wateren and Dunai, 2001; Codilean *et al*., 2008), the western escarpment of South Africa (Kounov *et al*., 2007) the Drakensberg (southeastern) escarpment (Fleming *et al*., 1999) and the Malapa caves region, central eastern plateau (Dirks *et al*., 2010). In order to compliment these datasets, new sample sites were chosen from previously unstudied areas in the region.

The locations of the 22 sample sites presented in this study are shown in **Figure 5.1**. The sample name, geographic coordinates, elevation and surface inclination at each site is listed in **Table 5.1**, together with the latitude- and altitude-dependent cosmogenic nuclide production scaling factors of Lal (1991) and of Dunai (2000a). The local topographic shielding factor S, calculated in CosmoCalc version 1.6 (http://cosmocalc.googlepages.com) from the surface dip and the azimuths and elevations of objects on the horizon, is also given.

Samples were collected from two major areas in the Republic of South Africa:

1) A large western region ranging from south of the southern escarpment zone in the southern Cape region to the Orange River - a region recently studied by Tinker *et al.* (2008a) using fission track thermochronology (**Figures 5.2** and **5.3**).

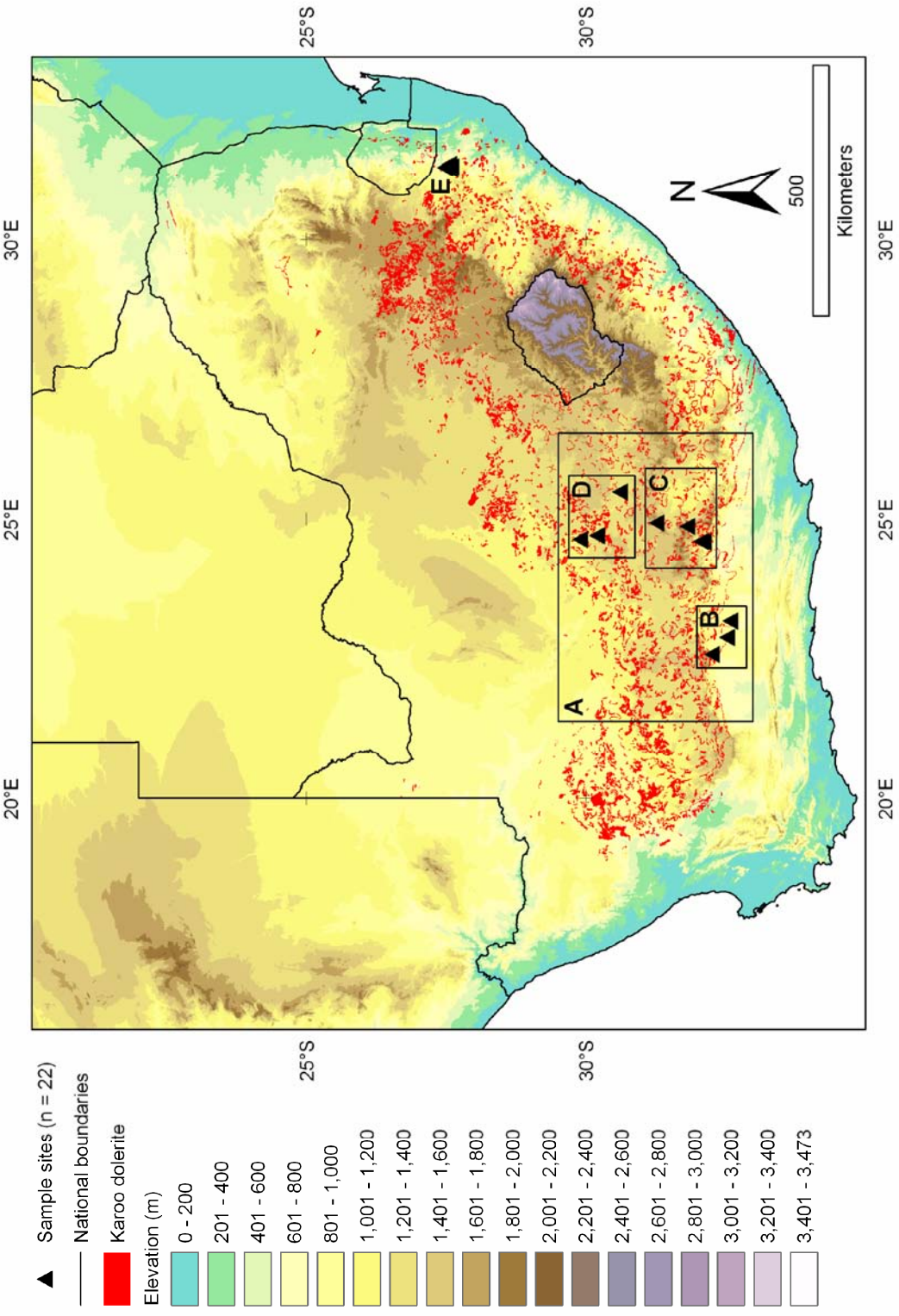

Figure 5.1: The topography of southern Africa according to the SRTM digital elevation model (Jarvis *et al*., 2006), the extent of Karoo dolerite outcrop in South Africa, Lesotho and Swaziland (AEON database) and the locations of sites sampled for cosmogenic nuclide analysis. Sites are shown in more detail in maps A to E in **Figures 5.2**, **5.3** and **5.4**

Sample	Latitude (°)	Longitude(°)	Elevation (m)	Nuclide production scaling factor (Lal, 1991)	Nuclide production scaling factor (Dunai, 2000a)	Surface dip (°)	Surface class	Topographic shielding factor, S
BW3	-32.2552	22.5818	1121	2.06	1.84	90	Vertical	0.460
CB1	-31.2623	24.9396	1632	2.89	2.63	44	Inclined	0.926
DV5	-32.5217	22.8831	855	1.70	1.50	0	Horizontal	1.000
DV6	-32.5216	22.8836	858	1.70	1.51	0	Horizontal	1.000
DV9	-32.5762	23.1796	907	1.77	1.57	10	Sub-horizontal	0.999
GD1	-30.6122	25.4923	1494	2.59	2.33	90	Vertical	0.499
GD2	-30.6128	25.4920	1494	2.59	2.33	10	Sub-horizontal	0.999
GD3	-30.6128	25.4920	1494	2.59	2.33	12	Sub-horizontal	0.999
GR1	-32.1066	24.6029	1176	2.13	1.91	0	Horizontal	0.997
GR2	-32.1065	24.6020	1187	2.15	1.93	0	Horizontal	1.000
GR3	-32.0528	24.6110	1260	2.26	2.03	10	Sub-horizontal	0.999
GR5	-31.8117	24.8762	1647	2.96	2.70	0	Horizontal	0.999
IT1	-27.5579	31.3586	1101	1.84	1.62	0	Horizontal	1.000
IT3	-27.5905	31.3156	1252	2.05	1.81	0	Horizontal	1.000
IT5	-27.4824	31.2918	919	1.60	1.41	4	Sub-horizontal	1.000
IT6	-27.4774	31.2969	876	1.55	1.36	90	Vertical	0.499
IT8	-27.5713	31.2756	1386	2.25	2.00	0	Horizontal	1.000
IT9	-27.5713	31.2756	1386	2.25	2.00	0	Horizontal	1.000
IT10	-27.5705	31.2766	1393	2.26	2.01	0	Horizontal	1.000
OR1	-29.8958	24.6319	1163	2.01	1.79	30	Inclined	0.977
OR2	-29.8963	24.6447	1205	2.07	1.84	0	Horizontal	1.000
OR3	-30.1993	24.7119	1236	2.13	1.90	6	Sub-horizontal	1.000

Table 5.1: Geographic locations and elevations of sample sites, as well as cosmogenic nuclide production rate scaling factors and shielding factors.

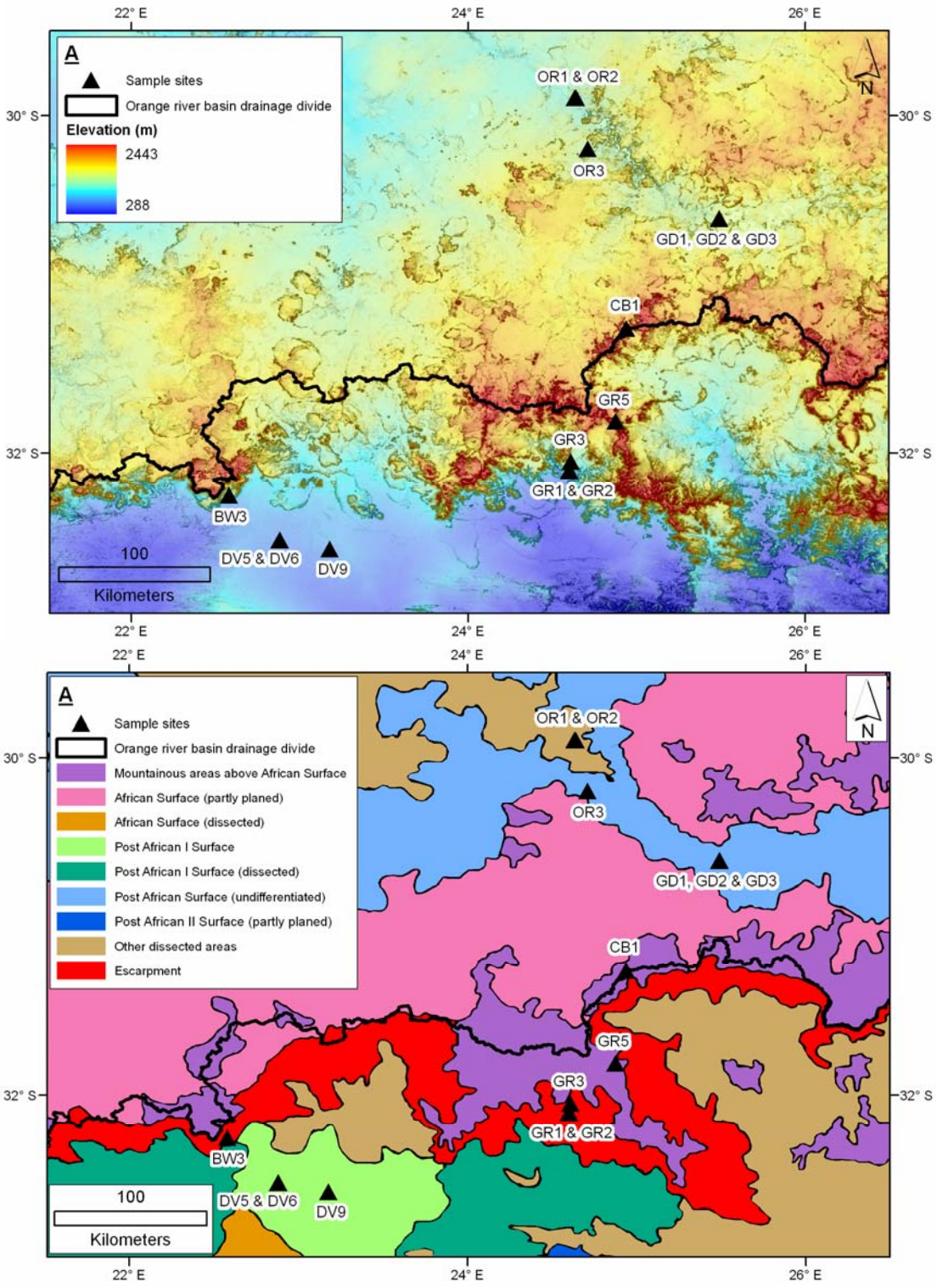

Figure 5.2: Locations of sample sites in box A of **Figure 5.1** relative to relief-shaded elevation (top), and the erosion surfaces of Partridge and Maud (1987) as digitized from the authors' 1:2,500,000 scale map by C. Mielke (bottom). The drainage divide of the northward-draining Orange River basin according to Schulze (2007) is also shown.

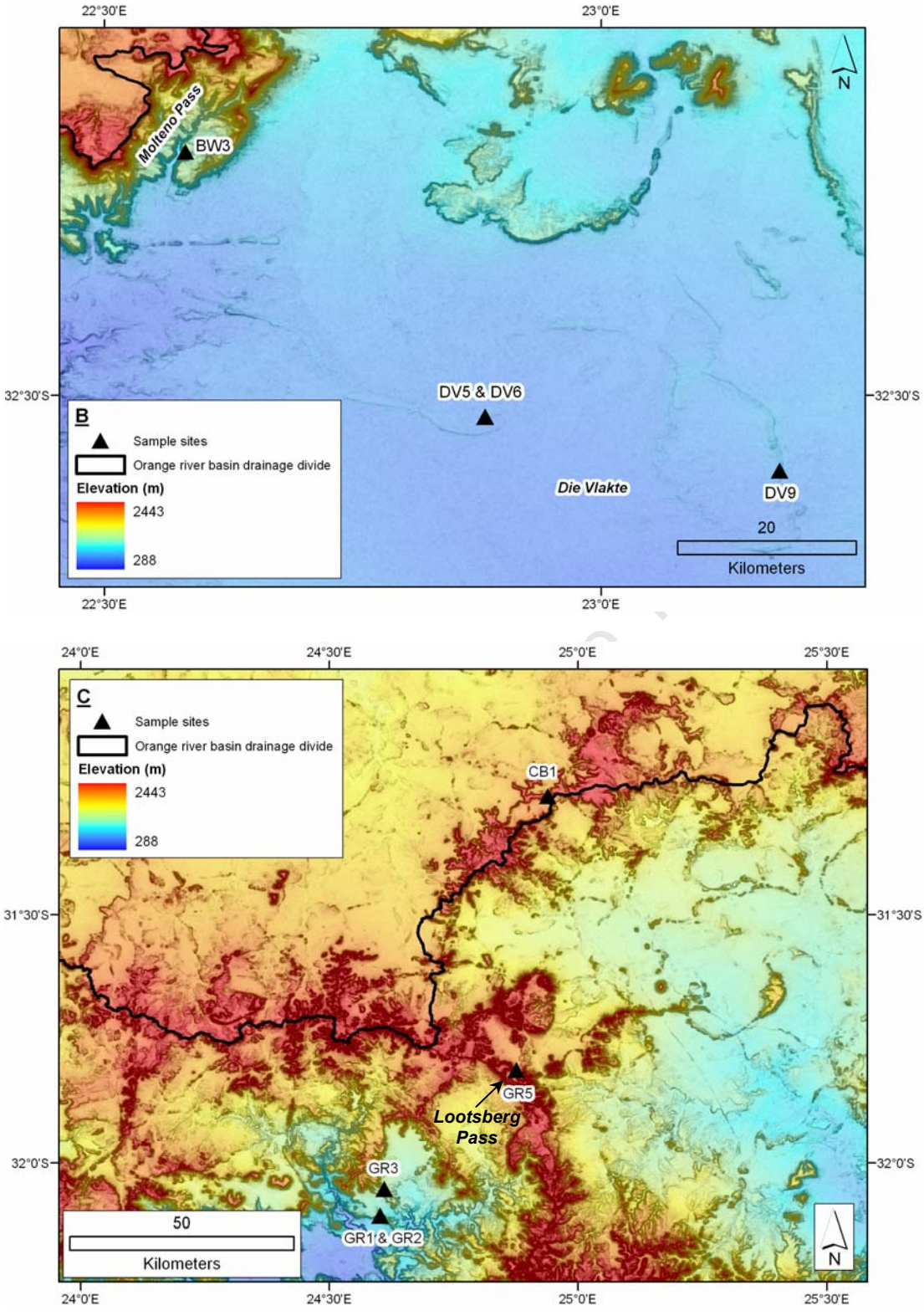

Figure 5.3: *(Continued on following page).*

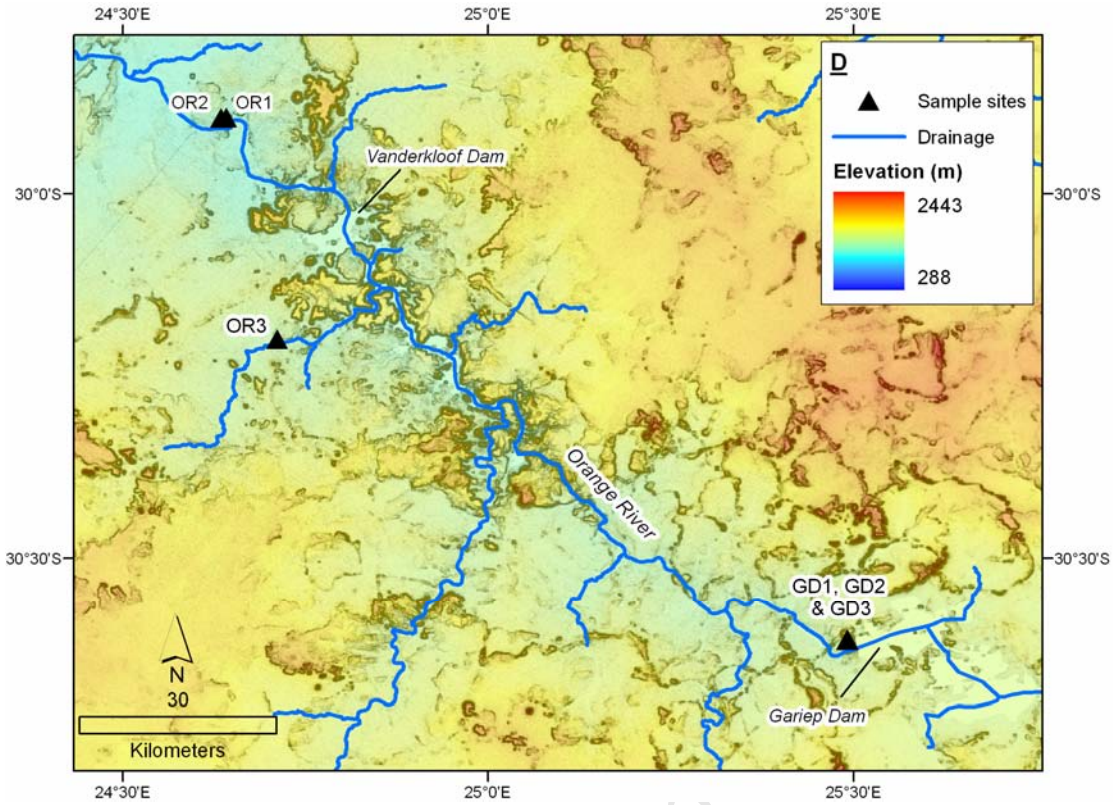

Figure 5.3: *(Continued from previous page):* Locations of sample sites in boxes B, C and D of **Figure 5.1** and in **Figure 5.2** relative to relief-shaded elevation**.** Geographical features mentioned in the text are also shown for reference. The course and tributaries of the Orange River (Strahler stream order ≥ 2; data from the Department of Water Affairs and Forestry: www.dwaf.gov.za) are shown in D.

2) A smaller, eastern region in northeastern Kwazulu-Natal province of South Africa, south of Swaziland and near the deeply incised Pongola River (**Figure 5.4**).

5.3 Regional context

Southern Africa displays a distinct longitudinal climatic gradient, with more arid conditions in the west and more humid conditions in the east. The median January rainfall, median July rainfall and mean annual precipitation for South Africa, Lesotho and Swaziland according to Schulze (2007) is displayed in **Figure 5.5**. Mean January temperature, mean July temperature and mean annual temperature from Schulze (2007) is shown in **Figure 5.6**.

Most of the region is dominated by distinctly seasonal rainfall during the warm austral summer (January), with only the southwestern regions receiving higher winter (July) rainfall. As such, winter rainfall is uniformly low for all dolerite sample sites, but summer rainfall is significantly greater for the more eastern sample sites. If weathering rates depend on both runoff and temperature (e.g. Dessert *et al*., 2003), temporal coincidence of elevated rainfall and elevated temperature for these sample sites suggests that a correlation between rainfall and weathering rates might be expected.

As discussed in Chapter 3, Weinert (1965) derived a dimensionless climatic proxy for dolerite weathering in southern Africa, N:

$$N = 12\frac{E_J}{P_a} \tag{3.9}$$

where P_a is mean annual precipitation and E_J is potential evaporation in the same units in January. When N > 5, physical weathering is taken to be dominant in Karoo dolerites, and when N < 5 chemical weathering is taken to be dominant.

A map of N values for South Africa, Lesotho and Swaziland (**Figure 5.7**) was calculated using the raster calculator in ArcGIS Spatial Analyst, with E_J and P_a values from Schulze (2007). As with mean annual precipitation, N values display a strong longitudinal gradient, with a dominance of physical weathering processes proposed

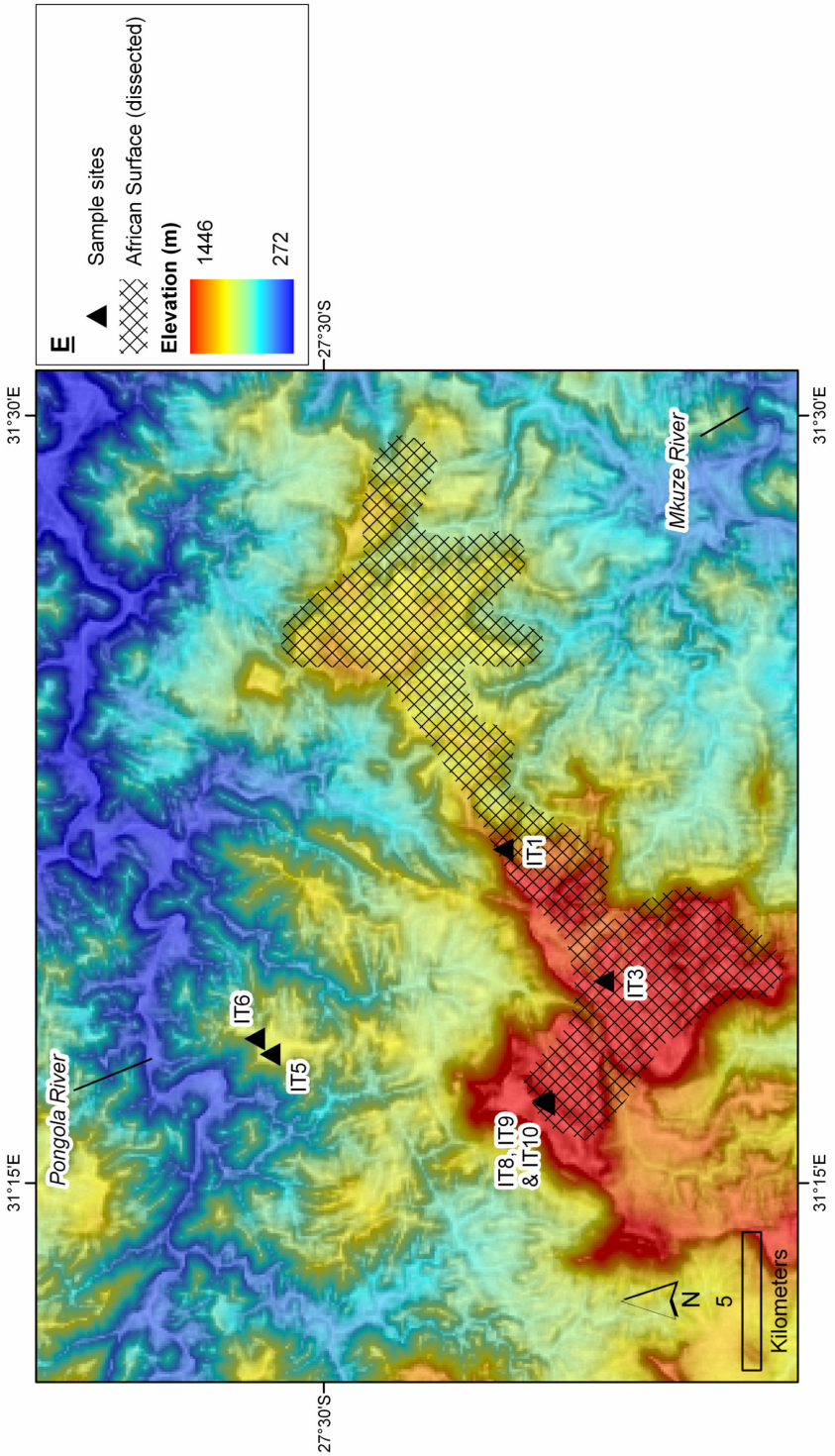

Figure 5.4: Locations of sample sites in area E of **Figure 5.1** relative to relief-shaded elevation. The courses of the Pongola and Mkuze rivers (Strahler stream order ≥ 2) are also given. The approximate extent of Partridge and Maud's (1987) "African Surface (dissected)", according to their 1:2,500,000 erosion surface map, is shown with cross-hatching. These authors classified the remaining area of this figure as a part of "other dissected areas".

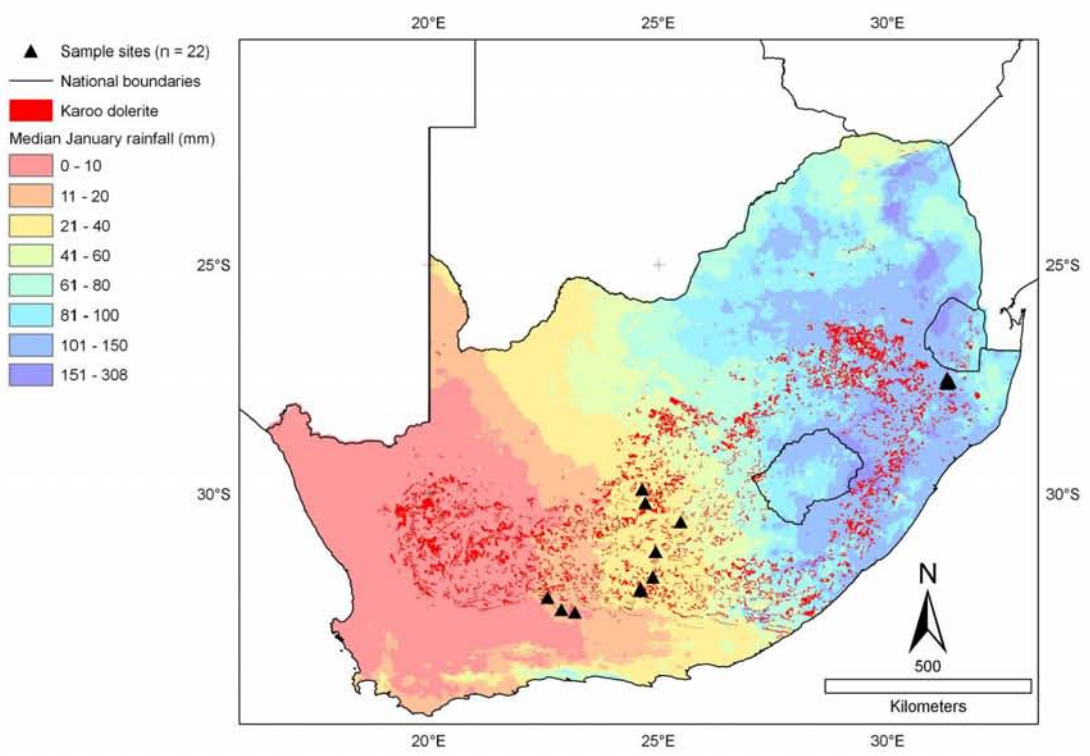

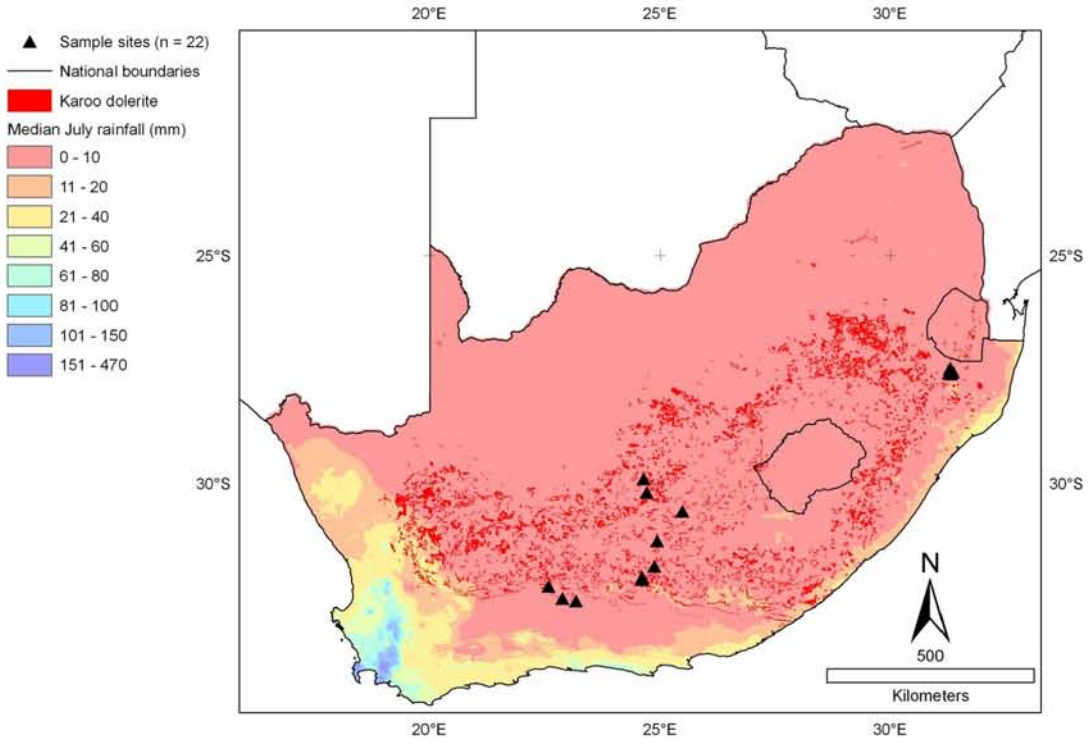

Figure 5.5: *(Continued on following page).*

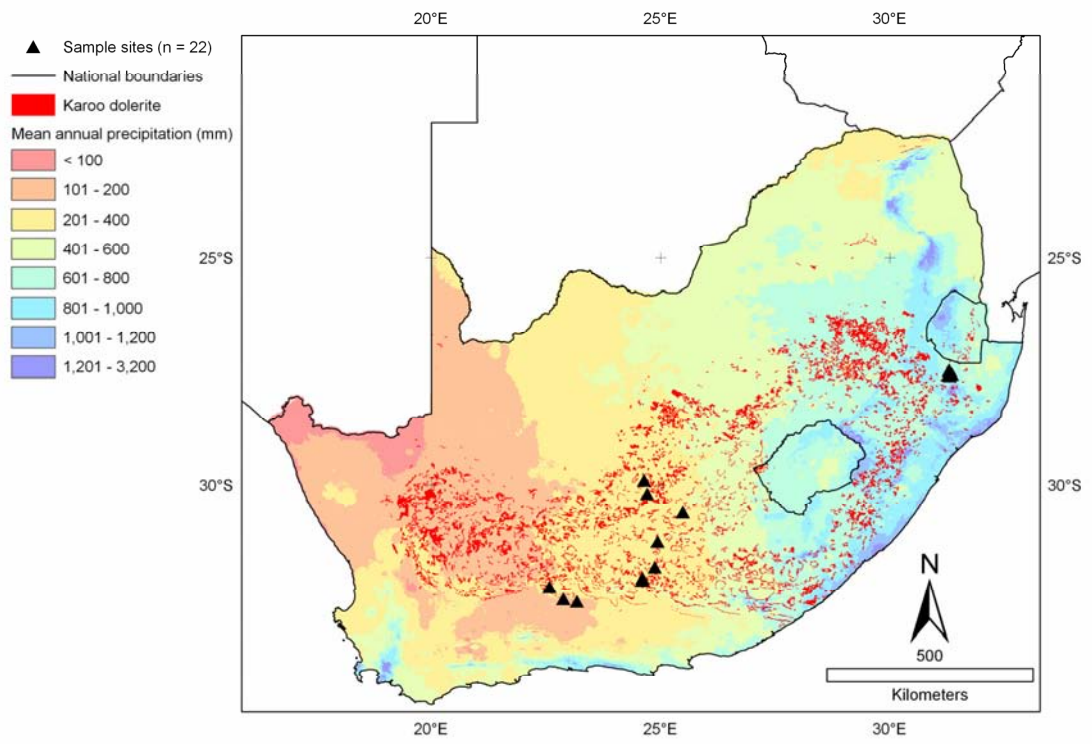

Figure 5.5: *(Continued from previous page):* Locations of sample sites, dolerite outcrop, and median January rainfall (austral summer; previous page, top), median July rainfall (austral winter; previous page, bottom), and mean annual precipitation (above) according to Schulze (2007). Rainfall and precipitation data is interpolated from stations with ≥ 15 years of daily records (Schultz, 2007).

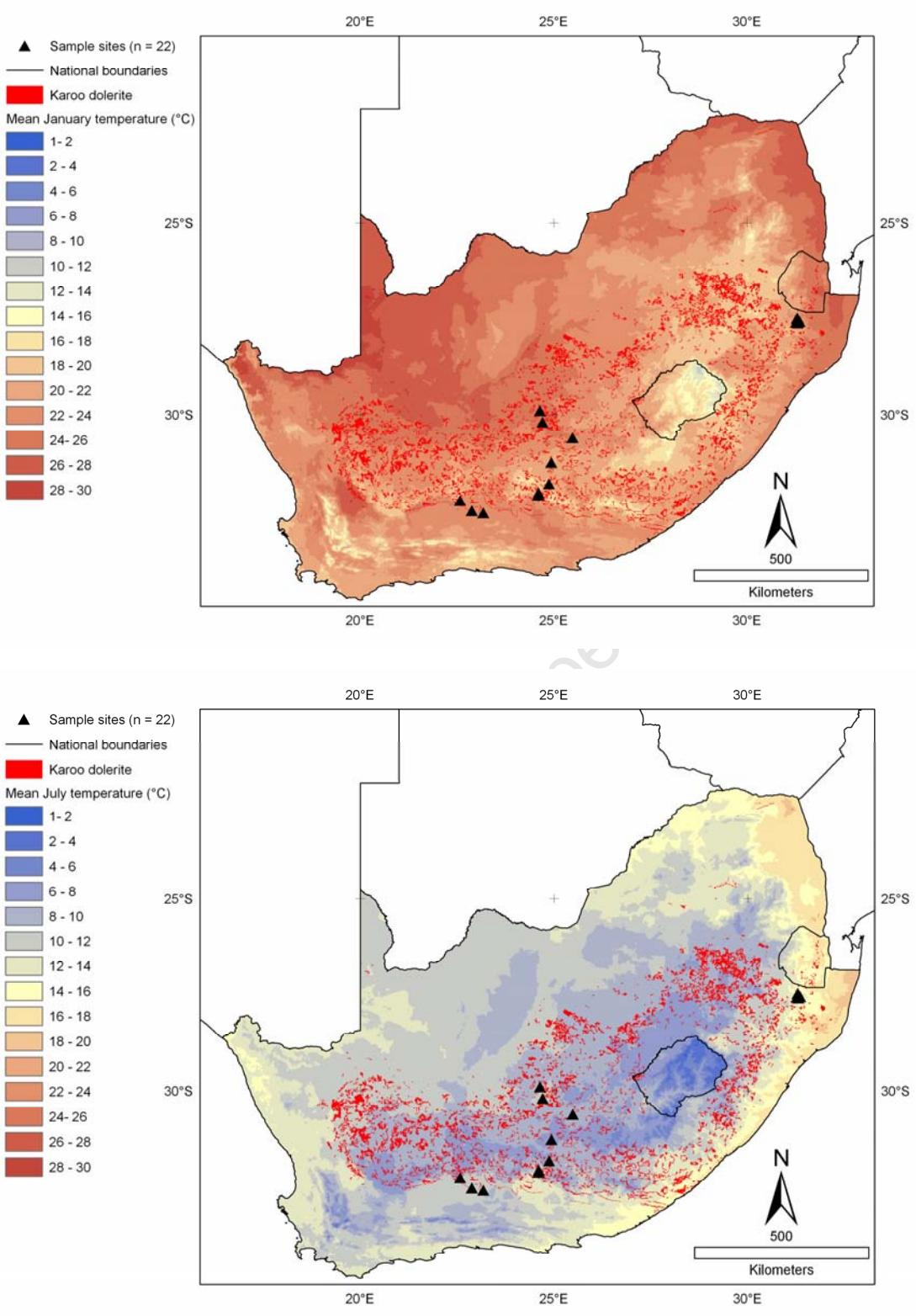

Figure 5.6: *(Continued on following page).*

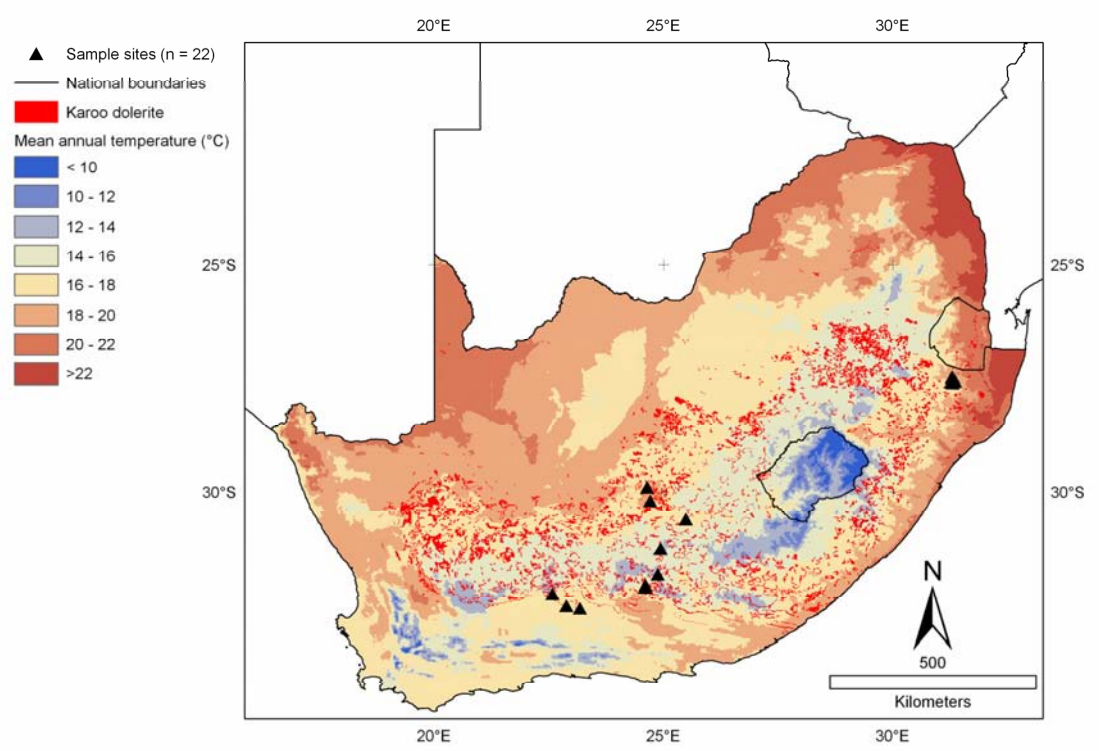

Figure 5.6: *(Continued from previous page):* Locations of sample sites, dolerite outcrop, mean January temperature (austral summer; previous page, top), mean July temperature (austral winter; previous page, bottom) and mean annual temperature (above) according to Schulze (2007). Data is interpolated from stations with daily records ranging from 3 to > 75 years (Schultz, 2007).

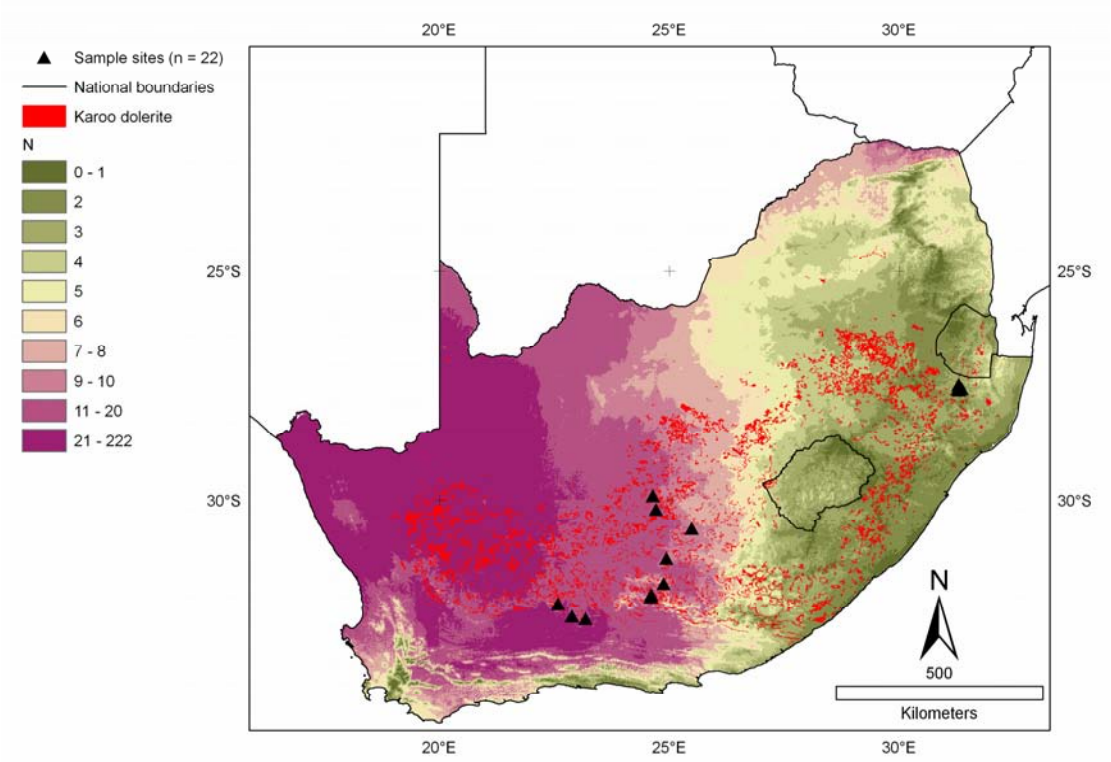

Figure 5.7: Locations of sample sites, dolerite outcrop and Weinert's (1965) dolerite weathering index, $N = 12(E_{Jan}/P)$, where E_{Jan} is potential evaporation in January and P is mean annual precipitation. N is calculated from the E_{Jan} and P values of Schulze (2007).

for the western regions and a dominance of chemical weathering processes proposed for the eastern regions.

The sample sites also correspond to a number of the cyclic erosion surfaces proposed by Partridge and Maud (1987). The positions of the sample sites relative to these surfaces are also shown in **Figure 5.2** and **Figure 5.4**. It should be noted that the map of Partridge and Maud (1987) was produced at a 1:2,500,000 scale, making the exact correlation of sample sites with proposed erosional surfaces potentially ambiguous in topographically complex areas. Mean annual precipitation, mean annual temperature and N values (Weinert, 1965), as well as river catchments and theoretical erosion surfaces (Partridge and Maud, 1987) corresponding to each sample site are given in **Table 5.2**.

5.4 Strategy and bias in sampling

Not only were sample sites limited to Karoo dolerite outcrops, but these outcrops had to be suitable for cosmogenic nuclide analysis. Horizontal surfaces were selected if they were the highest points locally, in order to minimize the chances of a complex exposure history (i.e. intermittent sediment cover). Similarly, vertical surfaces were selected that did not appear to have been influenced by human activities (e.g. road construction). Care was also taken not to sample rocks that may have experienced an influx of cosmic-ray neutrons from more than one surface (e.g. small boulders and the crests of cliffs) or samples that may have experienced movement during their exposure history.

Only dolerite outcrops that appeared to be fresh enough to potentially yield unweathered dolerites with pristine pyroxenes suitable for cosmogenic noble gas analysis were selected. As such, sampling was biased towards less weathered dolerite outcrops. It was noted during fieldwork that suitably fresh outcrop was more frequently observed in the drier western regions than in the more humid eastern regions. Some samples collected in the field were later rejected during sample preparation as they did not yield sufficient fresh pyroxene.

Lastly, most samples were collected near major roads and where landowners permitted access to their land.

Sample	Mean annual precipitation (mm)*	Mean annual temperature (°C)*	Weinert's (1965) dolerite weathering index, N**	River catchment	Theoretical erosion surface*** Name	Inception age
BW3	280	15.8	14	Gouritz	Escarpment	
CB1	334	17.0	11	Orange	Mountainous area above African	
DV5	188	14.4	21	Groot	Post-African 1	Early Miocene
DV6	188	17.4	21	Groot	Post-African 1	Early Miocene
DV9	195	17.4	21	Groot	Post-African 1	Early Miocene
GD1	354	17.0	10	Orange	Post-African (undifferentiated)	Early Miocene-Pliocene
GD2	354	16.4	10	Orange	Post-African (undifferentiated)	Early Miocene-Pliocene
GD3	354	13.1	10	Orange	Post-African (undifferentiated)	Early Miocene-Pliocene
GR1	314	17.3	12	Sundays	Escarpment	
GR2	314	17.1	12	Sundays	Escarpment	
GR3	324	17.1	11	Sundays	Escarpment	
GR5	353	17.1	10	Great Fish	Mountainous area above African	
IT1	722	18.5	3	Pongola	African (dissected, original on interfluves)	Early Cretaceous
IT3	746	18.5	2	Pongola	African (dissected, original on interfluves)	Early Cretaceous
IT5	791	16.5	3	Pongola	Other dissected areas	Various
IT6	791	16.5	3	Pongola	Other dissected areas	Various
IT8	1025	18.0	2	Pongola	African (dissected, original on interfluves)	Early Cretaceous
IT9	1025	18.0	2	Pongola	African (dissected, original on interfluves)	Early Cretaceous
IT10	1025	18.3	2	Pongola	African (dissected, original on interfluves)	Early Cretaceous
OR1	305	18.0	13	Orange	Other dissected areas	Various
OR2	322	16.5	12	Orange	Other dissected areas	Various
OR3	328	16.4	12	Orange	Post-African (undifferentiated)	Early Miocene-Pliocene

*From Schulze (2007)
**Calculated from data in Schulze (2007)
***According to Partridge and Maud (1987)

Table 5.2: Mean annual precipitation, mean annual temperature and Weinert's (1965) N values, as well as river catchments and theoretical erosion surfaces (Partridge and Maud, 1987), corresponding to Karoo dolerite sample sites.

5.5 Field observations

A brief description of each sample site follows, with accompanying field photographs of the sample sites. Sample sites are listed from west to east along the southern escarpment zone, from south to north from the escarpment towards the Orange River, and in order of ascending elevation for samples from the Pongola River region. The position of the samples relative to major drainage and the erosional surface map proposed by Partridge and Maud (1987) is also discussed.

BW3:

Sampled from the vertical exfoliating scarp face of a dolerite sill on the eastern side of Molteno Pass, east of the town of Beaufort West, within the escarpment zone at 1121m above sea level (**Figure 5.8**). The summit of the escarpment in this region was sampled for cosmogenic nuclide analysis by Kounov *et al*. (2007).

DV5; DV6; DV9:

Samples DV5, DV6 and DV9 were taken from the horizontal surfaces of dolerite sills outcropping in the low relief region *Die Vlakte* between Beaufort-West and Graaff-Reinet, at elevations of 855m, 858m and 905m above sea level, respectively (**Figure 5.9, Figure 5.10** and **Figure 5.11**). This region is bound in the north by the southern escarpment and in the south by the mountains of the Cape Fold Belt, and has been classified as part of the Miocene Post-African I surface by Partridge and Maud (1987). Dolerite outcrops form slight local topographic highs. A thin (millimetres to centimetres) calcrete coating is formed in places on the dolerite surface sampled by DV6.

GR1; GR2:

Samples collected from a dolerite ridge north of Graaff-Reinet at elevations of 1176 and 1187 m, respectively (**Figure 5.12**). The surface of the ridge comprises boulders that are in various stages of exfoliation. Sample GR1 is from a rock layer that has recently separated from the underlying material, whereas GR2 is from a rock surface that appears to have lost material more recently. This region has been classified as part of the escarpment zone by Partridge and Maud (1987), but lies within the Sundays River catchment, and approximately 50 km to the south of the main drainage divide with the Orange River basin.

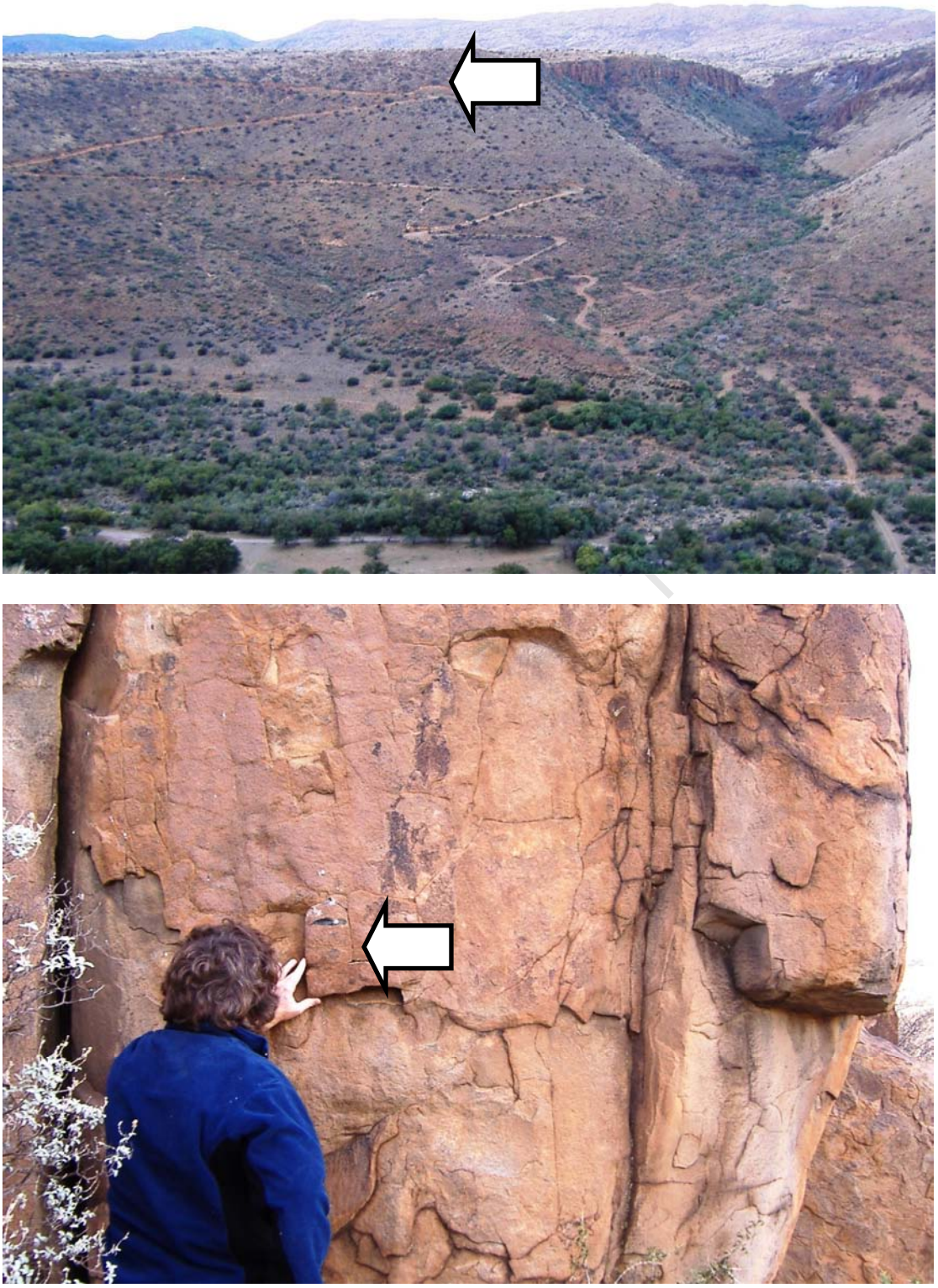

Figure 5.8: Top: BW3 sample site (arrow) on scarp face of dolerite sill, viewed from Molteno Pass, looking east. Bottom: Close-up view of sample BW3, viewed towards the south. Sample is being held back in place after removal from the exfoliating dolerite face.

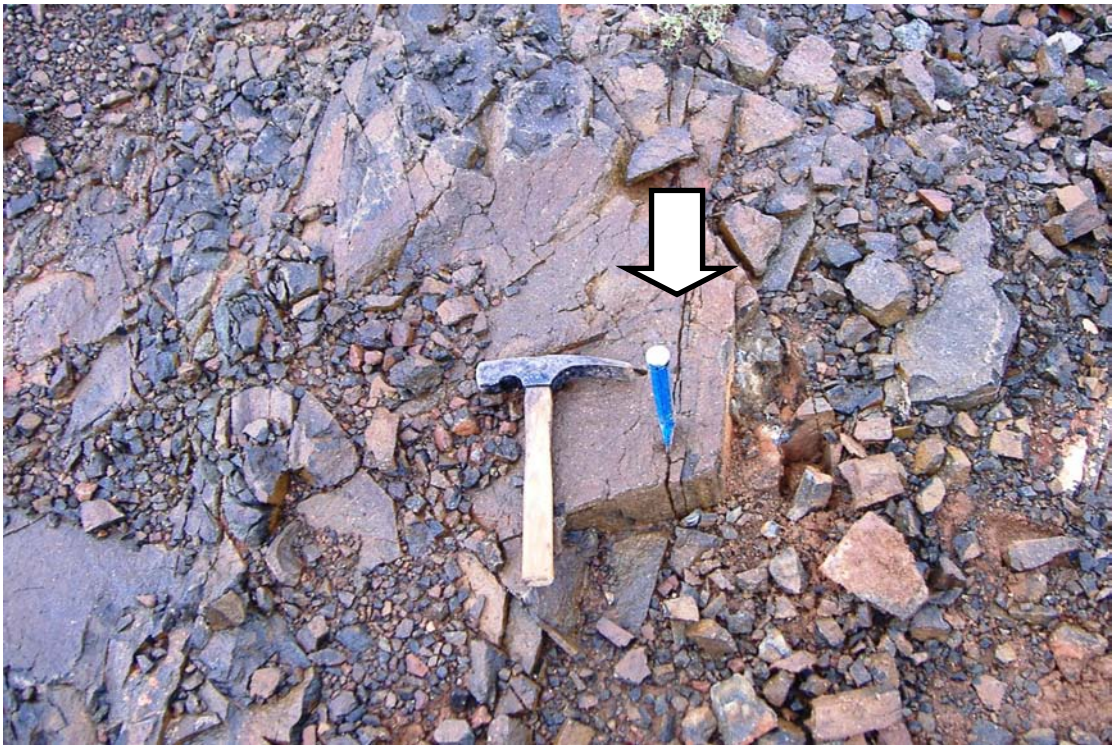

Figure 5.9: Sample DV5 from the low relief region, *Die Vlakte*, south of the escarpment zone between Beaufort West and Graaff Reinet.

Figure 5.10: Sample DV6, viewed to the north, with the escarpment zone on the horizon. A thin, white calcrete coating on the dolerite is observable in the right foreground.

Figure 5.11: Sample DV9 viewed towards the south. The dolerite sill from which the sample is collected forms a slight local topographic high on the low relief plain. The mountains of the Cape Fold Belt are faintly visible on the horizon.

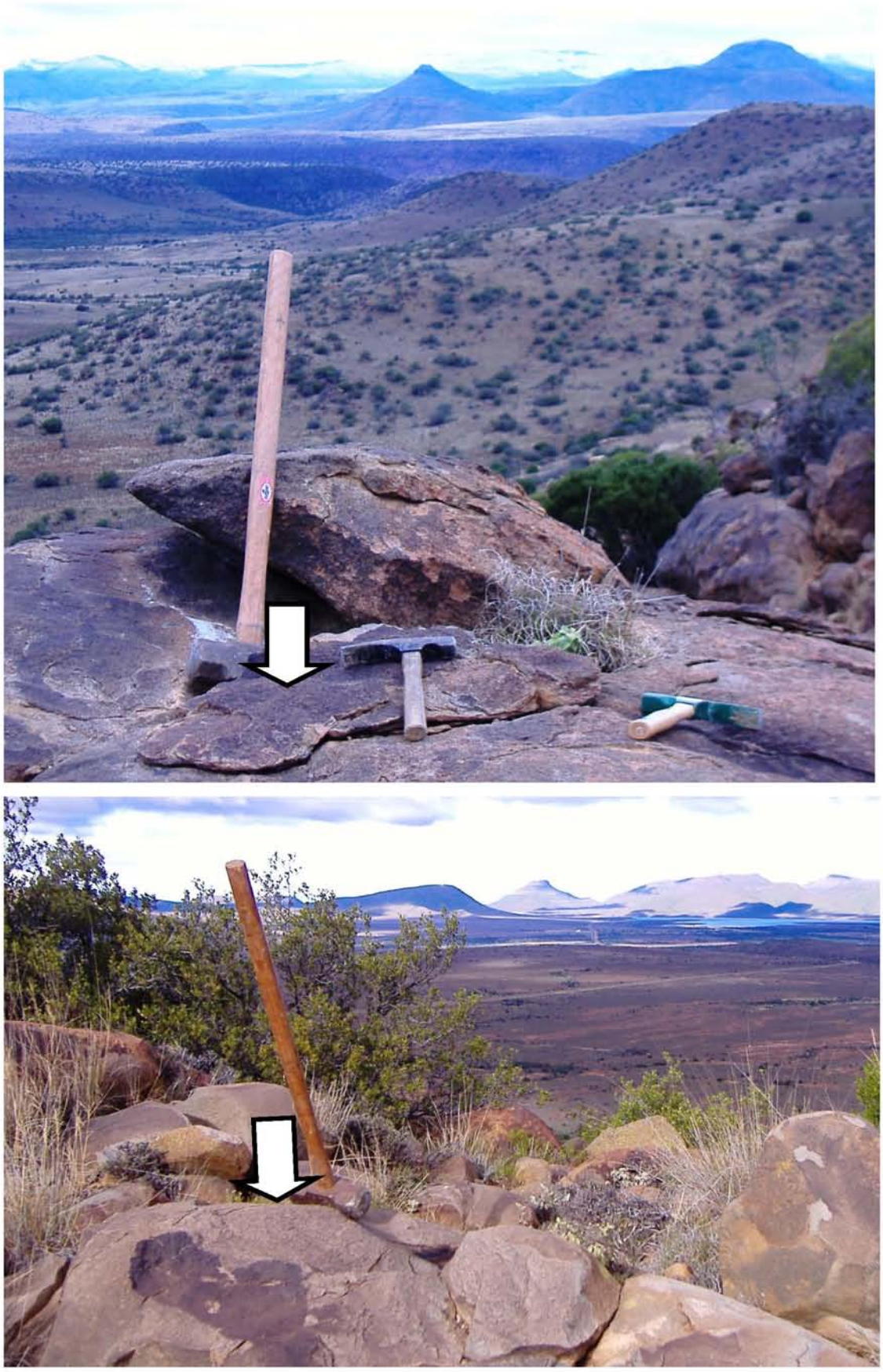

Figure 5.12: Samples GR1 (top) viewed towards the east and GR2 (bottom) viewed towards the south from a dolerite ridge north of Graaff-Reinet.

GR3:

Horizontal surface sample from a dolerite sill at 1260 m above sea level, outcropping on the edge of a plain within the escarpment zone outcrop north of Graaff-Reinet (**Figure 5.13**).

GR5:

Horizontal surface sample from a dolerite sill at the top of Lootsberg Pass, at an elevation of 1647 m above sea level (**Figure 5.14**). Although at a high elevation, and classified as "above the African surface" by Partridge and Maud (1987), the site lies to the south of the Orange River drainage basin, and is situated on the northeastern side of the high elevation drainage divide between two southward-draining rivers: the Sundays River catchment to the west and the Great Fish River catchment to the east.

CB1:

At an elevation of 1632 m above sea level, this sample is from an inclined surface with a 44º dip to the north, on the north side of the Orange River drainage divide (i.e. within the Orange River drainage basin) and in an area "above the African surface" according to Partridge and Maud (1987) (**Figure 5.15**).

GD1; GD2; GD3:

Samples from a flat-topped hill or *koppie* overlooking Gariep Dam on the Orange River (**Figure 5.16**). The flat summit of the *koppie* (1494 m above sea level) is formed by a dolerite sill caprock overlying Karoo sedimentary rocks of the Beaufort Group. Sample GD1 is taken from the vertical cliff face of the dolerite (**Figure 5.17**), whereas samples GD2 and GD3 are situated on the summit, a few metres adjacent to each other (**Figure 5.17** and **Figure 5.18**).

OR3:

Sample from the top surface of a dolerite inselberg/tor comprising a pile of *in situ* dolerite corestones, near a tributary of the Orange River between Colesberg and Vanderkloof Dam (**Figure 5.19**). Sample site elevation is at 1236 m above sea level.

Figure 5.13: Sample site GR3 from a dolerite sill north of Graaf-Reinet, viewed towards the north.

Figure 5.14: Sample site GR5 from a dolerite outcrop at the top of Lootsberg Pass.

Figure 5.15: Sample site CB1 from an inclined exfoliating scarp face south of Colesburg.

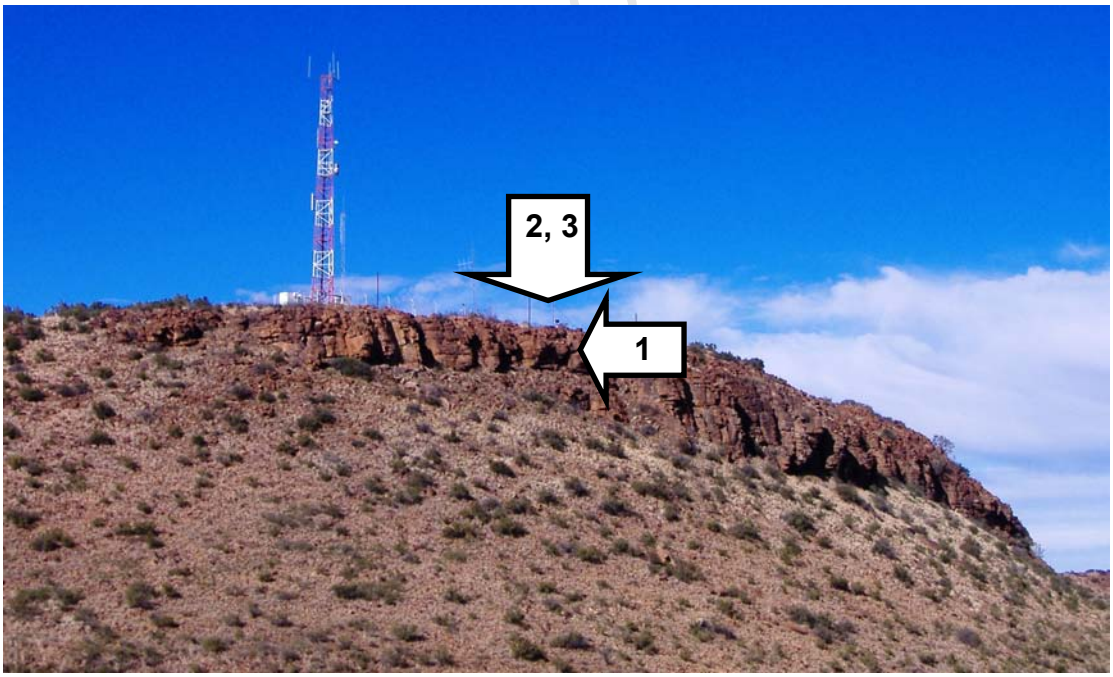

Figure 5.16: Sample sites GD1 (arrow 1), GD2 and GD3 (arrow 2,3), from a dolerite sill forming the resistant caprock to a flat-topped hill, or *koppie*, overlooking Gariep Dam on the Orange River. Photograph viewed towards the south.

Figure 5.17: Samples GD1 (arrow 1, above) and GD2 (arrow 2, below, with Gariep Dam in the background), both viewed towards the south.

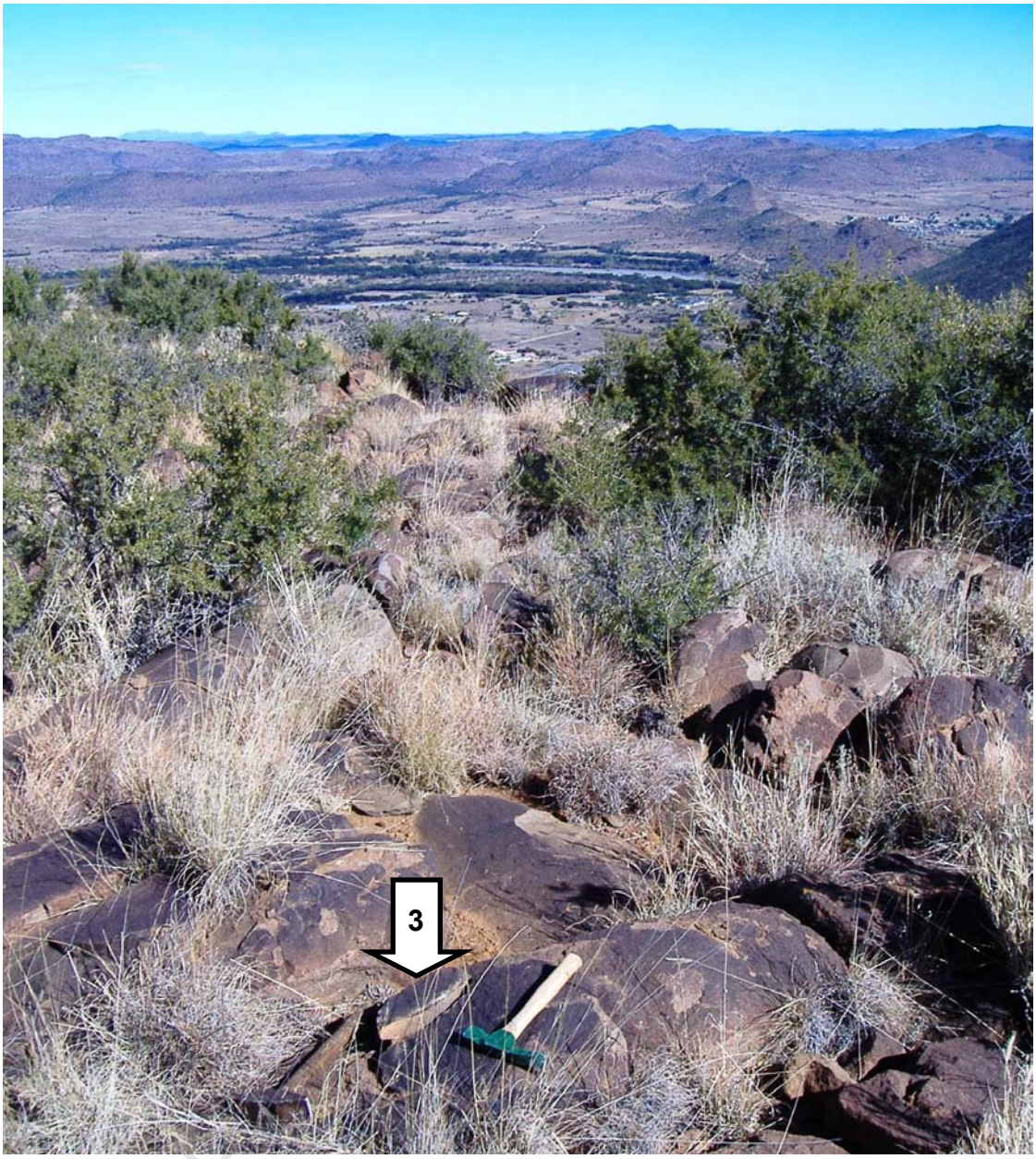

Figure 5.18: Sample GD3 (arrow 3) viewed to the west, a few metres adjacent to sample GD2, with the Orange River in the background.

Figure 5.19: Sample OR3 from the top corestone of a dolerite inselberg or tor between Colesberg and Vanderkloof Dam. Photograph viewed to the east.

Figure 5.20: Sample OR1 from an inclined dolerite hillslope near Vanderkloof Dam on the Orange River. Photograph viewed to the west.

OR1; OR2:

Samples from an inclined dolerite hillslope (OR1; **Figure 5.20**; 1163 m) and the summit of a dolerite hill (OR2; **Figure 5.21**; 1205 m) overlooking the Orange River, north (downstream) of Vanderkloof Dam. A quarry in the side of the hill sampled by OR2 is shown in **Figure 5.22,** and reveals orthogonal joints within unweathered dolerite, as well as unweathered dolerite corestones surrounded by saprolite. This suggests that corestones form through weathering along joints, and that tors of corestones, such as that sampled by OR3, may form though the subsequent erosion of the saprolitic matrix.

IT6:

Sample from a vertical cliff face at 876 m above sea level, overlooking the incised meanders of the Pongola River, in Ithala Game Reserve, north-east KwaZulu Natal (**Figure 5.23**). The dolerite intrudes between the base of the Karoo Supergroup sandstones and shales (Vryheid Formation) and the underlying Archean metasedimentary basement of Pongola Group. The accordant summit heights surrounding the Pongola River appear to coincide with the sub-Karoo basal unconformity, i.e. these summits constitute erosional remnants of an exhumed Palaeozoic planation surface. This area has been described as a "dissected" region by Partridge and Maud (1987), who propose that the incised meandering drainage patterns of rivers within the region constitute superimposed drainage from the "African" cycle of erosion initiated in the early Cretaceous.

IT5:

Sample from the horizontal surface of the same dolerite sill sampled by IT6, at 919 m elevation (**Figure 5.24**).

IT1:

Sample from a dolerite sill intruded higher in the Karoo stratigraphy at 1101 m above sea level (**Figure 5.25**). This site and those that follow lie within an area described as part of the "dissected African surface" by Partridge and Maud (1987), with original African surface remnants preserved on interfluves.

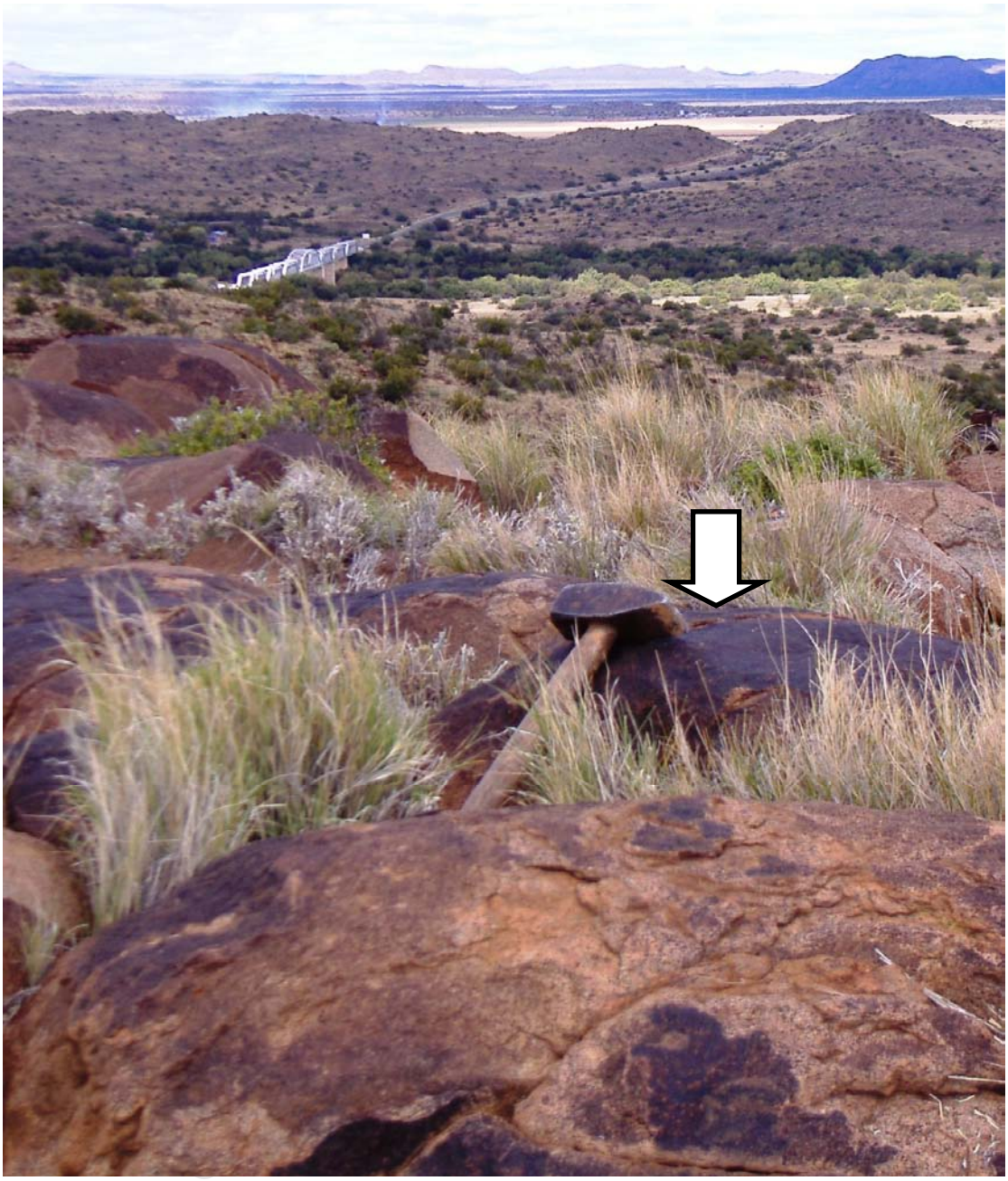

Figure 5.21: Sample OR2 from the summit of a *koppie* overlooking the Orange River near Vanderkloof Dam. Photograph viewed to the west, with a bridge crossing the Orange River in the background.

Figure 5.22: Stone quarry from the side of the koppie from which OR2 is sampled, displaying unweathered dolerite corestones within a weathered saprolite. The upper rock face (background) displays orthogonal joints within the dolerite. In the foreground, subsurface weathering along the joints of the dolerite has resulted in the development of fresh corestones surrounded by saprolite.

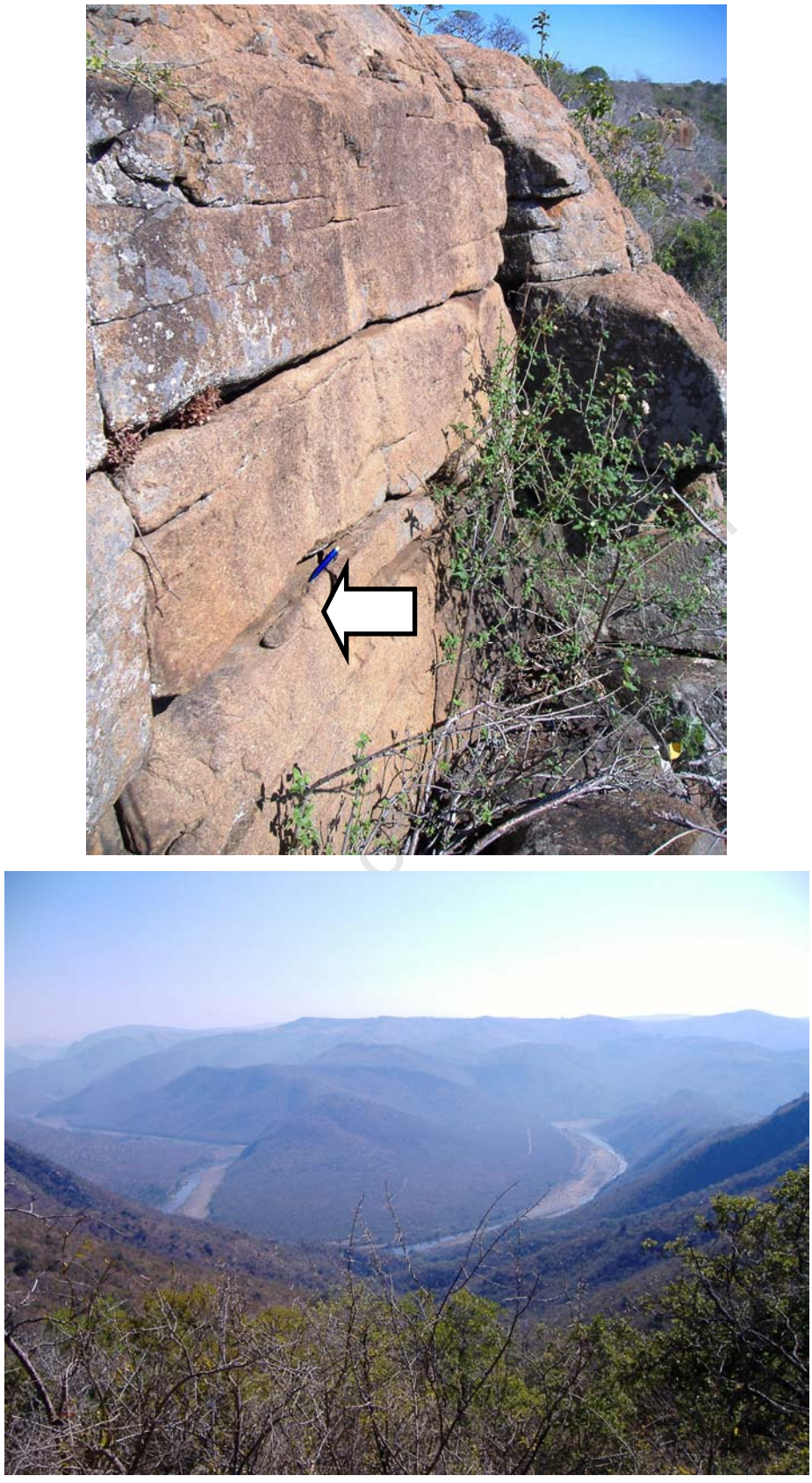

Figure 5.23: Sample IT6 from a dolerite sill (top, viewed to the southwest), overlooking the incised meanders of the Pongola River (bottom, viewed to the northwest).

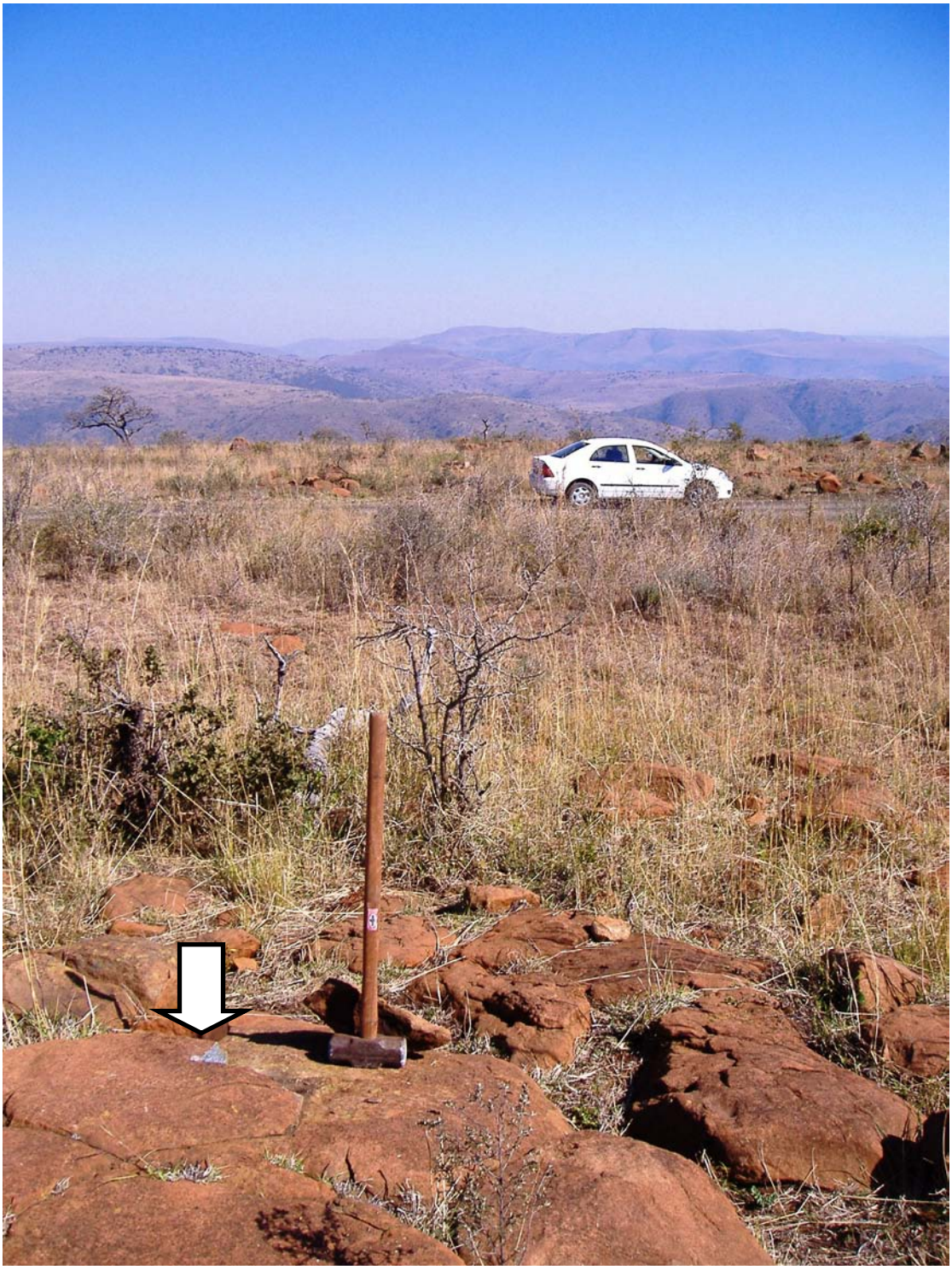

Figure 5.24: Sample IT5 from a dolerite sill at the base of the Karoo sedimentary sequence, viewed to the west. Valley of a Pongola River tributary in the background.

Figure 5.25: Sample IT1, viewed towards the northwest.

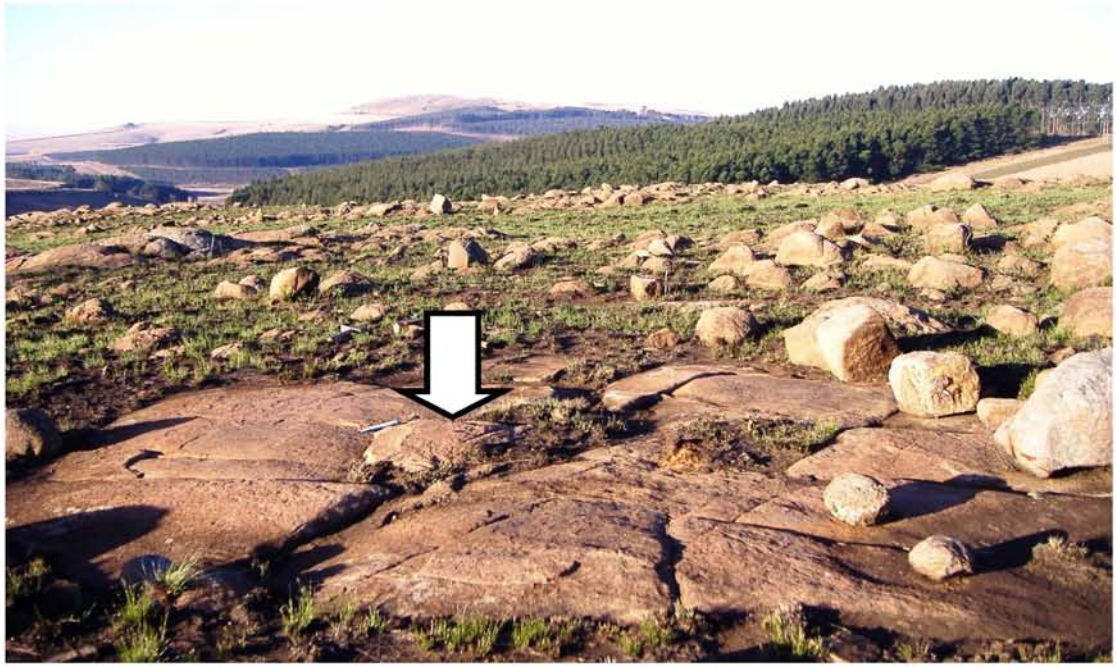

Figure 5.26: Sample IT3, from an exposed dolerite pavement littered with dolerite boulders.

IT3:

Sample from the horizontal surface of an extensive, jointed dolerite pavement at 1252 m elevation (**Figure 5.26**). Boulders of dolerite lie scattered across the undulating surface.

IT8; IT9:

Adjacent samples from the horizontal surface, an exfoliating dolerite pavement at 1386 m elevation (**Figure 5.27**), at the top of a flat-topped and steep-sided hill between the Pongola and Mkuze river catchments.

IT10:

Upper surface of a dolerite boulder near the IT8 and IT9 sites, at the summit of the hill south of the Pongola river (1393 m, **Figure 5.28**). The steep scarps surrounding this hill are formed by Karoo sandstones, and the summit of the hill is capped with dolerite.

5.6 Petrography

A brief pretrographic description of each rock sample is summarized in **Table 5.3**, based on optical microscopy. Each sample's mineralogy reflects the presence of primary igneous phases, hydrothermal alteration phases and weathering products. Two predominant igneous textures were observed:

1) Ophitic textures characterised by clinopyroxene phenocrysts encapsulating plagioclase laths (**Figure 5.29**), and
2) Cumulates characterised by euhderal plagioclase phenocrysts with interstitial anhedral pyroxene (**Figure 5.30**).

The major primary phases for all samples were plagioclase feldspar and pyroxene, with accessory opaque phases. In addition, olivine and interstitial alkali feldspar were often present in minor amounts.

When present, olivine displayed varying degrees of alteration to "iddingsite", a red-brown mixture of smectite, chlorite and goethite/hematite, or "bowlingite", a green mixture of smectite, chlorite and serpentine with minor talc, mica and quartz (Deer *et al.*, 1992; **Figure 5.31**). Pyroxenes were commonly altered to amphiboles, and

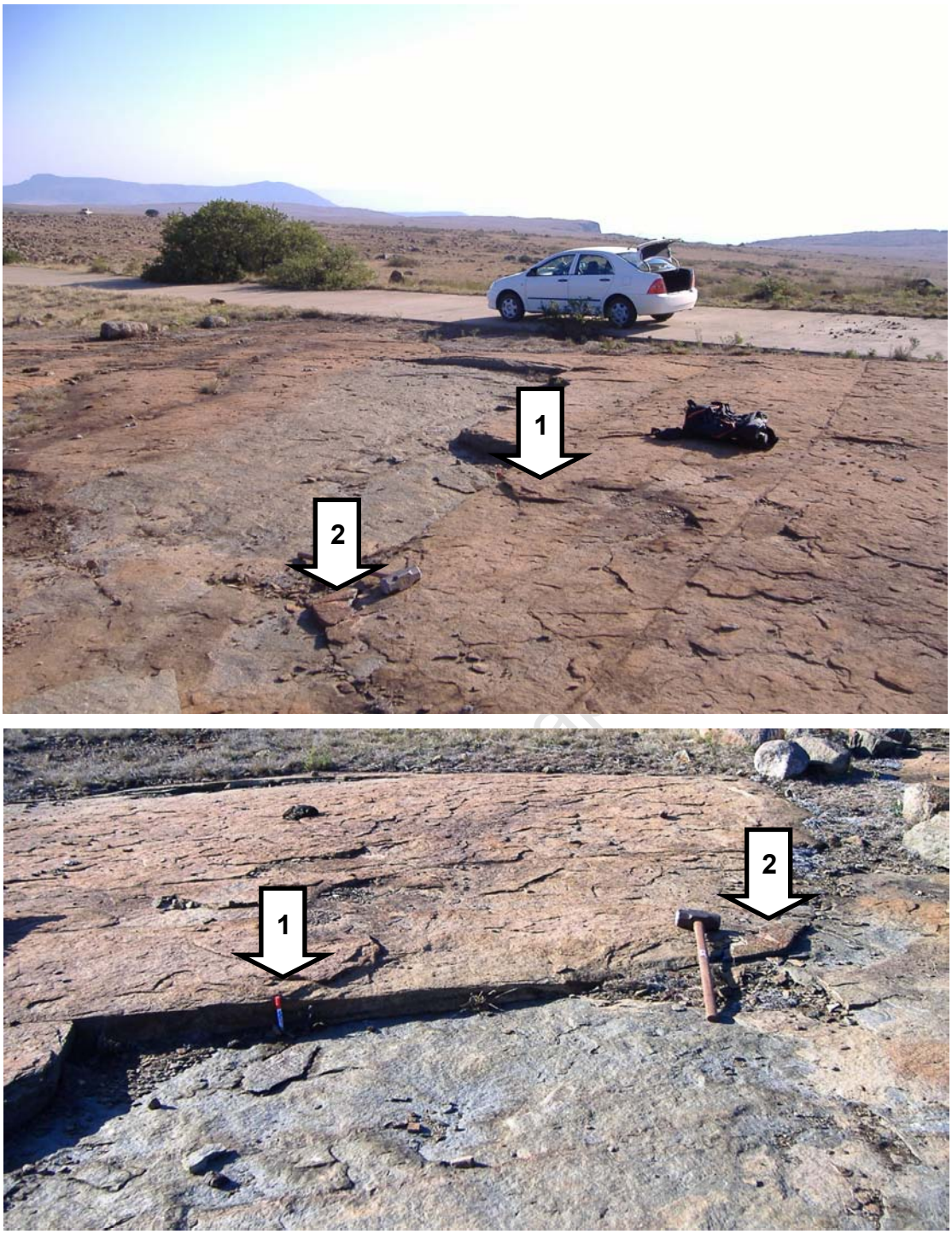

Figure 5.27: Samples IT8 (arrow 1) and IT9 (arrow 2) from an exfoliating dolerite pavement, viewed towards the southwest (top) and the north (below).

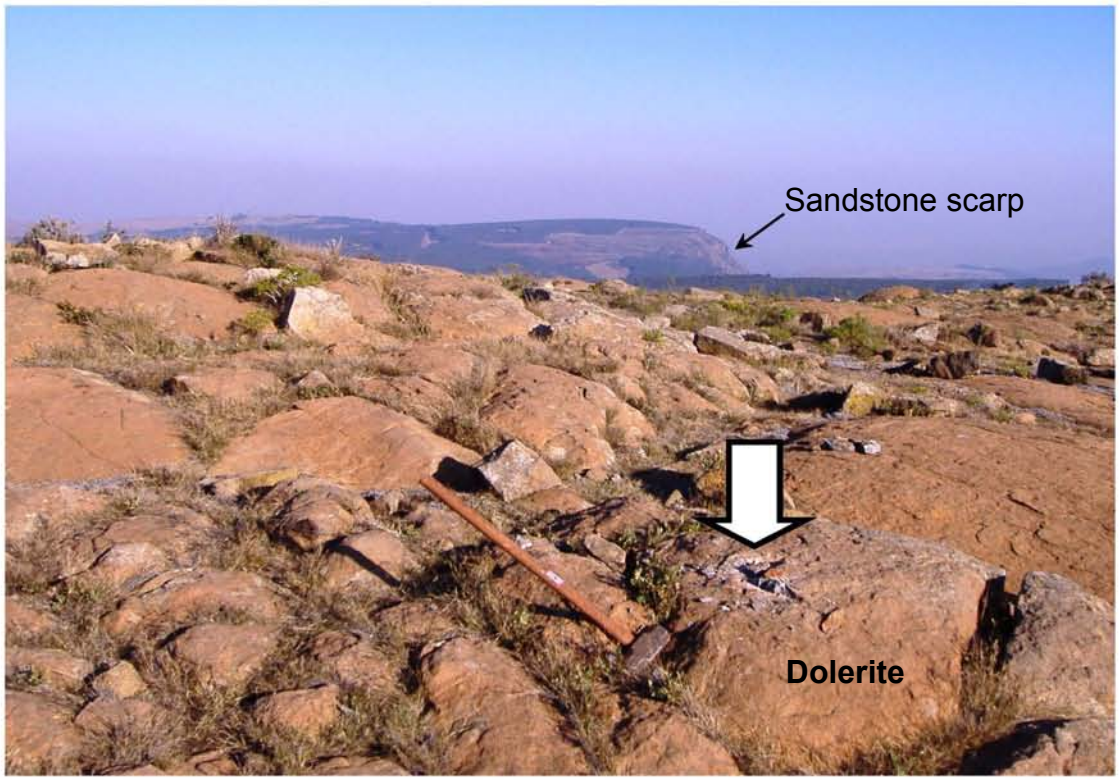

Figure 5.28: Sample IT10 viewed towards the south.

Sample	Plagioclase	Pyroxene	Olivine	Alkali feldspar	Amphibole	Biotite	White mica	Chlorite	"Iddingsite-Bowlingite"	Clays	opaques	Serpentine	Texture	Plagioclase grain size (mm)	Pyroxene grain size (mm)
BW3	30	50	psdm		10	a	10	a	a	a	a		op	0.3 - 0.75	0.5 - 3
CB1	60	30			a	10	a	a	a	a	a		pc	0.3 - 3	0.5 - 1.5
DV5	50	40		a	10	a	a			a	a		pc	0.15 - 6	0.1 - 1
DV6	50	40		a	10	a	a			a	a		pc	0.15 - 2	0.1 - 1
DV9	50	40		a	10	a	a			a	a		pc	0.1 - 2	0.1 - 0.75
GD1	50	50	a			a	a		a	a	a	a	op	0.1 - 0.5	0.15 - 4
GD2	50	50	a			a			a	a	a	a	op	0.1 - 0.75	0.15 - 4
GD3	50	50	a			a			a	a	a	a	op	0.1 - 1.5	0.15 - 3
GR1	50	50	a		a	a				a	a		op	0.3 - 1.5	0.5 - 4
GR2	50	50	a		a	a				a	a		op	0.3 - 1.5	0.5 - 3
GR3	60	30		a	10	a	a	a		a	a		pc	0.15 - 2	0.1 - 2
GR5	40	60	a		a	a	a	a	a	a	a		op	0.1 - 0.5	0.1 - 3
IT1	50	40	a	a	a	10	a	a	a	a	a		pc	0.1 - 5	0.1 - 1
IT3	40	40		a	a	a	a	a		10	a		pc	0.1 - 4	0.15 - 1.5
IT5	50	40		a	a	a	a			10	a		pc	0.15 - 4	0.1 - 2
IT6	50	40		a	a	a	10	a		10	a		pc	0.2 - 3	0.1 - 1
IT8	50	40		a	a	a	a	a		10	a		pc	1.5 - 3	0.1 - 2
IT9	50	50		a	a	a	a	a		a	a		pc	0.1 - 3	0.1 - 1
IT10	50	40		a	a	a	a			10	a		pc	0.1 - 4	0.1 - 1.5
OR1	50	40	a	a	10	a	a	a	a	a	a		pc	0.15 - 1.6	0.2 - 2
OR2	50	40	a	a	10	a	a	a	a	a	a		pc	0.2 - 1.5	0.2 - 2
OR3	50	50	a		a	a	a	a	a	a	a		op	0.1 - 0.7	0.75 - 3

Table 5.3: Petrographic summary of the samples analysed for cosmogenic noble gases, with estimated mineral concentration given as percentages. Abbreviations are as follows: psdm = pseudomorph, a = accessory, op = ophitic pyroxene, pc = plagioclase cumulate. Modal percentages are estimated from thin section. Accessory phases are defined as those that consititute less than 10 % of the rock volume.

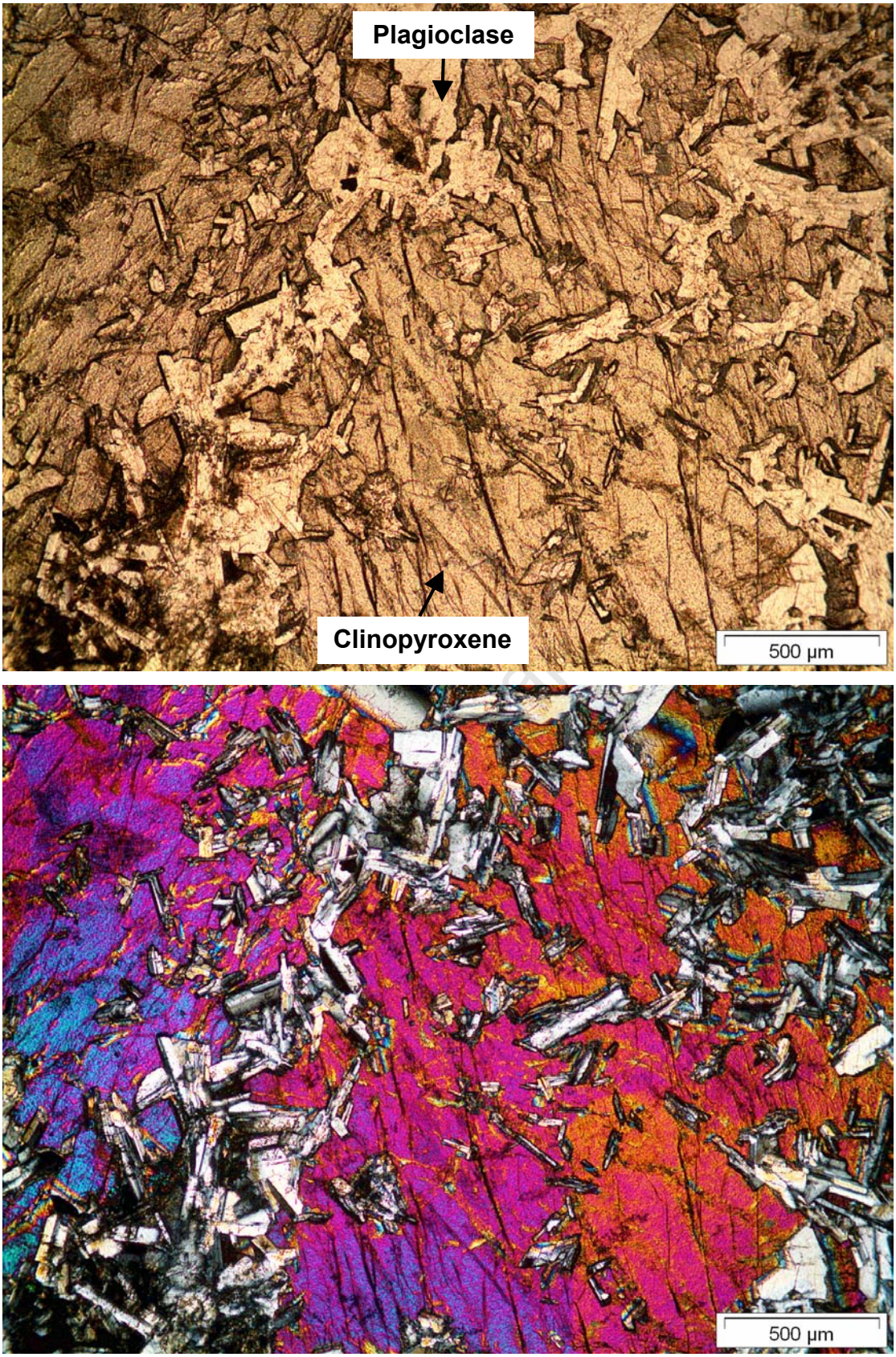

Figure 5.29: Photomicrographs of sample GR5 in plane-polarised light (PPL, top) and cross-polarized light (XPL, bottom), displaying an ophitic texture with euhedral laths of plagioclase enclosed by a clinopyroxene phenocryst.

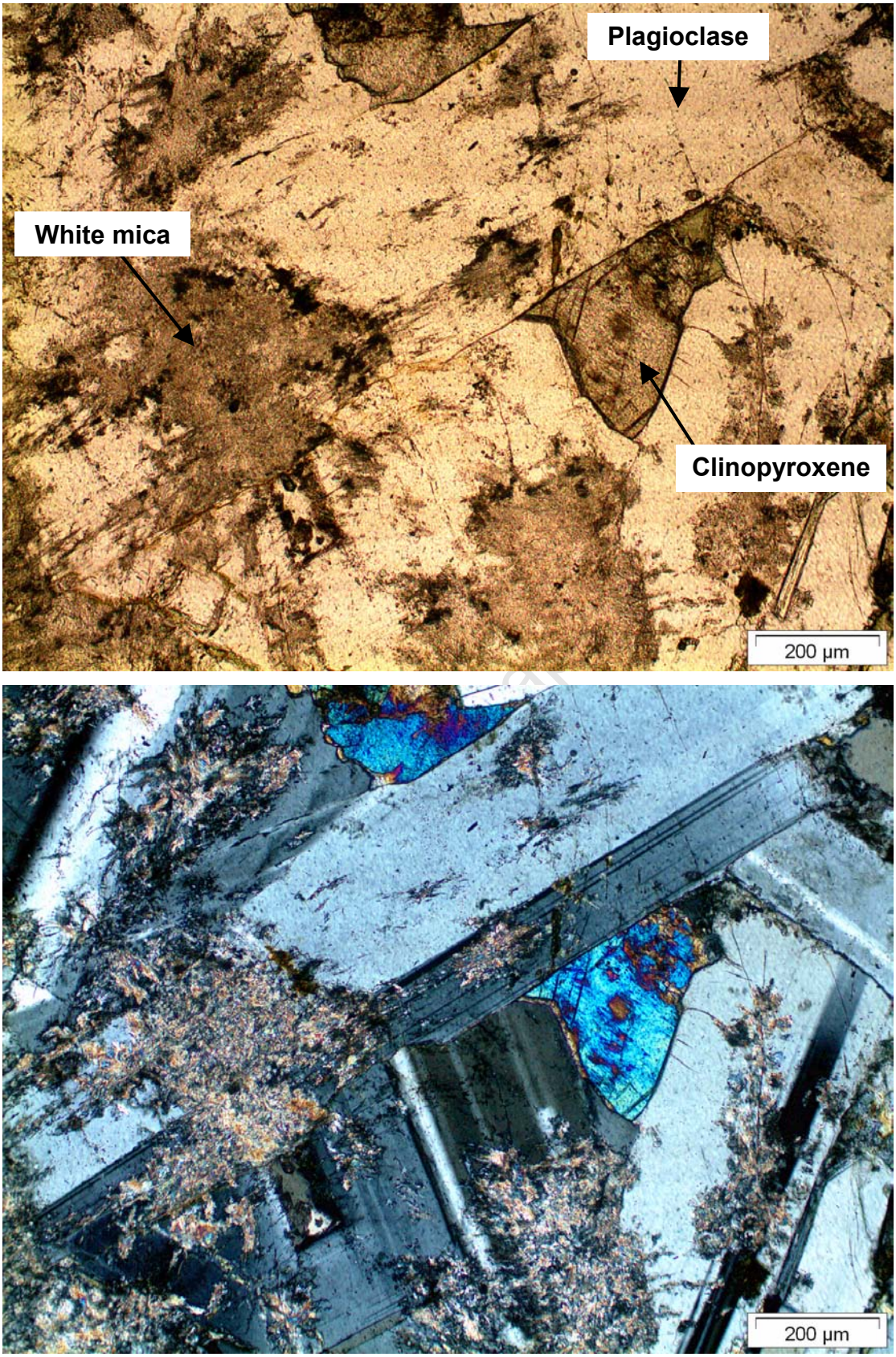

Figure 5.30: Sample IT8 (PPL top; XPL bottom), a plagioclase cumulate with intercumulate pyroxene. Note the extensive alteration of plagioclase feldspar to white mica ("sericitisation").

Figure 5.31: Sample OR2 (PPL top; XPL bottom), showing alteration of olivine to green "bowlingite" pseudomorphs. Besides pyroxene and plagioclase, biotite and chlorite are also present.

plagioclase to white mica ("sericitisation"); other alteration phases included biotite, chlorite, epidote and serpentine (**Figures 5.30, 5.32, and 5.33**). Clay minerals were also observed, particularly in association with white mica (**Figure 5.33)**. The overall degree of alteration (hydrothermal and weathering) of the primary igneous phases was estimated to vary between 5 and 30 %.

5.7 Pyroxene chemistry and cosmogenic ^{3}He and ^{21}Ne production rates

ICP-AES analysis of ~150 mg splits of the pyroxene separates used for noble gas analysis yielded weight percent concentrations of all major oxides other than SiO_2. The SiO_2 concentration was then assumed to be equal to the remainder from a total of 100%. Oxide concentrations were then converted to element concentrations according to each element's atomic mass. For every sample, all Fe was assigned to the FeO oxidation state in order to yield a total cation to anion molar ratio of ~0.67, as required by ideal pyroxene stoichiometry. Whilst minimal Fe may be present as Fe_2O_3, the effect on the net cosmogenic nuclide production rates would be negligible. Even a weight percent ratio of $Fe_2O_3/FeO = 0.1$ for these pyroxenes, equivalent to the whole rock ratio assumed for karoo dolerites by le Roex and Reid (1978), yields differences in the net nuclide production rates that are less than 0.1 atom/g/yr. The oxide and element concentrations for all samples are given in **Table 5.4**.

The element concentrations were then used to determine the net cosmogenic production rates for ^{3}He and ^{21}Ne according to Masarik and Reedy (1996), Kober *et al*. (2005) and Fenton *et al*. (2009); these are given as P1, P2 and P3 respectively in **Table 5.5**, and represented graphically in **Figure 5.34.** Cosmogenic production rates for ^{38}Ar are more complicated to determine, and are discussed later in Section 6.5. Ratios of P1, P2 and P3 to each other (as percentages), production rate ratios of ^{21}Ne to ^{3}He, and average production rates for all samples are also shown for the sake of comparison. It should be noted that production rates are for a horizontal surface at sea level and high latitude with no topographic shielding.

In this study, net production rates for pyroxenes were calculated according to the elemental production rates of Fenton *et al*. (2009). For ^{3}He, production rates according to Fenton *et al*. (2009) are, on average, 5 % higher than according to Masarik and Reedy (1996), and 20 % lower than according to Kober *et al*. (2005). For

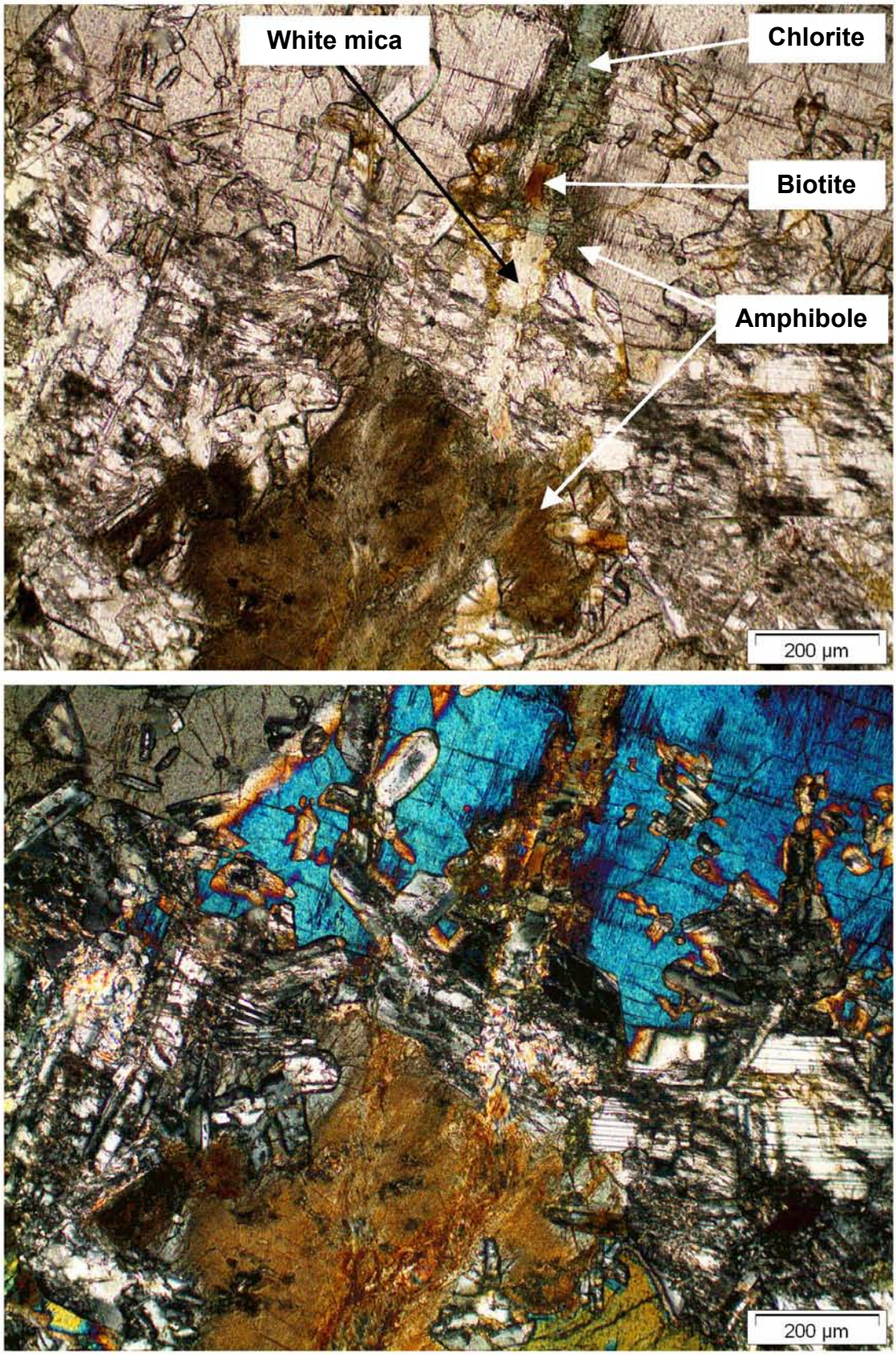

Figure 5.32: Sample BW3 (PPL top; XPL bottom), showing primary mineral phases cross-cut by a vein infilled with white mica, biotite and chlorite, and alteration of neighbouring pyroxene to a brown fibrous amphibole.

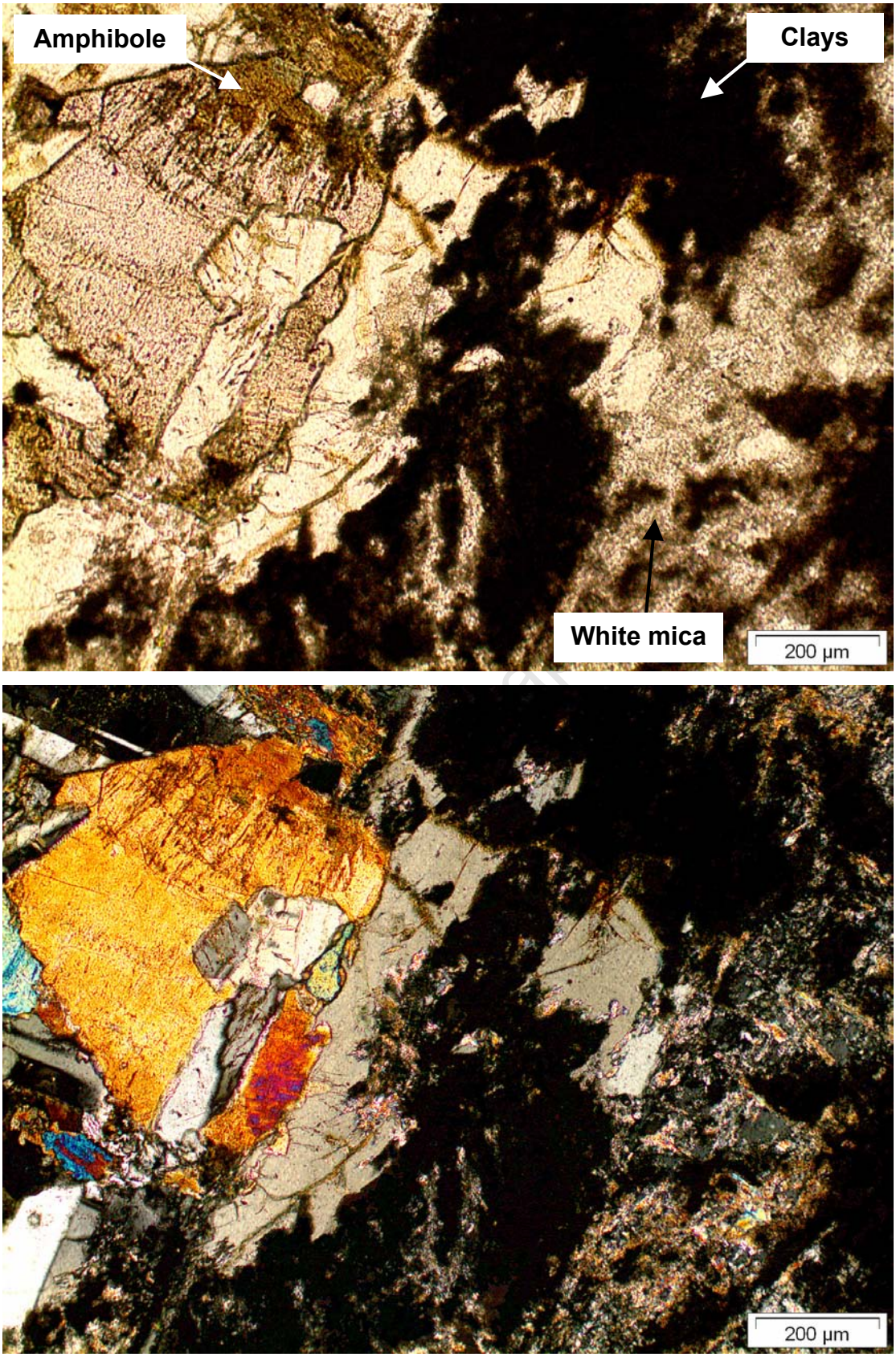

Figure 5.33: Sample DV9 (PPL top; XPL bottom) showing alteration of pyroxene to amphibole, and alteration of plagioclase to white mica. The white mica, in turn, displays extensive alteration to clay minerals.

Sample	Al_2O_3 (wt %)	CaO (wt %)	FeO (wt %)	MgO (wt %)	MnO (wt %)	K_2O (wt %)	Na_2O (wt %)	TiO_2 (wt %)
BW 3	2.92	17.61	8.27	16.94	0.22	<0.1	0.31	0.31
CB 1	2.73	16.30	9.99	16.60	0.25	<0.1	0.33	0.38
DV5	2.65	15.55	11.53	15.48	0.28	<0.1	0.29	0.50
DV6	2.82	14.94	12.97	15.45	0.30	<0.1	0.36	0.47
DV9	2.71	15.65	11.88	15.30	0.28	<0.1	0.31	0.49
GD 1	2.86	19.51	7.06	16.29	0.18	<0.1	0.29	0.36
GD 3	2.66	19.52	7.47	16.33	0.19	<0.1	0.28	0.37
GD2	2.56	18.26	8.20	16.35	0.21	<0.1	0.27	0.42
GR 2	4.37	14.50	11.04	16.37	0.27	<0.1	0.52	0.38
GR 5	2.57	19.09	7.51	17.26	0.20	<0.1	0.27	0.30
GR1	2.56	17.53	8.89	16.83	0.23	<0.1	0.26	0.37
GR3	1.93	15.50	11.56	16.34	0.28	<0.1	0.22	0.42
IT 5	3.08	15.80	14.17	14.18	0.30	<0.1	0.43	0.56
IT1	2.33	16.07	12.53	14.80	0.29	<0.1	0.28	0.51
IT3	1.83	8.36	20.51	17.02	0.39	<0.1	0.25	0.41
IT6	2.06	15.46	14.62	14.94	0.31	<0.1	0.28	0.59
IT8	2.00	10.90	16.41	16.42	0.34	<0.1	0.28	0.40
IT9	1.82	10.17	16.66	16.74	0.35	<0.1	0.23	0.43
IT10	2.09	12.30	15.54	15.69	0.32	<0.1	0.33	0.44
OR 2	2.88	17.52	8.26	16.86	0.21	<0.1	0.33	0.32
OR1	2.52	16.43	9.82	16.47	0.24	<0.1	0.46	0.37
OR3	2.43	17.99	8.26	16.87	0.22	<0.1	0.27	0.37

Sample	Al (%)	Ca (%)	Fe (%)	Mg (%)	Mn (%)	K (%)	Na (%)	Ti (%)	Si (%)	O (%)
BW3	1.54	12.6	6.43	10.2	0.17	<0.1	0.23	0.18	25.0	43.7
CB1	1.45	11.7	7.77	10.0	0.19	<0.1	0.24	0.23	25.0	43.5
DV5	1.40	11.1	8.96	9.34	0.22	<0.1	0.22	0.30	25.1	43.3
DV6	1.49	10.7	10.1	9.32	0.23	<0.1	0.26	0.28	24.6	43.0
DV9	1.43	11.2	9.23	9.23	0.22	<0.1	0.23	0.29	25.0	43.2
GD1	1.52	13.9	5.49	9.83	0.14	<0.1	0.22	0.21	25.0	43.7
GD2	1.35	13.1	6.37	9.86	0.16	<0.1	0.20	0.25	25.1	43.6
GD3	1.41	14.0	5.81	9.85	0.15	<0.1	0.21	0.22	24.9	43.6
GR1	1.35	12.5	6.91	10.2	0.18	<0.1	0.20	0.22	24.9	43.5
GR2	2.31	10.4	8.59	9.87	0.21	<0.1	0.39	0.23	24.6	43.5
GR3	1.02	11.1	8.99	9.85	0.22	<0.1	0.16	0.25	25.1	43.3
GR5	1.36	13.6	5.83	10.4	0.16	<0.1	0.20	0.18	24.7	43.5
IT1	1.23	11.5	9.74	8.93	0.22	<0.1	0.21	0.31	24.9	43.0
IT3	0.97	5.97	15.9	10.3	0.30	<0.1	0.18	0.25	24.0	42.2
IT5	1.63	11.3	11.0	8.55	0.23	<0.1	0.32	0.34	24.1	42.6
IT6	1.09	11.0	11.4	9.01	0.24	<0.1	0.21	0.35	24.2	42.5
IT8	1.06	7.79	12.8	9.90	0.26	<0.1	0.21	0.24	24.9	42.9
IT9	0.96	7.27	12.9	10.1	0.27	<0.1	0.17	0.26	25.1	43.0
IT10	1.11	8.79	12.1	9.46	0.25	<0.1	0.24	0.26	24.9	42.9
OR1	1.34	11.7	7.63	9.93	0.18	<0.1	0.34	0.22	25.1	43.5
OR2	1.52	12.5	6.42	10.2	0.16	<0.1	0.24	0.19	25.1	43.7
OR3	1.29	12.9	6.42	10.2	0.17	<0.1	0.20	0.22	25.1	43.6

Table 5.4: Results of ICP-AES analyses (above) and calculated major element compositions (below) for pyroxene separates.

Sample	^{3}He			^{21}Ne			^{3}He			^{21}Ne			^{21}Ne/^{3}He		
	P1	P2	P3	P1	P2	P3	P2/P1 (%)	P3/P1 (%)	P3/P2 (%)	P2/P1 (%)	P3/P1 (%)	P3/P2 (%)	P1	P2	P3
BW3	110.4	142.8	115.8	24.9	33.9	25.4	129.3	104.9	81.1	136.3	102.0	74.8	0.225	0.237	0.219
CB1	109.8	143.2	115.2	24.5	33.3	25.0	130.4	104.9	80.5	136.0	102.0	75.0	0.223	0.233	0.217
DV5	109.1	142.9	114.5	23.6	32.0	24.0	131.0	105.0	80.1	135.4	101.6	75.1	0.216	0.224	0.210
DV6	108.4	142.9	113.7	23.5	31.8	23.9	131.8	104.9	79.6	135.4	101.7	75.1	0.217	0.223	0.210
DV9	108.8	142.6	114.2	23.4	31.8	23.8	131.1	104.9	80.1	135.4	101.6	75.0	0.215	0.223	0.208
GD1	110.4	141.2	115.8	24.4	33.4	24.8	127.9	104.9	82.0	136.8	101.7	74.3	0.221	0.236	0.214
GD2	110.2	141.9	115.6	24.3	33.2	24.8	128.8	104.9	81.5	136.5	101.8	74.6	0.221	0.234	0.214
GD3	110.1	140.9	115.5	24.3	33.3	24.7	128.0	104.9	82.0	137.0	101.7	74.3	0.220	0.236	0.214
GR1	110.1	142.5	115.5	24.6	33.6	25.1	129.5	104.9	81.0	136.4	102.1	74.8	0.224	0.236	0.218
GR2	109.6	144.6	115.0	24.8	33.5	25.2	131.8	104.9	79.6	135.0	101.6	75.3	0.226	0.232	0.219
GR3	109.2	143.2	114.6	24.0	32.6	24.5	131.1	104.9	80.0	135.9	102.2	75.2	0.220	0.228	0.214
GR5	110.4	141.7	115.8	24.9	34.1	25.4	128.4	104.9	81.7	137.1	102.2	74.5	0.226	0.241	0.220
IT1	108.2	141.7	113.6	22.9	31.0	23.2	130.9	105.0	80.2	135.7	101.5	74.8	0.211	0.219	0.204
IT3	106.5	146.8	111.8	23.9	32.1	24.6	137.9	105.0	76.1	134.4	103.2	76.8	0.224	0.218	0.220
IT5	107.1	141.0	112.4	22.4	30.4	22.7	131.6	105.0	79.8	135.6	101.1	74.5	0.209	0.216	0.202
IT6	107.1	141.3	112.5	22.6	30.7	23.0	131.9	105.0	79.6	136.0	101.8	74.8	0.211	0.218	0.205
IT8	108.0	145.9	113.4	23.9	32.2	24.5	135.1	105.0	77.7	134.6	102.6	76.2	0.221	0.221	0.216
IT9	108.2	146.6	113.5	24.1	32.4	24.8	135.5	105.0	77.4	134.4	102.8	76.5	0.223	0.221	0.218
IT10	107.9	144.5	113.3	23.4	31.6	23.9	133.9	105.0	78.4	134.9	102.1	75.7	0.217	0.219	0.211
OR1	109.8	143.0	115.2	24.5	33.4	25.0	130.2	104.9	80.6	136.4	101.9	74.7	0.223	0.234	0.217
OR2	110.4	142.8	115.9	24.8	33.9	25.3	129.3	104.9	81.1	136.3	102.0	74.8	0.225	0.237	0.219
OR3	110.3	142.3	115.7	24.7	33.7	25.2	129.0	104.9	81.3	136.6	102.1	74.7	0.224	0.237	0.218
Average	***109.1***	***143.0***	***114.5***	***24.02***	***32.6***	***24.49***	***131.1***	***104.932***	***80.1***	***135.83***	***101.96***	***75.07***	***0.2202***	***0.2281***	***0.2140***
2 σ	***1.2***	***1.7***	***1.3***	***0.73***	***1.1***	***0.79***	***2.6***	***0.028***	***1.5***	***0.81***	***0.46***	***0.66***	***0.0050***	***0.0082***	***0.0054***

Table 5.5: Cosmogenic ^{3}He and ^{21}Ne production rates for pyroxene separates calculated according to Masarik and Reedy (1996), Kober *et al*. (2005) and Fenton *et al.* (2009), abbreviated as P1, P2 and P3, respectively. All production rates are in atoms per gram at sea level and high latitude (> 60º). Ratios and averages are also given for the purpose of comparison.

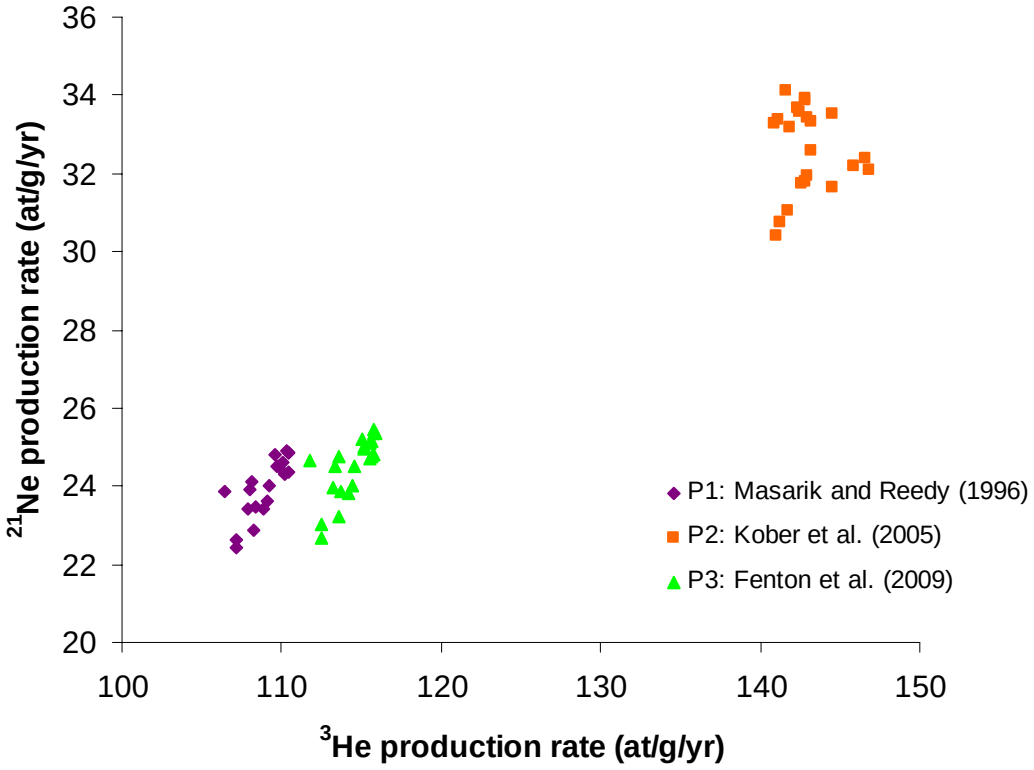

Figure 5.34: Comparative net cosmogenic production rates for ^{3}He and ^{21}Ne (normalized to sea level and at high latitude with no topographic shielding) for all pyroxene mineral separates. These are calculated from pyroxene mineral chemistry according to the elemental production rates of Masarik and Reedy (1996), Kober *et al*. (2005) and Fenton *et al*. (2009), and displayed as P1, P2 and P3, respectively.

^{21}Ne, the average production rate according to Fenton *et al.* (2009) is 2 % higher than according to Masarik and Reedy (1996), and 25 % lower than according to Kober *et al.* (2005).

Use of Fenton *et al.*'s (2009) production rates for these samples yields an average production rate ratio ^{21}Ne/^{3}He of 0.2140 ± 0.0054, in comparision with 0.2202 ± 0.0050 for Masarik and Reedy (1996), and 0.2281 ± 0.0082 for Kober *et al.* (2005). Note that all ^{3}He production rates determined for pyroxene separates in this study according to Fenton *et al.*'s (2009) elemental production rates (mean value 114.5 ± 1.3 at/g/yr) are within error of Goehring *et al.*'s (2010) global mean production rate for pyroxene and olivine of 119 ± 9 at/g/yr (as determined according to Lal, 1991 scaling).

CHAPTER 6: NOBLE GAS INVENTORIES, MINIMUM EXPOSURE AGES AND MAXIMUM EROSION RATES

6.1 Introduction

This chapter presents the noble gas inventories for the samples discussed in Chapter 5. The abundances of cosmogenic ^{3}He, ^{21}Ne and ^{38}Ar are determined, and the minimum exposure age and maximum erosion rate estimates based on this data are presented.

6.2 Helium and neon inventories

6.2.1 Nuclide abundances and ratios

The ^{4}He and ^{20}Ne concentrations for all analyses are presented in units of cm^{3} STP/g in **Table 6.1**, accompanied by the ratios ^{3}He/^{4}He, ^{22}Ne/^{20}Ne and ^{21}Ne/^{20}Ne. For all samples, results are reported for analyses at step heating temperatures of 900 ºC and 1750 ºC. For some samples, measurements made after heating to 600 ºC or after sample crushing *in vacuo* are also shown.

Total ^{4}He abundances range from 42.6 ± 1.4 × 10^{-8} cm^{3} STP/g (sample GD1) to 2980 ± 150 × 10^{-8} cm^{3} STP/g (sample IT3), and total ^{20}Ne abundances range from 39.2 ± 2.0 × 10^{-12} cm^{3} STP/g (sample IT8) to 1525 ± 66 × 10^{-12} cm^{3} STP/g (sample OR3). ^{4}He and ^{20}Ne abundances are lower for analyses at 600 ºC than for higher temperature analyses of the same sample, although no consistent distinction is observed between abundances at 900 ºC and 1750 ºC.

Total ^{3}He/^{4}He ratios vary from 0.0744 ± 0.0081 × 10^{-6} (sample BW3) to 7.14 ± 0.32 × 10^{-6} (sample GD3), total ^{22}Ne/^{20}Ne ratios range from 0.10120 ± 0.00028 (sample OR3) to 0.1265 ± 0.0023 (sample IT8), and total ^{21}Ne/^{20}Ne ratios range from 0.003233 ± 0.000054 to 0.0252 ± 0.0013 (also samples OR3 and IT8, respectively). ^{3}He/^{4}He ratios are lower for 1750 ºC analyses than for analyses at lower temperatures, signifying the release of most cosmogenic ^{3}He at temperatures of below 900 ºC. Conversely, ^{22}Ne/^{20}Ne and ^{21}Ne/^{20}Ne ratios are often higher at 1750 ºC than at 900 ºC, implying retention of most cosmogenic Ne within the crystal lattice until temperatures of above 900 ºC are achieved.

Sample	Mass g	T °C	^{4}He 10^{-8} cm^3 STP/g	± 2σ	^{20}Ne 10^{-12} cm^3 STP/g	± 2σ	^{3}He/^{4}He 10^{-6}	± 2σ	^{22}Ne/^{20}Ne	± 2σ	^{21}Ne/^{20}Ne	± 2σ
BW3	0.50102	600	13.91	0.70	16.74	0.92	0.449	0.083	0.1035	0.0024	0.00304	0.00040
		900	112.6	5.6	22.5	1.4	0.090	0.013	0.1032	0.0031	0.00325	0.00040
		1750	141.4	7.1	49.9	2.9	0.0251	0.0079	0.1037	0.0025	0.00392	0.00021
		Total	***267.9***	***9.1***	***89.1***	***3.4***	***0.0744***	***0.0081***	***0.1035***	***0.0017***	***0.00359***	***0.00017***
CB1	0.48028	900	129.9	6.5	38.9	2.3	0.194	0.020	0.1038	0.0028	0.00364	0.00025
		1750	59.8	3.0	32.3	2.2	0.045	0.011	0.1032	0.0024	0.00462	0.00035
		Total	***189.8***	***7.2***	***71.2***	***3.2***	***0.147***	***0.015***	***0.1035***	***0.0019***	***0.00408***	***0.00021***
DV5	0.50352	900	207	10	18.5	1.7	0.669	0.031	0.1086	0.0023	0.00860	0.00050
		1750	140.2	7.0	24.9	1.8	0.035	0.011	0.1103	0.0030	0.01211	0.00070
		Total	***347***	***13***	***43.4***	***2.4***	***0.413***	***0.022***	***0.1095***	***0.0020***	***0.01062***	***0.00046***
	0.51124	***Crushed***	***59.2***	***3.0***	***5.18***	***0.41***	***0.022***	***0.010***	***0.1032***	***0.0037***	***0.00314***	***0.00051***
DV6	0.50356	900	234	12	19.1	1.4	0.923	0.037	0.1076	0.0031	0.00647	0.00025
		1750	513	36	29.2	2.0	0.049	0.018	0.1201	0.0017	0.01911	0.00084
		Total	***748***	***38***	***48.3***	***2.5***	***0.322***	***0.023***	***0.1152***	***0.0016***	***0.01411***	***0.00060***
DV9	0.50052	900	377	19	46.4	2.9	0.439	0.028	0.1036	0.0025	0.00431	0.00032
		1750	544	38	50.6	2.9	0.0496	0.0083	0.1110	0.0019	0.00989	0.00042
		Total	***921***	***43***	***97.0***	***4.1***	***0.209***	***0.015***	***0.1075***	***0.0015***	***0.00722***	***0.00029***
GD1	0.50352	600	5.27	0.26	41.7	2.2	3.92	0.30	0.1027	0.0014	0.00298	0.00022
		900	15.30	0.77	38.5	2.2	4.43	0.33	0.1038	0.0018	0.00369	0.00027
		1750	22.0	1.1	337	17	1.044	0.083	0.10281	0.00049	0.003667	0.000067
		Total	***42.6***	***1.4***	***417***	***18***	***2.62***	***0.14***	***0.10289***	***0.00045***	***0.003600***	***0.000064***
GD2	0.51466	900	25.1	1.3	41.0	2.6	8.89	0.55	0.1032	0.0016	0.00443	0.00029
		1750	17.5	1.2	132.6	7.3	1.56	0.15	0.10588	0.00090	0.00649	0.00022
		Total	***42.6***	***1.8***	***173.6***	***7.7***	***5.88***	***0.36***	***0.10524***	***0.00078***	***0.00600***	***0.00018***
	0.52240	***Crushed***	***14.43***	***0.72***	***227***	***12***	***0.050***	***0.036***	***0.10214***	***0.00063***	***0.00299***	***0.00013***
GD3	0.48336	900	17.40	0.87	39.1	2.3	14.57	0.55	0.1032	0.0023	0.00367	0.00026
		1750	27.1	1.4	272	14	2.36	0.18	0.10447	0.00073	0.00540	0.00012
		Total	***44.5***	***1.6***	***311***	***14***	***7.14***	***0.32***	***0.10431***	***0.00070***	***0.00518***	***0.00011***
GR1	0.50178	900	178.0	8.9	32.6	2.0	0.734	0.037	0.1044	0.0032	0.00362	0.00026
		1750	422	21	255	13	0.0600	0.0027	0.1042	0.0029	0.00415	0.00017
		Total	***600***	***23***	***288***	***13***	***0.260***	***0.015***	***0.1042***	***0.0026***	***0.00409***	***0.00016***
GR2	0.50070	900	289	14	72.4	3.9	0.220	0.014	0.1033	0.0016	0.00340	0.00012
		1750	236	12	117.7	6.3	0.0425	0.0090	0.1032	0.0012	0.00431	0.00016
		Total	***525***	***19***	***190.1***	***7.4***	***0.140***	***0.009***	***0.1032***	***0.0010***	***0.00396***	***0.00011***
GR3	0.52566	900	329.8	16	41.3	2.5	0.401	0.028	0.10395	0.00088	0.00558	0.00046
		1750	148.7	7.4	36.9	2.1	0.128	0.020	0.1094	0.0014	0.00953	0.00049
		Total	***478***	***18***	***78.2***	***3.3***	***0.316***	***0.021***	***0.10650***	***0.00080***	***0.00744***	***0.00034***

Table 6.1: *(Continued on following page).*

Sample	Mass g	T ºC	^{4}He 10^{-8} cm^3 STP/g	± 2σ	^{20}Ne 10^{-12} cm^3 STP/g	± 2σ	^{3}He/^{4}He 10^{-6}	± 2σ	^{22}Ne/^{20}Ne	± 2σ	^{21}Ne/^{20}Ne	± 2σ
GR5	0.48144	900	118.7	5.9	71.5	4.1	2.031	0.078	0.1030	0.0013	0.00346	0.00019
		1750	318	16	245	13	0.207	0.011	0.10468	0.00070	0.00570	0.00017
		Total	***437***	***17***	***317***	***13***	***0.702***	***0.034***	***0.10430***	***0.00061***	***0.00520***	***0.00014***
IT1	0.52212	900	885.9	63	39.6	2.4	0.150	0.018	0.1061	0.0017	0.00554	0.00050
		1750	1236	88	45.0	2.6	0.054	0.011	0.1100	0.0013	0.00928	0.00033
		Total	***2120***	***110***	***84.7***	***3.5***	***0.094***	***0.010***	***0.1082***	***0.0010***	***0.00753***	***0.00030***
	0.53060	***Crushed***	***866***	***61***	***35.7***	***1.9***	***0.060***	***0.011***	***0.1044***	***0.0019***	***0.00397***	***0.00014***
IT3	0.50018	900	1063	75	91.9	4.9	0.342	0.025	0.1041	0.0014	0.00468	0.00011
		1750	1920	140	36.8	2.2	0.100	0.011	0.12352	0.00081	0.02157	0.00068
		Total	***2980***	***150***	***128.6***	***5.4***	***0.187***	***0.013***	***0.1096***	***0.0011***	***0.00951***	***0.00035***
IT5	0.50190	900	258	13	156.4	8.2	0.984	0.035	0.10284	0.00076	0.00367	0.00010
		1750	308	15	44.6	3.1	0.161	0.013	0.1153	0.0012	0.01608	0.00062
		Total	***566***	***20***	***201.0***	***8.7***	***0.536***	***0.023***	***0.10561***	***0.00067***	***0.00642***	***0.00025***
IT6	0.50024	600	62.9	3.1	9.54	0.69	0.490	0.044	0.1053	0.0038	0.00332	0.00014
		900	268	13	22.4	1.5	0.164	0.011	0.1057	0.0018	0.00411	0.00025
		1750	607	43	48.8	2.7	0.0989	0.0079	0.1091	0.0017	0.00693	0.00042
		Total	***938***	***45***	***80.7***	***3.2***	***0.144***	***0.007***	***0.1077***	***0.0012***	***0.00572***	***0.00027***
IT8	0.50388	900	795	56	18.3	1.3	0.497	0.057	0.1128	0.0029	0.00997	0.00071
		1750	966	68	20.8	1.5	0.151	0.016	0.1385	0.0032	0.0386	0.0019
		Total	***1761***	***88***	***39.2***	***2.0***	***0.307***	***0.028***	***0.1265***	***0.0023***	***0.0252***	***0.0013***
IT9	0.49022	900	1240	88	172.7	9.2	0.311	0.022	0.10301	0.00082	0.00420	0.00014
		1750	643	32	89.2	4.8	0.1382	0.0088	0.1097	0.0017	0.00874	0.00020
		Total	***1883***	***94***	***262***	***10***	***0.252***	***0.015***	***0.10531***	***0.00080***	***0.00575***	***0.00014***
IT10	0.50202	900	933	66	63.8	3.5	0.509	0.032	0.1052	0.0015	0.00558	0.00025
		1750	981	69	21.1	1.5	0.151	0.014	0.1413	0.0028	0.0417	0.0020
		Total	***1914***	***96***	***85.0***	***3.8***	***0.326***	***0.019***	***0.1142***	***0.0015***	***0.01456***	***0.00081***
OR1	0.50602	900	91.1	4.6	113.0	6.0	0.993	0.067	0.10230	0.00092	0.00331	0.00013
		1750	35.9	1.8	85.3	4.6	0.638	0.063	0.1047	0.0013	0.00576	0.00014
		Total	***127.0***	***4.9***	***198.2***	***7.6***	***0.893***	***0.052***	***0.10332***	***0.00076***	***0.00436***	***0.00010***
OR2	0.50038	900	49.3	2.5	92.2	4.9	3.25	0.16	0.1031	0.0014	0.00362	0.00020
		1750	21.3	1.1	48.5	2.9	1.40	0.11	0.11087	0.00078	0.01102	0.00040
		Total	***70.7***	***2.7***	***140.8***	***5.7***	***2.69***	***0.12***	***0.10579***	***0.00094***	***0.00617***	***0.00023***
OR3	0.50940	900	72.6	3.6	263	14	1.709	0.082	0.1018	0.0011	0.00304	0.00010
		1750	198.1	9.9	1262	65	0.254	0.013	0.10108	0.00026	0.003273	0.000062
		Total	***271***	***11***	***1525***	***66***	***0.644***	***0.031***	***0.10120***	***0.00028***	***0.003233***	***0.000054***

Table 6.1: *(Continued from previous page):* Results of all ^{4}He, ^{20}Ne, ^{3}He/^{4}He, ^{22}Ne/^{20}Ne and ^{21}Ne/^{20}Ne measurements after sample heating or crushing. Totals from heating measurements are also given for each sample.

6.2.2 Neon three-isotope diagrams

The $^{22}Ne/^{20}Ne$ and $^{21}Ne/^{20}Ne$ ratios for heating and crushing analyses are plotted in neon three-isotope diagrams for each sample in **Figures 6.1** to **6.22**. The experimentally-determined pyroxene spallation line of Schäfer *et al*. (1999), defined by the equation $^{22}Ne/^{20}Ne = (1.069\pm 0.035)*(^{21}Ne/^{20}Ne) + 0.099$, is also shown, as well as the composition of air ($^{21}Ne/^{20}Ne = 0.002959$; Eberhardt *et al*., 1965). Any measurements that do not plot within analytical error limits of the spallation line imply the non-negligible presence of a Ne component other than air and cosmogenic Ne (Niedermann *et al*., 1993). This has implications for the calculation of the cosmogenic ^{21}Ne abundance.

Of the crushing measurements, samples DV5 and GD2 yield measurements within 2σ error limits of the composition of air (**Figures 6.3** and **6.7** respectively), whilst sample IT1 yields $^{21}Ne/^{20}Ne$ and $^{22}Ne/^{20}Ne$ ratios higher than air (**Figure 6.13**). It is unlikely that the crushed IT1 measurement represents a significant component of cosmogenic Ne, because cosmogenic ^{21}Ne and ^{22}Ne are produced *in situ* within the crystal lattice, and crushing measurements reflect the composition of gases trapped along grain boundaries and in fluid inclusions. The crushed IT1 analysis might be interpreted to reflect the presence of *in situ*-produced nucleogenic ^{21}Ne and ^{22}Ne, as the sample has a relatively high (radiogenic) ^{4}He abundance of $2120 \pm 110 \times 10^{-8}$ cm^3 STP/g (**Table 6.1**). However, as with cosmogenic components, *in situ*-produced nucleogenic components are primarily produced within the crystal lattice. It is perhaps more likely that the crushed IT1 analysis reflects the trapping of nucleogenic Ne from the country rock, i.e. crustal Ne (e.g. Kennedy *et al*., 1990) during emplacement of the dolerite. Indeed, the crushed IT1 analysis also yielded a relatively high abundance of ^{4}He ($866 \pm 61 \times 10^{-8}$ cm^3 STP/g), suggesting that much of the ^{4}He originates from crustal fluids too.

All heating analyses, with the exceptions of the 900 ºC and 1750 ºC analyses of sample IT6 (**Figure 6.16**) and the 1750 ºC analysis of sample OR3 (**Figure 6.22**), plot within 2σ error limits of the pyroxene spallation line. The IT6 900 ºC and 1750 ºC analyses display $^{22}Ne/^{20}Ne$ ratios that are elevated relative to the pyroxene spallation line, implying that a significant additional ^{22}Ne component may be present: either crustal Ne, or *in situ*-produced nucleogenic ^{22}Ne. However, it may be noted that the

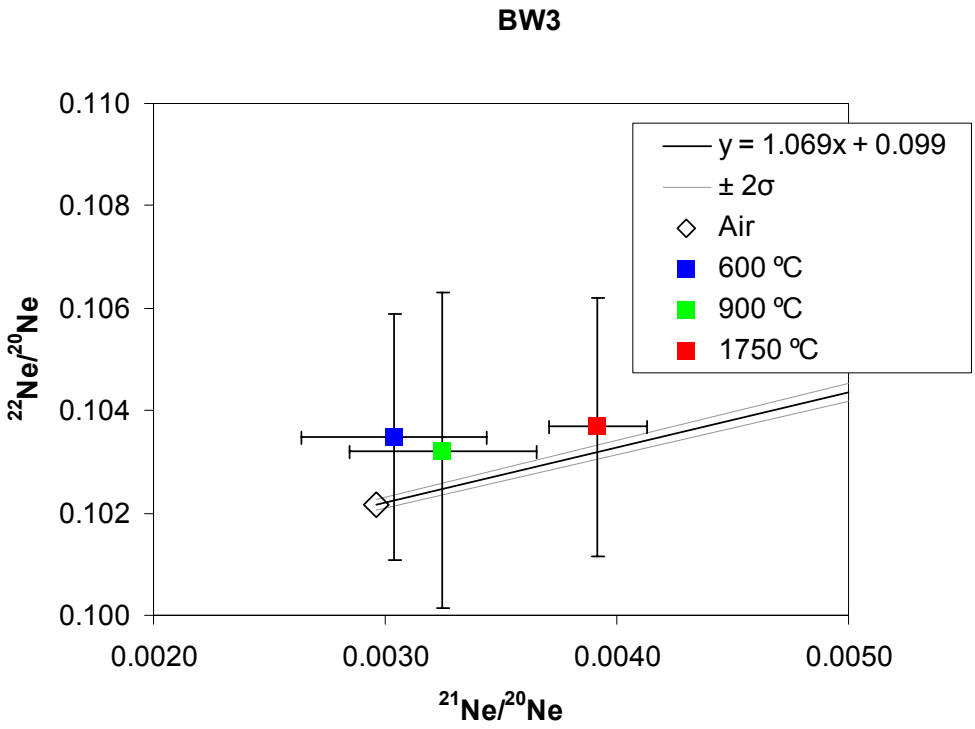

Figure 6.1: Neon three-isotope diagram of analyses of sample BW3 at 600 ºC, 900 ºC and 1750 ºC. Schäfer *et al.*'s (1999) pyroxene spallation line (y = (1.069 ± 0.035)x + 0.099) and the composition of air ($^{21}Ne/^{20}Ne = 0.002959$) are also shown here and in subsequent Ne three-isotope diagrams.

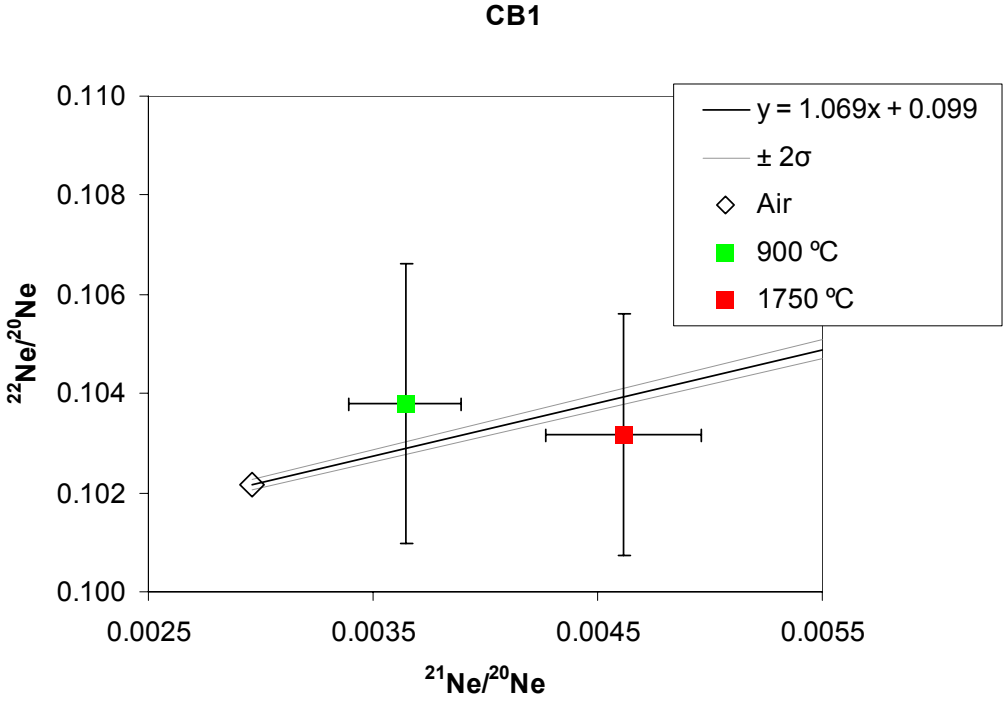

Figure 6.2: Neon three-isotope diagram of analyses of sample CB1 at 900 ºC and 1750 ºC.

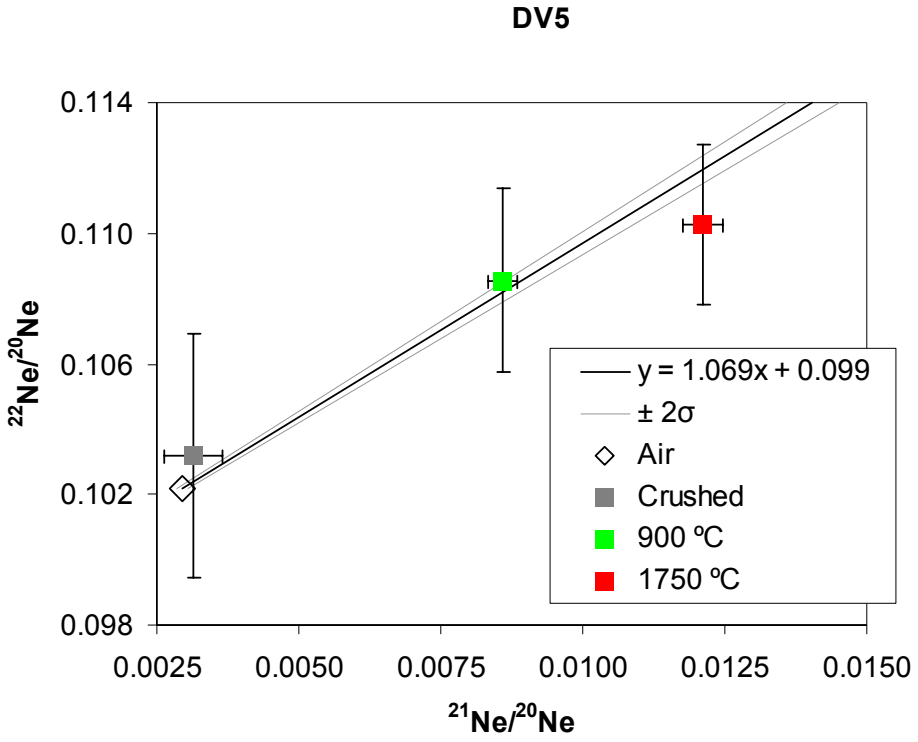

Figure 6.3: Neon three-isotope diagram of analyses of sample DV5 at 900 ºC and 1750 ºC, and after crushing *in vacuo*.

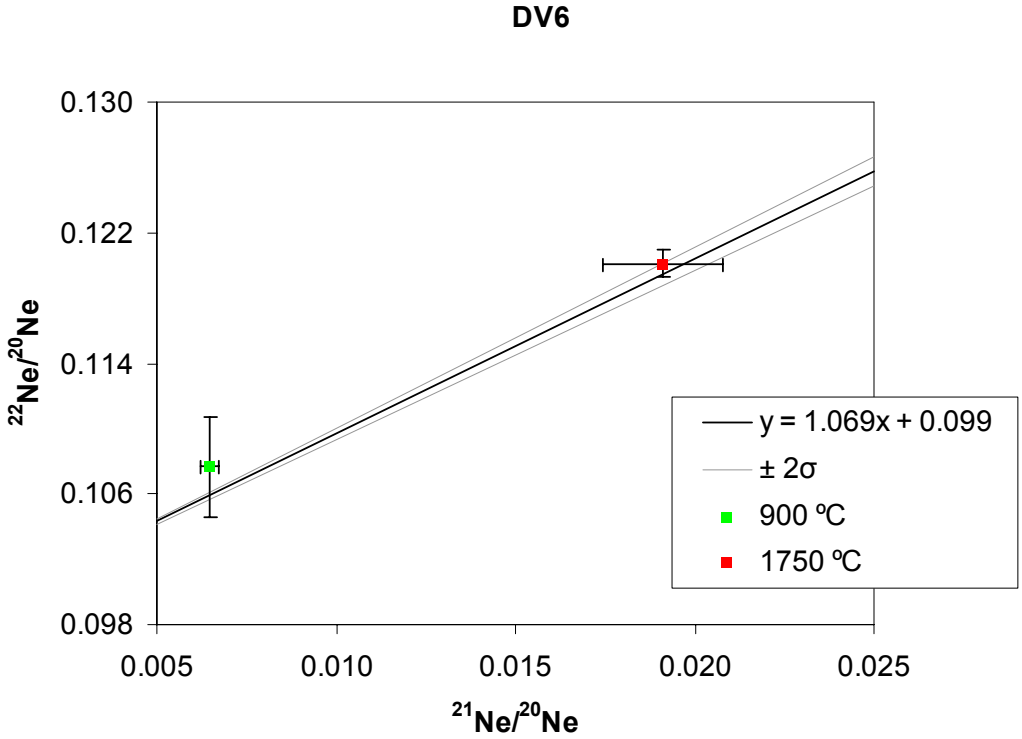

Figure 6.4: Neon three-isotope diagram of analyses of sample DV6 at 900 ºC and 1750 ºC.

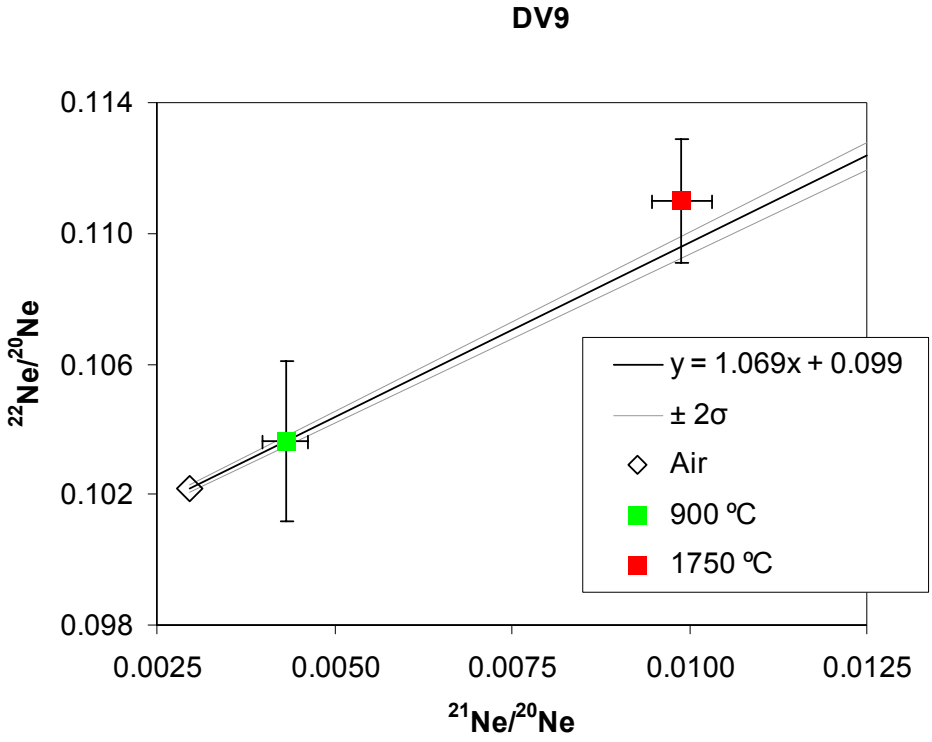

Figure 6.5: Neon three-isotope diagram of analyses of sample DV9 at 900 ºC and 1750 ºC.

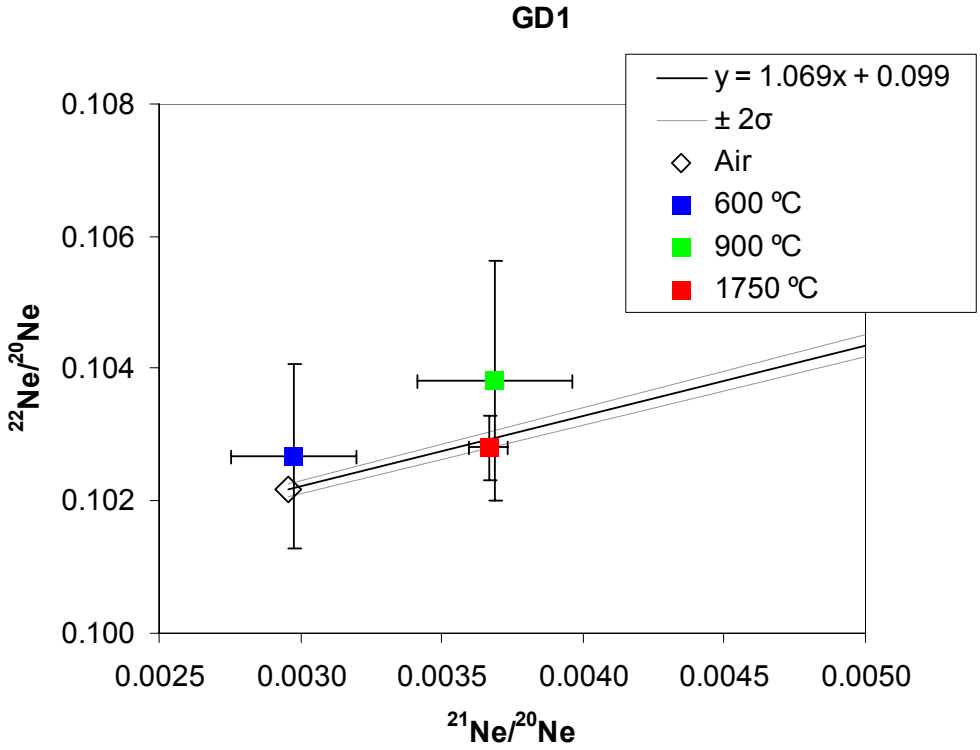

Figure 6.6: Neon three-isotope diagram of analyses of sample GD1 at 600 ºC, 900 ºC and 1750 ºC.

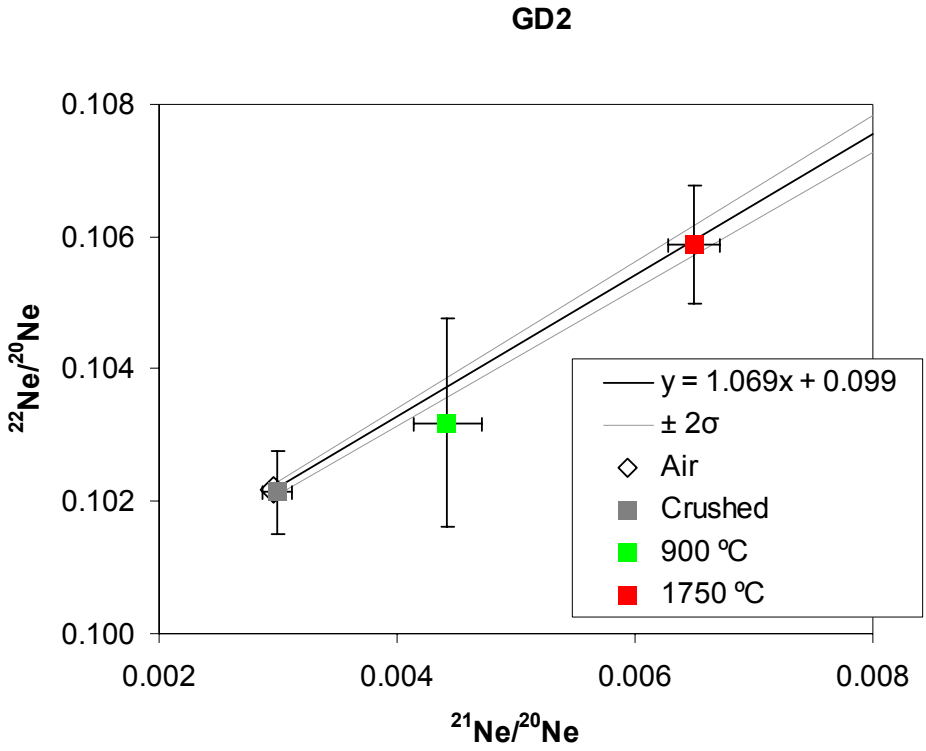

Figure 6.7: Neon three-isotope diagram of analyses of sample GD2 at 900 ºC and 1750 ºC, and after crushing *in vacuo*.

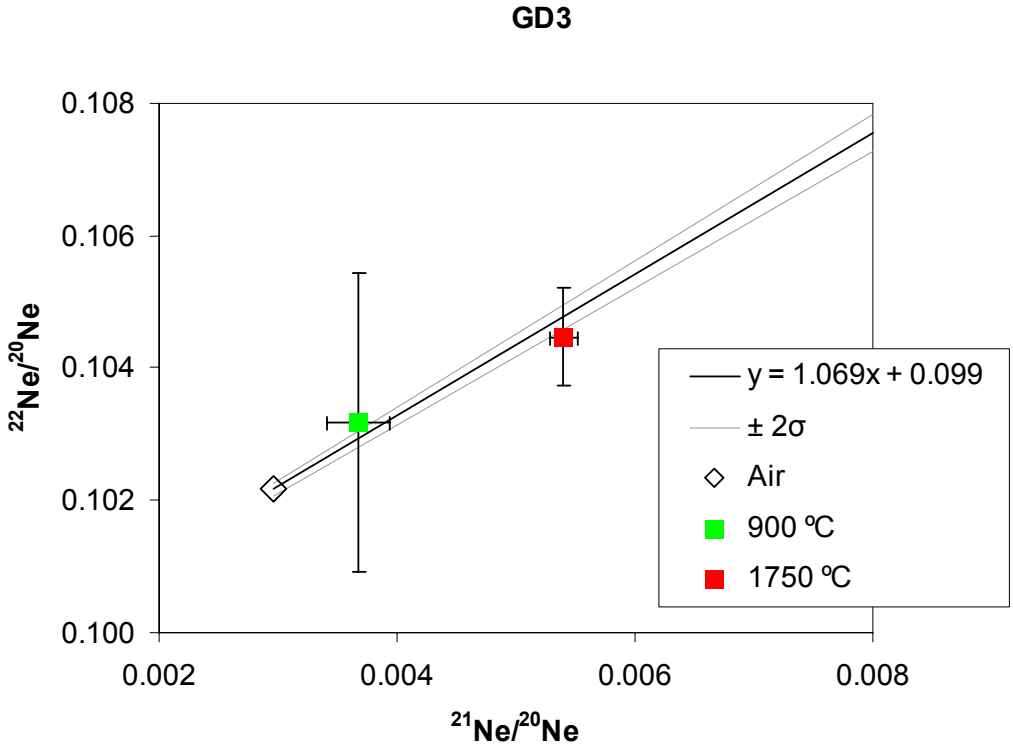

Figure 6.8: Neon three-isotope diagram of analyses of sample GD3 at 900 ºC and 1750 ºC.

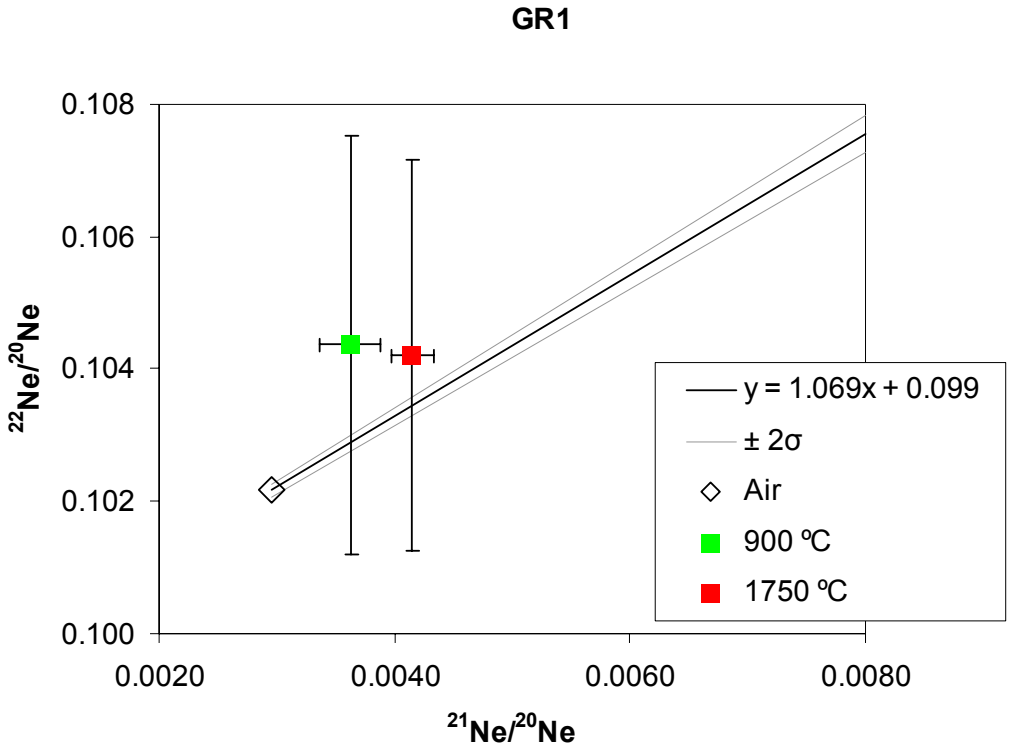

Figure 6.9: Neon three-isotope diagram of analyses of sample GR1 at 900 ºC and 1750 ºC.

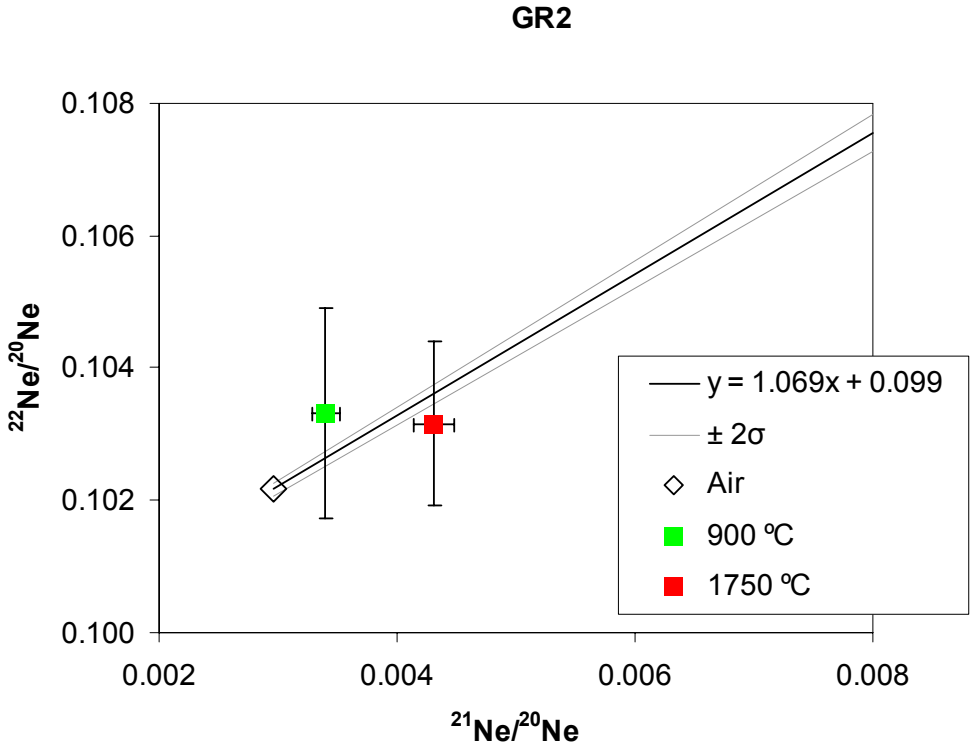

Figure 6.10: Neon three-isotope diagram of analyses of sample GR2 at 900 ºC and 1750 ºC.

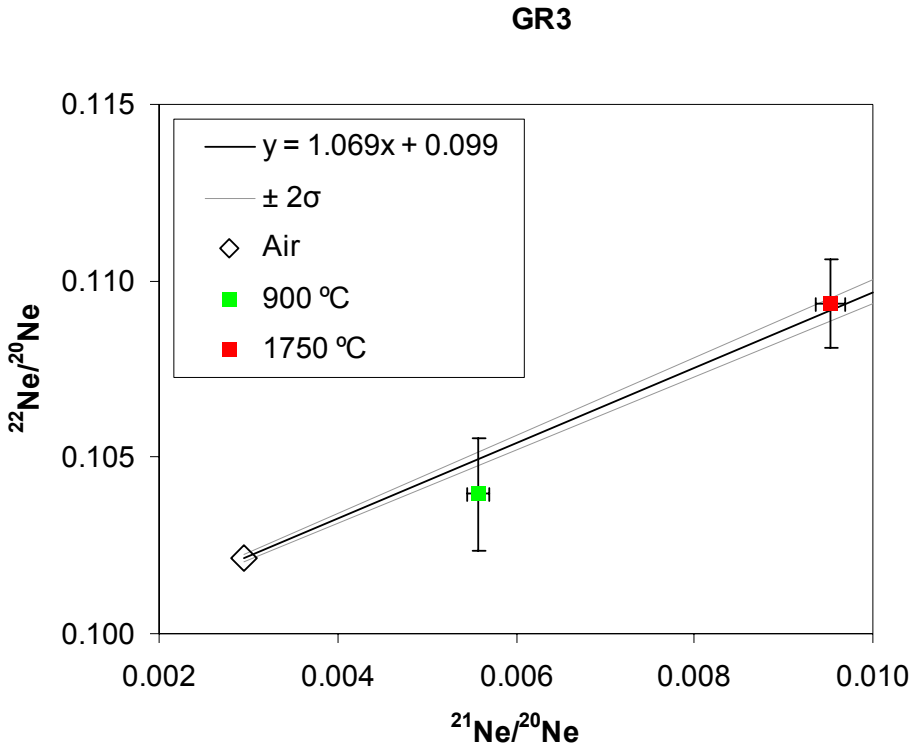

Figure 6.11: Neon three-isotope diagram of analyses of sample GR3 at 900 ºC and 1750 ºC.

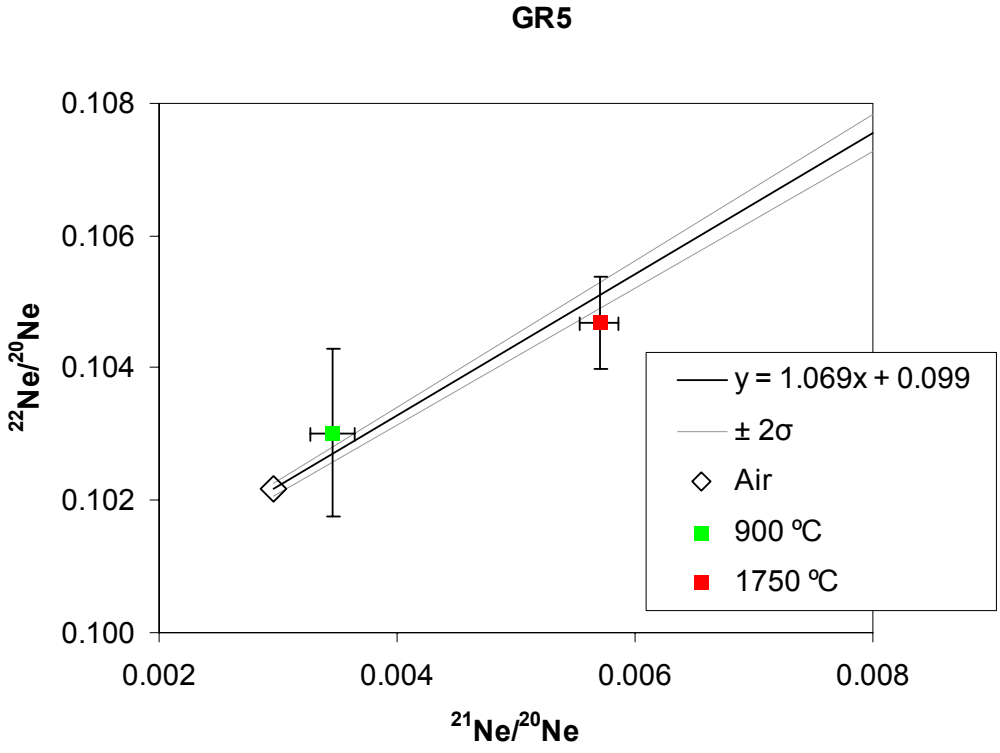

Figure 6.12: Neon three-isotope diagram of analyses of sample GR5 at 900 ºC and 1750 ºC.

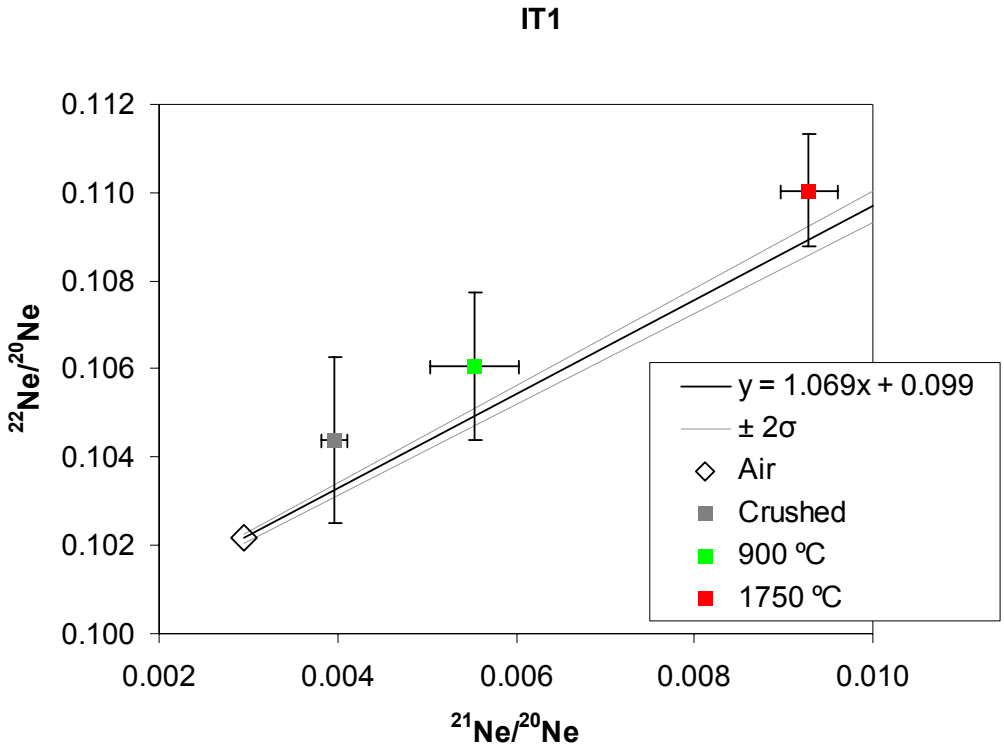

Figure 6.13: Neon three-isotope diagram of analyses of sample IT1 at 900 ºC and 1750 ºC, and after crushing *in vacuo*.

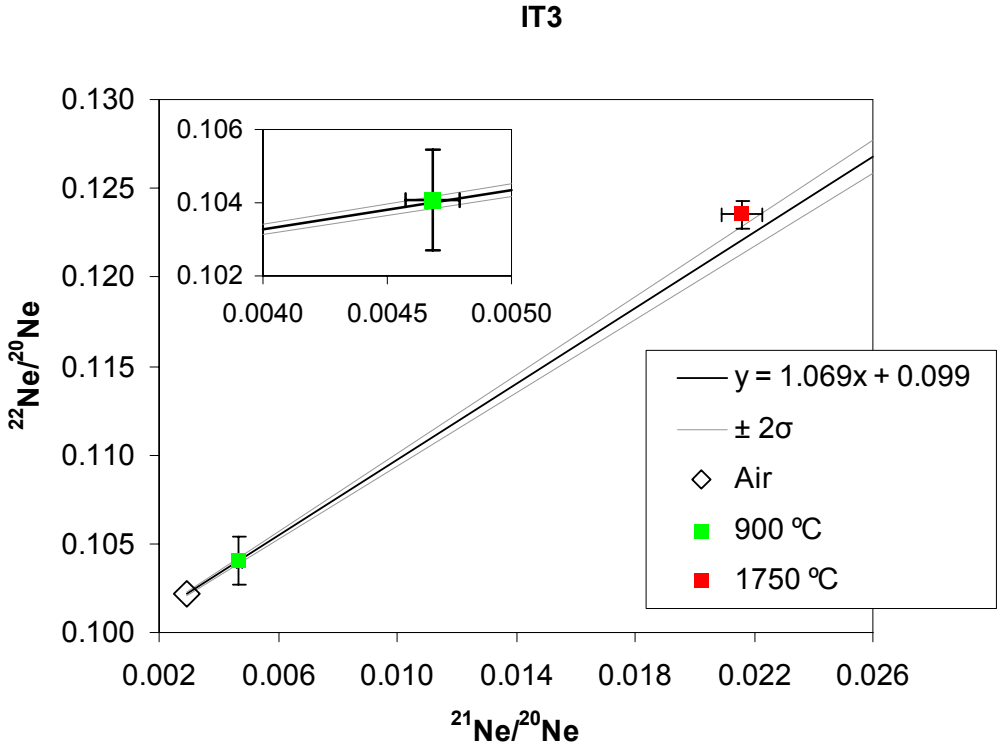

Figure 6.14: Neon three-isotope diagram of analyses of sample IT3 at 900 ºC and 1750 ºC. Detail of 900 ºC analysis is shown in inset.

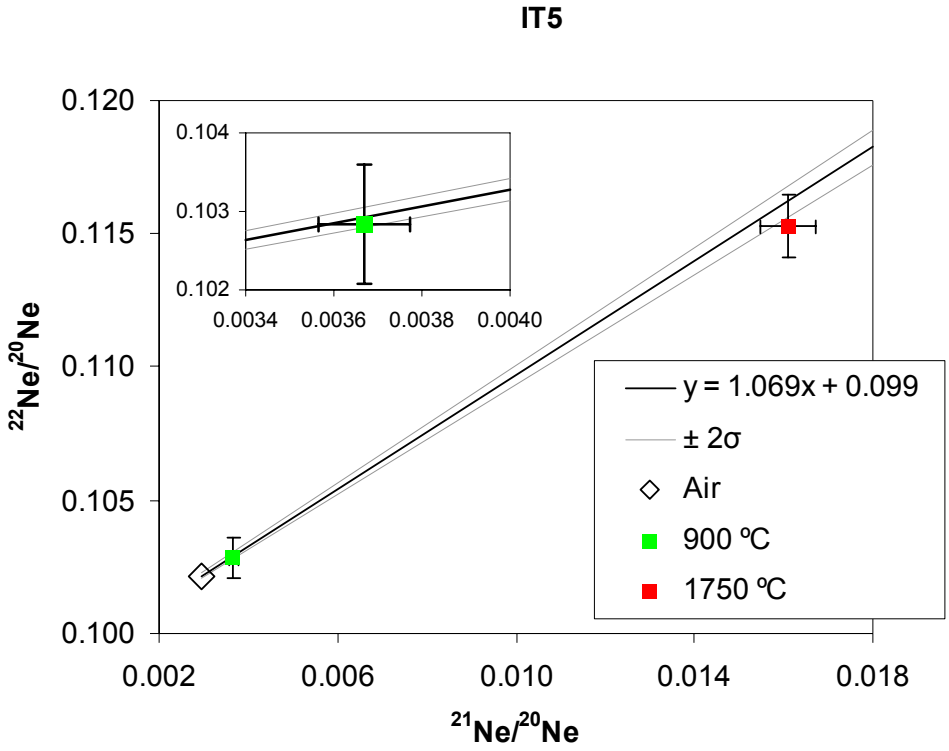

Figure 6.15: Neon three-isotope diagram of analyses of sample IT5 at 900 ºC and 1750 ºC. Detail of 900 ºC analysis is shown in inset.

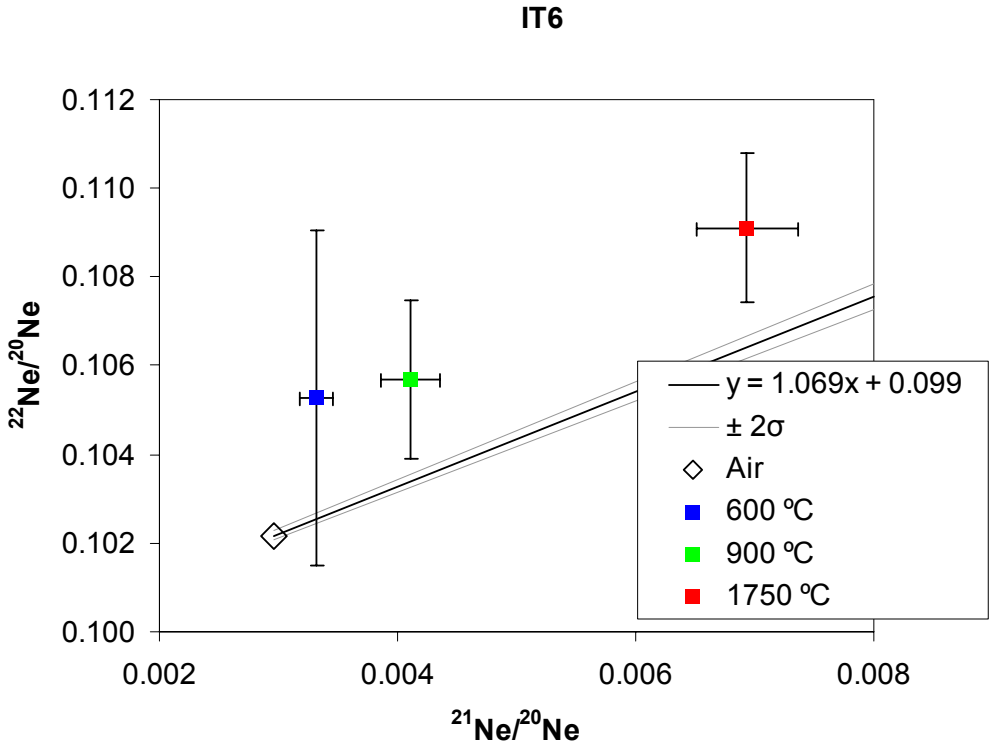

Figure 6.16: Neon three-isotope diagram of analyses of sample IT6 at 600 ºC, 900 ºC and 1750 ºC. Analyses at 900 ºC and 1750 ºC do not plot within 2σ error limits of the pyroxene spallation line, but display relative enrichment in ^{22}Ne.

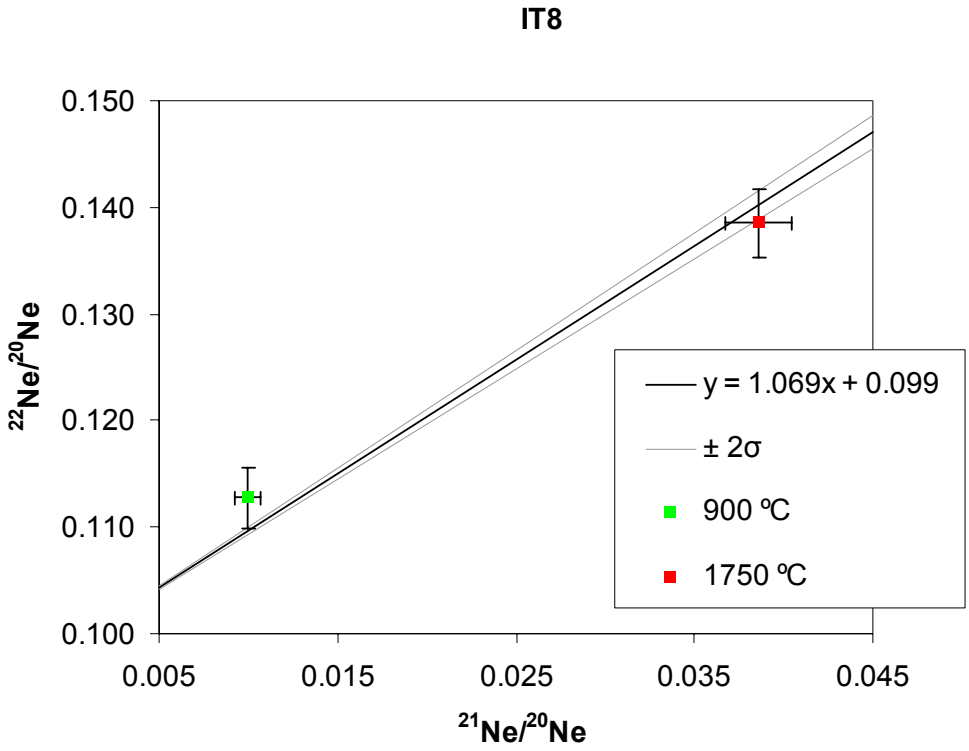

Figure 6.17: Neon three-isotope diagram of analyses of sample IT8 at 900 ºC and 1750 ºC.

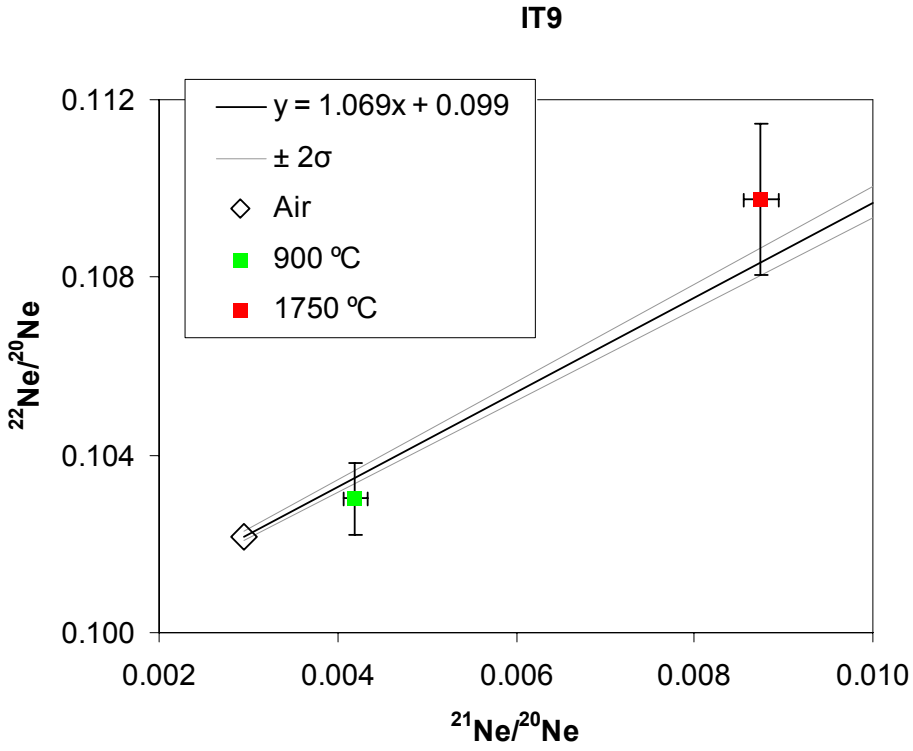

Figure 6.18: Neon three-isotope diagram of analyses of sample IT9 at 900 ºC and 1750 ºC.

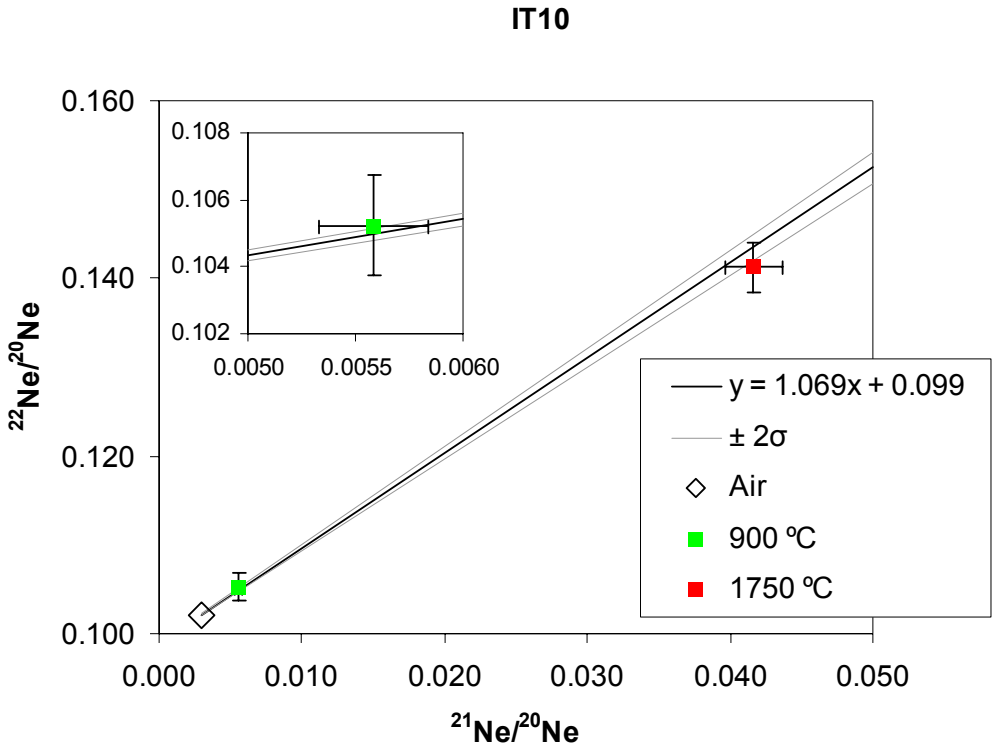

Figure 6.19: Neon three-isotope diagram of analyses of sample IT10 at 900 ºC and 1750 ºC. Detail of 900 °C analysis is shown in inset.

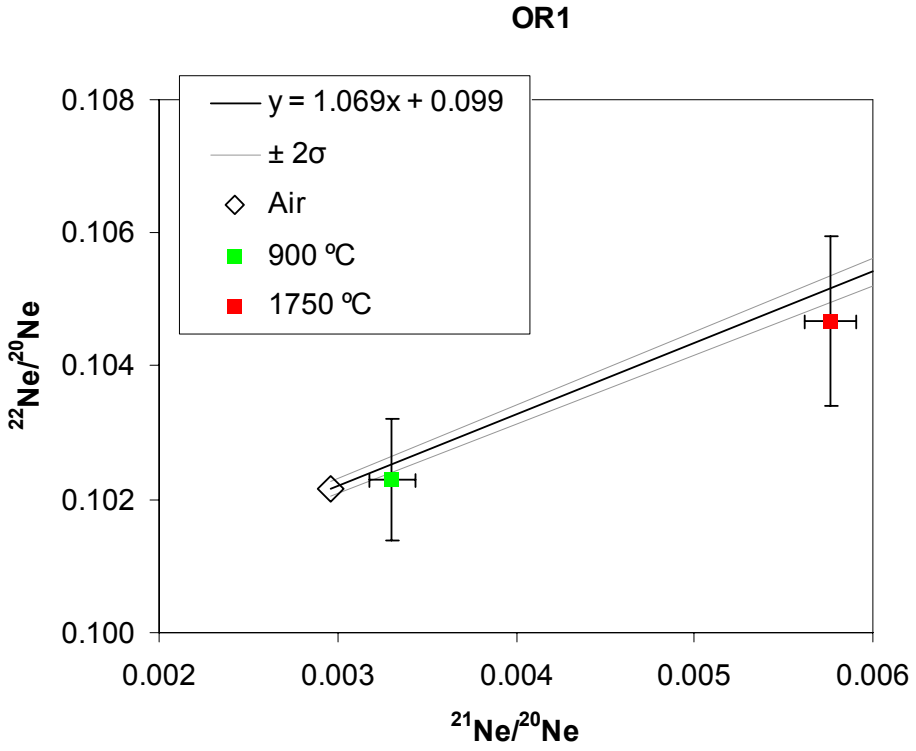

Figure 6.20: Neon three-isotope diagram of analyses of sample OR1 at 900 ºC and 1750 ºC.

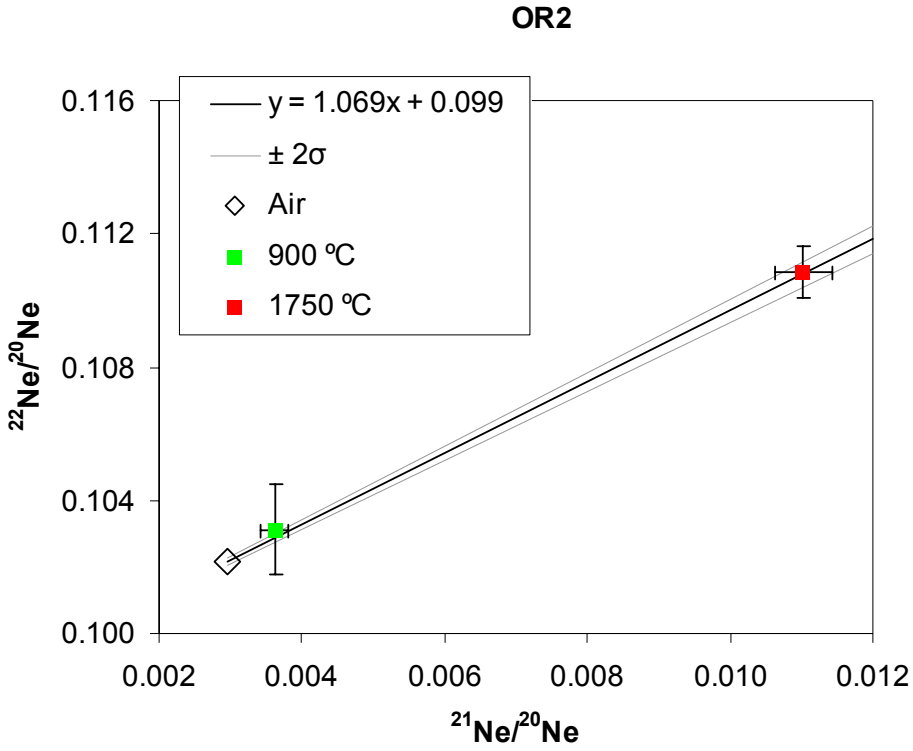

Figure 6.21: Neon three-isotope diagram of analyses of sample OR2 at 900 ºC and 1750 ºC.

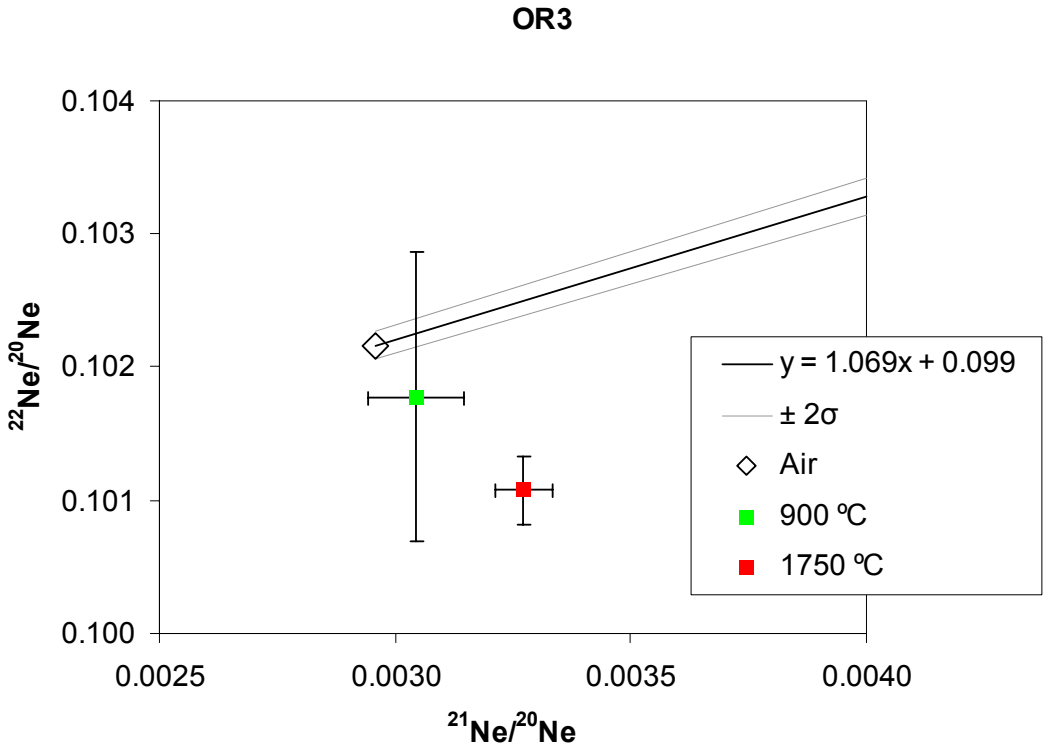

Figure 6.22: Neon three-isotope diagram of analyses of sample OR3 at 900 ºC and 1750 ºC. The analysis at 1750 ºC does not plot within 2σ error limits of the pyroxene spallation line, but displays a relative depletion in ^{22}Ne.

total ^{4}He abundance for sample IT6 (938 ± 45 x 10^{-8} cm^3 STP/g, **Table 6.1**) is not unusually high. Alternatively, sample IT6 may have a significant trapped component of fractionated atmospheric Ne, as the ^{22}Ne/^{20}Ne ratios at 600 ºC, 900 ºC and 1750 ºC lie almost equally elevated above the pyroxene spallation line (**Figure 6.16**).

The 1750 ºC analysis of sample OR3 yielded a ^{22}Ne/^{20}Ne ratio of 0.10108 ± 0.00026, lower than the ^{22}Ne/^{20}Ne ratio of air. ^{22}Ne/^{20}Ne ratios that are depleted relative to air may be indicative of a mantle Ne component, and have been reported for mid-ocean ridge basalts and ocean island basalts (e.g. Craig and Lupton, 1976; Sarda *et al*., 1988; Honda *et al*., 1991), as well as for continental flood basalts (Dodson *et al*., 1997). Alternatively, the low ^{22}Ne/^{20}Ne in sample OR3 may reflect some process of mass fractionation or contamination during emplacement. For instance, Rama and Hart (1965) observed significant isotopic fractionation of the ^{20}Ne/^{22}Ne ratio during Ne diffusion experiments using a permeable silica glass membrane. Furthermore, presumably fractionated ^{22}Ne/^{20}Ne ratios lower than air have been previously noted for rocks with high Ne abundances analysed at the GFZ noble gas laboratory (S. Niedermann, personal communication, 2009). Sample OR3 displays a ^{20}Ne abundance of 1262 ± 65 × 10^{-12} cm^3 STP/g at 1750 ºC, and a total ^{20}Ne abundance of 1525 ± 66 × 10^{-12} cm^3 STP/g - significantly higher than for any other sample in this study (**Table 6.1**).

6.3 ^{3}He and ^{21}Ne excesses

The calculation of ^{3}He and ^{21}Ne minimum exposure ages and maximum erosion rates requires the determination of the cosmogenic excesses of ^{3}He and ^{21}Ne. As discussed in Section 4.8, these excesses are calculated from equations 4.31 and 4.32, reproduced here for the sake of clarity:

$$^{3}He_{ex} = \left[\left(^{3}He/^{4}He\right)_{m} - \left(^{3}He/^{4}He\right)_{tr}\right] \times {}^{4}He_{m} \tag{4.31}$$

$$^{21}Ne_{ex} = \left[\left(^{21}Ne/^{20}Ne\right)_{m} - \left(^{21}Ne/^{20}Ne\right)_{tr}\right] \times {}^{20}Ne_{m} \tag{4.32}$$

where the subscripts *ex, m* and *tr* denote excess, measured and trapped. Thus values for the isotopic ratios of the trapped, non-cosmogenic components, (^{3}He/^{4}He)$_{tr}$ and (^{21}Ne/^{20}Ne)$_{tr}$, must be assumed.

6.3.1 The trapped $^{3}He/^{4}He$ ratio

For $(^{3}He/^{4}He)_{tr}$, measurements of $^{3}He/^{4}He$ made after crushing *in vacuo* are considered, as these measurements reflect the $^{3}He/^{4}He$ ratio of He trapped in fluid inclusions and grain boundaries. Crushing of samples DV5, GD2 and IT1 yielded $^{3}He/^{4}He$ ratios of $(0.022 \pm 0.010) \times 10^{-6}$, $(0.050 \pm 0.036) \times 10^{-6}$ and $(0.060 \pm 0.011) \times 10^{-6}$ respectively (**Table 6.1**). However, these measurements are likely overestimates for the true $(^{3}He/^{4}He)$ value of total non-cosmogenic He, because additional (radiogenic) ^{4}He is produced *in situ* within the crystal lattice of these relatively old (~183 Ma; Duncan *et al*., 1997) pyroxenes. Therefore, a $(^{3}He/^{4}He)_{tr}$ value of $(0.035 \pm 0.035) \times 10^{-6}$ was assumed for all samples in this study.

6.3.2 The trapped $^{21}Ne/^{20}Ne$ ratio

As discussed in Section 6.2.2, analyses of most samples (with the exception of samples IT1, IT6 and OR3) display Ne isotope ratios that are consistent with, although not necessarily indicative of, a mixture of air and cosmogenic Ne with no other significant components. Indeed, given the high concentrations of radiogenic ^{4}He in some samples ($> 1 \times 10^{-5}$ cm^3 STP/g), it is possible that nucleogenic ^{22}Ne and ^{21}Ne may be present in non-negligible quantities.

However, incorporating the possible effect of a non-air and non-cosmogenic Ne component when estimating $(^{21}Ne/^{20}Ne)_{tr}$ is problematic. Sample IT6 displays $^{22}Ne/^{20}Ne$ ratios at 900 ºC and 1750 ºC that are consistent with the presence of nucleogenic ^{22}Ne or a trapped atmospheric component with a fractionated $^{22}Ne/^{20}Ne$ ratio. However, whether nucleogenic ^{21}Ne is also present, or whether fractionation of the $^{21}Ne/^{20}Ne$ ratio of a trapped atmospheric component also occurred, is unknown. Similarly for sample OR3, a mantle component may be present or mass fractionation of the $^{22}Ne/^{20}Ne$ ratio may have occurred, with the effect on the $^{21}Ne/^{20}Ne$ ratio being uncertain. For sample IT1, the significant presence of crustal ^{21}Ne is suggested by the crushing analysis, although this would not have been suspected from the heating analyses alone (**Figure 6.13**). The other two crushing analyses (DV5 and GD2) yielded $^{21}Ne/^{20}Ne$ ratios which are compatible with the composition of air, as were two other crushing analyses reported by Kounov *et al*. (2007) for Karoo dolerite pyroxenes ($^{21}Ne/^{20}Ne = 0.00319 \pm 0.00037$ and 0.00299 ± 0.0010).

Given these considerations and for the sake of consistency, a $(^{21}Ne/^{20}Ne)_{tr}$ value of 0.002959 was assumed for all samples, corresponding to the composition of air (Eberhardt *et al*., 1965), with the caveat that should a sample yield a ^{21}Ne minimum exposure age (T) greater than (or a maximum erosion rate (ε) less than) that indicated by the ^{3}He data, preference will be given to the ^{3}He estimate when interpreting the sample's exposure history. Furthermore, ^{21}Ne exposure histories calculated on this basis for samples IT6 and OR3 must be treated with particular caution, and the ^{21}Ne T and ε values calculated for sample IT1 can only be considered to be maximum and minimum estimates for T and ε, respectively.

6.3.3 Comparison of excesses

$^{3}He_{ex}$ and $^{21}Ne_{ex}$ values were calculated for each heating step according to equations 4.3.1 and 4.3.2. The total $^{3}He_{ex}$ and $^{21}Ne_{ex}$ values for each sample are given in **Table 6.2** with 2σ analytical errors. Some $^{3}He_{ex}$ or $^{21}Ne_{ex}$ values bear asymmetric errors, because for analyses where 2σ relative errors for $(^{3}He/^{4}He)_{m\text{-}tr}$ or $(^{21}Ne/^{20}Ne)_{m\text{-}tr}$ are greater than 100 %, the negative 2σ error was set to 100 %. Similarly, where $(^{3}He/^{4}He)_{m\text{-}tr}$ was less than zero, this value was set to zero to calculate $^{3}He_{ex}$ and the negative 2σ error, and set to $(^{3}He/^{4}He)_{m}$ when calculating the positive 2σ error for $^{3}He_{ex}$. Values in **Table 6.2** are given in atom/g, converted from cm^3 STP/g according to the Loschmidt Constant, 2.686×10^{19} atom/cm^3 STP.

The $^{3}He_{ex}$ and $^{21}Ne_{ex}$ values from **Table 6.2** are plotted in **Figure 6.23**. Lines with slopes of 0.2202, 0.2281 and 0.2140, corresponding to average nuclide production ratios P1($^{21}Ne/^{3}He$), P2($^{21}Ne/^{3}He$) and P3($^{21}Ne/^{3}He$) in **Table 5.5,** are also shown for reference. These lines represent the average cosmogenic nuclide ratios expected from mineral chemistry and the elemental production rates of Masarik and Reedy (1996), Kober *et al*. (2005) and Fenton *et al.* (2009), respectively.

6.4 ^{3}He and ^{21}Ne minimum exposure ages and maximum erosion rates

Minimum exposure ages (T) and maximum erosion rates (ε) were calculated from $^{3}He_{ex}$ and $^{21}Ne_{ex}$ values in **Table 6.2** with the use of the Microsoft Excel add-in CosmoCalc version 1.6, downloaded free of charge from http://cosmocalc.googlepages.com. Details of the program are reported by Vermeesch (2007).

Sample	$^{3}He_{ex}$ (10^{6} atom/g)	2σ (+)	2σ (-)	$^{21}Ne_{ex}$ (10^{6} atom/g)	2σ (+)	2σ (-)
BW3	3.2	1.5	1.2	1.50	0.42	0.34
CB1	5.7	1.6	1.4	2.15	0.41	0.41
DV5	35.3	3.4	3.1	8.93	0.56	0.56
DV6	57.7	6.9	4.6	14.47	0.84	0.84
DV9	43.1	7.3	5.4	11.10	0.83	0.83
GD1	29.5	1.8	1.8	7.19	0.79	0.75
GD2	66.9	4.8	4.8	14.2	1.1	1.1
GD3	84.9	4.5	4.5	18.6	1.3	1.3
GR1	36.3	5.0	4.1	8.8	1.3	1.3
GR2	14.8	3.8	3.1	5.12	0.61	0.61
GR3	36.2	4.6	4.6	9.42	0.78	0.78
GR5	78.3	5.3	5.3	19.0	1.5	1.5
IT1	34	16	12	10.40	0.77	0.77
IT3	121	24	24	22.6	1.1	1.1
IT5	76.3	5.7	5.7	18.7	1.0	1.0
IT6	27.4	6.6	6.6	6.00	0.63	0.63
IT8	129	19	19	23.4	1.3	1.3
IT9	110	17	17	19.6	1.1	1.1
IT10	149	18	18	26.5	1.5	1.5
OR1	29.3	2.3	2.3	7.47	0.60	0.60
OR2	50.4	3.1	3.1	12.15	0.87	0.87
OR3	44.3	3.2	3.2	11.2	2.3	2.2

Table 6.2: ^{3}He and ^{21}Ne excesses calculated for all samples in 10^{6} atoms per gram of pyroxene.

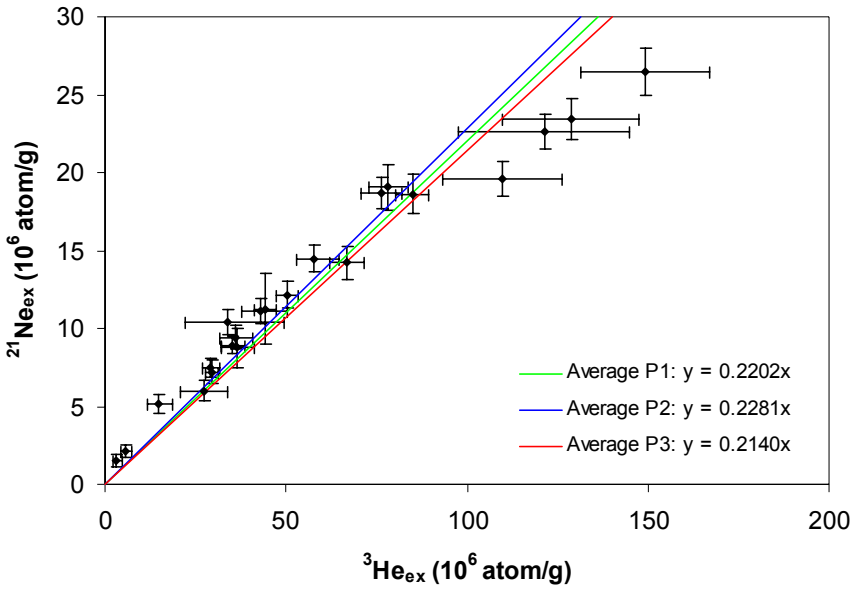

Figure 6.23: ^{3}He vs. ^{21}Ne excesses with 2σ analytical error for all samples in 10^6 atom/g. Lines corresponding to average expected cosmogenic nuclide ratios, based on mineral chemistry and three sets of elemental production rates (**Table 5.5**) are shown for reference.

Default settings were used, with the exception of the exponent of topographic shielding: m = 2.3 (e.g. Gosse and Phillips, 2001; Niedermann, 2002); the rock density: ρ = 3.0 g/cm^3 (e.g. Maré and Cole, 2006); and the sample-specific cosmogenic ^{3}He and ^{21}Ne production rates, where chemistry-dependent production rates calculated from Fenton *et al*. (2009) were used (P3 values in **Table 5.5**). Topographic shielding factors used are given in **Table 5.1**, and results are reported according to both Lal's (1991) and Dunai's (2000a) scaling factors.

Additionally, true erosion rates for inclined surfaces were calculated from apparent erosion rates determined in CosmoCalc by application of the numerical approximation of Hermanns *et al*. (2004) discussed in Section 4.6:

$$\varepsilon = \frac{\varepsilon^*}{\left(1 + \frac{\alpha^2}{5000}\right)} \tag{4.30}$$

where ε is the true erosion rate, ε* is the apparent erosion rate and α is the slope angle in degrees (surface dip values reported in **Table 5.1**).

The ^{3}He and ^{21}Ne minimum exposure ages and "true" maximum erosion rates for samples are given in **Tables 6.3** and **6.4,** respectively, and are shown graphically in **Figures 6.24**, **6.25** and **6.26**, according to all four nuclide and scaling factor combinations. Uncertainties for both the minimum exposure ages and maximum erosion rates reflect the standard propagation of the 2σ analytical uncertainties in $^3He_{ex}$ and $^{21}Ne_{ex}$. ^{3}He minimum exposure ages range from 18.5 +5.0/-4.7 ka for sample CB1 to 583 ± 69 ka for sample IT10 according to Lal's (1991) scaling method, or from 20.3 +5.6/-5.2 ka to 656 ± 78 ka for the same samples according to Dunai's (2000a) scaling. The corresponding ^{21}Ne minimum exposure ages for these samples are 32.1 ± 6.1 ka and 488 ± 27 (samples CB1 and IT10 respectively; Lal (1991) scaling) or 35.4 ± 6.7 ka and 550 ± 31 ka (also samples CB1 and IT10 respectively; Dunai (2000a) scaling). Whilst CB1 yields the lowest ^{21}Ne minimum exposure age, sample IT5 yields the highest ^{21}Ne minimum exposure age: 514 ± 28 ka (Lal (1991) scaling) or 587 ± 32 ka (Dunai (2000a) scaling).

Sample	Minimum exposure age											
	^{3}He						^{21}Ne					
	Lal (1991) scaling			Dunai (2000a) scaling			Lal (1991) scaling			Dunai (2000a) scaling		
	T (ka)	2σ (+)	2σ (-)	T (ka)	2σ (+)	2σ (-)	T (ka)	2σ (+)	2σ (-)	T (ka)	2σ (+)	2σ (-)
BW3	29	14	11	33	16	12	63	18	14	70	20	16
CB1	18.5	5.0	4.7	20.3	5.6	5.2	32.1	6.1	6.1	35.4	6.7	6.7
DV5	182	18	16	205	20	18	219	14	14	248	16	16
DV6	299	36	24	337	40	27	356	21	21	403	23	23
DV9	214	36	27	241	41	30	264	20	20	298	22	22
GD1	198	12	12	219	13	13	225	25	23	249	27	26
GD2	224	16	16	248	18	18	222	17	17	246	18	18
GD3	284	15	15	315	17	17	292	20	20	324	22	22
GR1	148	20	17	165	23	19	164	24	24	183	27	27
GR2	60	15	12	67	17	14	95	11	11	106	13	13
GR3	139	18	18	155	20	20	170	14	14	189	16	16
GR5	228	15	15	251	17	17	253	20	20	278	21	21
IT1	162	74	55	184	85	63	244	18	18	277	21	21
IT3	530	100	100	600	120	120	449	23	23	507	26	26
IT5	423	32	32	483	36	36	514	28	28	587	32	32
IT6	314	75	75	359	86	86	336	36	36	384	41	41
IT8	504	74	74	568	83	83	424	24	24	478	27	27
IT9	430	65	65	484	73	73	352	20	20	396	23	23
IT10	583	69	69	656	78	78	488	27	27	550	31	31
OR1	129	10	10	146	12	12	152	12	12	171	14	14
OR2	210	13	13	236	15	15	231	17	17	260	19	19
OR3	180	13	13	201	14	14	209	42	42	235	48	47

Table 6.3: ^{3}He and ^{21}Ne minimum exposure ages, according to the production rates calculated from Fenton *et al*. (2009). Results are reported according to the scaling factors of both Lal (1991) and Dunai (2000a).

Sample	Maximum erosion rate											
	^{3}He						^{21}Ne					
	Lal (1991) scaling			Dunai (2000a) scaling			Lal (1991) scaling			Dunai (2000a) scaling		
	ε (m/Myr)	2σ (+)	2σ (-)	ε (m/Myr)	2σ (+)	2σ (-)	ε (m/Myr)	2σ (+)	2σ (-)	ε (m/Myr)	2σ (+)	2σ (-)
BW3	6.9	2.5	3.3	6.2	2.3	3.0	3.26	0.75	0.92	2.91	0.67	0.82
CB1	20.8	5.3	5.7	18.9	4.8	5.2	12.0	2.3	2.3	10.9	2.0	2.0
DV5	2.94	0.26	0.28	2.60	0.23	0.25	2.43	0.15	0.15	2.15	0.14	0.14
DV6	1.79	0.14	0.21	1.58	0.13	0.19	1.497	0.087	0.087	1.325	0.077	0.077
DV9	2.45	0.31	0.41	2.17	0.27	0.37	1.98	0.15	0.15	1.76	0.13	0.13
GD1	1.031	0.063	0.063	0.929	0.057	0.057	0.905	0.094	0.099	0.817	0.085	0.090
GD2	2.33	0.17	0.17	2.11	0.15	0.15	2.36	0.18	0.18	2.12	0.16	0.16
GD3	1.82	0.10	0.10	1.644	0.088	0.088	1.78	0.12	0.12	1.60	0.11	0.11
GR1	3.61	0.41	0.49	3.23	0.37	0.44	3.25	0.48	0.48	2.91	0.43	0.43
GR2	8.9	1.8	2.3	8.0	1.6	2.1	5.64	0.67	0.67	5.05	0.60	0.60
GR3	3.75	0.47	0.47	3.37	0.43	0.43	3.08	0.25	0.25	2.77	0.23	0.23
GR5	2.33	0.16	0.16	2.13	0.14	0.14	2.11	0.16	0.16	1.92	0.15	0.15
IT1	3.3	1.1	1.5	2.9	1.0	1.3	2.19	0.16	0.16	1.92	0.14	0.14
IT3	1.01	0.20	0.20	0.89	0.17	0.17	1.189	0.060	0.060	1.052	0.053	0.053
IT5	1.257	0.094	0.094	1.101	0.082	0.082	1.034	0.056	0.056	0.905	0.049	0.049
IT6	0.65	0.16	0.16	0.57	0.14	0.14	0.606	0.064	0.064	0.530	0.056	0.056
IT8	1.06	0.15	0.15	0.94	0.14	0.14	1.258	0.071	0.071	1.116	0.063	0.063
IT9	1.24	0.19	0.19	1.10	0.17	0.17	1.516	0.087	0.087	1.346	0.077	0.077
IT10	0.92	0.11	0.11	0.813	0.097	0.097	1.092	0.061	0.061	0.969	0.054	0.054
OR1	3.49	0.28	0.28	3.10	0.25	0.25	2.97	0.24	0.24	2.64	0.21	0.21
OR2	2.54	0.16	0.16	2.26	0.14	0.14	2.30	0.16	0.16	2.05	0.15	0.15
OR3	2.95	0.21	0.21	2.63	0.19	0.19	2.53	0.50	0.51	2.26	0.45	0.45

Table 6.4: ^{3}He and ^{21}Ne maximum erosion rates, according to the production rates calculated from Fenton *et al*. (2009). Results are reported according to the scaling factors of both Lal (1991) and Dunai (2000a).

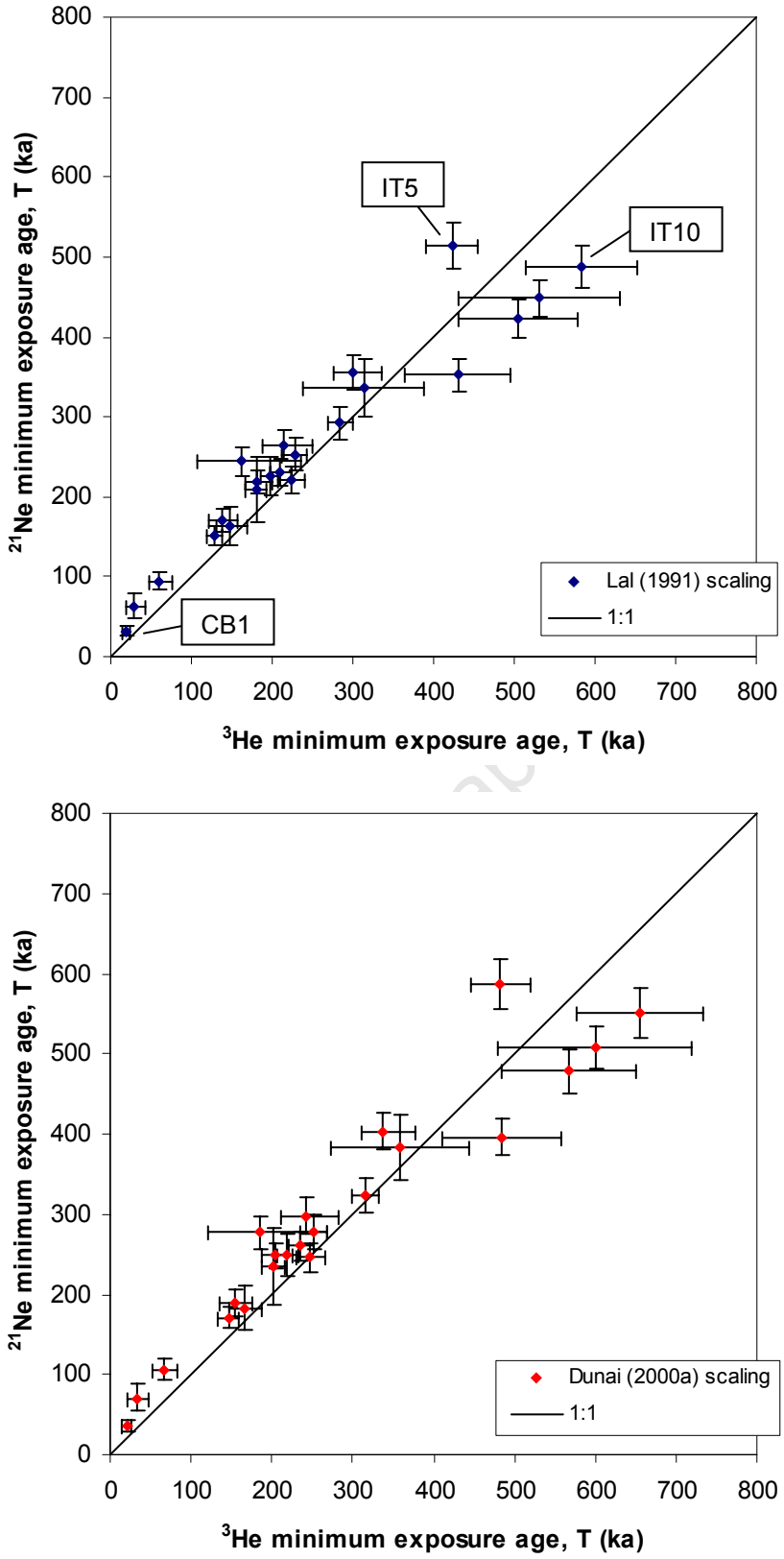

Figure 6.24: ^{3}He vs. ^{21}Ne minimum exposure ages according to the nuclide production rate of Fenton *et al.* (2009) and the scaling factors of Lal (1991), top, and Dunai (2000a), bottom.

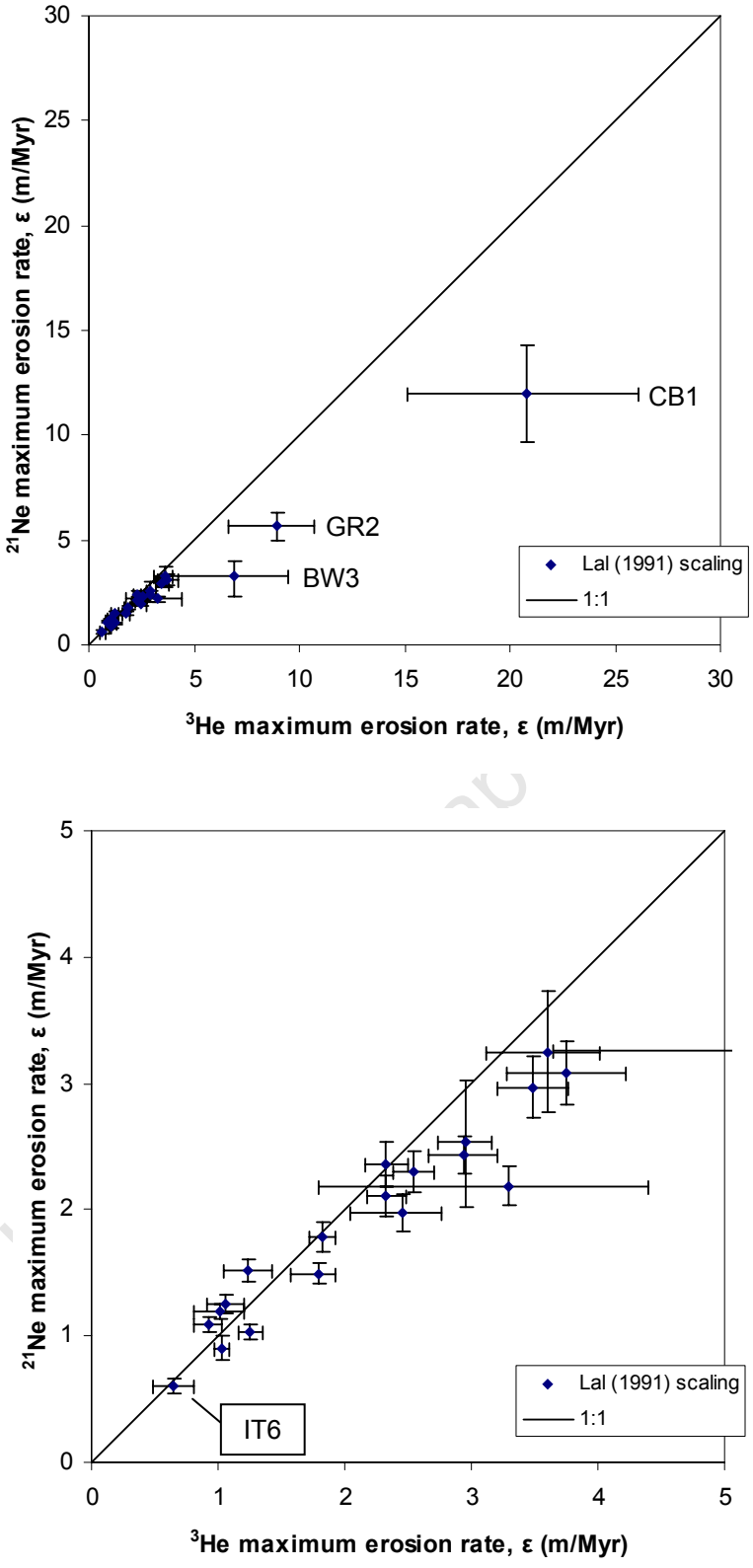

Figure 6.25: Top: ^{3}He vs. ^{21}Ne maximum erosion rates according to the nuclide production rate of Fenton *et al.* (2009) and the scaling factor of Lal (1991). Bottom: Detail of maximum erosion rates of 0-5 m/Myr.

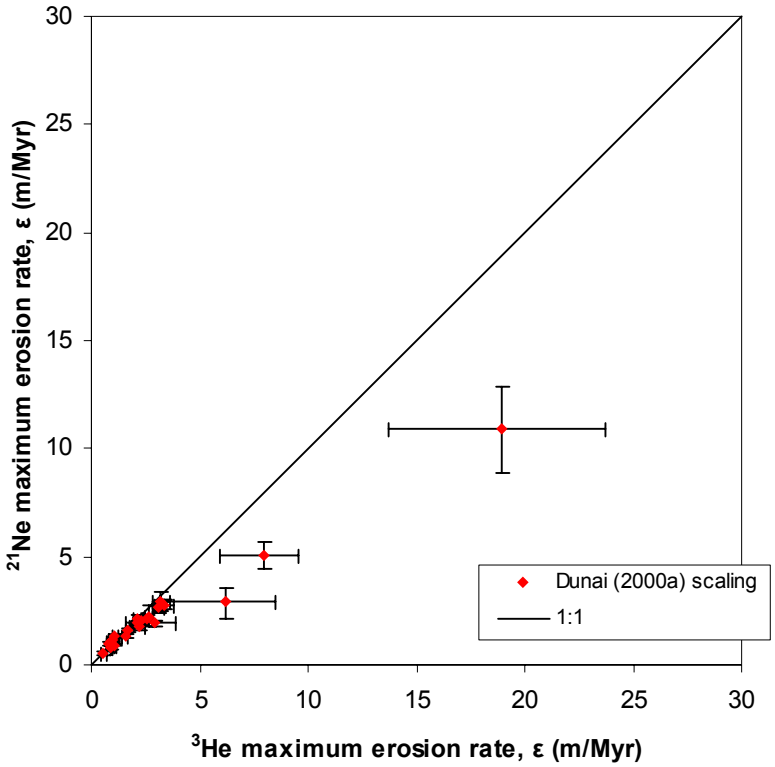

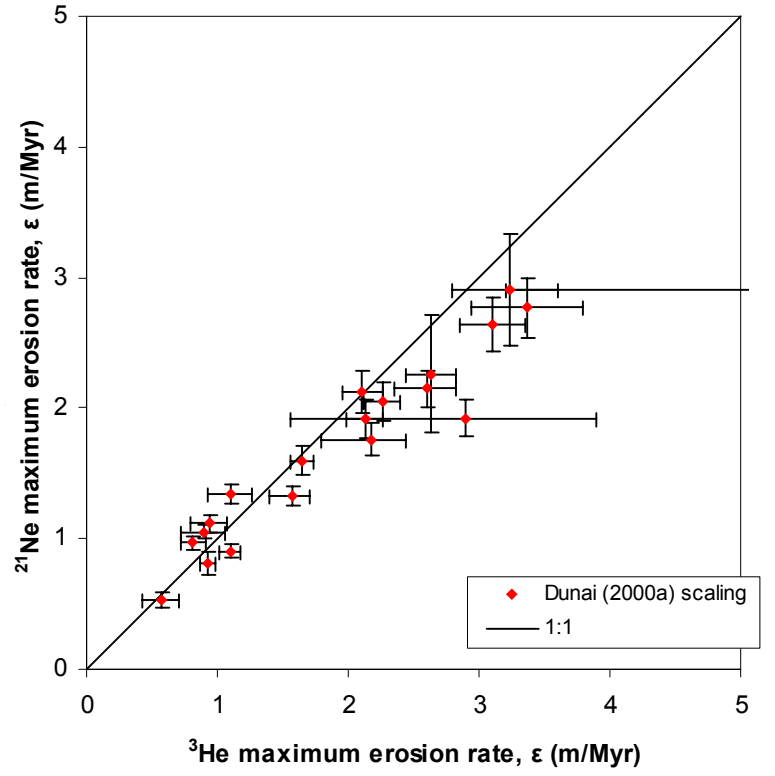

Figure 6.26: Top: ^{3}He vs. ^{21}Ne maximum erosion rates according to the nuclide production rate of Fenton *et al.* (2009) and the scaling factor of Dunai (2000a). Bottom: Detail of maximum erosion rates of 0-5 m/Myr.

Sample CB1 also yields the highest maximum erosion rate estimates: 20.8 +5.3/-5.7 m/Myr (Lal (1991) scaling) or 18.9 +4.8/-5.2 m/Myr (Dunai (2000a) scaling) for ^{3}He, and 12.0 ± 2.3 m/Myr (Lal (1991) scaling) or 10.9 ± 2.0 m/Myr (Dunai (2000a) scaling) for ^{21}Ne. Sample IT6 yields the lowest maximum erosion rate estimates: 0.65 ± 0.16 m/Myr (Lal (1991) scaling) or 0.57 ± 0.14 m/Myr (Dunai (2000a) scaling) for ^{3}He, and 0.606 ± 0.064 m/Myr (Lal (1991) scaling) or 0.530 ± 0.056 m/Myr (Dunai (2000a) scaling) for ^{21}Ne. It may be noted that with the exception of three samples (BW3, CB1 and GR2), the range of all other maximum erosion rate estimates, including analytical error, is less than 5 m/Myr for Lal (1991) scaling, or less than 4 m/Myr for Dunai (2000a) scaling (**Figures 6.25** and **6.26**).

6.4.1 Comparison of ^{3}He and ^{21}Ne minimum exposure ages

Of the 22 samples analysed in this study, ^{3}He and ^{21}Ne minimum exposure ages agree within 2σ analytical error limits for 16 samples using Lal (1991) scaling, and also agree for 16 samples using Dunai (2000a) scaling (**Table 6.3**). In all of the cases where ages do not agree (samples BW3, CB1, DV5, GR2, IT5 and OR1 for Lal (1991) scaling, and samples BW3, CB1, DV5, DV6, GR2 and IT5 for Dunai (2000a) scaling), ^{21}Ne ages are higher than ^{3}He ages. These samples include the three samples with the lowest ^{3}He and ^{21}Ne excesses, BW3, CB1 and GR2, suggesting that because these samples have a lower cosmogenic ^{21}Ne concentration, a nucleogenic ^{21}Ne component may become significant. Only 5 samples (GD2, IT3, IT8, IT9 and IT10 according to both scaling factors) yielded ^{3}He ages greater than, although within analytical error of, ^{21}Ne ages. Despite the reservations expressed in Section 6.3.2 over the accuracy of cosmogenic ^{21}Ne estimates for samples IT1, IT6 and OR3, the ^{21}Ne ages for these samples agree with the corresponding ^{3}He ages within error limits.

Whilst higher ^{21}Ne ages may be due to the presence of nucleogenic ^{21}Ne, this is difficult to verify or correct for. Although a high abundance of radiogenic ^{4}He may theoretically indicate a higher abundance of ^{21}Ne, as nucleogenic ^{21}Ne is a by-product of α-decay, no significant positive correlation between the difference between the ^{21}Ne and ^{3}He minimum exposure ages and the abundance of radiogenic ^{4}He exists (**Figure 6.27**). Indeed, some of the samples with the highest ^{4}He abundances yield ^{3}He ages that are higher than, although within error of, their corresponding ^{21}Ne ages. A higher ^{4}He abundance also suggests that the corresponding ^{3}He ages are unlikely to

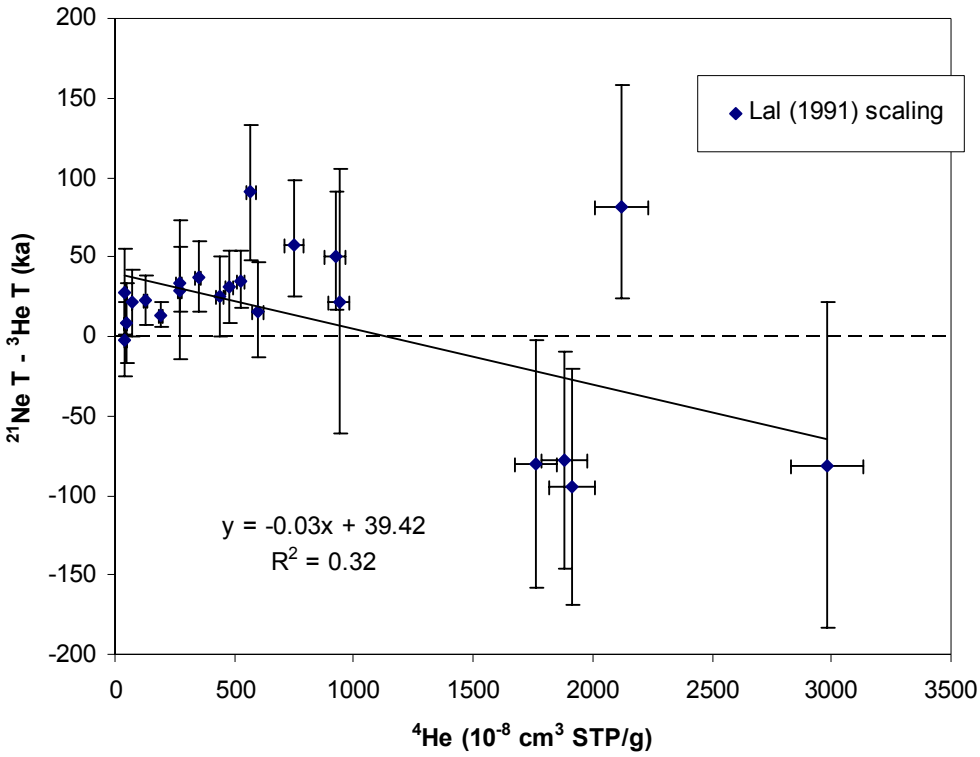

Figure 6.27: Comparison of the difference between ^{21}Ne and ^{3}He minimum exposure ages (according to Lal (1991) scaling) and ^{4}He abundances. A negative regression line where $R^2 = 0.32$ indicates that no positive correlation exists. Therefore, if higher ^{21}Ne T estimates are a result of a significant nucleogenic ^{21}Ne component, the ^{4}He abundance cannot be used as a proxy for the nucleogenic ^{21}Ne contribution.

be erroneously high as a result of the assumed value for $(^3He/^4He)_{tr}$ being too low. However, it may also be noted that samples with a high abundance of ^4He have relatively high analytical uncertainties, due to the small relative excesses in $^3He/^4He$ and the pumping of the mass spectrometer required for ^4He measurements greater than 10 V (Section 4.9).

6.4.2 Comparison of ^3He and ^{21}Ne maximum erosion rates

A comparison of the ^3He and ^{21}Ne maximum erosion rates corresponds closely with the comparison of the ^3He and ^{21}Ne minimum exposure ages given above. Five samples yielded ^3He and ^{21}Ne maximum erosion rates that do not agree within error limits for both Lal's (1991) and Dunai's (2000a) scaling factors. For four of these samples, CB1, DV5, GR2 and IT5, ^{21}Ne maximum erosion rates are lower than ^3He maximum erosion rates. The fifth sample, IT10, yielded ^3He maximum erosion rates lower than the corresponding ^{21}Ne maximum erosion rates. Just as samples GD2, IT3, IT8 and IT9 yielded ^3He minimum exposure ages greater than, although within analytical error of, their corresponding ^{21}Ne ages, these samples yielded ^3He maximum erosion rates lower than, although within error of, their corresponding ^{21}Ne maximum erosion rates.

6.5 Argon

The measured ^{40}Ar abundances, as well as the measured $^{40}Ar/^{36}Ar$ and $^{38}Ar/^{36}Ar$ ratios, are presented in **Table 6.5**. The ^{36}Ar abundances, calculated from the ^{40}Ar and $^{40}Ar/^{36}Ar$ measurements, are also given. $^{38}Ar/^{36}Ar$ ratios for all measurements are plotted in **Figure 6.28**. Although most samples plot within analytical error of the $^{38}Ar/^{36}Ar$ ratio of air, a number of analyses display elevated $^{38}Ar/^{36}Ar$ ratios that may be explained by the presence of a cosmogenic ^{38}Ar component.

6.5.1 Cosmogenic ^{38}Ar

The cosmogenic ^{38}Ar abundance, $^{38}Ar_c$, may be calculated according to equation 4.33 as discussed in Section 4.8, and reproduced below:

$$^{38}Ar_c = \frac{(38/36)_{sp}}{(38/36)_{sp} - (38/36)_{air}} \times \{36_{tot}\left[(38/36)_{tot} - (38/36)_{air}\right] + 36_{Cl}(38/36)_{air}\}$$

Sample	Mass	T	^{40}Ar		^{40}Ar/^{36}Ar		^{36}Ar		^{38}Ar/^{36}Ar	
	g	ºC	10^{-8} cm^3 STP/g	± 2σ		± 2σ	10^{-8} cm^3 STP/g	± 2σ		± 2σ
BW3	0.50102	600	11.87	0.59	308.6	1.7	0.0385	0.0019	0.1884	0.0013
		900	6.84	0.36	659	11	0.01039	0.00060	0.1891	0.0020
		1750	10.27	0.52	583.3	6.8	0.01760	0.00093	0.1883	0.0013
		Total	***28.98***	***0.87***	**436.1**	**5.3**	***0.0665***	***0.0022***	**0.18847**	**0.00087**
CB1	0.48028	900	26.1	1.3	416.4	3.0	0.0626	0.0032	0.1882	0.0011
		1750	13.25	0.67	823.7	7.8	0.01609	0.00085	0.1877	0.0017
		Total	***39.3***	***1.5***	**499.7**	**5.5**	***0.0787***	***0.0033***	**0.18807**	**0.00094**
DV5	0.50352	900	15.4	1.7	475.9	3.9	0.0324	0.0036	0.1881	0.0021
		1750	6.75	0.50	727	16	0.00928	0.00074	0.1930	0.0037
		Total	***22.2***	***1.7***	**531.7**	**7.3**	***0.0417***	***0.0036***	**0.1891**	**0.0018**
	0.51124	*Crushed*	*1.259*	*0.064*	*391.4*	*5.2*	*0.00322*	*0.00017*	*0.1886*	*0.0023*
DV6	0.50356	900	11.37	0.58	572.8	5.2	0.0199	0.0011	0.1879	0.0014
		1750	10.96	0.57	988	23	0.01109	0.00070	0.1947	0.0022
		Total	***22.33***	***0.82***	**722**	**11**	***0.0309***	***0.0013***	**0.1903**	**0.0012**
DV9	0.50052	900	12.3	1.2	638	11	0.0193	0.0019	0.1881	0.0018
		1750	15.0	1.5	844	14	0.0177	0.0018	0.1893	0.0027
		Total	***27.3***	***1.9***	**736**	**11**	***0.0370***	***0.0026***	**0.1886**	**0.0016**
GD1	0.50352	600	6.99	0.35	353.9	3.0	0.0197	0.0010	0.1882	0.0014
		900	5.82	0.31	564.0	7.8	0.01032	0.00060	0.1883	0.0015
		1750	32.6	1.6	378.1	1.9	0.0863	0.0044	0.18859	0.00098
		Total	***45.4***	***1.7***	**390.5**	**1.9**	***0.1164***	***0.0045***	**0.18850**	**0.00077**
GD2	0.51466	900	11.0	1.0	435.8	5.4	0.0253	0.0024	0.1877	0.0022
		1750	14.5	1.4	421.0	8.6	0.0344	0.0034	0.1893	0.0026
		Total	***25.5***	***1.7***	**427.3**	**5.5**	***0.0597***	***0.0042***	**0.1886**	**0.0018**
	0.52240	*Crushed*	*21.0*	*1.1*	*324.6*	*1.7*	*0.0647*	*0.0033*	*0.1877*	*0.0011*
GD3	0.48336	900	7.37	0.38	429.3	3.5	0.01718	0.00092	0.1884	0.0013
		1750	22.9	1.1	393.8	2.9	0.0580	0.0030	0.1892	0.0011
		Total	***30.2***	***1.2***	**401.9**	**2.4**	***0.0752***	***0.0031***	**0.18905**	**0.00088**
GR1	0.50178	900	11.62	0.59	418.2	2.7	0.0278	0.0014	0.1883	0.0015
		1750	19.9	1.0	352.1	1.8	0.0565	0.0029	0.1882	0.0012
		Total	***31.5***	***1.2***	**373.9**	**1.8**	***0.0843***	***0.0032***	**0.18824**	**0.00097**
GR2	0.50070	900	16.11	0.82	880.9	9.5	0.0183	0.0010	0.1879	0.0017
		1750	18.31	0.92	693.2	5.4	0.0264	0.0014	0.1878	0.0015
		Total	***34.4***	***1.2***	**770.0**	**6.0**	***0.0447***	***0.0017***	**0.1878**	**0.0011**
GR3	0.52566	900	16.4	1.5	394.3	5.4	0.0417	0.0039	0.1879	0.0018
		1750	10.5	1.0	829	14	0.0127	0.0012	0.1898	0.0025
		Total	***26.9***	***1.8***	**496**	**11**	***0.0544***	***0.0041***	**0.1883**	**0.0015**
GR5	0.48144	900	7.70	0.40	379.4	2.9	0.0203	0.0011	0.1879	0.0013
		1750	14.83	0.75	336.8	2.4	0.0440	0.0022	0.18942	0.00092
		Total	***22.52***	***0.85***	**350.3**	**2.0**	***0.0643***	***0.0025***	**0.18894**	**0.00074**
IT1	0.52212	900	16.6	1.5	573.8	6.3	0.0289	0.0027	0.1882	0.0021
		1750	21.4	2.0	1409	21	0.0152	0.0014	0.1887	0.0020
		Total	***38.0***	***2.5***	**862**	**26**	***0.0441***	***0.0031***	**0.1884**	**0.0016**
	0.53060	*Crushed*	*10.08*	*0.51*	*1249*	*12*	*0.00807*	*0.00042*	*0.1875*	*0.0015*
IT3	0.50018	900	15.56	0.79	538.8	4.4	0.0289	0.0015	0.1878	0.0013
		1750	21.7	1.1	1113	10	0.0195	0.0010	0.1910	0.0013
		Total	***37.3***	***1.3***	**770**	**11**	***0.0484***	***0.0018***	**0.18906**	**0.00095**
IT5	0.50190	900	20.6	1.0	709.5	6.2	0.0290	0.0015	0.1879	0.0014
		1750	28.3	1.4	1476	14	0.0192	0.0010	0.1909	0.0011
		Total	***48.9***	***1.8***	**1015**	**15**	***0.0482***	***0.0018***	**0.18905**	**0.00093**
IT6	0.50024	600	9.65	0.48	358.5	2.5	0.0269	0.0014	0.1887	0.0014
		900	8.95	0.46	1377	36	0.00650	0.00042	0.1895	0.0031
		1750	40.7	2.0	3266	41	0.01247	0.00067	0.1894	0.0018
		Total	***59.3***	***2.1***	**1293**	**40**	***0.0459***	***0.0016***	**0.1890**	**0.0010**
IT8	0.50388	900	7.84	0.41	538.7	5.4	0.01454	0.00080	0.1881	0.0012
		1750	11.61	0.59	1318	19	0.00880	0.00049	0.1958	0.0013
		Total	***19.44***	***0.71***	**833**	**15**	***0.02335***	***0.00093***	**0.19104**	**0.00091**
IT9	0.49022	900	43.8	2.7	345.6	3.7	0.1266	0.0079	0.1878	0.0023
		1750	56.8	3.4	352.6	2.9	0.1610	0.0098	0.1877	0.0019
		Total	***100.5***	***4.4***	**349.5**	**2.3**	***0.288***	***0.013***	**0.1877**	**0.0015**
IT10	0.50202	900	11.96	0.61	530.2	5.0	0.0226	0.0012	0.1881	0.0018
		1750	13.06	0.66	1523	24	0.00858	0.00048	0.1973	0.0013
		Total	***25.02***	***0.90***	**804**	**16**	***0.0311***	***0.0013***	**0.1906**	**0.0013**
OR1	0.50602	900	23.3	1.2	472.2	2.6	0.0494	0.0025	0.1880	0.0011
		1750	23.5	1.2	647.5	4.0	0.0363	0.0019	0.1885	0.0012
		Total	***46.8***	***1.7***	**546.4**	**3.8**	***0.0857***	***0.0031***	**0.18819**	**0.00081**
OR2	0.50038	900	11.74	0.60	460.4	3.7	0.0255	0.0013	0.1874	0.0015
		1750	12.11	0.61	545.7	5.8	0.0222	0.0012	0.1900	0.0015
		Total	***23.85***	***0.86***	**500.1**	**3.7**	***0.0477***	***0.0018***	**0.1886**	**0.0011**
OR3	0.50940	900	15.91	0.81	347.6	1.6	0.0458	0.0023	0.1877	0.0012
		1750	58.3	2.9	311.0	1.1	0.1874	0.0094	0.18929	0.00090
		Total	***74.2***	***3.0***	**318.2**	**1.0**	***0.2332***	***0.0097***	**0.18898**	**0.00076**

Table 6.5: Results of all ^{40}Ar, ^{40}Ar/^{36}Ar and ^{38}Ar/^{36}Ar measurements after heating or crushing. Calculated ^{36}Ar abundances and totals from heating measurements are also given.

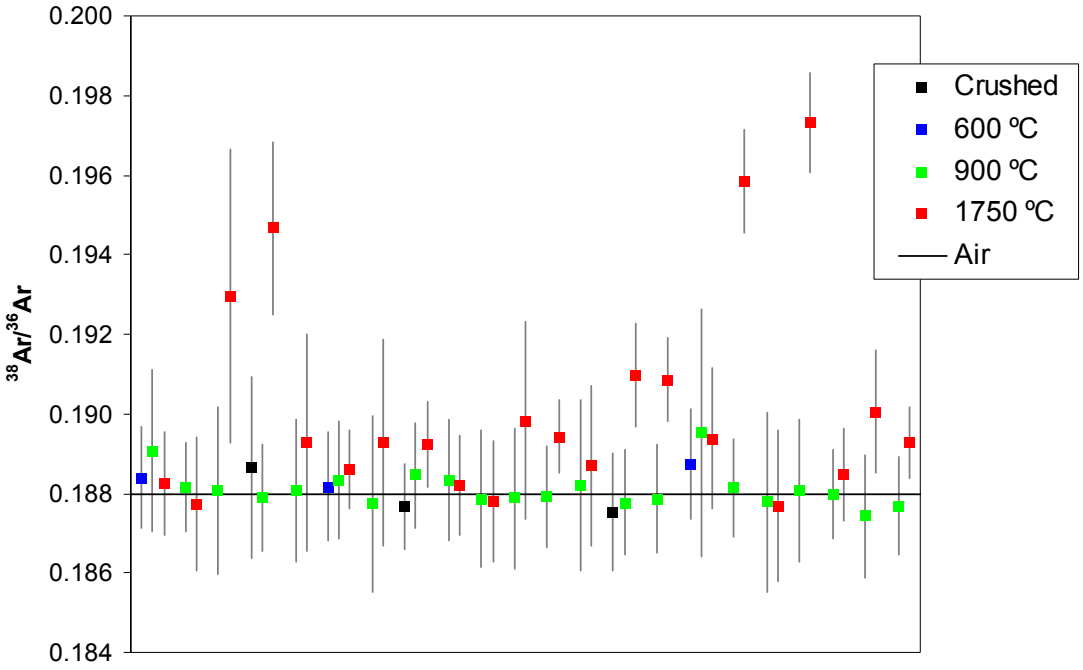

Figure 6.28: $^{38}Ar/^{36}Ar$ analyses presented in **Table 6.5**. Although the majority of analyses plot within error of the composition of air ($^{38}Ar/^{36}Ar$ = 0.1880; Nier, 1950), 10 of the analyses at 1750 ºC display significantly higher $^{38}Ar/^{36}Ar$ values, which may be attributed to a cosmogenic Ar component.

(4.33)

where 38 and 36 denote the respective Ar isotopes, the subscript *tot* denotes total measured, *air* denotes the assumed ratio in air, *sp* denotes the spallation production rate and *Cl* denotes the concentration produced by thermal and epithermal neutron capture of ^{35}Cl and subsequent decay of ^{36}Cl to ^{36}Ar (Niedermann *et al*., 2007).

The term $36_{tot}[(38/36)_{tot} - (38/36)_{air}]$, which is termed here simply as the ^{38}Ar excess, $^{38}Ar_{ex}$, was calculated based on an assumed $(38/36)_{air}$ value of 0.1880 (Nier, 1950). Whilst the isotopic composition of air has been more recently re-determined by Lee *et al.* (2006) as 0.1885 ± 0.0005, slightly higher than Nier's (1950) value of 0.1880 ± 0.0003, a value of 0.1880 is assumed because this value is used for calibration of the mass spectrometer (e.g. Niedermann *et al*., 2007). $^{38}Ar_{ex}$ values are given in **Table 6.6**.

6.5.2 The $^{38}Ar/^{36}Ar$ spallation production ratio

The term $(38/36)_{sp,}$ the ^{38}Ar/^{36}Ar spallation production ratio, is more complicated to determine. For Ca-bearing minerals with negligible K content, such as these pyroxene separates (**Table 5.4**), the production ratio $(38/36)_{sp}$ may be assumed to be equivalent to the inverse of the net time-dependent production ratio from Ca, $(^{36}Ar/^{38}Ar)_{Ca}$, given by Renne *et al*. (2001) as:

$$\left(\frac{^{36}Ar}{^{38}Ar}\right)_{Ca} = \frac{P(^{36}Ar_{Ca}) + P(^{36}Cl_{Ca}) \cdot (1 - e^{-\lambda t})}{P(^{38}Ar_{Ca})}$$

(6.1)

where $P(^{36}Ar_{Ca})$ and $P(^{38}Ar_{Ca})$ are the direct cosmogenic production rates of ^{36}Ar and ^{38}Ar from Ca, $P(^{36}Cl_{Ca})$ is the cosmogenic production rate of ^{36}Cl from Ca, λ is the decay constant for the β^- decay of ^{36}Cl to ^{36}Ar, and t is the exposure age of the sample in question.

For $P(^{38}Ar_{Ca})$, a value of 195.1 atom/g Ca/yr (at sea level and high latitude) is used in this study. This is calculated from the relation:

$$P(^{38}Ar_{Ca}) = 1.704 \times P(^{3}He_{tot})$$

(6.2)

Sample	$^{38}Ar_{ex}$			$(38/36)_{sp}$			^{36}Cl			$^{38}Ar_C$		
	10^6 atom/g	+ 2σ	- 2σ		+2σ	-2σ	10^6 atom/g	+ 2σ	- 2σ	10^6 atom/g Ca	+ 2σ	- 2σ
BW3	8	16	5	2.65	0.53	0.53	0.055	0.062	0.055	70	130	70
CB1	3	20	3	2.71	0.54	0.54	0.10	0.10	0.10	20	180	20
DV5	13	20	9	2.10	0.42	0.42	0.62	0.62	0.62	130	210	130
DV6	19.9	9.3	6.5	1.88	0.38	0.38	1.0	1.0	1.0	210	120	50
DV9	6	16	6	2.02	0.41	0.41	0.76	0.77	0.76	60	160	60
GD1	16	24	14	2.06	0.41	0.41	0.51	0.51	0.51	120	190	120
GD2	12	28	12	2.01	0.40	0.40	1.2	1.2	1.2	100	230	100
GD3	21	18	17	1.90	0.38	0.38	1.5	1.5	1.5	170	150	130
GR1	5	22	4	2.18	0.44	0.44	0.63	0.64	0.63	50	190	50
GR2	0	12	0	2.50	0.50	0.50	0.26	0.27	0.26	0	130	0
GR3	6	20	6	2.21	0.44	0.44	0.63	0.63	0.63	60	200	60
GR5	17	13	11	2.00	0.40	0.40	1.4	1.4	1.4	140	110	80
IT1	4	18	3	2.14	0.44	0.44	0.59	0.65	0.59	40	180	40
IT3	16	11	7	1.66	0.33	0.34	2.2	2.2	2.2	300	230	120
IT5	15	11	6	1.74	0.35	0.35	1.4	1.4	1.4	150	120	60
IT6	13	13	7	1.86	0.38	0.38	0.49	0.50	0.49	130	140	90
IT8	19.1	5.7	3.2	1.67	0.34	0.34	2.3	2.3	2.3	280	120	40
IT9	0	98	0	1.73	0.35	0.35	1.9	2.0	1.9	0	1500	0
IT10	22	11	3	1.63	0.33	0.33	2.6	2.7	2.6	300	170	60
OR1	4	18	4	2.24	0.45	0.45	0.51	0.51	0.51	40	170	40
OR2	12	11	9	2.03	0.41	0.41	0.87	0.87	0.87	110	100	80
OR3	65	47	45	2.10	0.42	0.42	0.77	0.77	0.77	560	430	330

Table 6.6: Estimates for the ^{38}Ar excess above air, $^{38}Ar_{ex}$, the $^{38}Ar/^{36}Ar$ neutron spallation production ratio, $(38/36)_{sp}$, the ^{36}Ar produced from thermal and epithermal neutron capture of ^{35}Cl and subsequent decay of ^{36}Cl, 36_{Cl}, and the Ca-normalised cosmogenic ^{38}Ar concentration, $^{38}Ar_c$, for each sample.

as determined by Niedermann *et al.* (2007), and based on an average $P(^{3}He_{tot})$ for these samples of 114.5 ± 1.3 atom/g/yr (**Table 5.5**) as calculated according to Fenton *et al.* (2009). An ^{38}Ar production rate of 195.1 atom/g Ca/yr also agrees well with the value of 191 ± 21 atom/g Ca/yr, one of the two "global means" proposed by Niedermann *et al.* (2007), and with Lal's (1991) estimate of ~200 atom/g Ca/yr. However, it is appreciably higher than Knight *et al.*'s (2003) preliminary estimate of ~100 atom/g Ca/yr.

The ^{36}Cl half-life is given by Renne *et al.* (2001) as 3×10^5 yr (i.e. $\lambda = 2.31 \times 10^{-6}$ yr^{-1}). Renne *et al.* (2001) also use a (sea level and high latitude) value of 69 atom/g/yr for $P(^{36}Ar_{Ca})$ and 67 atom/g/yr for $P(^{36}Cl_{Ca})$, after Lal (1991) and Phillips *et al.* (2001), respectively. However, it may be noted that the basis of the $P(^{36}Ar_{Ca})$ calculation of Lal (1991) is unclear (Renne *et al.*, 2001), and Schimmelpfennig *et al.* (2009) suggest that Phillips *et al.*'s (2001) estimate of $P(^{36}Cl_{Ca})$ may be overestimated due to an underestimation of ^{36}Cl produced through thermal neutron capture on ^{35}Cl in calibration samples with an underestimated Cl abundance. Nevertheless, use of all the constants above for long exposure ages of three or more ^{36}Cl half-lives, where $(1\text{-}e^{-\lambda t})$ → 1, yields $(^{36}Ar/^{38}Ar)_{Ca} \rightarrow 0.697$ (i.e. $(38/36)_{sp} \rightarrow 1.43$). As this value approximates the $(^{38}Ar/^{36}Ar)_{Ca}$ production ratio of 1.5 ± 0.2 proposed for shielded lunar material by Hohenberg *et al.* (1978), these values are adopted for this study.

Sample-specific $(38/36)_{sp}$ ratios were calculated using the ^{3}He minimum exposure ages (according to both Lal's (1991) and Dunai's (2000a) scaling factors) as values for t. An average $(38/36)_{sp}$ value was then calculated for each sample and multiplied by a factor of 1.0 ± 0.2 in order to account for possible unquantified uncertainties, such as those that may be associated with the $P(^{36}Ar_{Ca})$ and $P(^{36}Cl_{Ca})$ estimates. The final $(38/36)_{sp}$ ratios are given in **Table 6.6.**

6.5.3 Thermal neutron capture of ^{35}Cl

The remaining term in equation 4.33 that requires determination is 36_{Cl}, the ^{36}Ar concentration produced by thermal and epithermal neutron capture of $^{35}C1$ and subsequent decay of $^{36}C1$. 36_{Cl} estimates were derived from ^{3}He minimum exposure ages according to both Lal (1991) and Dunai (2000a) scaling factors, and a sea level and high latitude production rate of 2 ± 2 atoms/g/yr (Niedermann *et al.*, 2007) scaled

according to the nuclide production scaling factors and topographic shielding factors in **Table 5.1**. Niedermann *et al.*'s (2007) production rate of 2 ± 2 atoms/g/yr was a conservative estimate adopted for pyroxene samples with < 100 ppm Cl content. Although the Cl concentrations for these pyroxene samples are not known, they are likely to be similarly low. In any event, the potential effect of underestimating 36_{Cl} on the final determination of $^{38}Ar_c$ would be small, especially given the large analytical uncertainties and the uncertainties associated with $(38/36)_{sp}$.

6.5.4 Comparison of $^{38}Ar_c$ with $^{3}He_{ex}$ and $^{21}Ne_{ex}$

The $^{38}Ar_c$ concentrations are given in atom/g Ca for all samples in **Table 6.6**. In **Figure 6.29,** these concentrations are compared with the corresponding concentrations of $^{3}He_{ex}$ and of $^{21}Ne_{ex}$ normalized to Mg from **Table 6.2**. Normalization of $^{21}Ne_{ex}$ to Mg concentrations in **Table 5.4** was performed due the high relative production rate of ^{21}Ne from Mg (**Table 4.3**). Niedermann *et al.* (2007) demonstrated positive correlations of $^{38}Ar_c$/Ca with $^{3}He_{ex}$ and with $^{21}Ne_{ex}$/Mg for pyroxenes from dolerites from the Antarctic Dry Valleys, with long exposure histories of > 1 Ma. These relations, $^{38}Ar = 1.704 \times {}^{3}He$ (equation 6.2) and $^{38}Ar = 0.8763 \times {}^{21}Ne$ are also plotted in **Figure 6.29**.

Data from this study generally agrees within error limits with the relations proposed by Niedermann *et al.* (2007). This supports the ^{38}Ar production rate of 195.1 atom/g Ca/yr derived from the relation with ^{3}He. One notable outlier in this regard is sample OR3, with a high $^{38}Ar_c$ concentration of 560 +430/-330 × 10^6 atom/g Ca, but $^{3}He_{ex}$ and $^{21}Ne_{ex}$ concentrations of only 44.3 ± 3.2 × 10^6 atom/g and 110 ± 22 × 10^6 atom/g Mg respectively. This sample was noted in Section 6.3.2 to have an anomalous $^{22}Ne/^{20}Ne$ ratio lower than that of air, and it was suggested that this may have been due to some kind of mass fractionation. However, a similar fractionation effect for Ar would result in a relative deficit, rather than an over-abundance, of ^{38}Ar. Inspection of **Table 6.5** reveals that the 1750 ºC analysis of OR3 yielded an $^{38}Ar/^{36}Ar$ ratio of only 0.18929 ± 0.00090, i.e. almost within error of air (0.1880) but an unusually high ^{36}Ar abundance (0.1874 ± 0.0094 × 10^{-8} cm^3 STP/g), thus yielding a large nominal ^{38}Ar excess. However, the $^{38}Ar/^{36}Ar$ ratio was determined from a linear extrapolation of 11 measurements. It is possible that this linear extrapolation was not justified, as a mean value would have yielded a $^{38}Ar/^{36}Ar$ ratio within error of air, and thus an ^{38}Ar excess

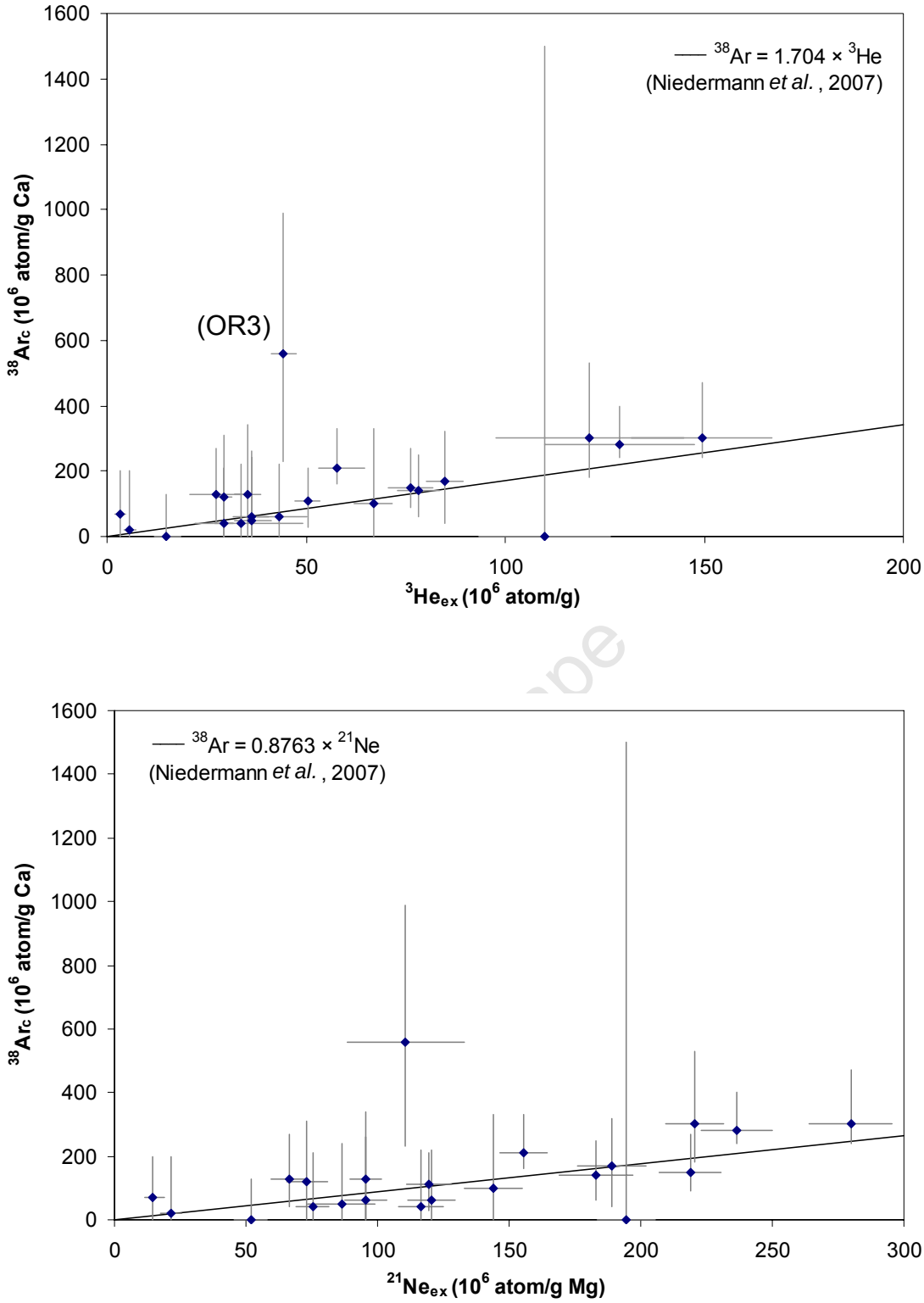

Figure 6.29: Comparison of $^{38}Ar_c$ concentrations normalized to Ca with ^3He (top) and with ^{21}Ne normalized to Mg (bottom). Lines defining the relations determined by Niedermann *et al.* (2007) are also shown.

within error of zero. Caution is therefore recommended in interpreting the $^{38}Ar_c$ estimate given for this sample.

6.5.5 ^{38}Ar minimum exposure ages and maximum erosion rates

Minimum exposure ages (T) and maximum erosion rates (ε) were calculated from $^{38}Ar_c$ concentrations and the ^{38}Ar production rate of 195.1 at/g Ca/yr according to the same procedures discussed for ^{3}He and ^{21}Ne in **Section 6.4**, with the exception of the error determination for ε. Due to ε being a reciprocal function of the cosmogenic nuclide abundance (equation 4.29), for samples with large relative uncertainties in $^{38}Ar_c$ (2σ typically > 50 % and +2σ often > 100 %), standard error propagation yields obviously unrealistic overestimates of negative uncertainties and underestimates of positive uncertainties for ε. Therefore, wherever relative errors in $^{38}Ar_c$ are > 50 %, error limits were determined for ε by calculating limiting ε values following the addition and subtraction of 2σ uncertainties for $^{38}Ar_c$. This condition applies to all cases with the exception of the negative $^{38}Ar_c$ errors (i.e. positive ε uncertainties) for samples DV6, IT3, IT5 and IT10, and the positive and negative $^{38}Ar_c$ errors for sample IT8. For samples where the negative uncertainties for $^{38}Ar_c$ are 100 %, this results in positive errors of infinity for ε.

The ^{38}Ar minimum exposure ages and maximum erosion rates are given in **Table 6.7** according to the scaling models of both Lal (1991) and Dunai (2000a). The ^{38}Ar minimum exposure ages are compared graphically with the ^{3}He and ^{21}Ne minimum exposure ages in **Figure 6.30.** In **Figure 6.31**, ^{38}Ar maximum erosion rates are compared with the ^{3}He and ^{21}Ne maximum erosion rates. For ease of reading, the three samples with the highest ^{38}Ar ε are not shown (CB1: ^{38}Ar ε = 8.3 +∞/-7.3 m/Myr, IT9: ^{38}Ar ε = 42 +∞/-42 m/Myr and GR2: ^{38}Ar ε = 440 +∞/-440 m/Myr, according to Lal's (1991) scaling).

Most ^{38}Ar minimum exposure ages and maximum erosion rates lie within error of the corresponding ^{3}He and ^{21}Ne estimates for the same samples. Two samples yield ^{38}Ar minimum exposure ages that are not within error of both the corresponding ^{3}He and ^{21}Ne ages: samples DV6 and OR3, which yielded higher ^{38}Ar T estimates as well as significantly lower ^{38}Ar ε estimates. Additionally, samples IT8 and IT10 yielded significantly higher T and lower ε estimates for ^{38}Ar than for ^{21}Ne. The ^{38}Ar

Sample	^{38}Ar minimum exposure age, T (ka)				^{38}Ar maximum erosion rate, ε (m/Myr)			
	Lal (1991) scaling		Dunai (2000a) scaling		Lal (1991) scaling		Dunai (2000a) scaling	
	2σ (+)	2σ (-)	2σ (+)	2σ (-)	2σ (+)	2σ (-)	2σ (+)	2σ (-)
BW3	390	730	390	430	810	430	0.53	∞	0.34	0.47	∞	0.31
CB1	50	350	50	50	380	50	8.3	∞	7.3	7.5	∞	6.6
DV5	390	620	390	440	700	440	1.38	∞	0.85	1.22	∞	0.75
DV6	630	350	150	710	390	170	0.85	0.21	0.30	0.75	0.18	0.27
DV9	190	460	190	210	520	210	2.8	∞	2.0	2.5	∞	1.8
GD1	490	770	490	540	850	540	0.42	∞	0.25	0.38	∞	0.23
GD2	200	470	200	220	520	220	2.6	∞	1.8	2.4	∞	1.6
GD3	340	300	250	370	330	280	1.5	4.4	0.7	1.4	4.0	0.6
GR1	120	470	120	130	520	130	4.6	∞	3.7	4.2	∞	3.3
GR2	0	300	0	0	340	0	440	∞	440	400	∞	400
GR3	140	460	140	160	510	160	3.7	∞	2.8	3.3	∞	2.5
GR5	240	190	130	260	210	150	2.2	2.9	1.0	2.0	2.7	0.9
IT1	120	490	120	140	560	140	4.5	∞	3.6	3.9	∞	3.2
IT3	760	560	300	860	640	330	0.70	0.27	0.30	0.62	0.24	0.27
IT5	480	380	180	540	440	210	1.12	0.43	0.50	0.98	0.37	0.44
IT6	840	890	600	1000	1000	700	0.24	0.59	0.13	0.21	0.52	0.11
IT8	640	270	90	720	310	110	0.83	0.12	0.35	0.74	0.11	0.31
IT9	0	3400	0	0	3900	0	42	∞	42	37	∞	37
IT10	650	380	130	740	430	140	0.82	0.16	0.30	0.72	0.14	0.27
OR1	110	450	110	120	520	120	4.1	∞	3.3	3.6	∞	2.9
OR2	270	260	210	300	290	230	2.0	7.0	1.0	1.8	6.3	0.9
OR3	1300	1000	800	1500	1200	900	0.40	0.56	0.17	0.35	0.50	0.15

Table 6.7: ^{38}Ar minimum exposure ages (T) and maximum erosion rates (ε) according to both Lal's (1991) and Dunai's (2000a) scaling factors.

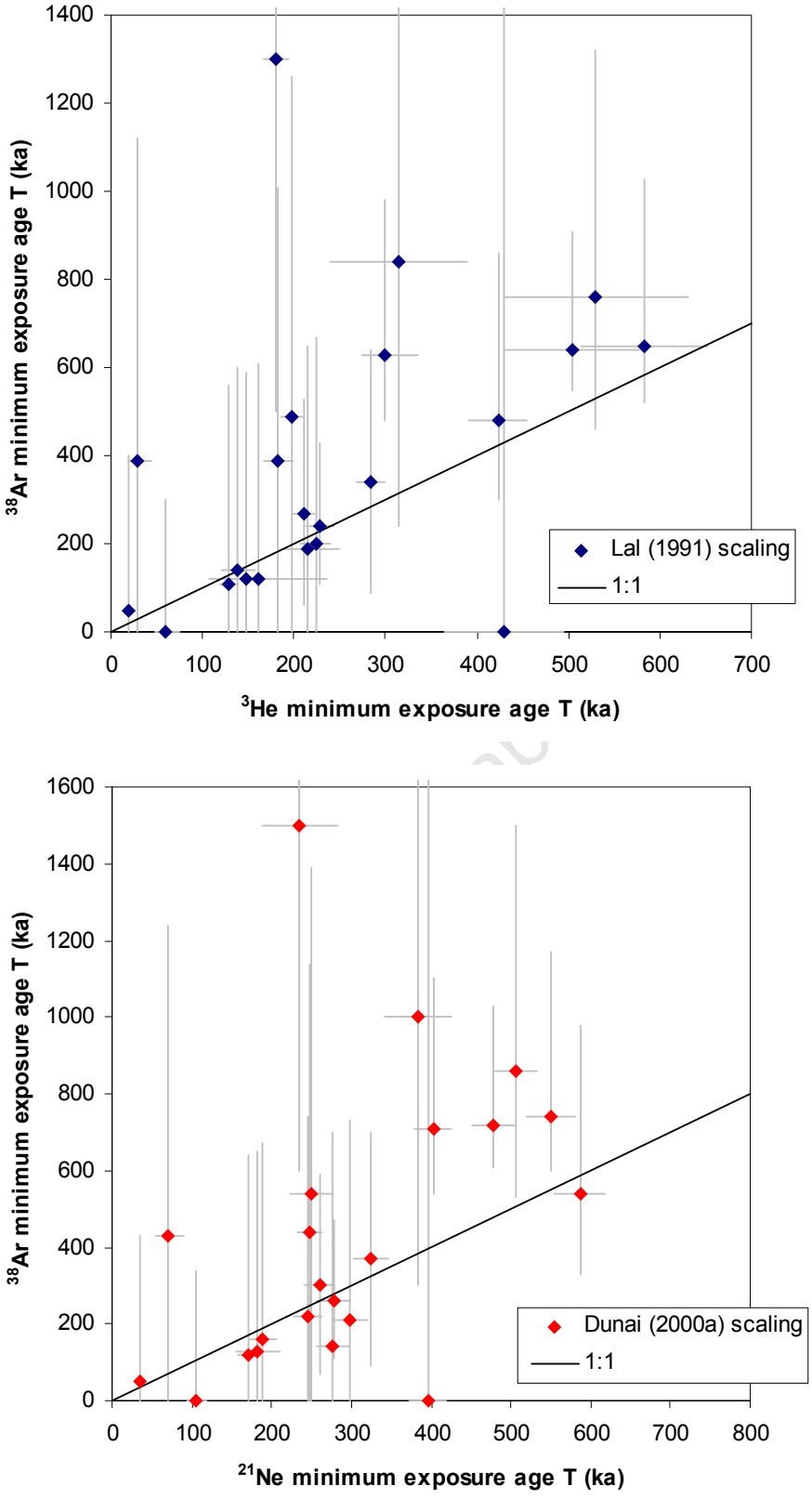

Figure 6.30: ^{38}Ar minimum exposure ages compared with the corresponding estimates from cosmogenic ^{3}He (top; Lal (1991) scaling) and ^{21}Ne (bottom; Dunai (2000a) scaling).

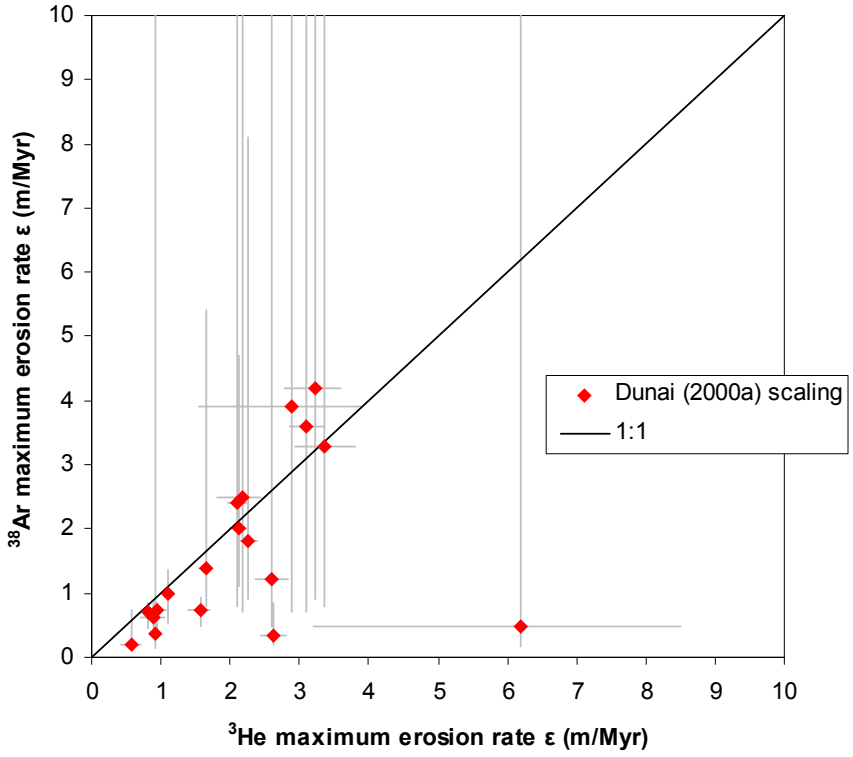

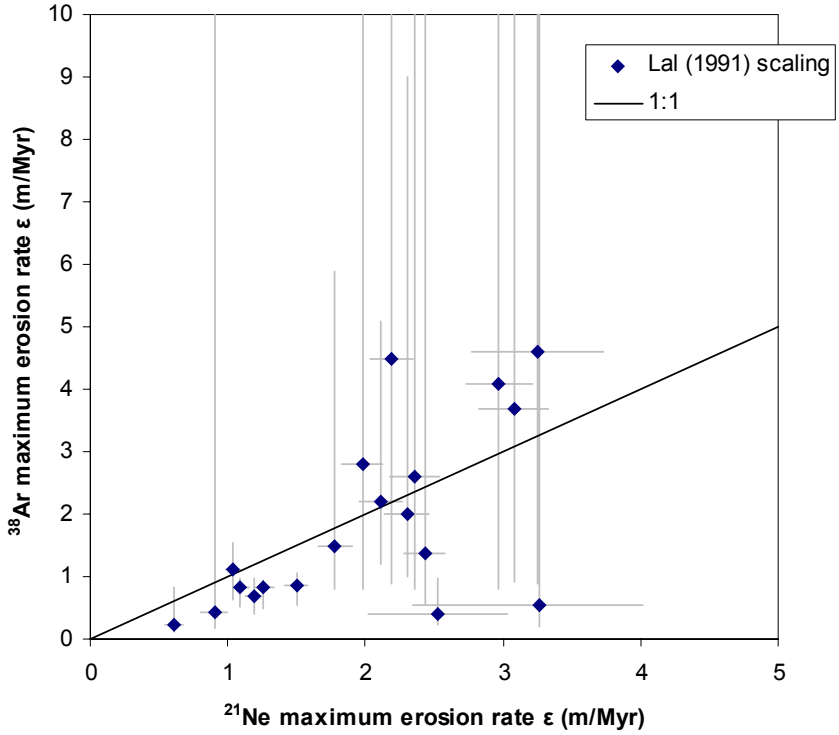

Figure 6.31: ^{38}Ar maximum erosion rates compared with the corresponding estimates from cosmogenic ^{3}He (top; Dunai (2000a) scaling) and ^{21}Ne (bottom; Lal (1991) scaling). The three samples with the highest ^{38}Ar ε values (CB1, GR2 and IT9) are not shown for the sake of clarity.

maximum erosion rate was also significantly lower than the corresponding ^{21}Ne maximum erosion rate for sample IT3.

If sample OR3 is excluded (cf. section 6.5.4), nine samples yield well-defined ^{38}Ar mimimum exposure ages that are not within error of zero (DV6, GD3, GR5, IT3, IT5, IT6, IT8, IT10 and OR2). The ^{38}Ar T estimates for these samples are compared with ^{3}He and ^{21}Ne T estimates in **Figure 6.32**. Although eight out of the nine ^{38}Ar T estimates plot within error of the corresponding ^{3}He T estimates, all ^{38}Ar T estimates are nominally higher. Similarly, seven of the nine samples have lower nominal ^{21}Ne T estimates than ^{38}Ar T estimates.

6.5.6 Discussion of ^{38}Ar ε and T estimates

To the author's knowledge, no prior studies determining minimum exposure ages and maximum erosion rates with terrestrial cosmogenic ^{38}Ar have been published. Considering the ongoing refinement of relevant nuclide production rates and the high analytical uncertainties involved when determining $^{38}Ar_c$, it is encouraging that most ^{38}Ar ε and T estimates reported in this study appear to be accurate within analytical error, albeit imprecise, when compared to corresponding ^{3}He and ^{21}Ne ε and T estimates. In fact, for some samples in this study, the precision for ^{38}Ar estimates is not radically lower than for ^{3}He and ^{21}Ne. For example, for Dunai (2000a) scaling, sample IT8 has an ^{38}Ar maximum erosion rate of 0.74 + 0.11/-0.31 m/Myr and a ^{3}He maximum erosion rate of 0.94 ± 0.14 m/Myr, i.e. both estimates have positive relative uncertainties of 15 %.

12 out of 22 samples yielded ^{38}Ar T in error of zero, and ^{38}Ar ε in error of infinity, meaning that only the maximum and minimum estimates for these variables are known. Although a maximum estimate for a minimum exposure age and a minimum estimate for a maximum erosion rate might seem somewhat meaningless, it must be remembered that the T and ε values refer to the specific cases of zero erosion since surface exposure and constant erosion (infinite surface exposure), respectively. As such, any limits placed on T and ε are potentially of geological significance. Two samples (GR2 and IT9) yielded only upper limits for the ^{38}Ar minimum exposure age, with ^{38}Ar maximum erosion rate estimates being unconfined ($+2\sigma = \infty$; -2σ = 100 %) when reported to two significant figures.

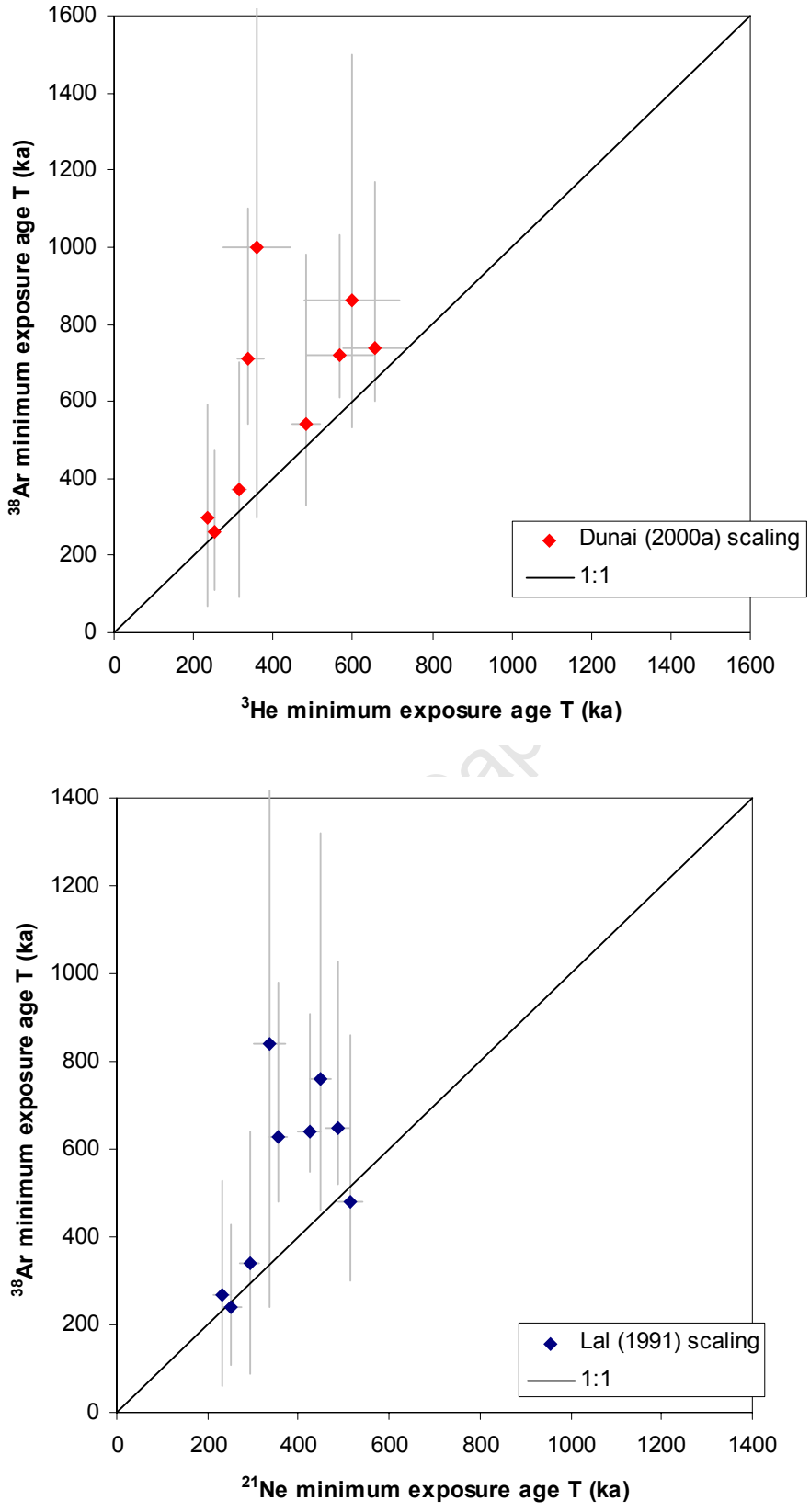

Figure 6.32: Comparison of ^{38}Ar minimum exposure ages with ^{3}He (Dunai (2000a) scaling; top) and ^{21}Ne estimates (Lal (1991) scaling; bottom) for nine samples where the ^{38}Ar T estimates do not plot within error of zero (sample OR3 excluded).

With the exception of sample OR3, the few discrepancies that are observed between the ^{38}Ar T and ε estimates and the corresponding ^{3}He and/or ^{21}Ne estimates might be due to a slight underestimation of the ^{38}Ar production rate and/or a slight overestimation of $^{38}Ar_c$. This is also consistent with the observation that for the nine more precisely constrained samples with ^{38}Ar miminum exposure ages not in error of zero (sample OR3 excluded), all samples have slightly higher ^{38}Ar T estimates than ^{3}He T estimates, and seven have slightly higher ^{38}Ar T estimates than ^{21}Ne T estimates. In turn, an overestimation of $^{38}Ar_c$ might be due to an underestimation of the ^{38}Ar production rate, an overestimation of the $^{36}Ar_{Ca}$ production rate and/or an overestimation of the $^{36}Cl_{Ca}$ production rate, with the latter having been suggested by Schimmelpfennig *et al.* (2009).

Nevertheless, cosmogenic ^{38}Ar clearly has potential as a useful tool for establishing constraints on surface exposure histories. ^{38}Ar is likely to be particularly useful for samples with long exposures (i.e. high ^{38}Ar/^{36}Ar ratios and where a constant ^{38}Ar/^{36}Ar production ratio may be assumed) and for Ca-bearing mineral phases where application of ^{3}He and ^{21}Ne is not possible due to diffusive loss. Feldspar is a clear future candidate mineral in this regard, although the production rate of ^{38}Ar from the other main target element K is yet to be accurately determined (Niedermann *et al*., 2007).

6.6 Krypton and Xenon

During samples analysis, ^{84}Kr and ^{132}Xe measurements were conducted concurrently with Ar measurements as a matter of routine. These measurements are of little direct relevance for surface exposure studies. Evidence of terrestrial cosmogenic Xe has been reported, but only through production from the target element Ba in barites (Srinivasan, 1976). Nevertheless, the existence of ^{84}Kr and ^{132}Xe data from this study warrants a brief appraisal.

^{84}Kr and ^{132}Xe abundances of all analyses, as well as totals for samples, are listed in **Table 6.8.** The resultant ^{84}Kr/^{132}Xe ratios are also shown, as well as the ^{36}Ar/^{132}Xe ratios for all samples. The ^{36}Ar/^{132}Xe ratios are calculated from ^{36}Ar abundances in **Table 6.5**. These values were not corrected for the presence of cosmogenic ^{36}Ar, as

Sample	Mass	T	^{84}Kr		^{132}Xe		^{84}Kr/^{132}Xe		^{36}Ar/^{132}Xe	
	g	ºC	10^{-12} cm^3 STP/g	± 2σ	10^{-12} cm^3 STP/g	± 2σ		± 2σ	10^4	± 2σ
BW3	0.50102	600	64.7	3.2	1.79	0.11	36.1	2.9		
		900	35.8	1.8	7.06	0.38	5.07	0.37		
		1750	17.86	0.92	21.7	1.3	0.821	0.064		
		Total	***118.4***	***3.8***	***30.6***	***1.3***	***3.87***	***0.21***	***21.7***	***1.2***
CB1	0.48028	900	27.7	1.4	2.69	0.15	10.28	0.79		
		1750	13.87	0.72	3.74	0.20	3.71	0.27		
		Total	***41.6***	***1.6***	***6.44***	***0.25***	***6.46***	***0.35***	***122.2***	***7.0***
DV5	0.50352	900	48.8	3.3	22.3	1.5	2.19	0.21		
		1750	6.65	0.42	2.56	0.18	2.60	0.25		
		Total	***55.5***	***3.4***	***24.8***	***1.6***	***2.24***	***0.19***	***16.8***	***1.8***
	0.51124	*Crushed*	*3.58*	*0.19*	*0.729*	*0.055*	*4.91*	*0.45*	*44.2*	*4.1*
DV6	0.50356	900	5.32	0.31	0.79	0.12	6.7	1.1		
		1750	8.79	0.48	1.181	0.081	7.44	0.65		
		Total	***14.11***	***0.57***	***1.97***	***0.14***	***7.16***	***0.59***	***157***	***13***
DV9	0.50052	900	18.8	3.3	6.64	0.93	2.84	0.64		
		1750	9.1	1.7	1.37	0.23	6.6	1.6		
		Total	***28.0***	***3.7***	***8.0***	***1.0***	***3.49***	***0.62***	***46.2***	***6.4***
GD1	0.50352	600	7.86	0.40	0.656	0.065	12.0	1.3		
		900	5.92	0.33	0.656	0.052	9.02	0.87		
		1750	25.2	1.3	3.75	0.21	6.71	0.51		
		Total	***39.0***	***1.4***	***5.07***	***0.23***	***7.69***	***0.44***	***230***	***14***
GD2	0.51466	900	14.3	2.5	3.03	0.45	4.7	1.1		
		1750	15.8	2.8	4.13	0.60	3.83	0.87		
		Total	***30.2***	***3.8***	***7.17***	***0.75***	***4.21***	***0.69***	***83***	***11***
	0.52240	*Crushed*	*15.99*	*0.81*	*1.053*	*0.070*	*15.2*	*1.3*	*614*	*51*
GD3	0.48336	900	8.86	0.47	1.394	0.086	6.36	0.52		
		1750	21.4	1.1	3.65	0.19	5.87	0.43		
		Total	***30.3***	***1.2***	***5.04***	***0.21***	***6.01***	***0.35***	***149.1***	***8.8***
GR1	0.50178	900	11.94	0.62	0.863	0.081	13.8	1.5		
		1750	17.92	0.94	3.00	0.17	5.97	0.46		
		Total	***29.9***	***1.1***	***3.86***	***0.19***	***7.73***	***0.47***	***218***	***13***
GR2	0.50070	900	11.10	0.58	2.18	0.16	5.09	0.46		
		1750	14.66	0.75	3.89	0.21	3.77	0.28		
		Total	***25.76***	***0.95***	***6.07***	***0.27***	***4.24***	***0.24***	***73.7***	***4.3***
GR3	0.52566	900	56.5	5.2	23.5	1.5	2.41	0.27		
		1750	7.14	0.67	2.37	0.17	3.01	0.36		
		Total	***63.7***	***5.2***	***25.9***	***1.5***	***2.46***	***0.25***	***21.0***	***2.0***
GR5	0.48144	900	10.42	0.55	1.77	0.10	5.90	0.46		
		1750	18.8	1.0	4.13	0.22	4.55	0.34		
		Total	***29.2***	***1.1***	***5.89***	***0.25***	***4.95***	***0.28***	***109.1***	***6.2***
IT1	0.52212	900	33.2	3.1	11.30	0.72	2.94	0.33		
		1750	9.82	0.94	4.80	0.35	2.05	0.25		
		Total	***43.1***	***3.2***	***16.10***	***0.80***	***2.67***	***0.24***	***27.4***	***2.4***
	0.53060	*Crushed*	*3.85*	*0.21*	*0.84*	*0.10*	*4.57*	*0.61*	*96*	*13*
IT3	0.50018	900	18.41	0.94	3.68	0.21	5.00	0.38		
		1750	10.57	0.55	2.60	0.16	4.06	0.33		
		Total	***29.0***	***1.1***	***6.28***	***0.26***	***4.61***	***0.26***	***77.0***	***4.4***
IT5	0.50190	900	18.7	1.0	3.22	0.18	5.81	0.44		
		1750	14.08	0.72	4.04	0.22	3.48	0.26		
		Total	***32.8***	***1.2***	***7.26***	***0.28***	***4.51***	***0.24***	***66.4***	***3.6***
IT6	0.50024	600	22.1	1.1	1.69	0.11	13.1	1.1		
		900	3.66	0.23	0.540	0.049	6.78	0.74		
		1750	6.13	0.32	0.991	0.089	6.19	0.64		
		Total	***31.9***	***1.2***	***3.22***	***0.15***	***9.92***	***0.58***	***142.5***	***8.1***
IT8	0.50388	900	30.1	1.5	16.68	0.84	1.80	0.13		
		1750	5.06	0.28	1.303	0.085	3.89	0.33		
		Total	***35.1***	***1.5***	***17.98***	***0.85***	***1.95***	***0.13***	***12.98***	***0.80***
IT9	0.49022	900	108.7	8.8	39.1	2.5	2.78	0.28		
		1750	128	10	48.4	2.9	2.64	0.27		
		Total	***236***	***13***	***87.43***	***3.82***	***2.70***	***0.19***	***32.9***	***2.0***
IT10	0.50202	900	37.6	1.9	16.44	0.83	2.29	0.16		
		1750	4.72	0.26	0.45	0.14	10.5	3.4		
		Total	***42.3***	***1.9***	***16.89***	***0.85***	***2.50***	***0.17***	***18.4***	***1.2***
OR1	0.50602	900	28.3	1.4	2.33	0.14	12.14	0.95		
		1750	19.1	1.0	5.11	0.28	3.74	0.28		
		Total	***47.4***	***1.7***	***7.44***	***0.31***	***6.37***	***0.35***	***115.1***	***6.4***
OR2	0.50038	900	14.72	0.76	2.86	0.15	5.16	0.38		
		1750	15.92	0.85	4.58	0.27	3.48	0.27		
		Total	***30.6***	***1.1***	***7.43***	***0.31***	***4.12***	***0.23***	***64.2***	***3.6***
OR3	0.50940	900	15.43	0.80	1.591	0.092	9.70	0.75		
		1750	49.6	2.5	5.41	0.34	9.17	0.74		
		Total	***65.0***	***2.6***	***7.00***	***0.35***	***9.29***	***0.60***	***333***	***22***

Table 6.8: Results of all ^{84}Kr and ^{132}Xe analyses. The ^{84}Kr/^{132}Xe ratios and the total ^{36}Ar/^{132}Xe ratios are also shown.

this was determined to be insignificant, with maximum estimates of the cosmogenic ^{36}Ar abundance ranging from 0.02 % to 0.2 % of the total ^{36}Ar.

Air is characterized by a $^{84}Kr/^{132}Xe$ ratio of 27.7 and a $^{36}Ar/^{132}Xe$ ratio of 1340 (Ozima and Podosek, 1983; and references therein). All total $^{84}Kr/^{132}Xe$ and $^{36}Ar/^{132}Xe$ ratios for samples are lower than for air. $^{84}Kr/^{132}Xe$ ratios range from 1.95 ± 0.13 (sample IT8) to 9.92 ± 0.58 (sample IT6), whilst $^{36}Ar/^{132}Xe$ ratios range from 18.4 ± 1.2 (sample IT10) to 333 ± 22 (sample OR3). Total $^{36}Ar/^{132}Xe$ ratios plotted against corresponding $^{84}Kr/^{132}Xe$ ratios display a linear positive correlation (R^2 = 0.79, **Figure 6.33**).

^{84}Kr and ^{132}Xe abundances are seldom reported in the literature. However, Valbracht *et al.* (1996) reported ^{36}Ar, ^{84}Kr and ^{132}Xe abundances for Hawaiian basaltic glasses and olivines, although the ^{84}Kr and ^{132}Xe data was not discussed. $^{36}Ar/^{132}Xe$ and $^{84}Kr/^{132}Xe$ ratios calculated from Valbracht *et al.*'s (1996) data are graphed for comparison in **Figure 6.34**, together with the total heating analyses and crushing analyses from this study. The composition of air is also shown. A regression line for all the data set to intercept the composition of air yields R^2 = 0.95. Thus both the Karoo and Hawaiian datasets may be interpreted to represent a mixture of predominantly two components: air, and a component enriched in ^{84}Kr relative to ^{132}Xe in air, and enriched in ^{132}Xe relative to ^{36}Ar in air, with an average $^{84}Kr/^{132}Xe$ ratio of ~2. Scatter in the data to the left of the regression line suggests the possibility of a third component being present in non-negligible quantities.

The origin of the non-atmospheric component(s) is uncertain, but at least two possible sources exist for enrichment in Kr and Xe relative to air. Firstly, the nuclides $^{83\text{-}86}Kr$ and $^{131\text{-}136}Xe$ may be produced through the spontaneous fission of U (e.g. Sabu, 1971). Srinivasan (1976) reported the Kr and Xe inventories of two Archean barites, and proposed that a significant fissiogenic component was present, estimating that approximately 52 % of the ^{132}Xe abundance was due to ^{238}U fission, with the remainder being atmospheric. $^{84}Kr/^{132}Xe$ ratios calculated from this data are 3.82 ± 0.54 and 6.98 ± 0.99 for these two barites. However, unpublished Xe isotope analyses for other Karoo pyroxene samples analysed by Kounov *et al.* (2007) yielded Xe isotope ratios indistinguishable from air (S. Niedermann, personal communication

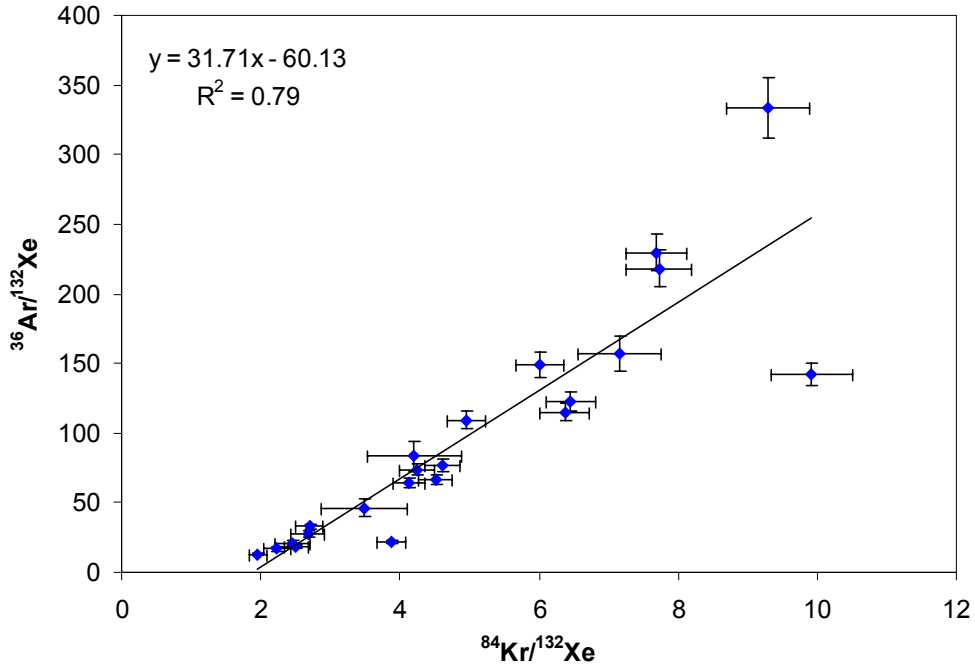

Figure 6.33: Total $^{36}Ar/^{132}Xe$ vs. $^{84}Kr/^{132}Xe$ ratios for samples in this study.

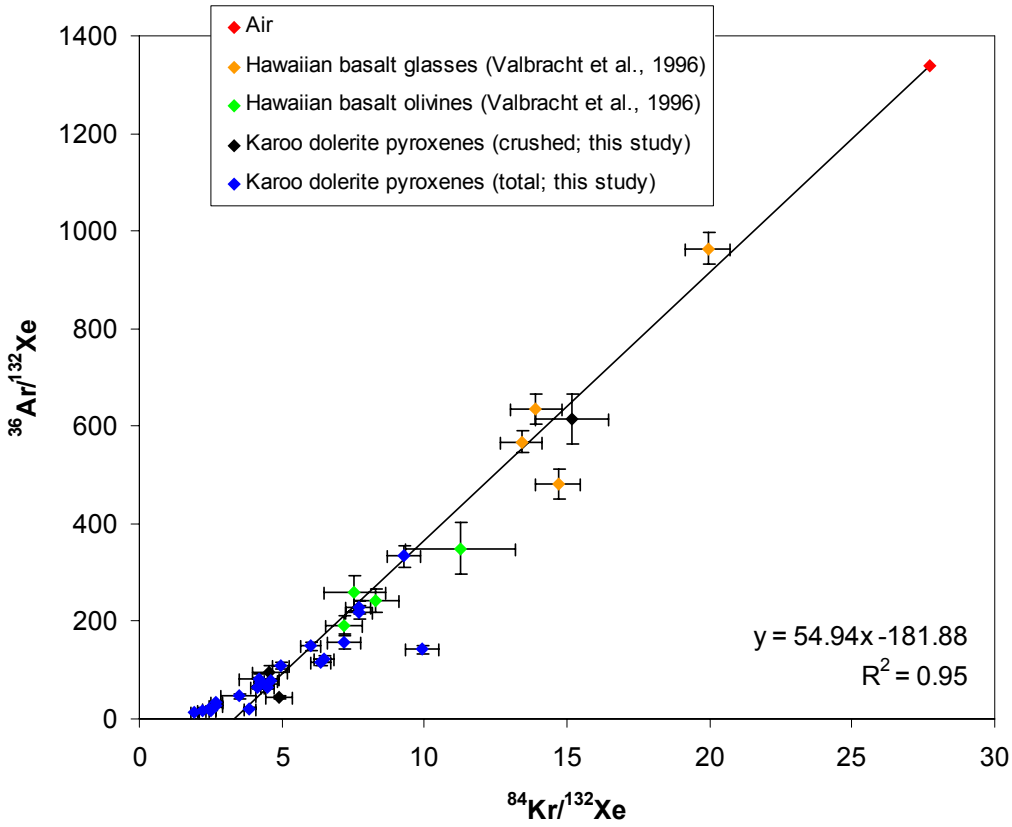

Figure 6.34: $^{36}Ar/^{132}Xe$ vs. $^{84}Kr/^{132}Xe$ ratios for crushing and total heating analyses in this study, compared with results from Hawaiian basalts (Valbracht *et al.*, 1996) and the composition of air.

2009). Furthermore, according to Sabu (1971) the relative fissiogenic yields of ^{84}Kr and ^{132}Xe from ^{238}U are (3.48 ± 0.02):(0.24 ± 0.05), i.e. $(^{84}Kr/^{132}Xe)_{fission}$ = 0.069 ± 0.014, substantially lower than the inferred average $^{84}Kr/^{132}Xe$ ratio of ~2 for the unknown component.

More probably, enrichment in ^{84}Kr and ^{132}Xe relative to air may be due to the significant presence of an adsorbed component derived from the atmosphere. Preferential adsorption of atmospheric Kr and Xe has been reported for a number of materials, including terrigenous sedimentary rocks (Fanale and Cannon, 1971; Podosek *et al*., 1980), lunar anorthosite breccias (Niedermann and Eugster, 1992) and meteoritic pyroxenes (Michel and Eugster, 1992). Niedermann and Eugster (1992) demonstrated experimentally that adsorption of a Xe-spiked gas to which lunar anorthosites were exposed was irreversible, with at least 75 % of the adsorbed component only being released at temperatures above 600 ºC.

CHAPTER 7: KAROO DOLERITE WEATHERING AND EROSION: PROCESSES, RATES AND IMPLICATIONS

7.1 Introduction

In Chapter 6, minimum exposure ages (T values) and maximum erosion rates (ε values) for Karoo dolerite surfaces were calculated, based on ^{3}He, ^{21}Ne and ^{38}Ar abundances. However, T and ε values only represent actual exposure ages and erosion rates for the model scenarios of instantaneous surface exposure with no subsequent loss of mass, and an infinite exposure period with a constant rate of surface denudation, respectively (Section 4.6). In this chapter, the ways in which these values may be used to interpret the erosional history of the southern African landscape and constrain the rate of Karoo dolerite weathering are explored.

First, various geomorphological processes that may result in the removal of mass from a rock surface are discussed. Then, the significance of cosmogenic nuclide data is discussed in view of these processes. Geomorphological interpretations of cosmogenic nuclide abundances are then presented for individual sample sites.

These interpretations are then used to:

1) Critically assess climate-dependent weathering models for Karoo dolerites specifically, and basaltic rocks in general;
2) Evaluate models of landscape development in southern Africa, particularly through the comparison of denudation rate estimates on various timescales;
3) Provide a geological perspective from which modern (20^{th} Century) rates of soil erosion and sediment yield in southern Africa may be discussed.

7.2 Rock weathering and erosion processes

As previously mentioned in Section 1.3, this study follows Sparks (1960) in using the following definitions:

- *Weathering:* Chemical or physical alteration of rock at the surface or subsurface.

- *Erosion:* Removal of rock mass from the surface, whether through physical (mechanical) processes, or through the removal of soluble ions in solution following chemical alteration and dissolution.
- *Denudation:* Synonymous with erosion as defined above.

In non-glacial landscapes, four general processes may be significant in the denudation of dolerites:

a) *Chemical weathering and granular disintegration:* One or more mineral phases may experience chemical alteration (e.g. hydration or oxidation), forming secondary (supergene) minerals and products that are removed in solution. Following this, the remaining rock may disintegrate and be removed through gravity, water or wind action (e.g. Sparks, 1960; **Figure 7.1**). Volumetric changes due to chemical alteration may also create stresses that cause fracturing and accelerate the disintegration of the rock, whilst plant acids may also accelerate chemical weathering (Section 3.3.2). If weathered material is removed as soon as it is produced, leaving behind a bare rock surface, the rock weathering rate may be said to determine the erosion rate of the surface, i.e. the removal of rock is weathering-limited.

b) *Exfoliation or spheroidal weathering:* The generation of rock sheets parallel to the surface is known as *exfoliation*, which is commonly observed at the surfaces of crystalline rocks (e.g. Sparks, 1960; **Figure 7.2**). The possible causes of exfoliation have been debated, but it is likely that exfoliation is due to tension release related to:
   1) Unloading and expansion of a surface, due to prior denudation,
   2) Temperature-induced rock expansion, either due to insolation or fire,
   3) Expansion of the rock along joints, due to incipient chemical weathering, or
   4) Frost wedging, through the freezing of water within joints (Sparks, 1960; Summerfield, 1991).

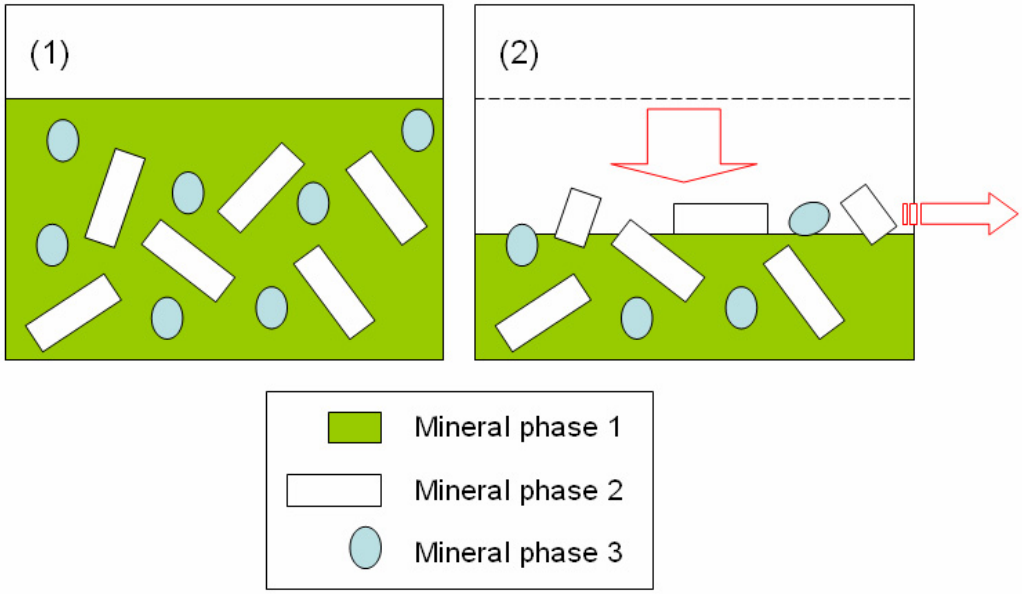

Figure 7.1: Schematic illustration of chemical weathering and granular disintegration. For a rock surface (1), one or more chemical mineral phases (e.g. mineral phase 1) may experience chemical alteration, followed by removal of the weathering products in solid state or in solution. This results in lowering of the surface (2), following which the remaining rock (e.g. mineral phases 2 and 3) may also experience chemical alteration on exposure, and/or be removed through gravity, water or wind action.

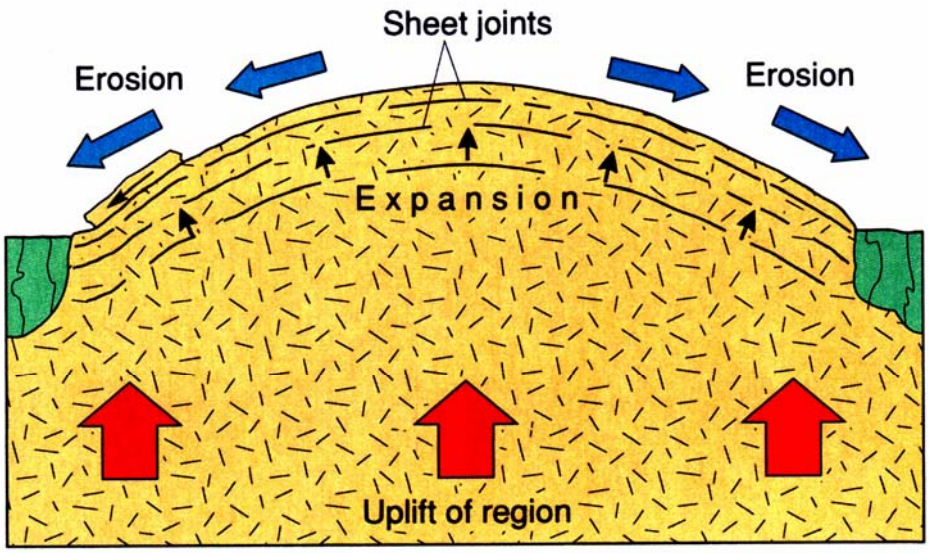

Figure 7.2: Schematic illustration of rock exfoliation, here resulting from pressure release, modified from Plummer and McGeary (1996). In this instance, a granitic dome experiences exhumation and unloading, due to surface denudation caused by regional uplift. This pressure release results in the formation of surface parallel joints, causing the detachment of rock sheets parallel to the surface (exfoliation). Tension release joints may also result from thermal expansion due to insolation or fire, incipient chemical weathering, or frost wedging.

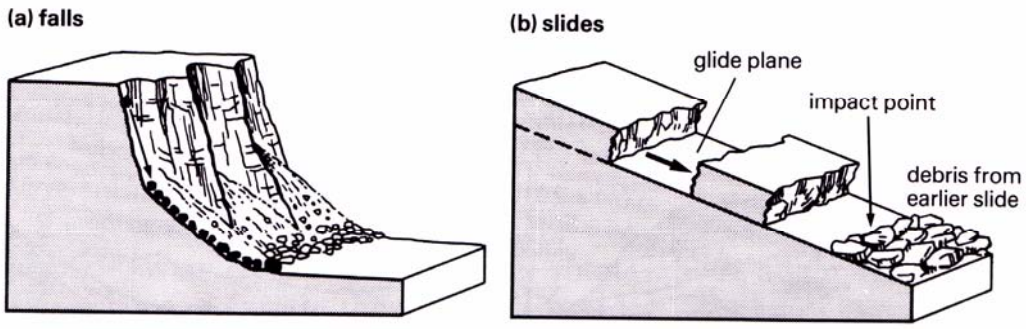

Figure 7.3: Schematic illustration of (a) rock falls and (b) rock slides, modified from Clowes and Comfort (1987). Rock falls occur at steep rock surfaces and generate scree slopes or debris cones below them, whereas rock slides occur along inclined planes of weakness, and result in less disruption of the mobile mass (Clowes and Comfort, 1987).

Exfoliation on a small scale, leading to the generation of rounded boulders, is known as *spheroidal weathering* (e.g. Plummer and McGeary, 1996) and may occur sub-aerially or below the surface.

c) *Slope failure:* Here a vertical or inclined rock surface loses mass through rock falls or rock slides that occur in response to gravity. Gravitational instability of the rock mass may result from:
   1) The erosion of downslope material following fluvial incision, or
   2) A decrease in the rock mass strength, due to the expansion of joints or fissures.

   Mass may be lost either as rock falls or as rock slides (e.g. Clowes and Comfort, 1987; **Figure 7.3**). Biotic activity may be a contributing factor towards slope failure, as plant acids may accelerate chemical weathering along joints, and blocks may be dislodged through the growth of plant roots and through animal activity.

d) *Regolith formation and subsequent erosion:* If the rate of chemical weathering exceeds the rate of erosion of the weathered material, a weathering mantle or regolith develops. Should this regolith be subsequently removed through an acceleration of the regolith erosion rate relative to the rock weathering rate, the exposed rock surface represents the exhumed subsurface weathering front (**Figure 7.4**). This model of initial chemical weathering and subsequent physical erosion has been invoked particularly for granitic rocks, where boulder piles (tors) have been proposed to represent residual corestones exhumed from the subsurface (e.g. Linton, 1955), or where inselbergs have been interpreted to represent the higher parts of a former subsurface weathering front (e.g. Sawyer, 1970; Buckle, 1978). Where a planation surface is interpreted to represent an exhumed palaeo-weathering front of significant aerial extent, the term *etchplain* (Wayland, 1934) may be applied. The concept of regolith formation and subsequent erosion was reviewed in detail by Twidale (2002), who cited Hassenfratz (1791) as one of the earliest workers to propose this hypothesis. Twidale (1988) also suggested that many of the *koppies* and plains characterising southern Africa may be etch forms rather than the products of scarp retreat. The possibility that some dolerite tors in

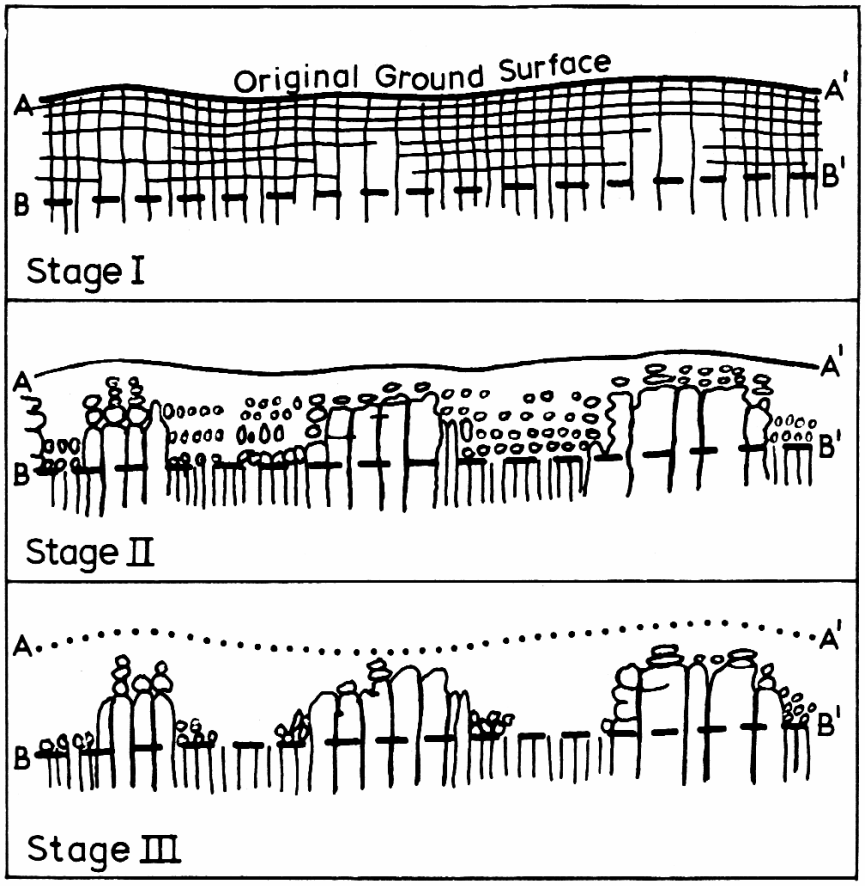

Figure 7.4: Schematic illustration of landscape denudation through initial chemical weathering followed by physical erosion, modified from Sawyer (1970). In Stage I, the rate of bedrock weathering along fractures exceeds the rate of erosion of the weathered material, leading to Stage II, where a regolith is formed and a subsurface weathering front (B-B') has developed beneath the ground surface (A-A'). Should the rate of physical erosion of the regolith then exceed the rate of chemical weathering of the bedrock, the weathering front is then exposed at the surface (Stage III).

southern Africa may be etch forms has already been mentioned in Section 5.5 (see also **Figures 5.19** and **5.22**).

It is important to note that a combination of these processes may be important in the denudation of a single rock surface. For instance, a surface may represent a subsurface weathering front that has been exhumed from beneath a regolith, and has subsequently lost mass incrementally through large episodic rock falls, whilst also steadily losing mass through chemical weathering and granular disintegration during times of slope stability.

7.3 Significance of cosmogenic nuclide data to weathering and erosion processes

7.3.1 The minimum exposure age, maximum erosion rate and characteristic erosion timescale

As discussed in Section 4.6, the minimum exposure age of a rock surface, T, is a function of the cosmogenic nuclide abundance, C, and the cosmogenic nuclide production rate at that surface, P_0:

$$T = \frac{C}{P_0} \tag{4.28}$$

In contrast, the maximum erosion rate, ε, is defined in Section 4.6 as follows:

$$\varepsilon = \frac{\Lambda \ P_0}{\rho \ C} \tag{4.29}$$

where Λ is the attenuation length for cosmogenic nuclide production and where ρ is rock density. The value of ε is thus valid for the time taken to erode the thickness of rock equivalent to one attenuation length, and this thickness of rock may be determined by dividing Λ by ρ. Hence the characteristic erosion timescale, T_ε may be defined as:

$$T_\varepsilon = \frac{(\Lambda/\rho)}{\varepsilon} \tag{7.1}$$

Substitution of equation 4.29 into equation 7.1 yields the relation:

$$T_\varepsilon = \frac{C}{P_0}$$

(7.2)

Therefore, the characteristic erosion timescale, T_ε, is equal to the minimum exposure age, T (equation 4.28).

7.3.2 Effective attenuation lengths

In order to assess how appropriate T and ε values are in describing surface process rates at a given sample site, it is neccessary to know the thickness of rock equivalent to the *effective* neutron spallation attenuation length at that site. For instance, for a cliff that is assumed to lose mass only through episodic rock falls, what thickness of rock must be lost during a single rock fall event for the minimum exposure age to approximate the age of the rock fall?

As discussed in Section 4.5, cosmogenic nuclide production is modelled to attenuate exponentially with depth, such that:

$$P(d) = P_0 e^{-\rho d / \Lambda} \tag{4.19}$$

where P(d) is the production rate P at depth d (Niedermann, 2002). For a horizontal, unshielded surface, the spallogenic neutron attenuation length Λ is 160 g/cm^2 (Gosse and Phillips, 2001), equivalent to a rock thickness of 53.3 cm for dolerite with a density of 3 g/cm^3. Thus where d = 53.3 cm for such a horizontal dolerite surface, $P/P_0 = e^{-1}$, i.e. the cosmogenic nuclide production rate is 37 % of the production rate at surface. Similarly, at depths of 107 cm, 160 cm, and 213 cm, the cosmogenic nuclide production rates are 14 %, 5.0 % and 1.8 %, respectively, of the production rate at surface (assuming negligible muogenic production).

As discussed in Section 4.6, the effective attenuation length perpendicular to a surface of dip > 0º depends on slope angle. In the same way that the true erosion rate for an inclined surface ε may be calculated from the apparent erosion rate ε* by using a numerical approximation (Section 4.6):

$$\varepsilon = \frac{\varepsilon^*}{\left(1 + \frac{\alpha^2}{5000}\right)} \tag{4.30}$$

where α is the dip of the surface (Hermanns *et al*., 2004), a true attenuation length Λ perpendicular to the surface length may be determined from the unshielded (apparent) attenuation length Λ*:

$$\Lambda = \frac{\Lambda *}{\left(1 + \frac{\alpha^2}{5000}\right)} \tag{7.3}$$

The effective attenuation lengths for non-horizontal dolerite surfaces sampled in this study were calculated according to equation 7.3, and are given in **Table 7.1**.

It may be noted that for a horizontal surface, obstructions on the horizon may also influence the effective attenuation length, but in such instances the effective attenuation length is greater than the unobstructed attenuation length, due to the lower energy of cosmic ray neutrons at lower angles of incidence (Dunne *et al*., 1999; Section 4.4). For rectangular obstructions, the ratio of the effective attenuation length Λ and the attenuation length for the unshielded surface Λ* is given by Dunne *et al*. (1999) as:

$$\frac{\Lambda}{\Lambda *} = \frac{1 - \sum_{i=1}^{n} \frac{\Delta\phi_i}{360°} \sin^{m+2}\theta_i}{1 - \sum_{i=1}^{n} \frac{\Delta\phi_i}{360°} \sin^{m+1}\theta_i} \tag{7.4}$$

for n obstructions which extend from the horizontal up to inclination angles of θ_i and subtend azimuthal angles of $\Delta\phi_i$ (in degrees), where m is the exponent of the topographic shielding correction (assumed here to be 2.3; Sections 4.4 and 6.4). For a horizontal surface with a triangular obstruction on the horizon of inclination angle θ_T < 50º, the ratio Λ/Λ* may be determined from the following numerical approximation:

$$\frac{\Lambda}{\Lambda *} = 1 + \left[0.08 \frac{1}{10e^{-0.09(\theta_T - 20°)} + 1} - 0.002\right] \times \frac{\Delta\phi}{360°} \tag{7.5}$$

$(\theta_T < 50º)$

where $\Delta\phi$ is the azimuthal angle in degrees subtended by the base of the obstruction (Dunne *et al*., 1999).

Sample	Surface dip, α (º)	Effective attenuation length, Λ (g/cm^2)	Depth (cm) where:			
			$P/P_0 = 0.37$	$P/P_0 = 0.15$	$P/P_0 = 0.050$	$P/P_0 = 0.018$
BW3	90	61	20	41	61	81
CB1	44	115	38	77	115	154
DV9	10	157	52	105	157	209
GD1	90	61	20	41	61	81
GD2	10	157	52	105	157	209
GD3	12	156	52	104	156	207
GR3	10	157	52	105	157	209
IT5	4	159	53	106	159	213
IT6	90	61	20	41	61	81
OR1	30	136	45	90	136	181
OR3	6	159	53	106	159	212

Table 7.1: Effective neutron spallation attenuation lengths (perpendicular to the sample surface) for non-horizontal surfaces (i.e. where surface dip, $\alpha > 0º$). Also shown are depths in cm equivalent to 1, 2, 3 and 4 effective attenuation lengths, where the cosmogenic nuclide production ratio is 37 %, 15 %, 5.0 % and 1.8 % of that at surface (based on a dolerite density of 3.0 g/cm^3).

Sample	T (ka)	2σ (+)	2σ (-)	ε (m/Myr)	2σ (+)	2σ (-)	Surface dip, α (º)
BW3	33	16	12	6.2	2.3	3.0	90
CB1	20.3	5.6	5.2	18.9	4.8	5.2	44
DV5	205	20	18	2.60	0.23	0.25	0
DV6	337	40	27	1.58	0.13	0.19	0
DV9	241	41	30	2.17	0.27	0.37	10
GD1	219	13	13	0.929	0.057	0.057	90
GD2	248	18	18	2.11	0.15	0.15	10
GD3	315	17	17	1.644	0.088	0.088	12
GR1	165	23	19	3.23	0.37	0.44	0
GR2	67	17	14	8.0	1.6	2.1	0
GR3	155	20	20	3.37	0.43	0.43	10
GR5	251	17	17	2.13	0.14	0.14	0
IT1	184	85	63	2.9	1.0	1.3	0
IT3	600	120	120	0.89	0.17	0.17	0
IT5	483	36	36	1.101	0.082	0.082	4
IT6	359	86	86	0.57	0.14	0.14	90
IT8	568	83	83	0.94	0.14	0.14	0
IT9	484	73	73	1.10	0.17	0.17	0
IT10	656	78	78	0.813	0.097	0.097	0
OR1	146	12	12	3.10	0.25	0.25	30
OR2	236	15	15	2.26	0.14	0.14	0
OR3	201	14	14	2.63	0.19	0.19	6

Table 7.2: ^{3}He minimum exposure ages and maximum erosion rates for Karoo dolerite surfaces analysed in this study, based on Fenton *et al.*'s (2009) production rates and Dunai's (2000a) scaling factors. The dip angle from the azimuth for each surface is also shown.

Effective attenuation lengths were determined in this manner for the two shielded, horizontal surfaces sampled in this study (GR1 and GR5), but it was found that the effect on Λ was $\leq$ 0.3 g/cm^2, i.e. smaller than the accuracy to which the assumed value of Λ^* (160 g/cm^2) is reported by Gosse and Phillips (2001). It is not apparent from the literature how the effective attenuation length for a non-horizontal surface with additional downslope shielding may be determined (S. Niedermann, personal communication, 2010), and five such surfaces were analysed in this study (BW3, CB1, GD1, GR3 and IT6). Nevertheless, the effect of downslope shielding on Λ would have also been insignificant for these surfaces had they been horizontal. The greatest effect would have been on the value for Λ for sample BW3 (1 g/cm^2, i.e. 0.6 % of Λ), but this is considerably less than the analytical uncertainty of +37 % / -48 % for the ^{3}He estimate of ε here. The effect of downslope topographic shielding on Λ is thus assumed to be negligible for these non-horizontal samples too.

The depths that are equivalent to 1, 2, 3 and 4 attenuation lengths (i.e. where nuclide production rates have decreased to 37 %, 14 %, 5.0 % and 1.8 %, respectively, of the production rates at surface) are also given in **Table 7.1**. The depth of rock d that corresponds to n number of effective attenuation lengths Λ may be calculated as follows:

$$d = \frac{n\Lambda}{\rho} \tag{7.6}$$

where ρ is the rock density. Thus for dolerite with a density of 3 g/cm^3, the effective attenuation length in g/cm^2 is numerically identical to the corresponding depth in cm equivalent to 3 effective attenuation lengths, i.e. P/P_0 = 5 % at 1.6 m depth where Λ = 160 g/cm^2. Therefore, if the minimum exposure age for a horizontal surface is to approximate a true exposure age with an accuracy of greater than 95 %, it is required that more than 1.6 m of rock was removed from that horizontal surface instantaneously.

7.3.3 Applicability of ε and T to weathering and erosion processes

In light of the considerations in Section 7.3.2, the usefulness of ε and T values in quantifying the weathering and erosion processes described in Section 7.2.1 is as follows:

a) *Chemical weathering and granular disintegration:* Erosion occurs here in increments that are small relative to the cosmic ray attenuation length, i.e. mass is lost either at the atomic scale or at the scale of individual mineral grains. Thus the maximum erosion rate ε may be assumed to be equal to the true erosion rate if chemical weathering and granular disintegration is judged to be the dominant process affecting the sampled rock surface. Furthermore, because the denudation of such a rock surface is weathering limited, ε may also be taken to signify the dolerite weathering rate in this case.

b) *Exfoliation or spheroidal weathering:* For the exfoliation of slabs of rock with thicknesses equivalent to > 3 effective attenuation lengths, the interpretation of cosmogenic nuclide data would be the same as for any surface that experiences the loss of large masses of rock through slope failure (see below). However, when thinner layers of rock are lost from a surface (e.g. exfoliating slabs of rock than are tens of cm thick), the minimum exposure age becomes less useful in describing the exposure history of the surface. The incremental nature of such a process would also mean that the maximum erosion rate is of limited applicability here in describing the denudation rate of the surface over time (e.g. Muzikar, 2009). Nevertheless, as the increments of mass lost become smaller (e.g. on a centimeter scale), the maximum erosion rate ε will approach the true erosion rate.

c) *Slope failure:* As with exfoliation, the relative usefulness of the ε and T constraints depends upon both the thicknesses of rock that are lost during slope failure events at a surface, and the effective cosmic ray attenuation length for that surface. In the case of a large rock fall at a cliff face, where the thickness of the rock fall is equivalent to ≥ 3 attenuation lengths (≥ 0.61 m of rock for a 90º cliff face) the minimum exposure age of the surface may be assumed to approximate to the age of the rock fall with an uncertainty of ≤ 5 %. However, the thickness of rock lost during the last large rock fall or rock slide is unlikely to be certain.

d) *Regolith formation and subsequent erosion:* Here the cosmogenic nuclide abundance is not dependent on the rate of rock weathering, but on the timing

of regolith erosion, assuming that the regolith was of sufficient maximum depth (i.e. corresponding to ≥ 3 neutron spallation attenuation lengths) at some point in time. Whether or not a minimum exposure age or a maximum erosion rate is more applicable depends on the rate at which the regolith is assumed to have been removed. If the overlying regolith was removed instantaneously, and the exposed rocks experienced negligible subsequent loss of mass, the minimum exposure age T is equal to the age of exhumation. Alternatively, it may be assumed that the regolith was removed at a constant rate and that the rock surface has only been subsequently exposed for an insignificant length of time. However, in such an instance, the maximum erosion rate ε is likely to be an underestimate of the regolith erosion rate, as the (unknown) density of the regolith would be less than that of the dolerite.

As noted in Section 7.2, it is unlikely that only one of these processes occurs for any given rock surface. Certainly, except for rocks that are exposed under exceptionally arid conditions, it is likely that most exposed rock surfaces lose mass continually through chemical weathering and granular disintegration, and that this process may continue, for example, between events of slope failure at a cliff face, or exfoliation of a boulder. For such surfaces, the value of the minimum exposure age T will underestimate the age of the last large rock fall at that surface, and the value of the maximum erosion rate ε will overestimate the true chemical weathering rate of the dolerite surface.

For cliff faces that primarily lose mass incrementally through slope failure, a model rate of scarp retreat at a cliff face may be derived from the minimum exposure age by assuming the average thickness of rock lost per rock fall, and relating the minimum exposure age to the average period between rock falls (e.g. Fleming *et al*., 1999). Thus a model rate of scarp retreat, E, may be defined as follows:

$$E = \frac{d}{T} \tag{7.7}$$

where T is the minimum exposure age and d is an estimate of the thickness of rock assumed to be lost during the average rock fall, in accordance with field evidence. As mentioned above, for the minimum exposure age to be within less than 5 % of the age

of the last rock fall, a thickness of rock equivalent to more than 3 effective attenuation lengths must be lost. In the instances where E values are determined in this study, d is calculated for the model case of n = 3 (equation 7.6), in which case an error of 5 % may be assumed for the value of E, in addition to the analytical uncertainty reported in the text. Note that the minimum exposure age may significantly underestimate the period between successive rock falls at a given site, *at least over the time period equal to the minimum exposure age*, as the time of sampling can only pre-date the future rockfall that would have occurred at a given site, making E an overestimate of the true rate of scarp retreat. On the other hand, E may be an underestimate of the true scarp retreat rate if the true value of d is greater than assumed.

The model scarp retreat rate, E, which assumes that mass is lost in large increments, should not be confused with the maximum erosion rate, ε, which assumes that mass is lost continuously at a constant rate. However, like ε, E is defined for the period T, and so extrapolation of this rate to longer timescales is particularly speculative. There seems little reason to assume that rock falls at a given site should occur periodically, and the magnitude and frequency of mass wasting events may rather, like earthquakes, be best described by fractal statistics (Bak, 1996; Hergarten, 2003). Indeed, any interpretation of the cosmogenic nuclide abundance of an incrementally eroding cliff face is subject to assumptions regarding both the magnitude of mass wasting events (unless a statistically significant number of samples can be analysed), and the time-correlation (periodicity versus episodicity) assumed for such events (e.g. Muzikar, 2008; 2009). Nevertheless, E values are useful for the forward modelling of scarp retreat rates. If it is assumed that E values are valid for a timescale of $>10^6$ yr, the time required to erode a landform of given dimensions may be calculated. This result may then be compared with independent stratigraphic constraints in order to assess the validity of the initial condition, i.e. whether or not erosion rates are likely to have remained relatively constant over the time period of interest.

7.4 Geomorphological interpretations of cosmogenic nuclide data

Geomorphological interpretations of the cosmogenic nuclide data are presented below for each sample site. Samples are grouped according to geographical proximity. All minimum exposure ages (T values) and maximum erosion rates (ε values) presented below are based on ^{3}He data and calculated according to Fenton *et al.*'s (2009)

cosmogenic nuclide production rates and Dunai's (2000a) scaling factors, unless specified otherwise. This data is summarised in **Table 7.2** (derived from **Tables 6.3** and **6.4),** together with surface dip angles from **Table 5.1.** Whilst the choice of Dunai (2000a) scaling over Lal (1991) scaling is arbitrary, ^{3}He estimates are chosen due to the possibility of a significant nucleogenic ^{21}Ne component being present in some samples, and due to the generally high analytical errors associated with ^{38}Ar estimates (Chapter 6). However, minimum exposure ages and maximum erosion rates based on ^{21}Ne data are also referred to for samples where ^{21}Ne T and ε values are not within error of the corresponding ^{3}He values (i.e. samples BW3, CB1, DV5, GR2, IT5 and IT10; Sections 6.4.1 and 6.4.2).

As discussed below, T and ε values are also plotted on topographic cross-sections, based on the SRTM digital elevation model (Jarvis *et al*., 2006). Due to the spatial resolution of the SRTM DEM (~90 m), possible artefacts and errors associated with the SRTM elevation data (Section 3.5.1), and possible inaccuracies in field GPS readings, note that the apparent absolute elevations of sample sites on topographic profiles may differ from those given in **Table 5.1**, particularly in areas of complex (high relief) topography. Nevertheless, these profiles provide an accurate illustration of the relative topography for each sample site.

7.4.1 Samples BW3, DV5, DV6 and DV9

The locations of samples BW3, DV5, DV6 and DV9 are shown in **Figure 7.5**. Minimum exposure ages and maximum erosion rates for these samples are displayed along a topographic profile in **Figure 7.6**, with a model scarp retreat rate for BW3 also shown.

BW3:

Sample BW3, from a vertical face in the escarpment zone near Beaufort West (**Figures 5.2** and **5.8**), yields T = 33 +16/-12 ka and ε = 6.2 +2.3/-3.0 m/Myr. This is the third highest maximum erosion rate, and the third youngest minimum exposure age in this study. These findings are compatible with field observations that suggest that this surface is actively losing mass through the episodic exfoliation of rock slabs that are centimetres to tens of centimetres thick. As such, the ε value is likely to be an overestimate of the dolerite weathering rate here. Furthermore, the field evidence also

suggests that the thickness of rock lost during single exfoliation events is typically less than the thickness of rock equivalent to the three effective attenuation lengths at this site (0.61 m). Assuming that the thickness of rock lost during this last rock fall was equivalent to 0.61 m, the model scarp retreat E is determined to be 13-29 m/Myr here. Use of ^{21}Ne data here (T= 70 +20/-16 ka); would, however, yield a lower scarp retreat rate, of 6.8 - 11 m/Myr, although Ne isotope systematics suggest that the assumed cosmogenic ^{21}Ne abundance for BW3 is an overestimate, due to a significant nucleogenic ^{21}Ne component (Section 6.4.1).

Vertical rock surfaces, such as the scarp from which BW3 was collected, pose the greatest challenges for the interpretation of cosmogenic nuclide data, as it is likely that such surfaces lose mass through both episodic and continuous mechanisms (i.e. mass wasting and chemical weathering). The model scarp retreat rate for BW3 is necessarily speculative, although Fleming *et al*. (1999) performed a similar thought experiment in order to determine rates of scarp retreat for the Drakensberg escarpment, by assuming intermittent shedding of 0.5 m thick basalt blocks. According to Fleming *et al*. (1999), the pediplanation models of King (1944) and Partridge and Maud (1987) imply an average scarp retreat rate of 1-1.5 km/Myr from the continental margin over the ~130 Myr since continental breakup, and this was found to be incompatible with Fleming *et al*.'s (1999) model escarpment retreat of 95 m/Myr for the Drakensberg escarpment (~150-200 km from the present-day coastline). For the escarpment at the location from which BW3 was collected, ~190 km from the present-day coastline, a similar rate of scarp retreat (~1.5 km/Myr) would be required for a constant scarp retreat rate scenario. This is up to two orders of magnitude higher than the model scarp retreat rate of 13-29 m/Myr determined here for sample BW3. At a scarp retreat rate of 29 m/Myr, less than 4 km of scarp retreat can occur in 130 Myr. Indeed, if T = 33 +16/-12 ka is taken to be the average period between rock fall events along the southern escarpment, rock falls with an average thickness of 32-74 m are required to achieve 190 km of scarp retreat.

DV5, DV6 and DV9:

These samples are from the low relief plains (*Die Vlakte*) south of the southern Escarpment (**Figures 5.3, 5.9, 5.10** and **5.11**), and from the east of sample BW3. Samples DV5, DV6 and DV9 yield minimum exposure ages of 205 +20/-18 ka, 337

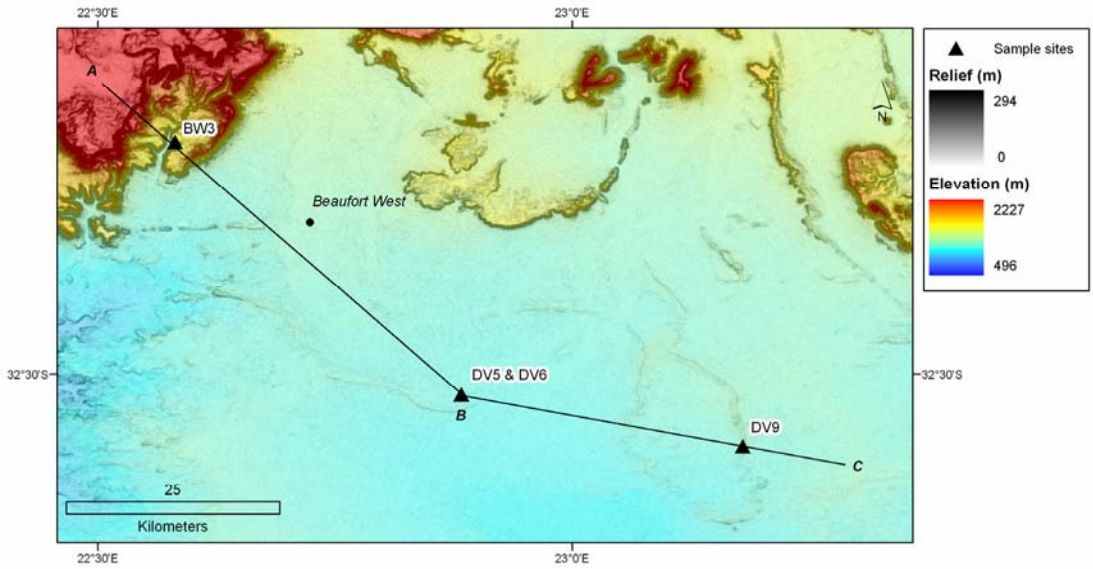

Figure 7.5: The positions of samples BW3, DV5, DV6 and DV9, relative to SRTM elevation and relief (Jarvis *et al*., 2006). The position of the topographic profile intersecting these sample sites along line A-B-C (**Figure 7.6**) is also shown.

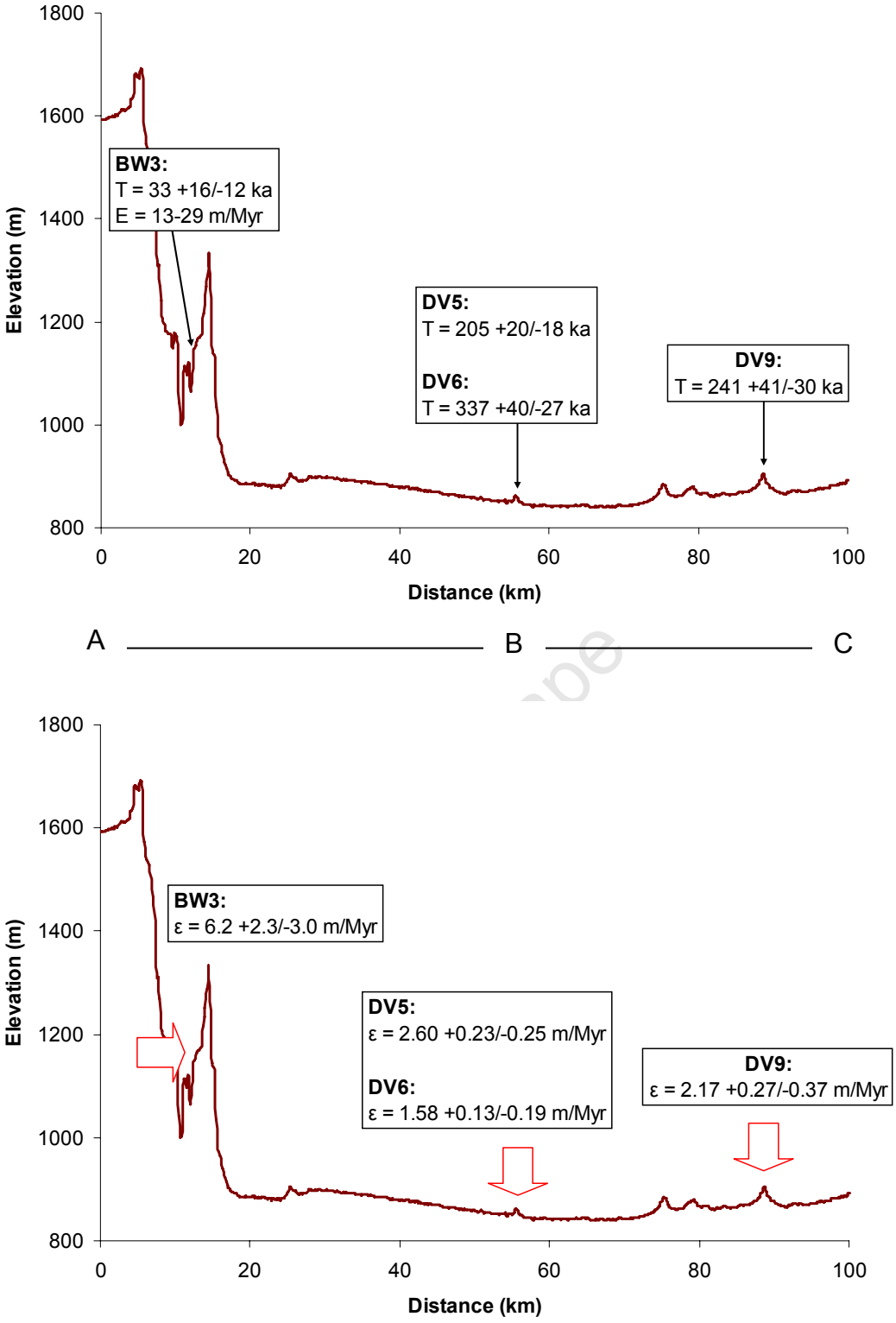

Figure 7.6: Topographic profile A-B-C from northwest to southeast (**Figure 7.5**), showing ^{3}He minimum exposure ages (T, above) and maximum erosion rates (ε, below) according to Fenton *et al.*'s (2009) production rates and Dunai's (2000a) scaling factors. The model scarp retreat rate, E, determined from the minimum exposure age of sample BW3, is also shown (above).

+40/-27 ka and 241 +41/-30 ka, respectively, and maximum erosion rates of 2.60 +0.23/-0.25 m/Myr, 1.58 +0.13/-0.19 m/Myr and 2.17 +0.27/-0.37 m/Myr. Samples DV5 and DV6 are from particularly flat surfaces, raising the possibility that sediment cover may have intermittently existed here. DV9 is from a local topographic high on these otherwise featureless plains, a testimony to the topographic significance of dolerite in even subdued topography. Nevertheless, these three samples all yielded old minimum exposure ages (> 200 ka) and low maximum erosion rates (< 3 m/Myr), with both the T and ε values of samples DV5 and DV9 being in analytical error of each other.

At elevations of ~850-900 m (**Table 5.1**), samples DV5, DV6 and DV9 lie at least 700 m lower than the ~1600 m high southern Escarpment directly to their north (**Figure 7.6**). Extrapolation of even the highest maximum erosion rate from these samples (2.60 +0.23/-0.25 m/Myr for sample DV5) demonstrates that the downwearing of 700 m of rock at such a rate would require 247-295 Myr, a length of time significantly longer than the emplacement age of the Karoo dolerite suite (~183 Ma; Duncan *et al*., 1997). This also assumes only negligible denudation at the summit of the escarpment over the past ~183 Ma, but this has surely not been the case, as the escarpment summit also comprises Karoo dolerites that must also have been emplaced subsurface, and that have been shown to yield maximum erosion rates that are similar to those of samples DV5, DV6 and DV9 (Kounov *et al*., 2007; see Section 7.6.1 below). Clearly, significantly higher denudation rates must have operated here in the past than during the more recent time periods addressed by the cosmogenic nuclide data.

Partridge and Maud (1987) assigned the low relief region, *Die Vlakte*, from which samples DV5, DV6 and DV9 were collected, to the Post African I erosion surface (hypothetical pediplain) for which an initial age of Early Miocene (i.e. ≤ ~23 Ma; Gradstein *et al*., 2004) is given (see discussion in Section 2.4.1). As illustrated schematically in **Figure 2.11**, the age of a pediplain is necessary diachronous, meaning that according to such a model, the Early Miocene age is a maximum estimate for when a northwards-retreating scarp would have passed this point. However, the oldest minimum exposure age here (DV6, T = 337 +40/-27 ka) is considerably younger than Early Miocene. Extrapolation of DV5's ε value would

also have resulted in surface lowering by at least 54-65 m of rock since 23 Ma. This thickness of rock is a minimum estimate, because possibly overlying sedimentary rocks are likely to have been more rapidly eroded than the resistant dolerite. Thus, if pediplanation had occurred here in the early Miocene, it seems unlikely that a pediplain would have survived intact since this time.

It may be noted that for samples DV5 and DV6, ^{21}Ne data yields still higher minimum exposure ages (248 ± 16 ka and 403 ± 23 ka, respectively), and lower maximum erosion rates (2.15 ± 0.14 m/Myr and 1.33 ± 0.14 m/Myr, respectively). Whilst this may be due to a significant nucleogenic ^{21}Ne component being present, use of this data would also support the inferences that a significant decline in vertical denudation rates must have occurred in this region since formation of the escarpment, and that at least ~50 m of rock must have been denuded here since the early Miocene at recent rates of erosion.

7.4.2 Samples GR1, GR2, GR3, GR5 and CB1

The locations of samples GR1, GR2, GR3, GR5 and CB1 are shown in **Figure 7.7**. Minimum exposure ages and maximum erosion rates for these samples are displayed along a topographic profile in **Figure 7.8**, where a model scarp retreat rate for sample CB1 is also shown.

GR1 and GR2:

These two horizontal surface samples were collected from boulders along the spine of dolerite ridge, within the southern "escarpment zone" as defined by Partridge and Maud (1987), to the east of samples BW3, DV5, DV6 and DV9, and to the south of the Orange River drainage divide. Both GR1 and GR2 were collected from horizontal rock surfaces where there was evidence of active spheroidal weathering. GR1 was collected from a rock slab that was partially detached from the underlying dolerite mass, whereas GR2 was collected from a dolerite surface that appeared to have exfoliated a rind of dolerite more recently than the surrounding rock (**Figure 5.12**).

These field observations suggested that sample GR2 was more likely to yield a younger minimum exposure age and higher maximum erosion rate than GR1. Indeed, this is borne out by the results of the cosmogenic nuclide analysis. For GR1, T = 165

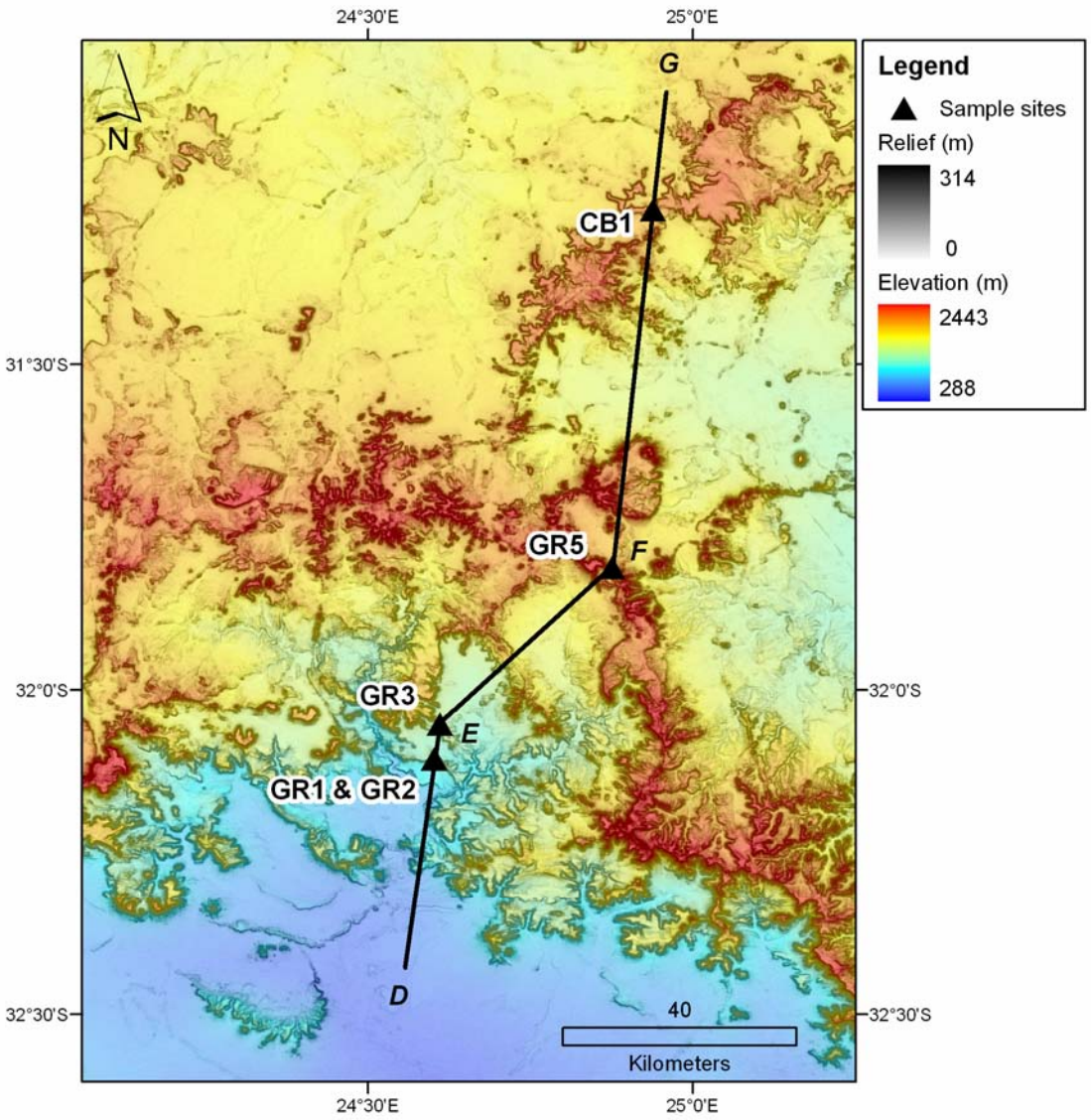

Figure 7.7: The positions of samples GR1, GR2, GR3, GR5 and CB1 relative to SRTM elevation and relief (Jarvis *et al.*, 2006). The position of the topographic profile intersecting these sample sites along line D-E-F-G (**Figure 7.8**) is also shown.

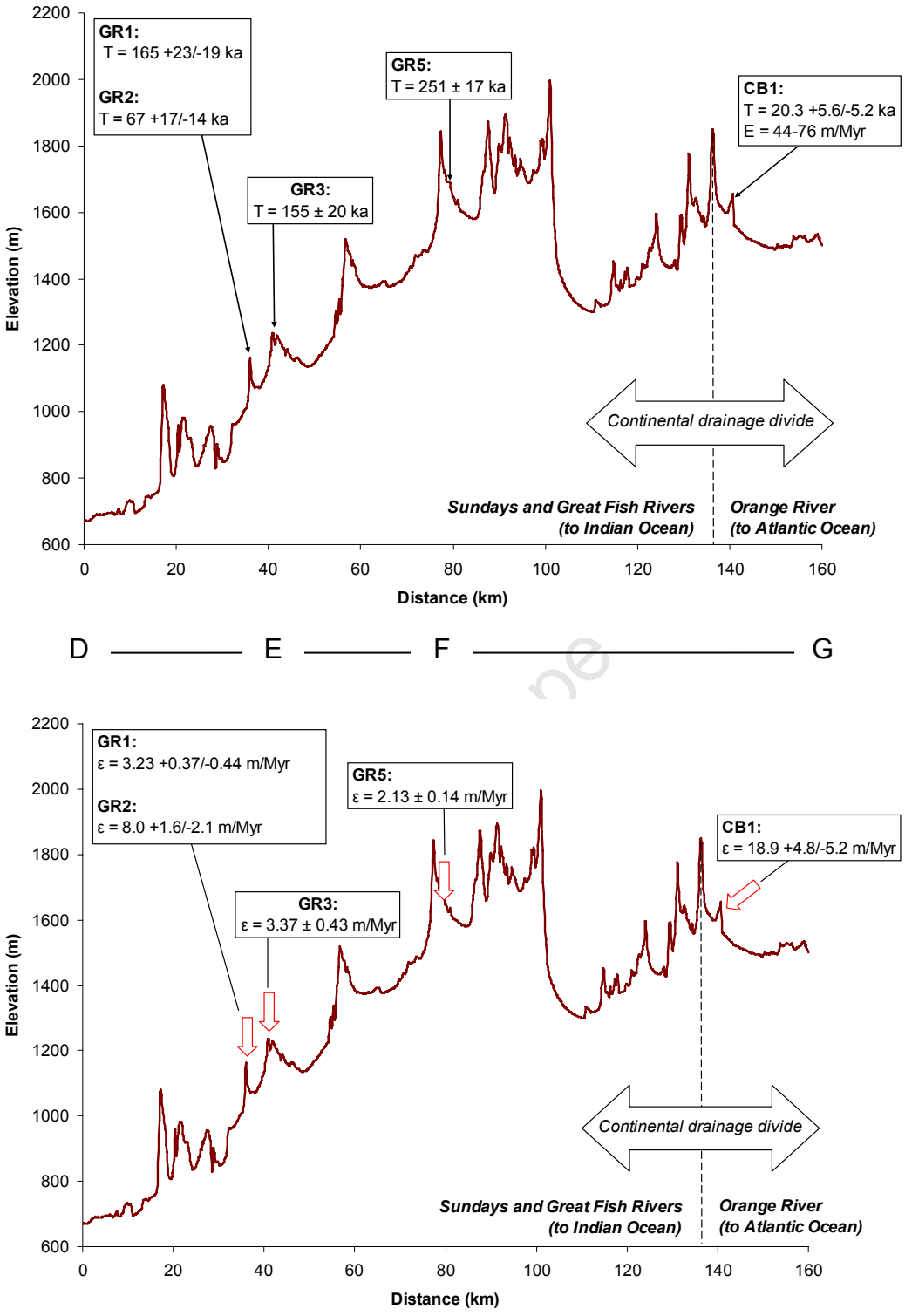

Figure 7.8: Topographic profile D-E-F-G from south to north (**Figure 7.7**), showing ^{3}He minimum exposure ages (T, above) and maximum erosion rates (ε, below) according to Fenton *et al.*'s (2009) production rates and Dunai's (2000a) scaling factors. The model scarp retreat rate, E, determined from the minimum exposure age of sample CB1, is also shown (above).

+23/-19 ka, and ε = 3.23 +0.37/-0.44 m/Myr, and for GR2, T = 67 +17/-14 ka and ε = 8.0 +1.6/-2.1 m/Myr. GR2 thus yields the second highest ε value and the third lowest T value in the study, which is also the highest ε value and lowest T value for all the horizontal and sub-horizontal surface samples. These results emphasise the potentially incremental nature of dolerite erosion even for locally horizontal surfaces, and the effect that this may have on T and ε values.

For sample GR1, ^{21}Ne abundances yield T and ε estimates (T = 183 ± 27 ka; ε = 2.91± 0.43 m/Myr) that are similar to those for ^{3}He, although for GR2, ^{21}Ne T values are substantially higher (T = 106 ± 13 ka), and ^{21}Ne ε values substantially lower (ε = 5.05 ± 0.60 m/Myr), than the corresponding ^{3}He estimates. Nevertheless, ^{21}Ne data still yields a younger minimum exposure and higher maximum erosion rate for GR2 than for GR1.

GR3 and GR5:

Samples GR3 and GR5 (**Figures 5.3, 5.13** and **5.14**) represent horizontal or sub-horizontal surface samples, collected from the coastward-draining Sundays and Great Fish River catchments, respectively. At 1260 m, the site from which sample GR3 was collected lies within the southern "escarpment zone", as defined by Partridge and Maud (1987), whereas sample GR5 (1647 m elevation) was collected from the "area above the African Surface", as defined by these same authors. For sample GR3, T = 155 ± 20 ka and ε = 3.37 ± 0.43 m/Myr, and for sample GR5, T = 251 ± 17 ka and ε = 2.13 ± 0.14 m/Myr. The T and ε values for GR5 are thus similar to those of other locally horizontal dolerite surfaces (e.g. DV5 and DV6), although GR3 yields a somewhat lower minimum exposure age and higher maximum erosion rate. However, the relative similarity of these ε values suggests that they may approximate a common subaerial weathering rate for Karoo dolerite that is < 3 m/Myr in this area.

CB1:

Sample CB1 (**Figures 5.2** and **5.15**), from an inclined (α = 44º) surface north of the southern drainage divide of the Orange River basin, yields T = 20.3 +5.6/-5.2 ka and ε = 18.9 +4.8/-5.2 m/Myr. As with sample BW3, field evidence suggests that this surface actively loses mass through the episodic exfoliation of rock slabs that are centimetres to tens of centimetres thick. Again, these increments are typically thinner

than the thickness of rock equivalent to three effective attenuation lengths here (1.15 m; **Table 7.1**). For CB1, the model scarp retreat rate, E, is greater than for BW3, at 44-76 m/Myr, due to CB1's younger minimum exposure age and longer effective attenuation length. It should be noted that this scarp retreat rate is a vector perpendicular to CB1's 44º surface, which may be resolved into horizontal and vertical components, of 31-53 m/Myr and 32-55 m/Myr, respectively (**Figure 7.9**).

It may be noted that ^{21}Ne minimum exposure ages are substantially higher than ^{3}He minimum exposure ages for this sample (T (^{21}Ne) = 35.4 ± 6.7 ka; Dunai (2000a) scaling). However, as with samples BW3 and GR2, ^{3}He data is especially preferred over ^{21}Ne data, due to the likelihood of significant nucleogenic ^{21}Ne components being present (Section 6.4.1). Use of the ^{21}Ne minimum exposure ages would result in a lower model scarp retreat rate, of 14-21 m/Myr (perpendicular to the surface).

7.4.3 Samples GD1, GD2, GD3

The locations of samples GD1, GD2 and GD3 are shown in **Figure 7.10**, with T, ε and E values on a topographic profile in **Figure 7.11**.

GD1:

GD1 (α = 90º) is from a cliff face below the summit of a *koppie* (inselberg) near Gariep Dam on the Orange River (**Figures 5.3; 5.16** and **5.17**). Instead of being characterised by exfoliating dolerite sheets (e.g. samples BW3 and CB1), the scarp face from which GD1 is sampled is characterised by angular dolerite blocks. This suggests that the mass wasting of dolerite blocks (rather than exfoliating sheets) is the dominant denudational process here. GD1 yields a minimum exposure age of 219 ± 13 ka, and three effective attenuation lengths here are equivalent to a thickness of 0.61 m. If it is assumed that this rock face only loses mass through the wasting of blocks > 0.61 m thick, then the age of the last rock fall is within 5 % of 219 ± 13 ka. A loss of 0.61 m every 219 ± 13 ka corresponds to a model scarp retreat rate of only 2.6 - 3.0 m/Myr. In comparison with sites BW3 and CB1, it is more plausible that for GD1, larger rock falls greater than 0.61 m may occur, but it is also obvious that the period from the last large rock fall here to the next (future) rock fall can only be greater than the minimum exposure age T.

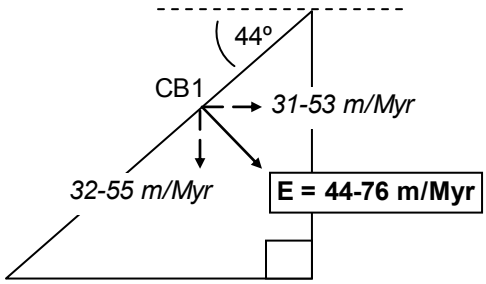

Figure 7.9: Schematic illustration of the slope from which CB1 is sampled. The model scarp retreat rate perpendicular to the scarp, E (determined from the minimum exposure age T, and an assumed rock fall thickness of 1.15 m, equivalent to 3 effective attenuation lengths here), may be resolved into horizontal and vertical components. For E = 44-76 m/Myr and an inclined surface of dip angle 44º, the erosion rate in the horizontal direction is 31-53 m/Myr, and the vertical downwearing rate is 32-55 m/Myr.

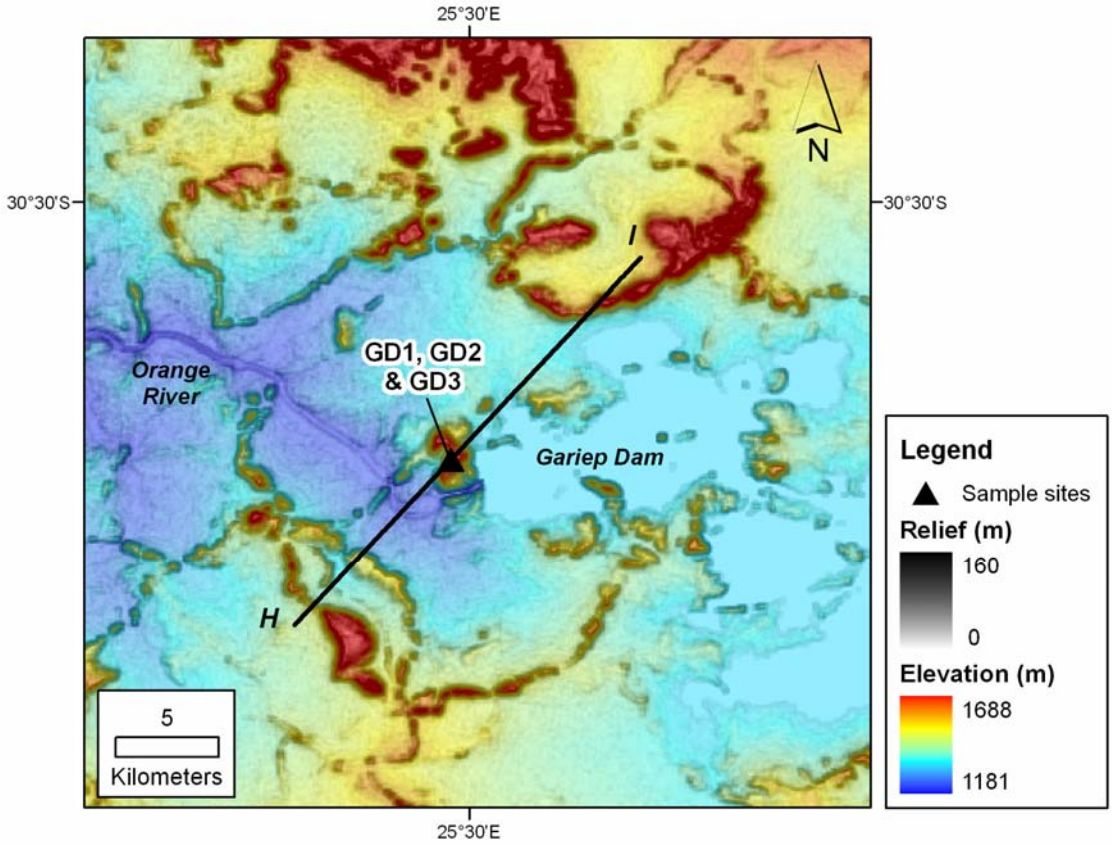

Figure 7.10: The positions of samples GD1, GD2 and GD3 relative to SRTM elevation and relief (Jarvis *et al*., 2006). The position of the topographic profile intersecting these sample sites along line H-I (**Figure 7.11**) is also shown.

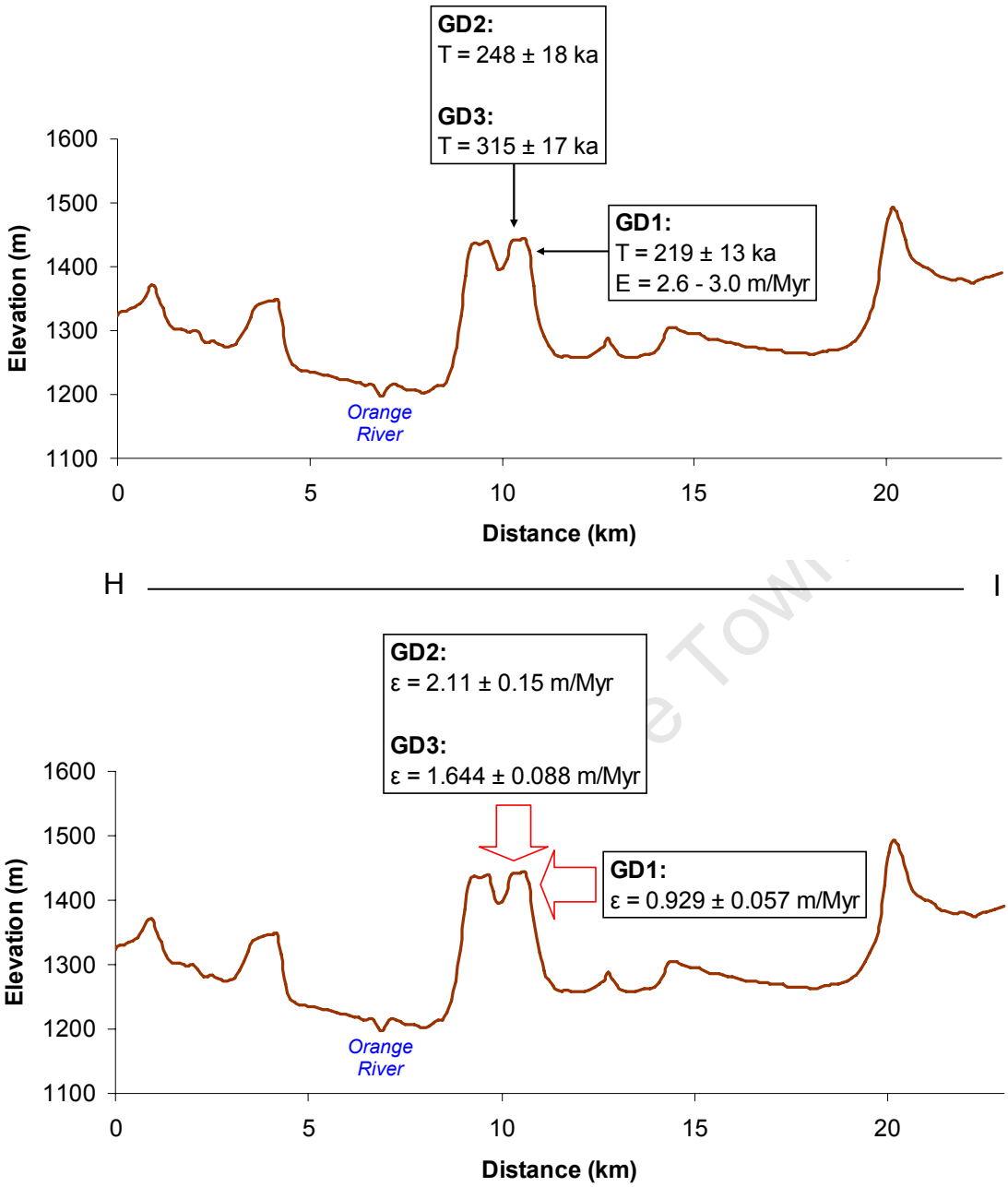

Figure 7.11: Topographic profile H-I from southwest to northeast (**Figure 7.10**), showing ^{3}He minimum exposure ages (T, above) and maximum erosion rates (ε, below) according to Fenton *et al.*'s (2009) production rates and Dunai's (2000a) scaling factors. The model scarp retreat rate, E, determined from the minimum exposure age of sample GD1, is also shown (above).

If the model of constant chemical weathering and granular disintegration is assumed here, then the rate at which mass is lost is even lower, with $\varepsilon = 0.929 \pm 0.057$ m/Myr over the characteristic timescale $T_\varepsilon = 219 \pm 13$ ka. Whichever model is assumed, GD1 represents a scarp face that has been stable over a surprisingly long period of time.

GD2 and GD3:

Samples GD2 and GD3 were collected from the summit of the *koppie* from which GD1 was sampled, and yield minimum exposure ages of 248 ± 18 ka and 315 ± 17 ka, respectively, corresponding to maximum erosion rates of 2.11 ± 0.15 m/Myr and 1.644 ± 0.088 m/Myr, respectively. Thus, despite these samples being collected only metres apart, neither their minimum exposure ages, nor their maximum erosion rates, are within analytical error of each other. This suggests that the ε values here do not only reflect the chemical weathering rate for both these samples, as there seems little reason why adjacent horizontal surfaces from the same dolerite surface should weather at different rates, although some past subtle topographic factor leading to the preferential accumulation of moisture on one of these surfaces, and thus a greater weathering rate, cannot be ruled out (e.g. Kounov *et al*., 2007). Instead, these surfaces may also lose mass incrementally through spheroidal weathering, and thus the variable ε values here reflect the asynchronous and localised nature of this process. Indeed, in **Figure 5.17** the boulder from which GD2 was sampled is seen to have an exfoliating surface, as do the more rounded boulders in the right background of **Figure 5.18**. If this interpretation is accepted, then the chemical weathering rate for dolerite here is less than or equal to the lower ε value, i.e. $\leq 1.644 \pm 0.088$ m/Myr.

Note that both T *and* ε values are higher for the summit samples GD2 and GD3 than for the scarp face sample GD1 (it should be remembered that ε is not simply inversely proportional to T, but is also dependent on the effective attenuation length Λ, which varies with slope angle). If the ε value for GD1 does represent the chemical weathering rate for this 90º scarp face, the lower ε value for GD1 than for GD2 and GD3 might be due to the more rapid drainage of moisture from this steeper surface. In any event, the generally similar constraints on the exposure histories of samples GD1, GD2 and GD3 suggest that a common process has been dominant in the denudation of these three surfaces. This suggests that both the vertical and horizontal surfaces at the summit of this *koppie* have been losing mass predominantly through chemical

weathering, although it is also possible that they all experienced exhumation from beneath a regolith and/or overlying boulders (with thicknesses > 3Λ/ρ) at a similar time.

7.4.4 Samples OR1, OR2 and OR3

The locations of samples OR1 and OR2 are shown in **Figure 7.12**, and the location of sample OR3 is shown in **Figure 7.14**. Due to the fine spatial resolution of these maps, base maps for **Figures 7.12** and **7.14** are derived from the digitised and georectified 1:50,000 scale topographic maps *2924DC Havengabrug* (Chief Director of Surveys and Mapping, 1988a) and *3024BA Petrusville* (Chief Director of Surveys and Mapping, 1988b). Minimum exposure ages and maximum erosion rates for these samples are shown on topographic profiles in **Figures 7.13** and **7.15**, with elevation data from the SRTM DEM.

OR1, OR2 and OR3:

Sample OR1, from the inclined (30º) slope of a *koppie* near Vanderkloof Dam (**Figure 5.20**), yields T = 146 ± 12 ka and ε = 3.10 ± 0.25 m/Myr. Sample OR2, a *koppie* summit near Vanderkloof Dam (**Figure 5.21**), yields a minimum exposure age of 236 ± 15 ka and a maximum erosion rate of 2.26 ± 0.14 m/Myr. Sample OR3, from the top of a tor (boulder pile) capping a dolerite *koppie* (**Figure 5.19**), yields a minimum exposure age of 201 ± 14 ka and a maximum erosion rate of 2.63 ± 0.19 m/Myr.

As with all dolerite surfaces, ε values for OR1, OR2 and OR3 may be considered to be maximum rates of Karoo dolerite weathering. However, if chemical weathering and granular disintegration is assumed to be the dominant process here, the chemical weathering rate may be higher for the inclined OR1 surface than for the more horizontal OR2 and OR3 surfaces in the same area, somewhat in contrast to the relation between ε values for GD1, GD2 and GD3, where the steeper surface yielded a lower maximum erosion rate. For sample OR1, the relatively smooth surface from which the sample was collected and the lower slope angle of 30º means that it is unlikely that this surface loses mass through slope failure in response to downslope erosion. However, episodic exfoliation of the dolerite remains a plausible mechanism

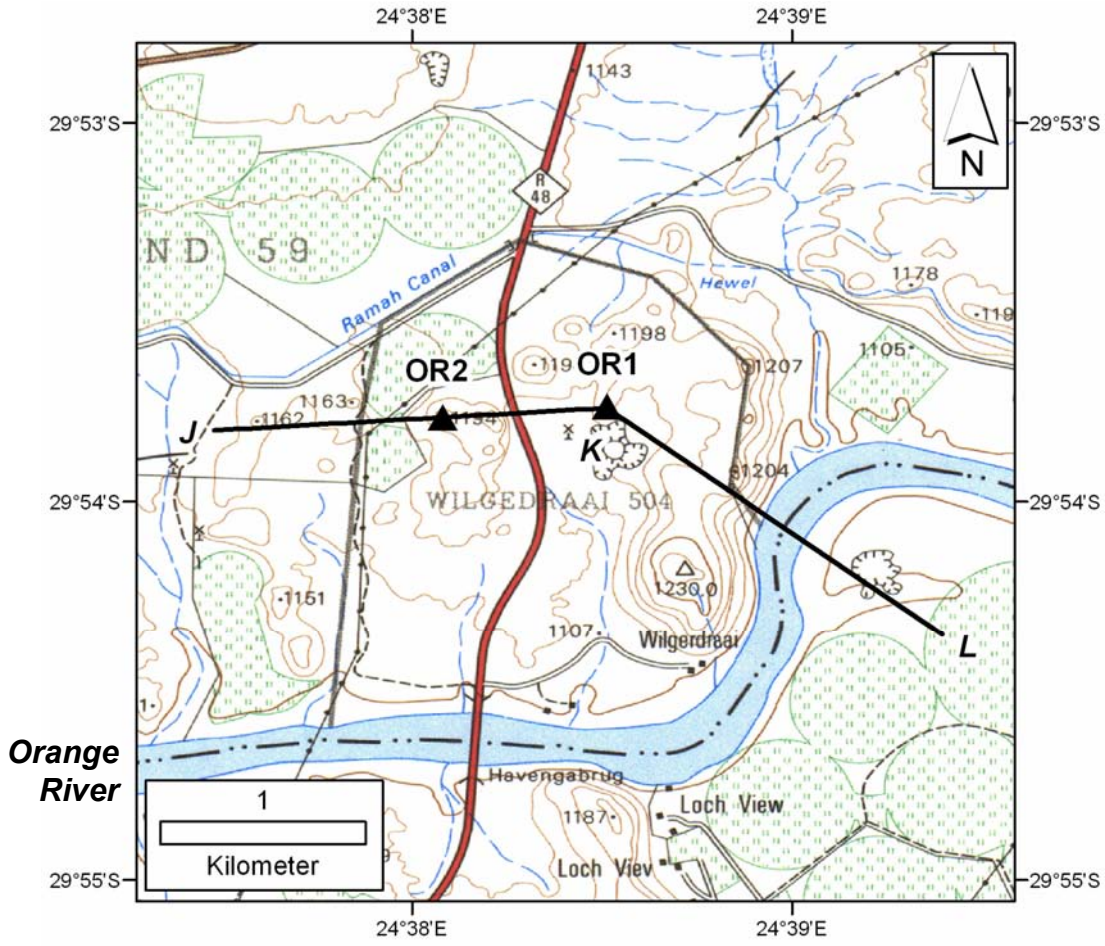

Figure 7.12: The location of samples OR1 and OR2 relative to the 1:50,000 topographic map *2924DC Havengabrug* (Chief Director of Surveys and Mapping, 1988a). The location of topographic profile J-K-L (**Figure 7.l3**) is also shown.

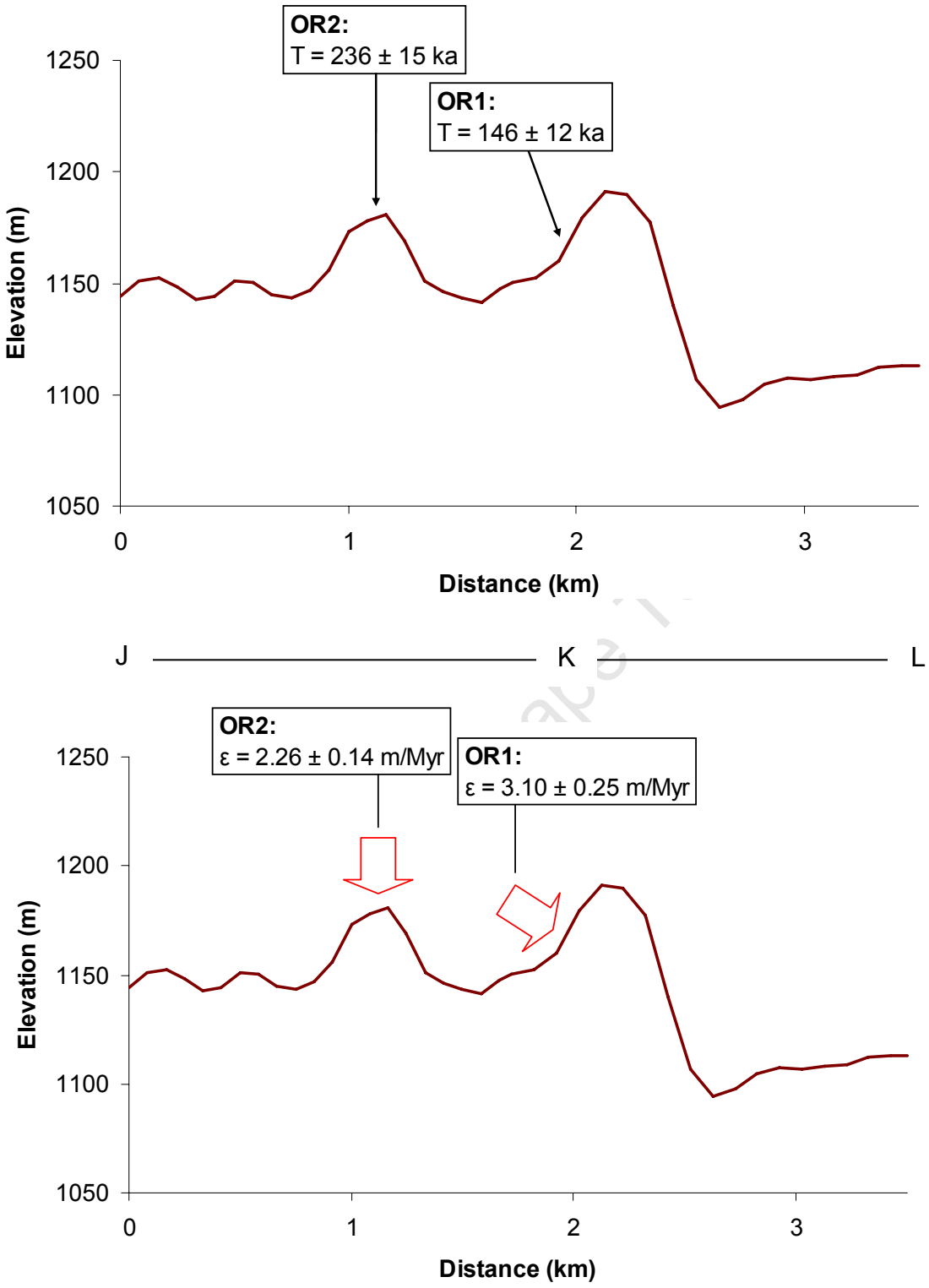

Figure 7.13: Topographic profile J-K-L from west to east (**Figure 7.12**), showing ^{3}He minimum exposure ages (T, above) and maximum erosion rates (ε, below) according to Fenton *et al.*'s (2009) production rates and Dunai's (2000a) scaling factors. Elevation is derived from the SRTM DEM (Jarvis *et al.*, 2006).

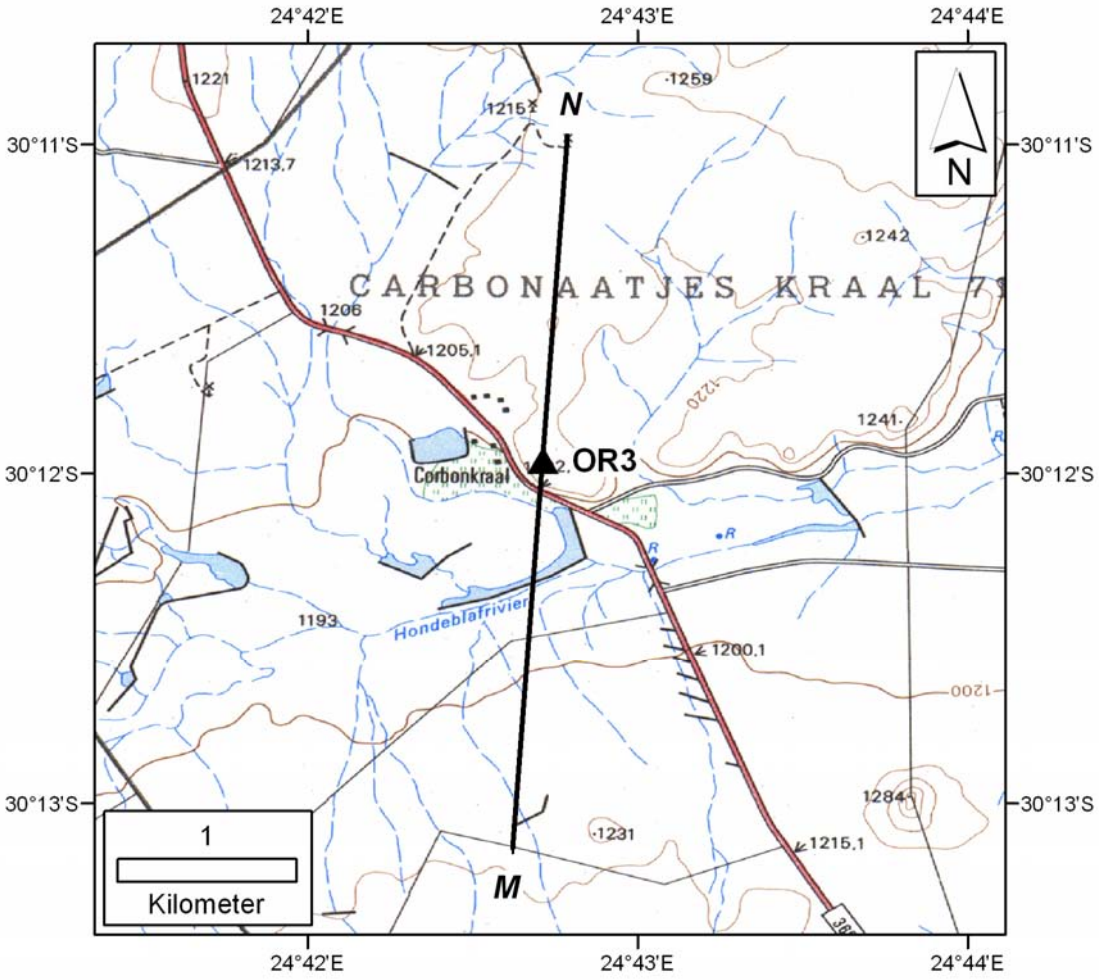

Figure 7.14: The location of sample OR3 relative to the 1:50,000 topographic map *3024BA Petrusville* (Chief Director of Surveys and Mapping, 1988b). The location of topographic profile M-N (**Figure 7.15**) is also shown.

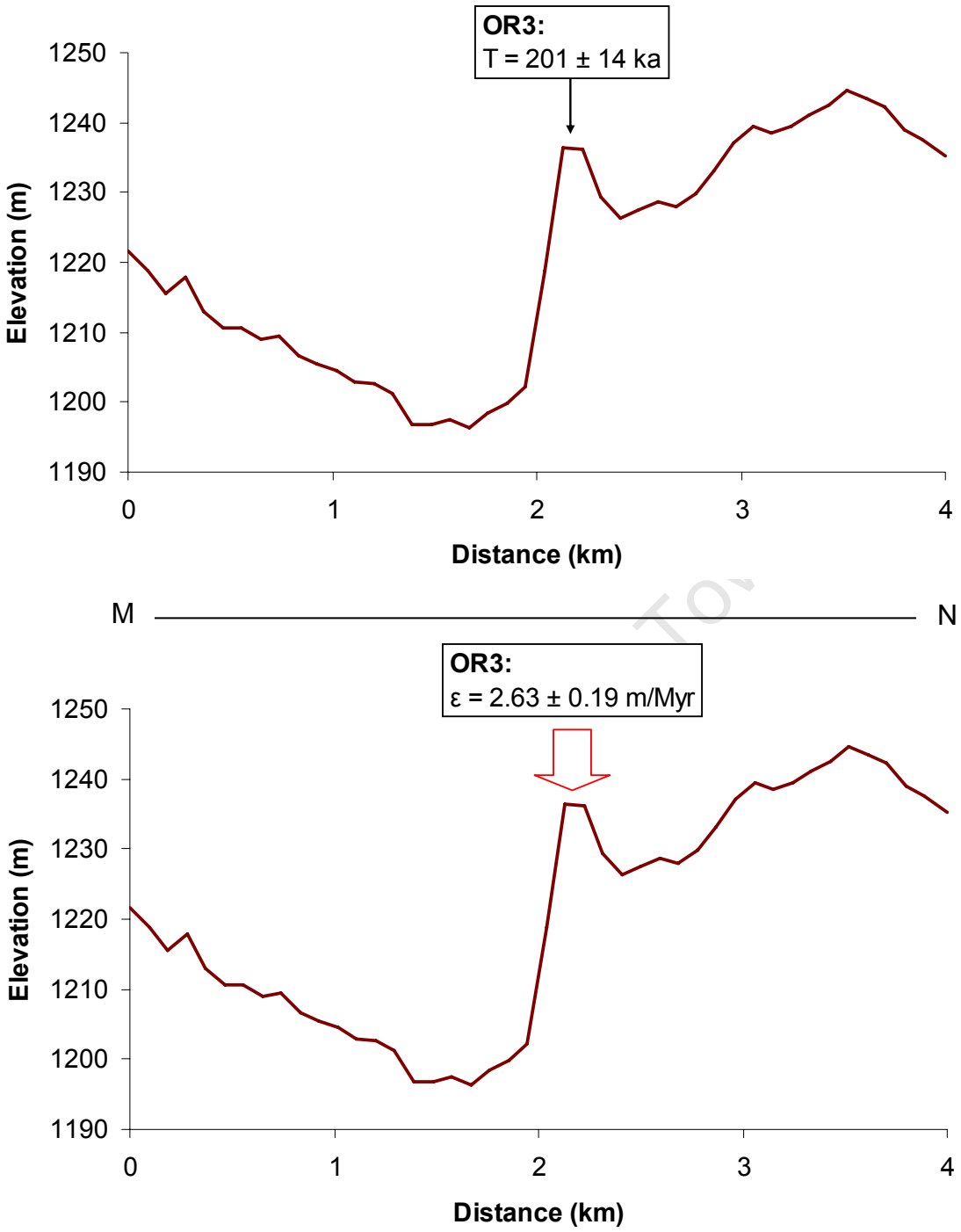

Figure 7.15: Topographic profile M-N from south to north (**Figure 7.14**), showing the ^{3}He minimum exposure age (T, above) and maximum erosion rate (ε, below) according to Fenton *et al.*'s (2009) production rates and Dunai's (2000a) scaling factors. Elevation is derived from the SRTM DEM (Jarvis *et al.*, 2006).

of erosion for this slope, and fissures in the dolerite that are semi-parallel to the hillslope surface are visible in **Figure 5.20**.

It is also possible that this area may have been subjected to regolith development and subsequent erosion, perhaps during some local base level fall event in the adjacent Orange River. Indeed, the tor from which OR3 was collected may represent the higher part of an exhumed weathering front, as depicted in Stage 3 in **Figure 7.2**. The accumulation of dolerite boulders on the upper parts of the hillslope from which OR1 was collected (**Figure 5.20**), and the subsurface weathering of Karoo dolerite in a quarry at the base of the *koppie* from which OR2 was collected (**Figure 5.22**) are also consistent with this hypothesis. If such an interpretation is valid, the minimum exposure ages for these surfaces represent minimum exhumation ages.

7.4.5 Samples IT1, IT3, IT5, IT6, IT8, IT9 and IT10

The locations of samples IT1, IT3, IT5, IT6, IT8, IT9 and IT10 are shown in **Figure 7.16**. Minimum exposure ages and maximum erosion rates for these samples are displayed along a topographic profile in **Figure 7.17**, where a geological cross section along the topographic profile and a model scarp retreat rate for sample IT6 are also shown.

IT6 and IT5:

Sample IT6 ($\alpha = 90^{o}$), is from a dolerite cliff face at the summit of the incised valley of the meandering Pongola River (**Figures 5.4** and **5.23**). Previously intruded between the base of the Karoo Supergroup and the underlying Pongola Group, the upper surface of this dolerite defines a small, dissected plateau at ~900 m elevation, with the Pongola River to the north and a scarp of Karoo sedimentary rocks to the south.

IT6 yields a minimum exposure age of 359 ± 86 ka and a maximum erosion rate of 0.57 ± 0.14 m/Myr, the lowest ε value determined in this study. This scarp face displayed no obvious signs of active exfoliation, but was partially lichen-covered and less angular in appearance than the scarp from which sample GD1 was collected. It is thus possible that the time interval since the last rock fall here has been so long that this surface has been losing mass predominantly through chemical weathering and granular disintegration over the characteristic time period of erosion (T_{ε} = 359 ± 86

ka). As with GD1, this particularly low weathering rate may be due, at least in part, to water draining rapidly from this vertical surface. The overall stability of the scarp might in turn be due to the Pongola Group meta-sediments and meta-volcanics that crop out downslope of this site being particularly resistant to erosion.

If T = 359 ± 86 ka is taken to be the age of the last rock fall of 0.61 m thickness, this yields a model scarp retreat rate of 1.4 – 2.2 m/Myr. As this scarp face is situated at the summit of the incised Pongola River valley, the T value is also the minimum age of initial incision for this > 400 m deep and > 7 km wide river valley (**Figure 7.17**). However, in order for the scarp face to retreat by even 1 km (less than the approximate horizontal distance between the site of IT6 and the current position of the Pongola River; **Figure 7.17**) at the rate of E, some 450-730 Myr are required - a period of time considerably longer than the emplacement age of the Karoo dolerite (~183 Ma; Duncan *et al*., 1997). Furthermore, if river incision here post-dated initial pediplanation of the "African Surface", as proposed by Partridge and Maud (1987), incision must have occurred during a still shorter time period (< 140 Myr; e.g. Gradstein *et al*., 2004). For 1 km of scarp retreat to have occurred within 140 Myr, the required average thickness of rock falls with an average periodicity of 359 ka is 2.8 m. No field evidence of large rock falls (e.g. downslope debris fans) was observed at this site. This suggests that a significant decrease in the rate of fluvial incision and valley widening has occurred here in the period before 359 ± 86 ka. As the steeply dipping Pongola Group lithologies crop out throughout the incised valley of the Pongola River (with the exception of Karoo dolerite at the summit), it would appear that a change in lithology with depth is an unlikely explanation for the change in incision rate with depth. Instead, major incision of the Pongola River may have occurred during a discrete period of local relative base level fall, with the landscape retaining a relatively steady-state form since that time.

Sample IT5 was collected from the upper surface of the same dolerite intrusion as IT6. For sample IT5 (**Figures 5.4** and **5.24**), T = 483 ± 36 ka and ε = 1.101 ± 0.082 m/Myr. These constraints for IT5 are thus similar to those of IT6 from the corresponding scarp face (T = 359 ± 86 ka; ε = 0.57 ± 0.14 m/Myr), but with a slightly higher minimum exposure age *and* maximum erosion rate, due to the dependence of ε on the slope angle. This is analogous to the differences observed

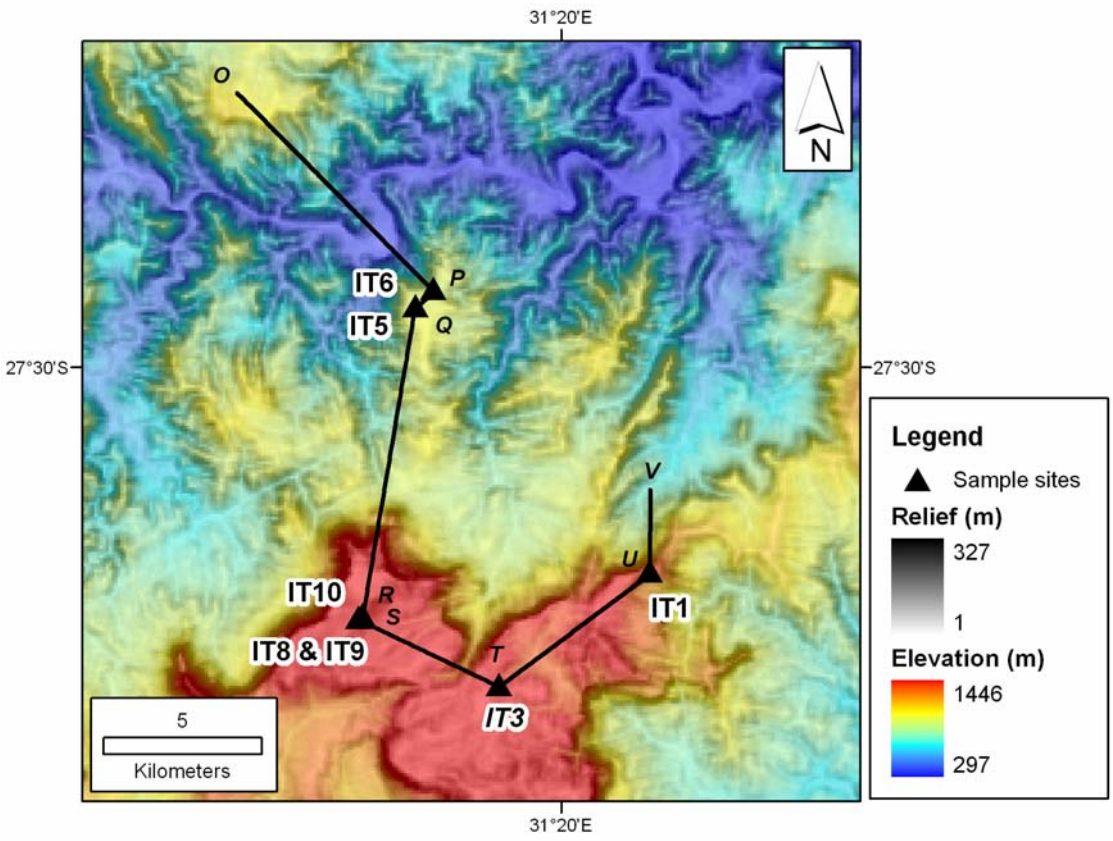

Figure 7.16: The positions of samples IT1, IT3, IT5, IT6, IT8, IT9 and IT10 relative to SRTM elevation and relief (Jarvis *et al*., 2006). The position of the topographic profile intersecting these sample sites along line O-P-Q-R-S-T-U-V (**Figure 7.17**) is also shown.

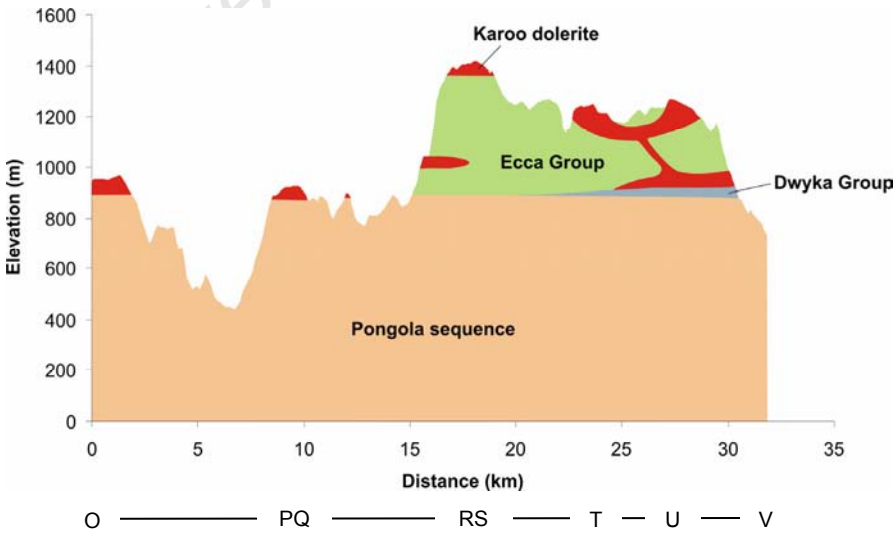

Figure 7.17: *(Continued on following page).*

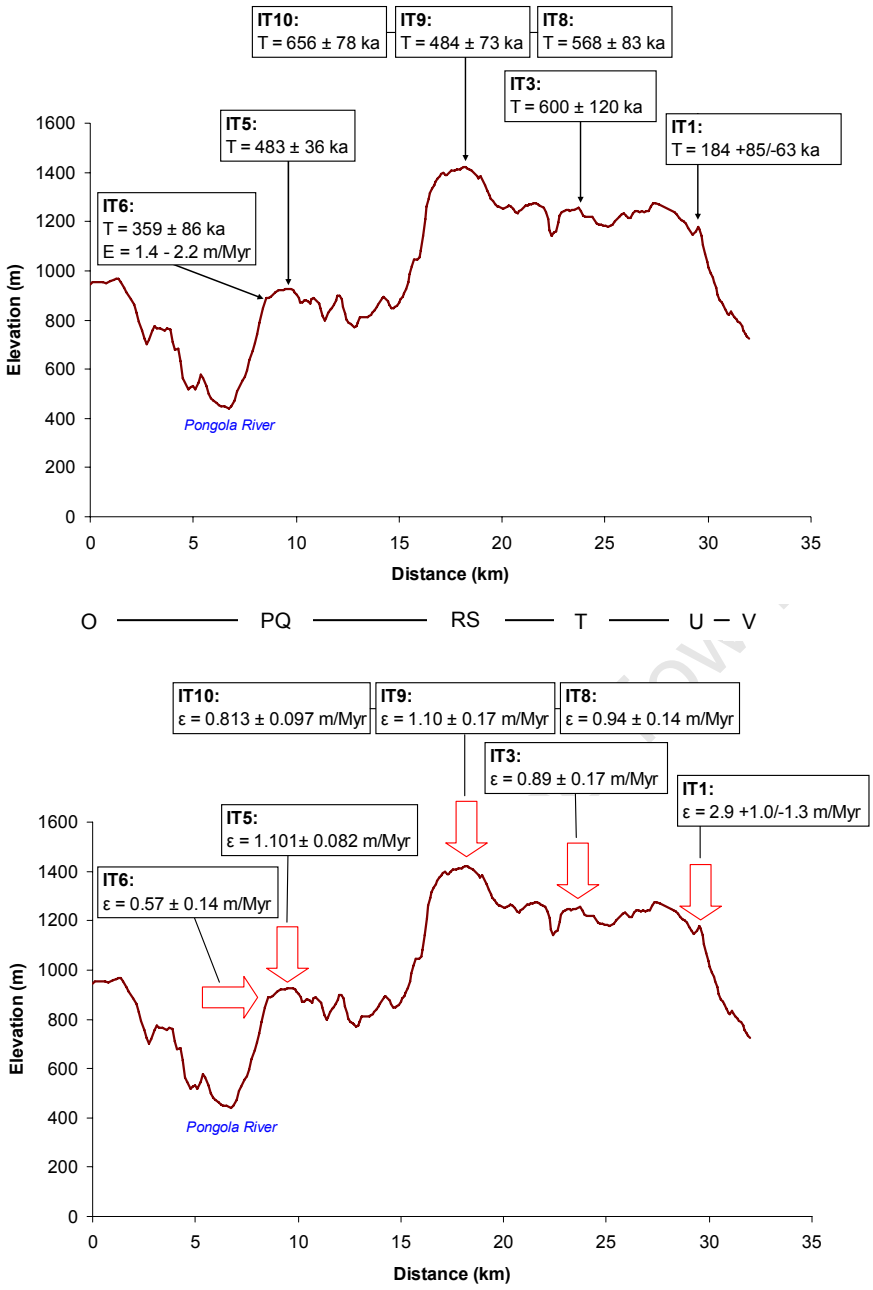

Figure 7.17: *(Continued from previous page).* Previous page: Schematic geological cross-section along topographic profile O-P-Q-R-S-T-U-V (**Figure 7.16**). This page: Topographic profile O-P-Q-R-S-T-U-V showing ^{3}He minimum exposure ages (T, above) maximum erosion rates (ε, below) according to Fenton *et al.*'s (2009) production rates and Dunai's (2000a) scaling factors. The model scarp retreat rate, E, determined from the minimum exposure age of sample IT6, is also shown (above).

between scarp sample GD1 and the corresponding summit samples GD2 and GD3 (Section 7.4.3), and it may be interpreted as evidence of lower chemical weathering rates for more easily drained, steeper rock surfaces. Note that ^{21}Ne data for IT5 yields a higher minimum exposure age of 587 ± 32 ka, and a lower maximum erosion rate of 0.905 ± 0.049 m/Myr. Whilst these values are not within analytical error of the ^{3}He estimates, they support the same geological interpretations.

IT1, IT3, IT8, IT9 and IT10:

These five samples were collected from across a higher region (1100-1400 m) south of the samples IT5 and IT6, which was assigned to the (Early Cretaceous) "African Surface" by Partridge and Maud (1987).

Sample IT1 (**Figures 5.4** and **5.25**) was collected from a dolerite boulder at an elevation of 1101 m, and yields T = 184 +85/-63 ka and ε = 2.9 +1.0/-1.3 m/Myr. Sample IT3 (**Figures 5.4** and **5.26**), from a dolerite pavement at 1252 m, yields a higher minimum exposure age of 600 ± 120 ka and a lower maximum erosion rate of 0.89 ± 0.17 m/Myr. IT8 and IT9 (**Figures 5.4** and **5.27**), adjacent samples collected from the same exfoliating dolerite pavement at 1386 m elevation, yielded T and ε values within analytical error of each other. For IT8, T = 568 ± 83 ka and ε = 0.94 ± 0.14 m/Myr; and for IT9, T = 484 ± 73 ka and ε = 1.10 ± 0.17 m/Myr. This confirms the reproducibility of this data, and also suggests that the exhumation of this dolerite pavement at such low rates is relatively homogeneous on this fine spatial scale. Finally, sample IT10 from the same dolerite intrusion and at the highest point in the immediate area (**Figures 5.4** and **5.28**), yields similar results, where T = 656 ± 78 ka and ε = 0.813 ± 0.097 m/Myr.

Maximum erosion rates for these five horizontal surface samples thus range from 0.813 ± 0.097 m/Myr (sample IT10) to 2.9 +1.0/-1.3 m/Myr (sample IT1). This relatively narrow range of ε values, which is also typical of most samples in this study, suggests that these estimates reflect a common rate of Karoo dolerite weathering in this region.

As noted above, samples IT1, IT3, IT8, IT9 and IT10 were collected from an area assigned to Partridge and Maud's (1987) "African Surface", with an Early Cretaceous

age of inception. However as with the Post-African I surface in the *Die Vlakte* area, the intact preservation of a pediplain since at least the time of initiation (Early Cretaceous, i.e. 140-100 Ma; Gradstein *et al*., 2004) seems unlikely. Even by extrapolating from the lowest maximum erosion rate here, ε = 0.813 ± 0.097 m/Myr (sample IT10), a vertical thickness of at least 72 - 91 m of rock would have been eroded from this area since 100 Ma.

7.4.6 Summary

T and ε values for all samples are compared in **Figure 7.18**. Note that because T is inversely proportional to ε for a given effective attenuation length, data from samples with the same dip angle define a hyperbola.

Vertical and inclined surfaces (α = 30º-90º; n = 5) yield variable T and ε values, with T values ranging from 20.3 + 5.6/-5.2 ka (CB1) to 359 ± 86 ka (IT6), and with ε values ranging from 18.9 +4.8/-5.2 m/Myr (CB1) to 0.57 ± 0.14 m/Myr (IT6). In contrast, horizontal and sub-horizontal surfaces (α = 0º-12º; n = 17) yield a wider range of T values, ranging from 67 +17/-14 ka (GR2) to 656 ± 78 ka (IT10), but with the exception of one sample where field evidence suggests recent exfoliation (GR2; ε = 8.0 +1.6/-2.1 m/Myr), these surfaces all display maximum erosion rates of less than 4 m/Myr, ranging from 3.37 ± 0.43 m/Myr (GR3) to 0.813 ± 0.097 m/Myr (IT10).

The main interpretations that emerge from this dataset may be summarised as follows:

1. T values for scarp faces where erosion through large rock falls is plausible (samples CB1, BW3, GD1 and IT6) may be used to define model rates of scarp retreat (E values) for the period T. Extrapolation of these E values over longer time periods (>10^6 yr) demonstrates that these rates are too low (by a factor of 2 to 4) to account for the development of features such as the incised Pongola river valley, and also too low (by more than an order of magnitude) for the southern escarpment to have retreated from a position close to the present coastline at a constant rate. Furthermore, present dolerite downwearing rates coastward of the escarpment are too low to have resulted in escarpment formation in the time elapsed since Karoo dolerite emplacement. This suggests

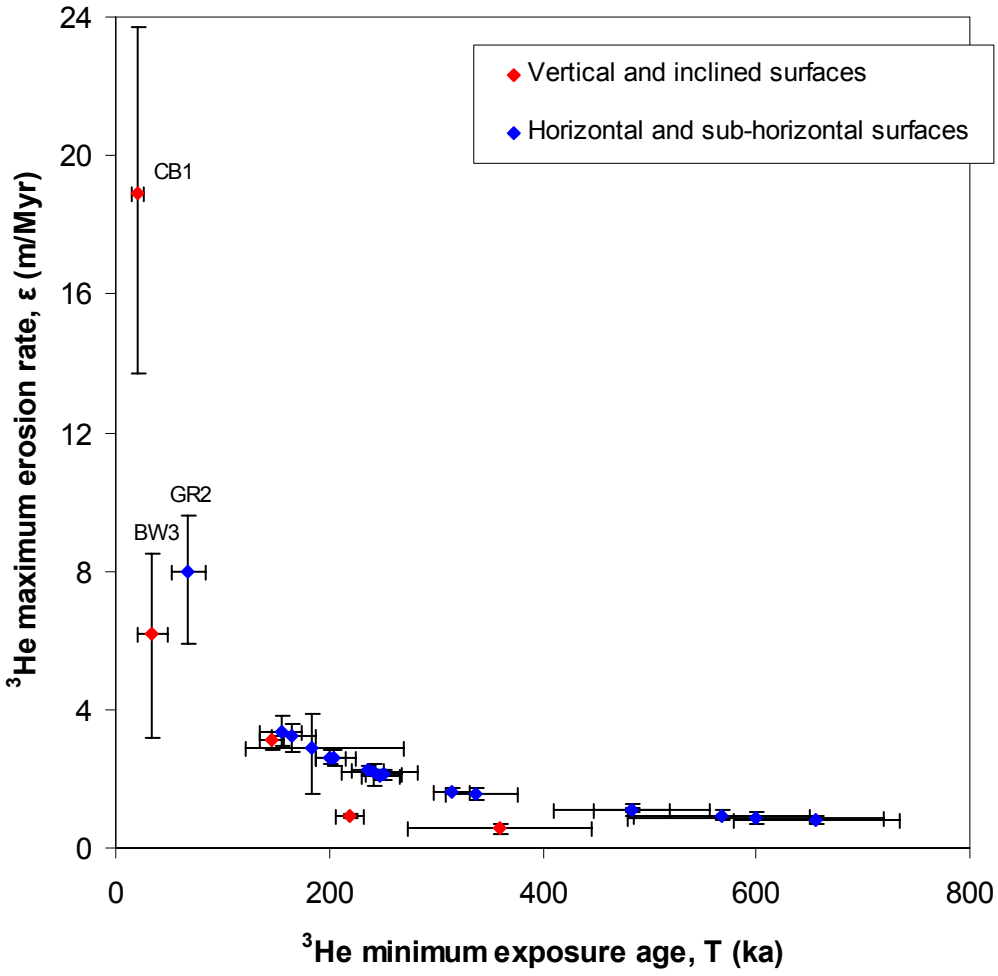

Figure 7.18: ^{3}He minimum exposure ages and maximum erosion rates, based on Dunai's (2000a) scaling factors and Fenton *et al.*'s (2009) cosmogenic nuclide production rates, for vertical and inclined surfaces (red diamonds, α = 90º - 30º) and horizontal surfaces (blue diamonds, α = 12º - 0º).

that these topographic features are relict forms which developed under significantly higher rates of erosion.

2. T and ε values for scarp faces and summits of *koppies* and plateaux suggest similar exposure histories (e.g. GD1 versus GD2 and GD3; OR1 versus OR2 and OR3; IT6 versus IT5), implying that these landforms are in a near-steady state, and that their overall form and position has changed little over the time period assessed by the cosmogenic nuclide data.

3. If a two-stage model of landscape development (initial weathering and regolith formation, followed by regolith erosion and bedrock exhumation) is assumed for *koppies* and dolerite tors on the southern African plateau near the Orange River, exhumation must have occurred before or during the Pleistocene (e.g. > 201 ± 14 ka for OR3).

4. With the exception of 3 samples (2 out of 5 vertical and inclined surfaces: CB1 and BW3, and 1 out of 17 horizontal and sub-horizontal surfaces: GR2), samples yield maximum erosion rates less than 4 m/Myr, even though minimum exposure ages range from 165 +23/-19 ka (GR1) to 656 ± 78 ka (IT10). Such consistently low ε values, even for some vertical scarp faces (e.g. GD1 and IT6), suggest that most maximum erosion rates approximate a relatively consistent rate of Karoo dolerite chemical weathering across the region.

5. Whilst most ε values may be related to the chemical weathering rates, it should also be noted that these are only maximum values, due to the incremental loss of mass at dolerite surfaces through exfoliation. The highest maximum erosion rates and lowest minimum exposure ages in this study are for samples where there is field evidence of active exfoliation (i.e. CB1, GR2 and BW3). Incremental exfoliation may also explain why adjacent boulders of the same dolerite intrusion may yield maximum erosion rates that are not within analytical error of each other (e.g. GR1 versus GR2 and GD2 versus GD3).

6. The extrapolation of even low maximum weathering rates suggests that significant thicknesses (on the order of $10^1 - 10^2$ m) of rock must have been eroded from areas that have been assigned to the "Post-African I" and "African" erosion surfaces (Partridge and Maud, 1987) since the proposed times of initial pediplanation. This suggests that the intact preservation of hypothetical pediplains on a $> 10^7$ yr timescale is unlikely

7.5 Possible influences on Karoo dolerite weathering rates

If the maximum erosion rates for samples with long exposure histories are assumed to approximate Karoo dolerite weathering rates, variations in ε values may be related to variables such as lithology, local drainage and climate. The relation between ε values and these variables is examined in detail below, in order to investigate possible controls on the weathering rate of Karoo dolerite in particular and basaltic rocks in general. The samples used for this investigation are the 19 samples where this is most plausible, i.e. where $\varepsilon < 4$ m/Myr. Samples CB1, BW3 and GR2 are thus excluded. However, as noted above, ε values are necessarily only maximum estimates for the true weathering rates of these 19 samples.

7.5.1 Lithology

As discussed in Section 5.6, dolerites sampled in this study exhibit two primary textures:

1) Ophitic textures, characterised by clinopyroxene phenocrysts encapsulating plagioclase laths, and
2) Cumulate textures, characterised by euhedral plagioclase phenocrysts with interstitial anhedral pyroxene.

These textural descriptions thus account for the relative sizes of the primary mineral phases (clinopyroxene and plagioclase). But even with all other factors being equal, the effect of texture on the weathering rate of a rock is likely to be complex. It has been proposed that finer-grained (ophitic textured) dolerites may exhibit faster weathering rates than coarser grained (cumulate textured) varieties, presumably due to a greater surface area of grain boundaries being available for alteration (Walker and Poldevaart, 1949). However, a more equigranular texture may also result in the weathering of the most susceptible mineral phase being less important to the overall

decomposition of the rock if the minerals in such a rock have an interlocking structure (e.g. Sparks, 1960). Moreover, the presence of more weatherable accessory phases or hydrothermal alteration phases may also play a role in accelerating the rate of dolerite weathering (e.g. Walker and Poldevaart, 1949; Bell and Jermy, 2000).

For each of the 19 samples, maximum erosion rates are plotted against median pyroxene grain size in **Figure 7.19**. Median pyroxene grain size, calculated as the average of the maximum and minimum pyroxene grain sizes for each sample in **Table 5.3**, serves as a semi-quantitative proxy for dolerite texture, with cumulate textures having values of ≤ 1.1 mm, and ophitic textures having values of ≥ 1.5 mm. As may be observed from **Figure 7.19**, no statistical correlation exists between these variables, with both groups of samples exhibiting a similar range of ε values. Other lithological variables reported in **Table 5.3**, such as the abundance of plagioclase or pyroxene, and the presence or absence of minor and accessory mineral phases, were also compared with maximum erosion rates, but no correlation exists with any of these variables either. One must therefore conclude that no evidence of any lithological control on the variation in weathering rates between Karoo dolerite samples may be determined from this study.

7.5.2 Local drainage

The efficiency with which moisture may drain from a surface may also affect the rate of weathering for a rock surface (e.g. Walker and Poldevaart, 1949; Kounov *et al.*, 2007). Thus, steeper surfaces may exhibit lower weathering rates than more horizontal surfaces where moisture may accumulate. It should be noted, however, that care was taken to collect samples from locally high points in the topography in all cases, in order to minimise the possibility that shielding sediments may have accumulated on a surface intermittently during its period of cosmic ray exposure.

The slope angle of a surface might be assumed to be a measure of the efficiency with which water may drain from it. Maximum erosion rates for the 19 samples are compared with slope angles in **Figure 7.20**, but no correlation exists between these variables. It is suggestive, however, that the two samples from 90º scarp faces (GD1 and IT6) display particularly low maximum erosion rates of < 1 m/Myr, especially compared with neighbouring samples from horizontal surfaces, as discussed in

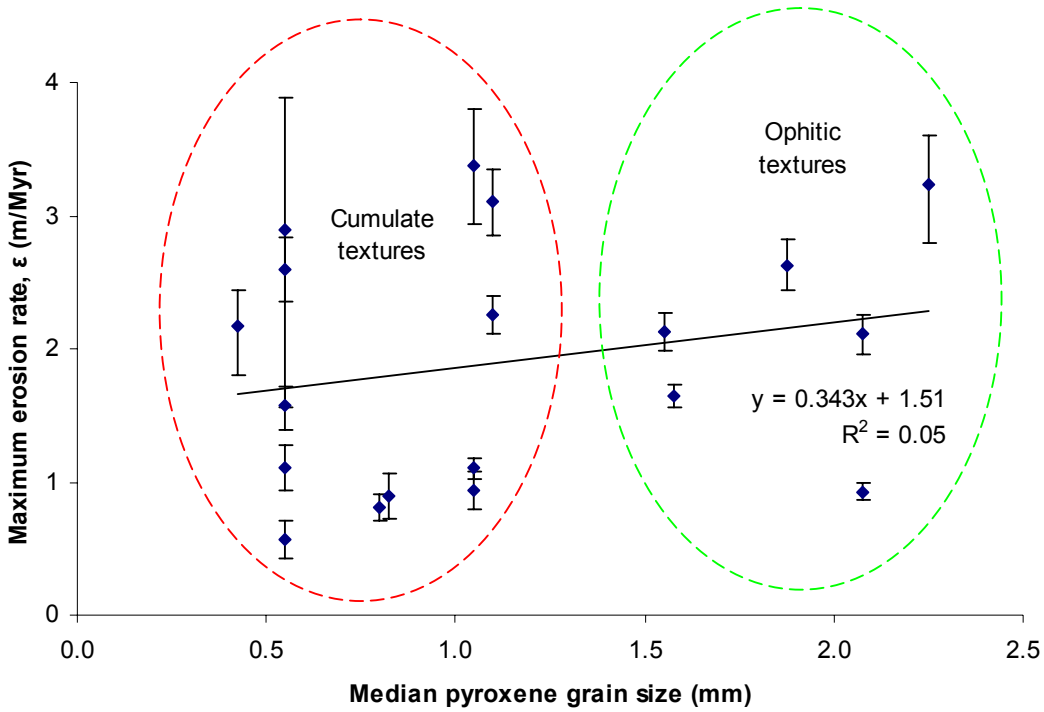

Figure 7.19: Maximum erosion rates and median pyroxene grain sizes of 19 samples where ε < 4 m/Myr. No statistical correlation exists between these variables, and samples that exhibit cumulate and ophitic textures, respectively, display similar ranges of ε values.

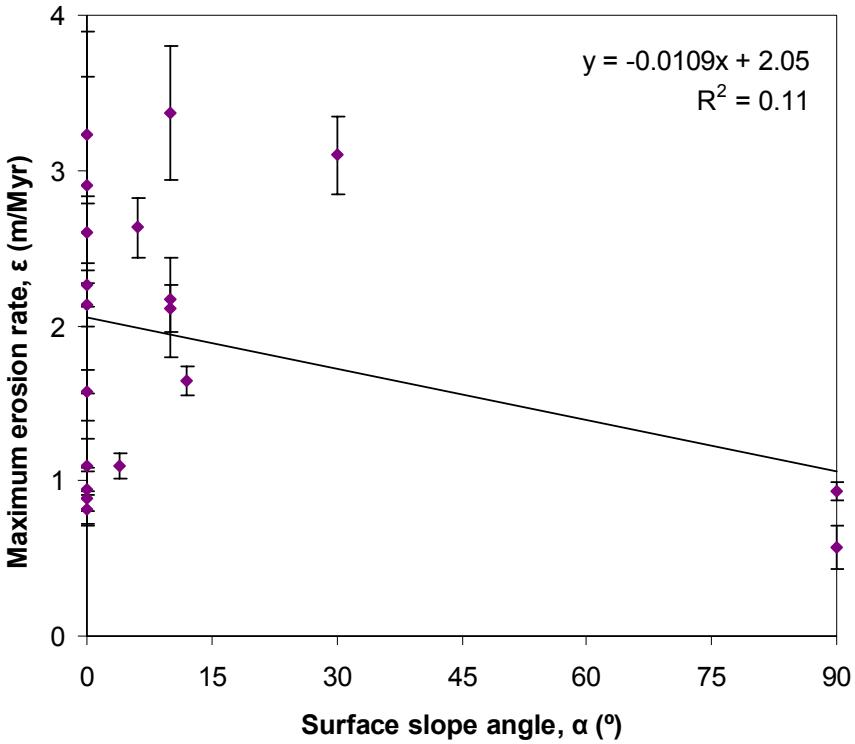

Figure 7.20: Maximum erosion rates and slope angles for 19 dolerite surfaces where ε < 4 m/Myr, displaying no statistical correlation.

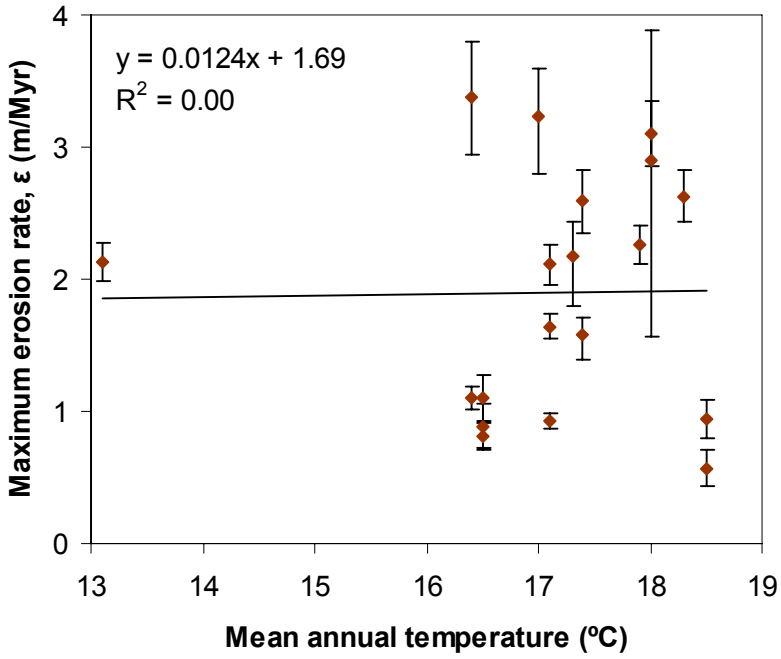

Figure 7.21: Maximum erosion rates and mean annual temperatures (Schulze, 2007) for 19 dolerite surfaces where ε < 4 m/Myr, displaying no statistical correlation.

Section 7.4.5. Note too, however, that samples BW3 and CB1 ($\alpha = 90^{o}$ and $\alpha = 44^{o}$, respectively) were excluded from this analysis due to their higher ε values. In summary then, the effect of slope angle on the dolerite chemical weathering rate is uncertain. However, the idea that vertical scarps may exhibit lower weathering rates due to rapid gravitational moisture loss is at least compatible with this data.

7.5.3 Climate

The possible effects of climate on the chemical weathering rates of basaltic rocks in general and Karoo dolerites in particular are discussed in Sections 3.3.1 and 3.3.3, respectively. The weathering rate of basaltic rocks may show a positive correlation with mean annual temperature and precipitation or runoff (Dessert *et al*., 2003; Gislason *et al*., 2009), and Karoo dolerite weathering may be dominated by chemical rather than mechanical processes where Weinert's (1965) N-value (the ratio of January evaporation to annual precipitation, multiplied by 12; equation 3.9) is lower than 5. In Sections 3.5.4 and 3.6 it was noted that the topographic expression of Karoo dolerites in southern Africa's eastern escarpment region is less prominent than in the southern escarpment region, and it was proposed that this may be due to higher rates of dolerite weathering in the more humid, eastern region.

Maximum erosion rates are compared with the mean annual temperatures of sample sites (**Table 5.2**; after Schulze, 2007) in **Figure 7.21**, but no correlation may be observed between these two variables. In **Figure 7.22**, maximum erosion rates are plotted against the mean annual precipitation at these sites (**Table 5.2**; after Schulze, 2007), but again, no statistically significant relationship exists. Indeed, for the seven samples from the more humid Pongola River region, where mean annual precipitation is greater 700 mm/yr, all samples except IT1 yield maximum erosion rates of ~1 m/Myr, which are among the lowest of the whole sample set.

In summary then, there is a general lack of correlation between maximum erosion rates on the one hand, and mean annual temperature and mean annual precipitation on the other. This suggests that either:

1) Mean annual temperature and mean annual precipitation do not significantly affect the rate of Karoo dolerite weathering;

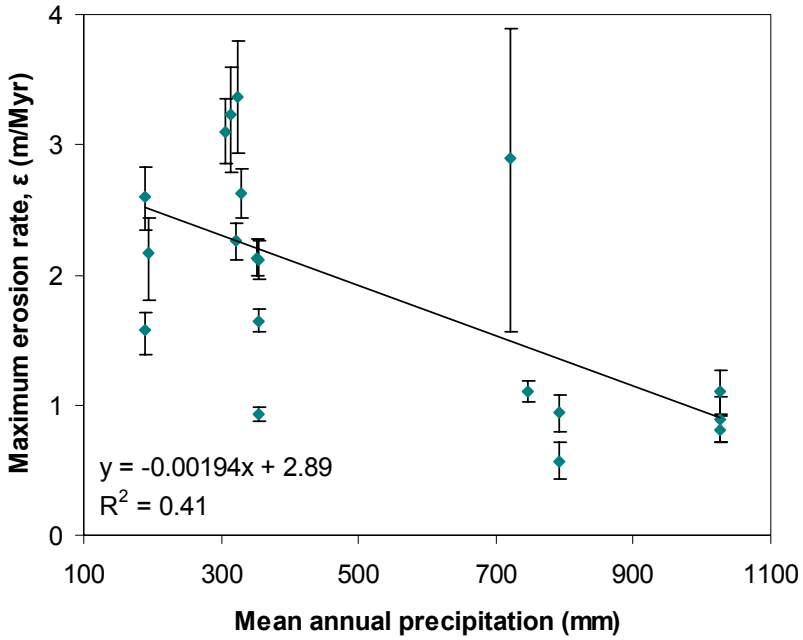

Figure 7.22: Maximum erosion rates and mean annual precipitation (Schulze, 2007) for 19 dolerite surfaces where ε < 4 m/Myr, displaying no statistical correlation.

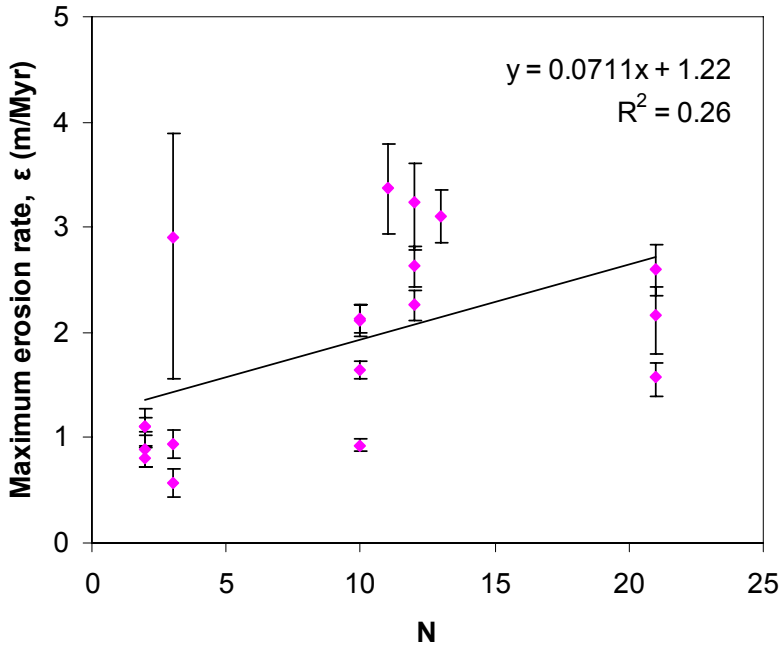

Figure 7.23: Maximum erosion rates and N values (Weinert, 1965, with data from Schulze, 2007) for 19 dolerite surfaces where ε < 4 m/Myr, displaying no statistical correlation. A negative correlation would be expected if ε values and N values both depended upon the absolute chemical weathering rate.

2) The maximum erosion rate is not an accurate indicator of the chemical weathering rate; or
3) Modern differences in mean annual temperature and mean annual precipitation across the region are not representative of the characteristic time periods of erosion addressed by the cosmogenic nuclide data.

The relative merits of these three possibilities are explored in Section 7.5.4 below.

Maximum erosion rates are compared with Weinert's (1965) N values (**Table 5.2;** calculated from data in Schulze, 2007) in **Figure 7.23**. N values were not proposed by Weinert (1965) as a proxy for the rate of dolerite chemical weathering *per se*, but rather as a measure of the dominance of chemical weathering relative to physical weathering. Thus a lower N value may be due to a higher absolute chemical weathering rate and/or a lower absolute physical weathering rate. Only if relative N values and relative ε values both depend on absolute rates of chemical weathering may a negative correlation be expected between N and ε. This might not be the case if either:

1) ε values do not accurately reflect the chemical weathering rate, but are compromised by episodic exfoliation (possibly physical weathering); or
2) Lower N values are due to lower rates of physical weathering rather than higher rates of chemical weathering.

In any event, no statistical correlation exists between maximum erosion rates and N values (**Figure 7.23**). Samples where N < 5 (chemical weathering dominated) also correspond to those in the Pongola River region where mean annual precipitation > 700 mm/yr, where all samples except IT1 display particularly low ε values of ~1 m/Myr. However, it is worth noting that the ε values > 4 m/Myr that were excluded from this analysis as being unlikely to accurately represent chemical weathering rates - CB1, BW3 and GR2 - all come from the more arid western areas that are supposedly dominated by physical weathering processes (N = 14, N = 11 and N = 12, respectively).

7.5.4 Comparison with model basaltic weathering fluxes

Maximum erosion rates for Karoo dolerites may be compared with model weathering rates for basaltic rocks, as proposed by Dessert *et al*. (2003). Based on global river

chemistry data, these authors suggested that for areas of basaltic rock outcrop, the weathering flux, f_w, in kg/km^2/yr, is climate dependent, and may be calculated as follows:

$$f_w = R_f \times 18.41 e^{0.0553T} \tag{3.6}$$

where R_f is the catchment mean annual run-off in mm/yr, and T is the mean annual temperature in °C (Dessert *et al*., 2003). Note that runoff may be defined as the total channel water flow that is generated from a catchment, comprising both surface water flow (from contemporaneous rainfall events) and base flow (from groundwater; Schulze, 2007). Values for the basaltic weathering flux, f_w, may be converted from units of kg/km^2/yr (mass per area per unit time) to units of m/Myr (depth per unit time) through division by a factor of 3×10^3 (assuming a dolerite density of 3 g/cm^3). Note that Equation 3.6 was derived for catchments of *basalt* outcrop - the finer-grained extrusive equivalent of a dolerite.

Because f_w values are, by definition, catchment specific, these values were calculated for the catchments from which samples were collected for cosmogenic nuclide analysis. Catchment areas used were the "quaternary catchments" of Schulze (2007), discussed earlier in Section 3.5.3, as Schulze (2007) reports mean annual runoff values for each of these catchments. Mean annual temperatures for each of these catchments were calculated in ArcGIS 9.3 by averaging the pixel values for mean annual temperature (also given by Schulze, 2007, **Figure 5.6**) over each catchment area.

The mean annual run-off, mean annual temperature and basaltic weathering flux (in m/Myr) is given in **Table 7.3** for each catchment corresponding to a dolerite sampling site; alpha-numeric catchment names from Schulze (2007) are also given for reference purposes. Values for f_w and ε, both in m/Myr, are compared graphically in **Figure 7.24** for the 19 samples where $\varepsilon < 4$ m/Myr.

Given that ε values determined in this study have already been shown to not correlate with either mean annual temperature or mean annual precipitation, the latter of which is a determining factor in the mean annual runoff of a catchment, it is unsurprising

Sample	Catchment*	Catchment mean annual temperature (ºC)**	Mean annual runoff, R_f (mm)*	Model basaltic weathering flux, f_w (m/Myr)
BW3	J21A	16.9	15.7	0.245
CB1	D32G	15.0	39.6	0.557
DV5	L11G	17.3	14.2	0.227
DV6	L11G	17.3	14.2	0.227
DV9	L12B	17.2	4.3	0.0683
GD1	D34A	16.3	71.1	1.07
GD2	D34A	16.3	71.1	1.07
GD3	D34A	16.3	71.1	1.07
GR1	N11B	15.9	27.3	0.404
GR2	N12C	16.5	57.0	0.871
GR3	N11B	15.9	27.3	0.404
GR5	Q22A	14.4	22.8	0.310
IT1	W31D	18.5	145.4	2.48
IT3	W31D	18.5	145.4	2.48
IT5	W42J	18.5	134.2	2.29
IT6	W42J	18.5	134.2	2.29
IT8	W42J	18.5	134.2	2.29
IT9	W42J	18.5	134.2	2.29
IT10	W42J	18.5	134.2	2.29
OR1	D33A	18.1	29.2	0.488
OR2	D33A	18.1	29.2	0.488
OR3	D31C	18.1	32.8	0.548

* after Schulze (2007)

** calculated from Schulze (2007)

Table 7.3: Mean annual temperature, mean annual runoff and the modeled basaltic weathering flux, as calculated in equation 3.6, according to Dessert *et al*. (2003), for catchments where dolerite samples were collected for cosmogenic nuclide analysis. Catchment names and runoff values are from Schulze (2007), and catchment mean annual temperatures are calculated from Schulze (2007) by averaging mean annual temperature pixel values in each catchment area.

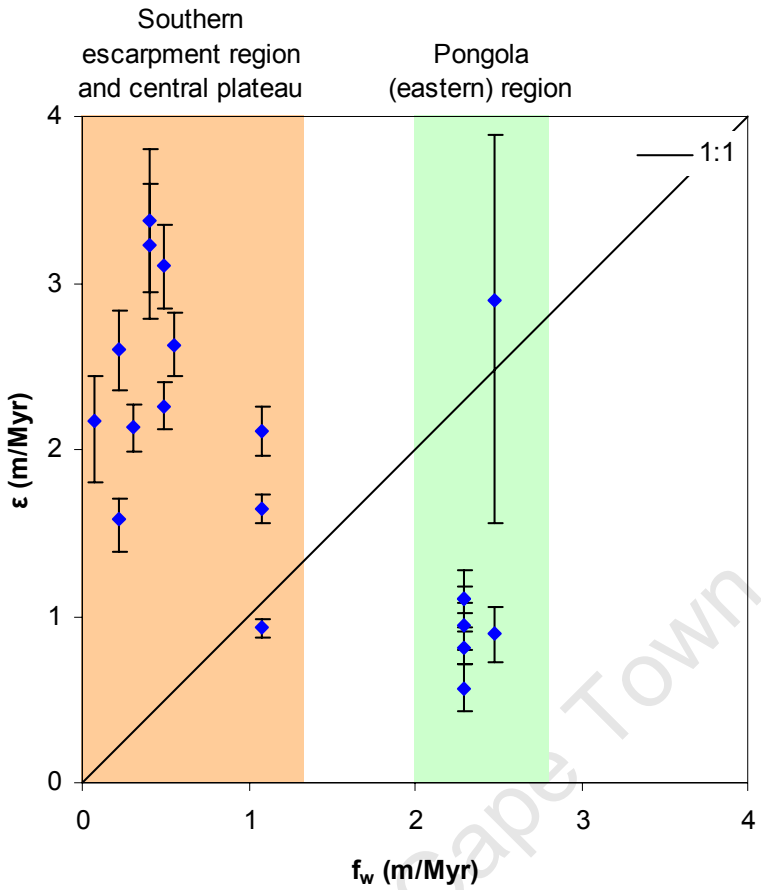

Figure 7.24: Maximum erosion rates and model basaltic weathering fluxes in the same units (calculated according to Dessert *et al*., 2003) for catchments corresponding to the 19 samples where ε < 4 m/Myr. No statistical correlation exists (R^2 = 0.42 for the best fit linear regression line, where y = -0.627x + 2.65, not shown for clarity). Model basaltic weathering fluxes yield a range of values < 3 m/Myr, similar to the range of values for maximum erosion rates. However, the model weathering fluxes are generally lower than maximum erosion rates in the more arid western (southern escarpment and central plateau) region, and generally higher than maximum erosion rates in the more humid eastern (Pongola) region.

that f_w values do not show a statistically significant correlation with ε values. It is remarkable, however, that values for Dessert *et al's* (2003) model basaltic weathering flux are all < 3 m/Myr, a similar range of values as the maximum erosion rates (< 4 m/Myr) for these 19 Karoo dolerite samples. Dessert *et al*.'s (2003) equation for predicting the basaltic weathering flux was derived from a global dataset of river chemistry, and uses contemporary climatic variables as inputs. Indeed, Dessert *et al*. (2003) also cite regional runoff and annual temperature estimates of 102 mm/yr and 19.3 ºC respectively for basaltic rocks in South Africa, which yield a model basaltic weathering flux of 1.8 m/Myr (and, according to their calculations, a CO_2 consumption flux of 2.4×10^{10} moles per year). This basalt weathering flux is very close to the average maximum erosion rate of 1.9 m/Myr yielded by the 19 dolerite samples discussed here.

The model basaltic weathering fluxes are thus integrated over larger spatial scales and shorter temporal scales than the maximum erosion rates, but the similarity in values between f_w and ε estimates strongly suggests that:

1) Weathering rates for basalts and (coarser-grained) dolerites are similar under similar conditions, and probably do not vary greatly with rock texture;
2) Both maximum erosion rates and model weathering fluxes approximate the true Karoo dolerite weathering rate with an accuracy of less than 3 m/Myr - the maximum difference between f_w and ε estimates; and
3) The chemical weathering rate of Karoo dolerites is, at least broadly, climate-dependent.

Note that Dessert *et al*. (2003) report measured weathering rates from basaltic catchments that are sometimes considerably higher, up to 342 ton/km^2/yr (114 m/Myr for a rock density of 3 g/cm^3) for Java (mean annual temperature: 24.8 ºC; runoff: 4052 mm/yr).

It is interesting that the model weathering fluxes are generally lower than the maximum erosion rates in the more arid western (southern escarpment and central plateau) region, and generally higher than maximum erosion rates in the more humid eastern (Pongola) region. This reflects the same non-correlation between maximum erosion rates and mean annual precipitation values discussed above. Higher maximum erosion rates than model basalt weathering fluxes may be accounted for by the

episodic exfoliation of dolerites, which is likely to be more prevalent in the more arid southern escarpment and central plateau regions, where Weinert's (1965) N-values suggest that physical weathering dominates. However, the generally lower maximum erosion rates in the Pongola region (6 out of 7 samples) require some further explanation. These 6 samples include those from flat dolerite pavements (e.g. samples IT3, IT8 and IT9) where local drainage conditions are likely to favour the accumulation of water, and theoretically promote chemical weathering.

One possible explanation why measured maximum erosion rates may be lower than model basaltic weathering fluxes is that the weathering rate of *bare* Karoo dolerite surfaces may be lower than that of Karoo dolerite within the subsurface. The basaltic weathering flux model is based on the chemistry of rivers with water sources from both groundwater flow and surface flow. The dolerite weathering rate beneath soil cover might be greater than for a bare rock surface from which water is likely to drain or evaporate more quickly. Field evidence of significant subsurface weathering of Karoo dolerites has already been discussed. On the other hand, thick soil or regolith may also serve to shield bedrock from chemical weathering, resulting in lower weathering rates than expected from climatic conditions (Gaillardet *et al*., 1999; Oliva *et al*., 2003; Section 3.3.2).

Another explanation for the apparent mismatch between relative maximum erosion rates and relative model basaltic weathering fluxes in southern Africa is that the general climatic conditions that prevailed over the characteristic erosion timescales were different from those of today. The maximum erosion rates for samples IT3, IT5, IT6, IT8, IT9 and IT10 range from 1.101 ± 0.082 m/Myr to 0.57 ± 0.14 m/Myr, a value range similar to the basaltic weathering fluxes predicted for the catchments in which samples CB1, GD1, GD2, GD3 and GR2 were sampled (f_w range: 1.07 m/Myr to 0.557 m/Myr). These latter catchments have a range of average mean annual temperatures between 15.0 ºC and 16.5 ºC (**Table 7.3**), and mean annual precipitation for these sample sites varies from 314 mm/yr to 354 mm/yr (**Table 5.2**). Thus, if one accepts Dessert *et al*.'s (2003) climatic dependence of the basaltic rock weathering rate, maximum erosion rates for Karoo dolerites determined from cosmogenic nuclides might be interpreted to indicate that mean annual temperatures in the Pongola region, integrated over the period 0 – 359 ± 86 ka (sample IT6), were lower

than those of today, by at least some 1.5 to 3 ºC, and mean annual precipitation integrated over this same period lower by at least 400 mm/yr. In other words, the more humid eastern region's average Quaternary climate may have been similar to the drier climate in the western part of southern Africa today.

Corroborating evidence from palaeo-climatic records is sparse, but generally compatible with this hypothesis. The 420 ka palaeo-temperature record from Vostok, Antarctica, based on deuterium and oxygen isotope proxies, indicates a strong 100 kyr Milankovitch cyclicity in global climate over this time period (Petit *et al*., 1999). Inspection of this dataset (Petit *et al*., 2001) reveals that Antarctic temperatures were estimated to be lower than at present by an average value of 4.5 ºC over the past ~420 ka, and lower throughout the period from ~120 ka to ~11 ka, by an average value of 5.4 ºC (note, however, that the distribution of temperature estimates with time is not uniform throughout the Vostok record). The Vostok temperature record after Petit *et al*. (1999; 2001) is shown in **Figure 7.25**. The characteristic time periods of erosion for the 19 samples where $\varepsilon < 4$ m/Myr are also shown, illustrating that these maximum erosion rates are integrated over periods of significant global climate change.

Unfortunately, southern Africa's palaeo-climatic record for the past few 100 kyr is generally of low resolution and poor continuity (Tyson, 1999). Sedimentological, micropalaeontological and chemostratigraphic proxies from sediment cores in the south Indian and south Atlantic oceans near southern Africa indicate that over the past 500 kyr, oceanographic oscillations in the region occurred in phase with global Milankovitch cycles (Shackleton, 1977; Prell *et al*., 1979; Rau *et al*., 2002, 2006). The highest resolution onshore palaeotemperature record for the late Quaternary in southern Africa is an oxygen isotope speleothem record from the Cango Caves (southern Cape region) that spans the past ~30 kyr, but including a hiatus from ~13.8 ka to ~5 ka (Talma and Vogel, 1992). According to these authors, temperatures were more of less constant (+1 ºC/-2 ºC) over the past 5000 yr, but were 4 – 7 ºC lower between 30 ka and 13.8 ka, with lowest temperatures between ~19 ka and ~17 ka (Talma and Vogel, 1992). It should be noted, however, that the interpretation of palaeoclimatic conditions from speleothems is complex, because temperature influences the stable oxygen isotope ratio in meteoric water and calcite precipitates in

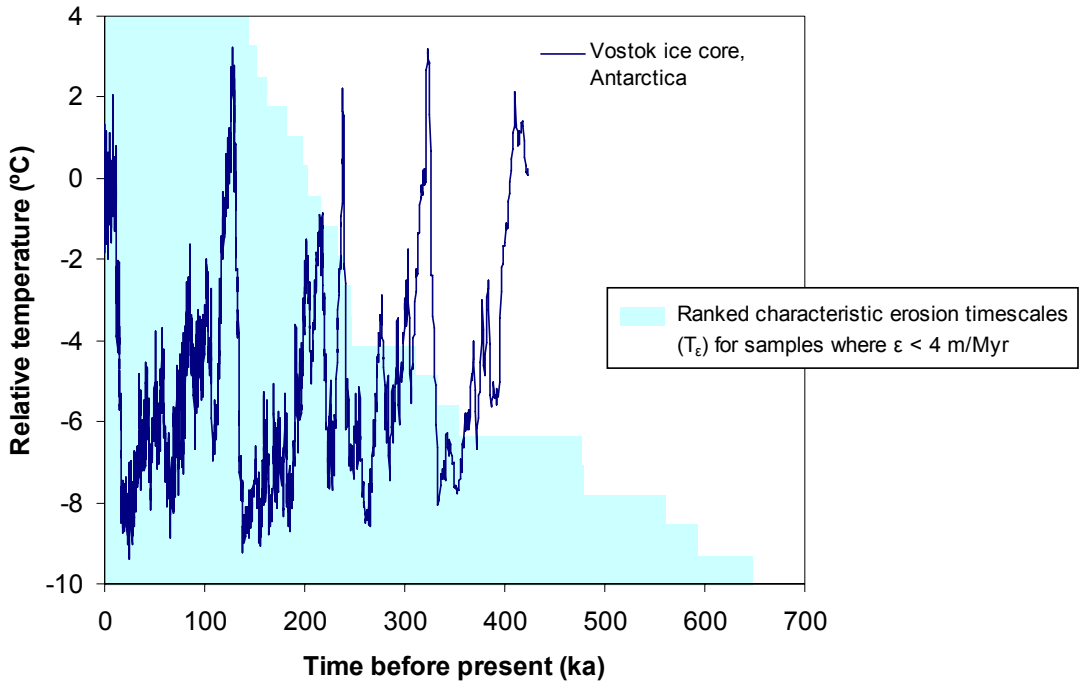

Figure 7.25: Antarctic atmospheric temperature relative to the present (dark blue line), according to deuterium and oxygen isotope proxies in the Vostok ice core (Petit *et al*., 1999; data from Petit *et al*., 2001). Individual Vostok core sample points are omitted for clarity. The characteristic erosion timescales (T_ε) of the 19 samples where the maximum erosion rate is < 4 m/Myr are superimposed on the background of the graph (blue bars), and ranked from longest (bottom) to shortest (top), with analytical error bars omitted for clarity. This illustrates that the maximum erosion rates for all these samples are integrated over time periods that experienced dramatic shifts in global climate.

different ways, and because oxygen isotope ratios in meteoric water may also vary in accordance with possible changes in the dominant direction of rain supply (e.g. Fairchild *et al*., 2006). In view of the possible influence of periglacial conditions on the mass wasting at dolerite scarps in southern Africa proposed by some workers (e.g. Marker, 1986; Section 3.3.3), it is interesting to note that according to both Lal (1991) scaling and Dunai (2000a) scaling, ^{3}He minimum exposure ages for 2 samples (CB1 and BW3) lie within analytical error of this last thermal minimum, although the minimum exposure ages of other steep slopes (i.e. GD1 and IT6) are considerably older.

Palaeo-precipitation records for the Quaternary in southern Africa are also scarce (Meadows, 2001). Based on a grain size analysis of lacustrine sediments, Partridge *et al*. (1997) presented a palaeo-precipitation record from Pretoria Saltpan (a.k.a. Tswaing Crater lake) on the north-eastern plateau in South Africa, a summer rainfall site with a present-day mean annual rainfall of ~630 mm/yr. Partridge *et al*. (1997) proposed that mean annual rainfall here, being dependent upon the summer monsoon, oscillated between ~535 mm/yr and ~900 mm/yr in accordance with ~23-19 kyr Milankovitch precessional cycles over the past ~200 kyr, with more arid conditions prevailing during glacials. This record has been widely referred to in the literature, for instance by Temme *et al*. (2008), who link these humid-arid cycles with cycles of deposition, pedogenesis and partial erosion recorded in the colluvial sediments of the Masotcheni Formation in KwaZulu-Natal (eastern South Africa) over the past 40 kyr. However, more recent work on Tswaing Crater lake sediments by Kristen *et al*. (2007) suggests that during the last glacial period (~80 – 10 ka), humid phases were out of phase with precessional insolation changes and possibly reflect southward migration of the Inter-Tropical Convergence Zone and/or changes in ocean circulation.

Whilst generally cooler and more arid conditions over the past few 100 kyr would mean that the model basaltic weathering flux in eastern southern Africa over this time would be in better agreement with the cosmogenic nuclide based maximum erosion rates, such conditions would also increase the mismatch between these two datasets in the more arid, western regions. However, according to Stuut *et al*.'s (2002) aeolian dust record from a marine sediment core from the Walvis Ridge (southern Atlantic

Ocean, ~20 ºS), glacial periods over the last 300 kyr in the western parts of southern Africa were characterised by an increase in both humidity and wind strength. The authors attribute this to the northward migration of the winter rainfall region of the southwestern Cape at these times in response to the equatorward movement of the polar front. Other supporting evidence from sedimentological, palynological, palaeontological and stable isotope studies in favour of an expanded western winter rainfall zone in southern Africa for the period ~32-17 ka during the last glacial period is reviewed by Chase and Meadows (2007). Thus, the more westerly sample sites in this study from the southern escarpment and central plateau regions might have in fact experienced generally more humid conditions during glacial periods, in contrast with sample sites from the more easterly (i.e. Pongola River) region.

In conclusion, given the variety of ways in which cosmogenic nuclide abundances may be interpreted and the number of unknown variables that may conspire to determine the exact weathering rate of a given rock surface (for instance, the possible effects of differences in vegetation and water chemistry across the region have yet to be explored), it would be premature to claim that maximum erosion rates in Karoo dolerites may serve as robust palaeoclimatic indicators. Rather, Dessert *et al.*'s (2003) basaltic weathering "law" and evidence from southern Africa's poorly constrained palaeoclimatic record are at least compatible with a palaeoclimate-dependent interpretation of the maximum erosion rate dataset for the 19 samples where $\varepsilon < 4$ m/Myr. It should also be noted that one dolerite sample (IT1) from the Pongola River region does in fact yield a maximum erosion rate within analytical error of the catchment's modern model basaltic weathering flux. Nevertheless, it seems likely that the time periods over which cosmogenic nuclides record weathering rates in southern Africa were characterized by significant spatial and temporal variations in climate. Cosmogenic nuclide abundances should therefore be interpreted within this context.

7.6 Comparisons and implications

7.6.1 Comparison with previous cosmogenic nuclide studies

Previously reported cosmogenic nuclide-based denudation rates for southern Africa were reviewed in Section 2.4.4 and summarized in **Figure 2.18** and **Table 2.2**. The results of this study are in excellent agreement with those of Kounov *et al*. (2007) for the southwestern escarpment and plateau, including their minimum exposure ages and

maximum erosion rates for Karoo dolerites (ε = 1.0 - 2.1 m/Myr, n = 7), also based on cosmogenic ^{3}He and ^{21}Ne in pyroxenes.

Fleming *et al.*'s (1999) ^{36}Cl-based rates for Drakenberg basalt denudation show more variable maximum erosion rates for horizontal surfaces (~10.0 m/Myr, ~6.7 m/Myr and ~1.4 m/Myr at the summit of the Drakensberg (2500-2900 m); and ~27 m/Myr at the summit of a ridge coastward of the escarpment). Although the range of values for the summit of the Drakensberg escarpment is similar to those determined for horizontal and sub-horizontal surfaces in this study (ε = 8.0 +1.6/-2.1 m/Myr (GR2) – 0.813 ± 0.097 m/Myr (IT10); n = 17), Fleming *et al.*'s (1999) denudation rate of ~27 m/Myr for a ridge seaward of the escarpment is substantially higher. Fleming *et al.* (1999) also report maximum erosion rates of ~48 m/Myr and ~62 m/Myr for two scarp face samples - both values being higher than the highest maximum erosion rate of 18.9 +4.8/-5.2 m/Myr determined for the 44º inclined scarp face, CB1. These authors note that the cause of the variability within their data is unclear, but may be due to local variability in slope, drainage conditions and substrate erodibility. In light of the smaller range of generally lower values for the larger Karoo dolerite dataset presented in this study, it is perhaps also worth noting that past and contemporary cryogenic processes (e.g. frost wedging), less significant or absent in lower areas of Karoo dolerite outcrop, may have been important in determining denudation rates at these high elevation (2500-2900 m) sites within the Drakensberg mountains (e.g. Grab *et al.*, 2005).

The maximum erosion rates determined for Karoo dolerites in this study are generally in close agreement with analogous values determined for other rock types in Namibia. Van der Wateren and Dunai's (2001) ^{21}Ne maximum erosion rates for quartz veins in granitic and metamorphic rocks are similar (~0.11 – 1.04 m/Myr), but include some especially low values (see discussion in Section 2.4.4). Cockburn *et al.*'s (1999; 2000) ^{10}Be and ^{26}Al data yields similar values for the denudation of quartzite at the escarpment summit (0.4 ± 0.1 m/Myr; n = 4) and of coastal bornhardts (5.1 ± 1.1 m/Myr; n = 6), as is the case with the ^{10}Be and ^{26}Al data of Bierman and Caffee (2001) for various outcrops both inland (3.2 ± 1.5 m/Myr; n = 9) and seaward (3.6 ± 1.9 m/Myr; n = 38) of the escarpment.

According to Cockburn *et al*. (1999, 2000), denudation rates for ridges and escarpments in Namibia are variable (2.1 ± 0.5 – 15.6 ± 3.7 m/Myr) and generally higher, at an average rate of 10 m/Myr (n = 10), presumably due to episodic physical erosion - rather than continuous chemical weathering - dominating the denudation of these rock surfaces. This is similar to the range of maximum erosion rates for Karoo dolerite surfaces such as CB1, BW3 and GR2, where there is field evidence of active Karoo dolerite exfoliation (6.2 +2.3/-3.0 – 18.9 +4.8/-5.2 m/Myr). However, values for maximum erosion rates are of limited significance at such sites if mass is not lost steadily. Nevertheless, according to Bierman and Caffee (2001), sediment from a small stream draining the Namibian escarpment yields a denudation rate of 16 m/Myr, higher than along the coastal plains (8 m/Myr) or in the highlands (5 m/Myr), and higher than in large rivers (6.4 ± 2.9 m/Myr; n = 4). Similar values were obtained by Codilean *et al*. (2008) for subcatchments within the Namib's Gaub river (8.0 ± 0.5 m/Myr – 14.1 ± 0.9 m/Myr). As discussed in Section 2.4.4, Codilean *et al*. (2008) also observed that, according to their data and that of Cockburn *et al*. (1999, 2000) and Bierman and Caffee (2001), erosion rates display a linear correlation with slope, which they interpreted as evidence that the western (Namibian) margin landscape is not in a topographic steady state. The results of the present study contrast somewhat with this interpretation, as some of the lowest rates of denudation may be recorded at vertical scarp faces (e.g. samples GD1 and IT6). Greater slope or relief is therefore not necessarily indicative of a higher erosion rate in southern Africa. Rather, the landscape may be in a state of equilibrium where form reflects the structure of the geological substrate, as is also suggested from the correlations between lithology and topography demonstrated in Chapter 3.

7.6.2 Comparison with long-term (> 10^6 yr) denudation rates

Long-term (> 10^6 yr) denudation rates for southern Africa were reviewed in Sections 2.4.2 and 2.4.3 and are summarized in **Figures 2.16** and **2.17** and **Table 2.1**. All reported denudation rates averaged over periods within the past 90 Myr are less than 30 m/Myr. In fact, only one estimate (Brown *et al*., 2002; for denudation seaward of the Drakensberg escarpment over the past 78 Myr) gives a denudation rate higher than 15 m/Myr. The shortest time period addressed by these estimates, the apatite fission track based estimate of Cockburn *et al*. (2000) for the western (Atlantic) margin yields an average denudation rate of 5 m/Myr for the past 36 Myr. This value is close

to the range of maximum erosion rate estimates (< 4 m/Myr) for the 19 samples where ε values may be assumed to reflect dolerite weathering rates, and is also within error of scarp sample BW3's maximum erosion rate. Maximum erosion rates for Karoo dolerites in this study are also in excellent agreement with the denudation rate of 3.4 m/Myr for the Drakensberg basalts over the past 87 Myr, as determined by Partridge and Maud (1987) and references therein from kimberlite facies analysis. However, other denudation rates averaged over the entire Cenozoic (Flowers and Schoene, in press) or the past 80-90 Myr (Brown *et al*., 2002; Tinker *et al*., 2008a; Hanson *et al*., 2009) all range from 10-15 m/Myr. Although this is similar to the cosmogenic nuclide based denudation rates for the Namibian escarpment determined by previous workers, as discussed in Section 7.6.1 above, it is nearly an order of magnitude higher than the average maximum erosion rate of 1.9 m/Myr for the 19 samples where $\varepsilon < 4$ m/Myr.

The general similarity between weathering rates determined in this study and the long-term rates determined by Cockburn *et al*. (2000) and Partridge *et al*. (1987) may be interpreted to signify that, during at least the past ~30 Myr, rock weathering (rather than physical erosion) has been the rate-determining step in the overall denudation of the landscape. This would imply that this was a period of general tectonic stability unassociated with regional uplift accompanied by fluvial incision and erosion, contrary to the opinion of Burke (1996) and Burke and Gunnell (2008). However, higher average denudation rates for the entire Cenozoic or the past 80-90 Myr suggest that denudation rates in the region may have declined over this time period. This may have been due to regional uplift in the Cretaceous, following which physical erosion rates due to fluvial incision may have decayed as southern Africa's landscape has approached a steady state form, with relief reflecting the relative erodibility of the geological substrate. Alternatively, a decline in denudation rates might be due, at least in part, to a decline in weathering rates following long term climate change during the Cenozoic.

Little is known about the climatic conditions that prevailed in southern Africa during the past ~65 Ma, due to the region's fragmentary stratigraphic record for the Cenozoic, which is mostly restricted to the currently arid, western coastal regions. However, in order to explain a significant (~1 order of magnitude) decrease in the Orange River's sediment discharge rate from the Palaeogene (early Tertiary, i.e.

Palaeocene, Eocene and Oligocene; ~65-23 Ma) and to the Neogene (late Tertiary; i.e. Miocene and Pliocene; ~23-2 Ma, as determined from offshore stratigraphy, Dingle and Hendey (1984) proposed that a decline in runoff occurred in southern Africa over this time.

According to the oxygen isotope record of benthic foraminifera through the Cenozoic, global temperatures have experienced a general cooling since a climatic optimum in the early Eocene at ~50 Ma (Zachos *et al*., 2001 and references therein). Available data from southern Africa is broadly consistent with this global cooling trend, according to Dingle *et al*.'s (1983) detailed review of the region's Tertiary palaeoclimatic record. For the Palaeogene, relative water temperature proxies from marine sediment cores and qualitative data inferred from plant and mammal fossils generally supports a warm, humid climate, although certain interpretations have been disputed (Dingle *et al*., 1983 and references therein). Neogene palaeoclimatic data from terrestrial floras, terrestrial and marine vertebrate and invertebrate fossils, as well as marine micropalaeontology, sedimentology and geochemistry also indicates generally warmer and wetter conditions than at present, at least along the west coast (Dingle *et al*., 1983 and references therein). Previous studies also point to the disappearance of extensive woodlands in the southwestern Cape and Namaqualand (western South Africa) in early Pliocene times, and their replacement with grassland, and ultimately fynbos/shrubland in Upper Pliocene and Pleistocene times, in response to cooler and progressively more arid conditions (Dingle *et al*., 1983 and references therein).

More recent palynological data from Udeze and Oboh-Ikuenobe (2005) for the Middle Miocene to Pliocene (~12 – 2 Ma) from sediment cores off southern Africa's west coast was interpreted by these authors as evidence that climate cooled from subtropical conditions in the late Middle Miocene (~12 Ma) to cool-temperate conditions in the Late Miocene (~11 – 5 Ma), but warmed temporarily to warm-temperate conditions in the Early to early Late Pliocene (~5 – 3 Ma), before the establishment of coastal upwelling and cooling along the west coast at the end of the Pliocene is indicated by multiple proxies (Etourneau *et al*., 2009). Some workers have proposed that aridity along southern Africa's west coast dates back to the Palaeogene and late Cretaceous (Ward *et al*., 1983; Ward, 1988), although this interpretation is

based on palaeosols and aoliantites of disputed age (Partridge, 1993). Note that geochronological dates quoted above are from Gradstein *et al*. (2004), with reference to Bohme (2003).

It thus seems reasonable to suggest that Tertiary weathering rates in southern Africa (at least for basalts and dolerites) have been higher than at present due to a generally warmer and wetter climate. Higher weathering rates for basaltic rocks occur elsewhere in the world today, and such locations may provide modern climatic analogues for southern Africa during the Tertiary. For instance, according to Dessert *et al*. (2003) and references therein, the Indian Ocean island of Réunion (~20 ºS) experiences a runoff of 2120 mm/yr (significantly higher than at present in any of the southern African catchments sampled in this study; **Table 7.3**), but a mean annual temperature of 17.1 ºC (similar to much of southern Africa today) and a basaltic weathering flux determined from river chemistry equivalent to 38.2 m/Myr (model basaltic weathering flux = 35.3 m/Myr for ρ = 3 g/cm^3). Another possible present-day analogue is the Deccan Traps of India, which display a more moderately elevated runoff of 463 mm/yr, but a significantly higher mean annual temperature of 27 ºC, and a basaltic weathering flux (also determined from river chemistry) equivalent to 12.4 m/Myr (model basaltic weathering flux = 12.6 m/Myr for ρ = 3 g/cm^3; Dessert *et al*., 2003 and references therein).

7.6.3 Comparison with Holocene sedimentation rates

Based on an analysis of the Holocene (~12 – 0 ka; Gradstein *et al*., 2004) mud belt along South Africa's west coast, Compton *et al*. (2010) concluded that mud from the Orange River had accumulated at an average rate of 5.1 × 10^{12} g/yr during the Holocene. These authors also noted that 5/6th's of the historical (20th Century) discharge from the 953 200 km^2 Orange River basin is mud (Dingle and Hendey, 1984; Bremner *et al*., 1990; Compton *et al*., 2010). Assuming a parent rock density of 2.6 g/cm^3 (e.g. Le Roux, 1990) this translates to a mean denudation rate of 2.5 m/Myr across this basin. However, given that the particulate load for rivers globally is estimated to be only 75 % to 90 % of the total load (Wilkinson, 2005), with the dissolved load being the remainder, an average Holocene denudation rate of 3.3 - 3.7 m/Myr may be assumed for the Orange River basin.

This value is similar to the average maximum erosion rate of ~2.1 m/Myr for the 6 Karoo dolerite samples (GD1, GD2, GD3, OR1, OR2 and OR3) in the Orange River basin where ε values are proposed to reflect weathering rates (CB1 excluded), and lies within the range of Karoo dolerite weathering rates (~0.5 - 4 m/Myr) determined in this study. Although these maximum erosion rates for Karoo dolerites are determined over time spans that are more than an order of magnitude longer than the Holocene, the similarity in values between Holocene sedimentation rates and dolerite surface denudation rates supports the argument ventured in Section 7.6.2 that rock weathering may be considered to be the rate determining step in the supply of sediment for much of this tectonically stable region.

Compton *et al*. (2010) consider that most of the Holocene sediment flux from the Orange River is delivered from surface exposures of the Elliot Formation adjacent to the western limits of the Drakensberg basalts, which also experiences relatively elevated precipitation for the Orange River basin (> 500 mm/yr). These authors thus embrace a scarp retreat model for the erosion of southern Africa above the Great Escarpment, with progressive eastward migration of the western Drakensberg margin (e.g. Moore and Blenkinsop, 2006; Hanson *et al*., 2009). No cosmogenic nuclide-based denudation rates are known from this immediate area, but the fact that denudation rates determined in this study from elsewhere in the Orange River catchment are compatible with Holocene sedimentation rates suggests that a scarp retreat model need not necessarily be invoked.

7.6.4 Comparison with "Anthropocene" rates of soil erosion and sediment yield

Rock weathering results in the production of soil, which is necessary for agriculture and the functioning of terrestrial ecosystems. Knowledge of the rate of soil erosion relative to the rate of soil formation is required, therefore, to assess the long-term sustainability of agricultural practices (Le Roux, 1990). Here, interpreted Karoo dolerite weathering rates (maximum erosion rates < 4 m/Myr) are compared with present-day rates of soil erosion or sediment yield.

Karoo dolerite weathering rates may be considered as maximum rates of doleritic soil production, because part of the mass lost from a dolerite surface will not be trapped as soil, but delivered to the oceans in suspension or in solution. Soils derived from

Karoo dolerites are typically more fertile than those derived from the Karoo sedimentary rocks, a fact reported to have been well known amongst traditional African farmers (Walker and Poldevaart, 1949). The mudstones and shales typical of Karoo sedimentary rocks units are probably more easily eroded in response to fluvial incision, but their weathering rates are unknown. However, the weathering rates of these rocks are likely reflected in the Orange River catchment's mean Holocene denudation rate of ~3 to 4 m/Myr calculated in Section 7.6.3 after Compton *et al*. (2010), and are thus possibly similar to Karoo dolerite weathering rates. The fact that *in situ*-produced soils in southern Africa (fluvial and aeolian deposits excluded) are generally < 1 m thick and thinner in arid areas of Karoo sedimentary rock outcrop (Schulze, 2007) suggests that weathering rates for most common rocks are unlikely to have been substantially faster than net erosion rates, at least during the Quaternary. Cosmogenic nuclide-based weathering rates for surfaces of rock types such as quartzites and granites are apparently similar to those of Karoo dolerites (**Table 2.2** and references therein). It should be noted that cosmogenic nuclide-based values record the weathering of bare rock surfaces only, although, as noted in Section 7.5.4, whether the presence of a soil cover over a rock surface serves to retard or enhance the rate of rock weathering is debatable.

The increasing movement of rock and soil by humans correlates strongly with the development of human societies. Humans are now arguably the most significant geomorphic agents that sculpt the Earth's landscape, and anthropogenic rates of erosion are estimated to have surpassed those resulting from all natural processes at the end of the first millennium A.D. (Hooke, 2000; Wilkinson, 2005). It has been projected that, following from the exponential growth in the human population, the total amount of earth moved by humans over the past 5000 years could double within the next 100 years, and high rates of global sediment production have been considered a distinct lithostratigraphic signal typical of a discrete geological epoch: the "Anthropocene" (Hooke, 2000 and references therein; Zalasiewicz *et al*., 2008). However, most material eroded by humans is not delivered to the oceans, but is deposited within catchments if the carrying capacity of rivers is exceeded. Thus, local soil erosion rates may be an order of magnitude greater than the net sediment yield (Martin, 1987; Garland *et al*., 1999; Wilkinson and McElroy, 2007; Keay-Bright and Boardman, 2009). On the other hand, modern global sediment yields may be higher

than the geological average partly because of increased sediment delivery following Quaternary glaciations (Wilkinson, 2005 and references therein).

Soil erosion has been a cause of concern in southern Africa since the early 20th Century (Garland *et al*., 1999), and it has been proposed that severely degraded areas in the region are likely to become even more vulnerable in future, according to predicted climate change scenarios (Meadows and Hoffman, 2003). Studies of badland and gully development focused on the Karoo region in particular are indicative of recent land degradation probably due to extensive stock farming over the past 150 years since European settlement (Boardman *et al*., 2003; Keay-Bright and Boardman, 2006, 2009). However, absolute estimates of regional soil erosion rates in southern Africa are variable and generally poorly constrained (Garland *et al*., 1999). Future regional studies applying improved monitoring, modeling and remote sensing technologies are required to address this deficiency (Le Roux *et al*., 2007). Nevertheless, some general inferences may be made through recourse to the available published data. Note that literature estimates of regional soil erosion rates, based on measurements of river sediment yield, are typically presented here after conversion to denudation-equivalent units (surface lowering per unit time).

In an early study, du Toit (1933 and references therein) estimated from the sediment flux below the Orange and Vaal river junction that soil erosion was lowering the landsurface by an average rate of 1 foot per 1500 years, i.e. ~200 m/Myr. Martin (1987) reported the sediment yield of southern Africa's east coast rivers and of the Limpopo river catchment to be 323 tons/km^2/yr and 265 tons/km^2/yr, equivalent to average surface denudation rates of 124 m/Myr and 102 m/Myr respectively, assuming a parent rock density of 2.6 g/cm^3. Compton *et al*. (2010) reported that the modern mud flux of the Orange River basin prior to the building of large dams (1930-1969) was ten times greater than mean Holocene mud flux, and attributed this to modern agricultural practices (Compton *et al*., 2010 and references therein).

For southern Africa, a number of soil erosion maps have been presented in the literature:

1) By extrapolating sediment yield rates determined from measuring stations and dam accumulations over larger areas of presumed similar erodability, a map of

maximum potential sediment yield rates in South Africa, Lesotho and Swaziland was presented by Rooseboom (1978) after Harmse (1975) and Rooseboom (1975). These values ranged from 50 ton/km^2/yr to 1000 ton/km^2/yr (i.e. denudation rates of 19 m/Myr to 385 m/Myr, assuming a rock density of 2.6 g/cm^3).

2) Le Roux (1990) produced a contoured map of denudation rates in this same area, based on dam accumulations, with contours ranging from 25 mm/kyr to 150 mm/kyr (units equivalent to m/Myr).
3) Schulze (2007) released a dataset of catchment-specific model sediment yields for the region, based on the Modified Universal Soil Loss Equation (MUSLE; Williams, 1975). Variable inputs for this model include the volumes and peak discharges of stormflow events, a soil erodilibity factor, slope length and slope gradient (Schulze, 2007).
4) Most recently, Compton *et al*. (2010) estimated soil erosion rates for magisterial districts within the Orange River catchment by combining literature estimates of the qualitative degree of soil degradation, measured rates of soil loss, and land use indices.

Estimated soil erosion rates for Karoo dolerite sample sites according to these four sources are given in **Table 7.4**. These estimates are compared graphically with ^{3}He maximum erosion rates for Karoo dolerites in **Figure 7.26**. For every samples site, all estimates of soil erosion rates are greater than the Karoo dolerite maximum erosion rate. The degree to which soil erosion rates exceed dolerite maximum erosion rates varies by between a factor of ~2 and ~280. As shown in **Table 7.4**, the average soil erosion rate for cosmogenic nuclide sample sites is variously estimated at 198 m/Myr (Rooseboom, 1978), 70 m/Myr (Le Roux, 1990), 76 m/Myr (Schulze, 2007) and 57 m/Myr (Compton *et al*., 2010). Note, however, that Rooseboom's (1978) estimates were maximum values, and that Compton *et al*.'s (2010) estimates were restricted to sample sites in the Orange River catchment (**Figure 7.26**).

The mean maximum erosion rate for Karoo dolerite in this study is 3.1 m/Myr, although the interpreted mean dolerite weathering rate (excluding samples BW3, CB1 and GR2) is still lower, at 1.9 m/Myr. If the latter value is assumed to be the rate of soil production through weathering, the rate of modern soil erosion in southern Africa

Sample site	Soil erosion rate estimates ($m^3/km^2/yr$ = mm/kyr = m/Myr)				
	Rooseboom (1978)[1]	Le Roux (1990)[2]		Schulze (2007)[3]	Compton *et al*. (2010)[4]
	Max.	Min.	Max.		
BW3	385	25	50	23	-
CB1	308	25	50	47	57
DV5	58	25	50	16	-
DV6	58	25	50	16	-
DV9	58	25	50	278	-
GD1	231	25	50	163	56
GD2	231	25	50	163	56
GD3	231	25	50	163	56
GR1	58	75	100	30	-
GR2	58	75	100	30	-
GR3	58	75	100	57	-
GR5	308	50	75	25	-
IT1	231	100	125	22	-
IT3	231	100	125	22	-
IT5	231	100	125	78	-
IT6	231	100	125	78	-
IT8	231	100	125	78	-
IT9	231	100	125	78	-
IT10	231	100	125	78	-
OR1	231	-	25	41	57
OR2	231	-	25	41	57
OR3	231	-	25	139	58
Average	***198***	***62***	***78***	***76***	***57***

[1]Converted from map of maximum averaged sediment yields in ton/ha/yr after Harmse (1975), assuming an average rock density of 2.6 g/cm^3

[2]Determined from map of surface lowering rate contours, given as mm/kyr for a rock density of 2.6 g/cm^3

[3]Converted from dataset of catchment-specific sediment yields in ton/ha/yr, assuming an average rock density of 2.6 g/cm^3

[4]Determined from supplementary table of erosion rates in ton/km^2/yr for magisterial districts in the Orange River catchment, assuming an average rock density of 2.6 g/cm^3

Table 7.4: Literature estimates of modern soil erosion rates for areas that encompass Karoo dolerite sample sites. Rooseboom (1978) provides only maximum values.

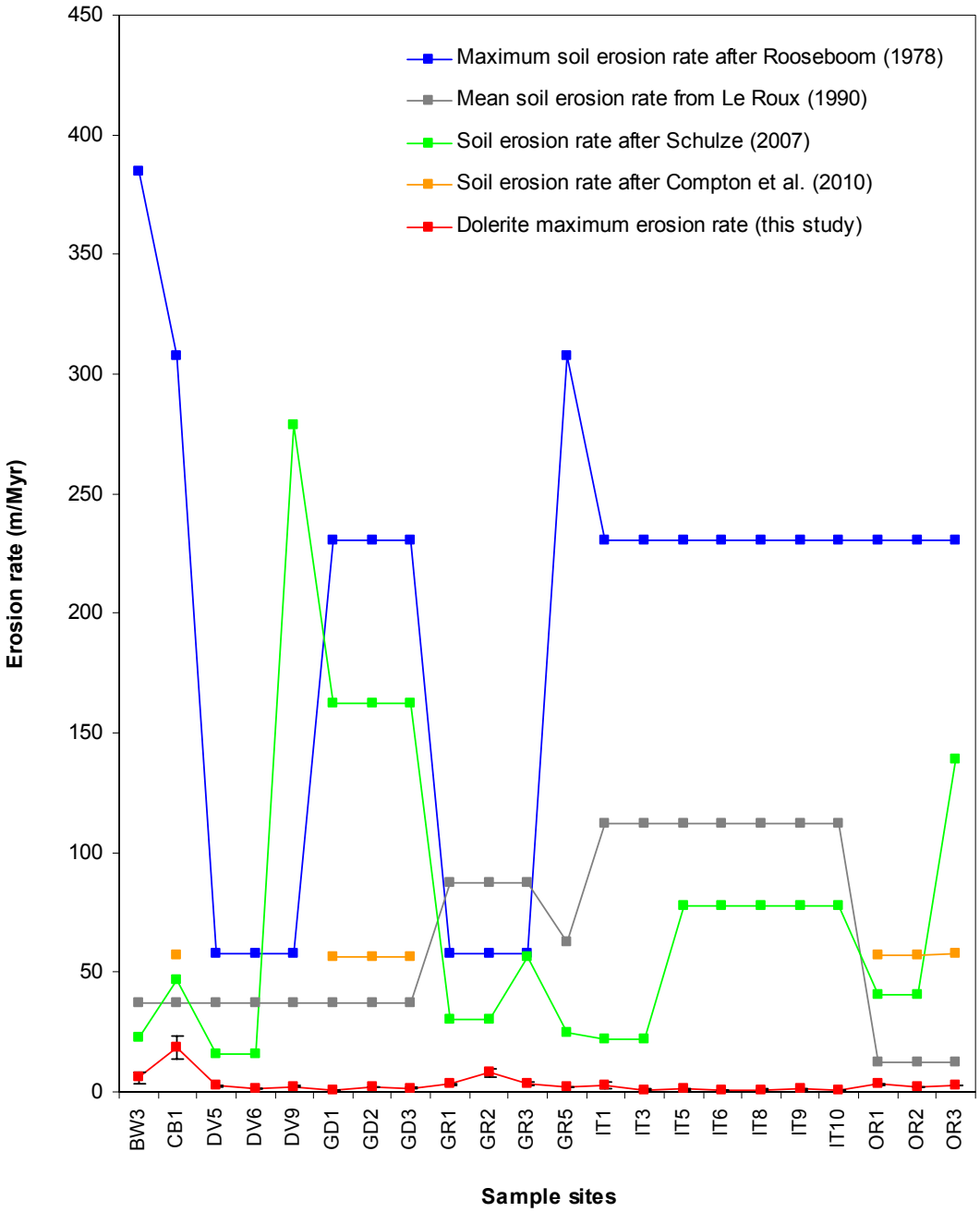

Figure 7.26: Comparison between ^{3}He maximum erosion rates for Karoo dolerites, according to Dunai (2000a) scaling and Fenton *et al.*'s (2009) production rates, and literature estimates of modern rates of soil erosion in the vicinity of sample sites, according to Rooseboom (1978), Le Roux (1990), Schulze (2007) and Compton *et al.* (2010). Note that if Karoo dolerite maximum erosion rates are assumed to represent soil production rates, soil erosion rates are higher than long-term production rates at any site by a factor of between ~2 and ~280.

is 30 to 100 times faster, on average, than the rate of soil production integrated over a 10^5 yr timescale. Le Roux (1990) tentatively assumed rock weathering rates in southern Africa to be considerably higher than shown in this study, at 10-40 m/Myr, and thus noted that soil was being lost more than 2 or 3 times faster than it was being produced. In fact, soil erosion and production rates in southern Africa are apparently even further from equilibrium than Le Roux (1990) imagined. The results of this comparison are instead similar to the findings of Hewawasam *et al*. (2003), who compared natural erosion rates in Sri Lanka, based on cosmogenic ^{10}Be in quartz from sediments and soils, with present-day rates of soil loss. They observed that sediment was being lost 1 to 2 orders of magnitude faster than it was being produced, and attributed this to extensive deforestation.

A referral to the long-term denudation record of southern Africa (**Figure 2.16**) reveals that such high soil erosion rates are apparently unprecedented in the Cenozoic – at least on a > 10^6 yr timescale. It is sobering to consider that the region has not experienced long-term denudation rates in excess of 50 m/Myr since the Cretaceous (Brown *et al*., 2002; Tinker *et al*., 2008a, Kounov *et al*., 2009). It may thus be said that humans are now mimicking the "Kalahari epeirogeny" (de Wit, M.J., 2007) in sculpturing the landscape. On the other hand, the rates of irregularly occurring processes such as erosion are timescale-dependent (Gardner *et al*., 1987), and thus present soil erosion rates may possibly be less geologically significant for southern Africa than a direct comparison with long-term rates would suggest. What is apparent, however, is that "Anthropocene" rates of soil erosion in southern Africa are unsustainable under prevailing tectonic and climatic conditions.

CHAPTER 8: SUMMARY AND CONCLUSIONS

8.1 Introduction

The findings of this thesis are summarized below in point form with reference to the key questions outlined in Section 1.3. Following this, some recommendations for future work and concluding remarks are presented.

8.2 The topography of southern Africa

8.2.1 How did key regional topographic features develop?

- Cosmogenic nuclide studies reported here show that denudation rates over the past 10^5 yr have been low, and generally < 4 m/Myr for Karoo dolerite surfaces (Section 8.3). Various extrapolations of data demonstrate that current denudation rates are of insufficient intensity to have formed the extant landscape over any geologically reasonable period of time. Thus it would appear that southern Africa displays what is predominantly a stable and relict landscape.

- This is compatible with denudation thermochronology studies over the last two decades that yield a consensus that most denudation in the region occurred during the Cretaceous, and that denudation rates in southern Africa have decreased since that time.

- It seems most probable, therefore, that epeirogenic uplift of southern Africa occurred during the Cretaceous, possibly in response to a significant thermal perturbation of the asthenospheric mantle (Nyblade and Robinson, 1994), resulting in the formation of the Great Escarpment.

8.2.2 Do cyclic landsurfaces exist (or, is their existence falsifiable)?

- Cyclic pediplanation surfaces defined by King (1951, 1967) and Partridge and Maud (1987) were proposed to have formed through scarp retreat following episodic isostatic uplift in response to a threshold amount of denudation. However, scarp retreat through pediplanation is incompatible with denudation thermochronology data and is unsupported by cosmogenic nuclide data. Also,

more recent work suggests that the isostatic response of uplift to denudation is continuous rather than episodic over such long timescales (Gilchrist and Summerfield, 1991).

- Cosmogenic noble gas abundances in Karoo dolerites show that the minimum exposure ages for rock surfaces are more than two orders of magnitude lower than the presumed ages of the pediplanation surfaces to which they were assigned by Partridge and Maud (1987), i.e. 10^5 a versus 10^7 a.

- For the true exposure age of a surface to be older than the minimum exposure age, it is required that the rock surface has lost mass since initial exposure. Extrapolation of these denudation rates over time periods equivalent to the presumed ages of the pediplanation surfaces implies that surfaces have lost at least tens of metres of rock since initial exposure. Whether such theoretical surfaces may be preserved intact is thus a question of semantics, but their successful recognition and correlation on the basis of elevation seems unlikely.

- Arguments for the existence of cyclic pediplanation surfaces in southern Africa are based on outdated geodynamic theory and are not supported by modern geochronological data. It is suggested that referral to theoretical pediplanation surfaces no longer provides a useful paradigm for geomorphological studies in southern Africa, but may instead lead to the entrenchment of erroneous theoretical assumptions.

8.2.3 To what degree is topography structurally (lithologically) controlled?

- Based on a GIS comparison of topography and lithology within catchments where Karoo dolerites crop out, it is apparent that Karoo dolerites generally display greater elevation and relief than their host (country) rocks.

- However, the relative topographic prominence of Karoo dolerites is variable and depends upon both host rock lithology and intrusion geometry. The hypothesis that the more subdued topography of Karoo dolerites in the eastern

escarpment region may be due to a higher dolerite weathering rate here is not supported by the cosmogenic nuclide data.

- The position of the Great Escarpment in the southern Cape generally coincides with the southern limit of Karoo dolerite, and becomes more poorly defined in areas where Karoo dolerites crop out closer to the coast.

- The mean elevations of different lithologies within catchments generally co-vary, demonstrating a common dependence upon the overall catchment elevation. However, the average relief values for different rock types do not co-vary. This shows that there is no evidence of any non-lithological control on relief, such as regions of axial uplift or planation, on the scale of these analyses.

- A strong lithological control on topography is consistent with an equilibrium landscape in a topographic steady state.

8.3 Weathering and erosion rates

8.3.1 What are the current rates of weathering and erosion of landforms?

- The abundance of a cosmogenic nuclide may be used to determine a rock surface's minimum exposure age, or its maximum erosion rate over the same time period.

- The determination of such values relies upon the scaling of cosmogenic nuclide production rates with altitude and latitude, as well as the absolute production rates of these nuclides from various target nuclei.

- Constraints on the surface exposure histories of Karoo dolerites may be gained from determining the abundances of the cosmogenic noble gases ^{3}He, ^{21}Ne and ^{38}Ar in pyroxene separates from Karoo dolerites.

- ^{3}He minimum exposures ages range from 18.5 +5.0/-4.7 ka to 583 ± 69 ka (using the scaling factors of Lal, 1991) or from 20.3 +5.6/-5.2 ka to 656 ± 78

ka (using the scaling factors of Dunai, 2000a). ^{3}He maximum erosion rates range from 0.65 ± 0.16 m/Myr to 20.8 +5.3/-5.7 m/Myr (using the scaling factors of Lal, 1991) or from 0.57 ± 0.14 m/Myr to 18.9 +4.8/-5.2 m/Myr (using the scaling factors of Dunai, 2000a).

- ^{21}Ne minimum exposures ages range from 32.1 ± 6.1 ka to 514 ± 28 ka (Lal, 1991 scaling) or from 35.4 ± 6.7 ka to 587 ± 32 ka (Dunai, 2000a scaling). ^{21}Ne maximum erosion rates range from 0.606 ± 0.064 m/Myr to 12.0 ± 2.3 m/Myr (Lal, 1991 scaling) or from 0.530 ± 0.056 to 10.9 ± 2.0 m/Myr (Dunai, 2000a scaling).

- ^{38}Ar minimum exposures ages that are not within analytical error of zero range from 240 +190/-130 ka to 1300 +1000/-800 ka (Lal, 1991 scaling) or from 260 +210/-150 ka to 1500 +1200/-900 ka (Dunai 2000a scaling). ^{38}Ar maximum erosion rates that are not within analytical error of infinity range from 0.24 +0.59/-0.13 m/Myr to 2.2 +2.9/-1.0 m/Myr (Lal, 1991 scaling) or from 0.21 +0.52/-0.11 m/Myr to 2.0 +2.7/-0.9 m/Myr (Dunai, 2000a scaling).

- Minimum exposure ages and maximum erosion rates determined from cosmogenic ^{3}He, ^{21}Ne and ^{38}Ar abundances are generally in good agreement with each other. The ^{21}Ne excess above air sometimes includes a significant nucleogenic/crustal ^{21}Ne component, and cosmogenic ^{38}Ar abundances are usually only known with a relatively high degree of analytical uncertainty. Cosmogenic ^{3}He abundances thus yield the most useful dataset for determining rates of weathering and erosion.

- 19 out of 22 samples yield ^{3}He maximum erosion rates less than 3.75 ± 0.47 m/Myr (Lal 1991 scaling) or less than 3.37 ± 0.43 m/Myr (Dunai 2000a scaling). Thus, 86 % of samples have maximum erosion rates in the range ~0.5-4 m/Myr.

- These low and generally consistent values for maximum erosion rates, combined with field observations, suggest that the maximum erosion rates for

these 19 surfaces closely approximate their weathering rates, but may be slight overestimates in places due to episodic surface exfoliation.

- The three surfaces with maximum erosion rates > 4 m/Myr all show evidence of active exfoliation, in which case maximum erosion rates are likely to be more significant overestimates of the dolerite weathering rate for such surfaces.

- For scarp faces, minimum exposure ages may be used to define model rates of scarp retreat. In such instances, it is assumed that the minimum exposure age is the time period between successive rockfalls where thicknesses of rock equivalent to 3 cosmic ray attenuation lengths (i.e. 0.61 m for a vertical dolerite cliff) are lost.

- The model scarp retreat rates are too low to laterally erode various landforms within geologically reasonable periods of time. This suggests a significant decline in the rate of weathering and erosion in southern Africa over time.

8.3.2 How and why have erosion rates changed over time?

- Literatures estimates of denudation rates in southern Africa based on apatite fission track and (U-Th)/He thermochronology indicate that denudation rates generally declined from the Cretaceous to the Tertiary by up to an order of magnitude (e.g. 125-175 m/Myr to 10-15 m/Myr in the southern Cape; Tinker et al., 2008a). The mean maximum erosion rate determined in this study for the late Quaternary is approximately an order of magnitude lower still (3.1 m/Myr, or 1.9 m/Myr for samples where $\varepsilon < 4$ m/Myr, according to cosmogenic ^{3}He abundances and Dunai 2000a scaling).

- High rates of denudation in the Cretaceous may have been due to epeirogenic uplift at this time (Section 8.2), and evidence that the Great Escarpment pre-dates the Cenozoic (Flowers and Schoene, in press) suggests that this was when major uplift of southern Africa took place. Lower denudation rates

during the Cenozoic may be viewed as indicating that the landscape was approaching a steady state form over this time.

- The similarity between Holocene sedimentation rates and late Quaternary cosmogenic nuclide based weathering rates suggests that sedimentation rates have been principally a function of weathering rates rather than due to active river incision over this time period. Together with the low denudation rate observed for the incised Pongola river valley, this supports the argument for a lack of significant regional mid-Cenozoic or late Cenozoic uplift in southern Africa, contrary to Partridge and Maud (1987) and Burke (1996).

- Literature estimates of soil erosion rates in southern Africa since the early 20th Century are highly variable, but average estimates for areas of dolerite sampling sites regionally vary from 57 m/Myr (Compton *et al*., 2010) to 198 m/Myr (Rooseboom, 1978). These "Anthropocene" soil erosion rates are more than one or two orders of magnitude higher than the mean rate of soil production from Karoo dolerites integrated over the late Quaternary, meaning that current agricultural practices in southern Africa are unsustainable.

8.3.3 Do weathering rates depend on climatic conditions?

- Maximum erosion rates for Karoo dolerites are generally within the same range of values predicted by a climate-dependent basaltic weathering law derived from a global database of present-day river chemistry (Dessert *et al*., 2003). According to this law, the weathering rate of basaltic rocks is a function of runoff and temperature (i.e. climate).

- However, interpreted Karoo dolerite weathering rates ($\varepsilon < 4$ m/Myr) do not vary across the region as a function of present-day climate.

- If the climatic dependence of dolerite weathering is accepted, and because dolerite weathering rates are integrated over time periods of $> 10^5$ years, this data suggests that present-day climatic trends in southern Africa did not prevail over the late Quaternary. Generally more arid conditions are implied

for eastern (presently humid) parts, and generally more humid conditions are implied for western (presently arid) parts. Available evidence from southern Africa's sparse late Quaternary climatic record supports this hypothesis.

8.4 Recommendations for future work

A number of observations may support the argument that Karoo dolerite denudation rates are representative of the catchments in which they occur:

1) Minimum exposure ages for some scarp faces formed by dolerite cap rocks are very similar to those of horizontal dolerite surfaces, implying that no recent undercutting by faster erosion of the underlying country rocks is occurring.
2) The mean elevation and mean relief of different rock types within a catchment varies consistently, suggesting an adjustment of form to mechanical strength, and an equality of erosive action across the landscape.
3) There is a close similarity between average Holocene rates of denudation for the Orange River catchment as determined by offshore sediment volume calculations (Compton *et al*., 2010), and dolerite maximum erosion rates.
4) Average denudation rates for southern Africa during the whole Cenozoic as determined by denudation thermochronology are no more than 1 order of magnitude greater than average dolerite maximum erosion rates over the late Quaternary. Southern Africa's palaeoclimatic record suggests that the Tertiary was, in general, warmer and more humid than the Quaternary, and this would probably have lead to increased weathering rates.

Nevertheless, catchment-averaged denudation rates could be determined in future by measuring cosmogenic ^{10}Be and ^{26}Al abundances in quartz from stream sediments in the Karoo Basin and surrounding areas. The cosmogenic noble gases alone are not well suited to such a task, as ^{3}He is not quantitatively retained in quartz, and ^{21}Ne data alone may be compromised by the presence of a significant but unquantified nucleogenic component. ^{10}Be and ^{26}Al analyses could also be applied to sediments in the area of the Elliot Formation outcrop west of the Drakensberg basalts, in order to test Compton *et al*.'s (2010) hypothesis of higher denudation rates here and inland scarp retreat. The Cape Fold Belt also constitutes a useful field area for such studies. Whilst apatite fission track data suggests that the Cape Fold Belt was exhumed largely

during the Cretaceous, the possibility of later uplift resulting in, for instance, fluvial incision and the creation of gorges, cannot be discounted (Tinker *et al*., 2008a). It has been proposed that Cenozoic uplift may have occurred here along a flexural axis during the Plio-Pleistocene (Partridge and Maud, 1987; Moore, 1999) or as a relatively continuous (~10^4 – 10^5 yr) isostatic response to denudational unloading (Gilchrist and Summerfield, 1991; Van der Beek *et al*., 2002). If recent local flexural uplift has occurred in the Cape Fold Belt, appreciably higher rates of denudation may be expected here.

Although numerous apatite fission track studies have been conducted in southern Africa, apatite (U-Th)/He thermochronology has only been applied in one recent study of the eastern escarpment (Flowers and Schoene, in press). As this technique is sensitive to lower temperatures than apatite fission track studies, its application to other parts of southern Africa may provide new insights into southern Africa's long-term denudation. If the geochronological dating of the Karoo dolerite weathering products proves to be possible, this may yield further insights into whether some dolerite *koppies* are indeed etch forms exhumed from an earlier, subsurface weathering front.

Small scale cosmogenic nuclide studies of specific landforms (e.g. a single *koppie*) may also prove insightful. A study in which a statistically significant number of samples are recovered from a single scarp face could be used to characterise the magnitudes of mass wasting events that occur at such a surface (e.g. Muzikar, 2008; 2009). The relationship between weathering rates and the erosion rate of weathered material may also be explored through the combined major element and cosmogenic nuclide analysis of soils and saprolites (e.g. Riebe *et al*., 2003, 2004; Green *et al*., 2006; Granger and Riebe, 2007 and references therein; Burke *et al*., 2009; Schaller *et al*., 2009). Whilst soils profiles in much of southern Africa are often thin and poorly developed, this approach would allow for an appraisal of the degree to which overall denudation rates in southern Africa may be weathering limited.

The highly variable estimates of present-day soil erosion rates, based on generally old data, emphasises the need for more research in this arena, particularly given the socio-economic and environmental relevance of this issue. Weathering studies based on the

chemistry of southern Africa rivers may also provide critical information on the relations between weathering, erosion and climate in the region. Further geomorphometric studies using recently available high resolution digital elevation data are also likely to yield new ways to map and interrogate southern Africa's landforms.

Finally, an understanding of southern Africa's geomorphology requires the integration of data based on different techniques and conducted by researchers from a variety of disciplines, including geochronologists, water chemists, soil scientists and GIS specialists. Some future integration of these studies under a regional geomorphological research programme may prove to be beneficial.

8.5 Concluding remarks

This thesis began with an introduction to two pioneers of geomorphological theory: W.M. Davis and G.K. Gilbert. The dominant effect of lithology on topography, as championed by Gilbert, is supported by this study for southern Africa. However, notable features such as incised river valleys, an interior plateau, a regional Great Escarpment and *koppies* that express the geometry of Karoo dolerite intrusions, all attest to southern Africa's unique geomorphological history. L.C. King once considered that southern Africa's landscape epitomises the cyclical development of landscapes through time, and that its history was globally applicable. Instead, it is the opinion of the present author that the landscape of southern Africa records the response of surface processes to regional epeirogenic uplift and climate change since the time of Gondwana breakup. Rather than recording a cyclical and repetitive narrative, it documents a unique history of changes in the rates of weathering and erosion, in which humans are writing the latest paragraph.

REFERENCES

Andreoli, M.A.G., Viola, G., Kounov, A., Scheepers, J., Heidbach, O. and Stengel, I., 2009. History of stress at Vaalputs, Namaqualand, South Africa: evidence for a Mid-Cretaceous "Wegener-type Orogeny" in western southern Africa. 11th SAGA biennial Technical Meeting and Exhibition, Swaziland, 16-18 September, 515-520.

Bak, P., 1996. How Nature Works. Springer-Verlag (New York), 205 p.

Baulig, H., 1952. Surfaces d'aplanissement. Annales de Géographie 61, 161-183 & 245-262.

Beater, B.E., 1947. Chemical composition of some Natal coastal dolerites and their alteration products. Soil Science 64 (2), 85-96.

Bell, F.G. and Jermy, C.A., 2000. The geotechnical character of some South African dolerites, especially their strength and durability. Quarterly Journal of Engineering Geology and Hydrogeology 33, 59-76.

Berger, L.R., de Ruiter, D.J., Churchill, S.E., Schmid, P., Carlson, K.J., Dirks, P.H.G.M. and Kibii, J.M., 2010. *Australopithecus sediba*: A New Species of *Homo*-Like Australopith from South Africa. Science 9 328 (5975), 195 – 204.

Berner, R.A., 1991. A model for atmospheric CO_2 over geological time. American Journal of Science 291, 339-376.

Berner, R.A., 1998. The carbon cycle and CO_2 over Phanerozoic time: the role of land plants. Philosophical Transactions of the Royal Society of London B 353, 75-82.

Bierman, P. and Turner, J., 1995. ^{10}Be and ^{26}Al Evidence for Exceptionally Low Rates of Australian Bedrock Erosion and the Likely Existence of Pre-Pleistocene Landscapes. Quaternary Research 44, 378-382.

Bierman, P.R. and Caffee, M., 2001. Slow rates of rock surface erosion and sediment production across the Namib desert and escarpment, Southern Africa. American Journal of Science 301, 326-358.

Bierman, P.R. and Caffee, M., 2002. Cosmogenic exposure and erosion history of Australian bedrock landforms. GSA Bulletin 114 (7) 787-803.

Boardman, J., Parsons, A.J., Holland, R., Holmes, P.J. and Washington, R., 2003. Development of badlands and gullies in the Sneeuberg, Great Karoo, South Afrca. Catena 50, 165-184.

Boelhouwers, J.C. and Meiklejohn, K.I., 2002. Quaternary periglacial and glacial geomorphology of southern Africa: review and synthesis. South African Journal of Science 98, 47-55.

Bohme, M., 2003. The Miocene Climate Optimum: evidence from ectothermic vertebrates of Central Europe. Palaeogeography, Palaeoclimatology, Palaeoecology 195, 389-401.

Braun, J. and Beaumont, C., 1989. A physical explanation of the relation between flank uplifts and the breakup unconformity at rifted continental margins. Geology 17, 760-764.

Bremner, J.M., Rogers, J. and Willis, J.P., 1990. Sedimentological aspects of the 1988 Orange River floods. Transactions of the Royal Society of South Africa 47 (3), 247-294.

Broad, D.S., Jungslager, E.H.A., McLachlan, I.R. and Roux, J., 2006. Offshore Mesozoic Basins. In: Johnson, M.R., Anhaeusser, C.R. and Thomas, R.J. (ed.). The Geology of South Africa. Geological Society of South Africa (Johannesburg)/Council for Geoscience (Pretoria), 691 p.

Brown, L.F., Benson, J.M., Brink, G.J., Doherty, S., Jollands, A., Jungslager, E.H.A., Keenan, J.H.G., Muntingh, A. and van Wyk, N.J.S., 1995. Sequence stratigraphy in

offshore South African divergent basins: an atlas on exploration for Cretaceous lowstand traps by Soekor (Pty) Ltd. American Association of Petroleum Geologists (Tulsa), 184 p.

Brown, R.W., Rust, D.J., Summerfield, M.A., Gleadow, A.J.W., and de Wit, M.C.J., 1990. An Early Cretaceous phase of accelerated erosion on the south-western margin of Africa: Evidence from apatite fission track analysis and the offshore sedimentary record. Nuclear Tracks and Radiation Measurement 17, 339-350.

Brown, R., Gallagher, K. and Duane, M., 1994. A quantitative assessment of the effects of magmatism on the thermal history of the Karoo sedimentary sequence. Journal of African Earth Sciences 18 (3), 227-243.

Brown, R.W., Gallagher, K., Gleadow, A.J.W. and Summerfield, M.A., 2000. Morphotectonic evolution of South Atlantic margins of Africa and South America. In: Summerfield, M.A. (ed.). Morphotectonic evolution of the South Atlantic margins of Africa and South America. Wiley (Chichester), p. 255-281.

Brown, R.W., Summerfield, M.A. and Gleadow, A.J.W., 2002. Denudation history along a transect across the Drakensberg Escarpment of southern Africa derived from apatite fission track thermochronology. Journal of Geophysical Research 107 (B12), 2350, doi: 10.1029/2001JB000745.

Bruno, L.A., Baur, H., Graf, T., Schlüchter, C., Signer, P. and Wieler, R., 1997. Dating of Sirius Group tillites in the Antarctic Dry Valleys with cosmogenic ^{3}He and ^{21}Ne. Earth and Planetary Science Letters 147, 37-54.

Buckle, C., 1978. Landforms in Africa. Longman (Hong Kong), 249 p.

Büdel, J., 1963. Klima-genetische Geomorphologie. Geologische Rundschau 7, 269-286.

Büdel, J., 1969. Das system der klima-genetischen Geomorphologie. Erdkunde 23, 165-182.

Bull, W.B., 1975. Landforms that do not tend towards a steady state. In: Melhorn, W.N. and Flemal, R.C. (ed.), 1980. Theories of Landform Development: A proceedings volume of the Sixth Annual Geomorphology Symposia Series held at Binghamton, New York. September 26-27, 1975. Allen and Unwin (Boston), 306 p.

Burbank, D.W., Blythe, A.E., Putkonen, J.L., Pratt-Situala, B.A., Gabet, E.J., Oskin, M.E., Barros, A.P. and Ohja, T.P., 2003. Decoupling of erosion and climate in the Himalaya. Nature 426, 652-655.

Burke, B.C., Heimsath, A.M., Dixon, J.L., Chappell, J. and Yoo, K., 2009. Weathering the escarpment: chemical and physical rates and processes: south-eastern Australia. Earth Surface Processes and Landforms 34, 768-785.

Burke, K., 1996. The African Plate. South African Journal of Geology 99 (4), 341–409.

Burke, K. and Gunnell, Y., 2008. The African Erosion Surface: A Continental-Scale Synthesis of Geomorphology, Tectonics and Environmental Change over the Past 180 Million Years. Geological Society of America Memoir 201. GSA (Boulder), 66 p.

Cerling, T.E., 1990. Dating geomorphologic surfaces using cosmogenic ^{3}He. Quaternary Research 33, 148-156.

Cerling, T.E. and Craig, H., 1994. Cosmogenic ^{3}He production rates from 39 ºN to 46 ºN latitude, western USA and France. Geochimica et Cosmochimica Acta 58, 249-255.

Chase, B.M. and Meadows, M.E., 2007. Late Quaternary dynamics of southern Africa's winter rainfall zone. Earth-Science Reviews 84, 103-138.

Chevallier, L. and Woodford, A., 1999. Morpho-tectonics and mechanism of emplacement of the dolerite rings and sills of the western Karoo, South Africa. South African Journal of Geology 102 (1), 43-54.

Chief Director of Surveys and Mapping, 1988a. 2924DC Havengabrug (2nd edition). 1:50,000 topographic map series. Chief Director of Surveys and Mapping (Mowbray).

Chief Director of Surveys and Mapping, 1988b. 3024BC Petrusville (2nd edition). 1:50,000 topographic map series. Chief Director of Surveys and Mapping (Mowbray).

Clowes, A. and Comfort, P., 1987. Process and Landform: An outline of contemporary geomorphology. Oliver and Boyd (London), 335 p.

Cochran, M.F. and Berner, R.A., 1996. Promotion of chemical weathering by higher plants: field observations on Hawaiian basalts. Chemical Geology 132, 71-77.

Cockburn, H.A.P, Seidl, M.A. and Summerfield, M.A. 1999. Quantifying denudation rates on inselbergs in the central Namib Desert using in situ-produced cosmogenic ^{10}Be and ^{26}Al. Geology 27 (5), 399-402.

Cockburn, H.A.P., Brown, R.W., Summerfield, M.A. and Seidl, M.A., 2000. Quantifying passive margin denudation and landscape development using a combined fission-track thermochronology and cosmogenic isotope analysis approach. Earth and Planetary Science Letters 179, 429-435.

Codilean, A.T., Bishop, P., Stuart, F.M., Hoey, T.B., Fabel, D. and Freeman, S.P.H.T., 2008. Single-grain cosmogenic ^{21}Ne concentrations in fluvial sediments reveal spatially variable erosion rates. Geology 36 (2), 159-162.

Compton, J.S., Herbert, C.T., Hoffman, M.T., Schneider, R.R. and Stuut, J.-B., 2010. A tenfold increase in the Orange River mean Holocene mud flux: implications for soil erosion in South Africa. The Holocene 20 (1), 115-122.

Courtillot, V., Besse, J., Vandamme, D., Montigny, R., Jaeger, J.J. and Cappetta, H., 1986. Deccan flood basalt at the Cretaceous/Tertiary boundary? Earth and Planetary Science Letters 80, 361-374.

Cowling, R.M., Procheş, S. and Partridge, T.C., 2009. Explaining the uniqueness of the Cape flora: Incorporating geomorphic evolution as a factor for explaining its diversification. Molecular Phylogenetics and Evolution 51, 64-74.

Cox, K.G., 1992. Karoo igneous activity, and the early stages of the breakup of Gondwanaland. In: Storey, B.C., Alabaster, T. and Pankhurst, R.J. (eds.), 1992. Magmatism and the Causes of Continental Break-up. Special Publication of the Geological Society of London 68, 137-148.

Craig, H. and Lupton, J.E., 1976. Primordial neon, helium, and hydrogen in oceanic basalts. Earth and Planetary Science Letters 31 (3), 369-385.

Craig, H. and Poreda, R.J., 1986. Cosmogenic ^{3}He in terrestrial rocks: The summit lavas of Maui. Proceedings of the National Academy of Sciences USA 83, 1970-1974.

Cruden, D.M., 2003. The shapes of cold, high mountains in sedimentary rocks. Geomorphology 55 (1-4), 249-261.

Darwin, C., 1859. On the origin of species by means of natural selection, or the preservation of favoured races in the struggle for life. John Murray (London), 502 p.

Davis, G.L., 1977. The ages and uranium contents of zircons from kimberlites and associated rocks. Second International Kimberlites Conference (Abstract).

Davis, R. Jnr and Schaeffer, O.A., 1955. Chlorine-36 in nature. Annals of the New York Academy of Sciences 62, 107-121.

Davis, W.M., 1899. The Geographical Cycle. Geographical Journal 14, 481-504. In: Johnson, D.W. (ed.), 1909. Geographical Essays by William Morris Davis. Ginn and Company (Boston), 777 p.

Davis, W.M., 1905. The Geographical Cycle in an Arid Climate. The Journal of Geology 13, 381-407. In: Johnson, D.W. (ed.), 1909. Geographical Essays by William Morris Davis. Ginn and Company (Boston), 777 p.

Davis, W.M., 1932. Piedmont benchlands and the Primärrumpfe. Geological Society of America Bulletin 43, 399-440.

Deer, W.A., Howie, R.A. and Zussman, J., 1996. An introduction to the rock-forming minerals (2nd edition). Addison Wesley Longman Limited (Harlow), 696 p.

Desilets, D. and Zreda, M., 2001. On scaling cosmogenic production rates for altitude and latitude using cosmic-ray measurements. Earth and Planetary Science Letters 193, 213-225.

Desilets, D. and Zreda, M., 2003. Spatial and temporal distribution of secondary cosmic-ray nucleon intensities and applications to in situ cosmogenic dating. Earth and Planetary Science Letters 206, 21-42.

Desilets, D., Zreda, M. and Lifton, N.A., 2001. Comment on 'Scaling factors for production rates of in situ produced cosmogenic nuclides: a critical reevaluation' by Tibor J. Dunai. Earth and Planetary Science Letters 188, 283-287.

Desilets, D., Zreda, M. and Prabu, T., 2006. Extended scaling factors for in situ cosmogenic nuclides: New measurements at low latitude. Earth and Planetary Science Letters 246, 265-276.

Dessert, C., Dupré, B., François, L.M., Schott, J., Gaillardet, J., Chakrapani, G. and Bajpai, S., 2001. Erosion of Deccan Traps determined by river geochemistry: impact on the global climate and the $^{87}Sr/^{86}Sr$ ratio of seawater. Earth and Planetary Science Letters 188, 459-474.

Dessert, C., Dupré, B., Gaillardet, J., François, L.M. and Allègre, C.J., 2003. Basalt weathering laws and the impact of basalt weathering on the global carbon cycle. Chemical Geology 202, 257-273.

de Swardt, A.M.J. and Bennet, G., 1974. Structural and physiographic development of Natal since the late Jurassic. Transactions of the Geological Society of South Africa 77, 309-322.

de Swardt, A.M.J. and Bennet, G., 1976. Reply to: King, L.C., 1976. Comment upon two papers concerning the geomorphology of Natal. Transactions of the Geological Society of South Africa 79 (1), 149-151.

de Wit, M.C.J., 1993. Cainozoic Evolution of Drainage Systems in the North-Western Cape. Unpublished PhD thesis, University of Cape Town, 340 p.

de Wit, M.C.J., Ward, J.D., Bamford, M.K. and Roberts, M.J., 2009. The significance of the Cretaceous diamondiferous gravel deposit at Mahura Muthla, Northern Cape Province, South Africa. South African Journal of Geology 112, 89-108.

de Wit, M.J., 2007. The Kalahari Epeirogeny and climate change; differentiating cause and effect from core to space. South African Journal of Geology, Special Inkaba yeAfrica Volume 110, 367-392.

de Wit, M.J., Stankiewicz, J. and Reeves, C., 2008. Restoring Pan-African-Brasiliano connections: more Gondwana control, less Trans-Atlantic corruption. In: Pankhurst, R.J., Trouw, R.A.J., de Brito Neves, B.B. and de Wit, M.J. (eds.). West Gondwana: Pre-Cenozoic Correlations across the South Atlantic Region. Geological Society of London Special Publication 294, 399-412.

Dingle, R.V., Siesser, W.G. and Newton, A.R., 1983. Mesozoic and Tertiary geology of southern Africa. A.A. Balkema (Rotterdam), 375 p.

Dingle, R.V. and Hendey, Q.B., 1984. Late Mesozoic and Tertiary sediment supply to the eastern Cape Basin (SE Atlantic) and palaeo-drainage systems in southwestern Africa. Marine Geology 56, 13-26.

Dirks, P.H.G.M., Kibii, J.M., Kuhn, B.F., Steininger, C., Churchill, S.E., Kramers, J.D., Pickering, R., Farber, D.L., Mériaux, A.-S., Herries, A.I.R., King, G.C.P.,

Berger, L.R., 2010. Geological Setting and Age of *Australopithecus sediba* from Southern Africa. Science 328 (5975), 205 – 208.

Dodson, A., Kennedy, B.M. and DePaolo, D.J., 1997. Helium and neon isotopes in the Imnaha Basalt, Columbia River Basalt Group: Evidence for a Yellowstone plume source. Earth and Planetary Science Letters 150 (3-4), 443-451.

Doucouré, C.M. and de Wit, M.J., 2003. Old inherited origin for the present near-bimodal topography of Africa. Journal of African Earth Sciences 36, 371-388.

Douglass, J. and Schmeeckle, M., 2007. Analogue modeling of transverse drainage mechanisms. Geomorphology 84, 22-43.

Drever, J.I. and Stillings, L.L., 1997. The role of organic acids in mineral weathering. Colloids and Surfaces A: Physicochemical and Engineering Aspects 120, 167-18.

Dunai, T.J., 2000a. Scaling factors for production rates of in situ produced cosmogenic nuclides: a critical reevaluation. Earth and Planetary Science Letters 176, 157-169.

Dunai, T.J., 2000b. Erratum to "Scaling factors for production rates of in situ produced cosmogenic nuclides: a critical reevaluation" [Earth Planet. Sci. Lett. 176 (2000) 157-169]. Earth and Planetary Science Letters 178, 145.

Dunai, T.J., 2001a. Reply to comment on 'Scaling factors for production rates of in situ produced cosmogenic nuclides: a critical reevaluation' by Darin Desilets, Marek Zreda and Nathaniel Lifton. Earth and Planetary Science Letters 188, 289-298.

Dunai, T.J., 2001b. Influence of secular variation of the geomagnetic field on production rates of in situ produced cosmogenic nuclides. Earth and Planetary Science Letters 193, 197-212.

Dunai, T.J., González López, G.A. and Juez-Larré, 2005. Oligocene-Miocene age of aridity in the Acatama Desert revealed by exposure dating of erosion-sensitive landforms. Geology 33 (4), 321–324.

Duncan, A.R. and Marsh, J.S., 2006. The Karoo Igneous Province. In: Johnson, M.R., Anhaeusser, C.R. and Thomas, R.J. (ed.). The Geology of South Africa. Geological Society of South Africa (Johannesburg)/Council for Geoscience (Pretoria), 691 p.

Duncan, R.A., Hooper, P.R., Rehacek, J., Marsh, J.S. and Duncan, A.R., 1997. The timing and duration of the Karoo igneous event, southern Gondwana. Journal of Geophysical Research 102, 18127 – 18183.

Dunne, J., Elmore, D. and Muzikar, P., 1999. Scaling factors for the rates of production of cosmogenic nuclides for geometric shielding and attenuation at depth on sloped surfaces. Geomorphology 27, 3-11.

Dupré, B., Dessert, C., Oliva, P., Goddéris, Y., Viers, J., François, L., Millot, R. and Gaillardet, J., 2003. Rivers, chemical weathering and Earth's climate. C.R. Geoscience 335, 1141-1160.

du Toit, A.L., 1905. Geological survey of Glen Gray and parts of Queenstown and Wodehouse. Tenth Annual Report of the Cape Geological Commission, 97-140.

du Toit, A.L., 1920. The Karroo dolerites of South Africa: a study in hypabyssal injection. Transactions of the Geological Society of South Africa 23, 1-42.

du Toit, A.L., 1929. The volcanic belt of the Lebombo: a region of tension. Transactions of the Royal Society of South Africa 18, 189-217.

du Toit, A.L.,1933. Crustal movement as a factor in the geographical evolution of South Africa. South African Geographical Journal 16, 3-20.

du Toit, A.L., 1954. The Geology of South Africa (3rd edition). Oliver and Boyd (Edinburgh), 611 p.

Ebelmen, J.J., 1845. Sur les produits de la décomposition des espèces minérales de la famille des silicates. Annales des Mines 7, 3–66.

Eberhardt, P., Eugster, O. and Marti, K., 1965. A redetermination of the isotopic composition of atmospheric neon. Zeitschrift für Naturforschung 20a, 623–624.

Ebinger, C.J. and Sleep, N.H., 1998. Cenozoic magmatism throughout east Africa resulting from impact of a single plume. Nature 395, 788-791.

Encarnacion, J., Fleming, T.H., Elliot, H., and Eales, H.V., 1996. Synchronous emplacement of Ferrar and Karoo dolerites and the early breakup of Gondwana. Geology 24, 535 - 538.

England, P. and Molnar, P., 1990. Surface uplift, uplift of rocks, and exhumation of rocks. Geology 18, 1173-1177.

Etourneau, J., Martinez, P., Blanz, T. and Schneider, R., 2009. Pliocene-Pleistocene variability of upwelling activity, productivity, and nutrient cycling in the Benguela region. Geology 37, 871-874.

Fairchild, I.J., Smith, C.L., Baker, A., Fuller, L., Spötl, C., Mattey, D., McDermott, F. and E.I.M.F., 2006. Modification and preservation of environmental signals in speleothems. Earth-Science Reviews 75 (1-4), 105-153.

Fanale, F.P. and Cannon, W.A., 1971. Physical adsorption of rare gas on terrigenous sediments. Earth and Planetary Science Letters 11, 362–386.

Fenton, C.R., Niedermann, S., Goethals, M.M., Schneider, B. and Wijbrans, J., 2009. Evaluation of cosmogenic ^{3}He and ^{21}Ne production rates in olivine and pyroxene from two Pleistocene basalt flows, western Grand Canyon, AZ, USA. Quaternary Geochronology 4, 475–492.

Fleming, A., Summerfield, M.A., Stone, J.O.H., Fifield, L.K. and Cresswell, R.G., 1999. Denudation rates for the southern Drakensberg escarpment, SE Africa, derived

from in-situ-produced cosmogenic ^{36}Cl: initial results. Journal of the Geological Society, London 156, 209-212.

Flowers, R.M. and Schoene, B. (in press). Cretaceous topography in the eastern Kaapvaal craton and implications for Mesozoic elevation gain of the southern African Plateau. Geology.

Formento-Trigilio, M.L. and Pazzaglia, F.J., 1998. Tectonic geomorphology of the Sierra Nacimiento: Traditional and new techniques in assessing long-term landscape evolution in the southern Rocky Mountains. The Journal of Geology 106, 433–453.

Gabet, E.J. and Mudd, S.M., 2009. A theoretical model coupling chemical weathering rates with denudation rates. Geology 37, 151-154.

Gaillardet, J., Dupré, B., Louvat, P. and Allègre, C.J., 1999. Global silicate weathering and CO_2 consumption rates deduced from the chemistry of the large rivers. Chemical Geology 159, 3-30.

Gallagher, K. and Brown, R., 1999. Denudation and uplift at passive margins: the record on the Atlantic Margin of southern Africa. Philosophical Transactions of the Royal Society of London A 357, 835-859.

Gallagher, K., Brown, R. and Johnson, C., 1998. Fission track analysis and its applications to geological problems. Annual Review of Earth and Planetary Sciences 26, 519-572.

Gardner, T.W., Jorgensen, D.W., Shuman, C. and Lemieux, C.R., 1987. Geomorphic and tectonic process rates: Effect of measured time interval. Geology 15, 259-261.

Garland, G., Hoffman, T. and Todd, S., 1999. Chapter 6: Soil degradation. In: Hoffman, M.T., Todd, S., Ntshona, Z. and Turner, S. (eds.). Land degradation in South Africa. South African National Biodiversity Institute (Pretoria), 69-107.

Gilbert, G.K., 1877. Report on the Geology of the Henry Mountains. Geographical and Geological Survey of the Rocky Mountain Region, Department of the Interior (Washington D.C.), 160 p.

Gilchrist, A.R. and Summerfield, M.A., 1990. Differential denudation and flexural isostasy in the formation of rifted-margin upwarps. Nature 346, 739-742.

Gilchrist, A.R. and Summerfield, M.A., 1991. Denudation, isostasy and landscape evolution. Earth Surface Processes and Landforms 16, 555-562.

Gislason, S.R., Oelkers, E.H., Eiriksdottir,. E.S., Kardjilov, M.I., Gisladottir, G., Sigfusson, B., Snorrason, A., Elefsen, S., Hardardottir, J., Torssander, P. and Oskarsson, N., 2009. Direct evidence of the feedback between climate and weathering. Earth and Planetary Science Letters 277 (1-2), 213-222.

Goehring, B.M., Kurz, M.D., Balco, G., Schaefer, J.M., Licciardi, J. and Lifton, N., 2010. A reevaluation of *in situ* cosmogenic ^{3}He production rates. Quaternary Geochronology 5, 410-418.

Gosse, J.C. and Phillips, F.M., 2001. Terrestrial in situ cosmogenic nuclides: theory and application. Quaternary Science Reviews 20, 1475-1560.

Grab, S., van Zyl, C. and Mulder, N., 2005. Controls on basalt terrace formation in the eastern Lesotho highlands. Geomorphology 67, 473-485.

Gradstein, F., Ogg, J. and Smith, A., 2004. A Geologic Time Scale 2004. Cambridge University Press (Cambridge), 589 p.

Granger, D.E. and Riebe, C.S., 2007. Cosmogenic nuclides in weathering and erosion. In: Drever, J.I. (ed.) Surface and Ground Water, Weathering and Soils, Vol. 5. In: Turekian, K.K. and Holland, H.D. (eds.). Treatise on Geochemistry (online update). Elsevier-Pergamon (Oxford), 43 p. doi: 10.1016/B978-008043751-4/00238-8.

Green, E.G., Dietrich, W.E. and Banfield, J.F., 2006. Quantification of chemical weathering rates across an actively eroding hillslope. Earth and Planetary Science Letters 242, 155-169.

Haack, U., 1983. Reconstruction of the cooling history of the Damara Orogen by correlation of radiometric ages with geography and altitude. In: Martin, H. and Eder, F.W. (eds.). Intracontinental fold belts, Springer (Berlin), 873-884.

Hack, J.T., 1960. Interpretation of erosional topography in humid temperate regions. American Journal of Science, Bradley Volume 258-A, 80-97.

Hack, J.T., 1975. Dynamic equilibrium and landscape evolution. In: Melhorn, W.N. and Flemal, R.C. (ed.), 1980. Theories of Landform Development: A proceedings volume of the Sixth Annual Geomorphology Symposia Series held at Binghamton, New York. September 26-27, 1975. Allen and Unwin (Boston), 306 p.

Haddon, I.G. and McCarthy, T.S., 2005. The Mesozoic-Cenozoic interior sag basins of Central Africa: The Late-Cretaceous-Cenozoic and Okavango basins. Journal of African Earth Sciences 43, 316-333.

Hanson, E.K., Moore, J.M., Bordy, E.M., Marsh, J.S., Howarth, G. and Robey, J.V.A., 2009. Cretaceous erosion in central South Africa: Evidence from upper-crustal xenoliths in kimberlite diatremes. South African Journal of Geology 112, 125-140.

Harmse, H.J von M., 1975. Sedimentproduksiekaart van Suid-Afrika (unpublished).

Hart, M.G., 1986. Geomorphology: pure and applied. Allen and Unwin (London), 228 p.

Hassenfratz, J.H., 1791. Sur l'arrangement de plusieurs gros blocs de différentes pierres que l'on observe dans les montagnes. Annales de Chimie 11, 95–107.

Hatch, F.H. and Corstorphine, G.S., 1905. The Geology of South Africa. Macmillan and Co. (London), 336 p.

Hawthorne, J.B. (1975). Model of a kimberlite pipe. In: Ahrens, L.H., Dawson, J.B., Duncan, A.R. and Erlank, A.J. (eds.). Physics and Chemistry of the Earth 9, Pergamon (Oxford), 1-15.

Hergarten, S., 2003. Landslides, sandpiles, and self-organized criticality. Natural Hazards and Earth System Sciences 3, 505-514.

Hermanns, R.L., Niedermann, S., Ivy-Ochs, S. and Kubik, P.W., 2004. Rock avalanching into a landslide-dammed lake causing multiple dam failure in Las Conchas valley (NW Argentina) - evidence from surface exposure dating and stratigraphic analyses. Landslides 1 (2), 113–122.

Hewawasam, T., von Blanckenburg, F. Schaller, M. and Kubik, P., 2003. Increase of human over natural erosion rates in tropical highlands constrained by cosmogenic nuclides. Geology 31, 597-600.

Higgins, C.G., 1975. Theories of Landscape Evolution: A Perspective. In: Melhorn, W.N. and Flemal, R.C. (ed.), 1980. Theories of Landform Development: A proceedings volume of the Sixth Annual Geomorphology Symposia Series held at Binghamton, New York. September 26-27, 1975. Allen and Unwin (Boston), 306 p.

Hohenberg, C.M., Marti, K., Podosek, F.A., Reedy, R.C. and Shirck, J.R., 1978. Comparisons between observed and predicted cosmogenic noble gases in lunar samples. Proceedings of the 9th Lunar and Planetary Science Conference, 1419-1449.

Honda, M., McDougall, I., Patterson, D.B., Doulgeris, A. and Clague, D.A., 1991. Possible solar noble-gas component in Hawaiian basalts. Nature 349, 149-151.

Hooke, R. Le B., 2000. On the history of humans as geomorphic agents. Geology 28, 843-846.

Horton, R.E., 1945. Erosional development of streams and their drainage basins. Bulletin of the Geological Society of America 56 (1), 275-370.

Hutton, J., 1788. Theory of the earth. Transactions of the Royal Society of Edinburgh 1, 209-304.

Jamtveit, B., Svensen, H, Podladchikov, Y.Y. and Planke, S., 2004. Hydrothermal vent complexes associated with sill intrusions in sedimentary basins. In: Breitkreuz, C. and Petford, N. (eds.). Physical Geology of High-Level Magmatic Systems. Geological Society of London Special Publication 234, 233-241.

Jarvis, A., Rubiano, J., Nelson, A., Farrow, A. and Mulligan, M., 2004. Practical use of SRTM data in the tropics: Comparisons with digital elevation models generated from cartographic data. Working document 198, Centro Internacional de Agricultura Tropical (CIAT), Cali (Columbia), 32 p.

Jarvis, A., Reuter, H.I., Nelson, A. and Guevara, E., 2006. Hole-filled SRTM for the globe Version 3, available from the CGIAR-CSI SRTM 90m Database: http://srtm.csi.cgiar.org.

Johnson, D.W. (ed.), 1909. Geographical essays by William Morris Davis. Ginn and Company (Boston), 777 p.

Johnson, M.R., Anhaeusser, C.R. and Thomas, R.J. (ed.), 2006. The Geology of South Africa. Geological Society of South Africa (Johannesburg)/Council for Geoscience (Pretoria), 691 p.

Jokat, W., Boebel, T., König, M. and Uwe, M., 2003. Timing and geometry of early Gondwana breakup. Journal of Geophysical Research 108 (B9), 2428. doi:10.1029/2002JB001802.

Jourdan, F., Féroud, G., Bertrand, H., Kampunzu, A.B., Tshoso, G., Watkeys, M.K. and Le Gall, B., 2005. Karoo Large Igneous province: Brevity, origin, and relation to mass extinction questioned by new $^{40}Ar/^{39}Ar$ age data. Geology 33 (9), 745-748.

Jourdan, F., Féroud, G., Bertrand, H., and Watkeys, M.K., 2007. From flood basalts to the inception of oceanization. Example from the $^{40}Ar/^{39}Ar$ high-resolution picture of

the Karoo large igneous province. Geochemistry, Geophysics, Geosystems 8 (2), Q02002. doi: 10.

Jourdan, F., Féroud, G., Bertrand, H., Watkeys, M.K. and Renne, P.R., 2008. The $^{40}Ar/^{39}Ar$ ages of the sill complex of the Karoo large igneous province: implications for the Pliensbachian-Toarcian climate change. Geochemistry, Geophysics, Geosystems 9 (6), Q06009.doi: 10.1029/2008gc001994.

Keay-Bright, J. and Boardman, J., 2006. Changes in the distribution of degraded land over time in the central Karoo, South Africa. Catena 67, 1-14.

Keay-Bright, J. and Boardman, J., 2009. Evidence from field-based studies of rates of soil erosion on degraded land in the central Karoo, South Africa. Geomorphology 103, 455-465.

Kennedy, B.M., Hiyagon, H. and Reynolds, J.H., 1990. Crustal Neon: a striking uniformity. Earth and Planetary Science Letters 98, 277–286.

King, L.C., 1944. Geomorphology of the Natal Drakensberg. Transactions of the Geological Society of South Africa 47, 255-282.

King, L.C., 1951. South African Scenery (2nd edition). Oliver and Boyd (Edinburgh), 377 p.

King, L.C., 1953. Canons of landscape evolution. Geological Society of America Bulletin 64, 721-751.

King, L.C., 1955. Pediplanation and isostasy: an example from South Africa. Quarterly Journal of the Geographical Society 111, 353-359.

King, L.C., 1967. Morphology of the Earth (2nd edition). Oliver and Boyd (Edinburgh), 726 p.

King, L.C., 1976. Comment upon two papers concerning the geomorphology of Natal. Transactions of the Geological Society of South Africa 79 (1), 149-151.

King, L.C., 1983. Wandering Continents and Spreading Sea Floors on an Expanding Earth. John Wiley & Sons (Bath), 232 p.

Klausen, M.B., 2009. The Lebombo monocline and associated feeder dyke swarm: Diagnostic of a successful and highly volcanic rifted margin? Tectonophysics 468, 42-62.

Knight, K.B., Renne, P.R. and Farley, K.A., 2003. Preliminary estimate of production rates for terrestrial cosmogenic ^{38}Ar from calcium. Eos Transactions AGU 84, Abstract V22G-08.

Kober, F., Ivy-Ochs, S., Leya, I., Baur, H., Magna, T., Wieler, R. and Kubik, P.W., 2005. In situ cosmogenic ^{10}Be and ^{21}Ne in sanidine and in situ cosmogenic ^{3}He in Fe-Ti-oxide minerals. Earth and Planetary Science Letters 236, 404-418.

Kooi, H. and Beaumont, C., 1994. Escarpment evolution on high-elevation rifted margins: Insights derived from a surface processes model that combines diffusion, advection, and reaction. Journal of Geophysical Research 99 (B6), 12,191 – 12,209.

Kounov, A., Niedermann, S., de Wit, M.J., Viola, G., Andreoli, M. and Erzinger, J., 2007. Present denudation rates at selected sections of the South African escarpment and the elevated continental interior based on cosmogenic ^{3}He and ^{21}Ne. South African Journal of Geology 110, 235-248.

Kounov, A., Viola, G., de Wit, M.J. and Andreoli, M., 2008. A Mid Cretaceous paleo-Karoo River valley across the Knersvlakte plain (northwestern coast of South Africa): Evidence from apatite fission-track analysis. South African Journal of Geology 111, 409-420.

Kounov, A., Viola, G., de Wit, M. and Andreoli, M.A.G., 2009. Denudation along the Atlantic passive margin: new insights from apatite fission-track analysis on the western coast of South Africa. In: Lisker, F., Ventura, B. and Glasmacher, U.A. (eds). Thermochronological Methods: From Palaeotemperature Constraints to Landscape Evolution Models. Geological Society, London, Special Publications 324, 287-306.

Kristen, I., Fuhrmann, A., Thorpe, J., Röhl., U., Wilkes, H. and Oberhänsli, H., 2007. Hydrological changes in southern Africa over the last 200 Ka as recorded in lake sediments from the Tswaing impact crater. South African Journal of Geology 110, 311-326.

Kurz, M.D., Colodner, D., Trull, T.W., Moore, R.B. and O'Brien, K., 1990. Cosmic-ray exposure dating with *in situ* produced cosmogenic ^{3}He: results from young Hawaiian lava flows. Earth and Planetary Science Letters 97, 177-189.

Lal, D., 1991. Cosmic ray labeling of erosion surfaces: *in situ* nuclide production rates and erosion models. Earth and Planetary Science Letters 104, 424-439.

Lal, D. and Peters, B., 1967. Cosmic ray produced radioactivity on the earth. In: S. Flugg (Ed.), Handbook of Physics 46 (2), Springer, Berlin, 551-612.

Lee, J.-Y., Marti, K., Severinghaus, J.P., Kawamura, K., Yoo, H.-S., Lee, J.B. and Kim, J.S., 2006. A redetermination of the isotopic abundances of atmospheric Ar. Geochimica et Cosmochimica Acta 70, 4507–4512.

le Roex, A.P. and Reid, D.L., 1978. Geochemistry of Karroo Dolerite Sills in the Calvinia District, Western Cape Province, South Africa. Contributions to Mineralogy and Petrology 66, 351-360

Le Roux, F.G. (compiler), 1998. 3024 Colesburg. 1:250,000 geological map series, Council for Geoscience (Pretoria).

Le Roux, J.J., Newby, T.S. and Sumner, P.D., 2007. Monitoring soil erosion in South Africa at a regional scale: review and recommendations. South African Journal of Science 103, 329-335.

Le Roux, J.S., 1990. Spatial variations in the rate of fluvial erosion (sediment production) over South Africa. Water SA 16 (3), 185-194.

Libarkin, J.C., Quade, J., Chase, C.G., Poths, J. and McIntosh, W., 2002. Measurement of ancient cosmogenic ^{21}Ne in quartz from the 28 Ma Fish Canyon Tuff, Colorado. Chemical Geology 186, 199-213.

Libby, W. F., 1946. Atmospheric helium three and radiocarbon from cosmic radiation. Physics Review 69, 671-672.

Lifton, N.A., Bieber, J.W., Clem, J.M., Duldig, M.L., Evenson, P., Humble, J.E., Pyle, R., 2005. Addressing solar modulation and long-term uncertainties in scaling secondary cosmic rays for in situ cosmogenic nuclide applications. Earth and Planetary Science Letters 239, 140- 161.

Linton, D.L., 1955. The problem of tors. The Geographical Journal 121, 470–487.

Macmillan, I.K., 2003. Foraminiferally defined biostratigraphic episodes and sedimentation pattern of the Cretaceous drift succession (Early Barremian to Late Maastrichtian) in seven basins on the South African and southern Namibian continental margin. South African Journal of Science 99, 537-576.

Maré, L.P. and Cole, J., 2006. The Trompsburg Complex, South Africa: A preliminary three dimensional model. Journal of African Earth Sciences 44, 314-330.

Marker, M.E., 1986. Pleistocene evidence from the Eastern Cape South Africa: The Amatola screes tongues. In: Gardiner, V. (ed.). International Geomorphology II. Wiley (Chichester), 901-913.

Marsh, A. (compiler), 1979. 3222 Beaufort West. 1:250,000 geological map series, Council for Geoscience (Pretoria).

Marti, K. and Craig, H., 1987. Cosmic-ray-produced neon and helium in the summit lavas of Maui. Nature 325, 335-337.

Martin, A.K., 1987. Comparison of sedimentation rates in the Natal Valley, south-west Indian Ocean, with modern sediment yields in the east coast rivers of Southern Africa. South African Journal of Science 83, 716-724.

Masarik, J., 2002. Numerical simulation of in situ production of cosmogenic nuclides. Geochimica et Cosmochimica Acta 66 (15A), A491.

Masarik, J. and Reedy, R.C., 1995. Terrestrial cosmogenic-nuclide production systematics calculated from numerical simulations. Earth and Planetary Science Letters 136, 381-395.

Masarik, J. and Reedy, R.C., 1996. Monte Carlo simulation of *in situ* produced cosmogenic nuclides. Radiocarbon 38, 163-164.

Masarik, J., Frank, M., Schäfer, J.M., and Wieler, R., 2001. Correction of in situ cosmogenic nuclide production rates for geomagnetic field intensity variations during the past 800,000 years. Geochimica et Cosmochimica Acta 65 (17), 2995–3003.

Meadows, M.E., 2001. The role of Quaternary environmental change in the evolution of landscapes: case studies from southern Africa. Catena 42, 39-57.

Meadows, M.E. and Hoffman, T.M., 2003. Land degradation and climate change in South Africa. The Geographical Journal 169 (2), 168-177.

Melhorn, W.N. and Flemal, R.C. (ed.), 1980. Theories of Landform Development: A proceedings volume of the Sixth Annual Geomorphology Symposia Series held at Binghamton, New York. September 26-27, 1975. Allen and Unwin (Boston), 306 p.

Michel, Th. and Eugster, O., 1992. Acquisition of terrestrial Kr and Xe by meteoritic orthopyroxene. Abstracts of the Lunar and Planetary Science Conference 23, 905-906.

Mielke, C., 2009. Structural Analysis and Landscape Dynamics of the Cape Fold Belt, South Africa. Unpublished diploma thesis, Freie Universität Berlin, 163 p.

Molnar, P. 2003. Nature, nurture and landscape. Nature 426, 612-614.

Montelli, R., Nolet, G., Dahlen, F.A. and Masters, G., 2006. A catalogue of deep mantle plumes: new results from finite-frequency tomography. Geochemistry, Geophysics, Geosystems 7, Q11007, doi: 10/1029/2006GC001248.

Moore, A. and Blenkinsop, T., 2006. Scarp retreat versus pinned drainage divide in the formation of the Drakensberg escarpment, southern Africa. South African Journal of Geology 109, 599-610.

Moore, A.E., 1999. A reappraisal of epeirogenic flexure axes in southern Africa. South African Journal of Geology 102 (4), 363-376.

Murray, B.A., Lazarus, E., Ashton, A., Baas, A., Coco, G., Coulthard, T., Fonstad, M., Haff, P., McNamara, D., Paola, C., Pelletier, J. and Reinhardt, L., 2009. Geomorphology, complexity, and the emerging science of the Earth's surface. Geomorphology 103, 496–505.

Muzikar, P., 2008. Cosmogenic nuclide concentrations in episodically eroding surfaces: Theoretical results. Geomorphology 97, 407-413.

Muzikar, P., 2009. General models for episodic surface denudation and its measurement by cosmogenic nuclides. Quaternary Geochronology 4, 50-55.

Nelson, A., Reuter, H.I. and Gessler, P., 2009. DEM Production Methods and Sources. In: Hengel, T. and Reuter, H.I. (eds.). Geomorphometry Concepts, Software, Applications. Developments in Soil Science 33, 65-85.

Newton, A.R., Shone, R.W. and Booth, P.W.K., 2006. The Cape Fold Belt. In: Johnson, M.R., Anhaeusser, C.R. and Thomas, R.J. (eds.). The Geology of South Africa. Geological Society of South Africa (Johannesburg)/Council for Geoscience (Pretoria), 691 p.

Niedermann, S., 2000. The ^{21}Ne production rate in quartz revisited. Earth and Planetary Science Letters 183, 361-364.

Niedermann, S., 2002. Cosmic-ray-produced noble gases in terrestrial rocks: Dating tools for surface processes. In: Porcelli, D., Ballentine, C. J. and Wieler, R. (eds.): Noble gases in geochemistry and cosmochemistry. Reviews in Mineralogy and Geochemistry 47, 731-784.

Niedermann, S. and Eugster, O., 1992. Noble gases in lunar anorthositic rocks 60018 and 65315: Acquisition of terrestrial krypton and xenon indicating an irreversible adsorption process. Geochimica et Cosmochimica Acta 56, 493-509.

Niedermann, S., Graf, Th. and Marti, K., 1993. Mass spectrometric identification of cosmic-ray-produced neon in terrestrial rocks with multiple neon components. Earth and Planetary Science Letters 118, 65-73.

Niedermann, S., Graf, Th., Kim, J.S., Kohl, C.P., Marti, K. and Nishiizumi, K., 1994. Cosmic-ray-produced ^{21}Ne in terrestrial quartz: the neon inventory of Sierra Nevada quartz separates. Earth and Planetary Science Letters 125, 341-355.

Niedermann, S., Schaefer, J.M., Wieler, R. and Naumann, R., 2007. The production rate of cosmogenic ^{38}Ar from calcium in terrestrial pyroxene. Earth and Planetary Science Letters 257, 596-608.

Nier, A.O., 1950. A redetermination of the relative abundances of the isotopes of carbon, nitrogen, oxygen, argon and potassium. Physical Review 77, 789-793.

Nyblade, A.A. and Robinson, S.W., 1994. The African Superswell. Geophysical Research Letters 21(9), 765-768.

Ohno, M. and Hamano, Y., 1992. Geomagnetic poles over the past 10,000 years. Geophysical Research Letters 19, 1715-1718.

Oliva, P., Viers, J., Dupré, B., Fortuné, J.-P., Martin, F., Braun, J.-J., Nahon, D. and Robain, H., 1999. The effect of organic matter on chemical weathering: Study of a small tropical watershed : Nsimi-Zoétélé site, Cameroon. Geochimica et Cosmochimica Acta 63 (23/24), 4013-4035.

Oliva, P., Viers, J. and Dupré, B., 2003. Chemical weathering in granitic environments. Chemical Geology 202, 225-256.

Ollier, C., 1984. Weathering (2nd ed.). Longman (London), 270 p.

Ozima, M. and Podosek, F.A., 1983. Noble gas geochemistry. Cambridge University Press (New York), 367 p.

Pálfy, J. and Smith, P.L., 2000. Synchrony between Early Jurassic extinction, oceanic anoxia event, and the Karoo-Ferrar flood basalt volcanism. Geology 28, 747-750.

Paneth, F.A., Reasbeck, P. and Mayne, K.I., 1952. Helium 3 content and age of meteorites. Geochimica et Cosmochimica Acta 2 (5-6), 300-303.

Partridge, T.C., 1993. The evidence for Cainozoic aridification in southern Africa. Quaternary International 17, 105-110.

Partridge, T.C., 1998. Of diamonds, dinosaurs and diastrophism: 150 million years of landscape evolution in southern Africa. South African Journal of Geology 101 (3), 167-184.

Partridge, T.C. and Maud, R.R., 1987. Geomorphic evolution of southern Africa since the Mesozoic. South African Journal of Geology 90, 179-208.

Partridge, T.C., Demenocal, P.B., Lorentz, S.A., Paiker, M.J. and Vogel, J.C., 1997. Orbital forcing of climate over South Africa: A 200,00-year rainfall record from the Pretoria Saltpan. Quaternary Science Reviews 16, 1125-1133.

Partridge, T.C., Botha, G.A. and Haddon, I.G., 2006. Cenozoic deposits of the interior. In: Johnson, M.R., Anhaeusser, C.R. and Thomas, R.J. (eds.). The Geology of South Africa. Geological Society of South Africa (Johannesburg)/Council for Geoscience (Pretoria), 691 p.

Partridge, T.C., Dollar, E.S.J., Moolman, J. and Dollar, L.H., 2010. The geomorphoic provinces of South Africa, Lesotho and Swaziland: A physiographic subdivision for earth and environmental scientists. Transactions of the Royal Society of South Africa 65 (1), 1-47.

Penck, W., 1924. Die morphologische Analyse: ein Kapitel der Physikalischen Geologie. Engelhorns (Stuttgart), 284 p.

Penck, W., 1953. Morphological analysis of landforms: A contribution to physical geology. Translated by Czech, H. and Boswell, K.C. MacMillan (London), 429 p.

Petit, J.R., Jouzel, J., Raynauld, D., Barkov, N.I., Barnola, J.-M., Basile, I., Bender, M., Chappellaz, J., Davis, M., Delaygue, G., Delmotte, M., Kotlyakov, V.M., Legrand, M., Lipenkov, V.Y., Lorius, C., Pépin, L., Ritz, C., Saltzman, E. and Stievenard, M., 1999. Climate and atmospheric history of the past 420,000 years from the Vostok ice core, Antarctica. Nature 399, 429-436.

Petit, J.R., Jouzel, J., Raynauld, D., Barkov, N.I., Barnola, J.-M., Basile, I., Bender, M., Chappellaz, J., Davis, M., Delaygue, G., Delmotte, M., Kotlyakov, V.M., Legrand, M., Lipenkov, V.Y., Lorius, C., Pépin, L., Ritz, C., Saltzman, E. and Stievenard, M., 2001. Vostok Ice Core Data for 420,000 Years, IGBP PAGES/World Data Center for Paleoclimatology Data Contribution Series #2001-076. NOAA/NGDC Paleoclimatology Program, Boulder CO, USA. ftp://ftp.ncdc.noaa.gov/pub/data/paleo/icecore/antarctica/vostok/deutnat.txt.

Phillips, F.M., Stone, W.D. and Fabryka-Martin, J.-T., 2001. An improved approach to calculating low-energy cosmic-ray neutron fluxes near the land/atmosphere interface. Chemical Geology 175, 689-701.

Plummer, C.C. and McGeary, D., 1996. Physical Geology (7th ed.). Wm. C. Brown (Dubuque), 539 p.

Podosek, F.A., Honda, M. and Ozima, M., 1980. Sedimentary noble gases. Geochimica et Cosmochimica Acta 44, 1875–1884.

Poreda, R.J. and Cerling, T.E., 1992. Cosmogenic neon in recent lavas from the western United States. Geophysical Research Letters 19, 1863-1866.

Prell, W.L., Hutson, W.H. and Williams, D.F., 1979. The subtropical convergence and the late Quaternary circulation in the southern Indian Ocean. Marine Micropalaeontology 4, 225-234.

Pretorius, D.A, 1973. The crustal architecture of southern Africa (Alex du Toit memorial lecture 13). The Geological Society of South Africa (Pietermaritburg), 60 p.

Raab, M.J., Brown, R.W., Gallagher, K., Carter, A. and Weber, K., 2002. Late Cretaceous reactivation of major crustal shear zones in northern Namibia: constraints from apatite fission track analysis. Tectonophysics 349, 75-92.

Rabus, B., Eineder, M., Roth, A. and Bamler, R., 2003. The shuttle radar topography mission - a new class of digital elevation models acquired by spaceborne radar. ISPRS Journal of Photogrammetry and Remote Sensing 57, 241-262.

Rama, S.N.I. and Hart, S.R., 1965. Neon isotope fractionation during transient permeation. Science 147 (3659), 737-738.

Rau, A.J., Rogers, J., Lutjeharms, J.R.E., Giraudeau, J., Lee-Thorp, J.A., Chen, M.-T. and Waelbroeck, C., 2002. A 450-kyr record of hydrological conditions on the western Agulhas Bank Slope, south of Africa. Marine Geology 180, 183-201.

Rau, A., Rogers, J. and Chen M.-T., 2006. Late Quaternary palaeoceanographic record in giant piston cores off South Africa, possibly including evidence of neotectonism. Quaternary International 148, 65-77.

Raymo, M.E. and Ruddiman, W.F., 1992. Tectonic forcing of late Cenozoic climate. Nature 359, 117-122.

Raymo, M.E., Ruddiman, W.F. and Froelich, P.N., 1988. Influence of late Cenozoic mountain building on ocean geochemical cycles. Geology 16(7) 649-653.

Renne, P.R., Farley, K.A., Becker, T.A. and Sharp, W.D., 2001. Terrestrial cosmogenic argon. Earth and Planetary Science Letters 188, 435-440.

Riebe, C.S., Kirchner, J.W. and Finkel, R.C., 2003. Long-term rates of chemical weathering and physical erosion from cosmogenic nuclides and geochemical mass balance. Geochimica et Cosmochimica Acta 67 (22), 4411-4427.

Riebe, C.S., Kirchner, J.W. and Finkel, R.C., 2004. Sharp decrease in long-term chemical weathering rates along an altitudinal transect. Earth and Planetary Science Letters 218, 421-434.

Rodriguez, E., Morris, C.S. and Belz, J.E., 2006. A global assessment of the SRTM performance. Photogrammetric Engineering and Remote Sensing 72 (3), 249-260.

Rogers, A.W. and Schwarz, E.H.L., 1902. Report on parts of the divisions of Beaufort West, Prince Albert and Sutherland. Annual Report of the Cape Geological Commission, 97-128.

Römer, W., 2010. Multiple planation surfaces in basement regions: Implications for the reconstruction of periods of denudation and uplift in southern Zimbabwe. Geomorphology 114, 199-212.

Rooseboom, A., 1975. Sedimentproduksiekaart van Suid-Afrika. Techniese verslag 16, Departement van Waterwese, RSA.

Rooseboom, A., 1978. Sedimentafvoer in Suider-Afrikaanse Riviere. Water SA 4 (1), 14-17.

Rosenzweig, M.L. 1968. Net primary productivity of terrestrial communities: Prediction from climatological data. American Naturalist 102, 67-74.

Røyne, A., Jamtveit, B., Mathiesen, J. and Malthe-Sørenssen, A., 2008. Controls on rock weathering rates by reaction-induced hierarchical fracturing. Earth and Planetary Science Letters 275, 364-369.

Rubidge, B.S., Johnson, M.R., Kitching, J.W., Smith, R.M.H., Keyser, A.W. and Groenewald, G.H., 1995. An introduction to the biozonation of the Beaufort Group. In: Rubidge, B.S. (ed.). Biostratigraphy of the Beaufort Group (Karoo Supergroup). Biostratigraphic Series No. 1, South African Committee for Stratigraphy. Council for GeoScience (Pretoria), 46 p.

Rust, D.J. and Summerfield, M.A., 1990. Isopach and borehole data as indicators of rifted margin evolution in southwestern Africa. Marine and Petroleum Geology 7, 277-287.

Rutherford, M.C., 1997. Categorization of biomes. In: Cowling, R.M., Richardson, D.M. and Pierce, S.M. (eds.). Vegetation of Southern Africa. Cambridge University Press (Cambridge), 91-98.

Sabu, D.D., 1971. On mass-yield of xenon and krypton isotopes in the spontaneous fission of uranium. Journal of Inorganic and Nuclear Chemistry 33 (5), 1509-1513.

Sarda, P., Staudacher, T. and Allègre, C.J., 1988. Neon isotopes in submarine basalts. Earth and Planetary Science Letters 91, 73-88.

Sawyer, K.E., 1970. Landscape studies: an introduction to geomorphology. Edward Arnold (London), 149 p.

Schäfer, J.M., Ivy-Ochs, S., Wieler, R., Leya, I., Baur, H., Denton, G.H. and Schlüchter, C., 1999. Cosmogenic noble gas studies in the oldest landscape on earth:

surface exposure ages in the Dry Valleys, Antarctica. Earth and Planetary Science Letters 167, 215-226.

Schaller, M., Blum, J.D. and Ehlers, T.A., 2009. Combining cosmogenic nuclides and major elements from moraine soil profiles to improve weathering rate estimates. Geomorphology 106, 198-205.

Schimmelpfennig I., Benedetti L., Finkel R., Pik R., Blard P.-H., Bourles D., Burnard P., Williams A., 2009. Sources of in-situ ^{36}Cl in basaltic rocks. Implications for calibration of production rates. Quaternary Geochronology, 4 (6), 441-461.

Schulze, R.E., 2007. South African Atlas of Climatology and Agrohydrology. Water Research Commission, Pretoria, RSA.

Shackleton, N.J., 1977. The oxygen isotope stratigraphic record of the late Pleistocene. Philosophical Transactions of the Royal Society of London B 280, 169-182.

Shone, R.W., 2006. Onshore post-Karoo Mesozoic deposits. In: Johnson, M.R., Anhaeusser, C.R. and Thomas, R.J. (ed.). The Geology of South Africa. Geological Society of South Africa (Johannesburg)/Council for Geoscience (Pretoria), 691 p.

Smith, R.M.H., Eriksson, P.G. and Botha, W.J., 1993. A review of the stratigraphy and sedimentary environments of the Karoo-aged basins of southern Africa. Journal of African Earth Sciences 16, 143-169.

South African Committee for Stratigraphy, 1980. Stratigraphy of South Africa, Part 1 (Compiler: L.E. Kent). Lithostratigraphy of the Republic of South Africa, South West Africa/Namibia and the Republics of Bophuthatswana, Transkei and Venda. Handbook of the Geological Survey of South Africa 8, Department of Minerals and Engery Affairs (Pretoria), 690 p.

Sparks, B.W., 1960. Geomorphology. Longman (London), 371 p.

Srinivasan, B., 1976. Barites: Anomalous xenon from spallation and neutron-induced reactions. Earth and Planetary Science Letters 31, 129-141.

Stankiewicz, J., 2004. African River Basins: Their present geometry and recent past as a framework for their evolution. Unpublished Ph.D. thesis, University of Cape Town, 231 p.

Stankiewicz, J., Chevrot, S., van der Hilst, R.D. and de Wit, M.J., 2002. Crustal thickness, discontinuity depth and upper mantle structure beneath southern Africa: constraints from body wave conversions. Physics of Earth and Planetary Interiors 130, 235-251.

Steckler, M.S., 1985. Uplift and extension at the Gulf of Suez: indications of induced mantle convection. Nature 317, 135-139.

Strecker, M.R., Alonso, R.N., Bookhagen, B., Carrapa, B., Hilley, G.E., Sobel, E.R. and Trauth, M.H., 2007. Tectonics and Climate of the Southern Central Andes. Annual Review of Earth and Planetary Sciences 35, 747-787.

Stone, J.O., 2000. Air pressure and cosmogenic isotope production. Journal of Geophysical Research 105 (B10), 23,753-23,759.

Stuut, J.-B.W., Prins, M.A., Schneider, R.R., Weltje, G.J., Jansen, J.H.F. and Postma, G., 2002. A 300-kyr record of aridity and wind strength in southwestern Africa: inferences from grain-size distributions of sediments on Walvis Ridge, SE Alantic. Marine Geology 180, 221-223.

Summerfield, M.A., 1985. Plate tectonics and landscape evolution on the African continent. In: Morisawa, M. and Hack, J.T. (editors), Tectonic Geomorphology. Allen and Unwin (Concordia), p. 27-51.

Summerfield, M.A., 1991. Global geomorphology: an introduction to the study of landforms. Longman (New York), 537 p.

Summerfield, M.A., 2005a. A tale of two scales, or the two Geomorphologies. Transactions of the Institute of British Geographers 30, 402-415.

Summerfield, M.A., 2005b. The changing landscape of geomorphology. Earth Surface Processes and Landforms 30, 779-781.

Summerfield, M.A, Stuart, F.M., Cockburn, H.A.P., Sugden, D.E., Denton, G.H., Dunai, T. and Marchant, D.R., 1999. Long-term rates of denudation in the Dry Valleys, Transantarctic Mountains, southern Victoria Land, Antarctica based on in-situ-produced cosmogenic ^{21}Ne. Geomorphology 27, 113–129.

Sumner, P. and de Villiers, S., 2002. On the Pleistocene palaeo-environmental evidence from the Amatola screes. South African Journal of Science 98, 598-603.

Svensen, H., Planke, S., Chevallier, L., Malthe-Sørenssen, A., Corfu, F. and Jamtveit, B., 2007. Hydrothermal venting of greenhouse gases triggering Early Jurassic global warming. Earth and Planetary Science Letters 256, 554-566.

Talma, A.S. and Vogel, J.C., 1992. Late Quaternary paleotemperatures derived from a speleothem from Cango Caves, Cape Province, South Africa. Quaternary Research 37, 203-213.

Tankard, A.J., Jackson, M.P.A., Eriksson, K.A., Hobday, D.K., Hunter, D.R. and Minter, W.E.L., 1982. Crustal Evolution of Southern Africa – 3.8 Billion Years of Earth History. Springer-Verlag (New York), 523 p.

Temme, A.J.A.M., Baartman, J.E.M., Botha, G.A., Veldkamp, A, Jongmans, A.G. and Wallinga, J., 2008. Climate controls on late Pleistocene landscape evolution of the Okhombe valley, KwaZulu-Natal, South Africa. Geomorphology 99, 280-295.

Thamm, A.G. and Johnson, M.R., 2006. The Cape Supergroup. In: Johnson, M.R., Anhaeusser, C.R. and Thomas, R.J. (ed.). The Geology of South Africa. Geological Society of South Africa (Johannesburg)/Council for Geoscience (Pretoria), 691 p.

Thorn, C.E., 1988. An introduction to theoretical geomorphology. Allen and Unwin (Boston), 247 p.

Thorn, C.E. and Welford, M.R., 1994. The Equilibrium Concept in Geomorphology. Annals of the Association of American Geographers 84 (4), 666-696.

Tinker, J., de Wit, M.J. and Brown, R, 2008a. Mesozoic exhumation of the southern Cape, South Africa, quantified using apatite fission track thermochronology. Tectonophysics 455, 77–93.

Tinker, J., de Wit, M.J. and Brown, R, 2008b. Linking source and sink: Evaluating the balance between onshore erosion and offshore sediment accumulation since Gondwana break-up, South Africa. Tectonophysics 455, 94-103.

Tooth, S., McCarthy, T.S., Brandt, D., Hancox, P.J. and Morris, R., 2002. Geological controls on the formation of alluvial meanders and floodplain wetlands: The example of the Klip River, Eastern Free State, South Africa. Earth Surface Processes and Landforms 27, 797-815.

Tooth, S., Brandt, D., Hancox, P.J. and McCarthy, T.S., 2004. Geological controls on alluvial river behaviour: a comparative study of three rivers on the South African Highveld. Journal of African Earth Sciences 38, 79-97.

Twidale, C.R., 1973. Geomorphology: with special reference to Australia. Thomas Nelson (Hong Kong), 406 p.

Twidale, C.R., 1988. The missing link: Planation surfaces and etch forms in southern Africa. In: Dardis, G.F. and Moon, B.P. (eds). Geomorphological studies in southern Africa. A.A. Balkema (Rotterdam), p. 31-46.

Twidale, C.R., 1996. Derivation and Innovation in Improper Geology, aka Geomorphology. In: Rhoads, B.L. and Thorn, C.E (ed.): The Scientific Nature of Geomorphology: Proceedings of the 27th Binghamton Symposium in

Geomorphology held 27-29 September 1996. John Wiley & Sons Ltd. (Chichester), 481 p.

Twidale, C.R., 2002. The two-stage concept of landform and landscape development involving etching: origin, development and implications of an idea. Earth-Science Reviews 57, 37–74.

Tyson, P.D., 1999. Late-Quaternary and Holocene palaeoclimates of Southern Africa; a synthesis. South African Journal of Geology 102 (4), 335-349.

Udeze, C.U. and Oboh-Ikuenobe, F.E., 2005. Neogene palaeoceanographic and palaeoclimatic events inferred from palynological data: Cape Basin off South Africa, ODP Leg 175. Palaeogeography, Palaeoclimatology, Palaeoecology 219, 199– 223.

Urey, H. C., 1952. The Planets: Their Origin and Development. Yale University Pess (New Haven), 242 p.

U.S. Department of Commerce, National Oceanic and Atmospheric Administration, National Geophysical Data Center, 2001. 2-minute Gridded Global Relief Data (ETOPO2). http://www.ngdc.noaa.gov/mgg/fliers/01mgg04.html.

Valbracht, P.J., Staudigel, H., Honda, M., McDougall, I. and Davies, G.R., 1996. Isotopic tracing of volcanic source regions from Hawaii: decoupling of gaseous from lithophile magma components. Earth and Planetary Science Letters 144, 185-198.

van der Beek, P., Summerfield, M.A., Braun, J., Brown, R.W. and Fleming, A., 2002. Modeling postbreakup landscape development and denudational history across the southeast African (Drakensberg Escarpment) margin. Journal of Geophysical Research 107 (B12), 2351, doi:10.1029/2001JB000744.

Van der Wateren, F.M. and Dunai, T.J., 2001. Late Neogene passive margin denudation history – cosmogenic isotope measurements from the central Namib desert. Global and Planetary Change 30, 271–307.

van Niekerk, H.S., Gutzmer, J., Beukes, N.J., Phillips, D. and Kiviets, G.B., 1999. An $^{40}Ar/^{39}Ar$ age for supergene K-Mn oxyhydroxides in a post-Gondwana soil profile on the Highveld of South Africa. South African Journal of Science 95, 450-454.

van Zijl, J.S.V., 2006. Physical chracteristics of the Karoo sediments and mode of emplacement of the dolerites. South African Journal of Geology 109, 329-334.

Vasconcelos, P.M., 1999. K-Ar and $^{40}Ar/^{39}Ar$ geochronology of weathering processes. Annual Review of Earth and Planetary Sciences 27, 183-229.

Vermeesch, P., 2007. CosmoCalc: An Excel add-in for cosmogenic nuclide calculations. Geochemistry, Geophysics, Geosystems 8, Q08003, doi: 10.1029/2006GC001530.

Veselinovic-Williams, M. and Frost-Killian, S. (compilers), 2002. International Metallogenic Map of Africa, at a scale of 1:5 000 000. Council for Geoscience (South Africa) and Commission de la Carte Géologique du Monde / Commission for the Geological Map of the World (Paris, France).

Viola, G., Andreoli, M., Ben-Avraham, Z., Stengel, I. and Reshef, M., 2005. Offshore mud volcanoes and onland faulting in southwestern Africa: neotectonic implications and constraints on the regional stress field. Earth and Planetary Science Letters 231, 147– 160.

von Blanckenburg, F., 2005. The control mechanisms of erosion and weathering at basin scale from cosmogenic nuclides in river sediment. Earth and Planetary Science Letters 237, 462–479.

Vorster, C.J., 2001. Metallogenic Map of the Republic of South Africa and the Kingdoms of Lesotho and Swaziland, at a scale of 1:1,000,000, available on CD-ROM. Council for Geoscience (Pretoria).

Walker, F. and Poldevaart, A., 1949. Karroo dolerites of the Union of South Africa. Bulletin of the Geological Society of America 60, 591-706.

Walker, J.C.G., Hays, P.B. and Kasting, J.F., 1981. A negative feedback mechanism for the long-term stabilization of Earth's surface temperature. Journal of Geophysical Research 86 (C10), 9776-9782.

Ward, J.D., 1988. Eolian, fluvial and pan (playa) facies of the Tertiary Tsondab sandstone formation in the central Namib Desert, Namibia. Sedimentary Geology 55, 143-162.

Ward, J.D., Seely, M.K. and Lancaster, N., 1983. On the antiquity of the Namib. South African Journal of Science 79, 175-183.

Watchman, A.L. and Twidale, C.R. 2002. Relative and 'absolute' dating of land surfaces. Earth-Science Reviews 58, 1-49.

Watkeys, M.K., 2006. Gondwana break-up: a South African perspective. In: Johnson, M.R., Anhaeusser, C.R.and Thomas, R.J. (eds.). The Geology of South Africa. Geological Society of South Africa (Johannesburg)/Council for Geoscience (Pretoria), 691 p.

Wayland, E.J., 1934. Peneplains and some erosional landforms. Geological Survey of Uganda Annual Report. Bulletin 1, 77-79.

Wegener, A., 1920. Die Entstehung der Kontinente und Ozeane. Die Wissenschaft 66 (2), F. Vieweg & Sohn (Braunschweig), 135 p.

Weinert, H.H., 1961. Climate and weathered Karoo dolerites. Nature 191 (4786), 325-329.

Weinert, H.H., 1965. Climatic factors affecting the weathering of igneous rocks. Agricultural Meteorology 2, 27-42.

Wellington, J.H, 1955. Southern Africa: A Geographical Study, Volume I, Physical Geography. Cambridge University Press, New York, 528 p.

White, A.F. and Blum, A.E., 1995. Effects of climate on chemical weathering in watersheds. Geochimica et Cosmochimica Acta 59 (9), 1729-1747.

Wilkinson, B.H., 2005. Humans as geologic agents: A deep-time perspective. Geology 33(3), 161-164.

Wilkinson, B.H. and McElroy, B.J., 2007. The impact of humans on continental erosion and sedimentation. Geological Society of America Bulletin 119 (1/2), 140-156.

Williams, J.R. 1975. Sediment yield prediction with universal equation using runoff energy factor. In: Present and Prospective Technology for Predicting Sediment Yields and Sources, USDA-ARS, Washington DC, USA, 40, 244 - 252.

Wolmarans, L.G. (compiler), 1988. 2730 Vryheid. 1:250,000 geological map series, Council for Geoscience (Pretoria).

Woodford, A.C. and Chevallier, L., 2002. Regional charcterisation and mapping of Karoo fractured aquifer systems – an integrated approach using a geographical information system and digital processing. Water Research Comission 653/1/02, 192 p.

Zachos, J., Pagani, M., Sloan, L., Thomas, E. and Billup, K., 2001. Trends, rhythms, and aberrations in global climate 65 Ma to Present. Science 292, 686-693.

Zalasiewicz, J., Williams, M., Smith, A., Barry, T.L., Coe, A.L., Bown, P.R., Brenchley, P., Cantrill, D., Gale, A., Gibbard, P., Gregory, F.J., Hounslow, M.W., Kerr, A.C., Pearson, P., Knox, R., Powell, J., Waters, C., Marshall, J., Oates, M., Rawson, P. and Stone, P., 2008. Are we now living in the Anthropocene? GSA Today 18 (2), 4-8.